

Arumugam Manthiram
Yongzhu Fu *Editors*

Advances in Rechargeable Lithium–Sulfur Batteries

Modern Aspects of Electrochemistry

Volume 59

Series Editors

Constantinos G. Vayenas, Department Chemical Engineering, University of Patras,
Patras, Greece

Ralph E. White, Department Chemical Engineering, University of South Carolina,
Columbia, SC, USA

This well-respected series commenced publication in the early 1950s. Over the years it has earned an excellent reputation by offering high quality reviews of current research into all areas of electrochemistry and electrochemical engineering and their applications. The international magazine *Chemistry & Industry* notes that this series “deserves a place in electrochemistry libraries and should prove useful to electrochemists and related workers.” Starting with Number 43 in the series, two features have been introduced:

- Each volume is thematic and focuses on a new development in the field or reviews a well-established area that is regaining interest.
- Each volume is guest-edited. As in the past, all chapters are topical reviews.

Subjects covered in recent volumes include:

1. Modeling and Numerical Simulations
2. Progress in Corrosion Science and Engineering
3. Electrodeposition: Theory and Practice
4. Electrocatalysis: Theory and Experiments
5. Interfacial Phenomena in Fuel Cell Electrocatalysis
6. Diagnostics and Modeling of Polymer Electrolyte Fuel Cells
7. Applications of Electrochemistry and Nanotechnology in Biology and Medicine


More information about this series at <https://link.springer.com/bookseries/6251>


Arumugam Manthiram · Yongzhu Fu
Editors

Advances in Rechargeable Lithium–Sulfur Batteries

 Springer

Editors

Arumugam Manthiram 
Materials Science and Engineering
University of Texas at Austin
Austin, TX, USA

Yongzhu Fu 
College of Chemistry
Zhengzhou University
Zhengzhou, China

ISSN 0076-9924

ISSN 2197-7941 (electronic)

Modern Aspects of Electrochemistry

ISBN 978-3-030-90898-0

ISBN 978-3-030-90899-7 (eBook)

<https://doi.org/10.1007/978-3-030-90899-7>

© The Editor(s) (if applicable) and The Author(s), under exclusive license to Springer Nature Switzerland AG 2022

This work is subject to copyright. All rights are solely and exclusively licensed by the Publisher, whether the whole or part of the material is concerned, specifically the rights of translation, reprinting, reuse of illustrations, recitation, broadcasting, reproduction on microfilms or in any other physical way, and transmission or information storage and retrieval, electronic adaptation, computer software, or by similar or dissimilar methodology now known or hereafter developed.

The use of general descriptive names, registered names, trademarks, service marks, etc. in this publication does not imply, even in the absence of a specific statement, that such names are exempt from the relevant protective laws and regulations and therefore free for general use.

The publisher, the authors and the editors are safe to assume that the advice and information in this book are believed to be true and accurate at the date of publication. Neither the publisher nor the authors or the editors give a warranty, expressed or implied, with respect to the material contained herein or for any errors or omissions that may have been made. The publisher remains neutral with regard to jurisdictional claims in published maps and institutional affiliations.

This Springer imprint is published by the registered company Springer Nature Switzerland AG
The registered company address is: Gewerbestrasse 11, 6330 Cham, Switzerland

Preface

With the population and economic growth, the demand for energy is steadily increasing. Fossil fuels have been the primary energy source for human kind over a long time, resulting in large amounts of CO₂ emission and environmental pollution. In order to alleviate the environmental challenges and reduce our dependence on fossil fuels, we need to explore and develop alternative energy technologies based on renewable resources, such as solar and wind. However, the renewable energies are constrained by their intermittency and locations. Rechargeable batteries are one of the most feasible options for storing electricity garnered from renewable sources, which can enable a widespread utilization of renewable energies. Lead-acid, nickel-cadmium, nickel-metal hydride, and lithium-ion (Li-ion) are the most representative rechargeable batteries. Among them, Li-ion batteries have dominated the high-energy-demand markets, such as portable electronics and electric vehicles because of their intrinsic high operating voltages leading to high energy densities. The current Li-ion battery technology is based on lithium-insertion compounds, such as graphite anode with a specific capacity of 374 mA h g⁻¹ and transition-metal oxide cathodes with specific capacities of <200 mA h g⁻¹. In order to overcome the charge storage limitation of these insertion-compound electrodes, materials that can undergo conversion reactions while accommodating more ions and electrons are becoming a promising choice.

Rechargeable lithium–sulfur (Li–S) batteries consist of a lithium-metal anode and a sulfur cathode, and it has been investigated vigorously over the past decades. Lithium is the lightest metal possessing the highest specific capacity of 3,862 mA h g⁻¹. Lithium-metal stripping and plating are involved in the discharge and charge processes of a Li–S battery, which usually results in side reactions, low efficiency, and dendrite growth. Sulfur is one of the most abundant elements in the earth's crust. Its theoretical capacity is as high as 1,675 mA h g⁻¹. Each sulfur atom can accept two electrons and two lithium ions. The high capacity is attributed to the conversion reaction from sulfur to lithium sulfide (Li₂S). However, the process is accompanied by about 80% volume change. In addition, sulfur and Li₂S are both insulators, which require large amounts of conductive additives, e.g., carbon. Furthermore, the intermediate lithium polysulfides formed during cycling could dissolve in the liquid organic

electrolytes used in Li–S batteries. All of the above issues bring great challenges to the development of Li–S batteries for practical applications.

Over the past two decades, significant progress has been made around the world to advance the Li–S battery technology. The purpose of this book is to bring together and portray some of the recent advances. In this book, we first introduce the principles, history, and technical challenges of Li–S batteries, and then present sulfur-carbon composite and lithium-sulfide cathodes. The importance of physical and chemical adsorption of lithium polysulfides is also discussed. The recently proposed catalysis of polysulfides is presented. Lithium metal and other anodes are summarized, which are the key to enable the Li–S battery technology to advance to the next stage. In recent years, organosulfides and sulfur-containing polymer materials have attracted significant attention, which are a class of promising cathode materials. They have shown unique properties and electrochemical behaviors. Furthermore, advanced characterization techniques and a mechanistic understanding of Li–S batteries are discussed. Finally, computation and simulation of Li–S batteries is covered.

In conclusion, in this book, we describe the recent advances in Li–S batteries and provide a perspective for the future development of the Li–S battery field. The contributions are made by leading internationally renowned scientists and are based on substantial recent advances in Li–S batteries. To achieve the goal, the book provides chapters on basic principles, electrode materials, characterization, and understanding. At the same time, the book can also overcome some key education gaps and help to train a new generation of researchers with potential for innovation. We hope the book serves as a forward-looking episode and perspective for stimulating further intensive research and development to make Li–S batteries a sustainable energy-storage technology in the near future.

With this perspective, we are grateful to the authors for their hard work, passion, dedication, and enthusiasm to drive the assembly of the chapters in this book on Li–S batteries. We salute the sheer power and momentum of trans-regional collaboration. You made the difference! Thank you.

Austin, USA
Zhengzhou, China

Arumugam Manthiram
Yongzhu Fu

Contents

1 Principles and Challenges of Lithium–Sulfur Batteries	1
Abhay Gupta and Arumugam Manthiram	
2 Sulfur–Carbon Composite Cathodes	19
Ruopian Fang, Ke Chen, Zhenhua Sun, Da-Wei Wang, and Feng Li	
3 Li₂S Cathodes in Lithium–Sulfur Batteries	83
Hualin Ye, Yanguang Li, and Jun Lu	
4 Physical and Chemical Adsorption of Polysulfides	111
Baohua Li and Yuanming Liu	
5 Catalytic Conversion of Polysulfides in Li–S Batteries	165
Wenjia Qu, Chuannan Geng, Jingyi Xia, Wuxing Hua, Guowei Ling, Chen Zhang, and Quan-Hong Yang	
6 Lithium Metal and Other Anodes	225
Li-Peng Hou, Xue-Qiang Zhang, and Qiang Zhang	
7 Organosulfide Cathodes	247
Pengfei Sang, Dan-Yang Wang, Wei Guo, and Yongzhu Fu	
8 Sulfur-Containing Polymer Cathode Materials for Li–S Batteries	295
Yizhou Wang, Dong Zhou, and Guoxiu Wang	
9 Advanced Characterization Techniques and Mechanistic Understanding	331
Cheng Zhou, Binbin Shuai, Xu Xu, and Liqiang Mai	
10 Computation and Simulation	355
Ying Ma	
Index	397

Editors and Contributors

About the Authors

Arumugam Manthiram is currently the Cockrell Family Regents Chair in Engineering and Director of the Texas Materials Institute at the University of Texas at Austin (UT Austin). He received his B.S. and M.S. degrees from Madurai University, India, and his Ph.D. degree from the Indian Institute of Technology, Madras, all in chemistry. He then worked as a Postdoctoral Researcher with the 2019 Chemistry Nobel Laureate John Goodenough before becoming a faculty at UT Austin. His research focuses on batteries and fuel cells. He directs a large, productive research group in electrochemical energy technologies with about 35 graduate students and postdoctoral researchers. He has provided research training to 300 people, including the graduation of 66 Ph.D. students. He has authored 880 journal publications and 16 awarded patents, edited 9 books, and given 500 presentations.

Yongzhu Fu is a Professor in the College of Chemistry at Zhengzhou University in China. He received his B.E. degree from Tsinghua University in 2000; M.S. degree from Dalian Institute of Chemical Physics, Chinese Academy of Sciences in 2003; and Ph.D. degree in Materials Science and Engineering from the University of Texas at Austin, United States, in 2007. He was an Assistant Professor at Indiana University-Purdue University Indianapolis in the United States before joining Zhengzhou University in 2017. His research is focused on electrochemical energy materials for rechargeable batteries and fuel cells. He has authored more than 120 publications.

Contributors

Ke Chen Shenyang National Laboratory for Materials Science, Institute of Metal Research, Chinese Academy of Sciences, Shenyang, China;

School of Physical Science and Technology, Shanghai Tech University, Shanghai, China

Ruopian Fang School of Chemical Engineering, University of New South Wales, Sydney, Australia

Yongzhu Fu College of Chemistry, Zhengzhou University, Zhengzhou, P. R. China

Chuannan Geng State Key Laboratory of Chemical Engineering, Nanoyang Group, School of Chemical Engineering and Technology, Tianjin University and Collaborative Innovation Center of Chemical Science and Engineering, Tianjin, China

Wei Guo College of Chemistry, Zhengzhou University, Zhengzhou, P. R. China

Abhay Gupta Materials Science and Engineering Program & Texas Materials Institute, The University of Texas at Austin, Austin, TX, USA

Li-Peng Hou Beijing Key Laboratory of Green Chemical Reaction Engineering and Technology, Department of Chemical Engineering, Tsinghua University, Beijing, China

Wuxing Hua State Key Laboratory of Chemical Engineering, Nanoyang Group, School of Chemical Engineering and Technology, Tianjin University and Collaborative Innovation Center of Chemical Science and Engineering, Tianjin, China

Baohua Li Shenzhen Key Laboratory on Power Battery Safety Research and Shenzhen Geim Graphene Center, Tsinghua Shenzhen International Graduate School, Shenzhen, P.R. China

Feng Li Shenyang National Laboratory for Materials Science, Institute of Metal Research, Chinese Academy of Sciences, Shenyang, China;
School of Materials Science and Engineering, University of Science and Technology of China, Shenyang, China

Yanguang Li Jiangsu Key Laboratory for Carbon-Based Functional Materials and Devices, Institute of Functional Nano & Soft Materials (FUNSOM), Soochow University, Suzhou, China

Guowei Ling School of Marine Science and Technology, Tianjin University, Tianjin, China

Yuanming Liu Shenzhen Key Laboratory on Power Battery Safety Research and Shenzhen Geim Graphene Center, Tsinghua Shenzhen International Graduate School, Shenzhen, P.R. China

Jun Lu Chemical Sciences and Engineering Division, Argonne National Laboratory, Lemont, IL, USA

Ying Ma Department of Materials Science and Biomedical Engineering, University of Wisconsin-Eau Claire, Eau Claire, USA

Liqiang Mai State Key Laboratory of Advanced Technology for Materials Synthesis and Processing, Wuhan University of Technology, Wuhan, China

Arumugam Manthiram Materials Science and Engineering Program & Texas Materials Institute, The University of Texas at Austin, Austin, TX, USA

Wenjia Qu State Key Laboratory of Chemical Engineering, Nanoyang Group, School of Chemical Engineering and Technology, Tianjin University and Collaborative Innovation Center of Chemical Science and Engineering, Tianjin, China

Pengfei Sang College of Chemistry, Zhengzhou University, Zhengzhou, P. R. China

Binbin Shuai State Key Laboratory of Advanced Technology for Materials Synthesis and Processing, Wuhan University of Technology, Wuhan, China

Zhenhua Sun Shenyang National Laboratory for Materials Science, Institute of Metal Research, Chinese Academy of Sciences, Shenyang, China;
School of Materials Science and Engineering, University of Science and Technology of China, Shenyang, China

Da-Wei Wang School of Chemical Engineering, University of New South Wales, Sydney, Australia

Dan-Yang Wang College of Chemistry, Zhengzhou University, Zhengzhou, P. R. China

Guoxiu Wang School of Mathematical and Physical Sciences, Research Centre for Clean Energy Technology, University of Technology Sydney, Ultimo, Australia

Yizhou Wang School of Mathematical and Physical Sciences, Research Centre for Clean Energy Technology, University of Technology Sydney, Ultimo, Australia

Jingyi Xia State Key Laboratory of Chemical Engineering, Nanoyang Group, School of Chemical Engineering and Technology, Tianjin University and Collaborative Innovation Center of Chemical Science and Engineering, Tianjin, China

Xu Xu State Key Laboratory of Advanced Technology for Materials Synthesis and Processing, Wuhan University of Technology, Wuhan, China

Quan-Hong Yang State Key Laboratory of Chemical Engineering, Nanoyang Group, School of Chemical Engineering and Technology, Tianjin University and Collaborative Innovation Center of Chemical Science and Engineering, Tianjin, China;
Joint School of National University of Singapore and Tianjin University, International Campus of Tianjin University, Fuzhou, China

Hualin Ye Jiangsu Key Laboratory for Carbon-Based Functional Materials and Devices, Institute of Functional Nano & Soft Materials (FUNSOM), Soochow University, Suzhou, China;
Department of Chemical and Biomolecular Engineering, National University of Singapore, Singapore, Singapore

Chen Zhang School of Marine Science and Technology, Tianjin University, Tianjin, China

Qiang Zhang Beijing Key Laboratory of Green Chemical Reaction Engineering and Technology, Department of Chemical Engineering, Tsinghua University, Beijing, China

Xue-Qiang Zhang Beijing Key Laboratory of Green Chemical Reaction Engineering and Technology, Department of Chemical Engineering, Tsinghua University, Beijing, China

Cheng Zhou State Key Laboratory of Advanced Technology for Materials Synthesis and Processing, Wuhan University of Technology, Wuhan, China

Dong Zhou School of Mathematical and Physical Sciences, Research Centre for Clean Energy Technology, University of Technology Sydney, Ultimo, Australia

Chapter 1

Principles and Challenges of Lithium–Sulfur Batteries



Abhay Gupta and Arumugam Manthiram

Abstract The invention and adoption of lithium-ion batteries has catalyzed massive technological and societal progress over the past few decades. While lithium-ion batteries will continue to show considerable promise for a large range of applications, there are several critical use-cases that require order-of-magnitude increases in the battery's ability to store energy per unit mass. This will necessitate the development of novel battery chemistries with increased specific energy, such as the lithium–sulfur (Li–S) batteries. Using sulfur active material in the cathode presents several desirable properties, such as a low-cost, widespread geological abundance, and a high specific capacity. However, the Li–S conversion chemistry operates in a highly distinct manner from traditional insertion electrodes; discharge of elemental sulfur produces lithium polysulfide intermediates that dissolve into the liquid electrolyte and mediate the charge-transfer process in solution. This phenomenon is accompanied by the unique challenges presented from the reactive and unstable lithium-metal anode. In conjunction, this introduces tremendous complexity and opportunity in the analysis and design of Li–S batteries. In this chapter, the operating principles and challenges of Li–S batteries are first introduced, and then the historical progress and future directions are discussed on a component-by-component basis.

Keywords Lithium–sulfur batteries · Operating principles · Lithium-metal anode · Electrolyte · Critical metrics

1.1 Introduction

The discovery and introduction of lithium-ion batteries has enabled perhaps the single greatest technological leap in human history observed to date, comparable to the advent of the combustion engine during the Industrial Revolution. The ability to manipulate and store electrical energy in lightweight, energy-dense form factors has transformed almost every facet of the human experience. We can now instantaneously

A. Gupta · A. Manthiram (✉)

Materials Science and Engineering Program & Texas Materials Institute, The University of Texas at Austin, Austin, TX 78712, USA

e-mail: manth@austin.utexas.edu

access information on handheld smart phone computers, communicate with others on the opposite side of the planet, be transported in vehicles fueled solely by the power of renewable energy, and reliably overcome the intermittency inherent to photovoltaic solar and wind power. Each of these drastic shifts in human technological capability is grounded in the invention of the lithium-ion battery.

Lithium-ion batteries operate according to a “rocking chair” principle, where the working ion (Li^+) travels within a liquid electrolyte to neutralize electrochemical potential gradients induced between the anode and cathode [1]. Meanwhile, an electron, incapable of traversing the electronically insulating organic electrolyte, navigates an external circuit between the anode and cathode to maintain charge neutrality, performing electrical work in the process [2]. The anode and cathode are capable of hosting Li^+ cations within assigned sites in their constituent crystalline materials, in a process known as intercalation. Li-ion cells are typically assembled in the fully discharged state with a layered oxide cathode (Li_xMO_2 , $0 < x < 1$, where M is typically a combination of $\text{Ni}^{3+/4+}$, $\text{Mn}^{3+/4+}$, and $\text{Co}^{3+/4+}$) and a graphite anode host [3]. During charge, Li^+ ions proceed to deintercalate from the octahedral sites of the O3 layered oxide structure, migrate through the liquid organic carbonate electrolyte, and insert into the interstitial space between layered graphene sheets of the graphite electrode [4, 5]. Then, on discharge, the Li^+ cations migrate out of the graphite structure and insert into the lower energy layered oxide octahedral sites, a process that liberates approximately 4 V for useful work. This is illustrated in Fig. 1.1.

State-of-the-art lithium-ion batteries can yield a cell-level specific energy on the order of 250 Wh kg^{-1} , which has enabled widespread use in applications ranging from portable electronics to electrified mobility [3, 6]. As human technological prowess continues to grow over the coming decades, the rise of new applications will inevitably necessitate new battery chemistries with the ability to store even more energy per unit mass. This is particularly true for use-cases within the aerospace sector, where the efficient utilization of available payload mass is a key consideration [7–9]. A variety of other reasons exist for expanding the scope of existing energy storage technologies. The cost, geologic resource availability, and life cycle emissions of the nickel and cobalt precursors constituting layered oxide cathodes leaves much room for improvement [10, 11]. In addition, extreme conditions such as subzero low-temperature environments can present tremendous kinetic hurdles during operation of lithium-ion batteries, leading to stunted capacities, exacerbated degradation, and safety issues stemming from lithium-metal (Li-metal) plating upon the graphite anode [12, 13]. Due in part to all of these distinct factors, nascent battery chemistries, such as the lithium–sulfur (Li–S) battery have received tremendous research attention over the past few decades.

The Li–S battery can, in theory, present a path toward overcoming almost every single one of these challenges. In contrast to lithium-ion batteries, the Li–S redox couple consists of a Li-metal foil anode and a cathode made up of elemental sulfur (which predominantly exists natively as a S_8 octasulfur allotrope) [14, 15]. A Li–S cell is typically assembled in the charged state, and upon discharge, Li^+ cations are stripped from the surface of Li-metal, where they traverse an organic ether-based electrolyte and react with the elemental sulfur housed in the cathode. Rather

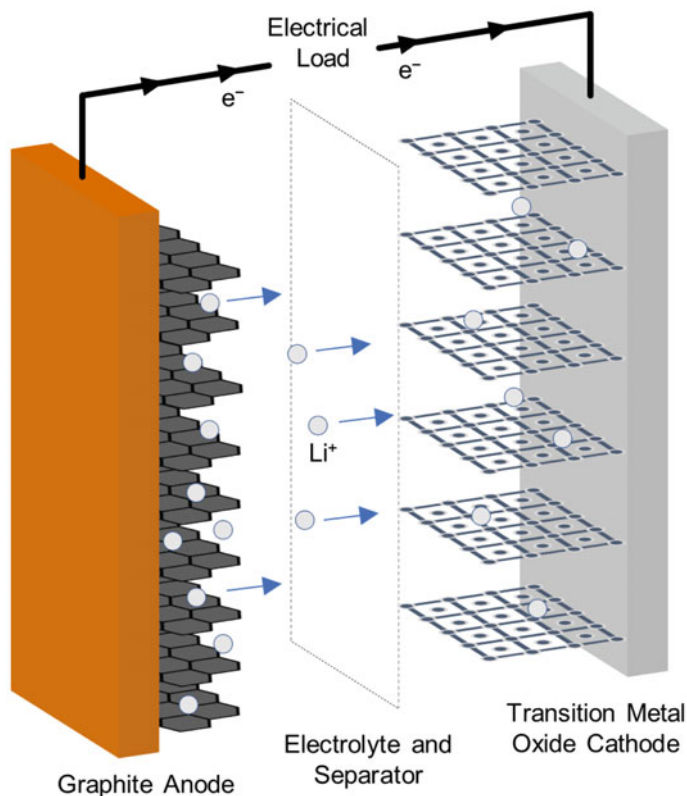


Fig. 1.1 A schematic illustration of the inner components of a lithium-ion cell undergoing discharge

than operating through an insertion mechanism, the reaction between sulfur and Li^+ proceeds through a conversion-type reaction. The internal operating environment of a Li–S cell is shown in Fig. 1.2.

Li-metal and elemental sulfur possess theoretical charge capacities of, respectively, 3,861 and 1,672 mA h g^{-1} [14]. At an average discharge potential of 2.1 V, the Li–S battery presents a theoretical electrode-level specific energy of $\sim 2,500 \text{ W h kg}^{-1}$, an order-of-magnitude higher than what is achieved in lithium-ion batteries. In practice, Li–S batteries are expected to achieve a cell-level specific energy on the order of 500 W h kg^{-1} , taking into account the weight of inactive components like the electrolyte, separator, and conductive filler materials [16]. The high specific energy of the Li–S battery is uniquely suited for enabling tremendous growth in weight-sensitive applications like unmanned aerial vehicles and CubeSats, while the use of a low-freezing point ether-based electrolyte could be compelling for applications requiring exposure to subzero low-temperature conditions [12]. Furthermore, sulfur is a relatively abundant element within the Earth’s crust. Being a direct waste byproduct of the petrochemical industry, elemental sulfur presents a low capital material primed for being massively scaled up for cathode production.

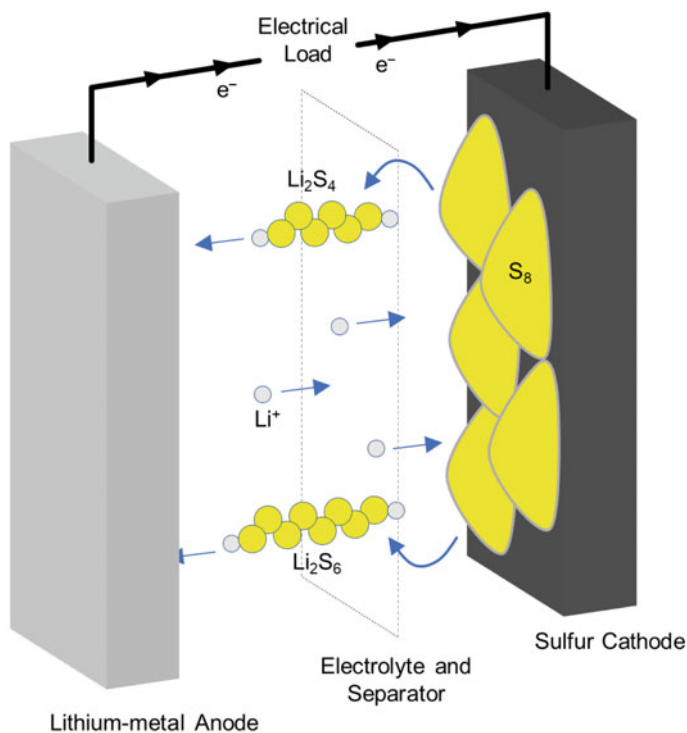


Fig. 1.2 An illustration of the inner components and operating mechanisms of a Li-S cell undergoing discharge

The invention of Li-S battery dates back to initial patents from the 1960s describing the use of lithium and sulfur electrodes in a nonaqueous electrolyte [17, 18]. Since then, there has been a multitude of scientific and engineering effort dedicated toward characterizing, understanding, and further improving the operation of the battery, with a particular surge of attention and publications seen during the past decade. However, it is notable that even after 60 years of development, the Li-S battery has not yet been implemented for widescale use. This is in stark contrast to the $LiCoO_2$ cathode material introduced by Goodenough in 1981 [19], which thereafter saw commercial implementation within the subsequent 10–15 years [20]. This speaks to the inherent chemical dynamics introduced in the conversion reaction between Li^+ and sulfur, which presents a variety of challenges and complex behaviors during operation. While the Li-S battery introduces considerable opportunity as a next chapter in the story of human technological progress, it also presents key hurdles that must be overcome.

1.2 Operating Principles and Challenges of the Li–S Redox Couple

During the discharge phase of a Li–S cell, sulfur is not directly converted to the lower energy Li_2S final discharge product, as would generally be the case in an insertion-type chemistry. Both S_8 and Li_2S are deeply ionically and electronically insulating, with resistivities on the order of $1 \times 10^{14} \Omega \text{ cm}$ [21]. This insulating nature presents a sizeable barrier to the bulk solid-state transport of electrons or Li^+ cations, which is necessary for the solid-state reduction and oxidation of sulfur-containing active material [22, 23]. However, the Li–S redox couple offers the ability to overcome these kinetically limiting surface-based electrochemical pathways through the generation of soluble lithium polysulfide (Li_2S_x , $2 < x \leq 8$) intermediates upon charge and discharge. As shown in Fig. 1.3a, rather than directly being converted from one to another, S_8 and Li_2S can, respectively, be reduced and oxidized to lithium-capped catenated chains of sulfur atoms; a range of higher order polysulfides (Li_2S_x , $4 \leq x \leq 8$) are immediately formed upon reduction of S_8 , corresponding to an upper voltage plateau with a potential averaging 2.3 V versus Li/Li^+ . A variety of polysulfide chain lengths are represented in solution at any single point of discharge, and through a combination of disproportionation and dissociation reactions, the order of a single lithium polysulfide unit can chemically and electrochemically modulate during operation. At the conclusion of the first stage of discharge, Li_2S_4 is the dominant average stoichiometry represented within solution [24]. Further reduction converts the liquid phase polysulfides to insoluble precipitates with a stoichiometry of Li_2S , the final discharge product. As shown in Fig. 1.3b, this phase change is represented through a second lower voltage plateau taking place at approximately 2.1 V versus Li/Li^+ [14].

The final Li_2S products at the conclusion of discharge precipitate and nucleate out of solution onto the cathode electrode scaffold, generally made up of a conductive sp^2 hybridized carbon-containing framework [25]. One problem often encountered during the precipitation of Li_2S is the nonideal buildup of the insulating product

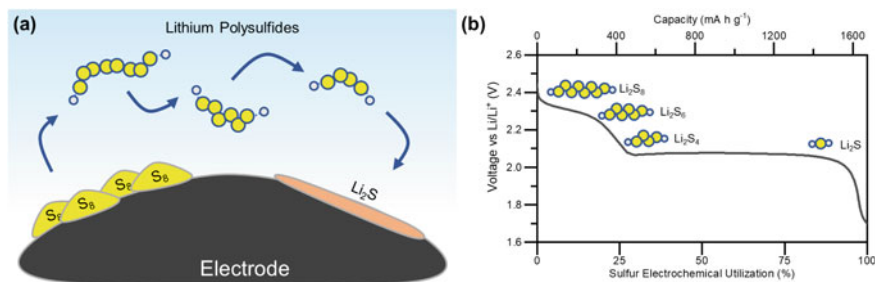


Fig. 1.3 **a** Illustration of the solution-mediated conversion process from S_8 to Li_2S that takes place during discharge of a Li–S cell. **b** The characteristic two-plateau voltage profile in Li–S cell discharge, with the upper plateau corresponding to the formation of soluble lithium polysulfides and the lower plateau corresponding to the nucleation and growth of insoluble Li_2S

on the cathode substrate, prematurely passivating the cathode from further electron transport before all the active material within the cell can be fully utilized [21, 26, 27]. For this reason, it is often the case that a sulfur cathode will be electrochemically utilized to only ~60% of its theoretical capacity before reaching the lower cutoff voltage. Regardless, through the solution-mediated behavior exhibited by lithium polysulfides, the Li–S redox chemistry overcomes most of its intrinsic restrictions towards bulk electron and ion-transport during the majority of discharge, still generally achieving a moderately high capacity on the order of $1,000 \text{ mA h g}^{-1}$. The active material dissolution intrinsic to the sulfur cathode material is thus the predominant basis by which active material is electrochemically utilized during operation [22, 23, 28, 29].

Within the Li–S system, the active material and liquid organic electrolyte are, therefore, indistinguishable and inextricably linked, a considerable distinction from the mechanisms underlying lithium-ion electrode materials. This is often represented and accounted for within the Li–S literature through the reporting of a key metric, the electrolyte-to-sulfur (E/S) ratio in $\text{mL}_{\text{electrolyte}} \text{ g}^{-1}_{\text{sulfur}}$ [16, 30]. Given the nature of active material dissolution, the electrochemical behavior can dynamically vary as a function of the available electrolyte present to solvate polysulfides, highlighting the importance of reporting E/S ratio alongside electrochemical data. This concentration dependence is particularly notable at low E/S conditions, where the high polysulfide concentrations achieved can drastically boost the viscosity of the electrolyte and impede solution-mediated charge transfer [30]. This leads to a subsequent loss in capacity, as shown in Fig. 1.4a. Minimizing the weight of inactive components is a key priority in the manufacturing of practically relevant Li–S cells, but for this reason, achieving favorable performance in Li–S batteries is often challenging under desired lean-electrolyte conditions.

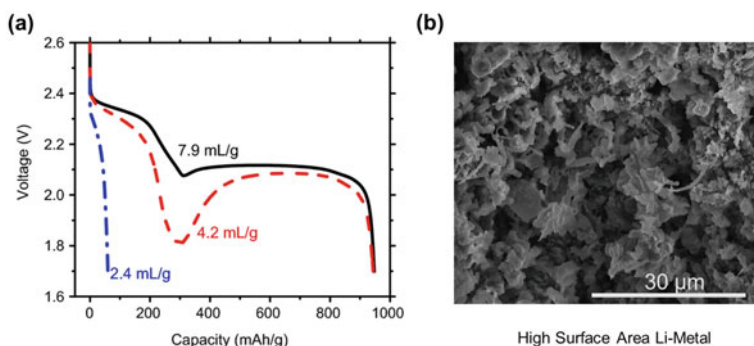


Fig. 1.4 **a** The variation in the discharge behavior with E/S ratio; at low E/S ratios, the solution-mediated behavior is kinetically inhibited, leading to poor performance. Reproduced with permission [30]. Copyright 2017, IOP Publishing. **b** Li-metal tends to evolve in a high surface area manner over the course of repeated electrochemical stripping and redeposition. Reproduced with permission [34]. Copyright 2020, Wiley–VCH

Another consequence of the use of non-lithiated elemental sulfur is the requirement to use a lithium-containing source like Li-metal as the counter electrode [31]. While this complements the high specific energy capability of sulfur, it also presents its own array of challenges. During discharge and charge, Li^+ cations are cyclically stripped and plated onto the surface of the foil electrode; the pits and valleys created on the Li-metal surface throughout this process serve as low energy nucleation sites for plating to occur on subsequent cycles [32, 33]. Over the course of cycling, this leads to high surface area mossy and dendritic growths, shown in Fig. 1.4b [34, 35]. This can ultimately provoke unsafe thermal events and rapid cell failure if the Li-metal pierces the delicate polymeric separator and internally shorts with the cathode. This is only exacerbated by the reactivity of Li-metal, whose electrochemical potential lies at a higher energy than the lowest unoccupied molecular orbital (LUMO) of the liquid electrolyte [36]. Thus, in contact with Li-metal, the electrolyte solvent and salt molecules are irreversibly reduced, forming a hybrid organic–inorganic mosaic of decomposition products, known as the solid–electrolyte interphase (SEI), on the surface of Li-metal [32].

Given the high surface area growths intrinsic to the electrochemical utilization of Li-metal, a considerable mass of electrolyte can be continually consumed through the SEI formation process. This presents a key obstacle for a battery system that is already challenged at lean-electrolyte conditions; subsequent decomposition with high-surface area lithium metal can completely consume the limited electrolyte available within the system initially [16]. The SEI decomposition products can passivate the Li-metal from further reduction of the surrounding electrolyte, but this is in no way a panacea. The thick SEI can also surround protruding growths of Li-metal, cutting off the exchange of electrons from the bulk structure and rendering the isolated Li-metal electrochemically inaccessible [37]. In combination, these key issues can lead to both shortened lifetimes and safety concerns during the manufacturing and operation of Li-metal containing cells.

While the sulfur cathode and Li-metal anode each possess their own intrinsic challenges, having both present simultaneously in one system introduces yet another emergent challenge: the “shuttling” of lithium polysulfide intermediates [14]. As mentioned, the electrolyte paired with a sulfur cathode can be better envisioned as an in situ formed “catholyte,” with polysulfide active material constituting one key component of the electrolyte along with the organic solvent and lithium salt compounds [23, 38–40]. As lithium polysulfides diffuse through the bulk electrolyte during operation, they will inevitably encounter the Li-metal anode surface. In contact with Li-metal, the decomposition process that normally takes place also extends to the dissolved polysulfides, leading to the parasitic loss of cathode active material and generation of a SEI rich in trapped sulfur active material [41, 42]. Thus, the polysulfide dissolution intrinsic to the sulfur cathode in many respects acts as a double-edged sword, both promoting the electrochemical utilization of cathode active material, but aiding in the deleterious and parasitic losses of the shuttling process [28].

While the Li–S battery chemistry provides tremendous opportunity as an advanced energy storage medium, its intrinsic operating principles facilitate key challenges during use. The electrochemical utilization of sulfur is uniquely predicated on the

ability of the electrolyte to solvate and incorporate active material. While this can lead to moderate capacity attainment, it also introduces the complex dependence on having ample electrolyte available in the cell, which runs counter to the practical desire of minimizing the weight of inactive cell components. Meanwhile, the use of Li-metal presents an array of challenges, including high surface area mossy growths, unceasing consumption of liquid electrolyte, and the loss of isolated, inaccessible pockets of SEI-laden Li-metal protrusions. Having both of these electrode materials present in a cell simultaneously gives rise to the polysulfide shuttling phenomenon, where polysulfide active material traverses to the anode surface and is irreversibly rendered inaccessible. However, though the challenges are steep, the potential improvements to society that could be brought through the successful implementation Li-S batteries loom even larger. This has beckoned countless scientists and engineers over the decades to work to address these problems. And indeed, through the collective effort of the Li-S research community, considerable progress has been made.

1.3 Enabling Li-S Batteries: The Collective Scientific and Engineering Effort

There has been an enormous amount of research attention devoted to understanding and overcoming the challenges listed above, with tens of thousands of scientific journal articles on Li-S batteries being published over the past decade alone [43, 44]. These investigations have dynamically ranged from developing highly capable sulfur cathodes to designing more stable and resilient Li-metal anodes to meticulously tailoring liquid electrolytes for Li-S batteries. In this section, the broad strokes and intents with which Li-S research has been carried out are described on a component-by-component basis.

1.3.1 Cathode

The sulfur cathode has received the most widespread research attention out of all the cell components constituting the Li-S battery. Within cathode research, the underlying research goals can be highly varied and diverse, though cathode studies generally fall into one of two broad thrust areas: (1) increasing the electrochemical utilization and capacity attainment of sulfur active material or (2) improving the cycle life by designing frameworks which physically or chemically trap dissolved polysulfides. Indeed, the primary intent of a specific research investigation can often times aim to address both goals at once. Over the past decade of research, the collective efforts of thousands of scientists have aimed to enable highly engineered sulfur cathodes with high active material loadings, long cycle lifetimes, and high capacity attainments, particularly under challenging conditions like low E/S ratios and high sulfur loadings [15].

As briefly mentioned earlier, the insulating nature of elemental sulfur and Li_2S necessitates the incorporation of an adequate amount of conductive filler material, generally conductive carbon, upon which to electrochemically nucleate and precipitate the solid phases [45, 46]. However, unlike in transition-metal oxide cathodes, where this conductive carbon can make up a small percentage of the cathode by mass, the amount of carbon utilized in sulfur cathodes can range as high as 50% [43]. This high carbon content can serve to boost both the capacity and cycle lifetimes of the cathode; the abundance of carbon sites provides a plentiful array of open sites for Li_2S nucleation, while the tortuous pathways presented by the high surface area framework can serve to delay the inevitable diffusion and shuttle of dissolved lithium polysulfides. However, the large usage of inactive conductive filler can deprecate the attained energy density of the cell. Moreover, given the low density of carbon, the porosity and surface area within the cathode is drastically heightened, which requires a larger volume of electrolyte to fully wet electrochemically active surfaces [16]. This is represented in Fig. 1.5a. Thus, sulfur–carbon composite cathodes with large fractions of carbon can deprecate the achieved energy density of a Li–S cell, and additionally, can tend to perform poorly under desirable low E/S conditions.

With this context, a key transition made over the past decade has been to move toward reducing the mass fractions of carbon filler while maintaining a high capacity and adequate cycle lifetime at low E/S ratios [15]. This transition has been concomitant with increasing both the sulfur content and sulfur loading within the cathode. Often times, these critical metrics go unreported within journal articles in the sulfur cathode literature. However, the potential implementation of Li–S batteries is dependent on their ability to outperform Li-ion batteries at the specific energy level. In order for this to occur, sulfur cathodes need to display an active material loading on the order of at least 5 mg cm^{-2} and a sulfur content ideally greater than 75% by which to offset the weight of inactive components like the current collector, separator, and conductive filler materials [16, 44].

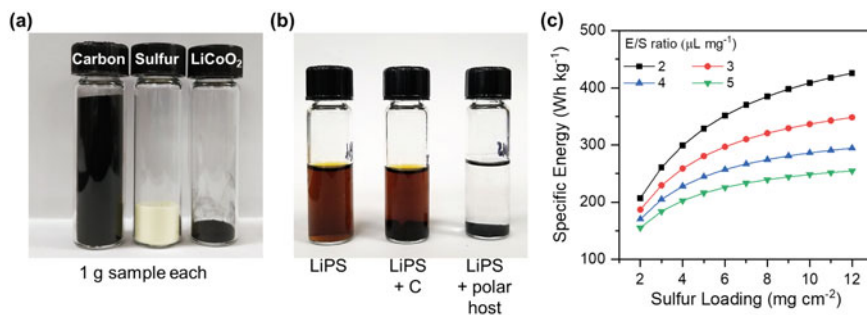


Fig. 1.5 **a** The variation in tap density between porous carbon black, elemental sulfur, and LiCoO_2 cathode material. **b** The ability of lithium polysulfides to be retained within the cathode framework is compared between carbon black and a polar host material, visualized by the degree of dissolution of polysulfides in the bulk electrolyte. **c** The theoretical relationship between specific energy and the sulfur mass loading in the cathode, as well as how this relationship varies as a function of E/S ratio. Reproduced with permission [16]. Copyright 2020, Elsevier

The transition toward achieving desirable performance metrics under practical conditions has been aided through the incorporation of novel cathode frameworks and materials. This will be explored in detail in later chapters, but briefly, has included a rich diversity of approaches like novel nanostructured designs which encapsulate sulfur, highly conductive polymeric binders, and electrocatalytic polar host materials (shown in Fig. 1.5b) that chemically bind and suppress the diffusion of dissolved polysulfides [45–52]. Indeed, today’s state-of-the-art sulfur cathode is highly engineered for optimized performance in both its composition and morphology, bearing little resemblance to a state-of-the-art sulfur cathode from the prior few decades. While much progress has been made, much work still remains to achieve high capacities and long cycle lifetimes under the conditions required for commercial implementation, including low carbon mass fractions, high sulfur loadings, and low E/S ratios [16]. A theoretical model relating these critical metrics to attainable specific energy is shown in Fig. 1.5c.

1.3.2 Anode

Another major focus within the Li–S research literature is the Li-metal anode. As discussed, Li-metal displays poor stability with the electrolyte solvent, which is only exacerbated by the presence of lithium polysulfides, high surface area mossy and dendritic growth, and the continuous growth of the thick, insulating SEI layer [32]. These effects are quite noticeable during the electrochemical cycling of Li–S cells, as seen through the generally short cycle lifetimes state-of-the-art Li–S cells possess in comparison to Li-ion cells [33]. In this regard, the Li-metal anode represents the most formidable obstacle in the pathway to implementation of the Li–S battery.

Just as in the case of the sulfur cathode, the reactive instability inherent to Li-metal becomes increasingly consequential under the practical cell construction constraints required for commercial implementation [53]. Under lean electrolyte conditions, for example, the continual formation of the anode-side SEI can consume and starve the cell of any remaining liquid electrolyte, leading to rapid cell failure [16]. This is demonstrated in Fig. 1.6a, b. Another critical cell constraint that exhibits dependencies with cell performance is the negative-to-positive (N/P) capacity ratio. Li–S cells generally contain an amount of Li-metal (negative electrode) well in excess of the capacity that would be generally required to stoichiometrically match that of the sulfur cathode (positive electrode), leading to a very high N/P ratio. This is governed by the thickness of commercial Li-foil, with a 50 μm Li-metal foil exhibiting an areal capacity on the order of 10 mA h cm^{-2} . In practical cell construction, however, it is desirable to minimize the N/P ratio to the largest extent possible, as this minimizes the contributions of inactive mass to the overall cell specific energy [16]. Unfortunately, the degradation of the Li-metal anode itself becomes increasingly more important as the amount of excess Li-metal is decreased, as excess Li-metal can help

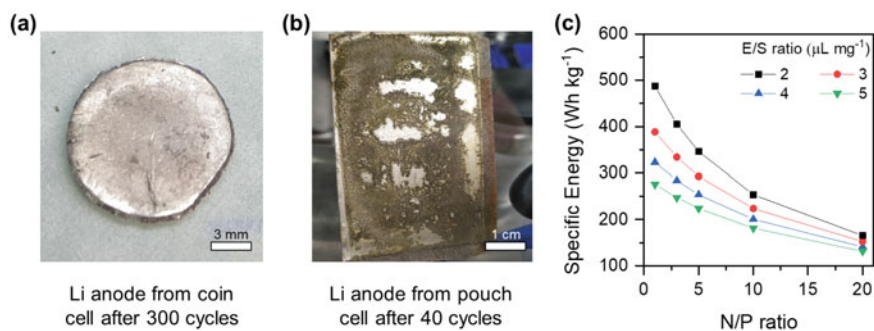


Fig. 1.6 **a** A relatively pristine Li-metal foil anode after undergoing 300 cycles in a coin cell with large excesses of electrolyte solvent. **b** A severely depredated Li-metal foil anode after undergoing only 40 cycles in a pouch cell with lean amounts of electrolyte solvent. **c** The theoretical relationship between specific energy and N/P ratio represented within the cell, as well as how this relationship varies as a function of E/S ratio. Reproduced with permission [16]. Copyright 2020, Elsevier

to offset and mask the losses to Li^+ charge carriers occurring over cycling [34, 54]. Thus, under either low E/S or low N/P conditions, the cycle lifetime of Li–S cells can precipitously decrease.

Therefore, over the past decade, the single largest driving force in Li-metal research has been to stem its inherent reactivity, often through the use novel inorganic and organic coating layers as well as altogether new anode frameworks to house and protect Li-metal [33, 55–60]. These improvements have been shown to shield and often partially passivate the Li-metal from the organic electrolyte, leading to improved cycle lifetimes. Just as in the case of the sulfur cathode, however, while significant progress has been shown for Li-metal, there is still plenty of room for improvement. The implementation of such improvements needs to be conducted in Li–S cells constructed under the critical metrics necessary for real-world use, including low E/S ratios and low N/P ratios (whose relation to attainable specific energy is modeled in Fig. 1.6c) [16].

1.3.3 Electrolyte

The final component receiving sizeable research attention within the Li–S area is the liquid electrolyte. As described throughout this chapter, the electrolyte is in many respects the most consequential and distinctive element of the Li–S battery, as the solution-mediated nature inherently ties and collates the solvent, salt, and polysulfide active material together in one liquid phase [23, 39, 40]. Furthermore, the electrolyte is the conduit by which the Li-metal anode and sulfur cathode active material are linked, and thus it requires a high ionic conductivity, little to no reactivity with lithium polysulfides, as well as sufficient stability in contact with Li-metal. Finally, given the deleterious shuttling dynamics introduced by polysulfides interacting with

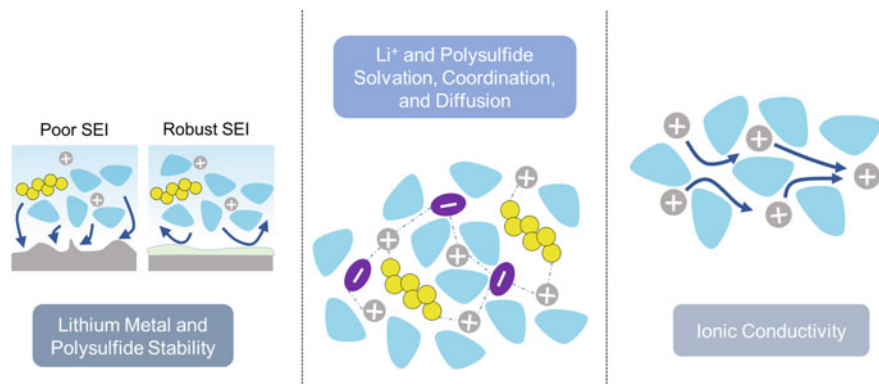


Fig. 1.7 A visual outline of the diverse and wide-ranging considerations that must be taken in the design of Li-S battery electrolytes. Reproduced and adapted with permission [12]. Copyright 2020, Wiley-VCH

Li-metal, it is desirable that the polysulfide diffusivity within the electrolyte remain low, without deprecating the solubility of polysulfides or ionic conductivity of Li^+ . This wide-ranging array of independent and often conflicting parametric constraints, which is outlined in Fig. 1.7, considerably reduces the number of solvent and salt compounds that can be reliably used in Li-S cells [16]. The predominantly used 1,3-dioxolane (DOL) and 1,2-dimethoxyethane (DME) ether-based solvents are among the few identified compounds that adequately address this myriad of considerations. There are several degrees of freedom when optimizing an electrolyte formulation, including the concentration and ratios of additives, salts, and solvents. This has led to a wide variety of scientific and engineering studies toward improving the Li-S electrolyte, making use of new salts, solvents, additives, and solvation frameworks [8, 26, 61–66]. However, the sheer number of performance constraints reliant on the electrolyte formulation have mostly stifled any major field-wide adoptions to the Li-S electrolyte over the past decade.

For example, an area for improvement within the DOL:DME electrolyte framework is the inevitable reactivity and decomposition in contact with Li-metal. This has led to significant research in highly concentrated electrolyte frameworks, which contain large excess of lithium salt dissolved in solution to stymie the inherent electrolyte consumption by Li-metal [67–69]. However, this can simultaneously present large losses to both polysulfide solubility and Li^+ mobility, often leading to a net loss in performance at room temperature [23, 65]. The opposite approach has also been assessed, where solvents with drastically boosted solubility towards lithium polysulfides are adopted; this boosts the capacity attainment in the initial cycles but leads to much worse reactivity with Li-metal and significantly deprecated cycle life [23, 65, 70]. These two examples illustrate the complex and often divergent considerations that need to be taken when tailoring the liquid electrolyte of the Li-S batteries. An addition which brings about an improvement to any one property of the Li-S electrolyte needs to be assessed in the context of every other critical attribute, including

polysulfide solubility, polysulfide diffusivity, polysulfide stability, Li-metal stability, and ionic conductivity. It may be the case, however, that an altogether new electrolyte will only be implemented after a landmark advance is made in either the anode or cathode framework, which may obviate the need for adherence to one of the parametric constraints described here.

There is significant opportunity for improvement of the Li–S battery electrolyte, if indeed a compound can outperform the current ether-based standard in the factors described. This is even more critical in the context of the E/S parameter necessary for practical implementation [16]. While the achievement of low E/S ratios is often contextualized as being predicated on a highly optimized sulfur cathode, the onus is just as much on the wetting and solvation properties of the liquid electrolyte, which are a function of the constraints described here. During the next decade, it will be exciting to see how the Li–S research community continues to build on the collective improvements initiated over the past several years, with a renewed focus on the critical metrics required for success.

1.4 Conclusion: The Next Decade of Li–S Battery Research

The Li–S battery is an intriguing and chemically rich system, with operating principles that differ considerably from the state-of-the-art Li-ion batteries. The chemical complexity arising from the solvation of the cathode active material and its subsequent dynamic behavior with the Li-metal anode presents an exciting challenge to researchers across the globe. Beyond just being interesting from a scientific perspective, however, taming the Li–S battery has the potential to unlock a new chapter in humanity’s ability to control and harness stored electrical energy. During the past few decades, the collective will and efforts of electrochemical researchers has advanced the Li–S battery to its current state, with considerable advances in the sulfur cathode, Li-metal anode, and electrolyte framework. As we move forward into the next decade of research, it is finally the prime opportunity to transition the Li–S battery from a lab-scale demonstration to a commercially implementable product.

In order to do this, it is of key importance to prioritize the attainment of critical metrics, including low carbon content ($\leq 5\%$) in the cathode, high sulfur loadings ($\geq 5 \text{ mg cm}^{-2}$), low N/P ratios (≤ 5), and low E/S ratios ($\leq 5 \text{ } \mu\text{L mg}^{-1}$) [16]. Equally important is the need to achieve high active material utilizations under such constraints, which can be expressed through the electrolyte-to-capacity (E/C) ratio, in $\mu\text{L (mA h)}^{-1}$. Along with the other mentioned metrics, it will likely be necessary for the E/C ratio in research-grade Li–S cells to be less than $5 \text{ } \mu\text{L (mA h)}^{-1}$ prior to commercial adoption. A quick heuristic for recalling the metrics outlined here is dubbed the “Five 5’s”, shown in Fig. 1.8 [16]. While it is feasible that the attainment of a practically implementable Li–S cell may not achieve every single one of these constraints, these metrics serve as idealized representations to keep in mind and strive for during the next decade of research, engineering, and deployment in the Li–S battery area.

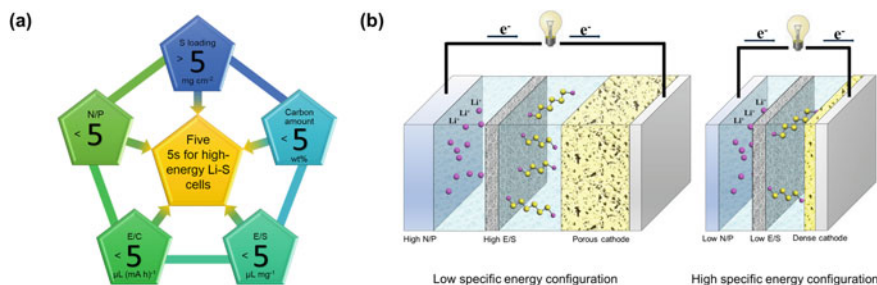


Fig. 1.8 **a** The critical metrics and guiding principles to heed during the next decade of research in Li–S batteries, dubbed the “Five 5s”. **b** A visual illustration of the properties and metrics dictating the specific energy attainment of Li–S cells. Reproduced with permission [16]. Copyright 2020, Elsevier

The quest to conquer the Li–S chemistry has made considerable progress over the years. We now enter the next phase of Li–S research, where the collective knowledge and understanding of the underlying chemistry is used as a tool toward effective and targeted deployment. By truly unlocking the potential of the Li–S battery, we add yet another exciting chapter to the story of humanity’s technological progress.

Acknowledgements This work was supported by the U.S. Department of Energy, Office of Basic Energy Sciences, Division of Materials Science and Engineering under award number DE-SC0005397.

References

1. Manthiram A (2020) A reflection on lithium-ion battery cathode chemistry. *Nat Commun* 11:1–9. <https://doi.org/10.1038/s41467-020-15355-0>
2. Goodenough JB (2018) How we made the Li-ion rechargeable battery. *Nat Electron* 1:204
3. Li W, Erickson EM, Manthiram A (2020) High-nickel layered oxide cathodes for lithium-based automotive batteries. *Nat Energy* 5:26–34. <https://doi.org/10.1038/s41560-019-0513-0>
4. Yamada Y, Iriyama Y, Abe T, Ogumi Z (2009) Kinetics of lithium ion transfer at the interface between graphite and liquid electrolytes: effects of solvent and surface film. *Langmuir* 25:12766–12770. <https://doi.org/10.1021/la901829v>
5. Xu K, Von Cresce A, Lee U (2010) Differentiating contributions to “ion transfer” barrier from interphasial resistance and Li⁺ desolvation at electrolyte/graphite interface. *Langmuir* 26:11538–11543. <https://doi.org/10.1021/la1009994>
6. Liu J, Zhang JG, Yang Z, Lemmon JP, Imhoff C, Graff GL, Li L, Hu J, Wang C, Xiao J, Xia G, Viswanathan VV, Baskaran S, Sprenkle V, Li X, Shao Y, Schwenzer B (2013) Materials science and materials chemistry for large scale electrochemical energy storage: from transportation to electrical grid. *Adv Funct Mater* 23:929–946. <https://doi.org/10.1002/adfm.201200690>
7. Halpert G, Frank H, Surampudi S (1999) Batteries and fuel cells in space. *Electrochem Soc Interface* 8:25–30
8. Gupta A, Bhargava A, Jones JP, Bugga RV, Manthiram A (2020) Influence of lithium polysulfide clustering on the kinetics of electrochemical conversion in lithium-sulfur batteries. *Chem Mater* 32:2070–2077. <https://doi.org/10.1021/acs.chemmater.9b05164>

9. Krishnamurthy V, Viswanathan V (2020) Beyond transition metal oxide cathodes for electric aviation: the case of rechargeable CF x. *ACS Energy Lett* 3330–3335. <https://doi.org/10.1021/acsenerylett.0c01815>
10. Sharma SS, Manthiram A (2020) Towards more environmentally and socially responsible batteries. *Energy Environ Sci* 13:4087–4097. <https://doi.org/10.1039/d0ee02511a>
11. Li L, Deshmane VG, Paranthaman MP, Bhave R, Moyer BA, Harrison S (2018) Lithium recovery from aqueous resources and batteries: a brief review. *Johnson Matthey Technol Rev* 62:161–176
12. Gupta A, Manthiram A (2020) Designing advanced lithium-based batteries for low-temperature conditions. *Adv Energy Mater* 10:2001972. <https://doi.org/10.1002/aenm.202001972>
13. Rodrigues M-TF, Babu G, Gullapalli H, Kalaga K, Sayed FN, Kato K, Joyner J, Ajayan PM (2017) A materials perspective on Li-ion batteries at extreme temperatures. *Nat Energy* 2:1–14. <https://doi.org/10.1038/nenergy.2017.108>
14. Manthiram A, Chung S-H, Zu C (2015) Lithium-sulfur batteries: progress and prospects. *Adv Mater* 27:1980–2006. <https://doi.org/10.1002/adma.201405115>
15. Hong-Jie P, Jia-Qi H, Xin-Bing C, Qiang Z (2017) Review on high-loading and high-energy lithium-sulfur batteries. *Adv Energy Mater* 7:1700260. <https://doi.org/10.1002/aenm.201700260>
16. Bhargav A, He J, Gupta A, Manthiram A (2020) Lithium-sulfur batteries: attaining the critical metrics. *Joule* 4:285–291. <https://doi.org/10.1016/j.joule.2020.01.001>
17. Herbert D, Ulam J (1962) Electric dry cells and storage batteries. United States Pat. Off. Pat. US3043986
18. Nole DA, Moss V (1968) Battery employing lithium-sulphur electrodes with non-aqueous electrolyte—Google Patents. United States Pat. Off. US3532543A
19. Mizushima K, Jones PC, Wiseman PJ, Goodenough JB (1981) Li_xCoO_2 ($0 < x \leq 1$): a new cathode material for batteries of high energy density. *Solid State Ionics* 3–4:171–174. [https://doi.org/10.1016/0167-2738\(81\)90077-1](https://doi.org/10.1016/0167-2738(81)90077-1)
20. Winter M, Barnett B, Xu K (2018) Before Li ion batteries. *Chem Rev* 118:11433–11456. <https://doi.org/10.1021/acs.chemrev.8b00422>
21. Liu Z, Mukherjee PP (2017) Mesoscale elucidation of surface passivation in the Li-sulfur battery cathode. *ACS Appl Mater Interfaces* 9:5263–5271. <https://doi.org/10.1021/acsami.6b15066>
22. Shen C, Xie J, Zhang M, Andrei P, Hendrickson M, Plichta EJ, Zheng JP (2017) Understanding the role of lithium polysulfide solubility in limiting lithium-sulfur cell capacity. *Electrochim Acta* 248:90–97. <https://doi.org/10.1016/J.ELECTACTA.2017.07.123>
23. Gupta A, Bhargav A, Manthiram A (2018) Highly solvating electrolytes for lithium-sulfur batteries. *Adv Energy Mater* 1803096. <https://doi.org/10.1002/aenm.201803096>
24. Cuisinier M, Hart C, Balasubramanian M, Garsuch A, Nazar LF (2015) Radical or not radical: revisiting lithium-sulfur electrochemistry in nonaqueous electrolytes. *Adv Energy Mater* 5:1401801. <https://doi.org/10.1002/aenm.201401801>
25. Manthiram A, Fu Y, Su Y-S (2013) Challenges and prospects of lithium-sulfur batteries. *Acc Chem Res* 46:1125–1134. <https://doi.org/10.1021/ar300179v>
26. Chu H, Noh H, Kim Y-J, Yuk S, Lee J-H, Lee J, Kwack H, Kim Y, Yang D-K, Kim H-T (2019) Achieving three-dimensional lithium sulfide growth in lithium-sulfur batteries using high-donor-number anions. *Nat Commun* 10:188. <https://doi.org/10.1038/s41467-018-07975-4>
27. Pan H, Han KS, Engelhard MH, Cao R, Chen J, Zhang JG, Mueller KT, Shao Y, Liu J (2018) Addressing passivation in lithium-sulfur battery under lean electrolyte condition. *Adv Funct Mater* 1707234:1–7. <https://doi.org/10.1002/adfm.201707234>
28. Mistry AN, Mukherjee PP (2018) “Shuttle” in polysulfide shuttle: friend or foe? *J Phys Chem C* 122:23845–23851. <https://doi.org/10.1021/acs.jpcc.8b06077>
29. Shin H, Baek M, Gupta A, Char K, Manthiram A, Choi JW (2020) Recent progress in high donor electrolytes for lithium-sulfur batteries. *Adv Energy Mater* 10:2001456. <https://doi.org/10.1002/aenm.202001456>

30. Fan FY, Chiang Y-M (2017) Electrodeposition kinetics in Li-S batteries: effects of low electrolyte/sulfur ratios and deposition surface composition. *J Electrochem Soc* 164:A917–A922. <https://doi.org/10.1149/2.0051706jes>
31. Cao R, Xu W, Lv D, Xiao J, Zhang JG (2015) Anodes for rechargeable lithium-sulfur batteries. *Adv Energy Mater* 5:1–23. <https://doi.org/10.1002/aenm.201402273>
32. Tikekar MD, Choudhury S, Tu Z, Archer LA (2016) Design principles for electrolytes and interfaces for stable lithium-metal batteries. *Nat Energy* 1:16114. <https://doi.org/10.1038/nenergy.2016.114>
33. Liu J, Bao Z, Cui Y, Dufek EJ, Goodenough JB, Khalifah P, Li Q, Liaw BY, Liu P, Manthiram A, Meng YS, Subramanian VR, Toney MF, Viswanathan VV, Whittingham MS, Xiao J, Xu W, Yang J, Yang XQ, Zhang JG (2019) Pathways for practical high-energy long-cycling lithium metal batteries. *Nat Energy* 4:180–186
34. Nanda S, Gupta A, Manthiram A (2020) Anode-free full cells: a pathway to high-energy density lithium-metal batteries. *Adv Energy Mater* 2000804. <https://doi.org/10.1002/aenm.202000804>
35. Xu W, Wang J, Ding F, Chen X, Nasybulin E, Zhang Y, Zhang J-G (2014) Lithium metal anodes for rechargeable batteries. *Energy Environ Sci* 7:513–537. <https://doi.org/10.1039/C3EE40795K>
36. Manthiram A (2016) Electrical energy storage: materials challenges and prospects. *MRS Bull* 41:624–630. <https://doi.org/10.1557/mrs.2016.167>
37. Fang C, Li J, Zhang M, Zhang Y, Yang F, Lee JZ, Lee MH, Alvarado J, Schroeder MA, Yang Y, Lu B, Williams N, Ceja M, Yang L, Cai M, Gu J, Xu K, Wang X, Meng YS (2019) Quantifying inactive lithium in lithium metal batteries. *Nature* 572:511–515. <https://doi.org/10.1038/s41586-019-1481-z>
38. Pan H, Wei X, Henderson WA, Shao Y, Chen J, Bhattacharya P, Xiao J, Liu J (2015) On the way toward understanding solution chemistry of lithium polysulfides for high energy Li-S redox flow batteries. *Adv Energy Mater* 5:1500113. <https://doi.org/10.1002/aenm.201500113>
39. Rajput NN, Murugesan V, Shin Y, Han KS, Lau KC, Chen J, Liu J, Curtiss LA, Mueller KT, Persson KA (2017) Elucidating the solvation structure and dynamics of lithium polysulfides resulting from competitive salt and solvent interactions. *Chem Mater* 29:3375–3379. <https://doi.org/10.1021/acs.chemmater.7b00068>
40. Andersen A, Rajput NN, Han KS, Pan H, Govind N, Persson KA, Mueller KT, Murugesan V (2019) Structure and dynamics of polysulfide clusters in a nonaqueous solvent mixture of 1,3-dioxolane and 1,2-dimethoxyethane. *Chem Mater* 31:2308–2319. <https://doi.org/10.1021/acs.chemmater.8b03944>
41. Li W, Yao H, Yan K, Zheng G, Liang Z, Chiang Y-M, Cui Y (2015) The synergetic effect of lithium polysulfide and lithium nitrate to prevent lithium dendrite growth. *Nat Commun* 6:7436. <https://doi.org/10.1038/ncomms8436>
42. Nanda S, Gupta A, Manthiram A (2018) A lithium-sulfur cell based on reversible lithium deposition from a Li₂S cathode host onto a hostless-anode substrate. *Adv Energy Mater* 8:1801556. <https://doi.org/10.1002/aenm.201801556>
43. Chung S-H, Chang C-H, Manthiram A (2018) Progress on the critical parameters for lithium-sulfur batteries to be practically viable. *Adv Funct Mater* 28:1801188. <https://doi.org/10.1002/adfm.201801188>
44. Hagen M, Hanselmann D, Ahlbrecht K, Maça R, Gerber D, Tübke J (2015) Lithium-sulfur cells: the gap between the state-of-the-art and the requirements for high energy battery cells. *Adv Energy Mater* 5:1401986. <https://doi.org/10.1002/aenm.201401986>
45. Thieme S, Brückner J, Meier A, Bauer I, Gruber K, Kaspar J, Helmer A, Althues H, Schmuck M, Kaskel S (2015) A lithium-sulfur full cell with ultralong cycle life: influence of cathode structure and polysulfide additive. *J Mater Chem A* 3:3808–3820. <https://doi.org/10.1039/C4TA06748G>
46. Ji X, Lee KT, Nazar LF (2009) A highly ordered nanostructured carbon-sulphur cathode for lithium-sulphur batteries. *Nat Mater* 8:500–506. <https://doi.org/10.1038/nmat2460>
47. He J, Manthiram A (2019) A review on the status and challenges of electrocatalysts in lithium-sulfur batteries. *Energy Storage Mater* 20:55–70. <https://doi.org/10.1016/J.ENSMS.2019.04.038>

48. Cha E, Patel MD, Park J, Hwang J, Prasad V, Cho K, Choi W (2018) 2D MoS₂ as an efficient protective layer for lithium metal anodes in high-performance Li–S batteries. *Nat Nanotechnol* 1. <https://doi.org/10.1038/s41565-018-0061-y>
49. Bugga RV, Jones SC, Pasalic J, Seu CS, Jones J-P, Torres L (2017) Metal sulfide-blended sulfur cathodes in high energy lithium-sulfur cells. *J Electrochem Soc* 164:A265–A276. <https://doi.org/10.1149/2.0941702jes>
50. Chen S, Wang D, Zhao Y, Wang D (2018) Superior performance of a lithium-sulfur battery enabled by a dimethyl trisulfide containing electrolyte. *Small Methods* 2:1800038. <https://doi.org/10.1002/smt.201800038>
51. Ye H, Lee JY (2020) Solid additives for improving the performance of sulfur cathodes in lithium-sulfur batteries—adsorbents, mediators, and catalysts. *Small Methods* 4:1900864. <https://doi.org/10.1002/smt.201900864>
52. Pang Q, Liang X, Kwok CY, Kulisch J, Nazar LF (2017) A comprehensive approach toward stable lithium-sulfur batteries with high volumetric energy density. *Adv Energy Mater* 7:1–9. <https://doi.org/10.1002/aenm.201601630>
53. Niu C, Lee H, Chen S, Li Q, Du J, Xu W, Zhang JG, Whittingham MS, Xiao J, Liu J (2019) High-energy lithium metal pouch cells with limited anode swelling and long stable cycles. *Nat Energy* 4:551–559. <https://doi.org/10.1038/s41560-019-0390-6>
54. Weber R, Genovese M, Louli AJ, Hames S, Martin C, Hill IG, Dahn JR (2019) Long cycle life and dendrite-free lithium morphology in anode-free lithium pouch cells enabled by a dual-salt liquid electrolyte. *Nat Energy* 4:683–689. <https://doi.org/10.1038/s41560-019-0428-9>
55. Yan K, Lu Z, Lee HW, Xiong F, Hsu PC, Li Y, Zhao J, Chu S, Cui Y (2016) Selective deposition and stable encapsulation of lithium through heterogeneous seeded growth. *Nat Energy* 1. <https://doi.org/10.1038/NENERGY.2016.10>
56. Cao X, Ren X, Zou L, Engelhard MH, Huang W, Wang H, Matthews BE, Lee H, Niu C, Arey BW, Cui Y, Wang C, Xiao J, Liu J, Xu W, Zhang JG (2019) Monolithic solid–electrolyte interphases formed in fluorinated orthoformate-based electrolytes minimize Li depletion and pulverization. *Nat Energy* 4:796–805. <https://doi.org/10.1038/s41560-019-0464-5>
57. Wang J, Huang W, Pei A, Li Y, Shi F, Yu X, Cui Y (2019) Improving cyclability of Li metal batteries at elevated temperatures and its origin revealed by cryo-electron microscopy. *Nat Energy* 4:664–670. <https://doi.org/10.1038/s41560-019-0413-3>
58. Li Y, Sun Y, Pei A, Chen K, Vailionis A, Li Y, Zheng G, Sun J, Cui Y (2018) Robust pinhole-free Li₃N solid electrolyte grown from molten lithium. *ACS Cent Sci* 4:97–104. <https://doi.org/10.1021/acscentsci.7b00480>
59. Chinnam PR, Wunder SL (2017) Engineered interfaces in hybrid ceramic–polymer electrolytes for use in all-solid-state Li batteries. *ACS Energy Lett* 2:134–138. <https://doi.org/10.1021/acscenergylett.6b00609>
60. Pathak R, Chen K, Gurung A, Reza KM, Bahrami B, Pokharel J, Baniya A, He W, Wu F, Zhou Y, Xu K, Qiao Q (Quinn) (2020) Fluorinated hybrid solid-electrolyte-interphase for dendrite-free lithium deposition. *Nat Commun* 11:1–10. <https://doi.org/10.1038/s41467-019-13774-2>
61. Chu H, Jung J, Noh H, Yuk S, Lee J, Lee J, Baek J, Roh Y, Kwon H, Choi D, Sohn K, Kim Y, Kim H (2020) Unraveling the dual functionality of high-donor-number anion in lean-electrolyte lithium-sulfur batteries. *Adv Energy Mater* 2000493. <https://doi.org/10.1002/aenm.202000493>
62. Gupta A, Bhargav A, Manthiram A (2020) Evoking high-donor-number-assisted and organosulfur-mediated conversion in lithium-sulfur batteries. *ACS Energy Lett* 224–231. <https://doi.org/10.1021/acscenergylett.0c02461>
63. Zheng J, Ji G, Fan X, Chen J, Li Q, Wang H, Yang Y, DeMella KC, Raghavan SR, Wang C (2019) High-fluorinated electrolytes for Li–S batteries. *Adv Energy Mater* 9:1803774. <https://doi.org/10.1002/aenm.201803774>
64. Yang B, Jiang H, Zhou Y, Liang Z, Zhao T, Lu YC (2019) Critical role of anion donicity in Li₂S deposition and sulfur utilization in Li–S batteries. *ACS Appl Mater Interfaces* 11:25940–25948. <https://doi.org/10.1021/acscami.9b07048>
65. Sun K, Li N, Su D, Gan H (2019) Electrolyte concentration effect on sulfur utilization of Li–S batteries. *J Electrochem Soc* 166:A50–A58. <https://doi.org/10.1149/2.0161902jes>

66. Zou Q, Lu Y-C (2016) Solvent-dictated lithium sulfur redox reactions: an operando UV–vis spectroscopic study. *J Phys Chem Lett* 7:1518–1525. <https://doi.org/10.1021/acs.jpcllett.6b00228>
67. Suo L, Hu Y-S, Li H, Armand M, Chen L (2013) A new class of solvent-in-salt electrolyte for high-energy rechargeable metallic lithium batteries. *Nat Commun* 4:1481. <https://doi.org/10.1038/ncomms2513>
68. Qian J, Adams BD, Zheng J, Xu W, Henderson WA, Wang J, Bowden ME, Xu S, Hu J, Zhang J-G (2016) Anode-free rechargeable lithium metal batteries. *Adv Funct Mater* 26:7094–7102. <https://doi.org/10.1002/adfm.201602353>
69. Chen L, Zhang J, Li Q, Vatamanu J, Ji X, Pollard TP, Cui C, Hou S, Chen J, Yang C, Ma L, Ding MS, Garaga M, Greenbaum S, Lee HS, Borodin O, Xu K, Wang C (2020) A 63 m superconcentrated aqueous electrolyte for high-energy Li-ion batteries. *ACS Energy Lett* 5:968–974. <https://doi.org/10.1021/acsenergylett.0c00348>
70. Li Z, Zhou Y, Wang Y, Lu YC (2019) Solvent-mediated Li₂S electrodeposition: a critical manipulator in lithium-sulfur batteries. *Adv Energy Mater* 9:1802207. <https://doi.org/10.1002/aenm.201802207>

Chapter 2

Sulfur–Carbon Composite Cathodes



Ruopian Fang, Ke Chen, Zhenhua Sun, Da-Wei Wang, and Feng Li

Abstract Carbon materials with various intriguing characteristics have been playing important roles in addressing the problematic issues during sulfur conversion reactions. Sulfur–carbon composite cathodes have demonstrated significantly improved electrochemical performances in terms of high sulfur utilization, long cycle life, and high areal capacities. In this chapter, an overview of the development of sulfur–carbon composite cathodes is presented. First, fundamentals of the role of carbon materials in improving the redox accessibility and reversibility of the sulfur cathode are discussed. A wide variety of sulfur–carbon composite cathodes are introduced, including the synthetic methods, material design principles, and functional applications. Finally, the significance of developing sulfur–carbon composite cathodes aiming for meeting practical requirements is remarked.

R. Fang · D.-W. Wang

School of Chemical Engineering, University of New South Wales, Sydney 2033, Australia
e-mail: ruopian.fang@unsw.edu.au

D.-W. Wang

e-mail: da-wei.wang@unsw.edu.au

K. Chen · Z. Sun · F. Li (✉)

Shenyang National Laboratory for Materials Science, Institute of Metal Research,
Chinese Academy of Sciences, Shenyang 110016, China
e-mail: fli@imr.ac.cn

K. Chen

e-mail: chenke@shanghaitech.edu.cn

Z. Sun

e-mail: zhsun@imr.ac.cn

K. Chen

School of Physical Science and Technology, Shanghai Tech University, Shanghai 201210, China

Z. Sun · F. Li

School of Materials Science and Engineering, University of Science and Technology of China,
Shenyang 110016, China

© The Author(s), under exclusive license to Springer Nature Switzerland AG 2022

A. Manthiram and Y. Fu (eds.), *Advances in Rechargeable Lithium–Sulfur Batteries*,

Modern Aspects of Electrochemistry 59, https://doi.org/10.1007/978-3-030-90899-7_2

Keywords Carbon materials · Electron conductors · Ion transport facilitators · Polysulfide immobilizer · Buffers for volume variation · Pore structure · Graphene · Carbon nanotube · Carbon fiber

2.1 Introduction

To make the Li–S battery technology viable, various strategies have been explored to tackle the problematic issues during sulfur conversion reactions that cause low active material utilization and fast capacity degradation [1]. These issues include low conductivity of sulfur, polysulfide dissolution and migration, and severe volumetric expansion upon lithiation. Basically, incorporation of conducting matrix is a requisite, aiming to facilitate electron and ion transport for enhanced redox reaction kinetics and impede irreversible loss of active materials from the cathode for improved cycling stability. In this respect, developing sulfur composite cathodes with tailored compositions, structures and properties has been the mainstream in recent years [2–5].

Carbon materials have intriguing characteristics of high electronic conductivity, tunable pore structure and surface functionality, good structural stability, and high versatility and availability, making them appealing for the design of high-performance sulfur composite cathodes [6–10]. In the past decade, sulfur–carbon composite cathodes have been playing a pivotal role in the development of Li–S batteries. Carbon materials with various morphologies and structures, including porous carbons, graphene, carbon nanotubes, carbon fibers, and carbon hybrids, have been reported for the construction of sulfur cathodes with high capacity and long cycle life. Moreover, carbon materials with excellent mechanical properties offer a good platform for the design of sulfur cathodes used for functional applications, such as bendable and stretchable devices [11].

In this chapter, we begin with a brief discussion on the fundamentals of the role of carbon materials in sulfur redox reactions. The development of various sulfur–carbon composite cathodes is comprehensively introduced, including the synthetic methods, composite material design principles, and electrode engineering. Recent advances of applying sulfur–carbon composite cathodes for flexible devices are also discussed. Finally, the significance of developing sulfur–carbon composite cathodes with practical reliability is remarked.

2.2 Fundamentals of the Role of Carbon Materials in Sulfur Redox Reactions

Generally, observed performance improvements of the sulfur composite cathode can be attributed to the advantages of carbon materials. More importantly, it is essential to obtain a general and objective understanding of how carbon materials benefit the

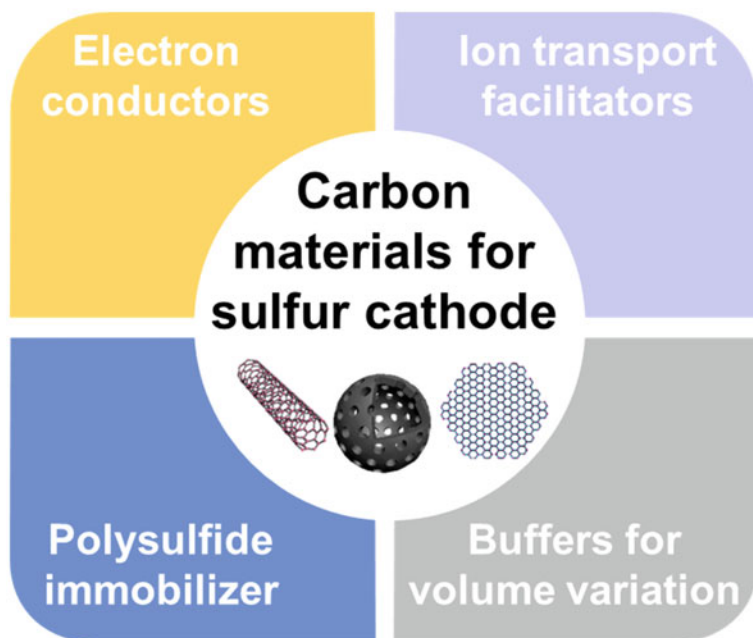


Illustration 2.1 The roles of carbon materials in sulfur redox reactions

sulfur conversion reactions and contribute to improved electrochemical behaviors. Fundamentally, the role of carbon materials in promoting the redox accessibility and reversibility of the sulfur cathode can be summarized as follows (Illustration 2.1):

1. **Electron conductors.** The active material utilization of the sulfur cathode is known to be limited by the insulating nature of both sulfur and its final discharge product Li_2S . Incorporating electron conductors in the sulfur cathode can provide sufficient electron transport paths for improved active material utilization. Meanwhile, electron conductors belong to inactive components that will decrease the overall energy density of the Li–S battery. Carbon materials feature high conductivity and light weight, which can effectively improve the conductivity of the sulfur cathode without compromising the overall capacity of the cathode.
2. **Ion transport facilitators.** Besides the electron transport parameters, good lithium-ion accessibility of the cathode is another determining factor that needs to be guaranteed for the implementation of sulfur redox reactions. For liquid electrolyte-based batteries, the liquid electrolyte serves as the ion-conducting phase, and fast lithium-ion transport behavior requires good penetration of liquid electrolytes through the cathode. The abundant pore structure and surface functional groups of carbon materials can enable good absorbability of the electrolytes to facilitate fast lithium-ion transport within the cathode for optimized electrochemical reaction kinetics.

3. Polysulfide immobilizer. The dissolution and diffusion of polysulfide intermediates cause severe irreversible loss of active material, resulting in low reversibility and fast capacity decay of the sulfur cathode. Introducing polysulfide immobilization sites in the sulfur cathode is beneficial for improved long-term cycling stability. This can be realized through either physical confinement effect of porous structures or chemical adsorption effect enabled by polar surface chemistry. Carbon materials with tailored pore structures and surface functional groups can provide sufficient immobilization sites to enhance the affinity of polysulfides with the cathode and effectively improve the reversibility and cycle life of the sulfur cathode.
4. Buffers for volume variation. Owing to the large volume expansion (~80%) going from sulfur to Li_2S , the sulfur cathode undergoes repeated volume variation during cycling, leading to pulverization of the cathode and loss of electrical contact of active materials. Carbon materials with adjustable pore structures can provide appropriate void spaces as buffers in the cathode to accommodate the volume change of active materials, contributing to improved structural stability of the cathode.

2.3 Synthetic Methods of Sulfur–Carbon Composites

The synthetic method of sulfur–carbon composite generally determines the dispersibility of sulfur within the carbon conducting matrix, which significantly influences the electrochemical utilization of sulfur. In early years, sulfur was often combined with conductive carbons via mechanical mixing methods, which often renders nonuniform sulfur agglomerates with poor electrical contact with the carbon matrix, resulting in low sulfur utilization during redox reactions [2]. Moreover, the dissolved polysulfides that cannot be well encapsulated in the cathode tend to diffuse to the anode side, leading to fast capacity degradation [12]. With substantial progress on the optimization of sulfur cathodes in recent years, various synthetic methods have been developed to prepare sulfur–carbon composites with improved electrochemical performance [13].

2.3.1 Melt-Diffusion

Melt diffusion is the most extensively used method to infiltrate sulfur into conductive carbon matrix with good dispersibility [14]. In this method, elemental sulfur and carbon first undergo premixing process such as mechanical grinding, followed by thermal treatment at the temperature where sulfur exists in the molten state with the lowest viscosity. The melting temperature of the most common cyclic orthorhombic sulfur (S_8) is 115.2 °C, above which the viscosity of sulfur gradually decreases with

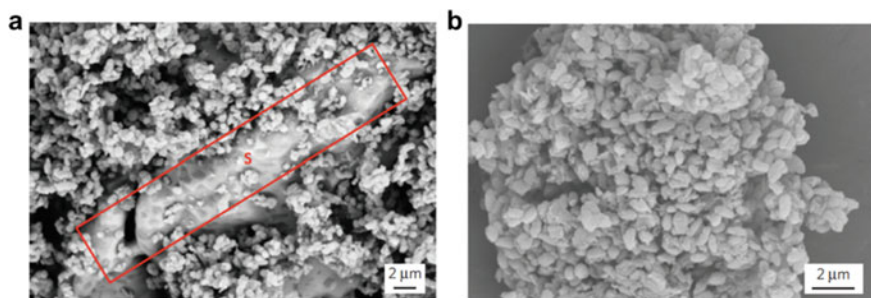


Fig. 2.1 SEM images of a sulfur-porous carbon composite prepared by **a** mechanical mixing method and **b** melt-diffusion method (reproduced with permission by the Nature Publishing Group from [14])

the temperature increasing, followed by drastic increase at 159 °C when the ring-opening polymerization of the cyclic S_8 rings is initiated [15]. Generally, the temperature of around 155 °C is considered to render minimum viscosity of the sulfur melt, which is often adopted for the melt diffusion of sulfur in conductive carbon materials [16]. The sulfur melt can be uniformly incorporated into the pores of the carbon matrix through capillary forces, resulting in intimate electrical contact of sulfur with the conductive carbon matrix. Figure 2.1 shows the comparison of scanning electron microscopy (SEM) images of sulfur-porous carbon composite prepared by mechanical mixing method (Fig. 2.1a) and melt-diffusion method (Fig. 2.1b), respectively [14]. Apparently, bulk sulfur evident in the SEM image of the mechanically mixed composite disappears after the melt-diffusion treatment, indicating well-dispersed sulfur within the conductive channels of porous carbon. In some cases, to ensure complete encapsulation of sulfur in the porous channels of the carbon matrix, a subsequent thermal treatment at 300–350 °C is applied to vaporize residual sulfur on the outer surface of the carbon matrix [17].

2.3.2 Vapor Phase Infusion

Different from the melt-diffusion method where sulfur exists in molten state, the vapor phase infusion method is implemented at higher temperature range of 300–600 °C to infuse gaseous sulfur into the carbon matrix [18–21]. The high penetration capability of gaseous sulfur enables uniform sulfur infiltration into the confining channels of carbon materials, especially the internal void space of hollow carbon spheres. The obtained sulfur–carbon composite material can ensure homogeneous distribution of sulfur without any post thermal treatment. Figure 2.2 shows the SEM image of sulfur-hollow carbon sphere composite prepared by vapor phase infusion of elemental sulfur, revealing the complete incorporation of sulfur into the carbon matrix [19]. In comparison to the melt-diffusion method, the vaporizing method requires more rigorous sealing of the reactor because of its higher operating temperature.

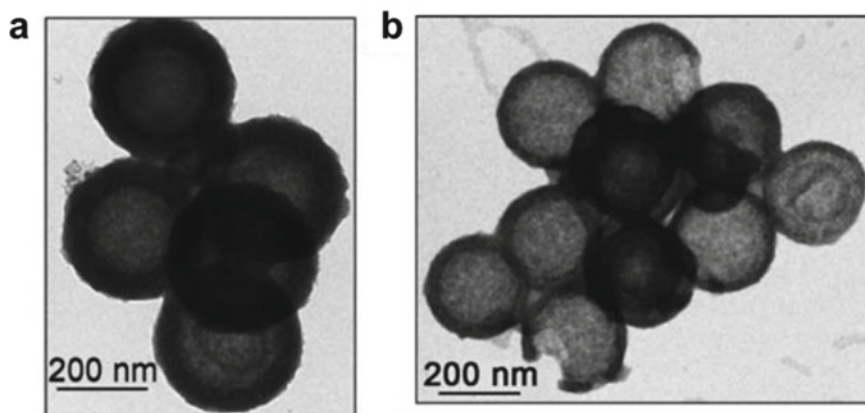
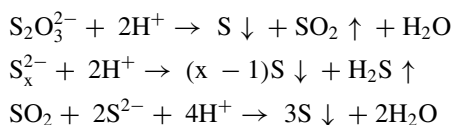


Fig. 2.2 SEM images of hollow carbon spheres **a** before and **b** after vapor phase infusion of elemental sulfur (reproduced with permission by Wiley-VCH from [19])

2.3.3 Heterogeneous Nucleation

In this method, elemental sulfur is generated through the chemical reactions between sulfur-containing salts and acids in aqueous solutions containing well-dispersed carbon materials [22–25]. Typical chemical reactions are shown as follows:



Sulfur heterogeneously nucleates on the surface of the carbon materials dispersed in the aqueous solutions to form sulfur–carbon composite materials. The size, morphology, and dispersion state of sulfur in the obtained sulfur–carbon composite materials can be adjusted by altering the reaction conditions, such as the relative proportions of the reactants and the surface functionality of carbon materials. Figure 2.3 shows the SEM images of sulfur–graphene composite prepared through heterogeneous nucleation of sulfur in aqueous solution, where sulfur particles with sizes less than 1 μm were uniformly wrapped by the graphene sheets [25]. This method is based on low-cost water-based chemical reactions without involving any toxic solvents, which is environmental-friendly and can be applicable in industrial productions.

Besides the above three representative methods, other methods have also been developed for constructing sulfur–carbon composites. For example, carbothermal reduction method was reported to prepare sulfur–carbon nanotube composite by sulfate-containing anodic aluminum oxide (AAO) template [26]. Template-directed chemical vapor deposition of carbon and carbothermal reduction of the sulfate by

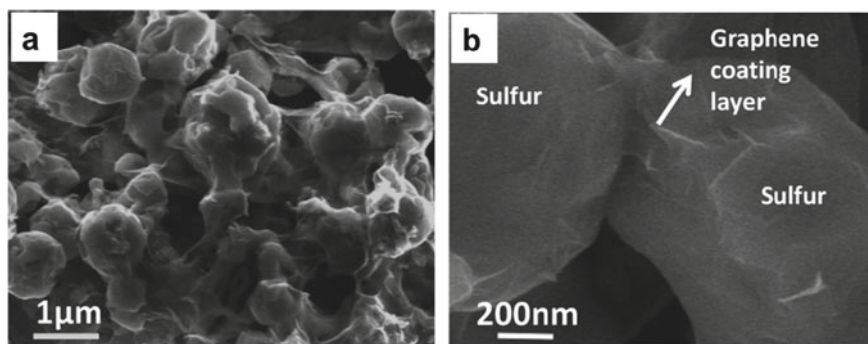


Fig. 2.3 SEM images of sulfur–graphene composite prepared through heterogeneous nucleation of sulfur in aqueous solution at **a** low and **b** high magnifications (reproduced with permission by American Chemical Society from [25])

carbon were integrated to grow the sulfur–carbon nanotube composite material where sulfur was confined in the walls of the nanotubes. A simple high-power ultrasonication method was reported to prepare sulfur–carbon nanotube-carbon black clusters with high sulfur content up to 90 wt% [27]. Carbon nanotubes and carbon black particles are homogeneously dispersed through the micrometer-sized sulfur particles to form an interconnected and embedded conductive network. A sulfur–graphene composite was synthesized by bubbling concentrated hydrogen sulfide (H_2S) into graphene oxide aqueous suspension, where graphene oxide was deoxygenated to reduce graphene oxide with improved conductivity and S^{2-} was transformed into elemental sulfur attached to the reduced graphene oxide layers [28]. This method realized both entirely “green” regeneration of pollutant H_2S gas and facile fabrication of sulfur composite cathode materials.

Overall, it is always highly desirable to explore more facile and powerful fabrication methods for optimizing sulfur–carbon composite cathodes. Basically, the following principles should be considered for the preparation of sulfur–carbon composite materials: (1) achieving high dispersibility of sulfur within the carbon conducting matrix, (2) minimizing the addition of inactive components, and (3) adopting economical and ecological synthetic routes.

2.4 Sulfur-Porous Carbon Composite Cathode

The structures and properties of porous carbons are considered highly effective to fulfill the requirements of an ideal sulfur host, such as improving the electronic conductivity, channeling the electrolytes, trapping the dissolved polysulfides, and accommodating the volumetric change [29, 30]. Generally, porous carbons have relatively low degree of graphitization and high diversity of pore structures. As defined

by the IUPAC, the pore size can be classified as micropore (<2 nm), mesopore (2–50 nm), and macropore (>50 nm) [31]. Pore size distributions of porous carbon exert an important influence on the sulfur redox reactions. Micropores have high adsorption capability towards the polysulfides, yet the small pore sizes pose an increased barrier to electrolyte penetration, leading to sluggish lithium-ion transport kinetics. Meso/macropores allow efficient electrolyte penetration through the sulfur cathode to ensure fast charge transport kinetics, but their capability to alleviate the polysulfide diffusion and migration is inferior to macropores [32, 33].

Besides the pore size distributions, the pore volume of porous carbon is another significant parameter that influences the performance of the sulfur-porous carbon composite cathode. Given that sulfur is completely encapsulated in the pore structures of porous carbon, the pore volume determines the sulfur content in the sulfur-porous carbon composite [34]. The relationship between the sulfur content ($S_{wt}\%$) in the sulfur-porous carbon composite material and the pore volume (V) of the porous carbon can be concluded by the following formula (considering the ~80% volumetric expansion from sulfur to Li_2S):

$$S_{wt}\% = \frac{\frac{V}{1.8} \times D}{\frac{V}{1.8} \times D + 1}$$

where D is the density of elemental sulfur (2.07 g cm^{-3}). It is known that low sulfur content leads to low energy density of the Li–S cell even high sulfur utilization can be achieved. High sulfur content requires the porous carbon to have high pore volume. For example, it has been estimated that the sulfur content in the cathode should reach at least 70 wt% for practical applications of Li–S batteries [35]. Considering the addition of conductive additives and binder during the common casting fabrication of the cathode (often 10–30 wt%), sulfur content of at least 80 wt% in the sulfur-porous carbon composite is needed, corresponding to high pore volume of $3.48 \text{ cm}^3 \text{ g}^{-1}$ for the carbon, as shown in Table 2.1.

Various porous carbons with different pore size distributions, pore volumes, and morphologies have been extensively investigated for constructing sulfur-porous carbon composite cathodes. In the following, the advances in the development of various sulfur-porous carbon composite cathode based on microporous, meso/macroporous, hierarchical porous, and hollow porous carbons will be introduced. A summary of pros and cons of porous carbon materials with different pore sizes as the sulfur host will be provided.

Table 2.1 Relationships between the pore volume of porous carbon (V) and the theoretical sulfur content ($S_{wt}\%$) in the sulfur-porous carbon composite

$S_{wt}\%$	50%	60%	65%	70%	75%	80%	85%	90%
$V \text{ (cm}^3 \text{ g}^{-1}\text{)}$	0.87	1.30	1.62	2.03	2.61	3.48	4.93	7.83

2.4.1 Microporous Carbon

Micropores can render high specific surface area and enable good immobilization of polysulfides by strong adsorption capability as the small pores can confine sulfur and restrict the dissolution and diffusion of polysulfides [36–38]. The microporous carbon spheres ranging in size from 200 to 300 nm were used for sulfur encapsulation, resulting in exceptional cycling stability of the cathode [17]. The carbon spheres have narrow micropore size distribution of about 0.7 nm, rendering a specific surface area of $844 \text{ m}^2 \text{ g}^{-1}$ and pore volume of $0.474 \text{ cm}^3 \text{ g}^{-1}$. The sulfur-microporous carbon sphere composite was prepared via melt-diffusion process at $149 \text{ }^\circ\text{C}$, followed by heat treatment at $300 \text{ }^\circ\text{C}$ to vaporize the superfluous sulfur on the outer surface of carbon spheres. With sulfur content of 42 wt% in the sulfur-microporous carbon sphere composite material, the Li–S cell delivered high initial discharge capacity of 1333 mAh g^{-1} at 40 mA g^{-1} and maintained long-term cycling stability with a capacity retention rate of 80% after 500 cycles at 400 mA g^{-1} . The obtained electrochemical performance could be ascribed to the narrow micropores of the carbon spheres, which not only enabled high dispersion of elemental sulfur inside the micropore structures for achieving high sulfur utilization but also trapped polysulfide intermediates by strong adsorption to impede irreversible loss of active materials.

To understand the underlying mechanism of the high cycling stability of sulfur confined in micropores, Wang et al. designed two-step adsorption-extraction method to differentiate the electrochemical behavior of micropore-confined sulfur from mesopore-confined sulfur [39]. A microporous-mesoporous carbon, with micropore sizes of 0.6–0.7 nm and mesopore sizes of 6–40 nm, was used for sulfur impregnation, followed by removal of sulfur in the mesopores using carbon sulfide (CS_2) washing. It was found that the sulfur cathode after CS_2 extraction was able to operate reversibly over 800 cycles at charge/discharge rate of 1.8 C (1 C corresponds to current density of 1675 mA g^{-1}), much better than that before CS_2 extraction, indicating the excellent efficacy of micropores in enhancing the cycling stability of sulfur. An ion-desolvation mechanism was proposed to interpret the high stability of sulfur in microporous carbons. As solvated ions tend to be desolvated in micropores with size close to the ion size [40], micropores below 1 nm can cause desolvation of the electrolyte ions, which prevent or at least slow the dissolution of polysulfides as the solvent concentration can be very low or likely nearly to zero in these microporous (Fig. 2.4a). Consequently, sulfur confined in the micropores reacts with desolvated ions in the absence of the solvents, and this solvent-deficient condition leads quasi-solid-state reaction of sulfur, which effectively eliminates the polysulfide dissolution issue and ensures good cycling stability.

Guo et al. further explored the electrochemical behavior of micropore-confined sulfur from the perspective of the existing forms of sulfur in the micropores [42]. According to theoretical calculations of the dimensions of different sulfur forms ranging from S_2 to S_8 molecules, microporous carbons with pore size of $<0.5 \text{ nm}$ are only able to accommodate the chain-like S_{2-4} molecules, rather than the cyclic S_{5-8} molecules as their sizes are $>0.5 \text{ nm}$ along at least two dimensions and cannot

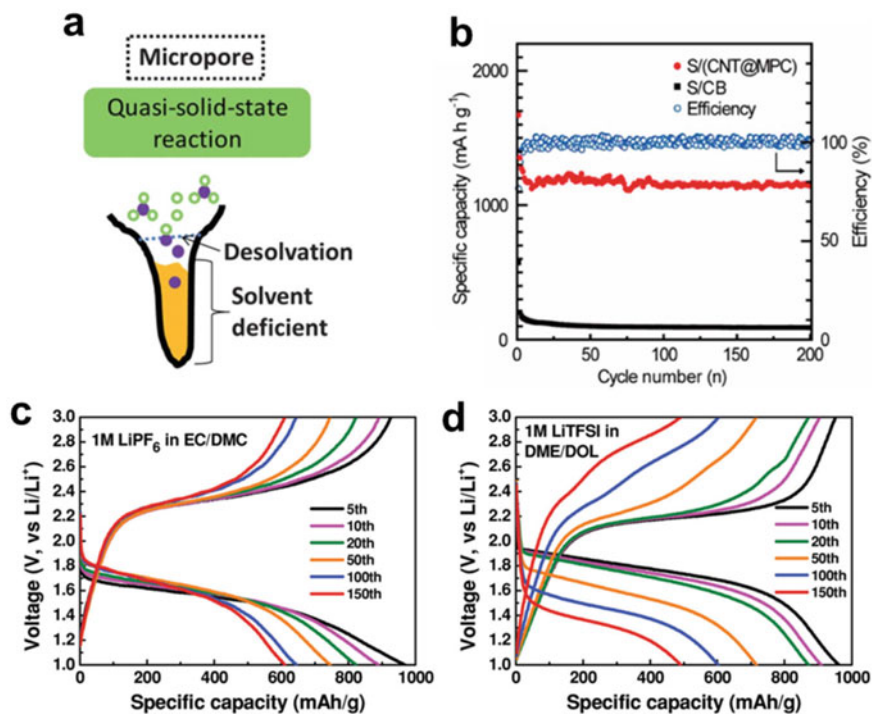


Fig. 2.4 **a** Illustration of the ion-desolvation mechanism for the quasi-solid-state reaction of sulfur confined in micropores (reproduced with permission by The Royal Society of Chemistry from [41]) **b** cycling performance and coulombic efficiency of sulfur-microporous carbon composite (S/CNT@MPC) cathode. S/CB referred to sulfur-carbon black composite (reproduced with permission by American Chemical Society from [42]) **c, d** Charge/discharge profiles of sulfur-microporous carbon composite cathodes at different cycles using **c** carbonate-based (EC/DMC) and **d** ether-based (DME/DOL) electrolytes (reproduced with permission by Wiley-VCH from [43])

fit such small micropores. Different from the cyclic sulfur molecules with high S–S bond rank, the chain-like sulfur molecules undergo direct solid to solid phase transition from S to Li₂S without the formation of polysulfide intermediates. Therefore, the polysulfide shuttle effect, which is considered as the main reason for capacity decay of the sulfur cathode, can be substantially inhibited, leading to high charge/discharge efficiency and exceptional cycling stability. As a result, the sulfur-microporous carbon composite cathode maintained high capacity retention rate and high coulombic efficiency after 200 cycles (Fig. 2.4b).

To obtain an in-depth understanding of the lithiation/delithiation mechanism of small S_{2–4} molecules confined in microporous carbons, Huang et al. explored the electrode mechanisms of the S_{2–4} molecule-based cathode from the perspective of electrolyte selection [43]. Two typical kinds of electrolytes were investigated, including ether-based and carbonate-based electrolytes. Ether-based electrolytes, using cyclic or linear ethers with ethoxy repeating units as the solvents, such as dimethyl ether

(DME) and 1,3-dioxolane (DOL), have been mostly used for Li–S batteries owing to their high solubility towards polysulfides. Carbonate-based electrolytes, using carbonate solvents such as ethylene carbonate (EC), dimethyl carbonate (DMC), and diethyl carbonate (DEC), commonly used in Li-ion batteries, are often considered not suitable for use in Li–S batteries because of the irreversible nucleophilic reactions between the carbonate solvents and sulfide anions. A microporous carbon with pore size of ~ 0.46 nm was used for accommodation of small S_{2-4} molecules. The differences in electrochemical behaviors of S_{2-4} in ether-based and carbonate-based electrolytes were systematically compared. It was found that, unlike the common cyclic sulfur molecules, the S_{2-4} molecules were able to perform good electrochemical properties in carbonate-based electrolytes (Fig. 2.4c), and the performance was even better than that in ether-based electrolytes (Fig. 2.4d). Therefore, the good cycling stability of S_{2-4} molecules can be explained by the synergic effect of small sulfur molecules, the microporous carbon matrix, and the electrolyte. First, the small micropores can physically prevent the contact between sulfur species and the electrolyte solvents, and the irreversible chemical reactions between carbonate solvents and nucleophilic sulfide anions can be avoided. Second, the short-chain structure of small S_{2-4} molecules gives rise to solid–solid reaction mechanisms without the formation of polysulfides. Third, the feasibility of using carbonate-based electrolytes in the S_{2-4} molecule-based cathode intrinsically eliminates the polysulfide dissolution and shuttle issues.

Based on the above discussions, it can be concluded that sulfur confined in microporous carbons has advantages of excellent cycling stability and good electrolyte compatibility. However, a large lithiation potential hysteresis can be observed in the discharge curve of the sulfur-microporous carbon composite cathode (Fig. 2.4c, d), resulting in low output voltage. This is indicative of additional energy required for overcoming the barrier for ion diffusion within the micropores. Meanwhile, low discharge cut-off voltage of 1 V versus Li^+/Li is often applied for full lithiation of sulfur confined in micropores, lower than the value of ~ 1.5 V versus Li^+/Li for sulfur confined in meso/macropores, which will be discussed in the following. Moreover, the sulfur content of sulfur-microporous carbon composite materials is mostly lower than 50 wt% owing to the low pore volume of microporous carbons for sulfur accommodation, which greatly offset the high-energy advantage of sulfur.

2.4.2 Meso/Macroporous Carbon

Meso/macroporous carbons with large pore sizes are beneficial for electrolyte penetration to facilitate lithium-ion transport for enhanced redox reaction kinetics [31, 44]. More importantly, large pore sizes render increased pore volumes that allow high sulfur content in the sulfur-meso/microporous carbon composite materials. As macroporous carbons with relatively open structures show insufficient adsorption capability toward polysulfides, they alone have been rarely utilized for the preparation

of sulfur composite cathodes [45]. In most cases, macropores are coupled with mesopores, serving the role of channeling the electrolyte for reduced lithium-ion diffusion distance during redox reactions, which will be discussed in the following sections. Sulfur-mesoporous carbon composite cathodes have been investigated extensively as they offer a reasonable balance between the capabilities of reaching high pore volume and trapping polysulfides via physical adsorption [46, 47].

A pioneering research work on sulfur-mesoporous carbon composite cathodes was the use of highly ordered mesoporous carbon (CMK-3) for sulfur nanofiller growth within the narrow mesoporous channels with uniform size of 3.3 nm (Fig. 2.5a), using melt-diffusion method at 155 °C [14]. The pore volume of the CMK-3 reached 2.1 cm³ g⁻¹, which enabled high sulfur content of 70 wt% in the sulfur-CMK-3 composite material. Owing to the uniform distribution of sulfur within the mesopores, the conductivity of the sulfur-CMK-3 composite material remained almost unchanged compared with that of the pristine CMK-3 (0.2 S cm⁻¹ vs. 0.21 S cm⁻¹). This indicated sufficient electrical contact between sulfur and the mesoporous carbon matrix, which guaranteed high sulfur utilization. The sulfur-CMK-3 composite cathode delivered the discharge capacity of 1005 mAh g⁻¹ along with high coulombic efficiency of 99.94% (Fig. 2.5b). Notably, its charge/discharge curves exhibited significantly decreased voltage polarization compared with that of the sulfur-microporous carbon composite cathode (Fig. 2.4c), indicating kinetically favorable sulfur redox reactions within the mesopores.

To explore the effect of mesopore size on the sulfur content, the specific capacity and cycling behavior of sulfur-mesoporous carbon composite cathode, Liu et al. systematically studied mesoporous carbons with tunable pore sizes (3, 7, 12, and 22 nm) and pore volumes (1.3–4.8 cm³ g⁻¹) for sulfur encapsulation [48]. The pore volume increased as the pore size increased, giving rise to increased sulfur content. Accordingly, a series of sulfur-mesoporous carbon composites using the four different mesoporous carbons were obtained with sulfur content ranging from 56 to 84 wt%. Notably, it was found that the sulfur-mesoporous carbon composite cathodes with different sulfur contents exhibited no significant difference in both the

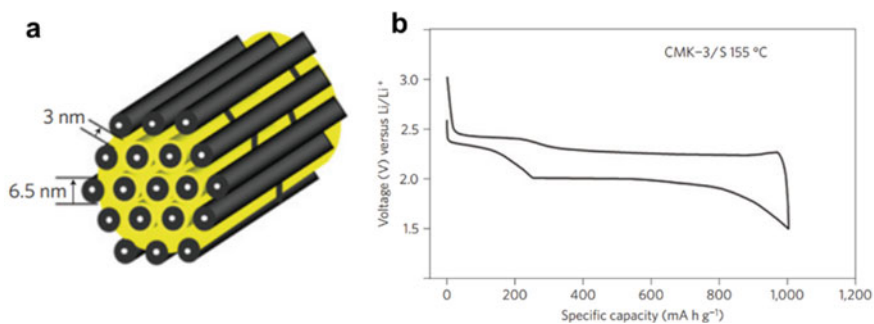


Fig. 2.5 **a** The schematic of sulfur (yellow) confined in the pore structure of mesoporous carbon, CMK-3. **b** Charge/discharge profiles of sulfur-CMK-3 composite cathode at current density of 168 mA g⁻¹ (reproduced with permission by the Nature Publishing Group from [14])

initial discharge capacity and capacity retention rate after 50 cycles (Fig. 2.6). These results could be explained by the fact that electrochemical reactions happen at the interface between sulfur and the conductive matrix, and sulfur within a certain range of the interface can participate in the electrochemical reactions and contribute to the capacity. When sulfur was fully encapsulated in the carbon mesopores, the intimate electrical contact between sulfur and the conductive carbon walls allowed sulfur to be electrochemically active, and the mesopores offered confining effect toward polysulfides to suppress their dissolution and migration. The similar discharge capacities and cycling stabilities of different sulfur-mesoporous carbon composite cathodes indicated that sulfur confined in these mesopores (3–22 nm) was within the electrochemical reaction range where sulfur exhibited a similar degree of electrochemical reactivity. This study suggested that mesoporous carbon with larger pore size and pore volume allowed an increased sulfur content along with uncompromised electrochemical performance, which contributed to increased overall capacity of sulfur–carbon composite cathode.

Besides the pore size distributions, the nanoscale morphology of mesoporous carbon is another important factor that determines the utilization efficiency of sulfur encapsulated in the mesopores, especially at high cycling current densities. Schuster et al. synthesized spherical ordered mesoporous carbon nanoparticles of 300 nm in diameter with 2D hexagonal mesostructured (Fig. 2.7a) [49]. The mesoporous carbon material has bimodal pore size distribution of small and large mesopores of 3.1 nm and 6 nm, rendering pore volume of $2.32 \text{ cm}^3 \text{ g}^{-1}$ and specific surface area of $2445 \text{ cm}^2 \text{ g}^{-1}$. Compared with bulk mesoporous carbon, the sulfur composite electrodes prepared from nano spherical mesoporous carbon exhibited obviously increased specific capacities (Fig. 2.7a), which could be largely attributed to the nanoscale morphology. The small particle size of the spherical mesoporous carbon allowed sulfur to distribute homogeneously at nanoscale, which could aid in highly efficient charge transfer and greatly enhanced the electrochemical behavior of the corresponding sulfur composite electrode.

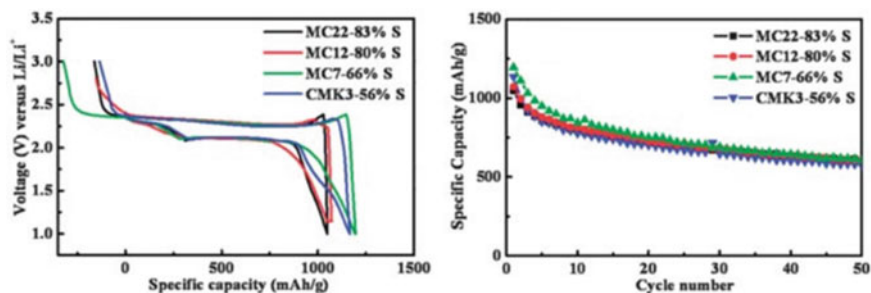


Fig. 2.6 Charge/discharge curves (left) and cycling stabilities (right) of sulfur-mesoporous carbon composite cathodes with different sulfur contents. The CMK-3, MC7, MC12, and MC22 refer to the mesoporous carbons with pore sizes of 3 nm, 7 nm, 12 nm, and 22 nm, respectively (reproduced with permission by The Royal Society of Chemistry from [48])

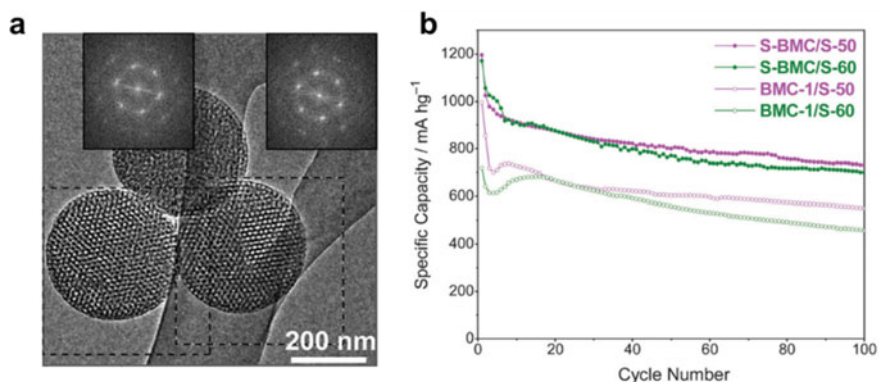


Fig. 2.7 **a** TEM micrograph of spherical ordered mesoporous carbon nanoparticles showing the 2D-hexagonal structure. **b** Comparison of cycling performance at 1675 mAh g^{-1} of sulfur composite electrodes prepared from nano spherical mesoporous carbon (BMC) and bulk mesoporous carbon (BMC-1) (reproduced with permission by Wiley-VCH from [49])

According to the above discussions, in comparison to micropores, meso/macropores are beneficial in achieving high sulfur content owing to the larger pore sizes and higher pore volume. However, the large pore sizes have lower adsorption capability toward polysulfides than microporous, leading to inferior cycling stability of the sulfur cathode. In terms of electrolyte selection, sulfur-meso/macroporous carbon composite cathodes require the use of ether-based electrolytes that have high solubility toward polysulfides, rather than the carbonate-based electrolytes used for most sulfur-microporous carbon composite cathodes. Advantages and disadvantages of meso/macropores and micropores of carbon in sulfur-porous carbon composite cathodes are summarized in Table 2.2, including the comparisons of adsorption capability, pore volume, sulfur content, electrolyte, overall cathode capacity, cycling stability and output voltage. It is worth noting that the marked “high” and “low” in Table 2.2 refer to the relative comparison between meso/macropores and micropores.

Table 2.2 Advantages and disadvantages of meso/macropores and micropores of carbon in sulfur-porous carbon composite cathodes

	Meso/macropores	Micropores
Adsorption capability	Low	High
Pore volume	High	Low
Sulfur content	High	Low
Electrolyte	Ether-based	Carbonate-based
Overall cathode capacity	High	Low
Cycling stability	Low	High
Output voltage	High	Low

2.4.3 Hierarchical Porous Carbon

As summarized in Table 2.1, it is difficult to simply determine the optimal pore size of carbon for use in the sulfur cathode as different pore sizes show different advantages in different aspects. To combine and make full use of the advantages of different pores, efforts have been devoted to designing hierarchical porous carbons that contain various pores, where different pores serve different roles during the sulfur redox reactions [39, 50–52]. Basically, micropores provide a high specific surface area for efficient adsorption of migrating polysulfides, and meso/macropores offer sufficient pore space for improved sulfur content and facilitate electrolyte penetration for rapid ion transport kinetics. Various hierarchical porous carbons, with micro-mesopores, meso-macropores, or micro-meso-macropores, have been explored to optimize the electrochemical properties of the sulfur cathode, including sulfur content, sulfur utilization, cycling stability, and output voltage [9, 32].

The pioneering research work that demonstrated the effect of micro-mesoporous carbons in the sulfur cathode utilized sulfur/bimodal porous carbon composite as the cathode material [53]. A porous carbon with uniform distribution of mesopores of 7.3 nm was synthesized through soft-template method, followed by potassium hydroxide activation process to create microporosity of less than 2 nm to the existing mesopores without deterioration of the integrity of the original mesoporous carbon. The hierarchically structured sulfur–carbon composite cathode exhibited improved cycling stability and sulfur utilization, compared to the cathodes with porous carbons containing micropores or mesopores only. However, the electrochemical performance showed significant degradation when the sulfur content in the sulfur-porous carbon composite material was increased to 50 wt%, probably owing to the insufficient pore volume that failed to provide essential electrical contact for high sulfur content. Inspired by this work, more bimodal porous carbons were fabricated via double-template approach to directly create pores with sizes split into ~2 nm and ~6 nm [54, 55]. The collaboration of bimodal pores resulted in high surface area over 2100 cm² g⁻¹ and large pore volume up to 2.0 cm³ g⁻¹. The small pores aided in suppressing the diffusion of polysulfides in the electrolyte, and the large pores favored fast ion transport during cycling, contributing to improved cycling stability and rate capability with sulfur content of 60 wt% in the sulfur-bimodal porous carbon composite.

Another approach to create micro-mesoporous carbons was to externally coat thin microporous carbon layer on the surface of mesoporous carbon to fabricate core–shell meso-microporous carbon materials as sulfur container [56]. In this architecture, the “core” with mesopores provided high pore volume to promise sufficient sulfur loading and high sulfur utilization, while the “shell” with micropores acted as a physical barrier to suppress the diffusion of polysulfides for improved cycling stability (Fig. 2.8a). The obtained sulfur–carbon composite with sulfur content of 61 wt% retained high capacity retention rate of 80 wt% after 200 cycles (Fig. 2.8b), which demonstrated the effectiveness of tailored combination of meso-micropore structure.

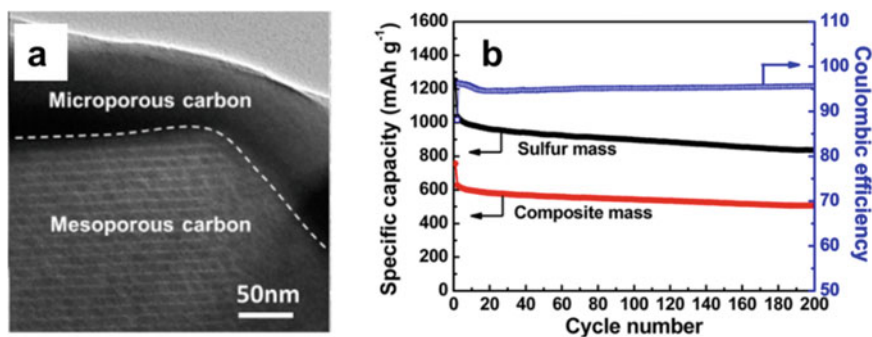


Fig. 2.8 **a** TEM image of the core-shell meso-microporous carbon. **b** Cycling performance of the sulfur-meso-microporous carbon composite cathode over 200 cycles at 0.5 C (reproduced with permission by American Chemical Society from [56])

As discussed in Sect. 2.4.2, macropores are often used in combination with mesopores owing to their inferior adsorption capability for polysulfide interception. This has inspired the design of hierarchical meso-macroporous carbons. For example, hierarchically ordered porous carbon (HOPC) with mesoporous walls and interconnected macropores was prepared by self-assembly of 350 nm colloidal poly(methyl methacrylate-butyl acrylate-acrylic acid) spheres and 9 nm silica spheres with sucrose as the carbon source and sulfuric acid as the catalyst [57]. The obtained HOPC had narrow mesopore size distribution of ~ 9 nm and macropore size of ~ 300 nm (Fig. 2.9a), with specific area of $850 \text{ cm}^2 \text{ g}^{-1}$ and pore volume of $1.4 \text{ cm}^3 \text{ g}^{-1}$. The mesopores walls of the HOPC encapsulated sulfur in highly dispersed state to inhibit aggregation of sulfur and generate essential electrical contact. The open and interconnected macropores allowed good penetration of electrolytes to promote the ion transport kinetics during redox reactions (Fig. 2.9b). The sulfur-HOPC composite cathode delivered high initial specific capacity of 1200 mAh g^{-1} and stable capacity

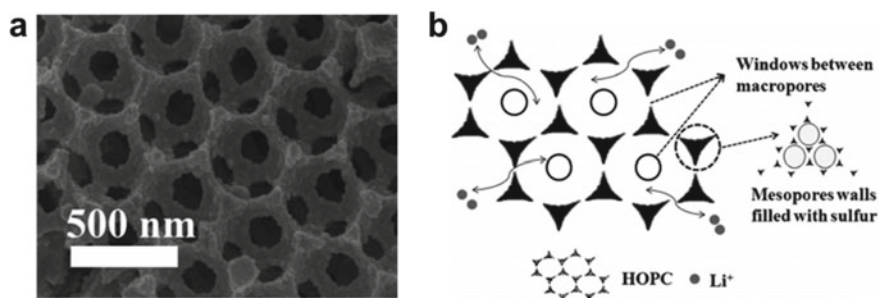


Fig. 2.9 **a** SEM image of the sulfur-hierarchically ordered porous carbon composite material. **b** Illustration of the sulfur redox process within the sulfur-hierarchically ordered porous carbon composite cathode (reproduced with permission by Wiley-VCH from [57])

of 884 mAh g⁻¹ after 50 cycles. It was anticipated that the electrochemical properties of S-HOPC composite cathode could be further optimized by modulating the nanopore structure of the HOPC.

To maximize the unique functions of different pores in sulfur cathode, hierarchical porous carbons that integrate micro-meso-macropores have been extensively studied [58–61]. Wei et al. reported a hierarchically structured porous carbon derived from pig bones, with abundant pores with diameters in three regions: 0.6–2.0, 2–10, and 10–100 nm [59]. The obtained micro-meso-macroporous carbon had specific surface area of 2160 cm² g⁻¹ and pore volume of 2.26 cm³ g⁻¹. With sulfur content of 63 wt%, the sulfur-micro-meso-macroporous carbon composite cathode exhibited initial discharge capacity of 1265 mAh g⁻¹, which is about 76% of the theoretical specific capacity of sulfur. Jung et al. fabricated hierarchical porous carbon sphere by ultrasonic spray pyrolysis using sucrose as carbon source and sodium carbonate and base catalyst for the efficient decomposition of sucrose [58]. The obtained hierarchical porous carbon spheres had meso- and macropores surrounded by outer micropores. The specific surface area was 2160 cm² g⁻¹, the micropores accounted for ~39% of the total pore volume (0.93 cm³ g⁻¹). Sulfur was mostly infiltrated in the inner meso- and macropores, while the outer micropores served as barrier to inhibit the dissolution and diffusion of intermediate polysulfides (inset in Fig. 2.10). At low current density of 100 mA g⁻¹, the sulfur hierarchical porous carbon composite cathode delivered high initial discharge capacity of 1412 mAh g⁻¹, and it maintained a capacity retention rate of 77% after 500 cycles at a current density of 4 A g⁻¹ (Fig. 2.10).

Overall, hierarchical porous carbons are beneficial to take full advantage of potential merits and circumvent limitations of different porous structures. Generally, the high surface area of porous carbons is mostly contributed by micropores, which, on one hand, enables high adsorption effect, yet on the other hand, leads to sluggish reaction kinetics. While meso/macropores allow good electrolyte penetration

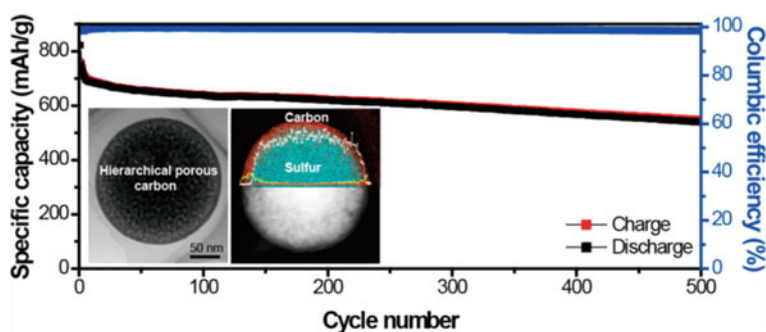


Fig. 2.10 Long-term cycling performance and coulombic efficiencies of the sulfur-hierarchical porous carbon composite cathode at current density of 4 A g⁻¹. Inset shows the TEM image and corresponding elemental maps showing the distribution of sulfur within the hierarchical porous carbon (reproduced with permission by American Chemical Society from [58])

for fast ion transport kinetics but have inferior adsorption capability. Combination of different pores can cause synergistic effects of their unique merits, contributing to further improved electrochemical behavior of the sulfur-porous carbon composite cathode.

2.4.4 *Hollow Porous Carbon*

Hollow porous carbons have structural features of large internal cavity volumes and porous outer shells, which provide them with the following merits as sulfur host: (1) maximizing the amount of sulfur sequestered by the hollow structure, (2) minimizing the polysulfide dissolution and migration in the electrolyte, (3) accommodating the volumetric expansion of sulfur during lithiation, (4) preserving good accessibility of lithium ions to the sequestered sulfur by facilitating good electrolyte penetration, (5) ensuring good conductivity for improved utilization of the poorly conducting sulfur [62, 63]. Basically, hollow porous carbon spheres belong to hierarchical porous carbons, where the interior void space provides macropores and the outer shell provide meso- and micropores [64]. The synthetic methods of hollow porous carbons often use the templating concept, including hard-templating, soft-templating, and self-templating strategies. The hard-templating strategy involves typical etching process for selective removal of the sacrificial hard template to create the internal void spaces (Fig. 2.11a), which is the most popular approach to fabricate hollow porous carbon materials. The soft-templating strategy usually employs the surfactant-stabilized micelles or microdroplets as templates (Fig. 2.11b). This route can produce fabricate hollow porous carbon materials without template removal process, as most surfactants are thermally decomposable. The self-templating strategy is often implemented by directly carbonizing hollow structured carbon precursors (Fig. 2.11c). Therefore, one advantage of hollow porous carbons over other hierarchical porous carbon is their highly controllable structural parameters of pore structures, morphologies, and components. Much effort has been devoted to designing sulfur-hollow porous carbon composites that allow for a high sulfur content while still maintaining high sulfur utilization and good cycling stability [65–68].

The pioneering work using hollow porous carbons for sulfur cathode was reported by Archer et al., using hard template method [19]. The obtained hollow porous carbon spheres had internal void size of ~200 nm, and specific surface area of 648 $\text{cm}^2 \text{g}^{-1}$ with 3 nm average pore size on the carbon walls. Sulfur was infiltrated in internal void space via vapor phase infusion process, resulting in sulfur content of 70 wt%. The sulfur-hollow porous carbon composite cathode could maintain a high reversible capacity of ~1000 mAh g^{-1} over 100 cycles at current density of 850 mA g^{-1} . Nazar et al. investigated the effect of different shell porosity of hollow porous carbon nanospheres (PCNS, Fig. 2.12a, b) on the electrochemical behavior of the sulfur composite cathode [69]. Three kinds of PCNS with different shell porosity were fabricated, denoted as low porosity, moderate porosity, and high porosity, respectively (Fig. 2.12c). It was found that the initial discharge capacities of

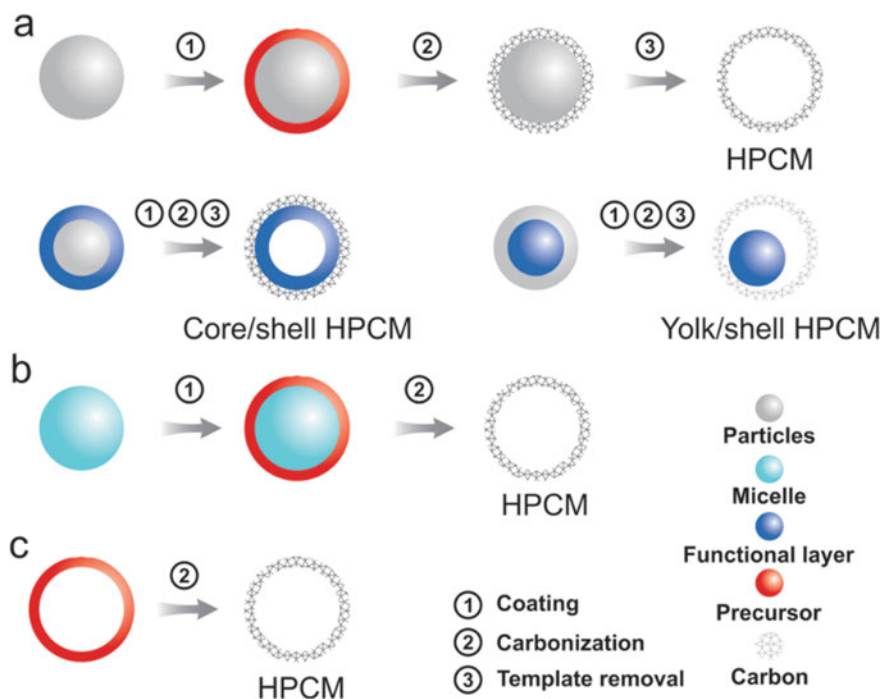


Fig. 2.11 Schematic illustrations of typical synthetic methods of hollow porous carbon materials (HPCM): **a** hard-templating strategy, **b** soft-templating strategy, **c** self-templating strategy (reproduced with permission by Wiley-VCH from [62])

the S-PCNS composite cathodes increased with shell porosity. This could be ascribed to the more uniform distribution of sulfur within the PCNS with higher shell porosity that gave rise to higher capillary force during sulfur infiltration. However, in the case of the most porous shell, despite the highest initial discharge capacity, the cell suffered the most severe capacity degradation, presumably owing to the structural instability of the carbon shells with large porosity. With sulfur content of 70 wt% in the S-PCNS composite material, the optimized sulfur electrode using PCNS with moderate shell porosity exhibited good cycling stability at various current densities (Fig. 2.12d). This work demonstrated the significance of tuning the porosity and maintaining intact carbon shells of hollow porous carbons in achieving both high specific capacity and stable cycling behavior of the sulfur cathode. Xiao et al. systematically studied three kinds of hollow carbon spheres with pore sizes of 4.1, 3.2, and 2.8 nm, respectively, to elucidate the effect of pore sizes on sulfur confinement [70]. When the pore size was 2.8 nm, sulfur that impregnated into the internal void of the hollow carbon could remain stable under the scanning transmission electron microscopy (STEM), which provided visible evidence that sulfur could be confined well within the porous carbon shell. In comparison, when the pore size was 4.1 or 3.2 nm, the preloaded sulfur

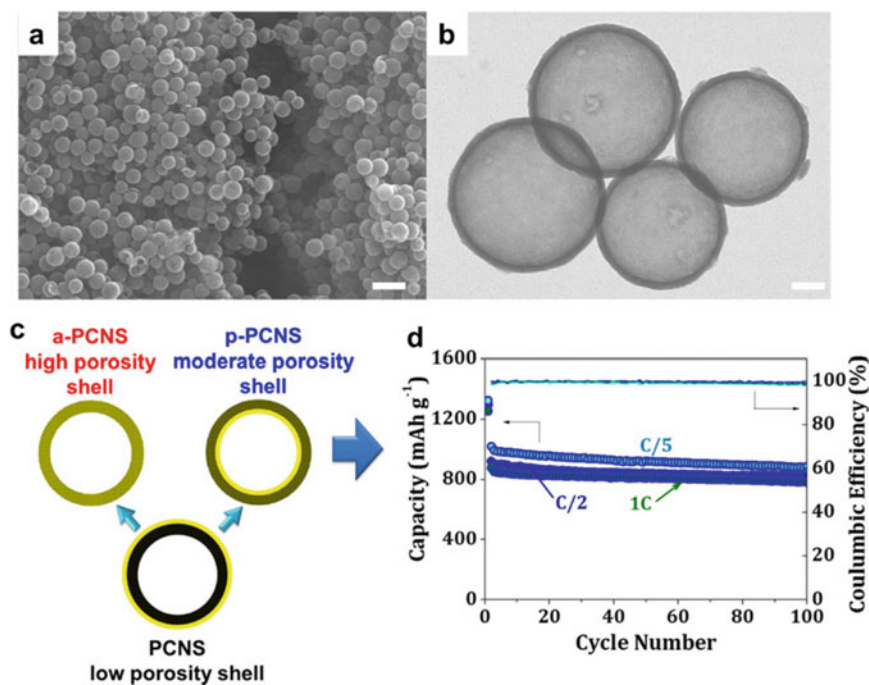


Fig. 2.12 **a** SEM image and **b** TEM image of the hollow porous carbon nanospheres. Scale bars: 400 nm (**a**) and 50 nm (**b**). **c** Illustrations of hollow porous carbon nanospheres with low porosity, moderate porosity, and high porosity shells. **d** Cycling performance of the sulfur electrode using PCNS with moderate shell porosity at different current densities (reproduced with permission by American Chemical Society from [69])

in the hollow carbon easily sublimed under STEM. Correspondingly, the sulfur-hollow porous carbon composite cathode with the 2.8 nm pore size delivered the best cycling stability and coulombic efficiency, indicating good polysulfide restriction effect. These results revealed that decreasing the pore size of the hollow porous carbon shells could provide strong confining effect towards both sulfur and polysulfides and thus contributes to improved electrochemical performance of the sulfur cathode.

Besides the single-shelled hollow porous carbons, multi-shelled porous carbons have also been designed and fabricated for sulfur infiltration [71]. Lou et al. developed double-shelled hollow porous carbon spheres using hollow SnO₂ as the hard template and glucose as the carbon precursor [72]. The double shells connected by carbon “links” formed highly porous structure with specific surface area of 748 cm² g⁻¹ and pore volume of 1.69 cm³ g⁻¹ (Fig. 2.13). The sulfur-double-shelled hollow porous carbon composite material was designed to host high amount of sulfur, suppress the outward diffusion of dissolved polysulfides, and buffer the volumetric changes of the active materials upon cycling. Zheng et al. employed multiple coating strategies for the synthesis of hollow-in-hollow-structured porous carbon spheres

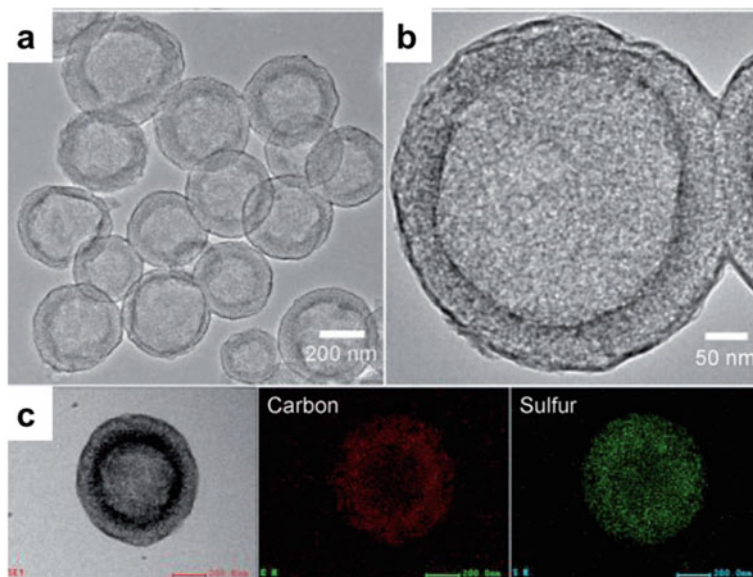


Fig. 2.13 a, b TEM image of the sulfur-double-shelled hollow porous carbon composite. c TEM image and corresponding elemental maps of a single sulfur-double-shelled hollow porous carbon sphere (reproduced with permission by Wiley-VCH from [72])

[73]. With similar porosities, the sulfur-hollow-in-hollow porous carbon composite cathode exhibited better cycling stability than that with single-shelled hollow porous carbon spheres. The improved performance could be ascribed to the double outer carbon shells that provided an enhanced interception effect to trap the polysulfides generated from the inner core of the hollow carbon sphere.

2.5 Sulfur–Graphene Composite Cathode

Graphene is a two-dimensional (2D) allotrope of carbon consisting of one-atom thick 2D planar carbon sheets where the carbon atoms are hexagonally packed in regular sp^2 -bonded configuration. Graphene has advantageous physicochemical properties of large theoretical specific surface area ($2630 \text{ m}^2 \text{ g}^{-1}$), high electrical conductivity, and good mechanical strength and flexibility [74–76]. Modification or functionalization of the 2D planar graphene sheets leads to the formation of chemically modified graphene, such as graphene oxide and reduced graphene oxide [77–79]. Graphene oxide contains large amounts of oxygen-containing functional groups and structural defects on the carbon backbone. Typical oxygen-containing functional groups include carbonyl, epoxy, hydroxyl, and carboxyl [80]. Particularly, hydrogen-containing groups such as hydroxyl and carboxyl can be entirely

or partially removed by thermal or chemical reductions, resulting in the formation of reduced graphene oxide with improved conductivity [77, 81]. Therefore, chemically modified graphene has highly adjustable surface hydrophilicity and electrical conductivity. These features make graphene highly favorable to construct sulfur composite cathodes with advantages in the following aspects: (i) facilitating the electron transfer for insulating sulfur and lithium sulfides to improve the active material utilizations; (ii) immobilizing the migrating polysulfides to alleviate irreversible active material loss from the cathode; (iii) accommodating the volume variation of sulfur during cycling to prevent electrode pulverization [82–85].

When graphene is used for sulfur infiltration, the obtained sulfur–graphene composites typically exhibit two kinds of microstructures: graphene-wrapped sulfur particle (Fig. 2.14a) and sulfur molecules dispersed on graphene sheets (Fig. 2.14b) [86]. The lone pairs of the S $3p_z^2$ electrons can interact with the antibonding conjugated π^* states of the graphene plane (Fig. 2.14c), resulting in strong interaction between sulfur and graphene in their composite structure. Besides, the contact angle of liquid sulfur droplet on graphene substrate (reproduced with permission by The Royal Society of Chemistry from [86])

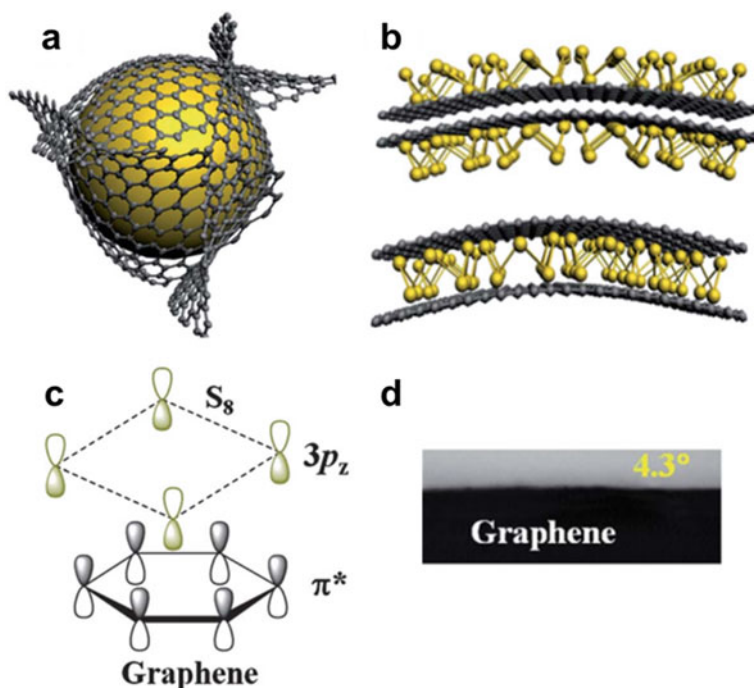


Fig. 2.14 Schematics illustrating two kinds of microstructures of sulfur–graphene composites: **a** graphene-wrapped sulfur particle and **b** sulfur molecules dispersed on graphene sheets. The octasulfur (S_8) molecule showing double-layer zigzag ring structure with four upper and four lower atoms is used for illustration. **c** Schematic of the electron orbit of sulfur and graphene. **d** The wetting property of liquid sulfur droplet on graphene substrate (reproduced with permission by The Royal Society of Chemistry from [86])

of liquid sulfur droplet on graphene substrate was found to be as small as 4.3° (Fig. 2.14d), indicative of strong interfacial interaction between the two materials [86]. This could be explained by the similar electronegativity of sulfur and carbon that gives rise to good wettability between them. Such strong interactions ensure intimate electrical contact of sulfur with the conductive graphene matrix, contributing to improved electrochemical activity of sulfur during redox reactions.

2.5.1 Conductive Graphene

The planar feature of graphene inspired the design of sandwich-like structure comprising of alternating graphene sheets and sulfur nanoparticle layers [87]. This structure enabled uniform distribution of sulfur particles within the graphene matrix at sulfur content of 72 wt%. The obtained sulfur–graphene cathode retained capacity retention rate of 75% over 100 cycles. Taking advantage of the high flexibility of graphene sheets, Dai et al. reported the synthesis of sulfur–graphene composite material by wrapping submicrometric sulfur particles with graphene sheets decorated by carbon black nanoparticles [25]. The graphene coating served to accommodate volume expansion of the coated sulfur particles during discharge, trap the dissolved polysulfide intermediates and provide essential electrical contact for the sulfur particles. The resulting sulfur–graphene composite cathode delivered a specific capacity of $\sim 600 \text{ mAh g}^{-1}$ over 100 cycles. In another approach, sulfur–graphene composite with sulfur content up to 87 wt% was obtained by heterogeneous nucleation of sulfur on graphene sheets through one-pot in-situ acid oxidation of sodium polysulfide species (Fig. 2.15a) [88]. The sulfur particles were completely enfolded by the graphene sheets (Fig. 2.15b), which served as an electrical conduit for insulating sulfur and barrier to retard polysulfide dissolution. It was found that large amounts of conductive additives were not required for efficient operation of such sulfur–graphene composite cathode, indicating the high efficiency of graphene for electron conduction. To further improve the conductivity of sulfur–graphene composites for improved sulfur utilization, Lin et al. reported the synthesis of low-defect graphene sheets through sulfur-assisted exfoliation of graphite [86]. The intimate interaction between sulfur and graphene, deriving from their similar electronegativities, was stronger than the *van der Waals* forces between the adjacent π - π stacked graphene layers. This led to exfoliation of the graphite layers when the sulfur molecules stuck to the surface and edges of the graphite, analogous to micromechanical exfoliation process. Meanwhile, sulfur molecules were uniformly anchored on the graphene sheets with sulfur content of 73 wt%. The exfoliated graphene exhibited high conductivity of 1820 S cm^{-1} , which suggested the low-defect feature of the graphene prepared from this approach. The obtained sulfur–graphene composite exhibited good electrochemical behavior at a high rate of 2 C.

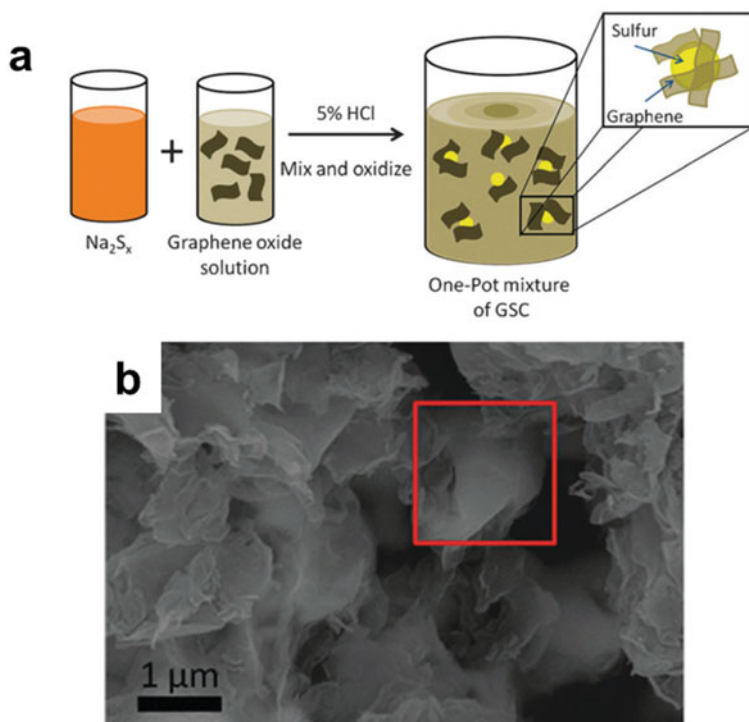


Fig. 2.15 **a** Schematic of the one-pot synthesis of the sulfur–graphene composite (GSC). **b** SEM image of the sulfur–graphene composite, the red square highlighted sulfur particles enveloped by graphene sheets (reproduced with permission by The Royal Society of Chemistry from [88])

2.5.2 Chemically Modified Graphene

The functional groups on chemically modified graphene can not only serve as active sites for uniform sulfur nucleation and growth but also render strong adsorbing ability to anchor polysulfides via chemical interactions [89]. It has been theoretically calculated that both epoxy and hydroxyl groups on the graphene oxide could increase the binding between sulfur atoms in polysulfides and carbon atoms in graphene due to the induced ripples by the functional groups (Fig. 2.16a) [90]. Therefore, the functional groups on graphene oxide exhibit good immobilization effect toward polysulfides, which effectively impede the irreversible active material loss caused by polysulfide dissolution and migration. A sulfur–graphene oxide composite was synthesized via a melt-diffusion method. The melted sulfur was diffused into the pores of the graphene oxide due to the strong adsorption effects derived from both the high surface area and the functional groups on the surface of graphene oxide, resulting in homogeneous distribution of sulfur within the graphene oxide (Fig. 2.16b, c). Meanwhile, the low temperature heat treatment process for sulfur infiltration could partially

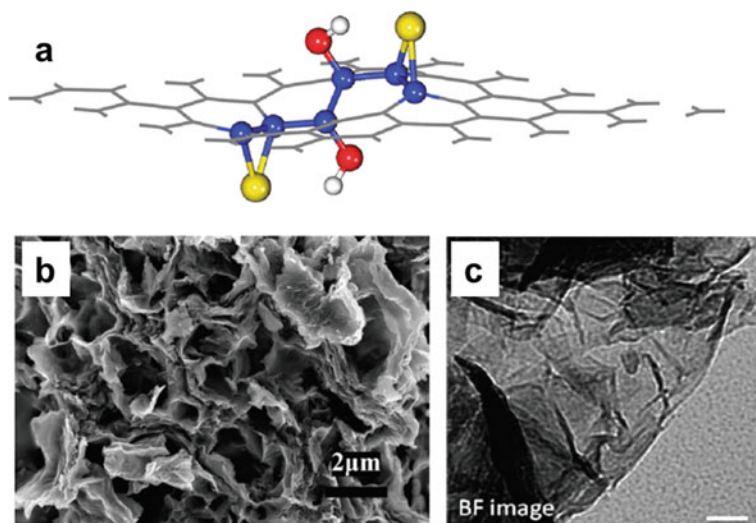


Fig. 2.16 **a** Representative pattern of graphene oxide immobilizing sulfur. The hydroxyl enhances the binding of S to the C–C bond due to the induced ripples by epoxy or hydroxyl group. Yellow, red, and white balls denote S, O, and H atoms, respectively, while the others are C atoms. The C atoms bonding to S or O are highlighted as blue balls. **b** SEM and **c** TEM images of the sulfur–graphene oxide composite. The scale bar in (c) is 50 nm (reproduced with permission by American Chemical Society from [90])

remove or chemical modify some of the functional groups on the graphene oxide surface, contributing to improved electronic conductivity of the sulfur–graphene oxide composite. The obtained sulfur–graphene oxide composite cathode demonstrated reversible capacity up to 1400 mAh g^{-1} and stable cycling behavior for more than 50 cycles at 168 mA g^{-1} . Rong et al. prepared sulfur–graphene oxide core–shell particles with different diameters ranging from 100 nm to $10 \mu\text{m}$ via a heterogeneous nucleation process [91]. The sulfur–graphene oxide composite cathode exhibited significant improvement in electrochemical performance over the sulfur particles without coating. A specific capacity of 800 mAh g^{-1} could be retained after 1,000 cycles at a current density of 1 A g^{-1} , indicating the effectiveness of graphene oxide in immobilizing the polysulfides for improved cycling stability.

2.5.3 Porous Graphene

Tailoring the nanopore structures of graphene has also proved an effective strategy to enhance the affinity of polysulfide intermediates within the sulfur–graphene composite cathode. Ding et al. created dense nanopores with size of $\sim 3.8 \text{ nm}$ on the surface of graphene through chemical activation process, rendering high specific surface area of $2313 \text{ m}^2 \text{ g}^{-1}$ (Fig. 2.17a) [92]. Sulfur was uniformly infiltrated into the

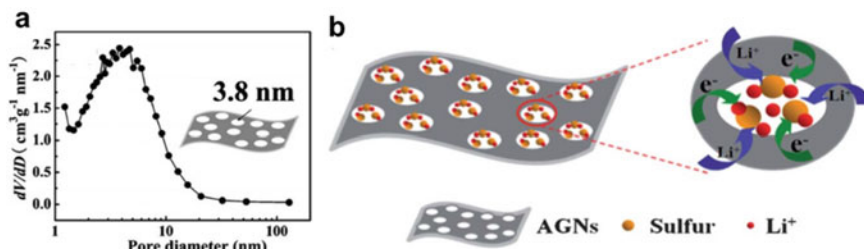


Fig. 2.17 **a** Pore size distributions of the activated graphene. **b** Schematic of the constrained redox reaction process within the sulfur-activated graphene composite (reproduced with permission by The Royal Society of Chemistry from [92])

nanopores of the activated graphene sheets with intimate electrical contact. During the sulfur conversion reactions, the nanopores could act as “micro-reactors” to suppress the migration of dissolved polysulfides while ensuring good electrolyte penetration for fast ion transport (Fig. 2.17b). The sulfur–graphene composite electrode delivered high initial capacity of 1380 mAh g^{-1} and maintained good cycling stability at different cycling rates. Guo et al. reported the use of activated graphene with hierarchical micro-mesopores as the sulfur host material [93]. The activated graphene had ultrahigh specific surface area of $3000 \text{ m}^2 \text{ g}^{-1}$, allowing a sulfur content of 75 wt%. The abundant pore structures with sizes ranging from 0.6 to 5 nm provided an effective adsorption effect toward polysulfides to inhibit their migration from the cathode matrix. The capacity retention of the obtained sulfur-porous graphene composite cathode could reach 76 wt% after 200 cycles at a current density of 1675 mA g^{-1} .

Considering the significance of developing high sulfur-loaded cathodes for high-energy-density Li–S batteries, graphene with high pore volume and high specific surface area has proved a promising conductive matrix to allow high sulfur content as well as high sulfur utilization and good cycling stability. Wang et al. reported the synthesis of highly crumpled graphene sheets via a simple thermally induced expansion strategy, rendering high pore volume of $5.4 \text{ cm}^3 \text{ g}^{-1}$ and specific surface area of $1158 \text{ cm}^2 \text{ g}^{-1}$ [94]. The highly crumpled graphene allowed high sulfur content of 80 wt% in the sulfur–graphene composite material and high areal sulfur loading of 5 mg cm^{-2} in the sulfur–graphene composite cathode. With such high sulfur content, the obtained sulfur–graphene composite exhibited uniform sulfur distribution without obvious sulfur agglomerates (Fig. 2.18). This indicated good electrical contact between sulfur and the conductive graphene sheets, which was beneficial for improved sulfur utilization. The sulfur-crumpled graphene composite cathode delivered high specific capacity over $1,200 \text{ mAh g}^{-1}$, along with high areal capacity of $\sim 5 \text{ mAh cm}^{-2}$ over 100 cycles. In another approach, highly porous graphene was prepared through thermal exfoliation of graphite oxide, leading to high pore volume of $3.5 \text{ cm}^3 \text{ g}^{-1}$ with broad pore size distribution ranging from 1 to 60 nm [34]. A sulfur-highly porous graphene composite with sulfur content of 80 wt% was obtained, where sulfur was uniformly encapsulated within the pore structures of graphene. Based on the use of the sulfur-highly porous graphene composite as

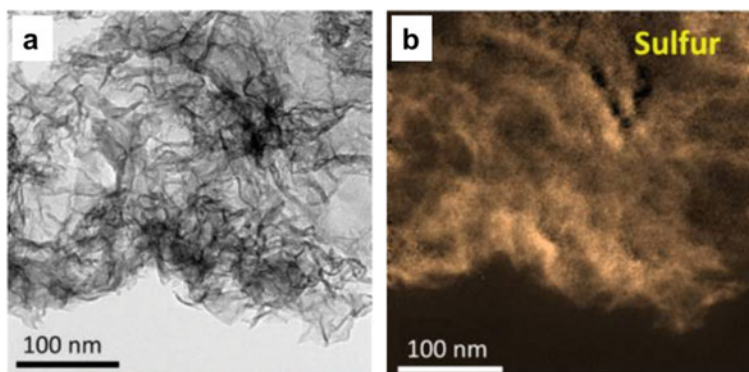


Fig. 2.18 **a** TEM image of the sulfur-encrusted graphene composite and **b** the corresponding elemental map of sulfur (reproduced with permission by American Chemical Society from [94])

the cathode material, all graphene cathode structure was further proposed for the sulfur cathode, with highly conductive graphene as the current collector and partially oxygenated graphene as a polysulfide-adsorption layer. This cathode design enabled a 5 mg cm^{-2} sulfur-loaded cathode showing both a high specific capacity of 1500 mAh g^{-1} and a high areal capacity of 7.5 mAh cm^{-2} .

Based on the above discussion, graphene can have a variety of characteristics and properties due to its different preparation routes. The conductivity, surface hydrophilicity, pore sizes, pore volumes, and morphologies of graphene are highly tunable to serve different functions in a sulfur–graphene composite cathode. These functions include improving the electrochemical activity of the electroactive sulfur, providing immobilization effect for polysulfides, accommodating the volume variations, and increasing the sulfur loading in the cathode, leading to significantly enhanced electrochemical performances of the sulfur–graphene composite cathode.

2.6 Sulfur–Carbon Nanotube Composite Cathode

Carbon nanotubes (CNTs) are one-dimensional (1D) carbon nanomaterials with large aspect ratio, which are generally divided into two categories: single-walled CNTs (SWCNTs) and multi-walled CNTs (MWCNTs) [95]. They have merits of high conductivity, good mechanical properties, and thermal stabilities. The 1D structural features of CNTs can provide long-range and interconnected electron paths through the electrode, contributing to significantly improved active material utilization [6, 96–100]. In early studies, CNTs were used as a conductive additive in sulfur cathode [101]. It was found that the 1D MWCNTs could provide a more efficient electron conductive network than the traditional conductive additives, such as carbon black nanoparticles, resulting in improved cycle life and rate capability. However, MWCNTs were not compatible with the conventional slurry-coating method for

cathode preparation, as it was difficult to disperse MWCNTs homogeneously in the cathode slurry [97]. Afterward, it was suggested that the low surface tension of melted sulfur could give rise to good wetting ability on the surface of CNTs [102], which greatly inspired the design of various sulfur–CNT composites.

2.6.1 Sulfur-Coated Carbon Nanotubes

Sulfur could be uniformly coated on the surface of CNTs via the melt-diffusion method [103–108]. Yuan et al. prepared sulfur-coated MWCNT composite material with core–shell structure [104]. The MWCNTs served as the core to provide electron conduction pathways for the coated sulfur. The sulfur–MWCNT composite cathode showed obviously enhanced cycling stability compared with the sulfur cathode using MWCNT as conductive additive. This work revealed the significance of uniform sulfur distribution on CNTs in promoting the electrochemical performances of sulfur–CNT composite cathode. Zhang et al. designed composite cathode containing sulfur–SWCNT coaxial nanocables prepared by melt-diffusion process [108]. Although the SWCNTs existed in bundles owing to the *van der Waals* interactions, the sulfur phase could still be uniformly distributed within the bundles (Fig. 2.19a). After sulfur infiltration, the micropores and mesopores of SWCNTs were occupied by sulfur, leading to decrease in the pore volume from 1.72 to 0.01 $\text{cm}^3 \text{g}^{-1}$ (Fig. 2.19b). This ensured good encapsulation of sulfur within the SWCNT conductive matrix. Benefiting from the large aspect ratio, high specific surface area, and interconnected electron pathways of the SWCNTs, the sulfur–SWCNT composite cathode exhibited good rate capabilities up to 10 C with sulfur content of 56 wt%.

Considering the significance of constructing high sulfur-loaded cathode, it is of great importance to fabricate sulfur–CNT composites with high sulfur content while preserving essential electrical contact. Li et al. proposed a theoretical model to investigate how different CNTs affect the sulfur content in sulfur–CNT composite [109].

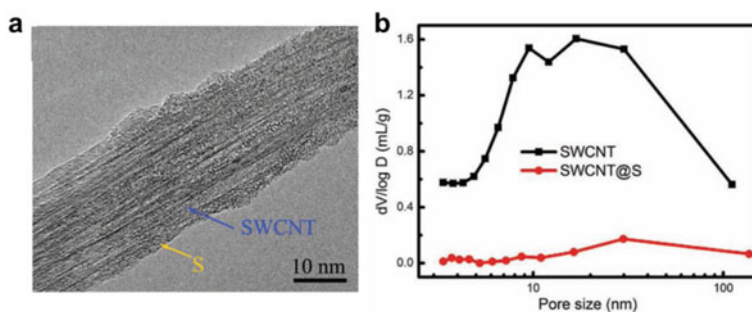


Fig. 2.19 **a** TEM image of the sulfur–SWCNT coaxial nanocables. **b** Pore size distributions of the SWCNT and sulfur–SWCNT coaxial nanocables sphere (reproduced with permission by Wiley-VCH from [108])

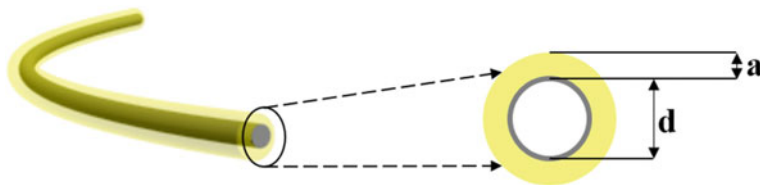


Fig. 2.20 Schematic for the calculation of the theoretical sulfur content in sulfur-coated CNT (reproduced with permission by Elsevier from [109])

Assuming that the sulfur–CNT composite has core–shell structure (Fig. 2.20), the theoretical sulfur content varies along with different CNT diameters. The relationship between the sulfur content ($S_{wt}\%$) and the CNT diameter (d) and sulfur coating thickness (a) can be concluded by the following formula:

$$S_{wt}\% = \frac{\rho_s * (4a^2 + 4ad)}{\rho_{CNT} * d^2 + \rho_s * (4a^2 + 4ad)}$$

where ρ_{CNT} represents the density of CNTs (taking 1.2 g cm^{-3} as typical value [110]) and ρ_s the density of sulfur (2.07 g cm^{-3}). It could be calculated that when the sulfur coating thickness on the CNTs was $\sim 3 \text{ nm}$, the theoretical sulfur content was only 54 wt% for CNTs with diameter of $\sim 20 \text{ nm}$, with this value drastically increasing to 90 wt% for CNTs with diameter of $\sim 4 \text{ nm}$. These results indicated that the diameter of CNTs largely determines the sulfur content. CNTs with small diameters show high electron conduction efficiency as they are capable to hold high sulfur content with short electron diffusion distance, which is desirable for achieving high sulfur utilization with high sulfur content.

Based on the above theoretical results, the ultralight SWCNT film with interconnected network structure was designed as conductive matrix for sulfur impregnation [109]. The diameter of the SWCNTs was only 2–3 nm, which rendered high sulfur content of 95 wt% with sulfur coating thickness of $\sim 6 \text{ nm}$ on the SWCNTs (Fig. 2.21). The high conductivity of the SWCNT network facilitated fast electron transport, and the interwoven network structure enabled effective polysulfide trapping during sulfur redox reactions. High initial discharge capacity of 1280 mAh g^{-1} was achieved at current density of 0.25 A g^{-1} , indicating high sulfur utilization. When the areal sulfur loading was increased to 7.2 mg cm^{-2} by stacking three layers of the sulfur-SWCNT composite electrode, high areal capacity of 8.6 mAh cm^{-2} was obtained.

2.6.2 Sulfur-Encapsulating Carbon Nanotubes

Apart from being coated on the exterior surface of CNTs, sulfur can also be encapsulated within the hollow interior of CNTs for better confinement effect [111–113]. Moon et al. developed the encapsulated sulfur–CNT composite cathode via vapor

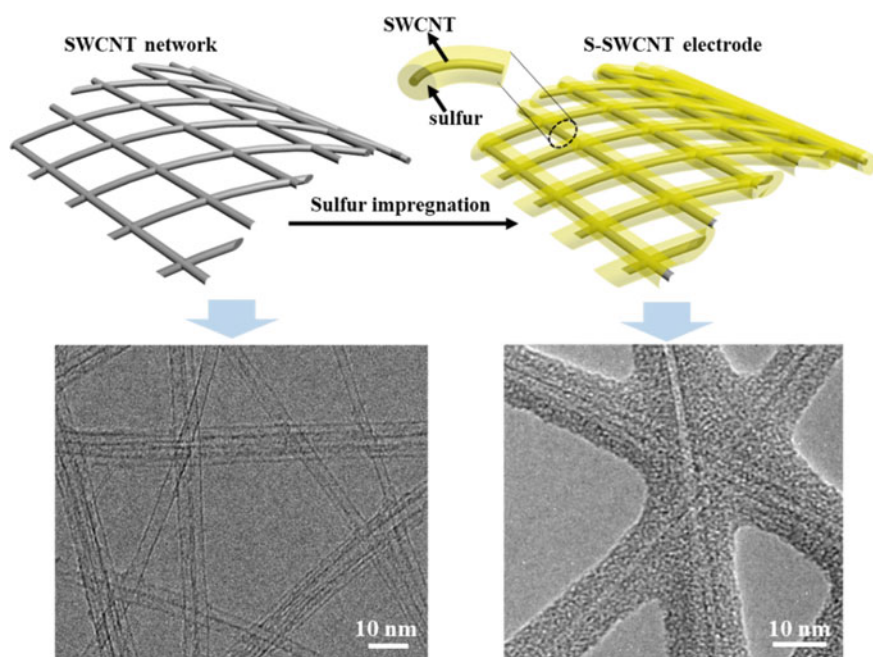


Fig. 2.21 Illustrations of the SWCNT network and the sulfur-SWCNT electrode with TEM images of the SWCNTs and the sulfur-SWCNT composite, respectively (reproduced with permission by Elsevier from [109])

phase infusion method by using the anodic aluminum oxide membrane as template for well-defined tube structures (Fig. 2.22a) [111]. Sulfur nanowires with diameter of ~ 75 nm were well encapsulated by the well-aligned CNT walls with a thickness of ~ 3 nm (Fig. 2.22b, c), leading to sulfur content of 81 wt% in the sulfur-CNT composite. The obtained freestanding sulfur-CNT composite cathode exhibited a high specific capacity of 1520 mAh g^{-1} , indicating that the CNTs contributed to improved electronic and ionic transport behavior for improved sulfur utilization. Particularly, the composite cathode exhibited exceptional rate capabilities. When the C rate was increased from 0.5 to 2 C, 76% of the original capacity (1234 mAh g^{-1}) could be retained. This could be ascribed to the nanostructured electrode design that facilitated short electron/ion pathways and thus ensured high electrochemical activity of the encapsulated sulfur.

2.6.3 Tube-in-Tube Structure

Wang et al. proposed CNT-based tube-in-tube structure with small-diameter CNTs (~ 20 nm) grown inside large-diameter CNT (~ 200 nm) for sulfur encapsulation

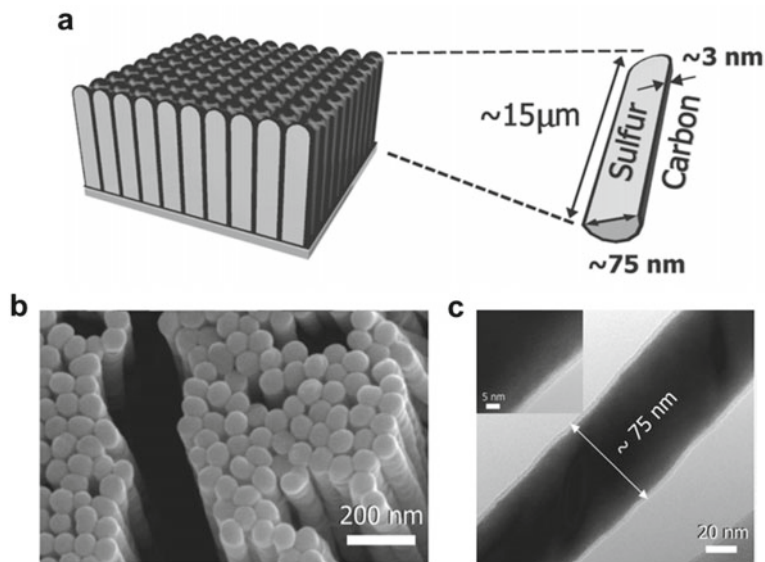


Fig. 2.22 **a** Illustration of the encapsulated sulfur–CNT composite. **b** SEM and **c** TEM images of the encapsulated sulfur–CNT composite (reproduced with permission by WILEY–VCH from [111])

(Fig. 2.23a) [114]. Sulfur was infiltrated into the hollow interior of the large-diameter CNT, and the small CNTs interlinked together and served as interconnected and embedded conductive network through the encapsulated sulfur (Fig. 2.23b). This gave rise to multiple electron transport pathways for fast electron transport kinetics during the sulfur redox reactions, highly desirable for high sulfur utilization. Moreover, the tube-in-tube structure could not only effectively alleviate the migration of polysulfide but also accommodate the volume variations of the active materials upon

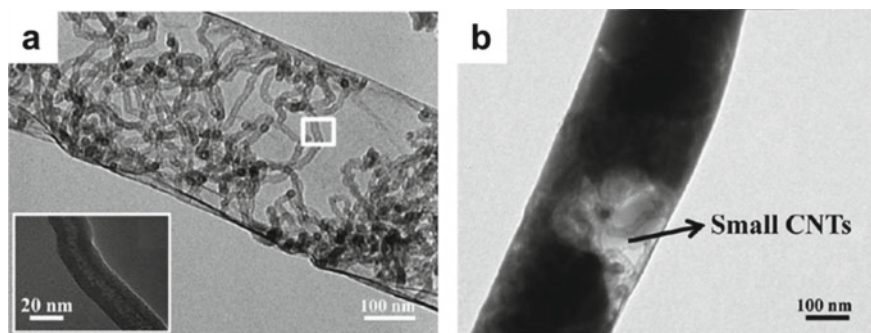


Fig. 2.23 TEM images of **a** the tube-in-tube CNTs and **b** the sulfur–CNT composite (reproduced with permission by American Chemical Society from [114])

cycling, contributing to improved cycling stability. With high sulfur content of 85 wt%, the sulfur–CNT composite cathode maintained high reversible specific capacity of $\sim 1,200 \text{ mAh g}^{-1}$ after 100 cycles. At high rate of 5 C, discharge capacity of 954 mAh g^{-1} could be stabilized after 150 cycles. The work demonstrated the effectiveness of novel structural design of sulfur–CNT composite cathode in achieving exceptional electrochemical performance with high sulfur content. In another approach, MWCNTs were encapsulated into the hollow interior of porous CNTs to obtain tube-in-tube structure for sulfur infiltration [115]. This structure could enhance the electrical conductivity, hamper the dissolution of lithium polysulfide, and provide large pore volume for sulfur impregnation. The obtained sulfur–CNT composite with 71 wt% sulfur content delivered high reversible capacity, good cycling performance as well as excellent rate capabilities. It remained a reversible capacity of 647 mAh g^{-1} at 2 A g^{-1} after 200 cycles. At high current density of 6 A g^{-1} , it delivered a capacity of 550 mAh g^{-1} .

2.6.4 Hierarchical CNT Network Structure

To improve the areal sulfur loading of sulfur–CNT composite cathode without sacrificing the sulfur utilization, Yuan et al. designed the hierarchical CNT network structure, using both short MWCNTs ($10\text{--}50 \mu\text{m}$) and long vertically aligned CNTs (VACNTs, $1000\text{--}2000 \mu\text{m}$) [116]. The short MWCNTs provide short range electrically conductive framework for sulfur impregnation, and the long VACNTs served as both long-range conductive network and interlinked mechanical scaffold (Fig. 2.24). With an areal sulfur loading of 6.3 mg cm^{-2} , the sulfur–CNT composite cathode retained reversible capacity of $\sim 700 \text{ mAh g}^{-1}$ after 150 cycles at current density of $0.38 \text{ mA mg cm}^{-2}$. When the areal sulfur loading was further increased to

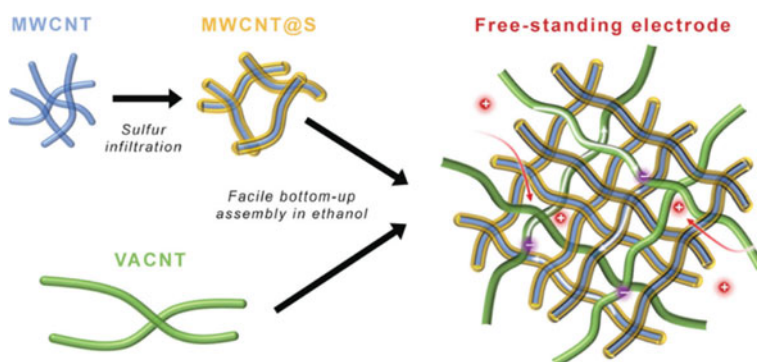


Fig. 2.24 Schematic of the hierarchical CNT network structure using both short MWCNTs and long vertically aligned CNTs (reproduced with permission by WILEY–VCH from [116])

17.3 mg cm⁻², high areal capacity of 15.1 mAh cm⁻² was achieved, indicating the high electron conduction efficiency of the hierarchical CNT network structure.

Therefore, the unique 1D nanotubular structure, good conductivity, and large aspect ratio of CNTs have proved effective in improving the electrochemical performance of sulfur–CNT composite cathodes. Sulfur can be either externally coated on the surface or impregnated inside the hollow interior of CNTs to gain good electrical contact for improved electrochemical activity. The self-weaving behavior of CNTs not only provides interconnected conductive framework for sulfur redox reactions but also enables restriction effect for the migrating polysulfides to prevent them from shuttling. The tubular hollow structure of CNTs can buffer the volume variation of sulfur during cycling. Moreover, the electrochemical behavior of sulfur–CNT composite cathodes can be further optimized by integrating CNTs with different structural features, which have shown great promise in constructing high sulfur-loaded cathodes.

2.7 Sulfur–Carbon Fiber Composite Cathode

Carbon fibers have 1D morphological characteristics similar to CNTs but without well-defined graphitic structure. The diameter of carbon fibers can range from hundreds of nanometers to several micrometers, with or without hollow voids [117]. Like CNTs, carbon fibers can interweave together to form long-range and interconnected conductive network to facilitate fast electron transport for sulfur redox reactions [118–121]. One favorable feature of carbon fibers is that various pores, including micro-, meso-, and macropores, can be created along their fibrous structure through various techniques [122–127]. As discussed in Sect. 2.4, pore structures have advantages including enabling uniform sulfur dispersion in the carbon matrix, trapping the migrating polysulfides, and permitting good electrolyte penetration [128]. Combining with the high electron conduction efficiency of the interwoven network structure, carbon fibers have been considered a promising sulfur host to fabricate sulfur–carbon fiber composite cathodes with improved electrochemical performances.

Zhang et al. reported the use of porous carbon fibers prepared by electrospinning polyacrylonitrile/poly(methyl methacrylate) mixture followed by carbonization process [129]. Polyacrylonitrile was used as the precursor for carbon fibers, while poly(methyl methacrylate) served as sacrificial template create pores in the fiber walls. After sulfur infiltration, sulfur-porous carbon fiber composite was obtained with sulfur content of 42 wt%. At low current density of 84 mA g⁻¹, the obtained composite cathode delivered discharge capacity of ~1400 mAh g⁻¹, indicating good electrical contact between sulfur and the porous carbon fibers. To achieve high sulfur content, efforts have been made to increase the porosity of carbon fibers to improve their capability for sulfur accommodation [126, 130–132]. Yang et al. fabricated hierarchically porous carbon fibers using metal–organic framework (MOF) as the precursor [126]. Carbonization of the microporous MOF precursor mainly produced

microporous carbons. While the metal ions in MOF could be reduced to the corresponding metal that subsequently served as the inner templates to form mesopores. Macropores could be formed owing to the synergic effect of organic material decomposition and gas activation during carbonization. Therefore, the obtained carbon fibers had hierarchical pores with specific surface area of $1906 \text{ m}^2 \text{ g}^{-1}$. The 1D cross-linking fibrous structure and the hierarchical pore structures contributed to fast transport for electrons and lithium ions during cycling and provided confinement effect for the dissolved polysulfides (Fig. 2.25). With sulfur content of 60 wt%, the sulfur-porous carbon fiber composite electrode demonstrated low capacity decay rate of 0.076% per cycle when cycled at a current density of 8.4 A g^{-1} over 500 cycles. Zhou et al. reported the synthesis of highly porous carbon fibers derived from polypyrrole with high specific surface area of $2642 \text{ m}^2 \text{ g}^{-1}$ [132]. The sulfur content could be increased to 77 wt% in the sulfur-carbon fiber composite. At a current density of $1,675 \text{ mA g}^{-1}$, the specific capacity of the obtained sulfur-carbon fiber composite cathode stabilized at 666 mAh g^{-1} after 200 cycles.

In attempts to construct sulfur cathodes with improved areal sulfur loading, Doron et al. reported the use of microporous activated carbon fibers in the form of monolithic carbon cloth for the preparation of binder-free sulfur cathode [133]. The active carbon fiber cloth had specific surface area of $2,000 \text{ m}^2 \text{ g}^{-1}$, which decreased to $1,200 \text{ m}^2 \text{ g}^{-1}$ after sulfur impregnation. Comparisons of the pore size distributions before and after sulfur incorporation revealed that sulfur was mainly encapsulated within the small micropores on the carbon fibers while large pores were preserved for electrolyte penetration (Fig. 2.26a). The sulfur-active carbon fiber composite exhibited smooth surface morphology (Fig. 2.26b), indicating well-confined sulfur within the nanopores of the active carbon fibers. With areal sulfur loading of 6.5 mg cm^{-2} , the sulfur-active carbon fiber composite cathode retained a reversible discharge capacity more than 800 mAh g^{-1} after 80 cycles. This work demonstrated the effectiveness of freestanding carbon fiber cloth in improving sulfur utilizations at high areal sulfur loading. However, as the non-hollow carbon fibers with large diameter of ($\sim 15 \mu\text{m}$) were densely packed in the monolithic structure, the areal density of the carbon fiber

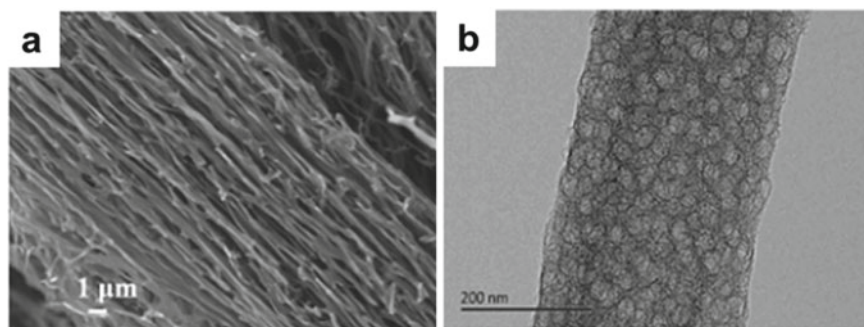


Fig. 2.25 **a** SEM and **b** TEM images of the hierarchically porous carbon fiber (reproduced with permission by The Royal Society of Chemistry from [126])

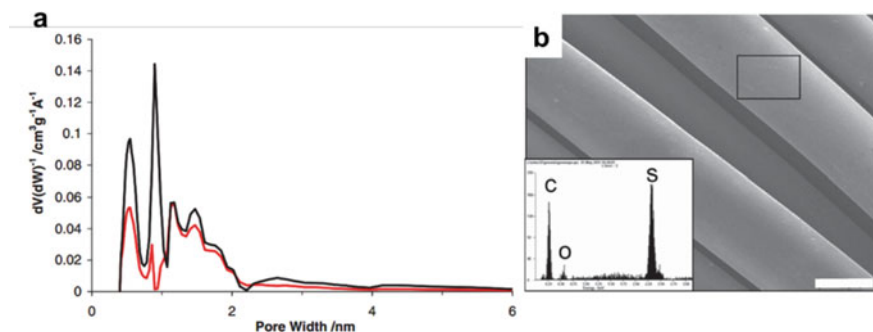


Fig. 2.26 **a** Pore size distributions of the activated carbon fiber cloth before (black) and after sulfur impregnation (red). **b** SEM image of the sulfur-activated carbon fiber composite (scale bar: 10 μm). The inset gave the Energy-dispersive X-ray spectroscopy (EDS) results of the area marked by the black squares (reproduced with permission by WILEY–VCH from [133])

cloth used in this work was as high as 13 mg cm^{-2} . This led to low sulfur content of 33.3 wt% in the sulfur–carbon fiber composite cathode, which might compromise both the gravimetric and volumetric energy densities of the Li–S cell.

Accordingly, Miao et al. reported the synthesis of hollow carbon fiber cloth by simply carbonizing cotton cloth [134]. Despite the similar densely packed structure as those in Fig. 2.26, the hollow structure of the carbon fibers led to obviously lower areal density of 4.8 mg cm^{-2} . The hollow carbon fibers with diameter of $\sim 7 \mu\text{m}$ presented in compact bundles were densely woven into an interconnected conductive network (Fig. 2.27a, b). Sulfur could be infiltrated inside and outside of the carbon fibers while ensuring uniform distribution (Fig. 2.27c), which guaranteed good electrical contact. A sulfur–carbon fiber composite cathode with areal sulfur loading of 6.7 mg cm^{-2} delivered high areal capacity of $\sim 7 \text{ mAh cm}^{-2}$. In another approach, hollow carbon fiber foam with low areal density of 4 mg cm^{-2} was synthesized by the carbonization of natural cotton [27]. Distinct from the compact structure introduced above, sufficient void space, tens of micrometers in size, was generated by the randomly interconnected hollow carbon fibers (Fig. 2.28a, b). Sulfur–carbon nanotube–carbon black clusters (90 wt% sulfur) were incorporated in the void space of the carbon fiber foam to fabricate the sulfur–carbon fiber composite electrode. The interconnected carbon fiber skeleton was capable of holding high, uniformly distributed concentration of the active materials within the interconnected void structures (Fig. 2.28c, d), enabling a high areal sulfur loading up to 21.2 mg cm^{-2} . The sulfur–hollow carbon fiber composite exhibited high areal capacity of 12.0 mAh cm^{-2} after 50 cycles with high sulfur loading of 16.5 mg cm^{-2} , indicating the high efficiency of the carbon fiber skeleton in promoting the sulfur redox reactions.

Qie et al. proposed facile layer-by-layer strategy for sulfur–carbon fiber composite cathodes with high areal capacities [135]. Freestanding porous carbon fiber layers with thickness of $\sim 60 \mu\text{m}$ were fabricated through vacuum filtration of commercial carbon fiber powers followed by chemical activation process (Fig. 2.29a).

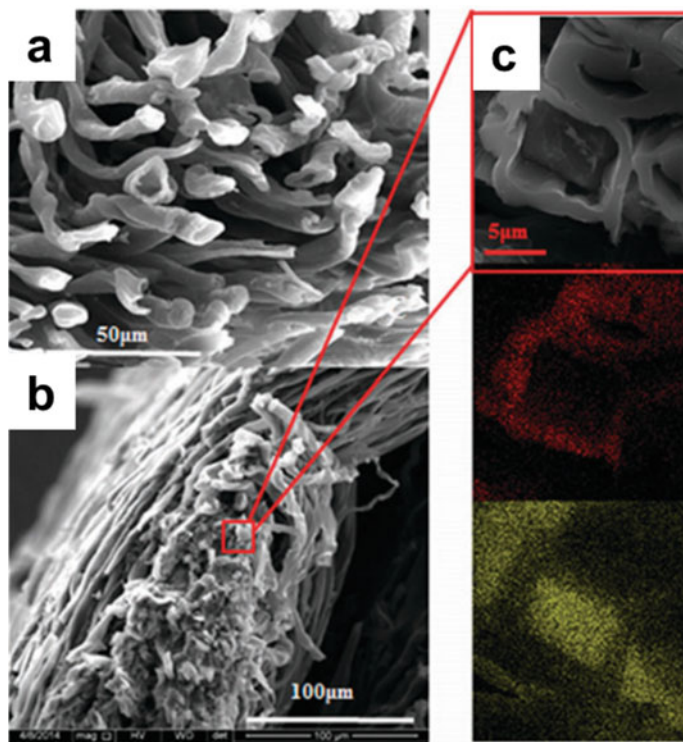


Fig. 2.27 a, b SEM images of the sulfur-hollow carbon fiber composite. c EDS maps of the cross-section of a sulfur-hollow carbon fiber (red: carbon, yellow: sulfur), with areal sulfur loading of 6.7 mg cm^{-2} (reproduced with permission by The Royal Society of Chemistry from [134])

Commercial sulfur powders were directly splinted between the porous carbon fiber layers (Fig. 2.29b). The areal sulfur loading could be easily increased by increasing the sulfur and porous carbon fiber layers. The porous carbon fiber layer provided interconnected conductive scaffold that not only facilitated fast electron transport but also effectively trap dissolved polysulfides within the cathode. The rate capability of the sulfur-porous carbon fiber composite cathode with three sulfur layers (5.7 mg cm^{-2}) exhibited no obvious degradation compared to that with one sulfur layer (1.9 mg cm^{-2}) (Fig. 2.29c). Moreover, the areal sulfur loading could be further increased to 11.4 mg cm^{-2} with six sulfur layers, leading to a high areal capacity of 11.3 mAh cm^{-2} .

Overall, carbon fibers can be prepared from various approaches with different structures and morphologies. Their 1D structural features can form interwoven conductive network with high electron conduction efficiency. Various pore structures can be created on the surface of carbon fibers to facilitate uniform sulfur infiltration and enable restriction effect toward migrating polysulfides. Moreover, carbon fibers can be easily assembled into freestanding and monolithic structure to fabricate

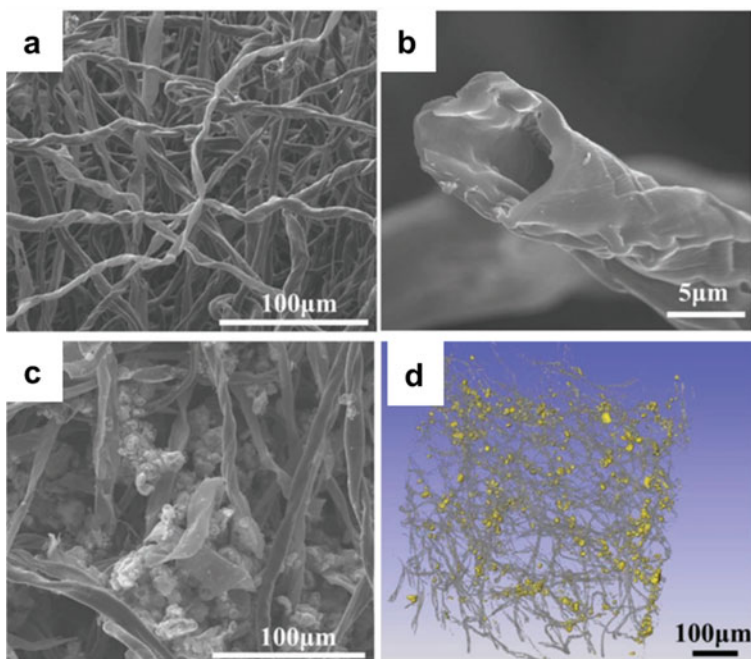


Fig. 2.28 a, b SEM images of the hollow carbon fiber foam. c SEM image and d 3D X-ray microtomography (XRM) image of the sulfur-hollow carbon fiber composite with areal sulfur loading of 10.8 mg cm^{-2} (reproduced with permission by WILEY-VCH from [27])

sulfur cathodes without additional conductive additives or binders. This has shown high effectiveness in constructing high sulfur-loaded cathodes that are desirable for high energy density of Li–S cells.

2.8 Sulfur-Functionalized Carbon Composite Cathode

The dissolution and migration of polysulfide intermediates in the electrolyte are known to cause the issues including fast capacity decay, high self-discharge rate, and low coulombic efficiency [12, 136, 137]. Therefore, introducing polysulfide immobilization sites within the sulfur cathode is requisite for achieving long-term stabilities of Li–S batteries [4, 5, 138, 139]. As discussed in the previous sections, carbon materials have shown effectiveness in polysulfide immobilization mainly by the adsorption effect derived from the pore structures. Nevertheless, from the perspective of fundamental chemistry, both sulfur and carbon both exhibit non-polar symmetric structures, while polysulfides have polar structures [140, 141]. The polar nature of polysulfide leads to relatively weak interaction with the non-polar carbon

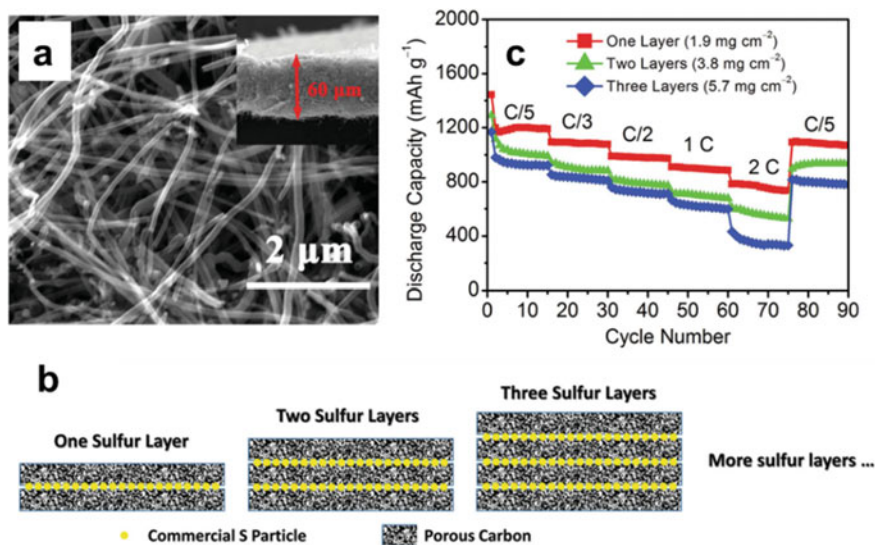


Fig. 2.29 **a** SEM image of the porous carbon fiber layers (inset showing the side view). **b** Schematic of the layer-by-layer sulfur-porous carbon cathodes. **c** Rate capabilities of sulfur-porous carbon cathodes with different layers (reproduced with permission by WILEY-VCH from [135])

matrix, which may offset the restriction effect of the pore structures toward polysulfides. It is worth mentioning that chemically modified graphene with oxygen-containing functional groups on the surface was found able to render chemical interactions with polysulfides for enhanced immobilization effect, as discussed Sect. 2.5. Therefore, adjusting the surface hydrophilicity of carbon materials is an effective approach to improve the interaction between polysulfides and the carbon matrix. This has triggered substantial research efforts on developing sulfur-functionalized carbon composite cathode [4, 142, 143]. Functionalization of carbon materials can modify their surface chemistry to render improved interactions with polysulfides to impede the polysulfide migration. Functionalization strategies mainly contain three categories: polymer decoration [144–147], heteroatom doping [148–152], and functional groups grafting [153–156].

2.8.1 Polymer Decoration

Nazar et al. adjusted the hydrophilicity of the carbon external surface by functionalizing the surface of the sulfur-mesoporous carbon composite with polyethylene glycol (PEG) coating layer [14]. The PEG-functionalized surface served to trap the polysulfide species by providing highly hydrophilic surface chemistry, resulting in improved cycling stabilities of the sulfur cathode. To visualize the evolution of interfacial interaction of carbon and sulfur upon lithiation, Cui et al. implemented ex-situ

TEM observations of sulfur-hollow carbon fiber composite cathode before and after electrochemical discharge [157]. Sulfur was initially encapsulated within the hollow voids of carbon fibers with good uniformity owing to the good wettability between sulfur and carbon (Fig. 2.30a). After discharging to 1.7 V, separation of the discharge product lithium sulfide from the carbon was obviously observed (Fig. 2.30b). While it is known that sulfur undergoes volume expansion after lithiation owing to the lower density of lithium sulfide than that of sulfur. The observed volume shrinkage in Fig. 2.30c indicated that the polysulfide intermediates had leaked out from the hollow carbon fibers through the opening tips. This could be ascribed to the weak interaction between polar polysulfides and non-polar carbon. The segregated polysulfides from the conductive matrix would lose electrical contact and cause capacity decay of the sulfur-hollow carbon fiber composite cathode. To improve the interaction between polysulfides and the carbon matrix, amphiphilic polyvinylpyrrolidone (PVP) was used to modify the interfacial properties of the hollow carbon fibers. After polymer functionalization, the encapsulated sulfur remained attached to the walls of hollow carbon fibers (Fig. 2.30d), indicating the effectiveness of the PVP polymer in stabilizing the polysulfides within the carbon fiber. Theoretical calculations were

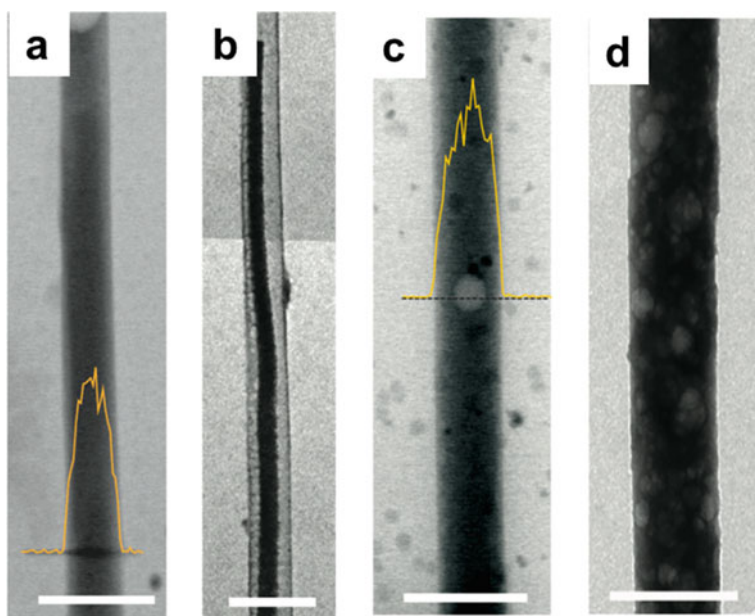


Fig. 2.30 **a** TEM image of the sulfur-hollow carbon fiber composite before discharge. **b** TEM image of the sulfur-hollow carbon fiber composite after fully discharge to 1.7 V. **c** TEM image of the sulfur-modified hollow carbon fiber composite before discharge. **d** TEM image of the sulfur-modified hollow carbon fiber composite after fully discharge to 1.7 V. The yellow line in **(a)** and **(c)** represented the EDS counts of the sulfur signal along the dark line. The scale bars are 500 nm (reproduced with permission by American Chemical Society from [157])

performed to study how the interaction between sulfur and carbon changes upon lithiation, and it was found that the binding energy between lithium sulfide and carbon experienced significant decrease. With the presence of PVP on the surface of carbon fibers, the lithium atoms in polysulfides could bind to the oxygen atoms in the PVP polymer, rendering increased binding energies between polysulfides and the carbon fibers. As a result, the PVP-modified sulfur-hollow carbon fiber composite electrode exhibited obviously improved cycling performance with a capacity retention rate of 80% over 300 cycles.

In order to minimize the influence of polymer decoration on the conductivity of the sulfur-carbon composite, Yang et al. proposed the use of conducting polymer poly(3,4-ethylenedioxythiophene)-poly(styrene sulfonate) (PEDOT:PSS) to modify the surface chemistry of the sulfur-porous carbon composite (Fig. 2.31a) [158]. PEDOT:PSS was uniformly coated on the surface of the porous carbon with thickness of several nanometers (Fig. 2.31b, c), serving as barrier layer to intercept polysulfides inside the porous carbon matrix. The polymer was also found between the porous carbon particles, acting as conductive binder to improve the adhesion between the particles (Fig. 2.31b). With the assistance of PEDOT:PSS coating, the capacity retention rate of the sulfur-porous carbon composite cathode was improved from 70 to 80% over 100 cycles, along with 10% increase in the discharge capacity. The coulombic efficiency was also improved from 93 to 97%. In another approach,

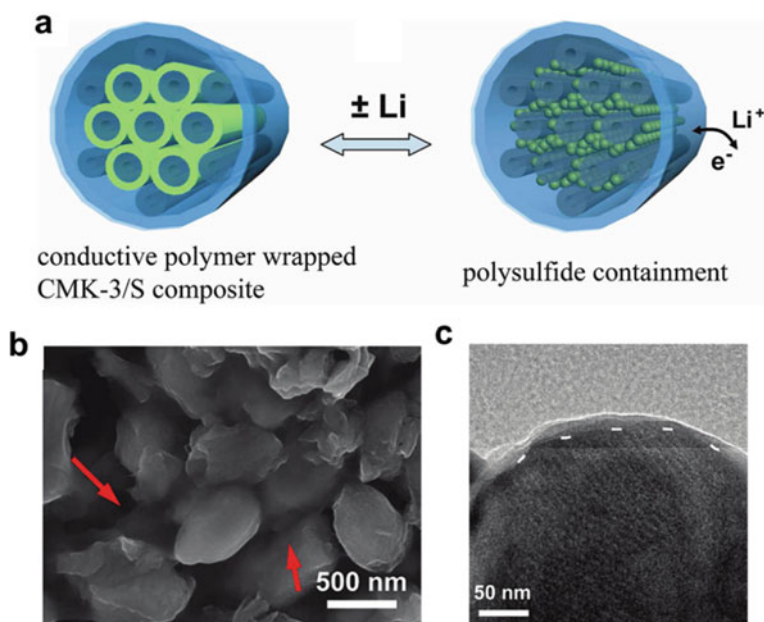


Fig. 2.31 a Schematic of the lithiation/delithiation processes of the PEDOT:PSS-coated porous carbon/sulfur composite. b SEM image and c TEM image of the PEDOT:PSS-coated porous carbon/sulfur composite (reproduced with permission by American Chemical Society from [158])

conducting polymer, polyaniline (PANI), was used to modify the surface properties of MWCNTs for enhanced interaction with polysulfides [159]. A sulfur-MWCNT composite was prepared by precipitating sulfur on MWCNTs via chemical reaction, followed with uniform surface coating of PANI. The presence of PANI on the surface not only helped mitigating the dissolution and diffusion of polysulfides but also provided additional electrical contact of sulfur coated on the MWCNTs. The PANI-modified composite cathode exhibited both improved cyclic stability and rate capability.

2.8.2 Heteroatom Doping

Modifying the carbon surface with heteroatom doping has been considered as effective approach to render strong chemical reaction with lithium polysulfides to minimize their diffusion in the electrolytes [160–162]. In this respect, nitrogen (N) doping has been most extensively studied [160, 161, 163–166]. Hou et al. performed systematic density functional theory calculation to investigate the effect of different doping atoms on the binding behaviors between the carbon matrix and polar lithium polysulfides [167]. Several rules of favoring strong anchoring effect for doped carbons were proposed: (1) the doping atom should have lone pair of electrons to serve as Lewis base to interact with the Lewis acidic lithium polysulfide; (2) the electronegativity of the doping atom should be higher than C to allow permanent dipole moment at the local doping site. Meanwhile, the radius of the doping atom oughts to be sufficiently small to pair with lithium to facilitate electrostatic dipole–dipole interaction; (3) the doping atom that forms π bond with the conjugated system should be capable of accepting additional charge from the π electrons to strengthen the dipole–dipole interaction; (4) the bond between the doping atom and the carbon matrix should have high bond stability. Based on these considerations, nitrogen was found most effective for monodoping, compared with other atoms, including oxygen (O), boron (B), fluorine (F), sulfur (S), phosphorus (P) and chlorine (Cl). The improved interaction strength of polysulfides with the N-doped carbon matrix can alleviate irreversible active material loss caused by the polysulfide diffusion and shuttle effect, contributing to improved cycling stabilities of the sulfur–carbon composite cathode.

Zhang et al. constructed sulfur-N-doped graphene composite where sulfur particles were wrapped inside the N-doped graphene sheets (Fig. 2.32) [168]. The role of the N dopants in immobilizing lithium polysulfides was confirmed by ab initio calculations. The results showed that N-doped graphene bind lithium polysulfides more strongly compared with the primitive graphene case, owing to the strong ionic attractions between N and Li atoms. This contributed to the alleviated dissolution of lithium polysulfides in the electrolyte, thereby improving the cycling stability of the sulfur-/N-doped graphene composite cathode. Peng et al. synthesized N-doped CNTs as conductive host for sulfur impregnation [169]. Conductivity measurements showed that the N-doped CNTs maintained good conductivity (798 S m^{-1}) compared with the pristine CNTs (1185 S m^{-1}). The positively charged lithium in the lithium

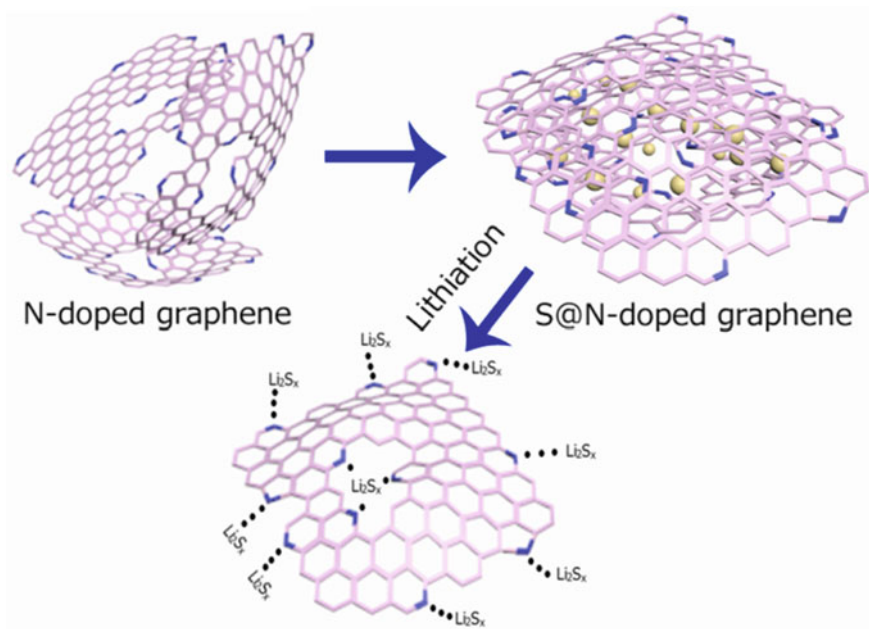


Fig. 2.32 Schematic of the sulfur-N-doped graphene composite and the effect of N dopants for polysulfide trapping (reproduced with permission by American Chemical Society from [168])

polysulfides could be adsorbed by negatively charged N dopants, leading to good polysulfide immobilization effect. The strong chemical adsorption effect as well as the high conductivity of the N-doped CNTs led to highly reversible and stable electrochemical performances, with high specific capacity of 1370 mAh g^{-1} and capacity retention rate over 70% during 200 cycles.

Yin et al. implemented comprehensive computational study to provide the fundamental understanding on the origin of the effective anchoring of lithium polysulfides by N-doped carbon materials [170]. It was shown that pyridinic and pyrrolic N dopant in graphene could render stronger binding energy with lithium polysulfides, compared to the graphitic N dopants. This could be ascribed to the existence of lone pair electrons in their atomic structures. They could serve as electron donors to bind with positively charged lithium in lithium polysulfides. Moreover, it was found that clustered pyridinic N dopants could further improve the binding energy with lithium polysulfides to effectively impede their migration and shuttling effect. The strong binding energies could derive from two aspects: (i) enhanced attraction between lithium ions in lithium polysulfides and pyridinic N-dopants and (ii) additional attraction between the sulfur anions in lithium polysulfides and lithium ions captured by the pyridinic N dopants. These findings could guide the design of more effective N-doped carbons for sulfur-carbon composite cathodes with optimized electrochemical performance.

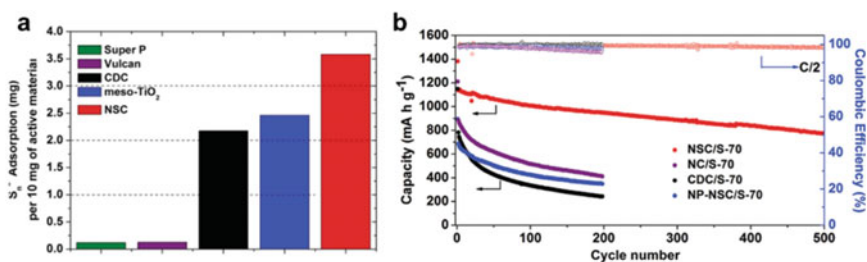


Fig. 2.33 **a** The polysulfide adsorptivity of non-doped carbon (CDC) and N, S dual-doped carbon (NSC), with comparison to Super P, Vulcan carbon, and commercial mesoporous TiO₂, evaluated by the electrochemical titration method ($n = 4$). **b** Comparisons of cycling stabilities of sulfur–carbon composite cathodes using different carbon matrix with sulfur content of 70 wt%. NC: N-doped carbon; NP-NSC: non-porous N, S dual-doped carbon (reproduced with permission by WILEY–VCH from [171])

Other than nitrogen monodoping, dual-doping strategy, using both nitrogen and other doping atoms, was proposed to further enhance the interaction of polysulfide with the carbon matrix [60, 171, 172]. Nazar et al. explored the use of N, S co-doped porous carbon as sulfur host material [171]. The dual doping of N and S atoms on the porous carbon was found able to greatly enhance the chemisorption of lithium polysulfides. Both the electrophilic Li⁺ and nucleophilic S_n²⁻ could be effectively bound to N, S dual-doped carbon, giving rise to doubled lithium polysulfide adsorptivity over N monodoping or non-doped carbons (Fig. 2.33a). Additionally, the electronic conductivity of the N, S dual-doped carbon was also greatly improved compared with non-doped carbon, favoring high-rate kinetics. The obtained sulfur–carbon composite cathode with dual dopants exhibited significantly improved specific capacity and cycling stabilities (Fig. 2.33b).

2.8.3 Functional Group Grafting

Grafting functional groups with polar features on the surface of carbon materials has also proved to be an effective way to enhance the affinity of polysulfides to the carbon matrix. A wide range of functional groups, such as hydroxyl, epoxy, carboxyl, sulfonate, amine, and amino, has been explored as chemical immobilizer grafted on the carbon matrix to impede the diffusion of polysulfides via polar–polar interactions [4]. These functional groups often consist of electronegative atoms with lone electron pairs in the outer *p* orbitals of their atomic structure, to serve as electron donors to interact with lithium polysulfides.

Manthiram et al. reported the use of hydroxylated graphene as substrate to produce sulfur–graphene nanocomposite [173]. The sonication hydrothermal method was used to graft hydroxyl groups homogeneously onto the graphene nanosheets. The

hydroxyl groups not only induced heterogeneous nucleation of sulfur nanoparticles on the graphene sheets but also rendered strong adsorption capabilities toward polysulfides during redox reactions. The sulfur-hydroxylated graphene composite cathode exhibited significantly improved cycling stabilities and specific capacities compared with the cathode using primitive unfunctionalized graphene. Archer et al. designed amine-functionalized CNTs by covalently attaching polyethylenimine (PEI) to hydroxyl- and carboxyl-functionalized CNTs [174]. The reactions between PEI and hydroxyl and carboxyl functional groups allowed a large number of amine groups grafted on the surface of CNTs, which rendered improved interactions between lithium polysulfide species and the amine-functionalized CNTs (Fig. 2.34a). With sulfur content of ~60 wt%, the sulfur-amine-functionalized CNT composite cathode exhibited significantly improved cycling stability compared with the cathode using the primitive CNTs (Fig. 2.34b). Meanwhile, the cycling behavior remained stable when increasing the sulfur content to 70 wt%, indicating the effectiveness of amine functional groups in immobilizing polysulfides via improved chemical interactions.

Lou et al. noticed that the detachment of lithium sulfides from the carbon matrix was an important contributing factor for the capacity decay of the sulfur cathode [175]. To mitigate this problem, amino-functionalized graphene was designed to stabilize sulfur and its discharge product. Ethylenediamine (EDA), composed of two electron-donating amine groups on carbon aliphatic ($\text{CH}_2\text{-CH}_2$) spacer, was grafted on the surface of graphene to implement the amino functionalization process. This unique molecular structure of EDA with high reactivity made it good crosslinker to join the polar lithium sulfides and nonpolar carbon surface together, which effectively prevented the irreversible loss of active materials. The strong affinity of lithium sulfides to the amino-functionalized graphene was verified by theoretical calculations, as demonstrated by the high binding energy between them. The sulfur cathode

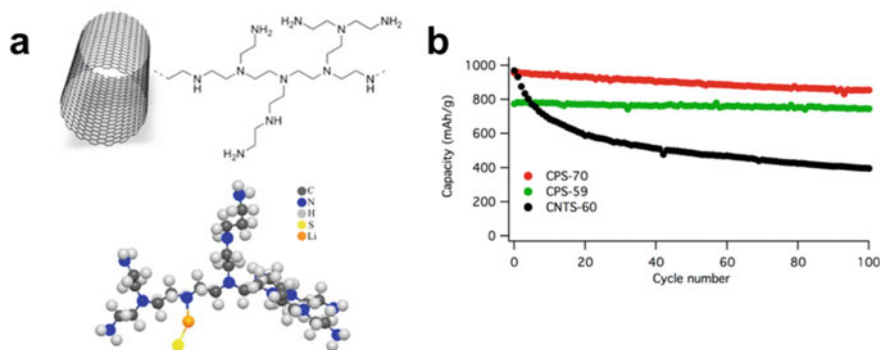


Fig. 2.34 **a** Schematic of amine-functionalized CNTs and their interaction with lithium polysulfide species. **b** Comparisons of cycling stabilities of different sulfur-CNT composite cathodes with 60 wt% sulfur content (CNTS-60) and sulfur-amine-functionalized CNT composite cathodes with 59 wt% (CPS-59) and 70 wt% (CPS-70) sulfur content (reproduced with permission by American Chemical Society from [174])

with amino-functionalized graphene exhibited high capacity retention rate of 80% after 350 cycles, much better than that with unfunctionalized graphene. The interaction between lithium sulfides and the amine groups was further investigated via ex-situ SEM observations of the cathode in the discharged state after cycling. For the cathode with unfunctionalized graphene, the graphene sheets exhibited a relatively bare surface as a result of significant detachment of the discharge products from carbon surface (Fig. 2.35a–c). While the discharge products were found to be uniformly distributed on the amino-functionalized graphene sheets to form a thick layer instead of discrete particles, indicative of strong interactions between them (Fig. 2.35d–f).

In another approach, lithium sulfonate (LiSO_3) groups were attached to the CMK-3 mesoporous carbon for surface functionalization (Fig. 2.36a) [176]. When used in the sulfur cathode with LiNO_3 -free electrolyte, the unfunctionalized CMK-3 suffers from severe polysulfide shuttling as evidenced by its low Coulombic efficiencies (Fig. 2.36b). While the sulfur cathode using LiSO_3 -functionalized CMK-3 exhibited significantly improved Coulombic efficiencies (Fig. 2.36c), indicating greatly reduced polysulfide shuttle with the presence of LiSO_3 groups. The cycling stability of the sulfur cathode with LiSO_3 -functionalized CMK-3 was also obviously better than that with unfunctionalized CMK-3. The observed performance improvement could be mainly attributed to the strong ionic interactions between lithium polysulfides and surface-bound sulfonate groups. Besides, the LiSO_3 groups could facilitate the hopping of lithium ions, contributing to improved lithium-ion transport kinetics during redox reactions.

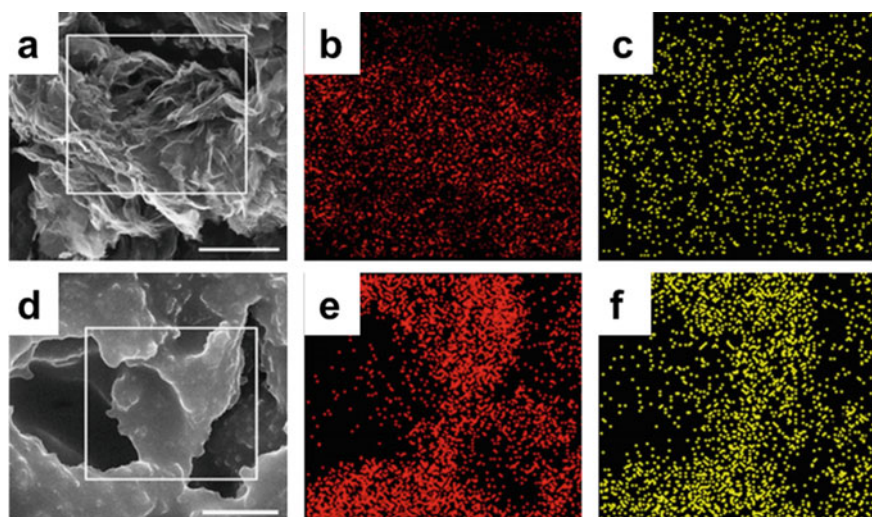


Fig. 2.35 **a** SEM image of the sulfur–graphene composite in the discharged state after 150 cycles. Scale bar: 1 μm . **b**, **c** Corresponding elemental mappings of **b** carbon and **c** sulfur in the composite. **d** SEM image of the sulfur-amino-functionalized graphene composite in the discharged state after 350 cycles. Scale bar: 5 μm . **e**, **f** Corresponding elemental mappings of **e** carbon and **f** sulfur in the composite content (reproduced with permission by the Nature Publishing Group from [175])

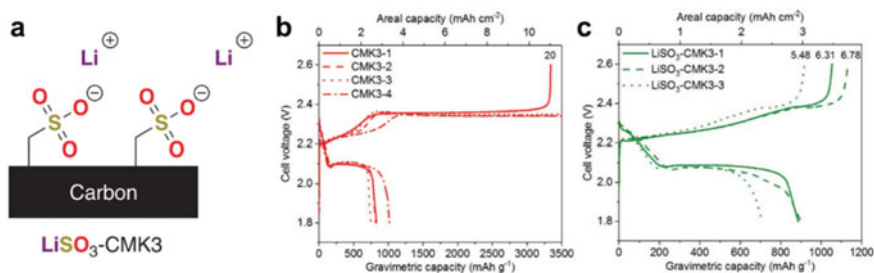


Fig. 2.36 a Schematic of LiSO₃-functionalized CMK-3 mesoporous carbon. Charge/discharge curves of the sulfur cathode with **b** unfunctionalized CMK-3 and **c** LiSO₃-functionalized CMK-3. The number above the charge curves corresponded to the charging time in hours (reproduced with permission by WILEY-VCH from [176])

2.9 Sulfur-Hybrid Carbon Composite Cathode

Sections 2.4–2.8 comprehensively discussed the design of various sulfur–carbon composite cathodes and their effect in improving the electrochemical performances of Li–S batteries. Carbon materials with different structures and properties exhibit different advantages during the sulfur redox reactions. To rationally integrate the merits of different types of carbon, hybrid carbon materials, composed of two or more carbon components, have been widely explored to achieve good comprehensive properties for further enhanced electrochemical properties of the sulfur–carbon composite cathode [115, 149, 177–182].

Zhang et al. proposed multi-dimensional carbon-based structure by combining vertically aligned CNTs (ACNTs) with horizontal graphene sheets [183]. ACNTs and graphene layers were anchored to each other to construct sandwich-like hierarchical architecture with efficient 3D electron transfer pathways and ion diffusion channels (Fig. 2.37). Nitrogen doping was further incorporated to the ACNT-graphene sandwiches to form nitrogen-doped ACNT/graphene (N-ACNT/G) hybrid, aiming to modify the interfacial properties for better polysulfide adsorption. The sandwich-like structure effectively prevented the self-aggregation of CNTs and re-stacking of graphene sheets, which gave rise to rapid electron transfer behavior along both horizontal and vertical directions. The interconnected mesoporous structure was beneficial for improved electrolyte immersion and diffusion, contributing to improved ion transfer kinetics. After sulfur impregnation, this hybrid enabled a high discharge capacity of 1,152 mAh g⁻¹ and retained 76% of its capacity after 80 cycles at 1 C rate. At high rate of 5 C, a reversible capacity of 770 mAh g⁻¹ could be achieved, indicating kinetically favorable redox processes.

Li et al. designed free-standing pie-like sulfur electrode, where sulfur was confined in the lotus root-like multichannel carbon nanofibers (S-LRC), and a thin layer of amino-functionalized graphene was coated on the surface of the S-LRC composite [184]. This design had multiple advantages. First, each S-LRC nanofiber had multiple channels with average diameter of 60 nm (Fig. 2.38a), which provided large void

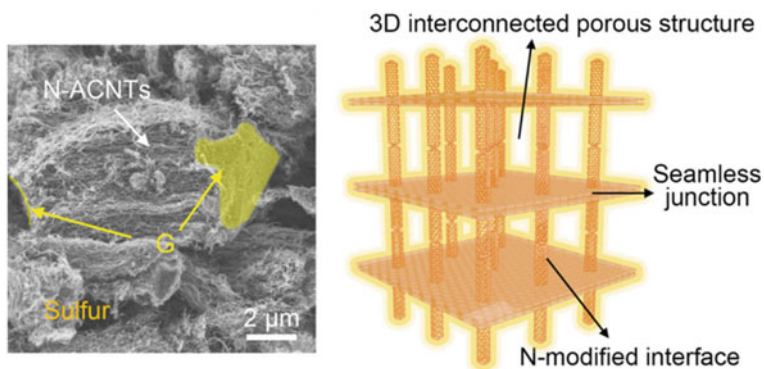


Fig. 2.37 SEM image and corresponding illustration of the sulfur-N-ACNT/G composite (reproduced with permission by WILEY–VCH from [183])

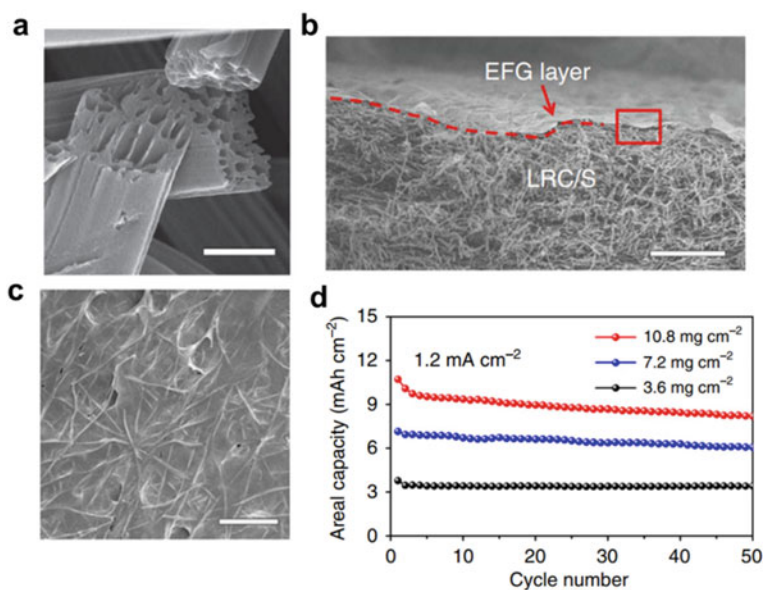


Fig. 2.38 **a** SEM image of the LRC nanofibers. Scale bar: 500 nm. **b** Cross-sectional SEM image of the S-LRC composite coated with amino-functionalized graphene (EFG). Scale bar: 20 μm. **c** SEM image showing the surface of amino-functionalized graphene-coated S-LRC composite. Scale bar: 1 μm. **d** Areal capacities of layer-by-layer structured sulfur-hybrid carbon composite cathodes (reproduced with permission by the Nature Publishing Group from [184])

space for sulfur accommodation to achieve high sulfur content. Second, the highly parallel channel walls inside each LRC nanofiber formed a continuous conducting framework that ensured close electrical contact between carbon and sulfur. This was beneficial for achieving high utilization efficiency of the active sulfur materials. Third, the functionalized graphene coating layer served as barrier to effectively suppress the diffusion of polysulfides (Fig. 2.38b, c), contributing to improved cycling stability. The sulfur content in the hybrid carbon structure could reach to 72.3%, with areal sulfur loading of 3.6 mg cm^{-2} . The obtained sulfur-hybrid carbon composite cathode delivered high specific capacity of $1,314 \text{ mAh g}^{-1}$ at 0.1 C, corresponding to areal capacity of 4.7 mAh cm^{-2} . The capacity retention rate of 78% could be maintained after 200 cycles at 0.2 C. Moreover, the areal capacity could be further boosted to more than 8 mAh cm^{-2} by stacking three layers of the sulfur-hybrid carbon composite cathode with an areal sulfur loading of 10.8 mg cm^{-2} (Fig. 2.38d).

In another approach, 3D multifunctional sponge-like architecture was designed as the cathode framework, where highly porous N-doped carbon fiber foam was used for sulfur accommodation and thin graphene layer was covered on the surface as polysulfide interception layer (Fig. 2.39a) [185]. The exceptionally high specific surface area ($2290 \text{ m}^2 \text{ g}^{-1}$) of the highly porous carbon fibers rendered uniform distribution of sulfur on their surface by strong capillary force (Fig. 2.39b). The interconnected carbon fibers provide long-range and continuous electric conducting pathways during the sulfur conversion reactions, contributing to high sulfur utilization. The N doping facilitated polysulfide immobilization within the cathode framework by enhanced chemical adsorption. The graphene interception layer provided not only extra conductive network for fast electron transport but also storage space for the migrating polysulfides. With areal sulfur loading of 7.7 mg cm^{-2} , high areal capacities up to 8.7 mAh cm^{-2} were attained together with excellent cycling stability over 500 cycles.

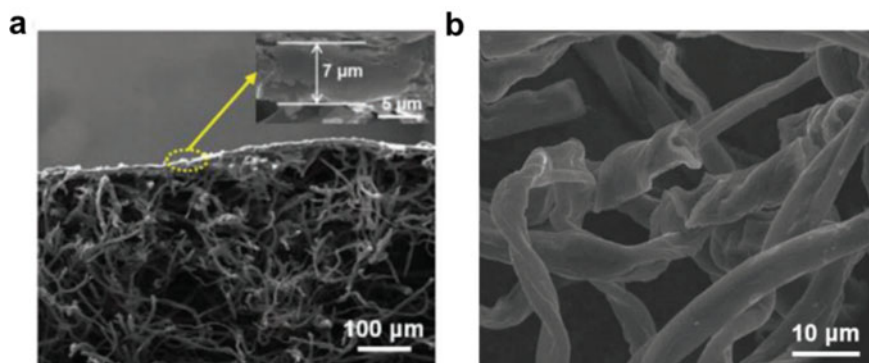


Fig. 2.39 **a** Cross-sectional SEM image showing the graphene interception layer coated on the surface of the carbon fiber foam. **b** SEM image of the sulfur-coated N-doped carbon fibers (reproduced with permission by WILEY-VCH from [185])

Overall, rational design of hybrid carbon materials can integrate multiple advantages from different carbon components, which provides a versatile platform for tailoring sulfur–carbon composite cathode for optimized electrochemical properties. The combination of delicately designed carbon components with tailored pore structure, conductivity, surface functionality, and morphology can render improved active material utilization, high cycling stability, high rate capability, and high areal capacity.

2.10 Flexible Sulfur–Carbon Composite Cathodes

Developing flexible batteries have become an important trend in recent years with the advent of bendable and stretchable electronic devices. Flexible batteries require their electrodes to perform well without structural failure under continuous deformation. Carbon materials have remarkable advantages for building flexible electrodes owing to their excellent mechanical properties [8, 11, 186–189]. Besides, carbon materials can be easily assembled into freestanding structures to provide robust and flexible scaffold for the flexible electrode. Various carbon fiber cloth/foams, with natural monolithic structure, are good flexible substrates for the design of flexible sulfur cathodes, as discussed in Sect. 2.7. Particularly, CNTs and graphene with the 1D and 2D nanostructures have an extremely small radius of curvature, leading to high durability under bending conditions [6, 190–194]. The strong interactions between CNT bundles and graphene sheets can effectively maintain structural integrity during repeated bending or stretching conditions. They have, therefore, been widely studied for use in flexible sulfur cathodes, either as flexible building units or independent current collectors.

Manthiram et al. reported the self-weaving behavior of MWCNTs for the construction of flexible sulfur cathodes (Fig. 2.40) [195]. MWCNTs were dispersed in $\text{Na}_2\text{S}_2\text{O}_3$ solution using isopropyl alcohol and Triton X-100 as wetting agent and dispersant to mitigate the hydrophobic behavior of the MWCNTs. Hydrochloric acid was then added to react with $\text{Na}_2\text{S}_2\text{O}_3$ to render heterogeneous nucleation of sulfur on the MWCNTs. The S-CNT products were vacuum-filtered and washed to obtain flexible S-CNT composite film. With sulfur content of 40 wt%, the flexible S-CNT composite cathode delivered specific capacity of 1352 mAh g^{-1} at 0.1 C. After 100 cycles, a reversible capacity of 915 mAh g^{-1} could be maintained. In another approach, MWCNTs were treated in concentrated $\text{H}_2\text{SO}_4/\text{HNO}_3$ solution to render a slightly oxidized surface, followed by vacuum filtration to obtain a flexible MWCNT membrane for sulfur infiltration [196]. With sulfur content of 65 wt%, the flexible S-MWCNT cathode delivered an initial discharge capacity of 1100 mAh g^{-1} and retained a capacity retention rate of 67% after 100 cycles.

Fan et al. exploited the use of super aligned CNTs for the construction of flexible sulfur cathodes [197, 198]. The super aligned CNTs had large aspect ratio ($\sim 10^4$) with strong van der Waals force among tubes and bundles. Abundant mesopores were introduced to the super aligned CNTs through controlled oxidation in air to

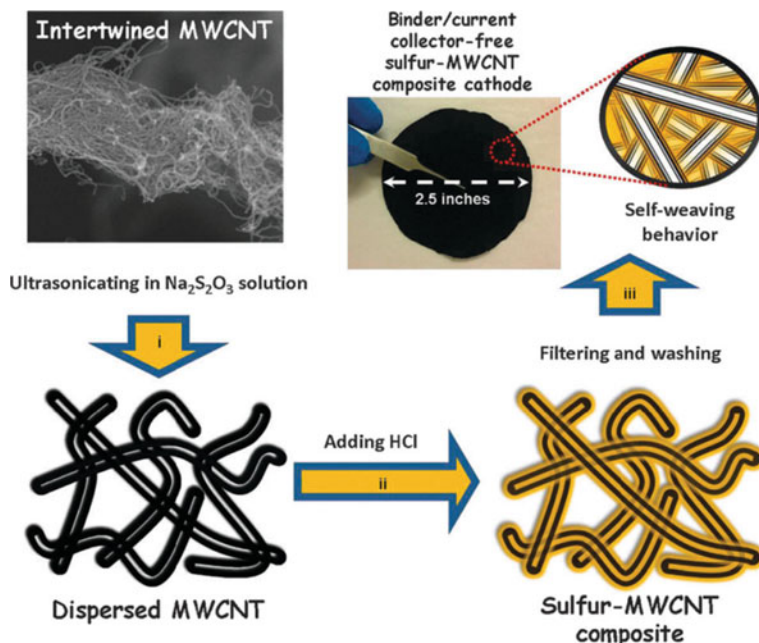


Fig. 2.40 Schematic of the fabrication process of the self-weaving sulfur-MWCNT composite cathode (reproduced with permission by The Royal Society of Chemistry from [195])

obtain porous CNTs (PCNTs) [197]. When employed as flexible sulfur host, the PCNTs could be assembled into continuous and interconnected conductive network with highly open and porous structures (Fig. 2.41). The flexible S-PCNT composite cathode had features of high conductivity, good polysulfide adsorption capability, and good mechanical strength. With high sulfur content of 70 wt%, the S-PCNT composite cathode maintained a specific capacity of 760 mAh g^{-1} after 100 cycles at 0.1 C.

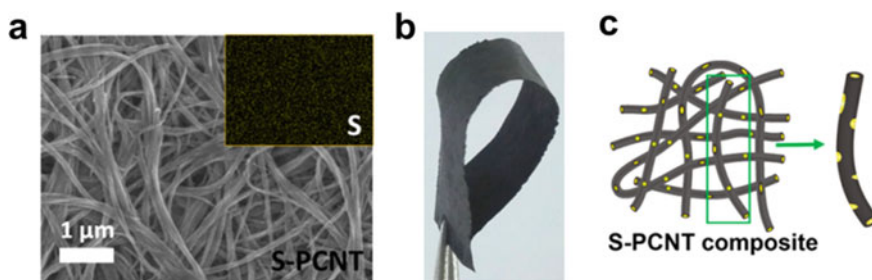


Fig. 2.41 a SEM image of the S-PCNT composite. Inset: corresponding elemental mapping of sulfur. b Photograph and c illustration of the S-PCNT composite electrode (reproduced with permission by American Chemical Society from [197])

Flexible sulfur–graphene composite cathodes could also be synthesized via vacuum infiltration. Wen et al. reported the synthesis of flexible self-supporting sulfur–graphene cathode with sulfur nanoparticles heterogeneously nucleated and deposited on the graphene sheets [199]. With sulfur content of 67 wt%, the reversible capacity of 600 mAh g^{-1} was retained after 100 cycles. Niu et al. reported the strategy to fabricate sulfur–graphene composite cathode with high flexibility by synchronously reducing and assembling graphene oxide sheets with sulfur nanoparticles on zinc metal surface [79]. The use of Zn metal could weaken the electrostatic repulsion between sulfur nanoparticles and the graphene sheets to promote their layer-by-layer crosslink. The sulfur nanoparticles were homogeneously attached on the surface of the interconnected graphene sheets (Fig. 2.42a, b), which ensured highly efficient transport of both electrons and lithium ions. The cross-linked porous network structures endowed the sulfur–graphene composite film with excellent mechanical properties, with tensile strength of 68 MPa and Young's modulus of 965 MPa (Fig. 2.40c). The flexible sulfur–graphene composite cathode delivered a high initial discharge capacity of $1,302 \text{ mAh g}^{-1}$ and retained a discharge capacity of 978 mAh g^{-1} after 200 cycles at 0.1 C.

Zhou et al. reported the use of graphene foam prepared from chemical vapor deposition method as flexible matrix for the sulfur cathode [200]. Thin layer of poly(dimethyl siloxane) (PDMS) was coated on the surface of the graphene foam to make the interconnected graphene network sufficiently robust, guaranteeing the flexibility of the cathode (Fig. 2.43a). The graphene foam could provide highly efficient conductive network, robust mechanical support, and sufficient space for high sulfur loading. The areal sulfur loading in the graphene foam-based electrodes could be tuned from 3.3 to 10.1 mg cm^{-2} , with uniform distribution of sulfur in the porous graphene network (Fig. 2.43b). The flexible sulfur–graphene foam electrode showed high electrical conductivity of 125 S m^{-1} , which remained unchanged after 22,000 bending cycles (Fig. 2.43c). With areal sulfur loading of 10.1 mg cm^{-2} , high areal capacity of 13.4 mAh cm^{-2} was obtained, along with low capacity decay rate per cycle of 0.07% over 1000 cycles.

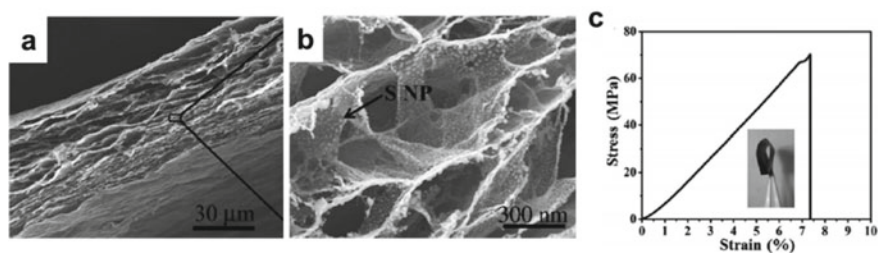


Fig. 2.42 a, b Cross-sectional SEM images of the flexible sulfur–graphene composite film. S NP: Sulfur nanoparticle. c Stress–strain curve of the sulfur–graphene composite film. Inset: photograph of bent sulfur–graphene composite film (reproduced with permission by WILEY–VCH from [79])

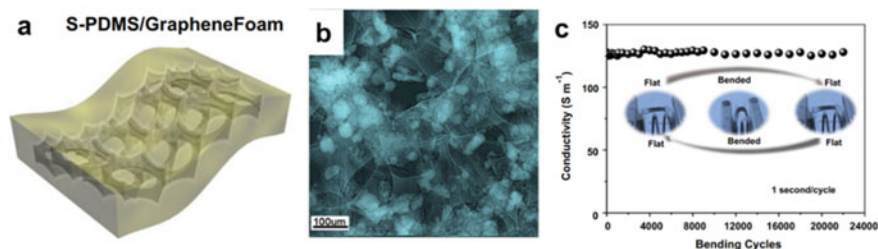


Fig. 2.43 **a** Illustration of the flexible sulfur–graphene foam electrode with thin layer of PDMS coating. **b** XRM 2D projections of the sulfur–graphene foam electrode. **c** Stability of sulfur–graphene foam electrode with 10.1 mg cm^{-2} sulfur loading in terms of electrical conductivity over 22,000 cycles (reproduced with permission by ELSEVIER from [200])

Overall, the intrinsic merits of carbon materials in electrical, mechanical, and thermal properties make them appealing for constructing flexible sulfur cathodes. The lightweight feature of carbon materials could further minimize their effect on the overall energy density of the flexible Li–S cells. The carbon components in flexible sulfur cathode could synchronously serve as the mechanical support and the conductive framework, contributing to uncompromised electrochemical properties while maintaining high flexibility.

2.11 Summary

Sulfur–carbon composite cathodes have attracted tremendous research interests, and the substantial progress on this research topic signifies their importance. The excellent properties of carbon materials, in the structural, electrical, and mechanical aspects, show great promise in constructing high-performance sulfur cathodes for Li–S batteries with high energy density, high power density, long cycle life, and low cost. The investigations of various sulfur–carbon composite cathodes suggested that carbon plays a significant role in improving the electronic conductivity of sulfur, inhibiting the dissolution and diffusion of polysulfide intermediates, and buffering the volume variations of the active materials during cycling. The high effectiveness of carbon materials in addressing the issues during sulfur conversion reactions has been verified by significantly improved electrochemical performances of the sulfur cathode in terms of high sulfur utilization, long cycle life, and high areal capacities.

A large variety of carbon materials have been developed to construct sulfur–carbon composite cathodes, including porous carbons, carbon nanotubes, graphene, carbon fibers, and their hybrids. The physicochemical properties of these carbon materials, such as pore structures, morphological structure, surface functionality and conductivity, exert a significant influence on the electrochemical behavior of sulfur–carbon composite cathode:

1. **Pore structures:** the role of pore structures in carbon materials is twofold. First, sulfur encapsulated in the nanosized pores exhibits improved electrochemical activity, owing to their nanoscale sizes that give rise to short electron and ion diffusion distance and the sufficient electrical contact with the carbon matrix. Second, the pore structures endow carbon materials with adsorption capability for polysulfide interception, alleviating their dissolution, diffusion, and shuttle. Pore size and pore volume are the two main parameters for pore structures. Decreasing pore size renders improved adsorption capability toward polysulfides but decreased pore volume for sulfur encapsulation. Besides, small pore sizes cause increased ion transport barrier, leading to sluggish redox reaction kinetics. Particularly, small sulfur molecules encapsulated in small micropores (<0.5 nm) undergo solid–solid conversion reaction process without the formation of polysulfide intermediates, exhibiting different electrochemical behavior from the common octasulfur. Therefore, optimization of pore structures in carbon materials requires comprehensive consideration of sulfur content, polysulfide adsorption capability, ion transfer kinetics, and sulfur redox mechanism.
2. **Morphological structure:** carbon materials can have various morphological structures, including particles (0D), tubes/fibers(1D), planar sheets (2D), and spheres. They can also be assembled into 3D monolithic structures with interconnected conductive network. The electron conduction efficiency, ion transfer channels, sulfur encapsulation capability, polysulfide interception property, and flexibility of carbon materials vary with different morphological structures. For example, CNTs with small diameter are beneficial to achieve a high sulfur content along with decreased ion and electron transfer length, compared with those with large diameters. Hollow carbon spheres can provide sufficient interior void space to encapsulate large amounts of sulfur. CNTs and graphene with the 1D and 2D nanostructures exhibit good flexibility owing to their small radius of curvature under bending conditions. Carbon hybrid structures, composed of two or more carbon components, can further combine the structural advantages of different carbon materials. It is essential to delicately tailor the morphological structures of carbon materials for sulfur cathode with improved electrochemical behavior and specific functions.
3. **Surface functionality and conductivity:** functionalization of carbon materials can adjust their surface hydrophilicity and render chemical interactions with polysulfides to inhibit their diffusion and shuttle effect. For example, chemically modified graphene with functional groups on the surface has proved effective to absorb polysulfides owing to their polar surface properties. N-doped carbon materials allow good polysulfide immobilization effect as the dopant with a lone pair of electrons can serve as Lewis base to interact with the Lewis acidic lithium polysulfide. Yet the defects, functional groups, and heteroatom doping of carbon materials have a great influence on their electronic conductivities. For example, graphene oxide without reduction treatment contains large amounts of oxygen-containing groups, which make it almost insulating. Therefore, it

is significant to consider the balance between high conductivity and modified surface functionality of carbon materials for the design of high-performance sulfur–carbon composite cathodes.

From the perspective of constructing Li–S batteries for practical applications, high energy/power density, long cycle life, affordable cost, and high safety have been long-lasting goals. With regard to the sulfur cathode, high sulfur content and high areal sulfur loading with uncompromised sulfur utilization and cycling stability are essential. In this respect, the following principles should be considered for the design of carbon materials used for the sulfur cathode: (1) the capability to accommodate high sulfur content while maintaining essential electrical contact; (2) high electron conduction efficiency to minimize their addition amount in the cathode; (3) rational combination of different pore structures; (4) balanced surface functionality and conductivity; (5) low-cost and facile synthetic route. Further optimization and understanding of the sulfur–carbon composite cathode would contribute to an acceleration in the development of commercially viable lithium-sulfur batteries.

Acknowledgements The authors acknowledge financial support from National Natural Science Foundation of China (Numbers 52020105010, 51525206, 51927803, 51972313, 52072378, and 51902316), National Key R&D Program of China (2016YFA0200102 and 2016YFB0100100), the Strategic Priority Research Program of the Chinese Academy of Sciences (XDA22010602), Liaoning Revitalization Talents Program (Number XLYC1908015), Youth Innovation Promotion Association of the Chinese Academy of Sciences (Number Y201942) and China Petrochemical Cooperation (Number 218025).

References

1. Bruce PG, Freunberger SA, Hardwick LJ, Tarascon JM (2012) Li-O₂ and Li-S batteries with high energy storage. *Nat Mater* 11(1):19–29
2. Huang L, Li J, Liu B, Li Y, Shen S, Deng S, Lu C, Zhang W, Xia Y, Pan G, Wang X, Xiong Q, Xia X, Tu J (2020) electrode design for lithium-sulfur batteries: problems and solutions. *Adv Funct Mater* 30(22):1910375
3. Dong C, Gao W, Jin B, Jiang Q (2018) Advances in cathode materials for high-performance lithium-sulfur batteries. *iScience* 6:151–198
4. Rana M, Luo B, Kaiser MR, Gentle I, Knibbe R (2020) The role of functional materials to produce high areal capacity lithium sulfur battery. *J Energy Chem* 42:195–209
5. Park J, Yu SH, Sung YE (2018) Design of structural and functional nanomaterials for lithium-sulfur batteries. *Nano Today* 18:35–64
6. Fang R, Chen K, Yin L, Sun Z, Li F, Cheng HM (2019) The regulating role of carbon nanotubes and graphene in lithium-ion and lithium-sulfur batteries. *Adv Mater* 31(9):1800863
7. Liang J, Sun ZH, Li F, Cheng HM (2016) Carbon materials for Li-S batteries: functional evolution and performance improvement. *Energy Storage Mater* 2:76–106
8. Zhao Y, Zhang Y, Bakenova Z, Bakenov Z (2015) Carbon/sulfur composite cathodes for flexible lithium/sulfur batteries: status and prospects. *Front Energy Res* 3:1–6
9. Bai Y, Li T, Wang Y, Jin H, Wang K, Xu H (2019) Novel construction of nanostructured carbon materials as sulfur hosts for advanced lithium-sulfur batteries. *Int J Energy Res* 44(1):70–91
10. Zhang L, Wang Y, Niu Z, Chen J (2019) Advanced nanostructured carbon-based materials for rechargeable lithium-sulfur batteries. *Carbon* 141:400–416

11. Wang Z, Xu X, Ji S, Liu Z, Zhang D, Shen J, Liu J (2020) Recent progress of flexible sulfur cathode based on carbon host for lithium-sulfur batteries. *J Mater Sci Mater* 55:56–72
12. Zhang SS (2013) Liquid electrolyte lithium/sulfur battery: fundamental chemistry, problems, and solutions. *J Power Sources* 231:153–162
13. Li S, Fan Z (2021) Encapsulation methods of sulfur particles for lithium-sulfur batteries: a review. *Energy Storage Mater* 34:107–127
14. Ji XL, Lee KT, Nazar LF (2009) A highly ordered nanostructured carbon-sulphur cathode for lithium-sulphur batteries. *Nat Mater* 8:500–506
15. Greenwood NN, Earnshaw A (1997) *Chemistry of the elements*, 2nd edn. Butterworth-Heinemann, Oxford, pp 645–662
16. Fang R, Xu J, Wang D-W (2020) Covalent fixing of sulfur in metal–sulfur batteries. *Energy Environ Sci* 13(2):432–471
17. Zhang B, Qin X, Li GR, Gao XP (2010) enhancement of long stability of sulfur cathode by encapsulating sulfur into micropores of carbon spheres. *Energy Environ Sci* 3(10):1531–1537
18. Xu YH, Wen Y, Zhu YJ, Gaskell K, Cychoz KA, Eichhorn B, Xu K, Wang CS (2015) Confined sulfur in microporous carbon renders superior cycling stability in Li/S batteries. *Adv Funct Mater* 25(27):4312–4320
19. Jayaprakash N, Shen J, Moganty SS, Corona A, Archer LA (2011) Porous hollow carbon@sulfur composites for high-power lithium-sulfur batteries. *Angew Chem Int Edit* 50(26):5904–5908
20. Carter R, Davis B, Oakes L, Maschmann MR, Pint CL (2017) A high areal capacity lithium-sulfur battery cathode prepared by site-selective vapor infiltration of hierarchical carbon nanotube arrays. *Nanoscale* 9(39):15018–15026
21. Li MY, Carter R, Douglas A, Oakes L, Pint CL (2017) Sulfur vapor-infiltrated 3D carbon nanotube foam for binder-free high areal capacity lithium-sulfur battery composite cathodes. *ACS Nano* 11(5):4877–4884
22. Sun H, Xu GL, Xu YF, Sun SG, Zhang XF, Qiu YC, Yang SH (2012) A composite material of uniformly dispersed sulfur on reduced graphene oxide: aqueous one-pot synthesis, characterization and excellent performance as the cathode in rechargeable lithium-sulfur batteries. *Nano Res* 5(10):726–738
23. Wei ZK, Chen JJ, Qin LL, Nemade AW, Zheng MS, Dong QF (2012) Two-step hydrothermal method for synthesis of sulfur-graphene hybrid and its application in lithium sulfur batteries. *J Electrochem Soc* 159(8):A1236–A1239
24. Su YS, Manthiram A (2012) A facile in situ sulfur deposition route to obtain carbon-wrapped sulfur composite cathodes for lithium-sulfur batteries. *Electrochim Acta* 77:272–278
25. Wang H, Yang Y, Liang Y, Robinson JT, Li Y, Jackson A, Cui Y, Dai H (2011) Graphene-wrapped sulfur particles as a rechargeable lithium-sulfur battery cathode material with high capacity and cycling stability. *Nano Lett* 11(7):2644–2647
26. Zhou G, Wang D-W, Li F, Hou P-X, Yin L, Liu C, Lu GQ, Gentle IR, Cheng H-M (2012) A flexible nanostructured sulphur-carbon nanotube cathode with high rate performance for Li-S batteries. *Energy Environ Sci* 5(10):8901–8906
27. Fang RP, Zhao SY, Hou PX, Cheng M, Wang SG, Cheng HM, Liu C, Li F (2016) 3D interconnected electrode materials with ultrahigh areal sulfur loading for Li-S batteries. *Adv Mater* 28(17):3374–3382
28. Zhang C, Lv W, Zhang W, Zheng X, Wu M-B, Wei W, Tao Y, Li Z, Yang Q-H (2014) Reduction of graphene oxide by hydrogen sulfide: a promising strategy for pollutant control and as an electrode for Li-S batteries. *Adv Energy Mater* 4(7):1301565
29. Wang LB, Hu XL (2018) Recent advances in porous carbon materials for electrochemical energy storage. *Chem Asian J* 13(12):1518–1529
30. Tian WJ, Zhang HY, Duan XG, Sun HQ, Shao GS, Wang SB (2020) Porous carbons: structure-oriented design and versatile applications. *Adv Funct Mater* 30(17):1909265
31. Evers S, Nazar LF (2013) New approaches for high energy density lithium sulfur battery cathodes. *Acc Chem Res* 46:1135–1143

32. Wang M, Xia X, Zhong Y, Wu J, Xu R, Yao Z, Wang D, Tang W, Wang X, Tu J (2019) Porous carbon hosts for lithium-sulfur batteries. *Chem Eng J* 25(15):3710–3725
33. Zhang ST, Zheng MB, Cao JM, Pang H (2016) Porous carbon/sulfur composite cathode materials for lithium-sulfur batteries. *Prog Chem* 28(8):1148–1155
34. Fang R, Zhao S, Pei S, Qian X, Hou PX, Cheng HM, Liu C, Li F (2016) Toward more reliable lithium-sulfur batteries: an all-graphene cathode structure. *ACS Nano* 10(9):8676–8682
35. Fang R, Zhao S, Sun Z, Wang D-W, Cheng H-M, Li F (2017) More reliable lithium-sulfur batteries: status, Solutions and Prospects. *Adv Mater* 29(48):1606823
36. Wu HB, Wei S, Zhang L, Xu R, Hng HH, Lou XW (2013) Embedding sulfur in MOF-derived microporous carbon polyhedrons for lithium-sulfur batteries. *Chem Eng J* 19(33):10804–10808
37. Han JK, Li Y, Li SW, Long P, Cao C, Cao Y, Wang WZ, Feng YY, Feng W (2018) A low cost ultra-microporous carbon scaffold with confined chain-like sulfur molecules as a superior cathode for lithium-sulfur batteries. *Sustain Energy Fuels* 2(10):2187–2196
38. Zhou JJ, Guo YS, Liang CD, Yang J, Wang JL, Nuli YN (2018) Confining small sulfur molecules in peanut shell-derived microporous graphitic carbon for advanced lithium sulfur battery. *Electrochim Acta* 273:127–135
39. Wang DW, Zhou G, Li F, Wu KH, Lu GQ, Cheng HM, Gentle IR (2012) A microporous-mesoporous carbon with graphitic structure for a high-rate stable sulfur cathode in carbonate solvent-based Li-S batteries. *Phys Chem Chem Phys* 14:8703–8710
40. Chmiola J, Yushin G, Gogotsi Y, Portet C, Simon P, Taberna PL (2006) Anomalous increase in carbon capacitance at pore sizes less than 1 nanometer. *Science* 313(5794):1760–1763
41. Wang D-W, Zeng Q, Zhou G, Yin L, Li F, Cheng H-M, Gentle IR, Lu GQM (2013) Carbon-sulfur composites for Li-S batteries: status and prospects. *J Mater Chem A* 1(33):9382–9394
42. Xin S, Gu L, Zhao NH, Yin YX, Zhou LJ, Guo YG, Wan LJ (2012) Smaller sulfur molecules promise better lithium sulfur batteries. *J Am Chem Soc* 134(45):18510–18513
43. Li Z, Yuan L, Yi Z, Sun Y, Liu Y, Jiang Y, Shen Y, Xin Y, Zhang Z, Huang Y (2013) Insight into the electrode mechanism in lithium-sulfur batteries with ordered microporous carbon confined sulfur as the cathode. *Adv Energy Mater* 4:1301473
44. Gueon D, Hwang JT, Yang SB, Cho E, Sohn K, Yang DK, Moon JH (2018) Spherical macroporous carbon nanotube particles with ultrahigh sulfur loading for lithium-sulfur battery cathodes. *ACS Nano* 12(1):226–233
45. Tachikawa N, Yamauchi K, Takashima E, Park JW, Dokko K, Watanabe M (2011) Reversibility of electrochemical reactions of sulfur supported on inverse opal carbon in glyme-Li salt molten complex electrolytes. *Chem Commun* 47(28):8157–8159
46. Eftekhari A, Fan ZY (2017) Ordered mesoporous carbon and its applications for electrochemical energy storage and conversion. *Mater Chem Front* 1(6):1001–1027
47. Xin W, Song YH (2015) Mesoporous carbons: recent advances in synthesis and typical applications. *RSC Adv* 5(101):83239–83285
48. Li XL, Cao YL, Qi W, Saraf LV, Xiao J, Nie ZM, Mietek J, Zhang JG, Schwenzer B, Liu J (2011) Optimization of mesoporous carbon structures for lithium-sulfur battery applications. *J Mater Chem* 21(41):16603–16610
49. Schuster J, He G, Mandlmeier B, Yim T, Lee KT, Bein T, Nazar LF (2012) Spherical ordered mesoporous carbon nanoparticles with high porosity for lithium-sulfur batteries. *Angew Chem Int Edit* 51(15):3591–3595
50. Rybarczyk MK, Peng HJ, Tang C, Lieder M, Zhang Q, Titirici MM (2016) Porous carbon derived from rice husks as sustainable bioresources: insights into the role of micro-/mesoporous hierarchy in hosting active species for lithium-sulphur batteries. *Green Chem* 18(19):5169–5179
51. Chen S, Sun B, Xie X, Mondal AK, Huang X, Wang G (2015) Multi-chambered micro/mesoporous carbon nanocubes as new polysulfides reservoirs for lithium-sulfur batteries with long cycle life. *Nano Energy* 16:268–280
52. Zhang YB, Zhao Y, Hao XF, Ma YC, Wu Y, Li GL, Cao JJ, Yan Y, Qiao LZ, Hao C (2019) Sulfur encapsulated in a wafer-like carbon substrate with interconnected meso/micropores for high-performance lithium-sulfur batteries. *Inorg Chem Front* 6(11):3264–3269

53. Liang C, Dudney NJ, Howe JY (2009) Hierarchically structured sulfur/carbon nanocomposite material for high-energy lithium battery. *Chem Mater* 21(19):4724–4730
54. He G, Ji XL, Nazar L (2011) High “C” rate Li-S cathodes: sulfur imbibed bimodal porous carbons. *Energy Environ Sci* 4(8):2878–2883
55. Chen SR, Zhai YP, Xu GL, Jiang YX, Zhao DY, Li JT, Huang L, Sun SG (2011) Ordered mesoporous carbon/sulfur nanocomposite of high performances as cathode for lithium-sulfur battery. *Electrochim Acta* 56(26):9549–9555
56. Li Z, Jiang Y, Yuan LX, Yi ZQ, Wu C, Liu Y, Strasser P, Huang YH (2014) A highly ordered meso@microporous carbon-supported sulfur@smaller sulfur core-shell structured cathode for Li-S batteries. *ACS Nano* 8(9):9295–9303
57. Ding B, Yuan CZ, Shen LF, Xu GY, Nie P, Zhang XG (2013) Encapsulating sulfur into hierarchically ordered porous carbon as a high-performance cathode for lithium-sulfur batteries. *Chem Eng J* 19(3):1013–1019
58. Jung DS, Hwang TH, Lee JH, Koo HY, Shakoor RA, Kahraman R, Jo YN, Park MS, Choi JW (2014) Hierarchical porous carbon by ultrasonic spray pyrolysis yields stable cycling in lithium-sulfur battery. *Nano Lett* 14(8):4418–4425
59. Wei SC, Zhang H, Huang YQ, Wang WK, Xia YZ, Yu ZB (2011) Pig bone derived hierarchical porous carbon and its enhanced cycling performance of lithium-sulfur batteries. *Energy Environ Sci* 4(3):736–740
60. Chen MF, Jiang SX, Huang C, Wang XY, Cai SY, Xiang KX, Zhang YP, Xue JX (2017) Honeycomb-like nitrogen and sulfur dual-doped hierarchical porous biomass-derived carbon for lithium-sulfur batteries. *Chemoschem* 10(8):1803–1812
61. Zhong Y, Xia XH, Deng SJ, Zhan JY, Fang RY, Xia Y, Wang XL, Zhang Q, Tu JP (2018) Popcorn inspired porous macrocellular carbon: rapid puffing fabrication from rice and its applications in lithium-sulfur batteries. *Adv Energy Mater* 8(1):1701110
62. Fu A, Wang C, Pei F, Cui J, Fang X, Zheng N (2019) Recent advances in hollow porous carbon materials for lithium-sulfur batteries. *Small* 15(10):e1804786
63. Jiang JM, Nie GD, Nie P, Li ZW, Pan ZH, Kou ZK, Dou H, Zhang XG, Wang J (2020) Nanohollow carbon for rechargeable batteries: ongoing progresses and challenges. *Nanomicro Lett* 12(1):183
64. Hou J, Tu X, Wu X, Shen M, Wang X, Wang C, Cao C, Pang H, Wang G (2020) Remarkable cycling durability of lithium-sulfur batteries with interconnected mesoporous hollow carbon nanospheres as high sulfur content host. *Chem Eng J* 401:126141
65. Sun Q, He B, Zhang XQ, Lu AH (2015) Engineering of hollow core-shell interlinked carbon spheres for highly stable lithium-sulfur batteries. *ACS Nano* 9(8):8504–8513
66. Zeng SZ, Yao Y, Huang L, Wu H, Peng B, Zhang Q, Li X, Yu L, Liu S, Tu W, Lan T, Zeng X, Zou J (2018) Facile synthesis of ultrahigh-surface-area hollow carbon nanospheres and their application in lithium-sulfur batteries. *Chem Eur J* 24(8):1988–1997
67. Li Z, Wu HB, Lou XW (2016) Rational designs and engineering of hollow micro-/nanostructures as sulfur hosts for advanced lithium-sulfur batteries. *Energy Environ Sci* 9(10):3061–3070
68. Xin S, Yin Y-X, Wan L-J, Guo Y-G (2013) Encapsulation of sulfur in a hollow porous carbon substrate for superior Li-S batteries with long lifespan. *Part Part Syst Charact* 30(4):321–325
69. He G, Evers S, Liang X, Cuisinier M, Garsuch A, Nazar LF (2013) Tailoring porosity in carbon nanospheres for lithium-sulfur battery cathodes. *ACS Nano* 7(12):10920–10930
70. Zhou W, Wang C, Zhang Q, Abruña HD, He Y, Wang J, Mao SX, Xiao X (2015) Tailoring pore size of nitrogen-doped hollow carbon nanospheres for confining sulfur in lithium-sulfur batteries. *Adv Energy Mater* 5(16):1401752
71. Zhang YZ, Zong XL, Zhan L, Yu XY, Gao J, Xun CC, Li PY, Wang YL (2018) Double-shelled hollow carbon sphere with microporous outer shell towards high performance lithium-sulfur battery. *Electrochim Acta* 284:89–97
72. Zhang CF, Wu HB, Yuan CZ, Guo ZP, Lou XW (2012) Confining sulfur in double-shelled hollow carbon spheres for lithium-sulfur batteries. *Angew Chem Int Edit* 51(38):9592–9595

73. Zang J, An TH, Dong YJ, Fang XL, Zheng MS, Dong QF, Zheng NF (2015) Hollow-in-hollow carbon spheres with hollow foam-like cores for lithium-sulfur batteries. *Nano Res* 8(8):2663–2675
74. Novoselov KS, Fal'ko VI, Colombo L, Gellert PR, Schwab MG, Kim K (2012) A roadmap for graphene. *Nature* 490(7419):192–200
75. Ren WC, Cheng HM (2014) The global growth of graphene. *Nat Nanotechnol* 9(10):726–730
76. Lv W, Li Z, Deng Y, Yang Q-H, Kang F (2016) Graphene-based materials for electrochemical energy storage devices: opportunities and challenges. *Energy Storage Mater* 2:107–138
77. Zhu YW, Murali S, Cai WW, Li XS, Suk JW, Potts JR, Ruoff RS (2010) Graphene and graphene oxide: synthesis, properties, and applications. *Adv Mater* 22(35):3906–3924
78. Kim JW, Ocon JD, Park DW, Lee J (2014) Functionalized graphene-based cathode for highly reversible lithium-sulfur batteries. *Chemosuschem* 7(15):1265–1274
79. Cao J, Chen C, Zhao Q, Zhang N, Lu QQ, Wang XY, Niu ZQ, Chen J (2016) A flexible nanostructured paper of a reduced graphene oxide-sulfur composite for high-performance lithium-sulfur batteries with unconventional configurations. *Adv Mater* 28(43):9629–9636
80. Bagri A, Mattevi C, Acik M, Chabal YJ, Chhowalla M, Shenoy VB (2010) Structural evolution during the reduction of chemically derived graphene oxide. *Nat Chem* 2(7):581–587
81. Gao W (2016) Graphene oxide: reduction recipes, spectroscopy, and applications. Springer International Publishing
82. Yu M, Li R, Wu M, Shi G (2015) Graphene materials for lithium-sulfur batteries. *Energy Storage Mater* 1:51–73
83. Sun CB, Liu YQ, Sheng JZ, Huang QK, Lv W, Zhou GM, Cheng HM (2020) Status and prospects of porous graphene networks for lithium-sulfur batteries. *Mater Horizons* 7(10):2487–2518
84. Chen K, Sun Z, Fang R, Li F, Cheng H-M (2018) Development of graphene-based materials for lithium-sulfur batteries. *Acta Phys-Chim Sin* 34(4):377–390
85. Wu SP, Ge RY, Lu MJ, Xu R, Zhang Z (2015) Graphene-based nano-materials for lithium-sulfur battery and sodium-ion battery. *Nano Energy* 15:379–405
86. Lin T, Tang Y, Wang Y, Bi H, Liu Z, Huang F, Xie X, Jiang M (2013) Scotch-tape-like exfoliation of graphite assisted with elemental sulfur and graphene-sulfur composites for high-performance lithium-sulfur batteries. *Energy Environ Sci* 6(4):1283–1290
87. Cao Y, Li X, Aksay IA, Lemmon J, Nie Z, Yang Z, Liu J (2011) Sandwich-type functionalized graphene sheet-sulfur nanocomposite for rechargeable lithium batteries. *Phys Chem Chem Phys* 13(17):7660–7665
88. Evers S, Nazar LF (2012) Graphene-enveloped sulfur in a one pot reaction: a cathode with good coulombic efficiency and high practical sulfur content. *Chem Commun* 48(9):1233–1235
89. Hu GJ, Xu C, Sun ZH, Wang SG, Cheng HM, Li F, Ren WC (2016) 3D graphene-foam-reduced-graphene-oxide hybrid nested hierarchical networks for high-performance Li-S batteries. *Adv Mater* 28(8):1603–1609
90. Ji L, Rao M, Zheng H, Zhang L, Li Y, Duan W, Guo J, Cairns EJ, Zhang Y (2011) Graphene oxide as a sulfur immobilizer in high performance lithium/sulfur cells. *J Am Chem Soc* 133(46):18522–18525
91. Rong JP, Ge MY, Fang X, Zhou CW (2014) Solution ionic strength engineering as a generic strategy to coat graphene oxide (GO) on various functional particles and its application in high-performance lithium-sulfur (Li-S) batteries. *Nano Lett* 14(2):473–479
92. Ding B, Yuan CZ, Shen LF, Xu GY, Nie P, Lai QX, Zhang XG (2013) Chemically tailoring the nanostructure of graphene nanosheets to confine sulfur for high-performance lithium-sulfur batteries. *J Mater Chem A* 1(4):1096–1101
93. You Y, Zeng WC, Yin YX, Zhang J, Yang CP, Zhu YW, Guo YG (2015) Hierarchically micro/mesoporous activated graphene with a large surface area for high sulfur loading in Li-S batteries. *J Mater Chem A* 3(9):4799–4802
94. Song J, Yu Z, Gordin ML, Wang D (2016) Advanced sulfur cathode enabled by highly crumpled nitrogen-doped graphene sheets for high-energy-density lithium-sulfur batteries. *Nano Lett* 16(2):864–870

95. Jia X, Wei F (2017) Advances in production and applications of carbon nanotubes. *Top Curr Chem* 375(1):18–52
96. Guo JC, Xu YH, Wang CS (2011) Sulfur-impregnated disordered carbon nanotubes cathode for lithium-sulfur batteries. *Nano Lett* 11(10):4288–4294
97. Fang R, Zhao S, Wang D-W, Sun Z, Cheng H-M, Li F (2019) Micro-macroscopic coupled electrode architecture for high-energy-density lithium-sulfur batteries. *ACS Appl Energy Mater* 2:7393–7402
98. Landi BJ, Ganter MJ, Cress CD, DiLeo RA, Raffaele RP (2009) Carbon nanotubes for lithium ion batteries. *Energy Environ Sci* 2(6):638–654
99. Razaq AA, Yao YZ, Shah R, Qi PW, Miao LX, Chen MZ, Zhao XH, Peng Y, Deng Z (2019) High-performance lithium sulfur batteries enabled by a synergy between sulfur and carbon nanotubes. *Energy Storage Mater* 16:194–202
100. Fan XL, Ping LQ, Qi FL, Ghazi ZA, Tang XN, Fang RP, Sun ZH, Cheng HM, Liu C, Li F (2019) Oriented outperforms disorder: thickness-independent mass transport for lithium-sulfur batteries. *Carbon* 154:90–97
101. Han SC, Song MS, Lee H, Kim HS, Ahn HJ, Lee JY (2003) Effect of multiwalled carbon nanotubes on electrochemical properties of lithium sulfur rechargeable batteries. *J Electrochem Soc* 150(7):A889–A893
102. Dujardin E, Ebbesen TW, Hiura H, Tanigaki K (1994) Capillarity and wetting of carbon nanotubes. *Science* 265(5180):1850–1852
103. Yuan W, Zhang Y, Cheng L, Wu H, Zheng L, Zhao D (2016) The applications of carbon nanotubes and graphene in advanced rechargeable lithium batteries. *J Mater Chem A* 4(23):8932–8951
104. Yuan LX, Yuan HP, Qiu XP, Chen LQ, Zhu WT (2009) Improvement of cycle property of sulfur-coated multi-walled carbon nanotubes composite cathode for lithium/sulfur batteries. *J Power Sources* 189(2):1141–1146
105. Geng X, Rao M, Li X, Li W (2012) Highly dispersed sulfur in multi-walled carbon nanotubes for lithium/sulfur battery. *J Solid State Electrochem* 17(4):987–992
106. Liu XF, Zhang Q, Huang JQ, Zhang SM, Peng HJ, Wei F (2013) Hierarchical nanostructured composite cathode with carbon nanotubes as conductive scaffold for lithium-sulfur batteries. *J Energy Chem* 22(2):341–346
107. Mi K, Jiang Y, Feng J, Qian Y, Xiong S (2016) Hierarchical carbon nanotubes with a thick microporous wall and inner channel as efficient scaffolds for lithium-sulfur batteries. *Adv Funct Mater* 26(10):1571–1579
108. Zhang S-M, Zhang Q, Huang J-Q, Liu X-F, Zhu W, Zhao M-Q, Qian W-Z, Wei F (2013) Composite cathodes containing SWCNT@S coaxial nanocables: facile synthesis, surface modification, and enhanced performance for Li-ion storage. *Part Part Syst Charact* 30(2):158–165
109. Fang R, Li G, Zhao S, Yin L, Du K, Hou P, Wang S, Cheng H-M, Liu C, Li F (2017) Single-wall carbon nanotube network enabled ultrahigh sulfur-content electrodes for high-performance lithium-sulfur batteries. *Nano Energy* 42:205–214
110. Huang H, Liu CH, Wu Y, Fan SS (2005) Aligned carbon nanotube composite films for thermal management. *Adv Mater* 17(13):1652–1656
111. Moon S, Jung YH, Jung WK, Jung DS, Choi JW, Kim DK (2013) Encapsulated monoclinic sulfur for stable cycling of Li-S rechargeable batteries. *Adv Mater* 25(45):6547–6553
112. Fu CY, Oviedo MB, Zhu YH, Cresce AV, Xu K, Li GH, Itkis ME, Haddon RC, Chi MF, Han Y, Wong BM, Guo JC (2018) Confined lithium-sulfur reactions in narrow-diameter carbon nanotubes reveal enhanced electrochemical reactivity. *ACS Nano* 12(10):9775–9784
113. Hu G, Sun Z, Shi C, Fang R, Chen J, Hou P, Liu C, Cheng H-M, Li F (2017) A sulfur-rich copolymer@CNT hybrid cathode with dual-confinement of polysulfides for high-performance lithium-sulfur batteries. *Adv Mater* 29(11):1603835
114. Jin F, Xiao S, Lu L, Wang Y (2016) Efficient activation of high-loading sulfur by small CNTs confined inside a large CNT for high-capacity and high-rate lithium-sulfur batteries. *Nano Lett* 16(1):440–447

115. Zhao Y, Wu WL, Li JX, Xu ZC, Guan LH (2014) Encapsulating MWNTs into hollow porous carbon nanotubes: a tube-in-tube carbon nanostructure for high-performance lithium-sulfur batteries. *Adv Mater* 26(30):5113–5118
116. Yuan Z, Peng H-J, Huang J-Q, Liu X-Y, Wang D-W, Cheng X-B, Zhang Q (2014) Hierarchical free-standing carbon-nanotube paper electrodes with ultrahigh sulfur-loading for lithium-sulfur batteries. *Adv Funct Mater* 24(39):6105–6112
117. Yang SN, Cheng Y, Xiao X, Pang H (2020) Development and application of carbon fiber in batteries. *Chem Eng J* 384:123294
118. Lee JS, Kim W, Jang J, Manthiram A (2017) Sulfur-embedded activated multichannel carbon nanofiber composites for long-life, high-rate lithium-sulfur batteries. *Adv Energy Mater* 7(5):1601943
119. Ren WC, Ma W, Zhang SF, Tang BT (2018) Nitrogen-doped carbon fiber foam enabled sulfur vapor deposited cathode for high performance lithium sulfur batteries. *Chem Eng J* 341:441–449
120. He MX, Li YQ, Liu SS, Guo R, Ma YL, Xie JY, Huo H, Cheng XQ, Yin GP, Zuo PJ (2020) Facile carbon fiber-sewed high areal density electrode for lithium sulfur batteries. *Chem Commun* 56(73):10758–10761
121. Shih HJ, Chang JY, Cho CS, Li CC (2020) Nano-carbon-fiber-penetrated sulfur crystals as potential cathode active material for high-performance lithium-sulfur batteries. *Carbon* 159:401–411
122. Zhang YZ, Zhang Z, Liu S, Li GR, Gao XP (2018) Free-standing porous carbon nanofiber/carbon nanotube film as sulfur immobilizer with high areal capacity for lithium-sulfur battery. *ACS Appl Mater Interfaces* 10(10):8749–8757
123. Chung S-H, Han P, Singhal R, Kalra V, Manthiram A (2015) Electrochemically stable rechargeable lithium-sulfur batteries with a microporous carbon nanofiber filter for polysulfide. *Adv Energy Mater* 5(18):1500738
124. Wang H, Zhang C, Chen Z, Liu HK, Guo Z (2015) Large-scale synthesis of ordered mesoporous carbon fiber and its application as cathode material for lithium-sulfur batteries. *Carbon* 81:782–787
125. He G, Mandlmeier B, Schuster J, Nazar LF, Bein T (2014) Bimodal mesoporous carbon nanofibers with high porosity: freestanding and embedded in membranes for lithium-sulfur batteries. *Chem Mater* 26(13):3879–3886
126. Yang XF, Yu Y, Yan N, Zhang HZ, Li XF, Zhang HM (2016) 1-D oriented cross-linking hierarchical porous carbon fibers as a sulfur immobilizer for high performance lithium-sulfur batteries. *J Mater Chem A* 4(16):5965–5972
127. Pan H, Cheng Z, Chen J, Wang R, Li X (2020) High sulfur content and volumetric capacity promised by a compact freestanding cathode for high-performance lithium-sulfur batteries. *Energy Storage Mater* 27:435–442
128. Zheng G, Yang Y, Cha JJ, Hong SS, Cui Y (2011) Hollow carbon nanofiber-encapsulated sulfur cathodes for high specific capacity rechargeable lithium batteries. *Nano Lett* 11(10):4462–4467
129. Ji LW, Rao MM, Aloni S, Wang L, Cairns EJ, Zhang YG (2011) Porous carbon nanofiber-sulfur composite electrodes for lithium/sulfur cells. *Energy Environ Sci* 4(12):5053–5059
130. Zhou L, Lin XJ, Huang T, Yu AS (2014) Nitrogen-doped porous carbon nanofiber webs/sulfur composites as cathode materials for lithium-sulfur batteries. *Electrochim Acta* 116:210–216
131. Zhang XQ, Sun Q, Dong W, Li D, Lu AH, Mu JQ, Li WC (2013) Synthesis of superior carbon nanofibers with large aspect ratio and tunable porosity for electrochemical energy storage. *J Mater Chem A* 1(33):9449–9455
132. Yang J, Xie J, Zhou XY, Zou YL, Tang JJ, Wang SC, Chen F, Wang LY (2014) Functionalized N-doped porous carbon nanofiber webs for a lithium-sulfur battery with high capacity and rate performance. *J Phys Chem C* 118(4):1800–1807
133. Elazari R, Salitra G, Garsuch A, Panchenko A, Aurbach D (2011) Sulfur-impregnated activated carbon fiber cloth as a binder-free cathode for rechargeable Li-S batteries. *Adv Mater* 23(47):5641–5644

134. Miao LX, Wang WK, Yuan KG, Yang YS, Wang AB (2014) A lithium-sulfur cathode with high sulfur loading and high capacity per area: a binder-free carbon fiber cloth-sulfur material. *Chem Commun* 50(87):13231–13234
135. Qie L, Manthiram A (2015) A facile layer-by-layer approach for high-areal-capacity sulfur cathodes. *Adv Mater* 27(10):1694–1700
136. Ren WC, Ma W, Zhang SF, Tang BT (2019) Recent advances in shuttle effect inhibition for lithium sulfur batteries. *Energy Storage Mater* 23:707–732
137. Zhang H, Wang Z, Ren J, Liu J, Li J (2020) Ultra-fast and accurate binding energy prediction of shuttle effect-suppressive sulfur hosts for lithium-sulfur batteries using machine learning. *Energy Storage Mater* 35:88–98
138. Zhang L, Wan F, Wang X, Cao H, Dai X, Niu Z, Wang Y, Chen J (2018) Dual-functional graphene carbon as polysulfide trapper for high-performance lithium sulfur batteries. *ACS Appl Mater Interfaces* 10(6):5594–5602
139. Chen K, Sun ZH, Fang RP, Shi Y, Cheng HM, Li F (2018) Metal-organic frameworks (MOFs)-derived nitrogen-doped porous carbon anchored on graphene with multifunctional effects for lithium-sulfur batteries. *Adv Funct Mater* 28(38):1707592
140. Fang R, Zhao S, Sun Z, Wang D-W, Amal R, Wang S, Cheng H-M, Li F (2018) Polysulfide immobilization and conversion on a conductive polar MoC@MoOx material for lithium-sulfur batteries. *Energy Storage Mater* 10:56–61
141. Hong XD, Wang R, Liu Y, Fu JW, Liang J, Dou SX (2020) Recent advances in chemical adsorption and catalytic conversion materials for Li-S batteries. *J Energy Chem* 42:144–168
142. Wang HQ, Zhang WC, Xu JZ, Guo ZP (2018) Advances in polar materials for lithium-sulfur batteries. *Adv Funct Mater* 28(38):1707520
143. Chung SH, Manthiram A (2014) A polyethylene glycol-supported microporous carbon coating as a polysulfide trap for utilizing pure sulfur cathodes in lithium-sulfur batteries. *Adv Mater* 26(43):7352–7357
144. Huang J-Q, Zhang Q, Zhang S-M, Liu X-F, Zhu W, Qian W-Z, Wei F (2013) Aligned sulfur-coated carbon nanotubes with a polyethylene glycol barrier at one end for use as a high efficiency sulfur cathode. *Carbon* 58:99–106
145. Hu QQ, Liu SL, Lu JQ, Zhong HX, Ren YL, Hu YJ, Cao SB, Li TL, Zhang LZ, Hong Y (2020) Strategy for practically constructing high-capacity sulfur cathode by combining sulfur-hierarchical porous graphitic carbon composite with surface modification of polydopamine. *Electrochim Acta* 356:136815
146. Hong X, Liu Y, Li Y, Wang X, Fu J, Wang X (2020) Application progress of polyaniline, polypyrrole and polythiophene in lithium-sulfur batteries. *Polymers (Basel)* 12(2):331
147. Wang X, Zhang S, Zhang H, Gao S, Han S, Xu Q, Xu J, Lu W, Wu X, Chen L (2019) 3D porous spherical sulfur/carbon cathode materials with in situ vapor-phase polymerized polypyrrole coating layer for high-performance lithium-sulfur batteries. *ACS Sustain Chem Eng* 7(20):17491–17499
148. Su DW, Cortie M, Wang GX (2017) Fabrication of N-doped graphene-carbon nanotube hybrids from prussian blue for lithium-sulfur batteries. *Adv Energy Mater* 7(8):1602014
149. Ding YL, Kopold P, Hahn K, van Aken PA, Maier J, Yu Y (2016) Facile solid-state growth of 3D well-interconnected nitrogen-rich carbon nanotube-graphene hybrid architectures for lithium-sulfur batteries. *Adv Funct Mater* 26(7):1112–1119
150. Arias AN, Villarroel-Rocha J, Sapag K, Mori MF, Planes GA, Tesio AY, Flexer V (2020) High nitrogen content carbons: morphological and chemical changes with synthesis temperature and application in lithium-sulfur batteries. *Electrochim Acta* 359:136942
151. Zeng S, Arumugam GM, Liu X, Yang Y, Li X, Zhong H, Guo F, Mai Y (2020) Encapsulation of sulfur into N-doped porous carbon cages by a facile, template-free method for stable lithium-sulfur cathode. *Small* 16(39):e2001027
152. Ren J, Zhou YB, Wu HL, Xie FY, Xu CG, Lin DM (2019) Sulfur-encapsulated in heteroatom-doped hierarchical porous carbon derived from goat hair for high performance lithium-sulfur batteries. *J Energy Chem* 30:121–131

153. Li F, Tao JY, Zou ZJ, Li C, Hou ZH, Zhao JJ (2020) Aminomethyl-functionalized carbon nanotubes as a host of small sulfur clusters for high-performance lithium-sulfur batteries. *Chemoschem* 13(10):2761–2768
154. Shen XW, Xu N, Liu XJ, Liu J, Qian T, Yan CL (2020) Strongly trapping soluble lithium polysulfides using polar cysteamine groups for highly stable lithium sulfur batteries. *Nanotechnology* 31(48)
155. Xu YW, Zhang BH, Li GR, Liu S, Gao XP (2020) Covalently bonded sulfur anchored with Thiol-modified carbon nanotube as a cathode material for lithium-sulfur batteries. *ACS Applied Energy Mater* 3(1):487–494
156. Rana M, He Q, Luo B, Lin TE, Ran LB, Li M, Gentle I, Knibbe R (2019) Multifunctional effects of sulfonyl-anchored, dual-doped multilayered graphene for high areal capacity lithium sulfur batteries. *ACS Central Sci* 5(12):1946–1958
157. Zheng G, Zhang Q, Cha JJ, Yang Y, Li W, Seh ZW, Cui Y (2013) Amphiphilic surface modification of hollow carbon nanofibers for improved cycle life of lithium sulfur batteries. *Nano Lett* 13(3):1265–1270
158. Yang Y, Yu GH, Cha JJ, Wu H, Vosgueritchian M, Yao Y, Bao ZA, Cui Y (2011) Improving the performance of lithium-sulfur batteries by conductive polymer coating. *ACS Nano* 5(11):9187–9193
159. Li XG, Rao MM, Chen DR, Lin HB, Liu YL, Liao YH, Xing LD, Li WS (2015) Sulfur supported by carbon nanotubes and coated with polyaniline: Preparation and performance as cathode of lithium-sulfur cell. *Electrochim Acta* 166:93–99
160. Yuan H, Zhang W, Wang J-G, Zhou G, Zhuang Z, Luo J, Huang H, Gan Y, Liang C, Xia Y, Zhang J, Tao X (2018) Facilitation of sulfur evolution reaction by pyridinic nitrogen doped carbon nanoflakes for highly-stable lithium-sulfur batteries. *Energy Storage Mater* 10:1–9
161. Gulzar U, Li T, Bai X, Colombo M, Ansaldo A, Marras S, Prato M, Goriparti S, Capiglia C, Proietti Zaccaria R (2018) Nitrogen-doped single-walled carbon nanohorns as a cost-effective carbon host toward high-performance lithium-sulfur batteries. *ACS Appl Mater Interfaces* 10(6):5551–5559
162. Wu X, Fan L, Wang M, Cheng J, Wu H, Guan B, Zhang N, Sun K (2017) Long-life lithium-sulfur battery derived from Nori-based nitrogen and oxygen dual-doped 3D Hierarchical biochar. *ACS Appl Mater Interfaces* 9(22):18889–18896
163. Fang R, Zhao S, Pei S, Cheng Y, Hou P, Liu M, Cheng H-M, Liu C, Li F (2016) An integrated electrode/separator with nitrogen and nickel functionalized carbon hybrids for advanced lithium/polysulfide batteries. *Carbon* 109:719–726
164. Fang R, Zhao S, Chen K, Wang D-W, Li F (2020) Binary graphene-based cathode structure for high-performance lithium-sulfur batteries. *J Phys Energy* 2(1):015003
165. Sun F, Wang J, Chen H, Li W, Qiao W, Long D, Ling L (2013) High efficiency immobilization of sulfur on nitrogen-enriched mesoporous carbons for Li-S batteries. *ACS Appl Mater Interfaces* 5(12):5630–5638
166. Niu S, Zhang S-W, Shi R, Wang J, Wang W, Chen X, Zhang Z, Miao J, Amini A, Zhao Y, Cheng C (2020) Freestanding agaric-like molybdenum carbide/graphene/N-doped carbon foam as effective polysulfide anchor and catalyst for high performance lithium sulfur batteries. *Energy Storage Mater*. 33:73–81
167. Hou TZ, Chen X, Peng HJ, Huang JQ, Li BQ, Zhang Q, Li B (2016) Design principles for heteroatom-doped nanocarbon to achieve strong anchoring of polysulfides for lithium-sulfur batteries. *Small* 12(24):3283–3291
168. Qiu Y, Li W, Zhao W, Li G, Hou Y, Liu M, Zhou L, Ye F, Li H, Wei Z, Yang S, Duan W, Ye Y, Guo J, Zhang Y (2014) High-rate, ultralong cycle-life lithium/sulfur batteries enabled by nitrogen-doped graphene. *Nano Lett* 14(8):4821–4827
169. Peng HJ, Hou TZ, Zhang Q, Huang JQ, Cheng XB, Guo MQ, Yuan Z, He LY, Wei F (2014) Strongly coupled interfaces between a heterogeneous carbon host and a sulfur-containing guest for highly stable lithium-sulfur batteries: mechanistic insight into capacity degradation. *Adv Mater Interfaces* 1(7):1400227

170. Yin LC, Liang J, Zhou GM, Li F, Saito R, Cheng HM (2016) Understanding the interactions between lithium polysulfides and N-doped graphene using density functional theory calculations. *Nano Energy* 25:203–210
171. Pang Q, Tang J, Huang H, Liang X, Hart C, Tam KC, Nazar LF (2015) A nitrogen and sulfur dual-doped carbon derived from polyrhodanine@cellulose for advanced lithium-sulfur batteries. *Adv Mater* 27(39):6021–6028
172. Mi K, Chen S, Xi B, Kai S, Jiang Y, Feng J, Qian Y, Xiong S (2017) Sole chemical confinement of polysulfides on nonporous nitrogen/oxygen dual-doped carbon at the kilogram scale for lithium-sulfur batteries. *Adv Funct Mater* 27(1):1604265
173. Zu C, Manthiram A (2013) Hydroxylated graphene-sulfur nanocomposites for high-rate lithium-sulfur batteries. *Adv Energy Mater* 3(8):1008–1012
174. Ma L, Zhuang HL, Wei S, Hendrickson KE, Kim MS, Cohn G, Hennig RG, Archer LA (2016) Enhanced Li-S batteries using amine-functionalized carbon nanotubes in the cathode. *ACS Nano* 10(1):1050–1059
175. Wang Z, Dong Y, Li H, Zhao Z, Wu HB, Hao C, Liu S, Qiu J, Lou XW (2014) Enhancing lithium-sulphur battery performance by strongly binding the discharge products on amino-functionalized reduced graphene oxide. *Nat Commun* 5:5002–5009
176. Fretz SJ, Pal U, Girard GMA, Howlett PC, Palmqvist AEC (2020) Lithium sulfonate functionalization of carbon cathodes as a substitute for lithium nitrate in the electrolyte of lithium-sulfur batteries. *Adv Funct Mater* 30(35):2002485
177. Wu R, Wang DP, Rui X, Liu B, Zhou K, Law AW, Yan Q, Wei J, Chen Z (2015) In-situ formation of hollow hybrids composed of cobalt sulfides embedded within porous carbon polyhedra/carbon nanotubes for high-performance lithium-ion batteries. *Adv Mater* 27(19):3038–3044
178. Xiang M, Wu H, Liu H, Huang J, Zheng Y, Yang L, Jing P, Zhang Y, Dou S, Liu H (2017) A flexible 3D multifunctional MgO-decorated carbon foam@CNTs hybrid as self-supported cathode for high-performance lithium-sulfur batteries. *Adv Funct Mater* 27(37):1702573
179. Zhang Z, Jing H-K, Liu S, Li G-R, Gao X-P (2015) Encapsulating sulfur into a hybrid porous carbon/CNT substrate as a cathode for lithium-sulfur batteries. *J Mater Chem A* 3(13):6827–6834
180. Li ZQ, Li CX, Ge XL, Ma JY, Zhang ZW, Li Q, Wang CX, Yin LW (2016) Reduced graphene oxide wrapped MOFs-derived cobalt-doped porous carbon polyhedrons as sulfur immobilizers as cathodes for high performance lithium sulfur batteries. *Nano Energy* 23:15–26
181. Yang W, Yang W, Song A, Sun G, Shao G (2018) 3D interconnected porous carbon nanosheets/carbon nanotubes as a polysulfide reservoir for high performance lithium-sulfur batteries. *Nanoscale* 10(2):816–824
182. Zhang Z, Kong L-L, Liu S, Li G-R, Gao X-P (2017) A high-efficiency sulfur/carbon composite based on 3D graphene nanosheet@carbon nanotube matrix as cathode for lithium-sulfur battery. *Adv Energy Mater* 7(11):1602543
183. Tang C, Zhang Q, Zhao MQ, Huang JQ, Cheng XB, Tian GL, Peng HJ, Wei F (2014) Nitrogen-doped aligned carbon nanotube/graphene sandwiches: facile catalytic growth on bifunctional natural catalysts and their applications as scaffolds for high-rate lithium-sulfur batteries. *Adv Mater* 26:6100–6105
184. Li Z, Zhang JT, Chen YM, Li J, Lou XW (2015) Pie-like electrode design for high-energy density lithium-sulfur batteries. *Nat Commun* 6:8850–8857
185. Zhao S, Fang R, Sun Z, Wang S, Veder J-P, Saunders M, Cheng H-M, Liu C, Jiang SP, Li F (2018) A 3D multifunctional architecture for lithium-sulfur batteries with high areal capacity. *Small Methods* 2(6):1800067
186. Gao P, Xu S, Chen Z, Huang X, Bao Z, Lao C, Wu G, Mei Y (2018) Flexible and hierarchically structured sulfur composite cathode based on the carbonized textile for high-performance Li-S batteries. *ACS Appl Mater Interfaces* 10(4):3938–3947
187. Wang Z, Shen J, Liu J, Xu X, Liu Z, Hu R, Yang L, Feng Y, Liu J, Shi Z, Ouyang L, Yu Y, Zhu M (2019) Self-supported and flexible sulfur cathode enabled via synergistic confinement for high-energy-density lithium-sulfur batteries. *Adv Mater* 31(33):1902228

188. Kong L, Tang C, Peng HJ, Huang JQ, Zhang Q (2020) Advanced energy materials for flexible batteries in energy storage: a review. *SmartMat*. <https://doi.org/10.1002/smm2.1007>
189. Wang ZS, Xu XJ, Ji SM, Liu ZB, Zhang DC, Shen JD, Liu J (2020) Recent progress of flexible sulfur cathode based on carbon host for lithium-sulfur batteries. *J Mater Sci Technol* 55:56–72
190. Wen L, Li F, Cheng HM (2016) Carbon nanotubes and graphene for flexible electrochemical energy storage: from materials to devices. *Adv Mater* 28(22):4306–4337
191. Mao YY, Li GR, Guo Y, Li ZP, Liang CD, Peng XS, Lin Z (2017) Foldable interpenetrated metal-organic frameworks/carbon nanotubes thin film for lithium-sulfur batteries. *Nat Commun* 8:14628
192. Sun ZX, Fang SY, Hu YH (2020) 3D graphene materials: from understanding to design and synthesis control. *Chem Rev* 120(18):10336–10453
193. Liu Y, Yao MJ, Zhang LL, Niu ZQ (2019) Large-scale fabrication of reduced graphene oxide-sulfur composite films for flexible lithium-sulfur batteries. *J Energy Chem* 38:199–206
194. Wang JN, Yang GR, Chen J, Liu YP, Wang YK, Lao CY, Xi K, Yang DW, Harris CJ, Yan W, Ding SJ, Kumar RV (2019) Flexible and high-loading lithium-sulfur batteries enabled by integrated three-in-one fibrous membranes. *Adv Energy Mater* 9(38):1902001
195. Su YS, Fu Y, Manthiram A (2012) Self-weaving sulfur-carbon composite cathodes for high rate lithium-sulfur batteries. *Phys Chem Chem Phys* 14(42):14495–14499
196. Jin KK, Zhou XF, Zhang LZ, Xin X, Wan GH, Liu ZP (2013) Sulfur/carbon nanotube composite film as a flexible cathode for lithium-sulfur batteries. *J Phys Chem C* 117(41):21112–21119
197. Sun L, Wang D, Luo Y, Wang K, Kong W, Wu Y, Zhang L, Jiang K, Li Q, Zhang Y, Wang J, Fan S (2016) Sulfur embedded in a mesoporous carbon nanotube network as a binder-free electrode for high-performance lithium-sulfur batteries. *ACS Nano* 10(1):1300–1308
198. Sun L, Li M, Jiang Y, Kong W, Jiang K, Wang J, Fan S (2014) Sulfur nanocrystals confined in carbon nanotube network as a binder-free electrode for high-performance lithium sulfur batteries. *Nano Lett* 14(7):4044–4049
199. Jin J, Wen ZY, Ma GQ, Lu Y, Cui YM, Wu MF, Liang X, Wu XW (2013) Flexible self-supporting graphene-sulfur paper for lithium sulfur batteries. *RSC Adv* 3(8):2558–2560
200. Zhou G, Li L, Ma C, Wang S, Shi Y, Koratkar N, Ren W, Li F, Cheng H-M (2015) A graphene foam electrode with high sulfur loading for flexible and high energy Li-S batteries. *Nano Energy* 11:356–365

Chapter 3

Li₂S Cathodes in Lithium–Sulfur Batteries



Hualin Ye, Yanguang Li, and Jun Lu

Abstract Lithium–sulfur (Li–S) batteries have attracted considerable research attentions in recent years, but their practical production is still challenging owing to several technical issues particularly the use of metallic Li anodes. Using fully lithiated sulfur (or Li₂S) as the cathode to pair with non-lithium anodes provides a feasible solution to circumvent the safety problem of Li metal and thereby may hold a greater potential for practical applications. However, Li₂S is almost electrochemically inert and has to overcome a large oxidation overpotential at the beginning of the charge process. In this chapter, we first discuss the underlying mechanism of the large oxidation overpotential of Li₂S and current understanding of the activation process. We then summarize various strategies developed in the past few decades to activate Li₂S cathodes and enhance their electrochemical performances in both half-cell and full-cell configurations. At last, some perspectives are provided for the future development of Li₂S cathodes.

Keywords Lithium–sulfur batteries · Lithium sulfide · Charging overpotential · Electrochemical activation

H. Ye · Y. Li (✉)

Jiangsu Key Laboratory for Carbon-Based Functional Materials and Devices, Institute of Functional Nano & Soft Materials (FUNSOM), Soochow University, Suzhou 215123, China
e-mail: yanguang@suda.edu.cn

H. Ye

Department of Chemical and Biomolecular Engineering, National University of Singapore, Singapore 119260, Singapore

J. Lu (✉)

Chemical Sciences and Engineering Division, Argonne National Laboratory, 9700 South, Cass Avenue, Lemont, IL 60439, USA
e-mail: junlu@anl.gov

3.1 Introduction

Lithium–sulfur (Li–S) batteries have been frequently advocated as an appealing energy–storage solution due to the large theoretical capacity (1675 mAh g^{-1}) and low price of sulfur ($< \$150 \text{ ton}^{-1}$) [1–5]. However, the large-scale application of Li–S batteries is yet unsuccessful due to several technical challenges [3–5]. One of the most serious problems is the use of highly reactive metallic Li anodes, which poses safety and cyclability concerns [6–8]. Using Li_2S as the cathode to pair with non-lithium anodes (e.g., Si, P, Sn, and SnO_2) provides an alternative solution to bypass the use of the problematic Li anode [9–12]. Hence, problems associated with the use of Li anodes including the dendritic or mossy Li growth, side reactions with polysulfides, and severe electrolyte depletion can be largely minimized (Fig. 3.1). The use of Li_2S cathode in Li–S batteries also has many other advantages. First, Li_2S has a high theoretical capacity of $\sim 1166 \text{ mAh g}^{-1}$ which exceeds most conventional positive electrodes (e.g., LiFePO_4 , LiCoO_2 , and LiMnO_2) of Li-ion batteries (LIBs) [10–12]. Second, Li_2S has a high melting point ($\sim 938 \text{ }^\circ\text{C}$) which affords Li_2S with high thermal stability. As such, it is feasible to prepare Li_2S -based composites under high temperatures which is however difficult for sulfur due to its low melting point of $115 \text{ }^\circ\text{C}$ [13–17]. For instance, compact carbon encapsulated Li_2S nanoparticles could be prepared through burning Li in CS_2 vapor or carbothermal reduction of Li_2SO_4 under high temperatures [18, 19]. Third, Li_2S has a low-mass density of $\sim 1.66 \text{ g cm}^{-3}$ which enables it to accommodate the volume change during cycling as Li_2S is already in the state of maximal volume. As a result, the Li_2S cathode can be roll-pressed into dense electrodes to guarantee the high volumetric energy density

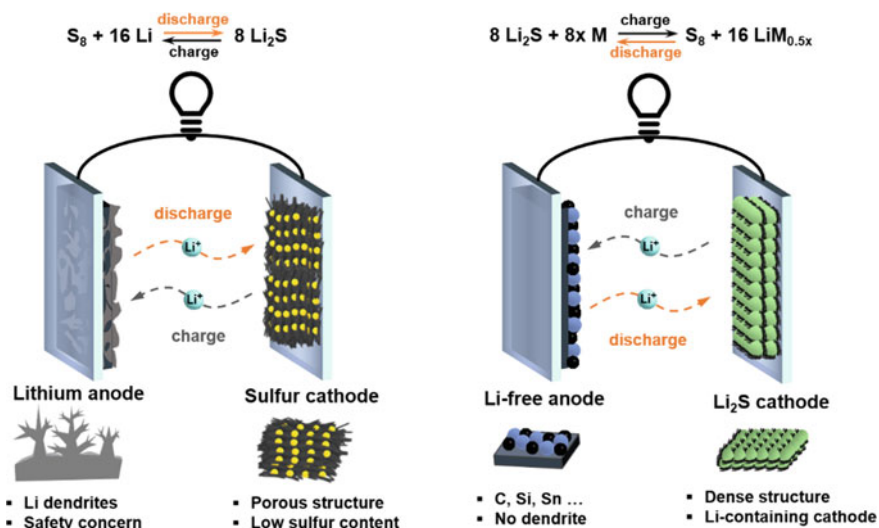


Fig. 3.1 Schematic cell types with sulfur (left) or Li_2S (right) as the cathode material, [11]. Reproduced with permission from Ref. [11]. Copyright 2020, American Chemical Society

while sulfur cathodes have to be porous in order to buffer the volume expansion. Thanks to these unique advantages, Li₂S may have great potential over sulfur for practical applications [20–23].

Unfortunately, the commercial production of Li₂S cathodes has been impeded by several technical challenges. The research progress of Li₂S cathodes is slower relative to the significant research advance of sulfur cathodes [24]. Aside from some common issues such as the low ionic/electric conductivity and the polysulfide dissolution and shuttle [9, 25], commercial Li₂S nearly has no electrochemical activity between 1.0–3.0 V versus Li⁺/Li and requires a high activation potential (>3.6 V) to initiate its oxidation. The research on Li₂S has not attracted much attention until 2012 when Cui's group found that a large activation potential of ~3.8 V was necessary to activate the Li₂S cathode. Such a high charging potential can result in the decomposition of electrolytes and short cycle life of Li₂S cathodes. To overcome these challenges, many strategies have been reported to lower the activation potential over the past few decades.

3.2 Activation Mechanism of Li₂S

Different from the cyclic molecular structure of S₈, Li₂S has an anti-fluorite crystal structure (Fig. 3.2a). This structure renders Li₂S with high structural stability and strong bond energy (standard enthalpy of formation: –447 kJ mol^{–1}). Like sulfur, Li₂S also suffers from poor ionic conductivity (~10^{–13} S cm^{–1}) and low electronic conductivity (~10^{–9} S cm^{–1}) [26, 27]. Commercial micro-sized Li₂S is therefore electrochemically inactive between the operation potential range of 1.0–3.0 V and has to be charged to >3.5 V to initiate the oxidation of Li₂S (Fig. 3.2b) [24, 28]. Such a high overpotential is closely related to its crystal structure and oxidation reaction pathway. Compared with S₈, the high structural stability of anti-fluorite Li₂S causes its delithiation process to be thermodynamically unfavored [29, 30].

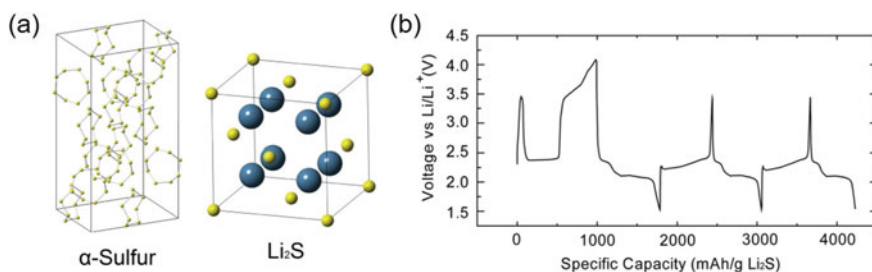


Fig. 3.2 **a** Crystal structures of α -sulfur and Li₂S, Reproduced with permission from Ref. [31]. Copyright 2015, American Chemical Society. **b** Voltage profile of a Li₂S electrode in different voltage ranges, Reproduced with permission from Ref. [28]. Copyright 2012, American Chemical Society

Moreover, the unique delithiation pathway of Li_2S also contributes to the large overpotential [31]. Cui's group studied the Li_2S reaction mechanism through in-situ synchrotron diffraction [28]. They found that a Li_2S core/ Li_{2-x}S shell structure was formed in the initial delithiation process, which was responsible for the initial potential rise. This was followed by the generation of soluble polysulfides until the charging potential reached ~ 3.5 V (Fig. 3.3a). After that, soluble polysulfides could serve as self-generated mediators to accelerate the reaction kinetics of Li_2S , thereby lowering the charging overpotential in the following cycles. As a result, the difficulty in forming soluble polysulfides was proposed to be the main reason of the initial charging overpotential of Li_2S . To further test this proposal, the authors added some soluble polysulfides to the electrolyte and observed that the activation potential was notably reduced.

There are also different views on the initial oxidation pathway of Li_2S . For instance, Zhang et al. detected the direct oxidation of Li_2S to sulfur without the formation of polysulfides through in-situ X-ray absorption spectroscopy (XAS) technique (Fig. 3.3b, c) [32]. In contrast to the rapid potential decrease shown in Fig. 3.2b, they observed that a high charging potential was always needed in the initial charge

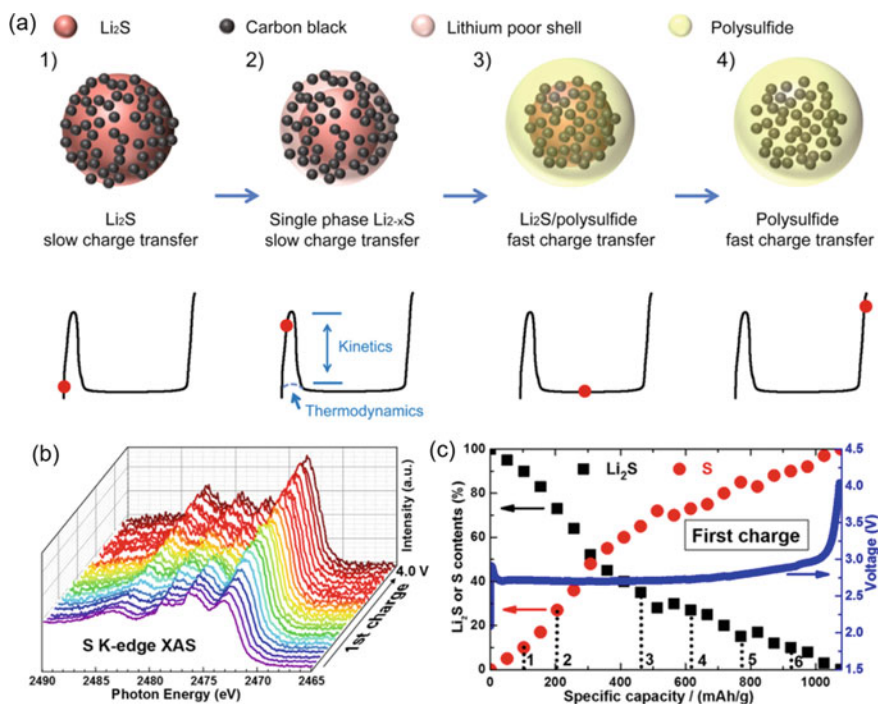


Fig. 3.3 **a** Schematic illustration of the initial delithiation mechanism of Li_2S , Reproduced with permission from Ref. [28]. Copyright 2012, American Chemical Society. **b** In situ S K-edge XAS spectra and **c** the corresponding contributions from Li_2S and sulfur species, Reproduced with permission from Ref. [32]. Copyright 2017, American Chemical Society

of Li₂S without the potential decrease (Fig. 3.3c). Similar phenomena were also observed by other research groups through in-situ XAS and UV-vis techniques [33, 34]. The different results observed in these in-situ characterizations might result from the different testing conditions. Dominko's group observed that the direct oxidation of Li₂S to sulfur was more likely to occur at low electrolyte-to-sulfur (E/S) ratios in which the polysulfide generation was more difficult [33]. The delithiation pathway could be changed under high E/S ratios [35].

3.3 Electrochemical Activation of Li₂S

Unlike Li–S batteries, LIBs with Li₂S cathodes (shorted as Li₂S batteries) are fabricated in the discharge state which requires a precharge process before use. Figure 3.1b presents the schematic working principle of a Li₂S cathode paired with a non-lithium anode. The electrochemical mechanism of Li₂S batteries follows the conventional principle of rocking-chair batteries without the safety concern of using reactive lithium. However, the aforementioned high overpotential of Li₂S can lead to the overcharge of Li₂S batteries to 4 V and may cause electrolyte decomposition. Given that the high charging overpotential is closely associated with the sluggish reaction kinetics of Li₂S and the difficulty of generating soluble polysulfides, many approaches have been reported to activate Li₂S for better performances, which include the structure engineering of Li₂S as well as the use of cathode electrocatalysts, redox mediators or electrolyte additives (Table 3.1).

3.3.1 Structural Engineering of Li₂S

Nanostructuring. Nanostructuring of Li₂S is able to reduce the Li⁺ ion transport distance and allow better contact between Li₂S particles and the conductive additive, thereby facilitating the charge transfer kinetics of Li₂S. Zhang's group prepared Li₂S–carbon nanocomposites through the ball milling of commercial Li₂S and carbon (Fig. 3.4a) [36]. The as-prepared Li₂S–C nanocomposite had an average size of ~400 nm and exhibited a notably low charging potential of ~2.52 V (Fig. 3.4b). When used as the cathode, it delivered a decent capacity of ~552 mAh g⁻¹ based on the mass of Li₂S at 0.2 C (1 C = 1166 mA g⁻¹). Unfortunately, the capacity retention was low (~74% after 50 cycles) as a result of the polysulfide dissolution in the electrolyte.

To simultaneously improve the electric conductivity and prevent the polysulfide shuttle, Yushin's group reported a facile approach to synthesize Li₂S nanoparticles with carbon encapsulation [37]. In a typical synthesis, commercial Li₂S powders were firstly mixed with polyvinylpyrrolidone (PVP) in ethanol. After the ethanol evaporation, the resultant powders were annealed at 700 °C to yield carbon encapsulated Li₂S (shorted as Li₂S@C) with a size distribution of 10–30 nm (Fig. 3.4c).

Table 3.1 A comparison of reported Li_2S -based cathodes

Cathodes	Li_2S loading (mg cm^{-2})	Activation barrier@Rate	Initial discharge capacity@Rate	Capacity retention (%)	References
$\text{Li}_2\text{S/C}$ mixture	1-1.5	3.5 V@0.05C	~950 mAh g^{-1} @0.1C	48% after 50 cycles	[28]
Ball-milled $\text{Li}_2\text{S/C}$	~0.54	2.6 V@0.02C	~552 mAh g^{-1} @0.2C	74% after 50 cycles	[36]
Carbon@ Li_2S	~0.75	3.2 V@0.05C	~925 mAh g^{-1} @0.2C	90% after 100 cycles	[37]
$\text{Li}_2\text{S@N,P-C}$	~1.2	2.7 V@0.1C	~650 mAh g^{-1} @1C	72% after 300 cycles	[38]
$\text{Li}_2\text{S@}$ graphene	~10	2.8 V@0.14C	~835 mAh g^{-1} @0.14C	67% after 200 cycles	[39]
Amorphous $\text{Li}_2\text{S/C}$	NA	2.4 V@0.05C	~1052 mAh g^{-1} @0.05C	76% after 36 cycles	[40]
Fe-doped Li_2S	~3	2.4 V@0.04C	~720 mAh g^{-1} @0.04C	69% after 10 cycles	[41]
$\text{VS}_2\text{-Li}_2\text{S}$	0.9-1.1	2.9 V@0.1C	~830 mAh g^{-1} @0.5C	84% after 300 cycles	[42]
3DCoS-C/ Li_2S	~8	2.3 V@0.1C	~1055 mAh g^{-1} @0.1C	90% after 200 cycles	[43]
$\text{LiTiO}_2/\text{Li}_2\text{S}$	~1.2	2.4 V@0.5C	~730 mAh g^{-1} @0.5C	88% after 400 cycles	[17]
$\text{Li}_2\text{S/C}$ with ethanol	1.2-2	2.9 V@0.2C	~1052 mAh g^{-1} @0.2C	32% after 100 cycles	[44]
PDSe- Li_2S	~1.0	2.2 V@0.5C	~780 mAh g^{-1} @0.5C	80% after 200 cycles	[45]
$\text{Li}_2\text{S/C}$ with DmFc	~3	2.9 V@0.2C	~750 mAh g^{-1} @0.2C	67% after 150 cycles	[46]
$\text{Li}_2\text{S/C}$ with LiI	~0.8	2.8 V@0.05C	~973 mAh g^{-1} @0.2C	92% after 100 cycles	[47]
$\text{Li}_2\text{S/C}$ with AQT	~4	2.5 V@0.3C	~600 mAh g^{-1} @0.1C	70% after 100 cycles	[48]
$\text{Li}_2\text{S/C}$ with Li_3PS_4	~1.5	2.8 V@0.05C	~597 mAh g^{-1} @0.025C	67% after 100 cycles	[49]

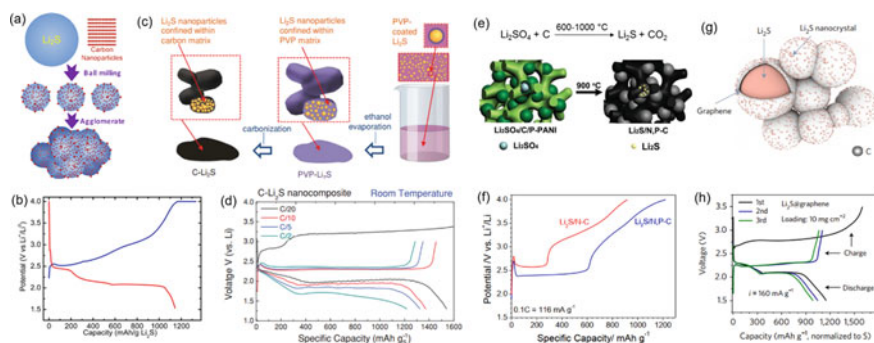


Fig. 3.4 **a** Schematic synthetic procedure and **b** charge–discharge curves of the ball-milled Li_2S -C nanocomposite, Reproduced with permission from Ref. [36]. Copyright 2012, American Chemical Society. **c** Schematic synthetic procedure and **d** charge–discharge curves of the liquid-phase prepared Li_2S -C nanocomposite, Reproduced with permission from Ref. [37]. Copyright 2014, Wiley-VCH. **e** Schematic synthetic procedure and **f** charge–discharge curves of the in-situ carbothermal reduced $\text{Li}_2\text{S}@N,P-C$ composite, Reproduced with permission from Ref. [38]. Copyright 2017, Wiley-VCH. **g** Schematic illustration and **h** charge–discharge curves of the $\text{Li}_2\text{S}@graphene$ nanocomposite, Reproduced with permission from Ref. [39]. Copyright 2017, Nature Publishing Group

Thanks to the carbon protection and nanocrystallization, the as-prepared Li_2S delivered a much lower activation barrier (<3.0 V) and showed a large discharge capacity of ~ 919 mAh g^{-1} (Fig. 3.4d). After that, many Li_2S -C nanocomposites via liquid-phase preparation methods have been demonstrated [15, 22, 50–52].

Since Li_2S is air-sensitive, it is often challenging to process commercial Li_2S from microsize to nanosize. Some studies reported that the indirect preparation of Li_2S -C nanocomposites from air-stable precursors could be an alternative solution. Archer's group first demonstrated a facile method to synthesize Li_2S -C nanocomposites from the high-temperature carbothermal reduction of Li_2SO_4 [53]. Li_2SO_4 powders were first uniformly dispersed on a resorcinol-formaldehyde aerogel. Li_2S was then obtained through the carbothermal reduction of Li_2SO_4 by carbon under elevated temperatures. Since this work, the carbothermal reduction strategy has been widely adopted in many studies [38, 54, 55]. For example, Yu's group prepared a Li_2S -N,P co-doped carbon nanocomposite ($\text{Li}_2\text{S}@N,P-C$) through the carbothermal reduction of Li_2SO_4 (Fig. 3.4e) [38]. The size of the resultant $\text{Li}_2\text{S}@N,P-C$ nanocomposite varied from 50 to 200 nm. More impressively, $\text{Li}_2\text{S}@N,P-C$ cathode exhibited a small charging potential of ~ 2.7 V (Fig. 3.4f) and delivered a long cycle life of 300 cycles. The long cycle stability could be attributed to the good polysulfide adsorption capability of N, P co-doped carbon.

Li_2S can also be synthesized from the reaction between S_8 and Li-based reductants such as LiH and $\text{Li}(\text{C}_2\text{H}_5)_3\text{BH}$ [55, 56]. These reactions are unfortunately not amenable to large-scale applications. In a recent study, Tan et al. reported a high-temperature approach to synthesize a Li_2S -C nanocomposite by burning metallic Li in CS_2 (Fig. 3.4g) [39]. Resultant Li_2S nanoparticles with sizes in the range of 40–60 nm

were encapsulated in few-layered graphene shells (denoted as $\text{Li}_2\text{S}@$ graphene). Impressively, the thus-obtained $\text{Li}_2\text{S}@$ graphene cathode displayed a large initial capacity of $\sim 835 \text{ mAh g}^{-1}$ at 0.14 C and a low charging potential of $\sim 2.8 \text{ V}$ (Fig. 3.4h).

Amorphization. Compared to crystalline Li_2S , amorphous Li_2S has lower lattice energy and weaker Li–S bonding, which are conducive to extracting lithium from Li_2S . Zhang's group conducted DFT simulations to analyze the influence of the Li_2S crystallinity on the charging overpotential [57]. The obtained results indicated that the dissociation energy barrier of amorphous Li_2S was noticeably lower than that of crystalline Li_2S (2.16 eV vs. 3.21 eV). This was an indicator of the easier delithiation of amorphous Li_2S than that of crystalline Li_2S . The preparation of amorphous materials usually requires the rapid nucleation and low reaction temperature to prevent the material crystallization [40, 57, 58]. For example, Elam's group synthesized amorphous Li_2S through the reaction between lithium tertbutoxide ($\text{LiOC}(\text{CH}_3)_3$) and H_2S via the atomic layer deposition [40]. The obtained Li_2S delivered a low charging overpotential of $\sim 2.4 \text{ V}$ and a large discharge capacity of $\sim 1000 \text{ mAh g}^{-1}$. However, it had short cycle life of only 36 cycles as a result of polysulfide dissolution and shuttle. In addition, Fu et al. reported that amorphous Li_2S could be prepared from the chemical reduction of Li_2S_6 by a lithiated carbon paper (CP) [59]. The amorphous structure of Li_2S was revealed by X-ray diffraction (XRD). Electrochemical measurements indicated that the as-prepared amorphous Li_2S exhibited nearly no charging overpotential. In a similar work, Passerini's group also reported the reaction between Li and S_8 in an amine-based solvent that led to the formation of amorphous Li_2S with negligible charging overpotential in Li_2S batteries [58].

Doping. Elemental doping can enhance the electric and ionic transport properties of Li_2S [60, 61]. The doping approach is inspired by previous reports that the introduction of transition metals (e.g., Co, Cu, Fe) to Li_2S could significantly decrease its charging overpotential [24, 62]. Wang's group conducted DFT simulations of the delithiation of metal-doped Li_2S [63]. They observed that Fe-doped Li_2S exhibited the lowest dissociation energy barrier, indicating that Fe doping was the most effective to reduce the charging overpotential of Li_2S . As such, Matsubara's group synthesized Fe-doped Li_2S through the ball milling of Li_2S and FeS [41]. Structural characterizations indicated that Fe-doped Li_2S retained the anti-fluorite structure of Li_2S with Fe ions partially occupying Li sites. The product had negligible charging overpotential, but unfortunately suffered from poor cycle life.

Besides metal doping, the non-metal doping of Li_2S is also a feasible approach to improve the charge transfer of Li_2S . For instance, Qian's group investigated the delithiation of Te-doped Li_2S [64]. Their DFT calculations indicated that the Te doping could significantly facilitate the Li^+ diffusion in the Li_2S crystal. As such, the Te doping afforded the Li_2S cathode with lower decomposition energy. Maier's group studied the charge transfer property of Cl-doped Li_2S through structure-performance analysis [60]. Their results indicated that Cl-doped Li_2S showed significantly enhanced ionic and electric conductivity.

3.3.2 Cathode Electrocatalysts

The use of catalysts is a common strategy to decrease the reaction activation barrier by modifying the reaction pathway. Electrocatalysts have been widely used in the field of electrochemistry to lower the reaction energy barrier [65]. Their introduction in Li–S batteries was first started with sulfur cathodes and then with Li₂S cathodes and were demonstrated to effectively decrease the activation barrier of Li₂S and accelerate the polysulfide conversion. As such, the polysulfide accumulation at the cathode was largely reduced [66–69].

Based on the results of their earlier studies, Cui's group investigated the electrocatalytic oxidation of Li₂S on transition metal sulfides (Fig. 3.5a) [42]. Six metal sulfides including VS₂, CoS₂, TiS₂, FeS, SnS₂, and Ni₂S₃ were compared to identify the possible catalytic effect by simulating the dissociation of Li₂S to LiS + Li⁺ on the catalyst surface (Fig. 3.5b). The authors found that the energy barrier was decreased in the following order: Ni₃S₂ > FeS > CoS₂ > SnS₂ > VS₂ > TiS₂ that was consistent with their experimental observations (Fig. 3.5c). The energy barrier was believed to be associated with the binding energy between Li atoms and the sulfur atoms of metal sulfides. Strong binding was favorable for breaking the Li–S bond in Li₂S.

In view of the low electric conductivity of most metal sulfides, Manthiram's group prepared metal sulfides (CoS, NiS, and MnS) decorated on three-dimensional (3D) carbon as the electrocatalysts for high-loading Li₂S batteries (Fig. 3.5d) [43]. Electrochemical investigations revealed no activation barriers when they were used as the cathode catalyst (Fig. 3.5e). It was the most impressive that among them, 3D CoS₂–Li₂S cathode exhibited 1055 mAh g⁻¹ and a long cycle life of 200 cycles.

In addition to metal sulfides, metal carbides, phosphides, and oxides have also been investigated as the potential catalysts to lower the charging potential of Li₂S cathodes [9, 12]. Yu's group synthesized a multi-layer Ti₃C₂/Li₂S cathode and observed a

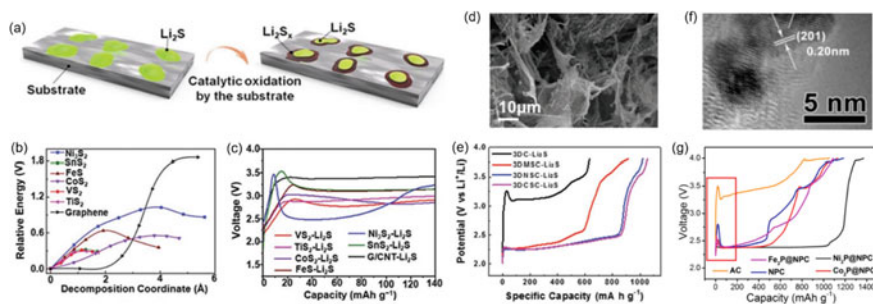


Fig. 3.5 **a** Schematic reaction mechanism, **b** decomposition energy profiles and **c** initial charge curves of Li₂S catalyzed by different transition metal sulfides, Reproduced with permission from Ref. [42]. Copyright 2017, National Academy of Sciences. **d** SEM image of 3DCoSC, **e** initial charge curves of different 3DTSC-Li₂S, Reproduced with permission from Ref. [43]. Copyright 2019, Wiley-VCH. **f** TEM image of Fe₂P@NPC, **g** initial charge curves of TMPs@NPC, Reproduced with permission from Ref. [70]. Copyright 2017 American Chemical Society

much decreased activation barrier between 2.8–3.5 V [71]. Tao's group investigated the effect of metal phosphides in lowering the activation barrier of Li_2S [72]. They prepared three kinds of metal phosphides (Ni_2P , Co_2P , and Fe_2P) anchored on N,P co-doped carbon (TMPs@NPC) (Fig. 3.5f). When mixed with Li_2S , TMPs@NPCs exhibited decreased activation potentials of 2.59, 2.51, and 2.44 V for Fe_2P @NPC, Co_2P @NPC, and Ni_2P @NPC, respectively (Fig. 3.5g). Furthermore, Yushin's group reported a Li_2S - LiTiO_2 core-shell cathode which displayed a negligible charging overpotential [17]. Their theoretical simulations indicated that the LiTiO_2 shell facilitated the delithiation of Li_2S and also had good polysulfide adsorption capability. As a result, the obtained LiTiO_2 @ Li_2S core-shell cathode demonstrated an initial capacity of ~ 730 mAh g^{-1} at 0.5 C with 88% capacity retention after 400 cycles.

3.3.3 Redox Mediators

Redox mediators have been widely used in $\text{Li}-\text{O}_2$ batteries to enhance the reaction kinetics [70, 73]. They act as charge carriers to participate in redox reactions and accelerate the charge transfer process (Fig. 3.6a, b). Aurbach's group first studied the effect of redox mediators in decreasing the charging overpotential of Li_2S [46]. They investigated five redox mediators with different redox potentials. The results indicated that only mediators possessing higher redox potentials than Li_2S could reduce the charging overpotential. Among the five mediators, Li_2S with decamethylferrocene showed the lowest activation potential of ~ 2.9 V (Fig. 3.6c). Yushin's group further reported that the concentration of LiI could also affect the charging overpotential of Li_2S [47]. Their results suggested that the activation potential decreased

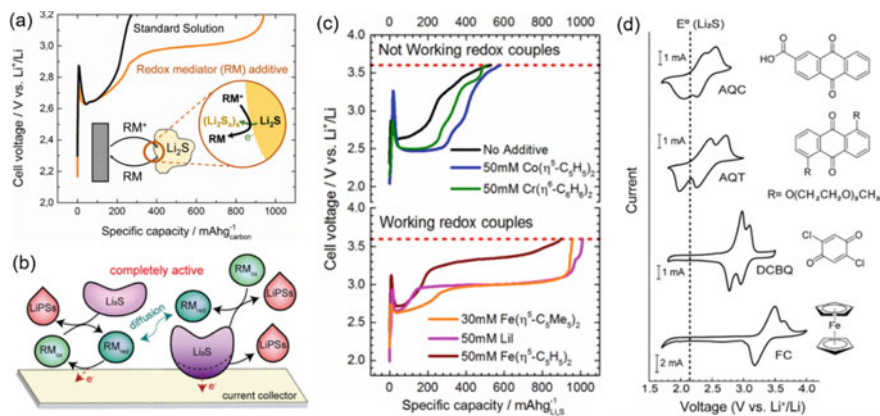


Fig. 3.6 a, b Schematic working mechanisms of redox mediators in Li_2S oxidation reaction, c initial charge curves of Li_2S in the presence of different redox mediators, d CV curves of different redox mediators, Reproduced with permissions from Ref. [46, 48]. Copyright 2014, American Chemical Society and Copyright 2019, Elsevier

from 2.9 to 2.8 V when the LiI concentration increased from 0.01 to 0.5 M. In a recent study, Bao and Cui et al. reported a class of quinone-based redox mediators that could considerably decrease the charging overpotential of Li₂S [48]. Quinones are well known for their advantages of tunable redox potential and high solubility in electrolytes. By tuning the molecular structure of quinone derivatives with different redox potentials, they observed that a quinone derivate (AQT) could significantly decrease the charging potential to 2.45 V (Fig. 3.6d). With the addition of AQT in the electrolyte, Li₂S cathode could exhibit a large capacity of ~600 mAh g⁻¹ with decent cycle stability.

The use of redox mediators is a simple but effective way to activate Li₂S. However, the dissolution of redox mediators in the electrolyte can cause side reactions with the lithium anode. In addition, the concentration of mediators is also a significant factor affecting the charging overpotential. It has been reported that the addition of soluble polysulfides could not decrease the charging overpotential if the concentration was decreased to 7 μL mg⁻¹ Li₂S [49]. The use of solid additives that can in-situ generate mediators can be an alternative solution. Li₃PS₄ is known as a solid-state electrolyte that has a slightly higher oxidation potential than that of Li₂S. Li et al. reported that the activation potential of Li₂S reduced from ~4.0 to ~2.7 V by simply mixing Li₃PS₄ with Li₂S as the cathode [49].

3.3.4 Electrolyte Additives

Since the charging overpotential of Li₂S is associated with its stable anti-fluorite crystal structure, the use of electrolyte additives to facilitate the solvation of Li₂S has also been demonstrated as a possible solution. Solvation of Li₂S can transform the conversion reaction from a solid phase to a liquid phase and thus can accelerate the reaction kinetics and decrease the activation barrier. Liang's group observed that adding P₂S₅ to the electrolyte could increase the dissolution of Li₂S [74]. Manthiram's group added P₂S₅ to the Li₂S cathode and observed that the charging potential of Li₂S was decreased to ~2.4 V [75]. In a recent study, Xiang's group found that a trace amount of ethanol in the electrolyte could assist in the partial solvation of Li₂S [44]. Their results indicated that the activation barrier can be reduced from 3.4 to 2.9 V with the addition of 250 ppm ethanol to the electrolyte. Similarly, Fu's group found that phenyl diselenide (PDSe) could also enhance the solvation of Li₂S as a result of the inductive effect between PDSe and Li₂S [45]. Their simulation results suggested that Se atoms of PDSe could strongly attract the Li atoms of Li₂S, weakening the Li–S bond of Li₂S. As a result, Li₂S cathodes with 0.5 M PDSe in the electrolyte displayed nearly no charging overpotential, concurrently with a promising specific capacity of ~780 mAh g⁻¹ at 0.5 C.

3.4 Full Cells Based on Li_2S Cathodes

The biggest strength of Li_2S over sulfur as the cathode is that it can be coupled with non-lithium anodes to bypass the use of metallic lithium. However, most research attentions have been focused on the evaluation of Li_2S in half cells, while relatively little has been explored on the combination of the Li_2S cathode and non-lithium anodes in full cells. The cyclability of Li_2S full cells with non-lithium anodes is in principle better than that with the lithium anode since the cyclability of lithium still faces many challenges. One of the main challenges is the formation of dendritic or mossy lithium during cycling. Brückner et al. observed that the dendritic lithium growth and electrolyte depletion were more severe in Li_2S batteries with lithium as the anode, compared those with non-lithium anodes [76].

3.4.1 Anode Materials for Li_2S Full Cells

Figure 3.7 summarizes the gravimetric energy densities of Li_2S full cells with different anode materials. It is indicated that the use of carbon-based anodes cannot promise Li_2S full cells with an energy density above 500 Wh kg^{-1} owing to the intrinsically low theoretical capacity of carbon ($\sim 375 \text{ mAh g}^{-1}$). Many high-capacity anodes such as Si, SnO, and Sn can afford the full cell with highly promising energy density, but unfortunately have problems of significant volume change and short

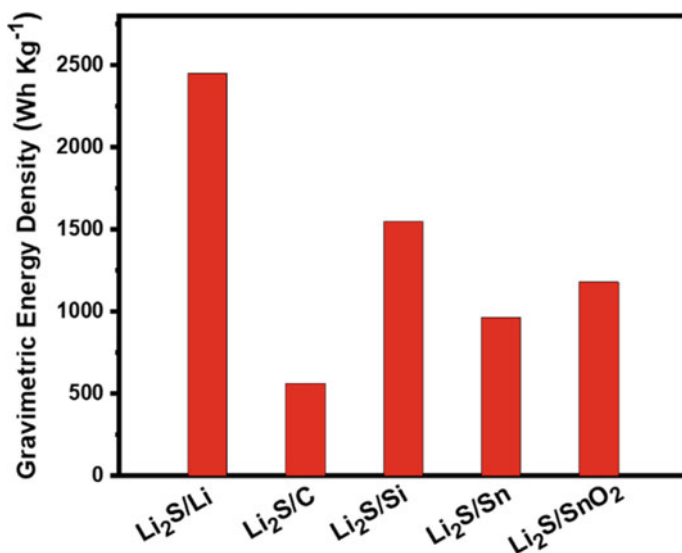


Fig. 3.7 Comparison of the gravimetric energy density of different Li_2S full cells normalized to the mass of all active materials

cycle life. As a result, most reported Li₂S full cells to date suffer from rapid capacity fade and short cycle life. The successful match of the Li₂S cathode with non-lithium anodes in full cells is tabulated in Table 3.2. All the reported capacity was normalized to the mass of Li₂S for a fair comparison.

Graphite has been successfully commercialized in LIBs for a few decades because of its applicable voltage plateau (~0.2 V) and excellent cyclability (>1000 cycles). Unfortunately, it is unstable in ether-based electrolytes due to the co-intercalation of ether molecules into graphite, resulting in the exfoliation of graphite [89]. To tackle with this issue, Lv et al. found that the use of high-concentrated ether-based electrolytes could effectively protect the graphite anode from the intercalation of solvent molecules [90]. Their electron microscopic characterizations indicated that a thin solid electrolyte interface (SEI) layer (100–200 nm) was formed on the graphite surface. Ye et al. further paired the graphite anode with a Li₂S cathode in a full cell in the high-concentrated electrolyte [77]. The assembled Li₂S/graphite full battery delivered a high discharge capacity of ~810 mAh g⁻¹ at 0.1 C and ~300 mAh g⁻¹ at 1 C after 600 cycles.

Carbonate electrolytes and ionic liquids have also been explored in Li₂S/graphite full cells. Zheng et al. prepared Li₂S nanoparticles embedded in microporous carbon (Li₂S/MC) as the cathode [78] and found that it could be cycled in carbonate electrolytes for hundreds of cycles. They attributed the good cyclability to the single-step solid–solid Li₂S ↔ Li₂S₄ conversion of the Li₂S/MC cathode in the carbonate electrolyte. Similar to the conversion mechanism of smaller sulfur (S_{2–4}) reported earlier [91], this single-step conversion does not involve the formation of soluble polysulfides. The assembled Li₂S/MC-graphite full cell exhibited a discharge capacity of ~680 mAh g⁻¹ at 0.14 C with a cycle life of 150 cycles. Watanabe's group reported a solvated electrolyte that was compatible with both Li₂S and graphite electrodes (Fig. 3.8a) [79]. In this electrolyte, the polysulfide shuttle and the intercalation of solvent molecules in graphite were largely suppressed. As a consequence, the full cell with the solvated electrolyte delivered a discharge capacity of ~820 mAh g⁻¹ at 0.08 C and a cycle life of 100 cycles (Fig. 3.8b).

Silicon is a promising anode material due to its earth abundance, low discharge potential (~0.3 V vs. Li⁺/Li), and high theoretical capacity (~4200 mAh g⁻¹) [93]. Yang et al. first introduced the nano-Si anode to pair with the CMK–Li₂S cathode (Fig. 3.8c) [84]. The fabricated CMK–Li₂S/Si full cell delivered an initial capacity of 430 mAh g⁻¹ at C/3 with 54% capacity retention after 20 cycles (Fig. 3.8d). The short cycle life of the CMK–Li₂S/Si full cell was not surprising since both the Li₂S cathode and Si anode suffer from rapid capacity fade and short cycle life. To improve the cycle stability of the Li₂S cathode, Hao et al. incorporated Li₂S nanoparticles into a hollow carbon as the cathode and added TiN into the cathode to anchor soluble polysulfides. When combined with a nano-Si anode, the as-prepared Li₂S-TiN/nano-Si full cell exhibited a large capacity of ~702 mAh g⁻¹ at 0.5 C with a cycle life of 200 cycles [16]. Besides the Li₂S cathode, Qiu's group further improved the cyclability of the Si anode by incorporating Si nanoparticles into hollow carbon nanofibers [85]. When combined with a carbon encapsulated Li₂S cathode, the obtained Li₂S/Si battery delivered a large discharge capacity of ~710 mAh g⁻¹ at 0.2 C. Although

Table 3.2. Summary of Li_2S full cells reported in literature. Note the specific capacity is normalized to the Li_2S mass

Cathode	Anode	Electrolyte	Li_2S loading (mg cm^{-2})	Initial discharge capacity@rate	Capacity retention (%)	References
$\text{Li}_2\text{S-C}$	Graphite	3 M LiTFSI in DOL/DME	2.0	~810 mAh g^{-1} @0.1 C	82% after 100 cycles	[77]
$\text{Li}_2\text{S/MC}$	Graphite	1.0 M LiPF ₆ in EC/DEC	1.0	~680 mAh g^{-1} @0.14 C	88% after 150 cycles	[78]
$\text{Li}_2\text{S/C}$	Graphite	Ionic liquid	0.5–2.2	~820 mAh g^{-1} @0.08 C	55% after 100 cycles	[79]
$\text{Li}_2\text{S/PC}$	Graphite	1 M LiTFSI in DOL/DME	1.0	~320 mAh g^{-1} @0.5 C	54% after 100 cycles	[80]
$\text{Li}_2\text{S/Graphene}$	Graphite	1 M LiTFSI in D2/DOL	2.0	~730 mAh g^{-1} @0.14 C	68% after 200 cycles	[39]
TG– Li_2S	Silicon	1 M LiTFSI in DOL/DME	1.0	~900 mAh g^{-1} @0.05 C	90% after 10 cycles	[81]
$\text{Li}_2\text{S/C/G}$	Silicon	1 M LiTFSI in DOL/DME	0.4	~600 mAh g^{-1} @0.1 C	50% after 30 cycles	[82]
$\text{Li}_2\text{S-MCMB}$	Silicon	1 M LiTFSI in TEGDME	1.0	~390 mAh g^{-1} @0.2 C	64% after 50 cycles	[83]
CMK– Li_2S	Silicon	1 M LiTFSI in DOL/DME	1.1–1.4	~430 mAh g^{-1} @ C/3	55% after 20 cycles	[84]
TiN/PHC@ Li_2S	Silicon	1 M LiTFSI in DOL/DME	3.4	~702 mAh g^{-1} @0.5 C	40% after 200 cycles	[16]

(continued)

Table 3.2 (continued)

Cathode	Anode	Electrolyte	Li_2S loading (mg cm^{-2})	Initial discharge capacity@rate	Capacity retention (%)	References
$\text{Li}_2\text{S-ZnS@NC}$	Silicon	1 M LiTFSI in DOL/DME	2.0	~710 mAh g^{-1} @0.2 C	64% after 200 cycles	[85]
$\text{Li}_2\text{S/C}$	Silicon	1 M LiTFSI in DOL/DME	2.0	~450 mAh g^{-1} @ 1 C	56% after 70 cycles	[86]
$\text{Li}_2\text{S/C}$	Tin	PEO-based	NA	~440 mAh g^{-1} @0.2 C	68% after 90 cycles	[87]
$\text{Li}_2\text{S/C}$	Tin oxide	1 M LiTFSI in DOL/DME	2.4	~703 mAh g^{-1} @0.5 C	92% after 200 cycles	[88]

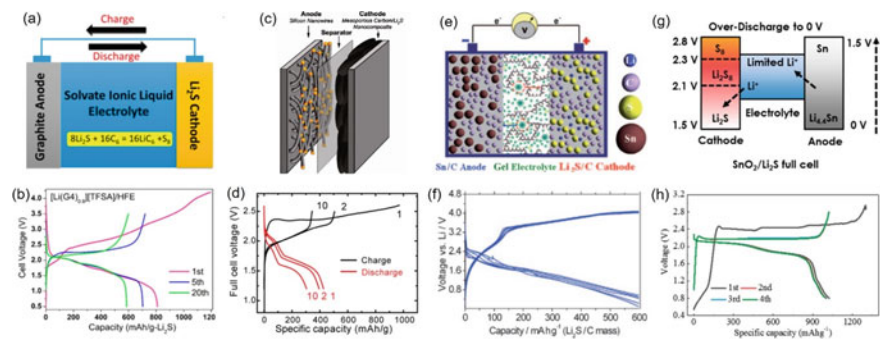


Fig. 3.8 **a** Schematic illustration and **b** charge–discharge curves of a Li_2S /graphite full cell, Reproduced with permission from Ref. [79]. Copyright 2016 American Chemical Society. **c** Schematic illustration and **d** charge–discharge curves of a CMK- Li_2S /Si full cell, Reproduced with permission from Ref. [84]. Copyright 2010 American Chemical Society. **e** Schematic illustration and **f** charge–discharge curves of a Li_2S /Sn full cell, Reproduced with permission from Ref. [87]. Copyright 2010 Wiley-VCH. **g** Schematic illustration and **h** charge–discharge curves of a $\text{SnO}_2/\text{Li}_2\text{S}$ full cell, Reproduced with permission from Ref. [94]. Copyright 2017 Elsevier

many $\text{Li}_2\text{S}/\text{Si}$ full cells were reported as shown in Table 3.2, very few of them could achieve long cycle life (>1000 cycles).

Metallic tin (Sn) is also regarded as a potential anode material. It has a larger theoretical capacity ($\sim 990 \text{ mAh g}^{-1}$) than graphite and suffers from less volume expansion ($\sim 260\%$) than silicon ($\sim 420\%$) [93]. Scrosati's group first reported the use of Sn anode in Li_2S full cells with a poly(ethylene oxide)-based polymer electrolyte to suppress the polysulfide shuttle (Fig. 3.8e) [87]. The prepared $\text{Li}_2\text{S}/\text{Sn}$ cell showed a discharge capacity of $\sim 440 \text{ mAh g}^{-1}$ at 0.2 C with 68% capacity retention after 90 cycles (Fig. 3.8f). Similar to metallic Sn, tin oxide (SnO_2) also has a large theoretical capacity ($\sim 1494 \text{ mAh g}^{-1}$) and relatively lower volume expansion ($\sim 250\%$) [88]. Liu et al. explored the performance of $\text{Li}_2\text{S}/\text{SnO}_2$ full cells (Fig. 3.8g). Their results showed that the full cell delivered a discharge capacity of $\sim 703 \text{ mAh g}^{-1}$ at 0.5 C and long cycle life of 200 cycles (Fig. 3.8h) [94].

3.4.2 Lithium Loss in Li_2S Full Cells

Li_2S -based full cells with non-lithium anodes should in principle have better cyclability than Li_2S -Li half cells. The practical performance is however the opposite based on current research results from literatures. One of the reasons is possibly due to the excessive amount of lithium (usually $>1000\%$) used in Li_2S -Li half cells, which can offset the lithium loss during cycling [4]. However, the lithium source only comes from the Li_2S cathode when used with lithium-free anodes. Since most lithium-free anodes suffer from low initial Coulombic efficiency (sometimes $<70\%$) [92], the lithium source from the Li_2S cathode is usually not enough to compensate

the lithium consumption for the SEI formation at the anode. It is therefore highly necessary to offset the initial lithium loss to guarantee the cyclability of Li₂S full cells.

The most common approach to offset the lithium loss is to use a slightly excessive amount of Li₂S. Jha et al. adopted this method to offset the initial lithium loss of the Si–C electrode by controlling the positive/negative capacity ratio to be ~1.1 (2.3 and 2.1 mAh cm⁻² for Li₂S and Si–C electrodes respectively) [86]. The thus-assembled cell exhibited an initial specific capacity of ~450 mAh g⁻¹ at 1 C with a decent cycle life. By comparison, the Li₂S–Li cell suffered from severe dendrite formation at the same testing conditions. Similar to the use of slightly excessive Li₂S, the addition of lithium-rich compounds to the Li₂S cathode is also a feasible solution. The lithium-rich compounds can release additional Li⁺ ions to compensate for the lithium loss during the initial charge process. Sun et al. found that Li₃N added to Li₂S electrodes could serve as a secondary lithium source to offset the lithium loss [95]. They also demonstrated that the LiCoO₂–Li₃N/graphite cell with 2.5 wt% Li₃N at the cathode delivered higher specific capacity and better cycle stability than the LiCoO₂/graphite cell without the Li₃N additive. Based on this discovery, they also introduced a mixture of transition metals and lithium oxide (M/Li₂O) as the lithium source to offset the initial lithium loss in a LiFePO₄/graphite full cell [96]. These methods can also be translated to Li₂S full cells to improve the cycle performance.

Another approach to offset the initial lithium loss is the prelithiation strategy. Yang's group reported a fast prelithiation approach to lithiate both the polyacrylonitrile-sulfur (PAN-S) cathode and the Si anode by immersing them in a lithium naphthalenide (Li-Naph) solution [20]. The final lithiated products were demonstrated to be PAN–Li₂S nanocomposite and partially lithiated Li_xSi. When combined in full cells, the assembled PAN–Li₂S/Si full cell exhibited an initial discharge capacity of ~620 mAh g⁻¹ at 0.08 C with 83% capacity retention after 50 cycles.

3.4.3 Electrolytes for Li₂S Full Cells

The choice of a suitable electrolyte is also a key factor to the performance of Li₂S full cells. Given the incompatibility between polysulfides and carbonate-based electrolytes, the most common electrolyte for Li₂S full cells is still ether-based electrolytes because of their low viscosity, high ionic conductivity, and electrochemical stability. Considerable progresses have been made in optimizing the ether-based electrolytes in Li₂S full cells. A typical example is the use of highly concentrated electrolytes. Chen et al. developed a fluorinated-ether electrolyte (TFE) for graphite/S full cells. The addition of TFE in the electrolyte decreased the polysulfide solubility and formed a stable SEI layer on the graphite surface. This SEI layer not only suppressed the polysulfide shuttle but also prevented the intercalation of solvent molecules to the graphite [97]. Ionic liquids have also received much attention in Li₂S full cells because of their nonflammability, high electrochemical stability, and low polysulfides

solubility [98]. Yang et al. reported a pyrrolidinium-based ionic liquid electrolyte in a lithiated Si-S full cell. The full cell exhibited a specific capacity of ~ 670 mAh g^{-1} after 50 cycles at 0.1 C. The low specific capacity and short cycle life were attributed to the high viscosity and low ionic conductivity of the ionic liquid electrolyte under investigation.

There are increasing emphases about lowering the E/S ratio in order to increase the practical energy density of Li-S batteries [99–103]. To reach an energy density of 500 Wh kg^{-1} , the E/S ratio is suggested to be kept below 3 μL mg^{-1} . Under this scenario, an insurmountable obstacle of Li-S batteries is the electrolyte depletion resulting from the polysulfide solvation and side reactions with the lithium anode [104]. To compete with the energy density of the state-of-art LIBs, the E/S ratio must be less than 5 [105]. One promising solution is the use of solvated ionic liquid electrolytes (or sparing solvating electrolytes) developed by Watanabe's group [79]. These sparing solvating electrolytes were prepared by diluting viscous ionic liquids with low-viscosity cosolvents. In comparison with ether-based electrolytes, sparing solvating electrolytes could significantly decrease the polysulfide solubility and shuttle between the cathode and anode. As a result, the Li_2S /graphite full cells with the solvating electrolyte exhibited a good cycle life of 300 cycles under the lean electrolyte condition [103].

Given the high safety concern of liquid organic electrolytes, solid electrolytes have also been frequently advocated as a promising solution [106]. Polymer electrolytes have been exploited in Li_2S full cells. Hassoun et al. first applied polymer electrolytes in Li_2S full cells [87, 107]. They prepared a polymer electrolyte with polyethylene oxide as the membrane matrix and 10 wt% zirconia ceramic fillers to improve the ionic conductivity. The finally assembled Li_2S /Sn cell with the polymer electrolyte exhibited a discharge capacity of ~ 440 mAh g^{-1} at 0.2 C with 68% capacity retention after 90 cycles. Although the use of polymer electrolytes has proven to be a feasible approach to fabricate all-solid-state Li_2S batteries, their cycle performance is still unsatisfactory due to the low ionic conductivity of polymer electrolytes. Compared with liquid electrolytes, considerable efforts are still needed to further enhance the ionic conductivity and stability of solid polymer electrolytes.

In addition to polymer electrolytes, inorganic electrolytes have also gained much attention for Li_2S batteries [108, 109]. The use of inorganic electrolytes has the potential to eliminate the polysulfide shuttle of Li_2S batteries. Tatsumisago's group reported an all-solid-state Li_2S -Cu/ Li_2S - P_2S_5 /In battery with a glass ceramic electrolyte [110]. The full cell exhibited a discharge capacity of ~ 490 mAh g^{-1} at 0.1 C. In a following study, Ogumi's group fabricated a Li_2S / Li_2S - P_2S_5 /graphite cell through a sintering fabrication process [111]. It reduced the interfacial resistance of the Li_2S cathode. The finally assembled full cell delivered a large capacity of ~ 750 mAh g^{-1} . In light of the good ionic conductivity of lithium superionic sulfide electrolytes, Liang's group pioneered the use of Li_3PS_4 solid electrolyte in Li_2S /Li cells [106]. To enhance the interfacial contact between Li_2S and solid electrolytes, they coated Li_2S with a thin Li_3PS_4 shell via an in-situ chemical reaction approach. Finally, the as-fabricated Li_2S / Li_3PS_4 /Li cell exhibited a large discharge capacity of ~ 848 mAh g^{-1} . Han et al. further prepared a Li_6PS_5Cl solid electrolyte and incorporated it into

the Li₂S cathode via a coprecipitation method in the PVP–ethanol solution [112]. After a carbonization process, Li₂S and Li₆PS₅Cl were homogeneously distributed in the PVP-derived carbon matrix. When assembled with an indium anode, the cell showed a high discharge capacity of ~830 mAh g⁻¹ at 50 mA g⁻¹.

3.5 Summary and Outlooks

In summary, replacing sulfur with Li₂S in Li–S batteries provides an alternative solution to utilize the high capacity of sulfur and can enable the use of non-lithium anodes instead of the reactive metallic lithium anode. Unfortunately, the electrochemical oxidation of Li₂S is subjected to a large overpotential during the initial charge. Considerable progresses have been made to decrease the charging overpotential and increase the cycle performance of Li₂S cathodes. As discussed in this chapter, various preparation methods have been developed for the production of Li₂S-based nanostructures as the cathode materials. The high activation barrier can also be reduced through the structure tuning of Li₂S as well as the use of electrolyte additives, mediators or electrocatalysts. Among different reports, Li₂S cathodes with mediators show considerably decreased charging overpotential, whereas Li₂S cathodes with electrocatalysts often result in good cycle life. Li₂S full cells with the graphite anode exhibit good cyclability but with low energy density (<200 Wh kg⁻¹). Full cells with the silicon anode has high energy density but are short of cycling stability (<100 cycles). At present, it is still difficult to simultaneously realize low oxidation potential (<2.4 V) and long cycle stability (>1000 cycles) for Li₂S cathodes. In our opinion, future works can be done from the following directions.

First, the preparation of nanostructured Li₂S cathodes with high capacity and long cyclability is still the priority of the Li₂S research. The ionic/electric conductivity is an important parameter to be considered when designing Li₂S cathode materials. Based on the current literature survey, the encapsulation of nanosized Li₂S with ultrathin carbon could be an effective approach to simultaneously enhance the electric and ionic conductivity of Li₂S cathodes. The carbon encapsulation can enable the Li₂S cathode with good electric conductivity while the nanosized Li₂S can shorten the Li⁺ diffusion length. However, the cyclability of the carbon encapsulated Li₂S can be impaired by its non-polar surface nature which has poor polysulfide adsorption capability. Hence, the doping of carbon with heteroatoms (e.g. N, P, Fe, Co) can be a possible approach to enhance its polysulfide adsorption capability and therefore improve the cyclability. In addition, solutions for suppressing the shuttle effect of polysulfide intermediates, such as using functional interlayers or separators can also be used in Li₂S cathodes to increase the cycle stability. With all these efforts taken, we aim to achieve high-performance Li₂S cathodes with large specific capacities of >800 mAh g⁻¹ at 1 C rate and long cycle stability of >1000 cycles under a high Li₂S loading of >5 mg cm⁻² and lean electrolyte condition ($E/S < 5 \mu\text{L mg}^{-1}$) in order to meet the energy density demand of next-generation batteries.

Second, we would have to deepen our understanding of the delithiation pathway of Li_2S . Although the generation of soluble polysulfides after the activation barrier was commonly observed in the literature, the exact structure evolution of Li_2S during the activation process has not been well understood. Some studies even detected the direct oxidation of Li_2S to sulfur under lean-electrolyte conditions. Future studies can combine in-situ characterizations and theoretical computations to provide a better understanding of the Li_2S reaction chemistry. Besides, the discovery of the direct conversion of Li_2S to sulfur can also inspire us to explore the possibility of the single solid–solid $\text{S} \leftrightarrow \text{Li}_2\text{S}$ reaction pathway without the generation of soluble polysulfides for better cyclability. The introduction of cathode electrocatalysts and electrolyte modification are two possible routes to achieve such a solid-solid electrochemical reaction pathway.

Third, more attention should be paid to the research on Li_2S full batteries. The greatest strength of Li_2S batteries is the use of non-lithium anodes (e.g., Sn, SnO_2 , and Si). Unfortunately, most current research still focuses on Li_2S half cells where the Li_2S cathode is often paired with an excessive amount of lithium in a flooded electrolyte condition. Promising data obtained in this configuration does not necessarily guarantee good full-battery performances. The selection of possible non-lithium anodes to match with the Li_2S cathode having satisfying energy/power density and cycle stability are the prerequisites of the commercialization of Li_2S full cells. However, the practical density of Li_2S full cells developed to date suffered from rapid capacity fade and short cycle life as shown in Table 3.2. Besides the mentioned issues from the Li_2S cathode, the cyclability of the anode also affects the full cell performance. In the future, we would have to look beyond the Li_2S cathode and evaluated the electrochemical performance of Li_2S in full cells. In particular, it is essential to consider the capacity balance between the cathode and anode and offset the lithium loss. Our target is to realize high-energy-density ($>500 \text{ Wh kg}^{-1}$) and long-cycle (>80 capacity retention after 1000 cycles) Li_2S full batteries with low cost ($<100 \text{ \$ kWh}^{-1}$).

Acknowledgements The work at Argonne National Laboratory was supported from the U. S. Department of Energy (DOE), Office of Energy Efficiency and Renewable Energy, Vehicle Technologies Office. Argonne National Laboratory is operated for DOE Office of Science by UChicago Argonne, LLC, under contract number DE-AC02-06CH11357. Y. Li acknowledged the support from the National Natural Science Foundation of China (51972219), the Priority Academic Program Development of Jiangsu Higher Education Institutions, and Collaborative Innovation Center of Suzhou Nano Science and Technology.

References

1. Evers S, Nazar LF (2013) New approaches for high energy density lithium-sulfur batteries. *Acc Chem Res* 46:1135–1143
2. Yang Y, Zheng G, Cui Y (2013) Nanostructured sulfur cathodes. *Chem Soc Rev* 42(7):3018–3032. <https://doi.org/10.1039/c2cs35256g>

3. Seh ZW, Sun Y, Zhang Q, Cui Y (2016) Designing high-energy lithium-sulfur batteries. *Chem Soc Rev* 45(20):5605–5634. <https://doi.org/10.1039/c5cs00410a>
4. Hagen M, Hanselmann D, Ahlbrecht K, Maça R, Gerber D, Tübke J (2015) Lithium-sulfur cells: the gap between the state-of-the-art and the requirements for high energy battery cells. *Adv Energy Mater* 5(16):1401986. <https://doi.org/10.1002/aenm.201401986>
5. Yin YX, Xin S, Guo YG, Wan LJ (2013) Lithium-sulfur batteries: electrochemistry, materials, and prospects. *Angew Chem* 52(50):13186–13200. <https://doi.org/10.1002/anie.201304762>
6. Cheng X-B, Yan C, Huang J-Q, Li P, Zhu L, Zhao L, Zhang Y, Zhu W, Yang S-T, Zhang Q (2017) The gap between long lifespan Li–S coin and pouch cells: the importance of lithium metal anode protection. *Energy Storage Mater* 6:18–25. <https://doi.org/10.1016/j.ensm.2016.09.003>
7. Zhao Y, Ye Y, Wu F, Li Y, Li L, Chen R (2019) Anode interface engineering and architecture design for high-performance lithium-sulfur batteries. *Adv Mater* 31(12):1806532. <https://doi.org/10.1002/adma.201806532>
8. Xu T, Gao P, Li P, Xia K, Han N, Deng J, Li Y, Lu J (2020) Fast-charging and ultrahigh-capacity lithium metal anode enabled by surface alloying. *Adv Energy Mater* 10:1902343. <https://doi.org/10.1002/aenm.201902343>
9. Son Y, Lee J-S, Son Y, Jang J-H, Cho J (2015) Recent advances in lithium sulfide cathode materials and their use in lithium sulfur batteries. *Adv Energy Mater* 5(16):1500110. <https://doi.org/10.1002/aenm.201500110>
10. Kaiser MR, Han Z, Liang J, Dou S-X, Wang J (2019) Lithium sulfide-based cathode for lithium-ion/sulfur battery: recent progress and challenges. *Energy Storage Mater* 19:1–15. <https://doi.org/10.1016/j.ensm.2019.04.001>
11. Ye H, Li M, Liu T, Li Y, Lu J (2020) Activating Li₂S as the lithium-containing cathode in lithium–sulfur batteries. *ACS Energy Lett* 5(7):2234–2245. <https://doi.org/10.1021/acsenergylett.0c00936>
12. Su D, Zhou D, Wang C, Wang G (2018) Toward high performance lithium-sulfur batteries based on Li₂S cathodes and beyond: status, challenges, and perspectives. *Adv Funct Mater* 28(38):1800154. <https://doi.org/10.1002/adfm.201800154>
13. Lee S-K, Lee YJ, Sun Y-K (2016) Nanostructured lithium sulfide materials for lithium-sulfur batteries. *J Power Sources* 323:174–188. <https://doi.org/10.1016/j.jpowsour.2016.05.037>
14. Jiang J, Fan Q, Chou S, Guo Z, Konstantinov K, Liu H, Wang J (2019) Li₂S-based Li-ion sulfur batteries: progress and prospects. *Small*:1903934. <https://doi.org/10.1002/sml.201903934>
15. Wu F, Lee JT, Fan F, Nitta N, Kim H, Zhu T, Yushin G (2015) A hierarchical particle-shell architecture for long-term cycle stability of Li₂S cathodes. *Adv Mater* 27(37):5579. <https://doi.org/10.1002/adma.201502289>
16. Hao Z, Chen J, Yuan L, Bing Q, Liu J, Chen W, Li Z, Wang FR, Huang Y (2019) Advanced Li₂S/Si full battery enabled by tin polysulfide immobilizer. *Small* 15:1902377. <https://doi.org/10.1002/sml.201902377>
17. Wu F, Pollard TP, Zhao E, Xiao Y, Olguin M, Borodin O, Yushin G (2018) Layered LiTiO₂ for the protection of Li₂S cathodes against dissolution: Mechanisms of the remarkable performance boost. *Energy Environ Sci* 11(4):807–817. <https://doi.org/10.1039/c8ee00419f>
18. Tan G, Xu R, Xing Z, Yuan Y, Lu J, Wen J, Liu C, Ma L, Zhan C, Liu Q, Wu T, Jian Z, Shahbazian-Yassar R, Ren Y, Miller DJ, Curtiss LA, Ji X, Amine K (2017) Burning lithium in CS₂ for high-performing compact Li₂S–graphene nanocapsules for Li–S batteries. *Nat Energy* 2(7). <https://doi.org/10.1038/nenergy.2017.90>
19. Wu F, Kim H, Magasinski A, Lee JT, Lin HT, Yushin G (2014) Harnessing steric separation of freshly nucleated Li₂S nanoparticles for bottom-up assembly of high-performance cathodes for lithium-sulfur and lithium-ion batteries. *Adv Energy Mater* 4(11). <https://doi.org/10.1002/aenm.201400196>
20. Shen Y, Zhang J, Pu Y, Wang H, Wang B, Qian J, Cao Y, Zhong F, Ai X, Yang H (2019) Effective chemical prelithiation strategy for building a silicon/sulfur Li-ion battery. *ACS Energy Lett* 4(7):1717–1724. <https://doi.org/10.1021/acsenergylett.9b00889>

21. He J, Chen Y, Lv W, Wen K, Li P, Qi F, Wang Z, Zhang W, Li Y, Qin W, He W (2016) Highly-flexible 3D Li_2S /graphene cathode for high-performance lithium sulfur batteries. *J Power Sources* 327:474–480. <https://doi.org/10.1016/j.jpowsour.2016.07.088>
22. He J, Chen Y, Lv W, Wen K, Xu C, Zhang W, Qin W, He W (2016) Three-dimensional CNT/graphene- Li_2S aerogel as freestanding cathode for high-performance Li-S batteries. *ACS Energy Lett* 1(4):820–826. <https://doi.org/10.1021/acseenergylett.6b00272>
23. Li S, Leng D, Li W, Qie L, Dong Z, Cheng Z, Fan Z (2020) Recent progress in developing Li_2S cathodes for Li-S batteries. *Energy Storage Mater* 27:279–296. <https://doi.org/10.1016/j.jensm.2020.02.010>
24. Obrovac MN, Dahn JR (2002) Electrochemically active Lithia/metal and lithium sulfide/metal composites. *Electrochem Solid-State Lett* 5:A70–A73. <https://doi.org/10.1149/1.1452482>
25. Li M, Chen Z, Wu T, Lu J (2018) Li_2S - or S-based lithium-ion batteries. *Adv Mater* 30(48):1801190. <https://doi.org/10.1002/adma.201801190>
26. Choi S, Yoon I, Nichols WT, Shin D (2018) Carbon-coated Li_2S cathode for improving the electrochemical properties of an all-solid-state lithium-sulfur battery using Li_2S - P_2S_5 solid electrolyte. *Ceram Int* 44(7):7450–7453. <https://doi.org/10.1016/j.ceramint.2018.01.104>
27. Chen YX, Kaghazchi P (2014) Metalization of Li_2S particle surfaces in Li-S batteries. *Nanoscale* 6(22):13391–13395. <https://doi.org/10.1039/c4nr03428g>
28. Yang Y, Zheng G, Misra S, Nelson J, Toney MF, Cui Y (2012) High-capacity micrometer-sized Li_2S particles as cathode materials for advanced rechargeable lithium-ion batteries. *J Am Chem Soc* 134(37):15387–15394. <https://doi.org/10.1021/ja3052206>
29. Wang L, Zhang T, Yang S, Cheng F, Liang J, Chen J (2013) A quantum-chemical study on the discharge reaction mechanism of lithium-sulfur batteries. *J Energy Chem* 22(1):72–77. [https://doi.org/10.1016/s2095-4956\(13\)60009-1](https://doi.org/10.1016/s2095-4956(13)60009-1)
30. Kim BS, Lee MS, Park KY, Kang K (2016) First-principles study on the charge transport mechanism of lithium sulfide (Li_2S) in lithium-sulfur batteries. *Chem Asian J* 11(8):1288–1292. <https://doi.org/10.1002/asia.201600007>
31. Park H, Koh HS, Siegel DJ (2015) First-principles study of redox end members in lithium-sulfur batteries. *J Phys Chem C* 119(9):4675–4683. <https://doi.org/10.1021/jp513023v>
32. Zhang L, Sun D, Feng J, Cairns EJ, Guo J (2017) Revealing the electrochemical charging mechanism of nanosized Li_2S by in situ and operando X-ray absorption spectroscopy. *Nano Lett* 17(8):5084–5091. <https://doi.org/10.1021/acs.nanolett.7b02381>
33. Vizintin A, Chabanne L, Tchernychova E, Arçon I, Stievano L, Aquilanti G, Antonietti M, Fellingner T-P, Dominko R (2017) The mechanism of Li_2S activation in lithium-sulfur batteries: can we avoid the polysulfide formation? *J Power Sources* 344:208–217. <https://doi.org/10.1016/j.jpowsour.2017.01.112>
34. Gorlin Y, Patel MUM, Freiberg A, He Q, Piana M, Tromp M, Gasteiger HA (2016) Understanding the charging mechanism of lithium-sulfur batteries using spatially resolved operando X-ray absorption spectroscopy. *J Electrochem Soc* 163(6):A930–A939. <https://doi.org/10.1149/2.0631606jes>
35. Cheng Q, Xu W, Qin S, Das S, Jin T, Li A, Li AC, Qie B, Yao P, Zhai H, Shi C, Yong X, Yang Y (2019) Full dissolution of the whole lithium sulfide family (Li_2S_8 to Li_2S) in a safe eutectic solvent for rechargeable lithium-sulfur batteries. *Angew Chem* 58(17):5557–5561. <https://doi.org/10.1002/anie.201812611>
36. Cai K, Song MK, Cairns EJ, Zhang Y (2012) Nanostructured Li_2S -C composites as cathode material for high-energy lithium/sulfur batteries. *Nano Lett* 12(12):6474–6479. <https://doi.org/10.1021/nl303965a>
37. Wu F, Kim H, Magasinski A, Lee JT, Lin HT, Yushin G (2014) Harnessing steric separation of freshly nucleated Li_2S nanoparticles for bottom-up assembly of high-performance cathodes for lithium-sulfur and lithium-ion batteries. *Adv Energy Mater* 4(11):1400196. <https://doi.org/10.1002/aenm.201400196>
38. Zhang J, Shi Y, Ding Y, Peng L, Zhang W, Yu G (2017) A conductive molecular framework derived $\text{Li}_2\text{S}/\text{N}$, P-codoped carbon cathode for advanced lithium-sulfur batteries. *Adv Energy Mater* 7(14):1602876. <https://doi.org/10.1002/aenm.201602876>

39. Tan G, Xu R, Xing Z, Yuan Y, Lu J, Wen J, Liu C, Ma L, Zhan C, Liu Q, Wu T, Jian Z, Shahbazian-Yassar R, Ren Y, Miller DJ, Curtiss LA, Ji X, Amine K (2017) Burning lithium in CS₂ for high-performing compact Li₂S–graphene nanocapsules for Li–S batteries. *Nat Energy* 2(7):17090. <https://doi.org/10.1038/nenergy.2017.90>
40. Meng X, Comstock DJ, Fister TT, Elam JW (2014) Vapor-phase atomic-controllable amorphous Li₂S for highperformance lithium sulfur batteries. *ACS Nano* 8:10963–10972
41. Takeuchi T, Kageyama H, Taguchi N, Nakanishi K, Kawaguchi T, Ohara K, Fukuda K, Sakuda A, Ohta T, Fukunaga T, Sakaebe H, Kobayashi H, Matsubara E (2018) Structure analyses of Fe-substituted Li₂S-based positive electrode materials for Li–S batteries. *Solid State Ionics* 320:387–391. <https://doi.org/10.1016/j.ssi.2018.03.028>
42. Zhou G, Tian H, Jin Y, Tao X, Liu B, Zhang R, Seh ZW, Zhuo D, Liu Y, Sun J, Zhao J, Zu C, Wu DS, Zhang Q, Cui Y (2017) Catalytic oxidation of Li₂S on the surface of metal sulfides for Li–S batteries. *Proc Natl Acad Sci* 114(5):840–845. <https://doi.org/10.1073/pnas.1615837114>
43. He J, Chen Y, Manthiram A (2019) Metal sulfide-decorated carbon sponge as a highly efficient electrocatalyst and absorbant for polysulfide in high-loading Li₂S batteries. *Adv Energy Mater* 9(20):1900584. <https://doi.org/10.1002/aenm.201900584>
44. Liang X, Yun J, Xu K, Shi P, Sun Y, Chen C, Xiang H (2019) Trace ethanol as an efficient electrolyte additive to reduce the activation voltage of the Li₂S cathode in lithium-ion-sulfur batteries. *Chem Commun* 55(68):10088–10091. <https://doi.org/10.1039/c9cc04877d>
45. Fan Q, Li B, Si Y, Fu Y (2019) Lowering the charge overpotential of Li₂S via the inductive effect of phenyl diselenide in Li–S batteries. *Chem Commun* 55(53):7655–7658. <https://doi.org/10.1039/c8cc09565e>
46. Meini S, Elazari R, Rosenman A, Garsuch A, Aurbach D (2014) The use of redox mediators for enhancing utilization of Li₂S cathodes for advanced Li–S battery systems. *J Phys Chem Lett* 5(5):915–918. <https://doi.org/10.1021/jz500222f>
47. Wu F, Lee JT, Nitta N, Kim H, Borodin O, Yushin G (2015) Lithium iodide as a promising electrolyte additive for lithium-sulfur batteries: mechanisms of performance enhancement. *Adv Mater* 27(1):101. <https://doi.org/10.1002/adma.201404194>
48. Tsao Y, Lee M, Miller EC, Gao G, Park J, Chen S, Katsumata T, Tran H, Wang L-W, Toney MF, Cui Y, Bao Z (2019) Designing a quinone-based redox mediator to facilitate Li₂S oxidation in Li–S batteries. *Joule* 3(3):872–884. <https://doi.org/10.1016/j.joule.2018.12.018>
49. Li M, Bai Z, Li Y, Ma L, Dai A, Wang X, Luo D, Wu T, Liu P, Yang L, Amine K, Chen Z, Lu J (2019) Electrochemically primed functional redox mediator generator from the decomposition of solid state electrolyte. *Nat Commun* 10(1):1890. <https://doi.org/10.1038/s41467-019-09638-4>
50. Wu F, Lee JT, Zhao E, Zhang B, Yushin G (2016) Graphene-Li₂S-carbon nanocomposite for lithium-sulfur batteries. *ACS Nano* 10(1):1333–1340. <https://doi.org/10.1021/acsnano.5b06716>
51. Wang C, Wang X, Yang Y, Kushima A, Chen J, Huang Y, Li J (2015) Slurryless Li₂S/reduced graphene oxide cathode paper for high-performance lithium sulfur battery. *Nano Lett* 15(3):1796–1802. <https://doi.org/10.1021/acs.nanolett.5b00112>
52. Zhou G, Paek E, Hwang GS, Manthiram A (2016) High-performance lithium-sulfur batteries with a self-supported, 3D Li₂S-doped graphene aerogel cathodes. *Adv Energy Mater* 6(2):1501355. <https://doi.org/10.1002/aenm.201501355>
53. Yang Z, Guo J, Das SK, Yu Y, Zhou Z, Abruña HD, Archer LA (2013) In situ synthesis of lithium sulfide–carbon composites as cathode materials for rechargeable lithium batteries. *J Mater Chem A* 1(4):1433–1440. <https://doi.org/10.1039/c2ta00779g>
54. Chen X, Peng L, Yuan L, Zeng R, Xiang J, Chen W, Yuan K, Chen J, Huang Y, Xie J (2019) Facile synthesis of Li₂S@C composites as cathode for Li–S batteries. *J Energy Chem* 37:111–116. <https://doi.org/10.1016/j.jechem.2018.12.008>
55. Yan Y, Cheng C, Zhang L, Li Y, Lu J (2019) Deciphering the reaction mechanism of lithium–sulfur batteries by in situ/operando synchrotron-based characterization techniques. *Adv Energy Mater* 9(18):1900148. <https://doi.org/10.1002/aenm.201900148>

56. Li X, Gao M, Du W, Ni B, Wu Y, Liu Y, Shang C, Guo Z, Pan H (2017) A mechanochemical synthesis of submicron-sized Li_2S and a mesoporous $\text{Li}_2\text{S}/\text{C}$ hybrid for high performance lithium-sulfur battery cathodes. *J Mater Chem A* 5(14):6471–6482. <https://doi.org/10.1039/c7ta00557a>
57. Ye F, Liu M, Yan X, Li J, Pan Z, Li H, Zhang Y (2018) In situ electrochemically derived amorphous- Li_2S for high performance $\text{Li}_2\text{S}/\text{graphite}$ full cell. *Small* 14(17):1703871. <https://doi.org/10.1002/sml.201703871>
58. Lodovico L, Milad Hosseini S, Varzi A, Passerini S (2019) Amorphous lithium sulfide as lithium-sulfur battery cathode with low activation barrier. *Energy Technol* 7(12):1801013. <https://doi.org/10.1002/ente.201801013>
59. Fu Y, Zu C, Manthiram A (2013) In situ-formed Li_2S in lithiated graphite electrodes for lithium-sulfur batteries. *J Am Chem Soc* 135(48):18044–18047. <https://doi.org/10.1021/ja409705u>
60. Lorgier S, Usiskin RE, Maier J (2018) Transport and charge carrier chemistry in lithium sulfide. *Adv Funct Mater* 29(6):1807688. <https://doi.org/10.1002/adfm.201807688>
61. Norris DJ, Efros AL, Erwin SC (2008) Doped nanocrystals. *Science* 319(5871):1776–1779. <https://doi.org/10.1126/science.1143802>
62. Zhou Y, Wu C, Zhang H, Wu X, Fu Z (2007) Electrochemical reactivity of $\text{Co-Li}_2\text{S}$ nanocomposite for lithium-ion batteries. *Electrochim Acta* 52(9):3130–3136. <https://doi.org/10.1016/j.electacta.2006.09.054>
63. Luo G, Zhao J, Wang B (2012) First-principles study of transition metal doped Li_2S as cathode materials in lithium batteries. *J Renew Sustain Energy* 4(6):063128. <https://doi.org/10.1063/1.4768814>
64. Xu K, Liu X, Liang J, Cai J, Zhang K, Lu Y, Wu X, Zhu M, Liu Y, Zhu Y, Wang G, Qian Y (2018) Manipulating the redox kinetics of Li-S chemistry by tellurium doping for improved Li-S batteries. *ACS Energy Lett* 3(2):420–427. <https://doi.org/10.1021/acscenergylett.7b01249>
65. Seh ZW, Kibsgaard J, Dickens CF, Chorkendorff I, Norskov JK, Jaramillo TF (2017) Combining theory and experiment in electrocatalysis: Insights into materials design. *Science* 355(6321):eaad4998. <https://doi.org/10.1126/science.aad4998>
66. Lim WG, Kim S, Jo C, Lee J (2019) A comprehensive review of materials with catalytic effects in Li-S batteries: enhanced redox kinetics. *Angew Chem* 58:2–14. <https://doi.org/10.1002/anie.201902413>
67. Al Salem H, Babu G, Rao CV, Arava LM (2015) Electrocatalytic polysulfide traps for controlling redox shuttle process of Li-S batteries. *J Am Chem Soc* 137(36):11542–11545. <https://doi.org/10.1021/jacs.5b04472>
68. Liu D, Zhang C, Zhou G, Lv W, Ling G, Zhi L, Yang QH (2018) Catalytic effects in lithium-sulfur batteries: promoted sulfur transformation and reduced shuttle effect. *Adv Sci* 5(1):1700270. <https://doi.org/10.1002/advs.201700270>
69. Ma L, Zhang W, Wang L, Hu Y, Zhu G, Wang Y, Chen R, Chen T, Tie Z, Liu J, Jin Z (2018) Strong capillarity, chemisorption, and electrocatalytic capability of crisscrossed nanostraws enabled flexible, high-rate, and long-cycling lithium-sulfur batteries. *ACS Nano* 12(5):4868–4876. <https://doi.org/10.1021/acsnano.8b01763>
70. Landa-Medrano I, Lozano I, Ortiz-Vitoriano N, Ruiz de Larramendi I, Rojo T (2019) Redox mediators: a shuttle to efficacy in metal- O_2 batteries. *J Mater Chem A* 7(15):8746–8764. <https://doi.org/10.1039/c8ta12487f>
71. Liang X, Yun J, Xu K, Xiang H, Wang Y, Sun Y, Yu Y (2019) A multi-layered $\text{Ti}_3\text{C}_2/\text{Li}_2\text{S}$ composite as cathode material for advanced lithium-sulfur batteries. *J Energy Chem* 39:176–181. <https://doi.org/10.1016/j.jechem.2019.02.002>
72. Yuan H, Chen X, Zhou G, Zhang W, Luo J, Huang H, Gan Y, Liang C, Xia Y, Zhang J, Wang J, Tao X (2017) Efficient activation of Li_2S by transition metal phosphides nanoparticles for highly stable lithium-sulfur batteries. *ACS Energy Lett* 2(7):1711–1719. <https://doi.org/10.1021/acscenergylett.7b00465>
73. Zhao Y, Ding Y, Li Y, Peng L, Byon HR, Goodenough JB, Yu G (2015) A chemistry and material perspective on lithium redox flow batteries towards high-density electrical energy storage. *Chem Soc Rev* 44(22):7968–7996. <https://doi.org/10.1039/c5cs00289c>

74. Lin Z, Liu Z, Fu W, Dudney NJ, Liang C (2013) Phosphorous pentasulfide as a novel additive for high-performance lithium-sulfur batteries. *Adv Funct Mater* 23(8):1064–1069. <https://doi.org/10.1002/adfm.201200696>
75. Zu C, Klein M, Manthiram A (2014) Activated Li₂S as a high-performance cathode for rechargeable lithium-sulfur batteries. *J Phys Chem Lett* 5(22):3986–3991. <https://doi.org/10.1021/jz5021108>
76. Brückner J, Thieme S, Böttger-Hiller F, Bauer I, Grossmann HT, Strubel P, Althues H, Spange S, Kaskel S (2014) Carbon-based anodes for lithium sulfur full cells with high cycle stability. *Adv Funct Mater* 24(9):1284–1289. <https://doi.org/10.1002/adfm.201302169>
77. Ye F, Noh H, Lee H, Kim HT (2018) An ultrahigh capacity graphite/Li₂S battery with holey-Li₂S nanoarchitectures. *Adv Sci* 5(7):1800139. <https://doi.org/10.1002/advs.201800139>
78. Zheng S, Chen Y, Xu Y, Yi F, Zhu Y, Liu Y, Yang J, Wang C (2013) In situ formed lithium sulfide/microporous carbon cathodes for lithium-ion batteries. *ACS Nano* 7(12):10995–11003. <https://doi.org/10.1021/nn404601h>
79. Li Z, Zhang S, Terada S, Ma X, Ikeda K, Kamei Y, Zhang C, Dokko K, Watanabe M (2016) Promising cell configuration for next-generation energy storage: Li₂S/graphite battery enabled by a solvate ionic liquid electrolyte. *ACS Appl Mater Interfaces* 8(25):16053–16062. <https://doi.org/10.1021/acsami.6b03736>
80. Wang N, Zhao N, Shi C, Liu E, He C, He F, Ma L (2017) In situ synthesized Li₂S@porous carbon cathode for graphite/Li₂S full cells using ether-based electrolyte. *Electrochim Acta* 256:348–356. <https://doi.org/10.1016/j.electacta.2017.10.053>
81. Zhang K, Wang L, Hu Z, Cheng F, Chen J (2014) Ultrasmall Li₂S nanoparticles anchored in graphene nanosheets for high-energy lithium-ion batteries. *Sci Rep* 4:6467. <https://doi.org/10.1038/srep06467>
82. Wang S, Chen H, Zhong Z, Hou X, Hu S, Wu J (2018) Graphene-decorated sphere Li₂S composite prepared by spray drying method as cathode for lithium-sulfur full cell. *Ionics* 24(11):3385–3392. <https://doi.org/10.1007/s11581-018-2493-7>
83. Agostini M, Hassoun J, Liu J, Jeong M, Nara H, Momma T, Osaka T, Sun YK, Scrosati B (2014) A lithium-ion sulfur battery based on a carbon-coated lithium-sulfide cathode and an electrodeposited silicon-based anode. *ACS Appl Mater Interfaces* 6(14):10924–10928. <https://doi.org/10.1021/am4057166>
84. Yang Y, McDowell MT, Jackson A, Cha JJ, Hong SS, Cui Y (2010) New nanostructured Li₂S/silicon rechargeable battery with high specific energy. *Nano Lett* 10(4):1486–1491. <https://doi.org/10.1021/nl100504q>
85. Yu M, Zhou S, Wang Z, Pei W, Liu X, Liu C, Yan C, Meng X, Wang S, Zhao J, Qiu J (2019) A molecular-cage strategy enabling efficient chemisorption–electrocatalytic interface in nanostructured Li₂S cathode for Li metal-free rechargeable cells with high energy. *Adv Funct Mater* 29(46):1905986. <https://doi.org/10.1002/adfm.201905986>
86. Jha H, Buchberger I, Cui X, Meini S, Gasteiger HA (2015) Li–S batteries with Li₂S cathodes and Si/C anodes. *J Electrochem Soc* 162(9):A1829–A1835. <https://doi.org/10.1149/2.0681509jes>
87. Hassoun J, Scrosati B (2010) A high-performance polymer tin sulfur lithium ion battery. *Angew Chem* 49(13):2371–2374. <https://doi.org/10.1002/anie.200907324>
88. Zoller F, Bohm D, Bein T, Fattakhova-Rohlfing D (2019) Tin oxide based nanomaterials and their application as anodes in lithium-ion batteries and beyond. *Chemsuschem* 12(18):4140–4159. <https://doi.org/10.1002/cssc.201901487>
89. Xu J, Dou Y, Wei Z, Ma J, Deng Y, Li Y, Liu H, Dou S (2017) Recent progress in graphite intercalation compounds for rechargeable metal (Li, Na, K, Al)-ion batteries. *Adv Sci* 4(10):1700146. <https://doi.org/10.1002/advs.201700146>
90. Lv D, Yan P, Shao Y, Li Q, Ferrara S, Pan H, Graff GL, Polzin B, Wang C, Zhang JG, Liu J, Xiao J (2015) High performance Li-ion sulfur batteries enabled by intercalation chemistry. *Chem Commun* 51(70):13454–13457. <https://doi.org/10.1039/c5cc05171a>
91. Zhu Q, Zhao Q, An Y, Anasori B, Wang H, Xu B (2017) Ultra-microporous carbons encapsulate small sulfur molecules for high performance lithium-sulfur battery. *Nano Energy* 33:402–409. <https://doi.org/10.1016/j.nanoen.2017.01.060>

92. Zubi G, Dufo-López R, Carvalho M, Pasaoglu G (2018) The lithium-ion battery: state of the art and future perspectives. *Renew Sustain Energy Rev* 89:292–308. <https://doi.org/10.1016/j.rser.2018.03.002>
93. Wu H, Cui Y (2012) Designing nanostructured Si anodes for high energy lithium ion batteries. *Nano Today* 7(5):414–429. <https://doi.org/10.1016/j.nantod.2012.08.004>
94. Liu M, Ren YX, Jiang HR, Luo C, Kang FY, Zhao TS (2017) An efficient Li₂S-based lithium-ion sulfur battery realized by a bifunctional electrolyte additive. *Nano Energy* 40:240–247. <https://doi.org/10.1016/j.nanoen.2017.08.017>
95. Sun Y, Li Y, Sun J, Li Y, Pei A, Cui Y (2017) Stabilized Li₃N for efficient battery cathode prelithiation. *Energy Storage Mater* 6:119–124. <https://doi.org/10.1016/j.ensm.2016.10.004>
96. Sun Y, Lee H-W, Seh ZW, Liu N, Sun J, Li Y, Cui Y (2016) High-capacity battery cathode prelithiation to offset initial lithium loss. *Nat Energy* 1(1):1–7. <https://doi.org/10.1038/energy.2015.8>
97. Chen S, Yu Z, Gordin ML, Yi R, Song J, Wang D (2017) A fluorinated ether electrolyte enabled high performance prelithiated graphite/sulfur batteries. *ACS Appl Mater Interfaces* 9(8):6959–6966. <https://doi.org/10.1021/acsami.6b11008>
98. Zhang S, Ueno K, Dokko K, Watanabe M (2015) Recent advances in electrolytes for lithium–sulfur batteries. *Adv Energy Mater* 5:1500117. <https://doi.org/10.1002/aenm.201500117>
99. Lee CW, Pang Q, Ha S, Cheng L, Han SD, Zavadil KR, Gallagher KG, Nazar LF, Balasubramanian M (2017) Directing the lithium-sulfur reaction pathway via sparingly solvating electrolytes for high energy density batteries. *ACS Cent Sci* 3(6):605–613. <https://doi.org/10.1021/acscentsci.7b00123>
100. Yanagi M, Ueno K, Ando A, Li S, Matsumae Y, Liu J, Dokko K, Watanabe M (2020) Effects of polysulfide solubility and Li ion transport on performance of Li–S batteries using sparingly solvating electrolytes. *J Electrochem Soc* 167(7). <https://doi.org/10.1149/1945-7111/ab7a81>
101. Gupta A, Bhargav A, Manthiram A (2019) Highly solvating electrolytes for lithium-sulfur batteries. *Adv Energy Mater* 9(6):1803096. <https://doi.org/10.1002/aenm.201803096>
102. Pang Q, Shyamsunder A, Narayanan B, Kwok CY, Curtiss LA, Nazar LF (2018) Tuning the electrolyte network structure to invoke quasi-solid state sulfur conversion and suppress lithium dendrite formation in Li–S batteries. *Nat Energy* 3(9):783–791. <https://doi.org/10.1038/s41560-018-0214-0>
103. Seita T, Matsumae Y, Liu J, Tatara R, Ueno K, Dokko K, Watanabe M (2020) Graphite-lithium sulfide battery with a single-phase sparingly solvating electrolyte. *ACS Energy Lett* 5(1):1–7. <https://doi.org/10.1021/acscenergylett.9b02347>
104. Peng H-J, Huang J-Q, Cheng X-B, Zhang Q (2017) Review on high-loading and high-energy lithium-sulfur batteries. *Adv Energy Mater* 7(24):1700260. <https://doi.org/10.1002/aenm.201700260>
105. Bhargav A, He J, Gupta A, Manthiram A (2020) Lithium-sulfur batteries: attaining the critical metrics. *Joule* 4(2):285–291. <https://doi.org/10.1016/j.joule.2020.01.001>
106. Lin Z, Liu Z, Dudney NJ, Liang C (2013) Lithium superionic sulfide cathode for all-solid lithium–sulfur batteries. *ACS Nano* 7(3):2829–2833. <https://doi.org/10.1021/nm400391h>
107. Hassoun J, Scrosati B (2010) Moving to a solid-state configuration: a valid approach to making lithium-sulfur batteries viable for practical applications. *Adv Mater* 22:5198–5201. <https://doi.org/10.1002/adma.201002584>
108. Yang X, Luo J, Sun X (2020) Towards high-performance solid-state Li–S batteries: from fundamental understanding to engineering design. *Chem Soc Rev* 49(7):2140–2195. <https://doi.org/10.1039/c9cs00635d>
109. Umeshbabu E, Zheng B, Yang Y (2019) Recent progress in all-solid-state lithium–sulfur batteries using high Li-ion conductive solid electrolytes. *Electrochem Energy Rev* 2(2):199–230. <https://doi.org/10.1007/s41918-019-00029-3>
110. Hayashi A, Ohtsubo R, Tatsumisago M (2008) Electrochemical performance of all-solid-state lithium batteries with Li₂S-Cu electrodes. *Solid State Ionics* 179:1702–1705. <https://doi.org/10.1016/j.ssi.2008.03.008>

111. Takeuchi T, Kageyama H, Nakanishi K, Ohta T, Sakuda A, Sakai T, Kobayashi H, Sakaebe H, Tatsumi K, Ogumi Z (2014) Application of graphite–solid electrolyte composite anode in all-solid-state lithium secondary battery with Li_2S positive electrode. *Solid State Ionics* 262:138–142. <https://doi.org/10.1016/j.ssi.2013.09.046>
112. Han F, Yue J, Fan X, Gao T, Luo C, Ma Z, Suo L, Wang C (2016) High-performance all-solid-state lithium-sulfur sbattery enabled by a mixed-conductive Li_2S nanocomposite. *ACS Nano* 10(7):4521–4527. <https://doi.org/10.1021/acs.nanolett.6b01754>

Chapter 4

Physical and Chemical Adsorption of Polysulfides



Baohua Li and Yuanming Liu

Abstract During the normal operation of sulfur cathode, the solid–liquid–solid reaction mechanism would facilitate the kinetics for sulfur transformation. However, once the sulfur species dissolved into the liquid electrolyte, it would move from cathode to the anode surface and react with Li metal anode, causing sulfur loss and capacity decay. This phenomenon is the notorious “shuttling effect” for sulfur cathode, and is also the main challenge that restrain the practical application of Li–S chemistry. In this chapter, starting from the basic principles, characterization techniques and prediction rules, we summarized the origin, phenomenon and solutions for the shuttling effect. Typically, the physical confinement of polysulfides via incorporating sulfur on carbon materials through Van der Waals interaction, the chemical adsorption of polysulfide toward various kinds of compounds by ways of polar–polar interaction, Lewis acid–base interaction and redox interaction, and a new configuration interlayer have been discussed and analyzed systematically. On top of this, the authors make outlooks for the future direction of polysulfides adsorption.

Keywords Lithium polysulfides · Shuttling · Physical adsorption · Chemical adsorption · Interlayer

4.1 Introduction

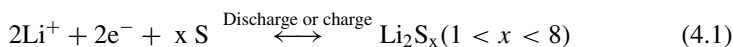
4.1.1 Basic Principles of Sulfur Cathode

Coupled with high-energy-density sulfur (S) cathode and lithium (Li) metal anode, Li–S batteries are considered as one of the most promising high-energy-density battery systems. It caters to the faster-changing energy requirements nowadays and has been extensively studied during the past decades. The dominating factors are the ultrahigh abundance of sulfur, its high energy density and its variation of oxidation

B. Li (✉) · Y. Liu

Shenzhen Key Laboratory on Power Battery Safety Research and Shenzhen Geim Graphene Center, Tsinghua Shenzhen International Graduate School, Shenzhen 518055, P.R. China
e-mail: libh@mail.sz.tsinghua.edu.cn

states. The basic electrochemistry of Li-S batteries is based on the following:



The reaction above has been given in the former chapter, thus we don't put more explanation on it.

4.1.2 Reaction Products of Sulfur Cathode

As shown in Eq. (4.1), many reaction intermediates would be generated during the sulfur reaction process, for example, Li_2S_8 , Li_2S_6 , Li_2S_4 , Li_2S_2 and Li_2S . Apart from these, some radicals such as S_3^{*-} and S_4^{*-} can also be generated and they do play important roles in sulfur transformation either. Typically, S_3^{*-} is extremely stable in nature and it was utilized to elucidate the functions of sulfur radicals during the electrochemical process [1].

As shown in Fig. 4.1, during the discharge process, S_8^{2-} is formed first via step (1) but then a disproportionation reaction appears as shown in step (1.1). There is an equilibrium between S_6^{2-} and S_3^{*-} radicals, and that is the reason why a sudden increase of S_3^{*-} concentration occurs once the discharge begins. At the end of 2.3 V, S_8^{2-} , S_6^{2-} (S_3^{*-}), and S_8 should reach an equilibrium. A single plateau is observed

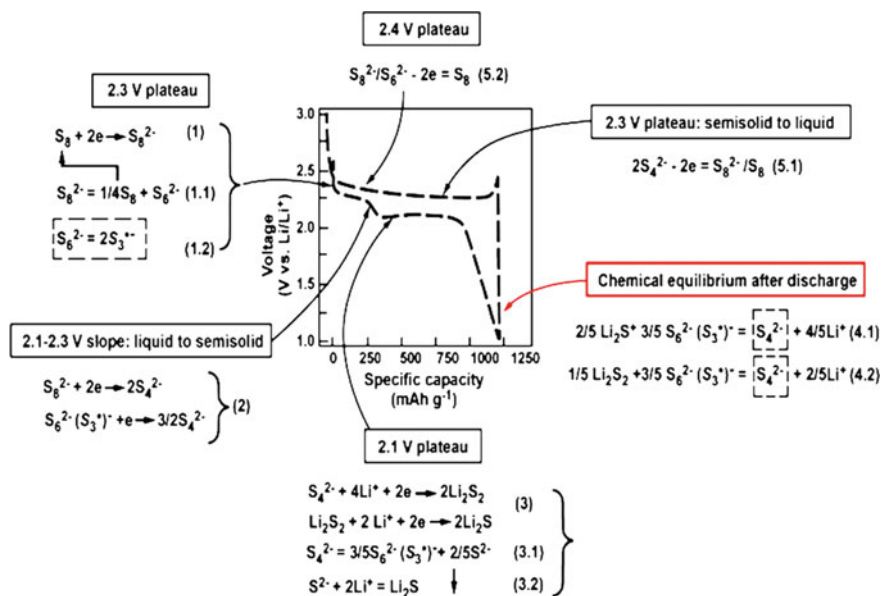


Fig. 4.1 Detailed reaction mechanisms of Li-S batteries. Reused with permission from Ref. [1], IOP

at 2.3 V because the reaction (1.1) is a chemical but not electrochemical route, and it reflects the two-phase transition between S_8 and Li_2S_8 . Continuing discharge, step 2 occurs at first and the S_8^{2-}/S_6^{2-} is electrochemically reduced to S_4^{2-} . The electrochemical reduction of Li_2S_4 to Li_2S_2 and then to Li_2S (step 3) take place by further lower degree scan. Both the electrochemical (step 3) and chemical reaction (steps 3.1 and 3.2) could produce Li_2S . At the end of discharge, a new equilibrium should be established among S_4^{2-} , S_3^{*-} (S_6^{2-}) and Li_2S_2/Li_2S (dominant species).

During the charge process, benefiting from the fast kinetics of semisolid-to-solid conversion in step (5.1), S_4^{2-} will be converted into S_8^{2-}/S_6^{2-} once the overpotential becomes large enough. Further, when the new S_8^{2-}/S_6^{2-} are produced, steps (4.1) and (4.2) would be initiated to produce more S_4^{2-} and facilitate the conversion of insoluble Li_2S_2/Li_2S . Therefore, more and more Li_2S_2/Li_2S is decomposed chemically rather than electrochemically.

As discussed above, the S_3^{*-} radicals play a significant role in the sulfur transformation, and it may help us to select the electrolyte system. For example, S_3^{*-} is highly reactive with a currently commercialized alkyl-carbonate solvent such as ethyl carbonate (EC)/dimethyl carbonate (DMC). The parasitic reactions between them will produce non-active byproducts, invalidating Li-S batteries. Therefore, the general electrolytes system for Li-S batteries are ether-based electrolytes or glymes, attributing to their stability toward sulfur radicals [2].

4.1.3 The Origin and Consequence of Shuttling Effect

Since it was suggested that the total or partial solubility of the cathode material may be the key for efficient sulfur utilization, various kinds of electrolyte system that could dissolve the sulfur intermediates had been explored [3]. For example, dimethyl sulfoxide (DMSO) or ethers like tetrahydrofuran (THF), for the reason that the polysulfide solubility as Li_2S_x can reach 10 M (or even more) in DMSO. Further researches of high polysulfide solubility electrolytes such as dioxolane (DOL) [4] and glyme solvents had been proved to be successful in boosting sulfur reaction kinetics. The high solubility of polysulfides imparts the ability to operate Li-S battery as a liquid cathode system whatever the starting sulfur is (solid as S_8 or soluble polysulfides). However, the lithium metal anode could sustain the corrosion from the soluble polysulfides due to its movement from cathode to anode (shuttling phenomenon). For example, the soluble polysulfides such as Li_2S_8 , Li_2S_6 would migrate from the cathode to the anode surface and then react with Li metal, producing Li_2S_2/Li_2S at the surface of Li metal and soluble lower-order polysulfide such as Li_2S_4 simultaneously. The newly formed Li_2S_4 would migrate to the sulfur cathode and further react with the solid sulfur to produce Li_2S_8 and Li_2S_6 (Fig. 4.1), and then migrate to anode. Therefore, the repeated transportation and reaction of soluble polysulfides would consecutively consume sulfur in the cathode and lithium metal simultaneously, causing irreversible capacity loss.

In 2004, Mikhaylik [5] proposed the basic shuttle Eq. (4.2) for various cell test conditions,

$$\frac{d[S_H]}{dt} = \frac{I}{q_H} - k_s[S_H] \quad (4.2)$$

where $[S_H]$ is the normalized concentration of polysulfide, t is the time, I is the normalized current during charge or discharge, q_H is the specific capacity that correspond to the first plateau (2.3 V) during sulfur transformation and k_s is the shuttle constant.

By comparing their theoretical data with experimental data, many kinds of phenomena such as the relations between the shuttling effect and overcharge, salt concentration and battery self-heating could be explained. Different electrolytes show different shuttle constants according to their concentrations, and the higher salt concentration means lower shuttle constant and lower Li corrosion rates.

In this chapter, we will concentrate on the basic rules and methods to tackle the shuttling effect of soluble lithium polysulfides, including physical and chemical adsorptions of polysulfides. Before this, the analytical techniques of shuttling effect are emphasized.

4.2 How to Characterize the Shuttling Effect of Polysulfides?

During the electrochemical process of Li–S batteries, intermediates such as Li_2S_8 , Li_2S_6 , Li_2S_4 , Li_2S_2 and Li_2S would be formed at different stages. These products are not inclusive of all the intermediate products definitely, but they are representative and can be utilized to describe the whole reaction process of Li–S batteries. Specifically, the former three (Li_2S_8 , Li_2S_6 and Li_2S_4) species are soluble in ether-based electrolyte, but the latter two (Li_2S_2 and Li_2S) species are insoluble. Therefore, there is a solid–liquid–solid transformation during the discharge or charge process. And the shuttling of polysulfides occurs during the liquid reaction process. Hence, it is reasonable to elucidate how the shuttling proceeds and how serious they are. There are mainly two series of methods to characterize the shuttling effect of polysulfides: in situ and ex situ method.

4.2.1 In Situ Method

4.2.1.1 In Situ Micro-scale Observation Techniques

The room temperature sulfur (S) to Li_2S solid-state transformation is kinetically too slow, and the dissolved polysulfide can facilitate the reversible charge–discharge

process of sulfur cathode. Therefore, when the shuttling effect of soluble lithium polysulfides was taken into consideration, both the solid to liquid and liquid to solid processes should be concerned. If the cathode electrode has some strong anchors of polysulfide species, the liquid to solid reaction would occur at these places at first. The distribution of liquid–solid charge/discharge products at different sites in the cathode is effective to verify this point [6]. As schematic in Fig. 4.2a, patterned hybrid tin-doped indium oxide (ITO) glassy carbon electrode was developed by sputtering, and the final electrode was constructed by ITO squares separated by carbon lines. Subsequently, the obtained electrode was assembled as a sulfur collector with Li metal and 2 M (the concentration based on sulfur) Li_2S_8 solution as anode and catholyte, respectively. After discharging the cell to 1.7 V, it was kept at this voltage until the discharge current decreased to $1 \mu\text{A cm}^{-2}$. As shown in Fig. 4.2b, c, after the whole discharge process, many particles appear on the ITO pattern while the C surface still looks smooth, suggesting that the final solid products have strong bonding with the ITO surface.

The more amount of solid product deposited on ITO means less shuttling effect of ITO electrode. If there is little solid product deposited on the cathode surface, it means that most of the dissolved polysulfide does not transfer into solid product and the shuttling effect is severe. Therefore, the amount of solid deposition products on specific materials can demonstrate its ability to restrain the shuttling effect. In other words, it can explain how serious the shuttling would be once this specific material was added into cathode. Actually, this method is not an in situ method, because that the SEM characterization and the Li_2S deposition processes are not carried out simultaneously. However, as the solid deposition could be visualized by optical microscopy, we defined this method to be “in situ” method either.

In addition, Chu et al. designed an in situ electrochemical cell to probe the supercooled sulfur deposition [7]. Typically, a nickel (Ni) grid electrode ($1 \mu\text{m}$ in line width, 50 nm in height) was deposited on a glass substrate via e-beam lithography and evaporation, while a Li metal was placed on the same plane to act as the

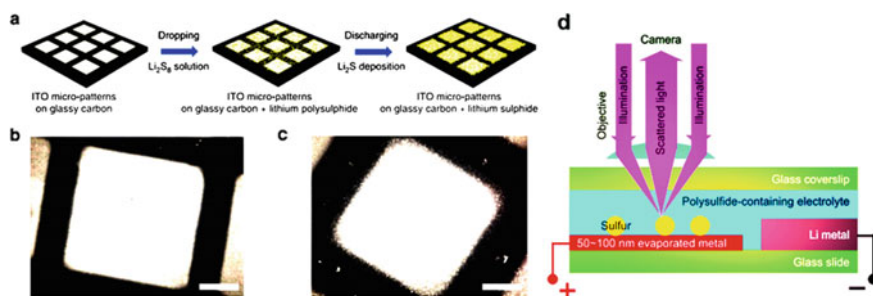


Fig. 4.2 a Schematic illustration of the tin-doped indium oxide (ITO) micro-pattern sulfur cathode. b and c SEM images of a fresh and Li_2S deposited ITO micropattern, respectively, the scale bar is $20 \mu\text{m}$. d Schematic showing the in situ dark-field light microscopy (DFLM) to observe the formation of supercooled sulfur at room temperature. Panels adapted with permission from: a, b, c Ref. [6], NPG; d Ref. [7], PNAS

counter/reference electrode (Fig. 4.2d). During the galvanostatic charge/discharge process at room temperature, sulfur would deposit on/strip from the working electrode, while the dark-field light microscopy (DFLM) images of a $180\ \mu\text{m} \times 135\ \mu\text{m}$ region on the surface of the Ni substrate were captured simultaneously. A white light source and a three-color-channel complementary metal-oxide semiconductor (CMOS) camera were used to record the color information. By using this technique, it is possible to optically observe multiple phenomena in lithium-sulfur (Li-S) batteries, including the generation of metastable liquid sulfur at room temperature electrochemically, rapid solidification of sulfur droplets upon crystal nucleation and sulfur plating/stripping via solution mechanism.

4.2.1.2 Optical Observation Techniques

Due to the fact that polysulfides are always colorful, the motion of polysulfide could be seen by eye sights directly. Therefore, an optically transparent Li-S cell was developed to probe the interaction between soluble polysulfide and cathode surface, as shown in Fig. 4.3a [8]. After discharging for 12 h, the electrolyte in the cell with S/Ketjen Black (75S/KB, the upper layer) is still yellow, showing severe loss of active sulfur. In contrast, for the 75S/MnO₂ cell, the electrolyte could maintain the color of faint yellow at 4 h, providing visual evidence for low content of soluble

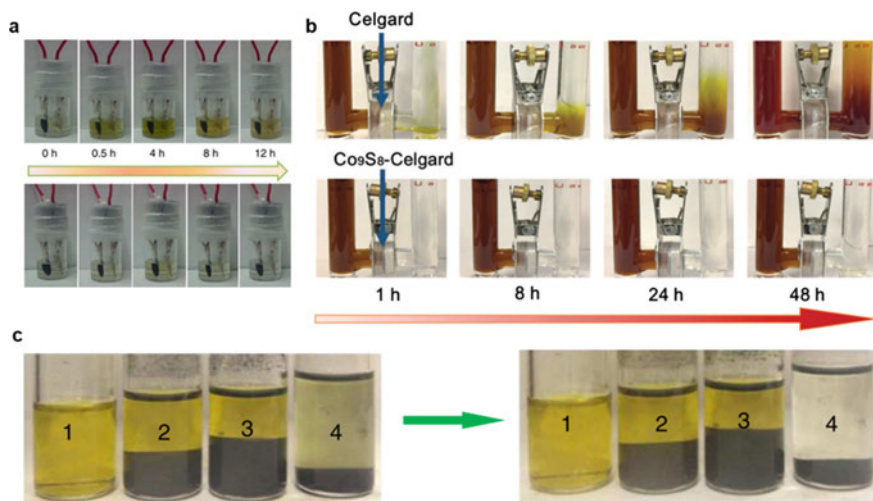


Fig. 4.3 **a** Digital photos of the electrochemical transparent cells to show the shuttling of sulfur cathode with (down) and without (up) MnO₂ additive. **b** Glass cells filling with LiPS (Li₂S₆) in DOL/DME solution (left chamber) and pure DOL/DME solvent (right chamber), and the top and bottom panels were inserted with Celgard and Co₉S₈-Celgard separator, respectively. **c** Sealed vials of the pristine Li₂S₄/THF solution after adding (1) nothing, (2) graphite, (3) VC carbon and (4) Ti₄O₇ (left side), and after 1 h stirring (right side). Panels adapted with permission from: **a** Ref. [8], NPG; **b** Ref. [9], RSC; **c** Ref. [10], NPG

polysulfide in the electrolyte and demonstrating the effective trapping effect of MnO_2 . Once fully discharged, the electrolyte tends to be completely decolorized, indicating the effective conversion of soluble lithium polysulfides to insoluble species. This method is effective in assessing the polysulfide trapping effect of sulfur cathode when the mediator was added into the cathode directly.

When the mediator was constructed on separator but not the sulfur cathode, the glass cells set up by Manthiram et al. [9] are helpful to demonstrate its polysulfide blocking ability, as shown in Fig. 4.3b. Typically, DOL/DME solvent with and without Li_2S_6 was filling in the left and right chambers, respectively. And then, the pristine separator (top panel) or the Co_9S_8 modified separator (bottom panel) was intercalated between these two chambers. Upon diffusion, for the cell with pristine separator, the right chamber changed to yellow-brown after 48 h, showing severe shuttling. In contrast, the cell with the Co_9S_8 modified separator shows almost unchanged color in the right chamber, proving that the shuttle of polysulfide can be mitigated by this modification significantly.

Further, as we can see, both the aforementioned methods could reflect the transportation of polysulfides to some extent. However, they are time-consuming and may not be that helpful if we want to know the results as soon as possible. Hence, Nazar et al. [10] prepared the $\text{Li}_2\text{S}_4/\text{THF}$ solution in a sealed vial at the first. Then the mediators such as graphite, VC carbon and Ti_4O_7 were added to it. Different from other candidates, once Ti_4O_7 was added, the Li_2S_4 solution changed to light yellow immediately, and almost completely decolorized after 1 h stirring, demonstrating the strong adsorption of Ti_4O_7 toward Li_2S_4 . This method is cheap yet convenient and could be utilized in many complicated circumstances.

All these methods can reflect the adsorption ability of the mediator toward soluble polysulfides but cannot explain the reason why the mediator can do this.

4.2.2 *Ex Situ Method*

The exhaustive searches for materials that show high electronic conductivity, substantial surface area and pore volume, and suitable physical/chemical properties to restrain the shuttling of polysulfides are still ongoing. We have discussed the in situ method to characterize the shuttling effect in Sect. 4.2.1. However, these methods can only reflect the superficial phenomenon and we need other techniques to disclose the covered part.

Therefore, a quantitative electro-oxidation reaction was designed to screen sulfur host candidates (Fig. 4.4b) [11]. Typically, the sample (Fig. 4.4b(i)) is prepared by dispersing a specific weight of the aimed host material into a Li_2S_4 solution (dissolved in tetraethylene glycol dimethyl ether (TEGDME)). Superfluous Li_2S_4 solution is added to guarantee the polysulfides saturation of host materials. Then the suspension is stirred until its color remained unchanged for 18 h. Next is the centrifugation of the suspension, and the resulted supernatant is collected for the titration (Fig. 4.4b(ii)). The following step is the electrochemical oxidation of the

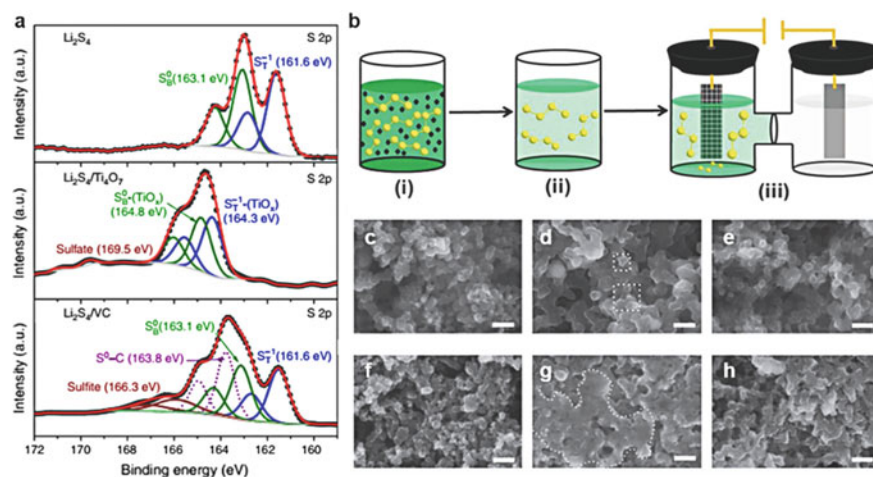


Fig. 4.4 **a** S 2*p* high-resolution spectra from the X-ray photoelectron spectroscopy (XPS) of Li_2S_4 , $\text{Li}_2\text{S}_4/\text{Ti}_4\text{O}_7$ and $\text{Li}_2\text{S}_4/\text{VC}$, respectively. **b** Schematic illustration of the electrochemical oxidation process to determine polysulfide adsorption capability. SEM images of the cycled morphologies of $\text{Ti}_4\text{O}_7/\text{S}$ and VC/S electrodes: **c**, **f** 0 cycles (pristine), **d**, **g** after first discharge, the dotted boxes and shapes are deposited Li_2S , **e**, **h** charged status after 500 cycles. Panels adapted with permission from: **a**, **c**, **d**, **e**, **f**, **g**, **h** Ref. [10], NPG; **b** Ref. [11], RSC

un-adsorbed polysulfides in a solution of $\text{LiClO}_4\text{-TEGDME}$ (Fig. 4.4b(iii)). A nickel foam was utilized as the current collector in the left compartment of an H-cell, and the right compartment is a Li foil counter electrode filled with adequate electrolyte: 1.0 M LiClO_4 in TEGDME with 2 wt% LiNO_3 . Then, a constant voltage charge at 3.0 V is carried out until the current is 0 mA. By this method, the capacity of the unreacted Li_2S_4 can be integrated over time. This allows one to determine the amount of polysulfide adsorbed on the matrix. As concluded, the non-polar materials (i.e., carbon-based materials such as Super P and Vulcan) adsorbed relatively few polysulfides compared to polar ones (i.e., metallic oxides such as TiO_2 and MnO_2). Although this method is similar to the sealed vial test aforementioned (Fig. 4.3c), it can assess the polysulfide adsorption ability quantitatively and thus we define it as a kind of ex situ method.

Other characterizations such as X-ray photoelectron spectroscopy (XPS, Fig. 4.4a), scanning electron microscopy (SEM, Fig. 4.4c–h) and so on are also effective in evaluating the shuttling effect of polysulfides [10]. By detecting the inner shell electron's chemical shift of specific atom, XPS is an effective tool in elucidating the electronic structure, macromolecular structure and chain structure of materials. For example, after getting touched with pristine materials for several hours, the Li_2S_4 were centrifuged, dried and then analyzed by high-resolution XPS, as shown in Fig. 4.4a. If there is no interaction between the substrate and Li_2S_4 (i.e., $\text{Li}_2\text{S}_4/\text{VC}$), the S 2*p* spectrum of the hybrid powder should be the same as the pristine Li_2S_4 powder. However, when there is a bond existing between the matrix and Li_2S_4

(i.e., $\text{Li}_2\text{S}_4/\text{Ti}_4\text{O}_7$), the binding energy of S 2p spectrum of the composite is different from the pristine Li_2S_4 . Further, the comparison of the cycled morphologies of sulfur electrodes is also indicative in demonstrating the shuttling effect of polysulfides. The final discharge products of sulfur cathode are Li_2S_2 and Li_2S . And severe polysulfides shuttling effect would hamper the liquid–solid transformation, resulting in less amount and non-uniform solid deposition (Fig. 4.4f, g, h).

4.3 Physical Confinement of Polysulfides Within Cathode

Originating from the Van der Waals force, the physical confinement of polysulfides can confine polysulfides inside sulfur cathodes through material and structure design. For example, by adopting porous materials or incorporating external barrier coatings, the shuttling effect of polysulfides could be physically restrained. Materials with natural pores are easily tailored to core–shell or layer structures might be good choices. Among these candidates, carbon-based materials have been recognized as one of the ideal ones for their large surface area, tunable structures and excellent electronic conductivity. Various kinds of carbon materials including carbon nanotubes (CNTs), graphene, and porous carbon nanofibers have been adopted to alleviate the ultralow electrical conductivity of sulfur and confine polysulfides shuttling simultaneously.

4.3.1 Carbon Materials for Physical Confinement

Due to the easy processing and high electrical conductivity properties, various kinds of carbon materials have been utilized as sulfur substrate. Apart from this, the non-polar sulfur could fill in its porous structure by capillary forces. Since the pioneering thought of melt-infusion sulfur into mesoporous CMK-3 substrate composed by Nazar et al. [12], various kinds of carbon materials with macro-, meso-, micropore and their mixture showed great potential in realizing high-performance sulfur cathode.

4.3.1.1 Macro-, Meso- and Microporous Carbon

As defined by the IUPAC, the pores in a material could be divided into macro (>50 nm), meso (2–50 nm) and micro (<2 nm). Carbon materials with different pore sizes have different functions for sulfur transformation.

Macroporous Carbon

Macroporous carbons have been little utilized to confine sulfur due to their open architecture, which is unable to sequester the shuttling of polysulfides. However, once the polysulfides' mobility is restrained by high-viscosity electrolyte, the macroporous carbon could be used as sulfur substrate either. For example, the sulfur-loaded ordered inverse opal carbon (IOP) was matched with a glyme–Li salt electrolyte with high viscosity for sulfur cathode [13]. This electrolyte contains purely $[\text{Li}(\text{glyme})]^+$ cations and TFSI^- anions only, and the final electrode delivered improved performance. However, the poor scalability of IOP, high cost of this electrolyte system and relatively small operation kinetics are restraining its large-scale applications.

Mesoporous Carbon

Most of the research on sulfur/carbon cathodes has paid attention to mesoporous carbons (MCs). By using mesoporous carbon (MC) with different pores (22 nm, 12 nm, 7 nm and 3 nm) and various pore volumes (up to $\sim 4.8 \text{ cm}^3 \text{ g}^{-1}$) as sulfur substrate, the fully or partially filling mesoporous porous sulfur (MCS) cathode could be obtained [14]. Typically, sulfur was dissolved in CS_2 first, then the MC was added and mixed with the sulfur solution. After the drying process, the composite was melt-flowed into the porous carbon. For the fully sulfur filling MCS (the pores of MC are fully filled), the higher sulfur loading could be realized by the MC with larger pore volume, while the performance of different MCS composites is almost the same. The partially sulfur filling MCS cathode (the pores are partially filled) can show an improved electrochemical performance compared with the fully filling ones, which may result from its improved electronic and ionic transport.

Microporous Carbon

The encapsulation of sulfur into micropores can be realized by thermal treatment of a mixture of sulfur and porous carbon materials [15]. Various kinds of precursors could be utilized to produce microporous carbon such as sucrose. As an example, a 5 wt% sucrose solution was prepared by dissolving sucrose in 6 M sulfuric acid. Then, the dissolved sucrose was placed in a flask and refluxed for 10 h at 120 °C. After infiltrating and washing the black suspension with distilled water several times, the product was air-dried and then calcined at 1000 °C under the protection of argon (Ar) atmosphere. The BET specific surface area of the resulting carbon spheres is $843.5 \text{ m}^2 \text{ g}^{-1}$. Further, it has a micropore size distribution of about 0.7 nm. The melt-infusion at 149 °C and further vaporization of excess sulfur at 300 °C was carried out to prepare the final C/S composite.

As shown in Fig. 4.5c (XRD), the melt-infusion process causes the disappearance of the sharp diffraction peaks of sulfur, indicating the fact that the sulfur

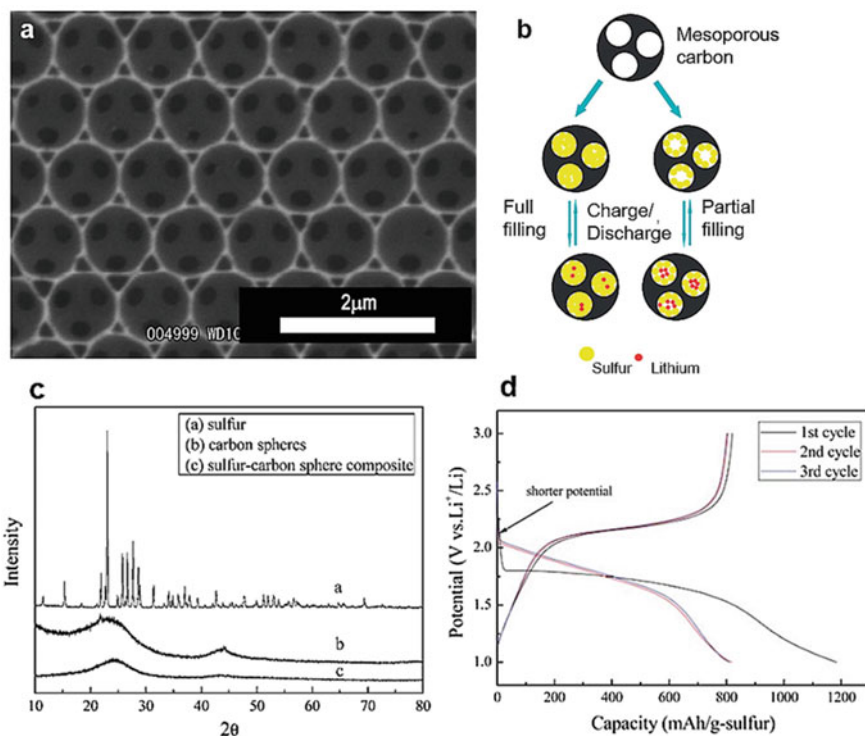


Fig. 4.5 **a** SEM image of 1 μm inverse opal carbon (IOC). **b** Schematic showing the working mechanism of sulfur mesoporous carbon (MC) composite cathode. **c** XRD patterns of a—sublimed sulfur, b—microporous carbon spheres and c—sulfur-carbon sphere composites with 42 wt% of sulfur. **d** Voltage–capacity curves of the sulfur–carbon sphere composite with 42 wt% sulfur. Panels adapted with permission from: **a** Ref. [13], RSC; **b** Ref. [14], RSC; **c, d** Ref. [15], RSC

inside the micropores is in a highly dispersed state with a low-molecular mono-layered coverage. During the electrochemical reaction of C/S composite, there is only one potential plateau at around 1.8 V (vs. Li^+/Li) shown after the first cycle, while the first cycle discharge has a very shorter potential plateau (2.25 V vs. Li^+/Li , Fig. 4.5d). This phenomenon is different from the traditional two potential plateaus of the sulfur/carbon matrix, and maybe result from the trace sulfur remained on the surface of C/S composite. The large potential hysteresis may result from the strong adsorption capability and the unstable properties of the sulfur at a high dispersion state.

4.3.1.2 Graphene

For its high electronic conductivity, large surface area and diverse surface properties (hydrophobicity/philicity), graphene has been extensively utilized as substrate, and conductive additive of sulfur cathode.

In 2011, Dai et al. found that the melt-infusion process can only improve the electronic conductivity of sulfur to some extent. However, once graphene was used as a sulfur scaffold, it is not effective in containing the polysulfides due to its irregular pore with widely distributed size [16]. Bearing this in mind, carbon black decorated graphene oxide sheets were wrapped on the sulfur particles coated with poly(ethylene glycol) (PEG). This method can change the insulating sulfur particles to be electrically conductive, trap the polysulfide intermediates and alleviate the volume expansion simultaneously. Besides, a highly scalable graphene/sulfur composite (GSC) cathode that exhibits a high sulfur content of 87 wt% was developed to resolve the large-scale technology of sulfur cathode [17]. Enveloped with reduced graphene oxide (rGO), the micron-sized sulfur particles deliver ultrahigh electronic conductivity. Typically, the micron-sized sulfur particles were produced by an in situ reaction between Na_2S_x and HCl solution, as schematic in Fig. 4.6a. If the sulfur particles are distributed properly, only little conductive additives are needed for efficient working of Li-S cell. In this regard, the 2D graphene seems to be ideal to accommodate sulfur.

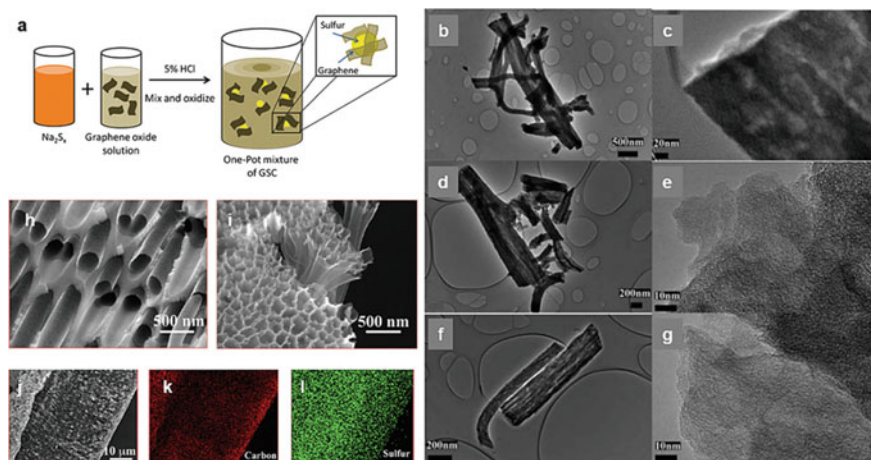
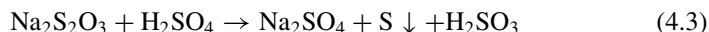


Fig. 4.6 a Schematic showing the one-pot synthesis process to fabricate graphene/sulfur composite (GSC). TEM images of **b, c** porous CNFs, **d, e** porous CNF-S nanocomposites after melt-infusion sulfur at 155 °C for 12 h and **f, g** porous CNF-S nanocomposites thermally treated at 155 °C for 12 h and further at 160 °C for 6 h. SEM images of **h** carbon-coated anodic aluminum oxide (AAO) template, **i** sulfur-impregnated hollow carbon nanofiber, **j** high-resolution TEM image of hollow carbon nanofiber/S array, and corresponding elemental mapping of carbon (**k**) and sulfur (**l**). Panels adapted with permission from: **a** Ref. [17], RSC; **b–g** Ref. [19], RSC; **h–l** Ref. [20], ACS

4.3.1.3 Carbon Nanotubes/Fibers

Multiwalled Carbon Nanotubes (MWCNTs)

Due to the 1D porous structure, multiwalled carbon nanotubes (MWCNTs) have long been utilized as either scaffold or conductive additive in Li–S batteries. For example, a well-dispersed sulfur-MWCNTs composite cathode was synthesized by a direct precipitation route listed below (Eq. 3.1) [18, 19]:



In this method, the acid-treated MWCNTs were dispersed in a 0.1 M $\text{Na}_2\text{S}_2\text{O}_3$ (sodium thiosulfate) solution and the obtained solution was further sonicated to disperse MWCNTs effectively. Then, 0.1 M H_2SO_4 was added dropwisely into the solution. After stirring for 1 h and infiltration, the precipitated sulfur-MWCNTs compound was washed by distilled water several times and the resulting composite was finally obtained after removing the solvent. Although the composite cathode exhibited a high initial sulfur utilization, its capacity fades to 63% only after 30 cycles. This suggests the limited effect of MWCNTs to restrain the shutting of polysulfides, which may result from their limitations in boosting Li-ion diffusion.

Carbon Nanofibers (CNFs)

Apart from MWCNTs, carbon nanofibers (CNFs) have also been developed as scaffolds of sulfur for their easy processing, adjustable pore structure and excellent mechanical strength.

Electrospinning is a low-cost, simple and environmentally benign method to fabricate multifunctional fibrous materials. In 2011, this method was adopted to fabricate porous CNFs as sulfur scaffolds. During the preparation process, 10 wt% PAN/PMMA (mass ratio of 1:1) bicomponent polymer was dissolved in DMF solvent at 60 °C first. After obtaining a homogeneous PAN/PMMA solution, a high voltage of ~12.5 kV was applied to carry out the electrospinning process. Once the electrospinning was terminated, a fibrous web was obtained at the collection plate, and it was collected for further usage. After being pre-oxidized and further carbonized under Ar atmosphere, the final porous CNFs were obtained. The CNF-S cathode was first prepared by the route in Fig. 4.6a, and then melt-infusion sulfur on CNFs. As shown in Fig. 4.6b, c, it is clear that the porous CNFs have many voids. After the first heat treatment step (155 °C for 12 h), almost all the open pores were filled with sulfur. At this stage, the sulfur content is about 60 wt% (Fig. 4.6d, e). Upon further heat treatment at 160 °C for 6 h, the thin interior pores reoccurred because of the partial evaporation of sulfur (Fig. 4.6f, g). At this stage, the sulfur content would be decreased to 42 wt%. For its extremely high surface area, the porous CNFs can adsorb and disperse sulfur efficiently, and further ameliorate the insulating nature of sulfur and shuttling effect of soluble polysulfides. Therefore, the final CNFs-S

composite cathode can deliver the initial discharge capacity of nearly 1400 mAh g⁻¹ at 0.05 C current density. From another perspective, the ultrahigh specific surface area of sulfur scaffold is detrimental for the cost of Li-S batteries, because it needs more electrolyte.

Ideal sulfur substrates should possess the following merits: (1) suitable porous structure for efficient polysulfides retainment; (2) limited sulfur-electrolyte contact; (3) sufficient space to alleviate the volumetric expansion of electrode; (4) faster transportations of both electrons and Li ions, especially under large current density; (5) sufficient electronic conductivity for deposition of Li₂S₂ and Li₂S and (6) suitable electrolyte to protect lithium metal anode [20]. However, some of these properties are conflicting with each other, especially the (2) and (5). On top of these, a hollow carbon nanofiber with vertical arrays was designed, as shown in Fig. 4.6j. Upon melt-infusion sulfur on this substrate, its high aspect ratio would boost the orderly diffusion of polysulfides in organic electrolyte, and its thin carbon wall would accelerate the transportation of lithium ions at the same time. Therefore, the final sulfur cathode delivered a reversible discharge capacity of around 730 mAh g⁻¹ after 150 cycles.

4.3.2 *Polymer Membranes for Physical Confinement*

Except for adsorption of soluble polysulfides via van der Waals interactions, coating ion-selective polymer layer on sulfur cathode can also sequester the shuttling effect effectively. Nowadays, various membranes have been widely applied in many fields such as gas separation, water desalination, fuel cells and batteries, for the reason that the flowing flux would scale inversely with the membrane thickness. In this regard, the high selectivity of one membrane needs to be thicker, but this would impair its permeability. It is influential in many areas to incorporate layer-by-layer (LBL) self-assembly technique via switching adsorption of oppositely charged polyelectrolytes. Benefiting from its ion conductivity, flexibility and self-healing properties, polyelectrolyte multilayers (PEMLs) can act as a membrane to impede polysulfide diffusion [21]. Typically, the outer surface of carbon/sulfur composite was encapsulated by adsorbing layer of branched poly(ethyleneimine chloride) (bPEI), which lays a foundation for the final PEMLs membrane. Following, upon exposing the carbon/sulfur composite to 0.5 M lithium chloride aqueous solutions of the polyanion sodium poly(styrene sulfonate) (PSS) or the polycation poly(dimethyldiallyl ammonium chloride) (PDADMA) alternatively, the PEMLs would be formed and the membrane thickness can be adjusted through the control of the number of layers. When the final composite cathode (PEML₃) is stained with the fluorescent dye fluorescein carboxylate YG, the green channel fluorescence microscopy directly shows the complete encapsulation of sulfur cathode (Fig. 4.7a). XPS characterization can provide more evidence for the complete encapsulation. As shown in Fig. 4.7b, the initial XPS spectrum (red line) of PEML₃ proves the existence of sulfonic acid functionality of the PSS layer in the PEML membrane (S (2p_{3/2}) peak located at 168.2 eV). With sputtering of the PEML₃ membrane, the PEML membrane was etched away (the absence

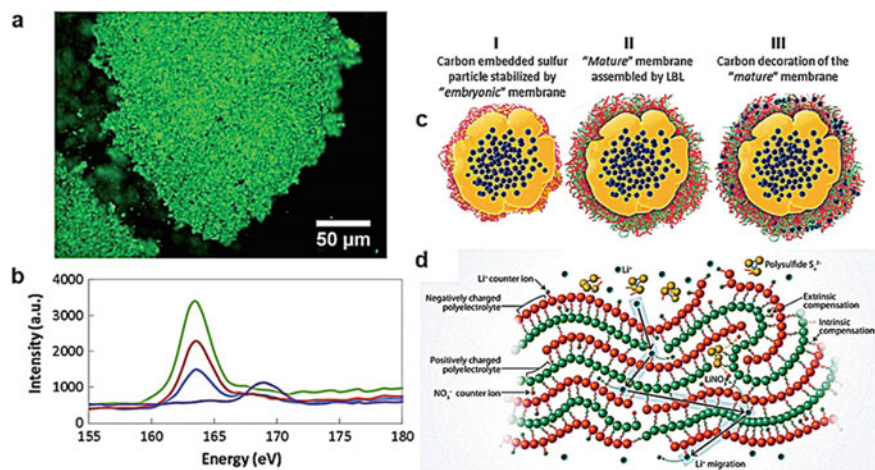


Fig. 4.7 **a** Fluorescence microscopy showing the homogeneous PEML coverage on carbon/sulfur composite. **b** XPS spectra of sample TDA57PEML3 at various sputtering time: 10 min (blue line), 20 min (garnet line) and 60 min (green line). **c** Schematic illustration of the preparation process of ion-selective, flexible and conductive carbon decorated LBL nanomembrane. **d** Diffusion procedure of the charged species through an LBL membrane. Panels adapted with permission from: **a, b** Ref. [21], RSC; **c, d** Ref. [23], RSC

of the peak at 168.2 eV) and the reappearance of the elemental sulfur contained in the pores of carbon substrate occurred (the emergence of a peak at 162 eV). The PEML membranes can selectively transport ions, and ions with a higher charge or larger size tend to move more slowly. In Li–S chemistry, except for the lithium polysulfides, almost all the other anion and cation in the electrolyte are singly charged. Therefore, the polymer network can show a strong sieving effect toward soluble polysulfides. Actually, there is a molecular weight threshold (~ 200) for the sieving effect of the PSS/PDADMA multilayer in an aqueous solution, and above which the rejection would be more efficient [22]. Such a limit shows that polysulfides would be greatly restrained by the PSS/PDADMA membrane.

Apart from this, a hollow carbon nanosphere decorating sulfur particle was encapsulated by an ion-selective, flexible and carbon-coated LBL nanomembrane [23], as vividly shown in Fig. 4.7c. Such architecture has the following merits: (1) the embedded hollow carbon spheres can promote the electronic conductivity of sulfur cathode; (2) the pores of carbon spheres can confine polysulfides and alleviate the volume expansion; (3) the ion-selective nanomembrane can restrain shuttling of polysulfides and permit the diffusion of lithium ions at the same time; (4) the nanocarbon decorated on the membrane can further promote the electronic conductivity. After a thin conductive polymer (PEDOT:PSS) coating, a fully selective membrane was assembled on top of it when this particle is exposed to the oppositely charged polyelectrolytes in an aqueous solution. Once assembled, the mature membrane exhibits the same functionality as the PEML membrane (Fig. 4.7d).

4.3.3 Summary

Physical confinement of polysulfides mainly comes from Van der Waals interactions. However, it is not strong enough to confine soluble polysulfides effectively. Hence, the physical adsorption of polysulfides in the carbon materials may be effective on short- and medium-term cycling only (within several hundred cycles). And the polysulfides would still shuttle to the anode surface, causing the capacity fading of batteries. On the other hand, due to its good electronic conductivity and light weight, carbon materials are helpful in boosting the electrochemical transformation of sulfur and maintaining its superior energy density. In addition, the easily tailored properties of carbon such as porosity, surface polarity and pore distribution of carbon are also beneficial to construct high sulfur loading cathode. Thus far, fabricating carbon materials with high electronic conductivity yet with high affinity to polysulfides still remained challenging.

4.4 Chemical Confinement of Polysulfides Within Sulfur Cathode

Upon reduction of sulfur, its asymmetric structure endows the soluble lithium polysulfides high polarity. When this polarity is taken into consideration, it is desirable to design sulfur hosts with strong polarity to adsorb polysulfides. The strong chemical interaction between the substrate and polysulfides can anchor the polysulfides, thus restraining its shuttling toward Li metal anode. Typically, three methods can be utilized to form bonding between sulfur substrates and polysulfides: (1) polar–polar interactions; (2) Lewis acid–base interactions; and (3) redox interactions. Generally, the first two are the main methods and the third one is similar to the catalytic conversion of sulfur cathode. Therefore, we discuss the former two parts meticulously and the third part briefly. Materials with sufficient bonding sites to build chemical interactions with polysulfides are useful to attain optimum chemical bonding. In this regard, porous materials with large pore volume and high specific surface area are ideal to load bonding sites and sulfur cathode.

4.4.1 Polar–Polar Interactions

Due to the structural asymmetry-induced polarity of polysulfides, the polar–polar interactions can be adopted for the polar materials to anchor polysulfides efficiently. Many materials with high polarity have been developed to chemically adsorb polysulfides, including heteroatom-decorated carbon materials, functional polymeric materials and metal compounds such as metal oxides, metal nitrides, metal sulfides and so on. It is worth noting that some of the metal compounds possess relatively poor

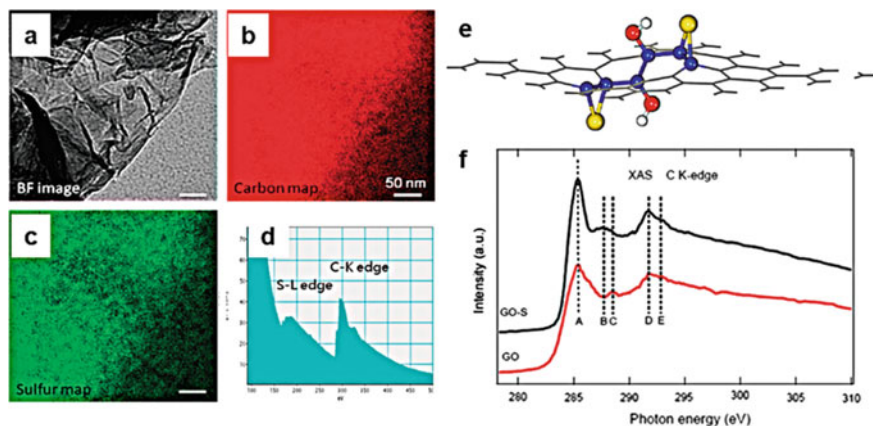


Fig. 4.8 **a**, **b** and **c** TEM bright-field image, mapping of elemental carbon and sulfur of GO-S nanocomposite, respectively. **d** Electron energy loss spectroscopy (EELS) spectrum of **(a)**, the scale bars are 50 nm. **e** Representative configuration of the sulfur immobilized by GO. The yellow, red and white balls denote sulfur, oxygen and hydrogen atoms, respectively, and the others are carbon atoms. **f** XAS carbon (C) K-edge spectra of pure GO and GO-S nanocomposites, respectively. Panels adapted with permission from Ref. [24], ACS

electronic conductivity, which is bad for sulfur transformation. Therefore, carbon materials with high electrical conductivity are often incorporated to improve sulfur cathode performance.

4.4.1.1 Heteroatom-Doped Carbon Materials

Decorated with heteroatoms (e.g., oxygen, nitrogen, sulfur and so on), the non-polar carbon materials can be converted to polar ones and these atoms can anchor polysulfides efficiently.

Oxygen Doping

Reduced graphene oxide (rGO) contains multiple functional groups, such as hydroxyl, carboxyl and ester, and it is effective in restraining the shuttling of polysulfides. In 2011, Zhang et al. first fabricated GO-S nanocomposite as a sulfur cathode [24]. A chemical reaction in a micro-emulsion system was adopted to deposit nano-sulfur onto the GO sheet. The following step is the heat treatment at 155 °C for 12 h, and it can remove some of the bulk S and reduce the GO simultaneously. The TEM image and its elemental mapping of carbon and sulfur can show the homogeneous dispersion of sulfur (Fig. 4.8a–d). Ab initio calculations discovered that due to the functional groups' induced ripples, both epoxy and hydroxyl groups can bind sulfur strongly (Fig. 4.8e). Soft X-ray adsorption spectroscopy (XAS) measurements

also proved that the sulfur incorporation would help in formatting the sp^2 -hybridized carbon structure. Moreover, the feature “carbon (C)” peak (possibly originating from C–O bond) of GO is weakened after heat treatment of GO-S nanocomposite, indicating the strong chemical interaction between sulfur and rGO (Fig. 4.8f). The rGO-S nanocomposite delivered a high specific capacity of 1000 mA h g^{-1} at the first cycle of 0.1 C and remained to be 954 mAh g^{-1} after 50 cycles (ionic electrolyte).

X-ray photoelectron spectroscopy (XPS, Fig. 4.9a–d) and near-edge X-ray absorption fine structure (NEXAFS, Fig. 4.9e, f) were also useful to investigate the electronic and chemical structure of rGO-S nanocomposite [25]. As shown in Fig. 4.9, the XPS and NEXAFS results can show the existence of C–S and O–S bonds. In addition, the results also demonstrate that the incorporation of sulfur can influence the valence band states of rGO. The following merits of rGO-S cathode might explain its excellent performance: (1) partially sulfur reduction on rGO induced higher electronic conductivity and (2) the preserved electronic properties of rGO and direct bonding of rGO with sulfur can significantly prevent the shuttling of polysulfides.

Nitrogen Doping

Nitrogen (N) doping is an effective method to endow carbon-based materials with high polarity. Generally, the thermal nitridation process in the NH_3 atmosphere can produce N-doped graphene (NG) sheets, as schematic in Fig. 4.10a [26]. The NG contains three kinds of nitrogen atoms: pyridinic N, pyrrolic N and graphitic N. The first two are dominant, and the N lone-pair electrons of them tend to form Li–N interactions with Li^+ ions. This interaction can confine lithium polysulfides and improve their solidification process upon cycling. Combining the high electronic conductivity ($\sim 270 \text{ S cm}^{-1}$), high surface area ($643.5 \text{ cm}^2 \text{ g}^{-1}$) and strong interaction between the N atoms and the soluble polysulfides, the final S@NG nanocomposite cathode can be cycled for over 2000 cycles at 2 C current density.

Graphitic carbon nitride ($g\text{-C}_3\text{N}_4$) is another kind of nitrogen and carbon-containing material constructed by continuous tri-s-triazine basic unit and analogous to graphite, and it possesses strong interaction with lithium polysulfides. Initially, a 2D sheet-like oxygenated carbon nitride (OCN, as shown in Fig. 4.11a) that contains micro- and mesopores, oxygen heteroatoms and many two-dimensional (2D) rippled sheets was incorporated as sulfur host material [27]. A one-step solid-state pyrolysis method was adopted to achieve the low-cost and large-scale production of OCN, and the N content of OCN can reach as high as 20.49%. Benefiting from the immobilization of lithium polysulfides enabled by suitable porous structure and heteroatom doping, the final S/OCN cathode present a high initial discharge capacity and long-term cycling (over 2000 cycles). Next, a hard-template (colloidal silica) method via polycondensation of cyanamide (CN_2H_2) was further developed to synthesize nanoporous $g\text{-C}_3\text{N}_4$ (Fig. 4.11b) [28]. Upon heating cyanamide at 550°C , a stepwise condensation of the melamine units occurs, and then the final $g\text{-C}_3\text{N}_4$ is obtained. The surface area and pore volume of the $g\text{-C}_3\text{N}_4$ are $615 \text{ m}^2 \text{ g}^{-1}$ and $0.97 \text{ cm}^3 \text{ g}^{-1}$, respectively. The DFT calculations were carried out to disclose the interaction between

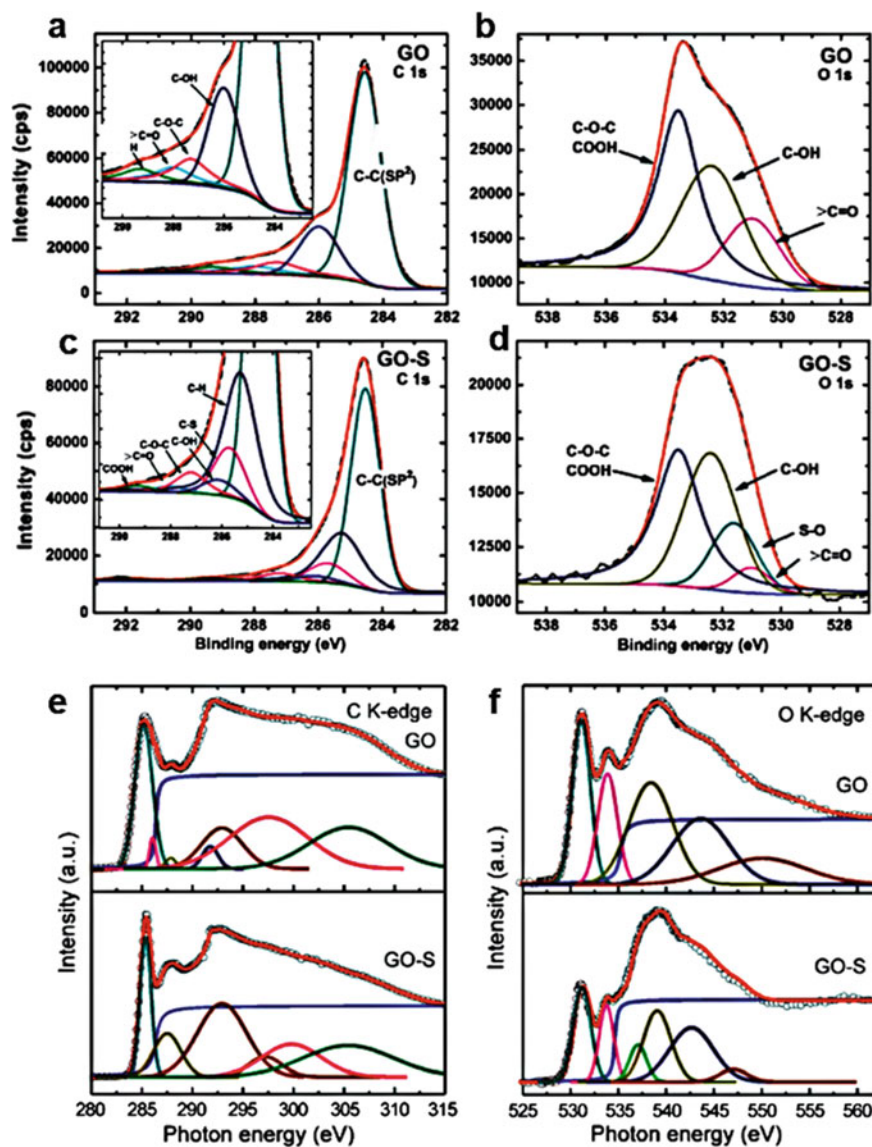


Fig. 4.9 a, c C1s, b, d O1s high-resolution spectra of the XPS of GO and GO-S nanocomposite, respectively. Insets of (a) and (c) are the enlarged C1s spectra after curve fitting. e, f NEXAFS carbon K-edge, oxygen K-edge spectra of GO and GO-S nanocomposite, respectively. Panels adapted with permission from Ref. [25], RSC

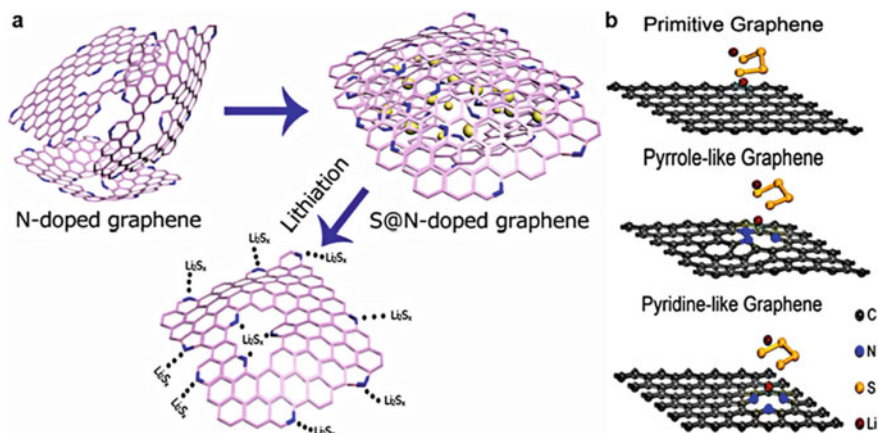


Fig. 4.10 **a** Schematic showing the function of N-doped graphene (NG) for sulfur transformation. **b** Adsorption structure of Li_2S_4 on the primitive graphene, pyrrole-like graphene and pyridine-like graphene through ab initio calculations, respectively. Panels adapted with permission from Ref. [26], ACS

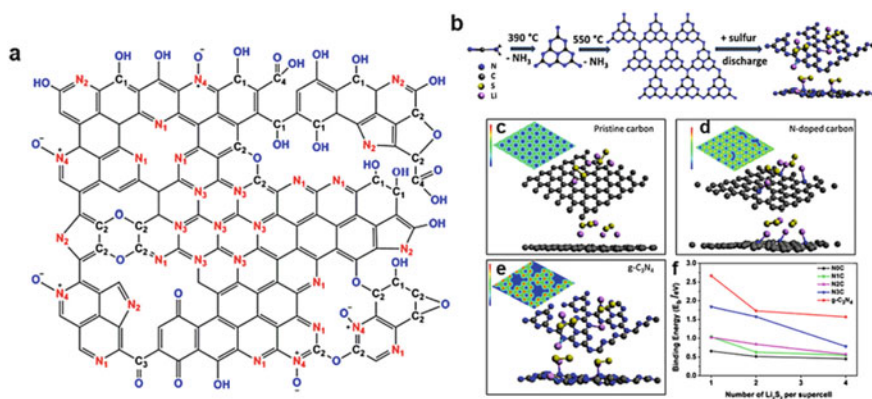


Fig. 4.11 **a** Schematic showing the structure of oxygenated carbon nitride (OCN). The N_1 is pyridinic N; N_2 is pyrrolic/pyridine N; N_3 is quaternary N; N_4 is the nitrogen of pyridine oxide, and C_1 , C_2 , C_3 and C_4 correspond to the C–N/C–O, C–O–C, C=N/C=O and C(O)OH, respectively. **b** Schematic diagram of the fabrication of g-C₃N₄ via cyanamide polycondensation. The calculated interact configurations of 2 Li_2S_2 molecules on **c** pristine carbon, **d** nitrogen (N)-doped carbon (3 N atoms, N3C), **e** g-C₃N₄ substrates; the bottom images are the side views of each configuration and the 2D charge distributions of the corresponding substrates are shown in the top left insets (accepting electrons—red, donating electrons—blue). Specifically, the gray, blue, purple and yellow balls represent carbon (C), nitrogen (N), lithium (Li) and sulfur (S) atoms, respectively. **f**, Binding energy variations of Li_2S_2 molecules (per Li_2S_2) on each substrate, which were calculated by Bader charge analysis. Panels adapted with permission from: **a** Ref. [27], ACS; **b–f** Ref. [28], ACS

g-C₃N₄ and polysulfides (Fig. 4.11c–f). Typically, 2D 2 × 2 g-C₃N₄ and 6 × 6 graphene supercells were constructed to build the corresponding supercell with only 4.0% structure difference. For the N doping graphene, the different nitrogen concentrations were achieved by varying the number of pyridinic N atoms per supercell (0, 1.4, 2.9 and 4.4%; denoted as N0C, N1C, N2C and N3C, respectively). And the Li₂S₂ was used as the representation of all the polysulfides. During the calculations, the binding capacity of the substrate was quantified according to the number of adsorbed molecules.

Upon calculations, a uniform charge distribution could be clearly observed from the pristine carbon (N0C), while a negative charge appears at the electron-rich pyridinic N in N-doped carbon (the red electron density contour curves). All the nitrogen atoms in g-C₃N₄ bear a negative charge. By normalizing the number of adsorbed Li₂S₂ molecules, the binding energy can be quantitatively defined (Fig. 4.11f). As vividly shown, no bonding is formed between Li₂S₂ and the pristine carbon substrate, and which is the reason why the binding energy between them is only 0.51 eV. For both N3C carbon and g-C₃N₄, the shortened Li–N bond distances (the average is 0.214 and 0.206 nm, respectively, compared with the 0.246 nm of pristine carbon) demonstrate that a favorable Li⁺ – N^{δ-} bond was formed between Li₂S₂ and the substrates. By further Bader charge analysis, one can find that there is a charge transfer from the substrate onto the S²⁻ cluster once they get touched. Even if Li₂S₂ possesses a higher concentration, a higher adsorption ability could be still achieved by g-C₃N₄, because it has more pyridinic N sites for polysulfide adsorption than N-doped carbon. Moreover, the binding energies between Li₂S₄, Li₂S and g-C₃N₄ show the same tendency with Li₂S₂, proving the high adsorption capability of g-C₃N₄.

Nitrogen and Oxygen Co-doping

Apart from the nitrogen (N) and oxygen (O) doping independently, the N-doping at the nearby of oxygen functional groups could promote the adsorption of sulfur either [29]. During the material preparation, a poly (melamine-co-formaldehyde) resin was used as a precursor, and tetraethyl orthosilicate, amphiphilic triblock copolymers and colloidal SiO₂ nanoparticles were used as porogens to fabricate the final N-doped mesoporous carbon (MPNC). The BET specific surface area and Barrett–Joyner–Halenda (BJH) pore volume of MPNC are 824.3 m² g⁻¹ and 1.38 cm³ g⁻¹, respectively. The MPNC possesses hierarchical pore structures composed of 2–3 nm, 4–8 nm and 10–20 nm diameter mesopores, respectively. The MPNC could only sustain a maximum amount of 80 wt% sulfur, and once the sulfur content reached this limit, the excess sulfur would not be confined. According to the X-ray absorption near-edge structure spectroscopy (XANES) analysis, the sulfur (S) loading would induce a significant oxygen coordination structure change of MPNC (Fig. 4.12a, b), indicating the existence of O–S bonding between MPNC and sulfur. In addition, upon increasing the sulfur content within the limit (80 wt%), the oxygen XANES spectra deliver a continuous line shift, implying that all the sulfur below the limit is accessible to these groups.

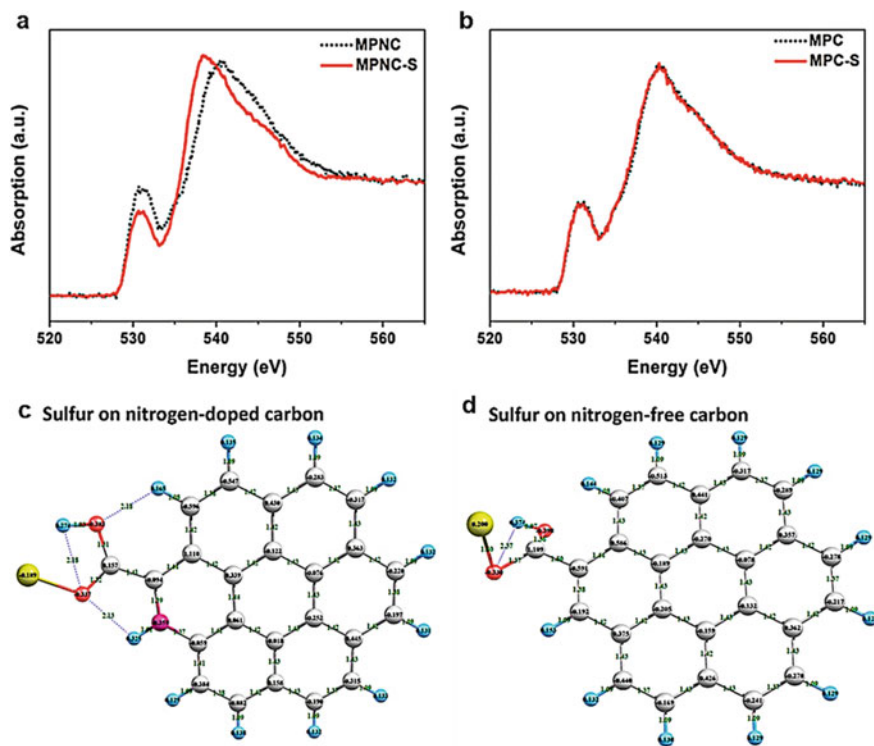


Fig. 4.12 **a** Oxygen (O) K-edge spectra of the XANES test of N-doped mesoporous carbon (MPNC) and MPNC-S nanocomposite. **b** O K-edge spectra of the XANES test of mesoporous carbon (MPC) and MPC-S nanocomposites. **c, d** the interaction between sulfur and pyridinic N-COOH functional group decorated carbon with and bare -COOH group decorated carbon (top views), respectively. All the balls represent yellow—sulfur (S), red—oxygen (O), magenta—nitrogen (N), silver gray—carbon (C) and blue—hydrogen (H) atom, respectively. Panels adapted with permission from Ref. [29], Wiley-VCH

When nitrogen is decorated on bare carbon materials, it can withdraw the electron from other atoms due to its high electronegativity (3.0 of nitrogen compared to 2.5 of carbon). Therefore, the polarization of the neighboring oxygen-containing groups (such as carbonyl and carboxyl groups) occurs and changes to be easily attacked by sulfur atoms. For the carboxyl group on the pyridinic-N-doped carbon, the calculated enthalpy change (ΔH) is $-56.88 \text{ kcal mol}^{-1}$. Moreover, the ΔH of the carbonyl group on the pyrrolic-N-doped carbon delivers the lowest ΔH value of $-117 \text{ kcal mol}^{-1}$. The above analyses manifest the enhanced sulfur transformation could be achieved by the nitrogen and oxygen co-doping carbon (Fig. 4.12c, d).

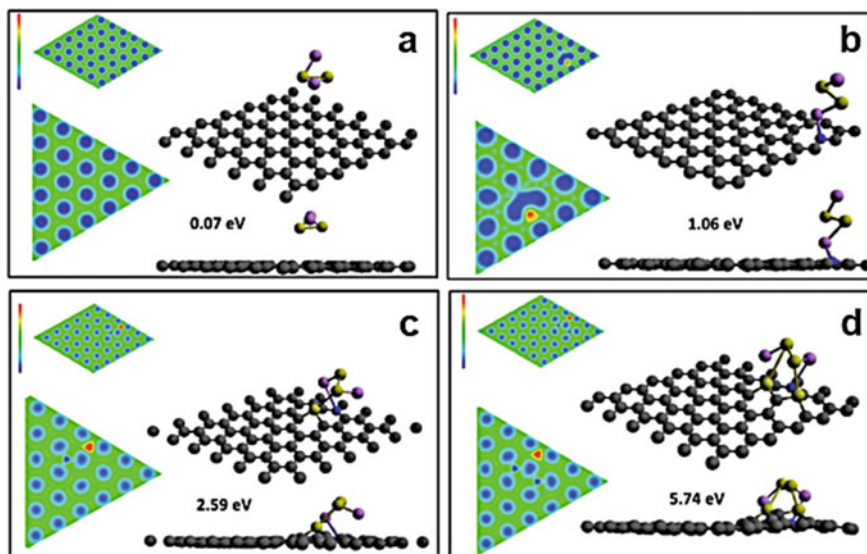


Fig. 4.13 The most stable Li_2S_2 configurations on various carbon substrates through ab initio calculations: **a** non-doped carbon, **b** 1 nitrogen (N), **c** 1 N + 1 sulfur (S) and **d** 1 N + 2 S-doped carbon (per supercell, the bottom right is the side view). The top left insets of each figure are the 2D charge contours of corresponding substrates, and the bottom left is the magnified versions. The gray, blue, purple and yellow balls represent carbon (C), N, lithium (Li) and S atoms, respectively. Panels adapted with permission from Ref. [30], Wiley-VCH

Nitrogen and Sulfur Co-doping

Element sulfur (S) and oxygen (O) come from the same main group, thus the sulfur existence of the nitrogen doping materials may also show great potential to be sulfur substrate [30]. Through DFT calculations, one can find a uniform charge density distribution on the non-doped graphene, whereas the pyrrolic N-doped carbon bears a charge of -0.81 (Fig. 4.13a, b). Moreover, as indicated by the dark electron density contour curves, the thiophene-like sulfur of the nitrogen and sulfur dual-doped carbon exhibits a charge of $+0.45$ (Fig. 4.13c). Consequently, there is a low binding energy of 0.07 eV between Li_2S_2 with the non-doped graphene because there is no specific bonding between them. However, for the co-doped condition, a favorable bonding between Li^+ and pyrrolic N, and S_T^{-1} and doped $\text{S}^{\delta+}$ could be observed; also the calculated binding energy between Li_2S_2 and nitrogen, sulfur dual-doped carbon is 2.59 eV. This number is over twofold that of bare N-doped carbon. Upon further increasing the S/N ratio to 2, the binding energy can be as high as 5.74 eV, indicating the highly favorable aspects of the nitrogen, sulfur dual-doping method (Fig. 4.13d). Furthermore, the high-rate redox kinetics of sulfur cathode could be largely augmented by the higher electronic conductivity of the dual-doped carbon than undoped carbon. Therefore, the final sulfur electrode could deliver a long cycle life of 1100 cycles at 2 C current density.

Porosity of Nitrogen Doping Carbon Materials and Other Configurations

The pore structure of nitrogen (N)-doping carbon materials can have a significant influence toward sulfur (S)/carbon (C) cathode. A comparison of the function for S/C cathode of three hollow carbons with pore sizes of 4.1, 3.2 and 2.8 nm was conducted [31]. The results showed that when the pore size was 2.8 nm, the internal void of the hollow carbon could be occupied by sulfur. The impregnated sulfur was stable at the chamber of STEM, which is under vacuum condition and has high irradiation, demonstrating the sulfur could be confined well within this porous carbon shell without any polymer coating. However, when the pore size is 3.2 or 4.1 nm, whatever the fully filled or partially filled state of sulfur, it would be easily sublimed off. These experiments also disclosed that sulfur could slightly spill out of the hollow carbon during the lithiation process, and gave visible evidence on the volume expansion of sulfur during discharge.

Because of the superior ability for polysulfides adsorption of N-doped carbon, various advanced frameworks based on N-doped carbon have been constructed to accelerate the sulfur reaction kinetics. For example, graphene wrapping nitrogen-doped double-shelled hollow carbon spheres (NDHCSs) were fabricated to load sulfur through a template method [32]. As schematic in Fig. 4.14a, the inner and outer surface of anatase TiO_2 hollow spheres was coated with dopamine at first, followed by carbonization and etching process, forming the NDHCSs. Sulfur was then melt-infused into the NDHCSs. After infiltrating graphene on NDHCSs-S composite, a flexible and hierarchical G-NDHCS-S hybrid paper was obtained (Fig. 4.14b, c). Benefiting from the N-doping-enabled polysulfide trapping, graphene wrapping improved electrical/ionic conductive network and pore accommodating of the volume change of sulfur via the sufficient space of NDHCSs. The final G-NDHCS-S electrode shows highly improved performance. In addition, mesoporous N-doped carbon spheres decorated with carbon nanotubes (MNCS/CNT) can enhance the confinement of lithium polysulfides either [33]. As schematic in Fig. 4.14d, the formation of MNCS/CNT composite relied on the evaporation-induced self-assembly (EISA) process. According to the comparison of polysulfides adsorption ability between MNCS/CNT composite and other reported adsorbents, the adsorption capability of the MNCS and MNCS/CNT materials is higher than other competitors (Fig. 4.14f). Specifically, MNCS can absorb almost fivefold soluble Li_2S_x species as the Al_2O_3 nanoparticles and mesoporous carbon (MPC) do. Although the MNCS possesses a smaller surface area and pore volume than SBA-15 and MPC, it can absorb tenfold more polysulfide. Moreover, after exposure to MNCS, the color of the Li_2S_x solution becomes much lighter than other competitors and indicates its adsorption capability toward Li_2S_x .

Although the N-doping is good for restraining the shuttling of polysulfides, an upper limit existed for the nitrogen content in carbon materials. Typically, the upper nitrogen content of N-doped carbons (NDCs) has correlation with its carbonization temperature (1000 °C for 14.32 wt% and 900 °C for 21.66 wt%), irrespective of the precursor or preparation conditions [34]. The energetically favorable N-doping architecture, in which nitrogen atoms are located on separate hexagon units as graphitic N,

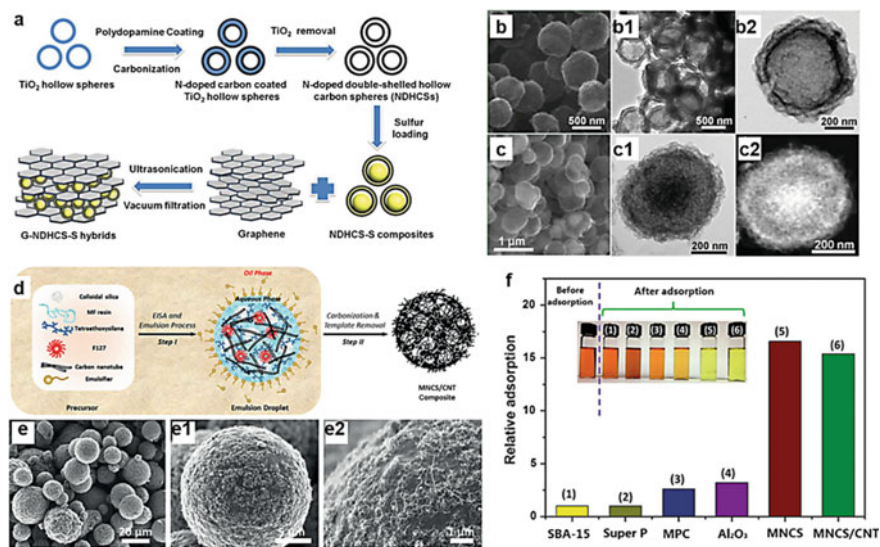


Fig. 4.14 **a** Schematic illustration of the preparation process of nitrogen (N)-doped double-shelled hollow carbon spheres (NDHCSs)-sulfur (S) composites and graphene wrapping NDHCSs (G-NDHCS)-S hybrid paper. **b** SEM and (**b1**, **b2**) TEM images of the NDHCSs. **c** SEM, (**c1**) TEM and (**c2**) STEM images of the sulfur encapsulated NDHCS. **d** Synthesis of the carbon-nanotube (CNT)—interpenetrated mesoporous N-doped carbon spheres (MNCS) composite (MNCS/CNT). SEM characterizations of the obtained composite with low (**e**), medium (**e1**) and high (**e2**) magnification. **f** Quantitative analysis of the adsorption capability for various adsorbents: mesoporous silica (SBA-15), Al_2O_3 , carbon black (Super P), mesoporous carbon (MPC), MNCS and MNCS/CNT. Digital photos of polysulfide solutions before and after adding adsorbents (insets of **f**). Panels adapted with permission from: **a**, **b**, **b1**, **b2**, **c**, **c1**, **c2** Ref. [32], Wiley-VCH; **d**, **e**, **e1**, **e2**, **f** Ref. [33], Wiley-VCH

results in NDCs with nitrogen contents and N/C values very close to those estimated from the experimental results. Despite these relationships, there is no clear evidence for the connection between the nitrogen content of precursors and NDCs. Therefore, designing N-doping carbon materials at the molecular level is still challenging and ongoing.

4.4.1.2 Functional Polymeric Materials

For its favorable electronic conductivity, abundant functional groups, suitable mechanical flexibility and facile synthetic routes, various kinds of polymers have been recognized as promising sulfur scaffolds. Specifically, the heteroatoms such as oxygen, nitrogen and the electronic conductivity of polymers can sequester soluble lithium polysulfides and boost the sulfur transformation, respectively.

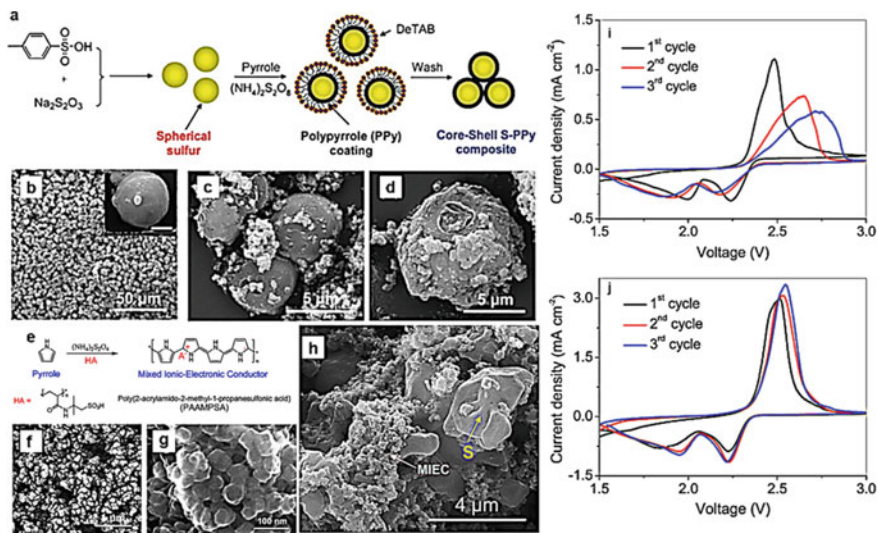


Fig. 4.15 **a** Schematic showing the preparation of sulfur-polypyrrole (S-PPy) composite with core-shell structure with the help of decyltrimethylammonium bromide (DeTAB), a cationic surfactant. **b** SEM image of the obtained sulfur particles, and its magnified SEM image is the inset (scale bar: 5 μm). **c** SEM image of the final S-PPy composites, and **d** single particle. **e** Schematic showing the preparation of PAAMPSA-doped polypyrrole mixed ionic-electronic conductor (MIEC). **f** SEM image of the obtained MIEC. **g**, **h** SEM image with higher magnification for the MIEC and S-MIEC, respectively. **i**, **j** The cyclic voltammograms (CV) at the first three cycles of the pristine sulfur and S-MIEC composites, respectively. Panels adapted with permission from: **a–d** Ref. [35], RSC; **e–j** Ref. [36], ACS

Oxygen and Nitrogen Containing Polymers

In 2009, a pioneering research reported that polyethylene glycol (PEG) coating on mesoporous carbon (CMK-3) can help in confining polysulfides [12]. Next, a core-shell sulfur-polypyrrole (PPy) composite cathodes was synthesized by Manthiram et al. [35] To fabricate sulfur particles, the reduction of sodium thiosulfate with *p*-toluenesulfonic acid (pTSA) was carried out first (Fig. 4.15a). The sulfonic acid on the pTSA can provide protons and form sulfur nucleation micelles, endowing the final sulfur particles with a uniform spherical shape and the diameter of which is 5–10 μm (Fig. 4.15b). In the meantime, the surface of sulfur particles still has small pores, which can facilitate electrolyte access. To get the surficial PPy coating, the as-synthesized sulfur was then dispersed into the aqueous solution of cationic surfactant (decyltrimethylammonium bromide (DeTAB)). With the help of DeTAB, the obtained PPy nanoparticles should nucleate at sulfur particles directly. After removal of the surfactant, the final PPy decorated sulfur was obtained as clearly shown in Fig. 4.15c, d. On top of this, a soft polymer-doped PPy has been fabricated as the mixed ionic-electronic conductor (MIEC) substrate of sulfur. Typically, the MIEC scaffolds could be obtained via the oxidation polymerization of

pyrrole monomer (oxidant is ammonium peroxydisulfate) in the presence of poly(2-acrylamido-2-methyl-1-propanesulfonic acid) (PAAMPSA) (Fig. 4.15e) [36]. As shown in Fig. 4.15f, g, the MIEC substrate is a 3D, well-connected nanoparticle matrix and the particles' surface is smooth. It looks like that a soft polymer layer is wrapped on the particles, which is likely to be PAAMPSA. The soft PAAMPSA can not only strongly bond to MIEC particles but also facilitate the transportation of Li^+ ions. Moreover, the sulfonic acid groups of the dispersed MIEC nanoparticles would cause the inhomogeneous charge (i.e., proton) distributions, forming the uniform crystalline sulfur domains (Fig. 4.15h). As shown in the cyclic voltammograms (CV) scanning, the slight shift for the narrower peaks of S-MIEC composite cathode upon cycling can demonstrate its functionality for sulfur transformation (Fig. 4.15i, j). Moreover, the two cathodic peaks of sulfur would increase upon cycling, indicating the improved kinetics and increased utilization of sulfur. The Coulombic efficiency (the specific value of the area under the two reduction peaks to that under the oxidation peaks) was further calculated to be 78.6% and 70.5% for the S-MIEC composite cathode and pristine sulfur cathode, respectively, demonstrating the enhanced trapping of soluble lithium polysulfides by MIEC nanoparticles.

During the discharge of C/S composite cathode, the final Li_xS ($x = 1, 2$) would detach from the carbon surface, as shown in Fig. 4.16a, b [37]. The final lithium sulfide would shrink and away from the carbon, indicating the leakage of intermediate polysulfides through the openings of hollow carbon nanofibers. Through DFT calculations, one can find that the C–C bond would adsorb sulfur atom ($x = 0$) and deliver a binding energy of 0.79 eV (Fig. 4.16e). Once being lithiated, the sulfur would bind weaker with carbon than the pristine sulfur. For LiS (with binding energy of 0.21 eV) and Li_2S (with binding energy of 0.29 eV) clusters, the distance between these sulfur atoms and graphene (C–C) are 0.338 nm and 0.367 nm, respectively, much larger than that of elemental sulfur and graphene (0.216 nm). To ameliorate this problem, poly(vinylpyrrolidone) (PVP) was incorporated to perfect the hydrophobic interface of carbon. According to the calculations, the lithium (Li) atoms in Li_xS species can bind the oxygen atom of NMP (bond length $\sim 0.185\text{--}0.189$ nm) and deliver binding energies of 1.29 and 1.01 eV for the LiS and Li_2S molecules, respectively (Fig. 4.16h, NMP is the modeling molecule of PVP because they have similar functional groups). As vividly shown in Fig. 4.16c, d, after the PVP modification, the final lithium sulfide would bind strongly with the carbon surface, even though there have some localized detachments.

Further research was also carried out to explore the best functional groups to bind Li_2S and other lithium polysulfides (Li_2S_n , $4 \leq n \leq 8$) (Fig. 4.17a–j) [38]. Ab initio simulations showed that the oxygen (O), nitrogen (N) and halogen atoms with lone pairs on electron-rich groups are capable of forming a coordination-like interaction with the lithium atoms of Li_2S . The carbonyl ($>\text{C}=\text{O}$) groups in esters, ketones and amides delivered the binding energies of 1.10, 0.96 and 0.95 eV with Li_2S , which was the strongest interaction. The lithium atoms in lithium polysulfides would bind to the doubly bonded oxygen atom in $>\text{C}=\text{O}$ group directly and form a strong lithium-oxygen (Li–O) bond, which is the relatively most stable configuration. This kind of strong force originates from the electron deficiency Li^+ and the electron donor oxygen

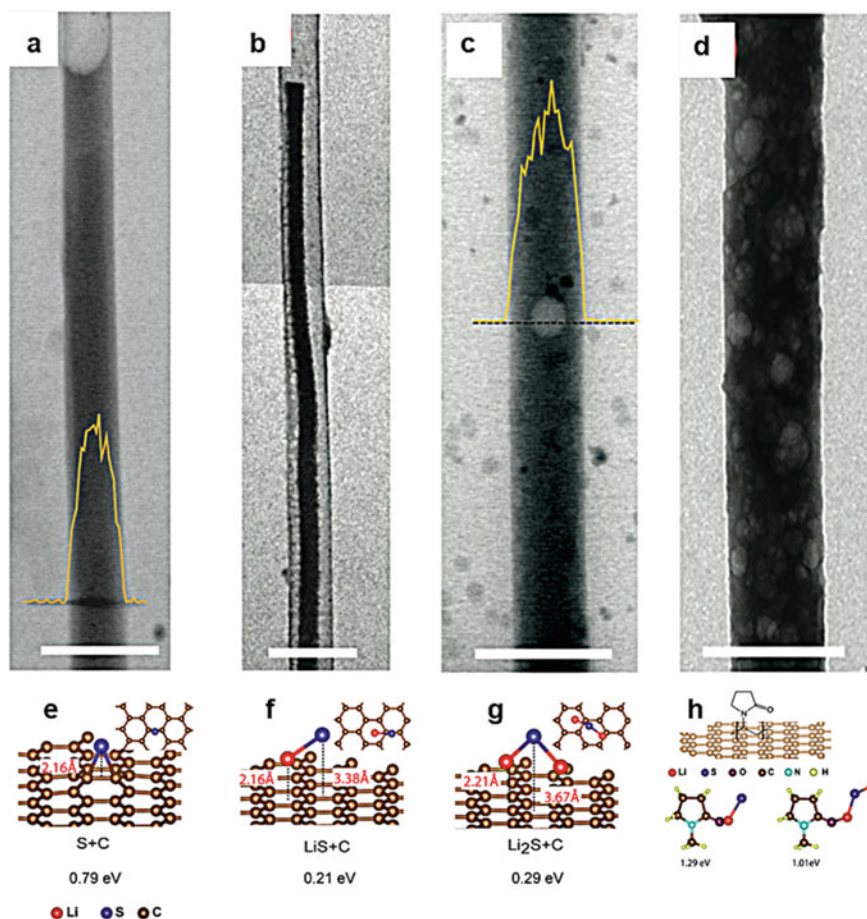


Fig. 4.16 **a, b** TEM images of the pristine S/C cathode and after discharge to 1.7 V. **c, d** TEM images of the pristine polymer functionalized S/C cathode and after discharge to 1.7 V. The yellow line is the EDS counts of the sulfur signal along the dashed line, and the scale bar is 500 nm. Calculated interactions between bare carbon and **e** S, **f** LiS and **g** Li₂S. **h** Schematic interaction between carbon and PVP (top panel), and the under panel are the interactions between the PVP and LiS/Li₂S via ab initio calculations, respectively. Panels adapted with permission from Ref. [37], ACS

atoms in $>C=O$ groups. In addition, the relevant end groups of polysulfides—Li–S-species (e.g., Li–S–S_{n-2}–S–Li; Li₂S_n in short, $4 \leq n \leq 8$) deliver the binding energies between 1.20 and 1.26 eV with $>C=O$ groups, which is the strongest interactions either. The most stable configuration of the bond between Li–S species and $>C=O$ groups is the same as the case of Li₂S. Therefore, a polymer has abundant $>C=O$ groups (poly(vinylpyrrolidone), PVP) that can endow much-improved kinetics for Li₂S cathodes. Another polymer, for example, poly(anthraquinonyl sulfide) (PAQS), had been utilized to confine polysulfide shuttling either (Fig. 4.17k–m) [39]. Both

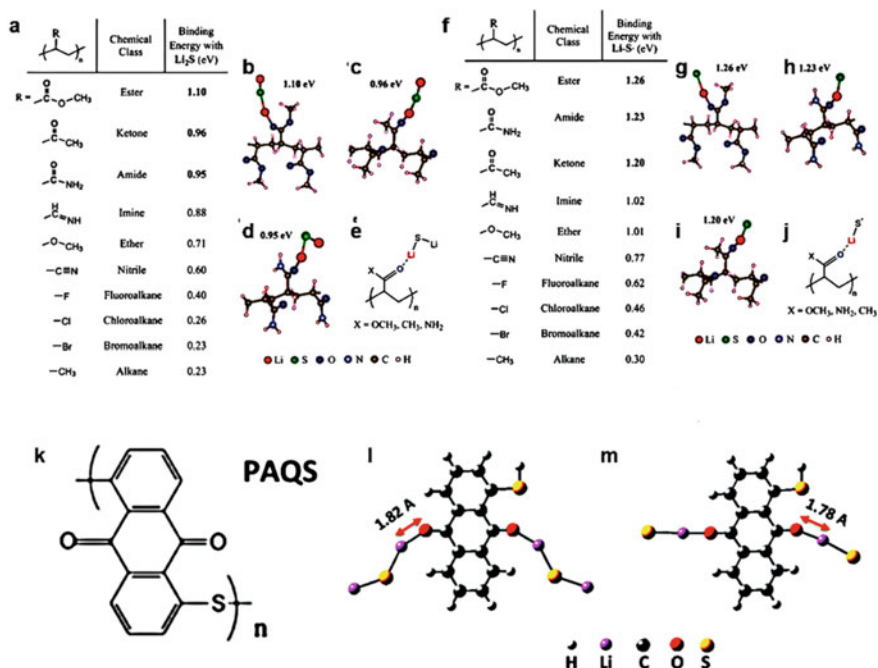


Fig. 4.17 **a** Calculated binding energies of Li₂S with various groups (R) functionalized vinyl polymers $-(\text{CH}_2-\text{CHR})_n-$. **b-d** Calculated configuration and binding energy of Li₂S with **b** ester, **c** ketone and **d** amide groups functionalized vinyl polymers. **e** Schematic showing the Li-O interaction between Li₂S and $>\text{C}=\text{O}$ group. **f** Calculated binding energies of Li-S species with various groups (R) functionalized vinyl polymers $-(\text{CH}_2-\text{CHR})_n-$. **g-i** Calculated configuration and binding energy of Li-S species with **g** ester, **h** ketone and **i** amide groups functionalized vinyl polymers. **j** Schematic showing the Li-O interaction between Li-S species and $>\text{C}=\text{O}$ groups. **k** Molecular formula of poly (anthraquinonyl sulfide) (PAQS). **l, m** The calculated adsorption configuration of Li₂S and Li-S species on PAQS. Panels adapted with permission from: **a-j** Ref. [38], RSC; **k-m** Ref. [39], ACS

PVP and PAQS are rich in $>\text{C}=\text{O}$ groups, but PAQS exhibits a stronger polysulfide trapping effect apparently. The binding energies between PAQS and Li₂S and Li-S-species are 2.1 and 2.5 eV, respectively, which are significantly stronger than that of PVP. Apart from the Li-O interaction, the more rigid molecular conformation of PAQS that resulted from its conjugated backbone units may incur its particularly strong interaction with Li₂S either.

Actually, the Li-O interaction between the lithium in lithium polysulfides and the oxygen in $>\text{C}=\text{O}$ group should be recognized as “Li bonds”. The thiol-ene chemistry was adopted by Goodenough et al. to fabricate cross-linked polymers with various functional groups such as 1,6-divinylperfluorohexane (FC), di(ethylene glycol) divinyl ether (EO), divinyladipate (ester), and 1,6-bis(vinylsulfone)hexane (sulfone) (Fig. 4.18a) [40]. Specifically, these groups were separately polymerized with tetrathiol cross-linker (pentaerythritol tetrakis (3-mercaptopropionate), PETT),

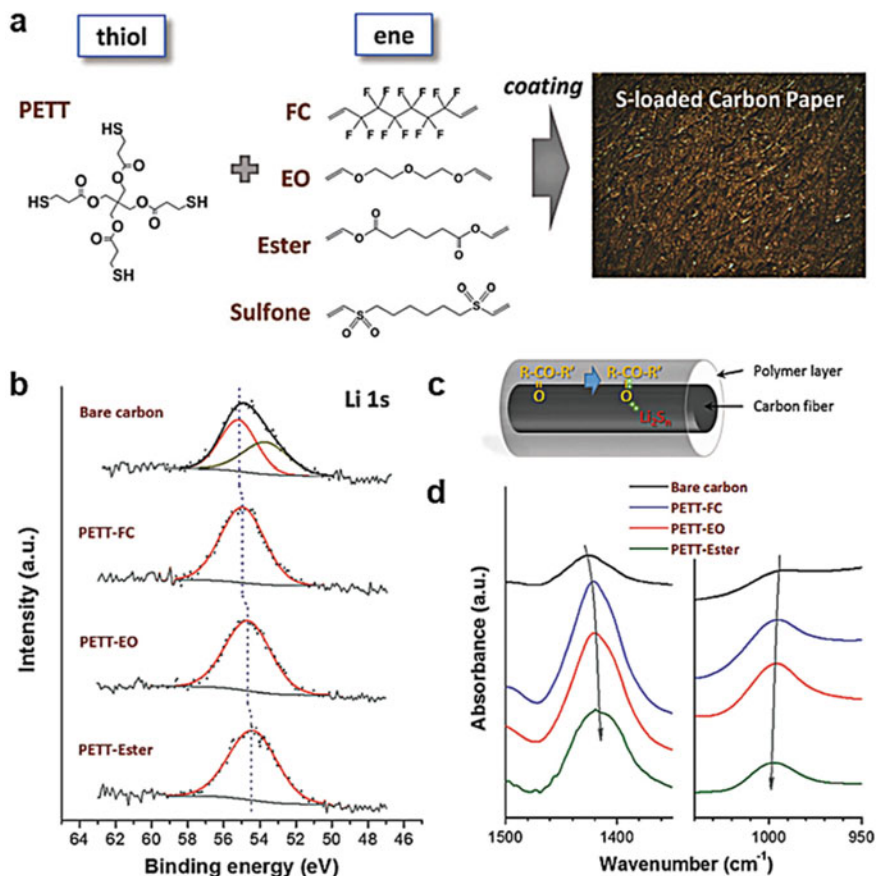


Fig. 4.18 **a** Schematic showing the thiol-ene reactions between a tetrathiol crosslinker and difunctional ene monomers, and the polymer decoration process on sulfur-loaded carbon paper electrodes. **b** Lithium (Li) 1s spectra of XPS test and **d** ATR-FTIR spectra of bare S/C composite, PETT-FC, PETT-EO and PETT-ester-coated composites after discharging to 1.5 V, respectively. **c** Schematic diagram of the "lithium bond" between lithium polysulfides and ester group. Panels adapted with permission from Ref. [40], RSC

and the final membranes were marked as PETT-FC, PETT-EO, PETT-ester, and PETT-sulfone, respectively (Fig. 4.18a). To sequester the shuttling of soluble lithium polysulfides, the S/C composite was coated with these neat membranes for electrochemical tests. As shown in Fig. 4.18b, d, the pristine S/C electrode has an additional peak located at 53.69 eV and indicates the decomposition of electrolyte (Li_2O is the decomposed byproduct). When the S/C electrode was coated with polymer membrane, the electrolyte stability could be improved because only one peak associated with Li_2S could be found. It is worth noting that the PETT-sulfone sample was not tested because the initial cycling would not produce Li_2S . As shown in the

Li 1 s XPS peaks of the bare, PETT-FC, PETT-EO and PETT-ester electrodes, the introduction of functional groups would shift these peaks to lower values gradually (55.19, 54.95, 54.65 and 54.40 eV, respectively) (Fig. 4.18b), demonstrating that the lithium of Li_2S would be partially reduced by these polymer coatings. As to the FTIR spectra, compared with the pristine sulfur electrodes, there is clear evidence for the red shifts of the COO stretch vibration and blue shifts of the CO vibration in the PETT-FC, PETT-EO and PETT-ester electrodes, respectively (Fig. 4.18d). All these results clearly manifest the fact that the carbonyl double bond would release charge to the lithium of lithium polysulfides, forming a lithium bond with asymmetric structures (Fig. 4.18c). The pure sulfur should interact with these groups through Van der Waals interaction. However, upon lithiation, the asymmetric bonding becomes the dominant one. In this regard, forming lithium bonds between some special functional groups in polymer backbone and polysulfides can alleviate the shuttling effect, and dramatically increase the electrochemical performance of sulfur cathode.

The peak shifting degree in XPS and FTIR signals can reflect the real density of the ester group in sulfur cathode, and if the ester groups have higher density, the shifts would be greater. For example, although PETT-FC and PETT-EO have the same amount of ester groups in their backbones, the PETT-FC can uptake more electrolytes and therefore deliver a lower density of ester. Therefore, the PETT-ester possesses the highest ester density, and its swelling degree is even lower than that of PETT-EO. Consequently, the neat membrane constructed by PETT-ester is more effective to bind lithium polysulfides, resulting in a high initial discharge capacity and a more stable cycle life. It should be noted that everything is a double-edged sword, because the abundant presence of electron-donating groups may impede Li^+ transportation in the meantime. Therefore, it is important to select a suitable electron-donating group that is capable of trapping lithium polysulfides yet does not hamper Li^+ diffusion simultaneously. Moreover, the amount of the polymerized functional groups should be adjusted to get the optimal value.

The lithium–nitrogen interaction can also be utilized to confine polysulfides shuttling. By encapsulating Li_2S with conducting polymer-polypyrrole (PPy) via in situ polymerization of pyrrole, a Li_2S -PPy composite sulfur cathode can be obtained [41]. On the one hand, the conductive PPy can facilitate the electronic conductivity of electrode. On the other hand, the N atoms in PPy polymer could form strong Li–N interaction with Li_2S , endowing PPy the ability to restrain the shuttling of soluble polysulfides. Specifically, the lone pair electrons on the N atoms in PPy are capable of forming a coordination-like interaction with the lithium of Li_2S (Fig. 4.19a, b). The calculated binding energy between Li_2S and PPy was 0.5 eV. Moreover, an analogical Li–N bond between PPy and Li–S-species, the corresponding end groups of long-chain lithium polysulfides, would empower PPy to restrain the shuttling of polysulfides during cycling. As evidence, the additional Li–N peak of Li 1 s high-resolution XPS spectroscopy and the red shift in the Raman peak position of the Li_2S -PPy composites prove the existence of Li–N bond (Fig. 4.19c, d).

Further, a more complicated molecule—alkoxy silane-functionalized amine and imidazolium chloride—was reported to possess higher binding energies for Li_2S_x than a nitrogen-rich polymer PAN [42]. For its preparation, a mixture of carbon, sulfur

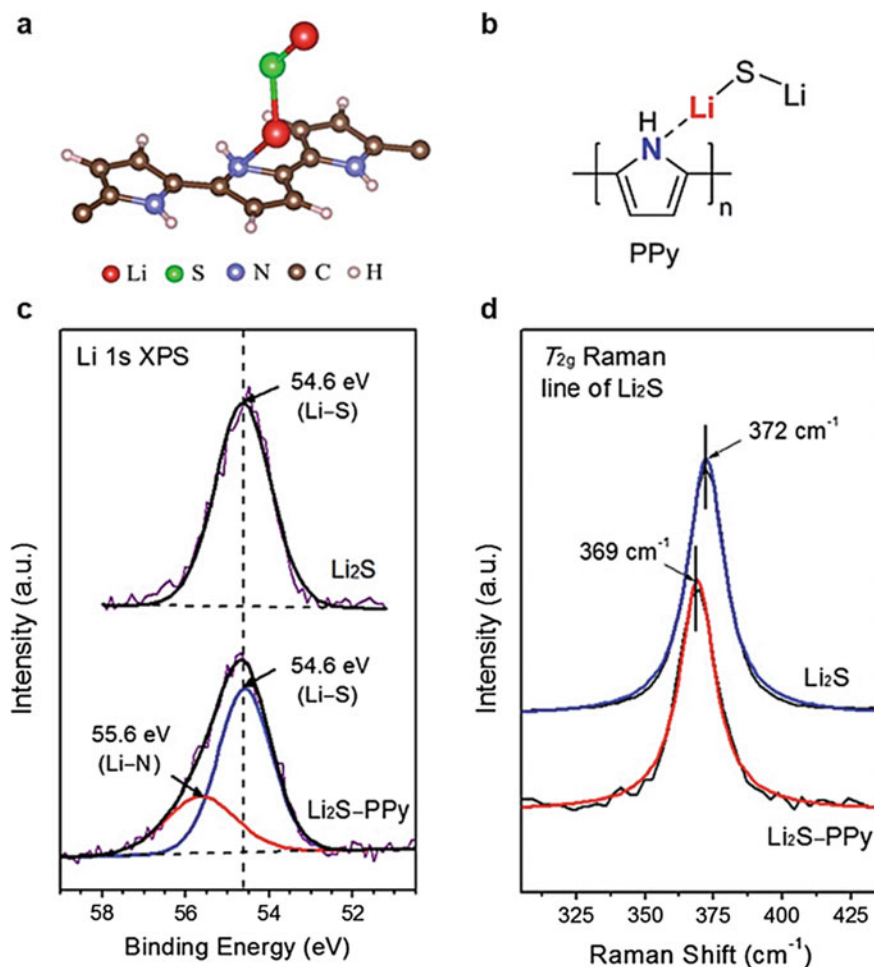


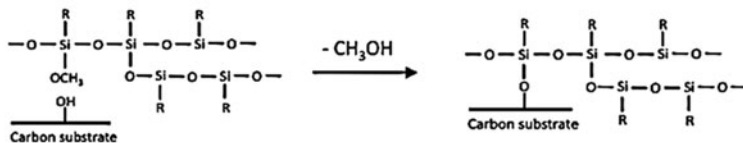
Fig. 4.19 a Structure and b molecular formula of the most stable Li-N interaction between Li_2S with PPy polymer through ab initio calculations, respectively. c High-resolution Li 1s spectra of XPS and d Fitted Raman spectra of the T_{2g} Raman peak of the pristine Li_2S and Li_2S -PPy composites, respectively. Panels adapted with permission from Ref. [41], RSC

and a nitrile-containing molecular sorbent was mixed in N-methyl-2-pyrrolidone (NMP) solvent followed by high-speed mixing firstly (Fig. 4.20a). During the heat treatment process of the slurry-coated electrode, trace amounts of moisture and the extra thermal energy would trigger the cross-link of alkoxysilane groups and the carboxylic acid, phenols, and other species present on the surface of the carbon to anchor sparsely to the surface of conductive additives (step 2). Upon battery discharge, a lithium-nitrile interaction between lithium polysulfides and tethered nitrile groups would be initiated (step 3), restraining the polysulfide loss to electrolyte (Fig. 4.20a).

a

1. Physical mixing of carbon, sulfur, silane-functionalized molecular sorbent, and polymer binder in NMP

2. After heating, the silane-functionalized sorbent molecules cross-link and bond to complementary functional groups on carbon



R : $\text{CH}_2\text{CH}_2\text{-NH-CH}_2\text{CH}_2\text{-NH-CH}_2\text{CH}_2\text{NH}_2$; $\text{C}_3\text{H}_4\text{ClN}_2$; or other nitrile-containing molecule

3. After discharge, Li_2S_x bond to nitrile groups tethered to carbon in the electrode

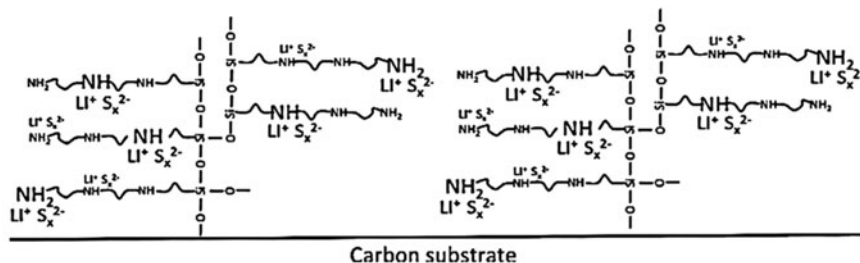
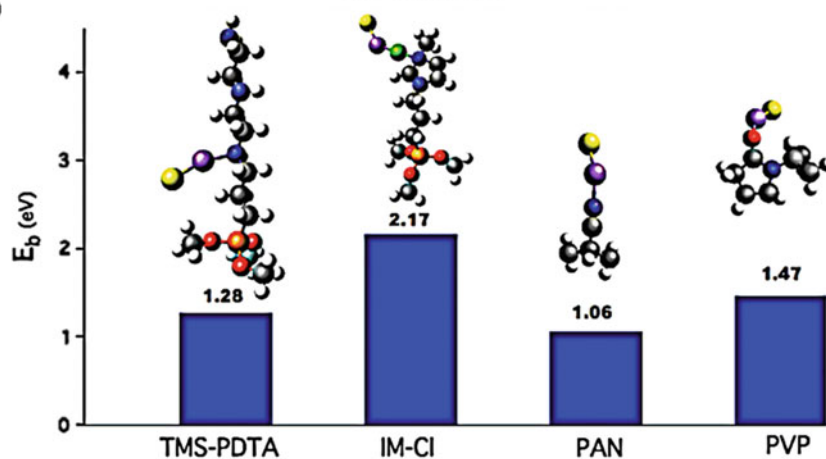
**b**

Fig. 4.20 **a** Methods to introduce Li-N interactions to sequester lithium polysulfides in S/C cathode. **b** Simulated structures and binding energies between the soluble lithium polysulfides and four nitrile-containing molecules such as (3-trimethoxysilylpropyl) diethylenetriamine (TMS-PDTA); 1-methyl-3-trimethoxysilane imidazolium chloride (IM-Cl); polyacrylonitrile (PAN); polyvinylpyrrolidone (PVP). The polysulfide species S_x^{2-} was represented by the yellow balls, while the purple is lithium, the blue is nitrogen, the gray is carbon, the orange is silicon, the red is oxygen, the white is hydrogen and the green is chlorine. Panels adapted with permission from Ref. [42], Wiley-VCH

The DFT calculated relaxed structures can explain the interaction between the nitrile groups and Li_2S_x molecules, as shown in Fig. 4.20b. For polymer like PAN which has isolated nitrile groups as an open-chain segment, the lithium atoms of Li_2S_x would bond with its nitrogen atoms directly. In addition, if one single molecule contains multiple nitrile groups, as in the case of TMS-PDPA, Li_2S_x would bond with it via lithium–nitrile interactions through its preference binding location. However, when the nitrile group is incorporated in a ring structure (e.g., IM-Cl and PVP), the Li_2S_x species would be confined by strong lithium–oxygen (e.g., PVP) and even stronger lithium–chlorine interactions (e.g., IM-Cl), but non-existent of lithium–nitrile interactions.

Conductive Polymers

As we have mentioned in the former section, the electronic conductivity of PPy can boost the electrochemical performance of Sulfur cathode. Therefore, other well-known conductive polymers such as polyaniline (PANI), and poly(3, 4-ethylenedioxythiophene) (PEDOT) may have this effect either (Fig. 4.19a) [43]. Typically, these conductive polymer-coated hollow sulfur cathodes were fabricated via in situ polymerization of the corresponding monomer on sulfur nanoparticles. As we have discussed before, the heteroatoms (such as oxygen, nitrogen and sulfur) with lone electron pairs are able to interact with the lithium atom in Li_xS ($0 < x \leq 2$) via strong Li–O, Li–N and Li–S interactions. As shown in Fig. 4.21b, c, both the oxygen and sulfur atom of PEDOT could form a chelated coordination structure with the lithium atom in Li_2S , giving a strong binding energy of 1.22 eV. In comparison, both the heteroatoms of PANI and PPy would bind with the lithium atoms of Li_2S via π - σ coordination, which delivers weak interaction (0.67 eV and 0.64 eV for PANI and PPy, respectively). As to the end Li–S species of soluble lithium polysulfides, PEDOT can still deliver an almost twofold binding energy (1.08 eV) than that of PANI (0.59 eV) and PPy (0.50 eV). The stronger binding affinity between PEDOT polymers and soluble lithium polysulfides can reduce the polysulfides shuttling more efficiently and result in a more stable cycling performance (Fig. 4.21d).

4.4.1.3 Metal Compounds

For its well-known polarization, various metal compounds have been reported to constrain polysulfides via polar–polar interactions through forming metal–sulfur or heteroatoms–lithium bonds. Oxides such as Ti_4O_7 , TiO_2 , Co_3O_4 , Fe_3O_4 , Al_2O_3 and sulfides such as Co_9S_8 , MoS_2 and TiS_2 have been incorporated to anchor polysulfides. Many phenomena, such as polar–polar interactions-induced charge transfer and configuration distortion, have been proved by both theoretical and experimental results. Besides, some metal nitrides and carbides may confine polysulfides either, and both of them deliver desirable electronic conductivity and structural stability. They may show the capability to confine soluble polysulfides, but their dominating

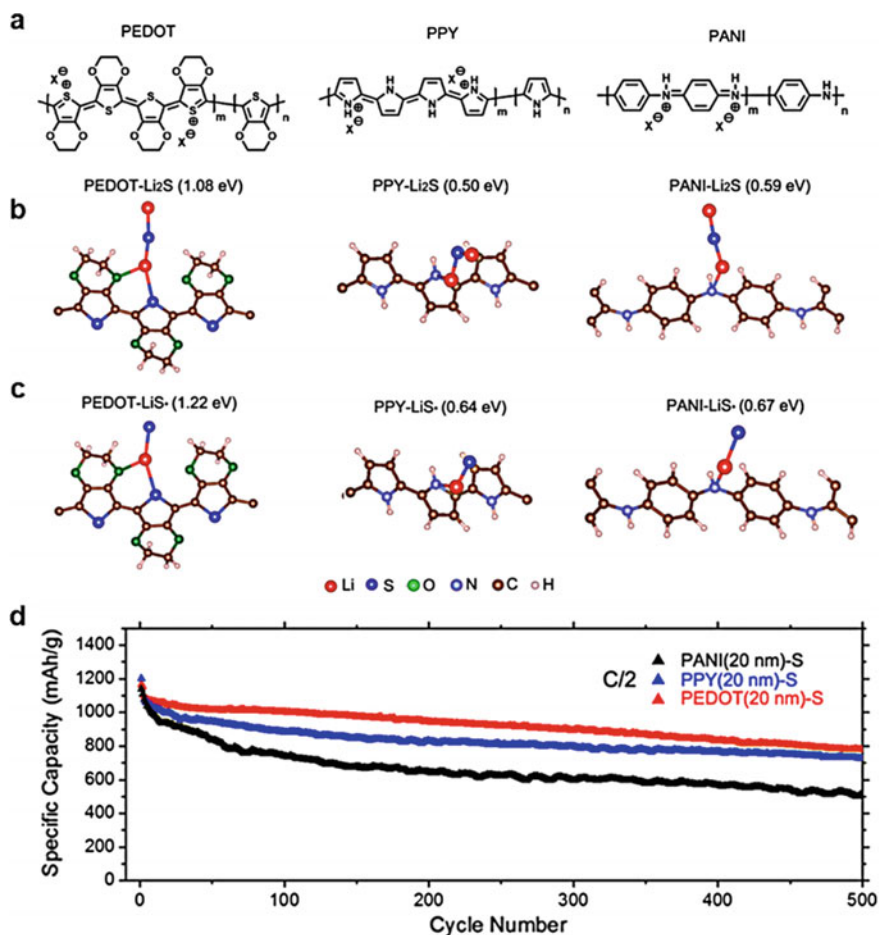


Fig. 4.21 **a** Structures of PEDOT, PPY, and PANI, the doped and undoped parts in these polymers are m and n separately, and the incorporated counterion during polymerization is X . **b, c** Calculated configurations and binding energies of **b** Li_2S and **c** Li-S species with PEDOT, PPY and PANI, respectively. **d** Cycle performances of hollow sulfur nanospheres cathodes decorated with ~ 20 nm PANI, PPY and PEDOT polymers, respectively. Panels adapted with permission from Ref. [43], ACS

effect should be the catalytic transformation of sulfur species, and we won't discuss these compounds in this chapter.

Oxides

In 2004, the nano $\text{Mg}_{0.6}\text{Ni}_{0.4}\text{O}$ particles were utilized as electrochemically inactive additive to improve the performance of sulfur cathode [44]. According to the

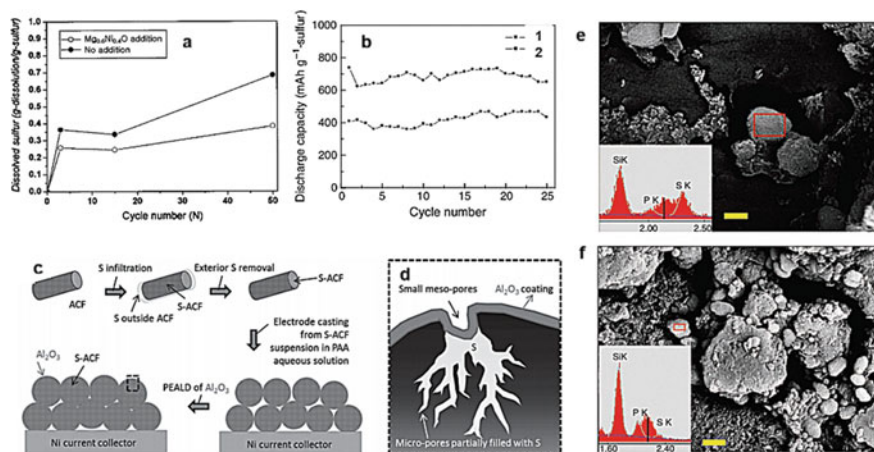


Fig. 4.22 **a** Sulfur content dissolved in liquid electrolyte upon cycling of Mg_{0.6}Ni_{0.4}O/S cathode. **b** Cycle performance of Li–S batteries: (1) without and (2) with nano Al₂O₃ (upper dot-line). **c** Schematic showing the preparation process of PEALD-coated S-ACFs electrode. **d** Schematic illustration of the gas exposure induced conformal alumina coating around S-ACF particles. **e** SEM image of sulfur electrode with SBA-15 particles after discharging to 2.15 V at the 40th cycle, scale bar is 200 nm. **f** SEM image of sulfur electrode with SBA-15 particles after discharging to 1.5 V at the 40th cycle, scale bar is 500 nm. Panels adapted with permission from: **a** Ref. [44], IOP; **b** Ref. [45], IOP; **c, d** Ref. [46], Wiley-VCH; **e, f** Ref. [47], NPG

sulfur quantitative analysis, the addition of Mg_{0.6}Ni_{0.4}O particles can reduce the content of dissolved lithium polysulfide, demonstrating its polysulfide adsorbing effect (Fig. 4.15a). In addition, the addition of nano Al₂O₃ particles can also give advantageous effects for restraining the shuttling effect, and improve the electrochemical performance of sulfur cathode (Fig. 4.22b) [45]. Most of the researches adopted a facile sol–gel route for the surface oxide coating of sulfur particles. However, this method would incur uneven coating and need pretty high oxide content to fully block the shuttling of polysulfides. In addition, the sol–gel process always has water remaining, which can cause significant cell degradation, especially for the high-temperature Li–S batteries. Furthermore, due to the high electrical resistance of metal oxides, additional electronic conductive additives are always needed to facilitate sulfur transformation, which sacrifices the merits of gravimetric and volumetric capacity of sulfur cathode.

Hence, a plasma-enhanced atomic layer deposition (PEALD) was developed to produce a thin but uniform Al₂O₃ coatings on the inner surface of sulfur particles (Fig. 4.22c) [46]. During the material preparation, it uses oxygen but not H₂O vapors as the oxidant, and this is in distinct contrast to the traditional atomic layer deposition (ALD) process. Therefore, the PEALD process on one electrode can avoid undesirable water-soluble binder swelling. In addition, the rapid PEALD of aluminum oxide was carried out after the electrode is fully dried, which is helpful in

retaining good electronic conductivity within the electrode and avoiding sulfur evaporation (Fig. 4.22d). Moreover, the PEALD process does not produce extra oxides in between the neighboring sulfur particles and does not increase the resistance of the electrode significantly. In all, the PEALD has the following merits: low operation temperature ($\sim 20^\circ\text{C}$), homogeneous coatings and faster deposition rates. It is a promising method to develop other metal compounds to confine lithium polysulfides.

Triblock copolymer-templated silica (SiO_2 , SBA-15) has long been utilized as substrate in repeatable drug delivery system, for its large pore volume, high surface area, interconnected pore structure and hydrophilic surface. Inspired by this, a carbon-sulfur nanocomposite with SBA-15 as additive was fabricated [47]. Typically, the addition of SBA-15 would help to confine the soluble lithium polysulfides within sulfur cathode. At the 40th cycle, the cell was discharged to 2.15 V and then the electrode material was extracted under the protection of inert atmosphere to determine the polysulfides adsorption capability of SBA-15. When it was discharged to 2.15 V, elemental sulfur would be completely converted to soluble polysulfide species (Li_2S_6). According to the SEM and EDX results in Fig. 4.22e, a collected sulfur/phosphorus (S/P) atomic ratio of 3.4 could be observed from the EDX signals from an SBA-15 particle (red square). In addition, the other two cells were discharged to 1.5 V at the 40th discharge process, and then the electrode material was further characterized to determine whether the adsorbed polysulfides at 2.15 V can be desorbed upon further discharging, as shown in Fig. 4.22f. According to the test results, the SBA-15 has a much lower average S/P ratio of 0.2. By comparing these results, one can estimate that almost $\sim 94\%$ of the sulfur species adsorbed on the SBA-15 particles would be reduced even after 40 cycles. Therefore, the addition of SBA-15 will significantly reduce the polysulfide anion concentration in the electrolyte, hinder the shuttling of soluble lithium polysulfides and, in turn, prevent active mass loss on both cathode and anode. These results are effective in manifesting the positive function of SiO_2 particles toward sulfur transformation, including the adsorption of soluble lithium polysulfides and following reduction of them.

Electropositive titania (TiO_2) can also be utilized to confine soluble lithium polysulfides [48]. From the FTIR and Raman spectroscopy of TiO_2 , Li_2S_4 and their composites, the interaction between TiO_2 and sulfur can be disclosed. As shown in Fig. 4.23a, Ti-O band (571 cm^{-1}) and S-S band (492 cm^{-1}) existed at the pure phase $\alpha\text{-TiO}_2$ and Li_2S_4 , respectively. However, if the Li_2S_4 was fabricated in the presence of $\alpha\text{-TiO}_2$, a new band would be formed at 534 cm^{-1} . This may originate from the sulfur and $\alpha\text{-TiO}_2$ interaction (forming S-Ti-O bond), namely the bond between $\alpha\text{-TiO}_2$ and Li_2S_4 . The Raman spectra of $\alpha\text{-TiO}_2$ and $\alpha\text{-TiO}_2/\text{Li}_2\text{S}_4$ can also support this. As shown in Fig. 4.23b, the two peaks of neat $\alpha\text{-TiO}_2$ at ~ 395 and $\sim 525\text{ cm}^{-1}$ would shift to ~ 410 and $\sim 515\text{ cm}^{-1}$ for the $\alpha\text{-TiO}_2/\text{Li}_2\text{S}_4$ sample. Both results show the fact that the surrounding chemical environment of the titanium atoms of $\alpha\text{-TiO}_2$ particles is altered by the addition of Li_2S_4 . To mitigate the volume change and shuttling effect of sulfur cathode simultaneously, a sulfur- TiO_2 yolk-shell composite was developed for sulfur cathode [49] (Fig. 4.23c). As shown in Fig. 4.23d, e, the internal void space could accommodate the large volumetric expansion ($\sim 80\%$) during the lithiation process, avoiding the broken of TiO_2 shell and minimizing polysulfide

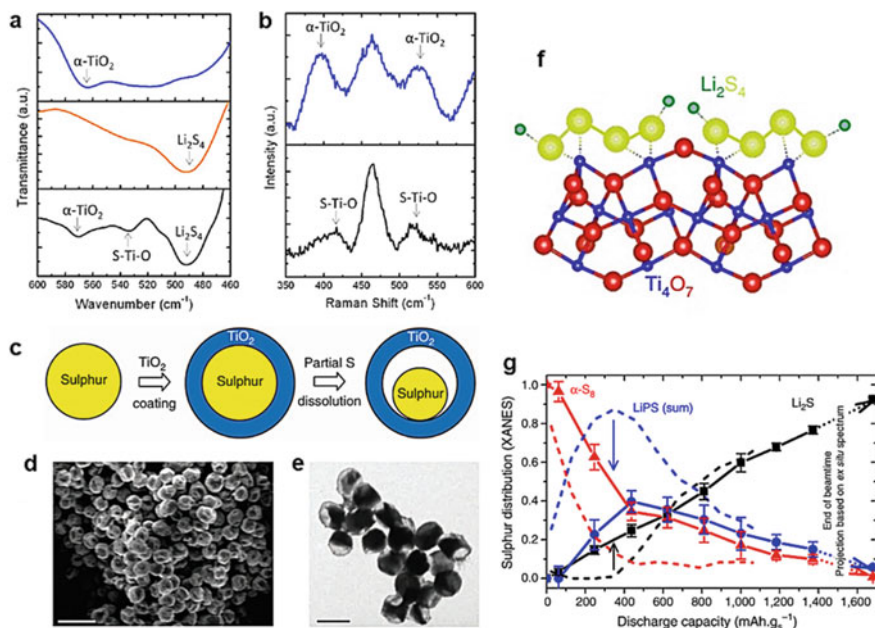


Fig. 4.23 **a** FTIR spectra of pure α -TiO₂ (top, blue), pure Li₂S₄ (middle, orange), and mixed α -TiO₂/Li₂S₄ (bottom, black) sample. **b** Raman spectra of pure α -TiO₂ (top, blue) and mixed α -TiO₂/Li₂S₄ (bottom, black). **c** Schematic showing the formation of sulfur-TiO₂ yolk-shell nanostructures. **d** SEM and **e** TEM of the as-synthesized yolk-shell nanostructures, the scale bars of **(d)** and **(e)** are 2 μ m and 1 μ m, respectively. **f** Schematic showing the electron transfer between Li₂S₄ and Ti₄O₇ (yellow: sulfur, green: lithium, blue: titanium, red: oxygen). **g** Operando XANES detected distribution of sulfur species during discharge. The black, blue and red represent the Li₂S, the sum of Li₂S₆ and Li₂S₄ and bare sulfur, respectively. Panels adapted with permission from: **a**, **b** Ref. [48], ACS; **c**, **d**, **e** Ref. [49], NPG; **f**, **g** Ref. [10], NPG

dissolution. Further, the high adsorption capability of TiO₂ toward soluble lithium polysulfides can also increase the utilization of active sulfur. Both of them are effective to boost the electrochemical reaction of sulfur cathode, and let the final cathode can be cycled over 1000 cycles at 0.5 C.

Ti₄O₇ is a substoichiometric Ti_nO_{2n-1} Magnéli phase and has always been used as catalyst support for its superior electronic conductivity (about threefold greater than graphite). By melt-infusion sulfur on the Ti₄O₇ host, the S-Ti₄O₇ cathode could achieve an excellent cycling performance [10]. According to the DFT calculations, a movement of electrons exists between the sulfur atoms in lithium polysulfides and the electropositive titanium and/or oxygen vacancies at the interface (Fig. 4.23f). And the terminal sulfur atom which has a higher electron density is more affected by this effect. According to the sulfur species distribution obtained from XANES K-edge spectra of Ti₄O₇/S electrode (Fig. 4.23g), the fraction of soluble lithium polysulfides (sum of Li₂S₆ and Li₂S₄) intermediates is significantly decreased at all discharge states (with the max of 40% for Ti₄O₇ and 87% for carbon, respectively),

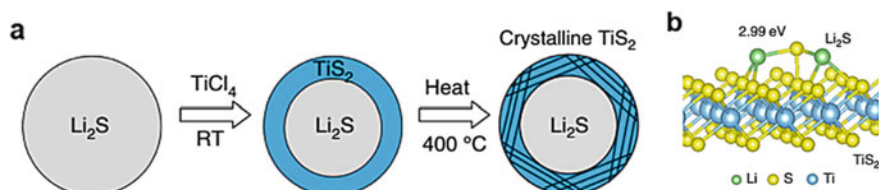


Fig. 4.24 **a** Schematic showing the preparation of nanosized $\text{Li}_2\text{S}@ \text{TiS}_2$ core–shell structures. **b** Calculated configuration of Li_2S on a single layer of TiS_2 , which delivers a binding energy of 2.99 eV. Panels adapted with permission from Ref. [50], NPG

and the final Li_2S would precipitate much earlier and more quickly at the existence of Ti_4O_7 . Therefore, the lithium polysulfides that chemically bonded with Ti_4O_7 are more readily to be reduced to Li_2S than that on the surface of carbon, demonstrating that the Ti_4O_7 host can empower a more efficient electron transfer to the electro-active sulfur species.

Sulfides

Since the interior strong polarization of metal sulfides, it would show significant chemical interaction with soluble lithium polysulfides. In addition, most of the lithiation of metal sulfides would occur at voltages lower than 1.5 V (vs. Li^+/Li), which is lower than a typical operating window of sulfur cathode (1.7–2.8 V). Therefore, metal sulfides can ensure their integrity when used as a sulfur substrate, avoiding harmful side reactions.

For the polar structure and high electronic conductivity, titanium disulfide (TiS_2), a two-dimensional (2D) layered transition metal disulfide, was utilized as the outer shell for Li_2S particles [50] (Fig. 4.24a). The electronic conductivity of the final $\text{Li}_2\text{S}@ \text{TiS}_2$ core–shell nanostructures is $5.1 \times 10^{-3} \text{ S cm}^{-1}$, which is 10 orders of magnitude higher than that of pure Li_2S ($10^{-13} \text{ S cm}^{-1}$). DFT calculations disclose the strong bonding between the lithium atoms of Li_2S and the sulfur atoms in TiS_2 , with 10 times higher binding energy (2.99 eV) than that between Li_2S and bare carbon substrate (single-layer graphene, Fig. 4.24b). Different from the graphene substrate which is covalently bonded and delivers a non-polar structure, the polar–polar interaction between TiS_2 and Li_2S is very strong. Due to the similar chemical environment of the lithium atoms of Li_2S_n species and Li_2S , the TiS_2 can bind Li_2S_n species through polar–polar interaction either. Benefiting from the excellent electronic conductivity and chemical bonding, the outer TiS_2 shell can effectively alleviate the problems of both sulfur and Li_2S cathodes during cycling.

The cobalt sulfides are also ideal sulfur substrate for their excellent thermal stability and electronic conductivity. For example, Co_9S_8 is a high-temperature peritectic phase of the Co–S compounds series and delivers an ultrahigh room temperature electronic conductivity of $0.29 \times 10^3 \text{ S cm}^{-1}$. This is good for the transformation kinetics of sulfur cathode. A rapid and scalable microwave solvothermal

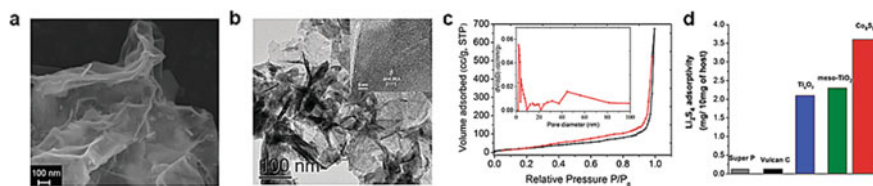


Fig. 4.25 **a, b** SEM and TEM image (the inset is the HRTEM), and **c** N_2 adsorption/desorption isotherm (the inset is the BJH method modeled pore size distribution) of the graphene-like Co_9S_8 . **d** The Li_2S_4 adsorption capability of Co_9S_8 measured by electrochemical titration, which was compared with meso- TiO_2 , nanosized Ti_4O_7 , Vulcan carbon and Super P. Panels adapted with permission from Ref. [51], RSC

method could be adopted to fabricate graphene-like Co_9S_8 , and its interconnected nanosheets would build a 3D network structure (Fig. 4.25a, b) [51]. The solvent dipole-microwave interaction would produce superheated regions rapidly and fabricate 3D porous Co_9S_8 within a very short time. Consequently, the final Co_9S_8 has a large pore volume ($1.07 \text{ cm}^3 \text{ g}^{-1}$, Fig. 4.25c). Through DFT calculations, one can find that there is a slight distortion of Li_2S_2 which adsorbed on Co_9S_8 , indicating the strong interaction between them. Moreover, the Li_2S_2 shows vibrational binding energy with a different crystallographic surface of Co_9S_8 . For example, 2.22 eV for (002) surface, 3.24 eV for (202) surface and 6.06 eV for (008) surface, respectively. The strongest binding energy of 6.06 eV results from the uncoordinated surface cobalt atoms in the (008) plane of Co_9S_8 . Therefore, a coupled interaction such as $\text{S}_n^{2-}-\text{Co}^{\delta+}$ (dominating) and $\text{Li}^+-\text{S}^{\delta-}$ (of Co_9S_8) exists between Co_9S_8 and Li_2S_n species. Through the quantitative analysis of the lithium polysulfides adsorption and the ability of various materials such as Co_9S_8 , Vulcan carbon, Super P, TiO_2 and Ti_4O_7 , one can find that the adsorbed content on Co_9S_8 (i.e., surface area normalized) is over five times that of titanium oxides, indicating the superiority of Co_9S_8 in confining soluble lithium polysulfides (Fig. 4.25d).

Another metal sulfide, CoS_2 , is half-metallic and has a pyrite-type crystal structure that has been utilized as conductive host for sulfur cathode either [52]. Compared with Co_9S_8 , CoS_2 possesses an even more higher room temperature electronic conductivity of $6.7 \times 10^3 \text{ S cm}^{-1}$. As shown in Fig. 4.26a, with the addition of CoS_2 , the dissolved lithium polysulfides were thoroughly decolorized, manifesting the existence of strong affinity between polar CoS_2 to Li_2S_4 through Co-S interaction. However, the graphene showed almost no sign of change in the color of $\text{Li}_2\text{S}_4/\text{DME}$ solution, indicating its faint interaction with Li_2S_4 . Furthermore, the calculated binding energies between Li_2S_4 and graphene or CoS_2 have a significant difference. As shown in Fig. 4.26b, the binding energy between CoS_2 and Li_2S_4 is 1.97 eV, which originates from the coupled interaction such as $\text{S}_n^{2-}-\text{Co}^{\delta+}$ and $\text{Li}^+-\text{S}^{\delta-}$ (of Co_9S_8) between CoS_2 and Li_2S_n species. However, unlike the Co_9S_8 with the dominating interaction of $\text{S}_n^{2-}-\text{Co}^{\delta+}$, the main force of CoS_2 is unknown yet.

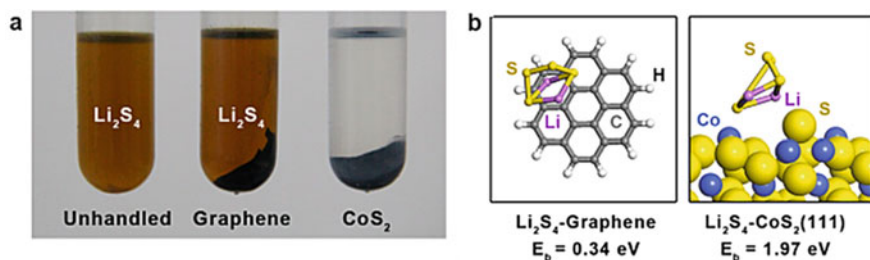


Fig. 4.26 **a** Digital photos of the Li₂S₄ adsorption on graphene and CoS₂ with the same contact area. **b** Calculated geometry and binding energy of one Li₂S₄ molecule on graphene (left), and (111) plane of CoS₂ (cobalt-terminated surface), respectively. Panels adapted with permission from Ref. [52], ACS

4.4.2 Lewis Acid–Base Interactions

Metal–organic framework (MOF) is constructed by coordinated outer organic linkers and inner metal ions, and it possesses adjustable composition, structures and porosity. From the perspective of electronic conductivity, MOFs are not suitable for sulfur transformation due to their insulating nature. However, the Lewis acidic metal ions inside one MOFs can anchor Lewis basic lithium polysulfide species. In addition, for its multiple porous structure, MOFs can realize high sulfur loading and deep electrolyte penetration and make them more suitable for sulfur scaffolds.

As aforementioned, the insulating nature of MOFs would limit its application in sulfur cathode, while it has multiple merits such as tunable chemical composition, structures and porosity. The successful application of LiFePO₄ gives people a lesson that the conductive coating can alter the electrochemical activity of insulating materials. Hence, Tarascon et al. first prepared the S@MOFs composite cathode by classical melt-diffusion sulfur at 155 °C (schematic illustration shown in Fig. 4.27)

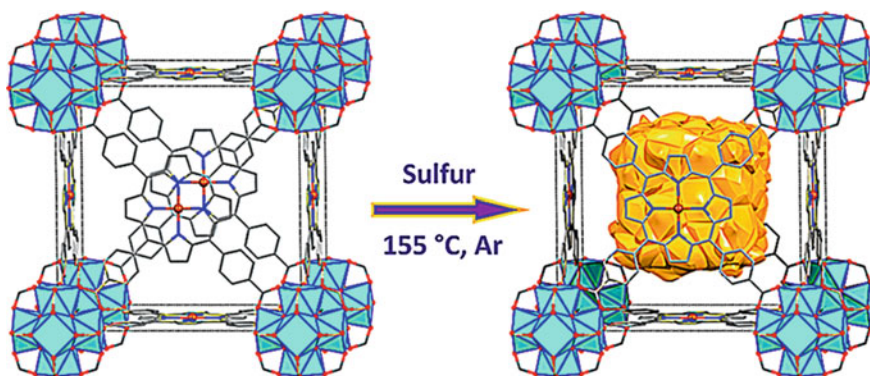


Fig. 4.27 Schematic illustration of the melt-infusion process of S@MOF composite cathode. Panel adapted with permission from Ref. [56], ACS

[53]. They chose MIL-100(Cr) (MIL: Matériaux Institut Lavoisier) as sulfur scaffold, for its pore volume could reach $\sim 1 \text{ cm}^3 \text{ g}^{-1}$ and unique structures. For example, its microporous pores (pentagonal, $\sim 0.5 \text{ nm}$; hexagonal, $\sim 0.9 \text{ nm}$) are connected with mesoporous cages ($\sim 2.5\text{--}2.9 \text{ nm}$). Compared with carbon materials with non-polar structure, both MOFs and mesoporous silica deliver polarized structure and this is the reason why they are capable of binding strongly with soluble polysulfides. Therefore, both S/silica and S/MOF composite cathodes exhibited better electrochemical performance compared to the S/C cathode (Fig. 4.28a). Furthermore, carbon materials such as graphene wrapping can build a good electron transport pathway as well as acting as a physical barrier for S@MOFs composite, improving its cycle stability and rate performance dramatically [54].

Further, Ni-MOF ($\text{Ni}_6(\text{BTB})_4(\text{BP})_3$, (BTB = benzene-1,3,5-tribenzoate and BP = 4,4'-bipyridyl), Fig. 4.28b) was found can immobilize polysulfides through both

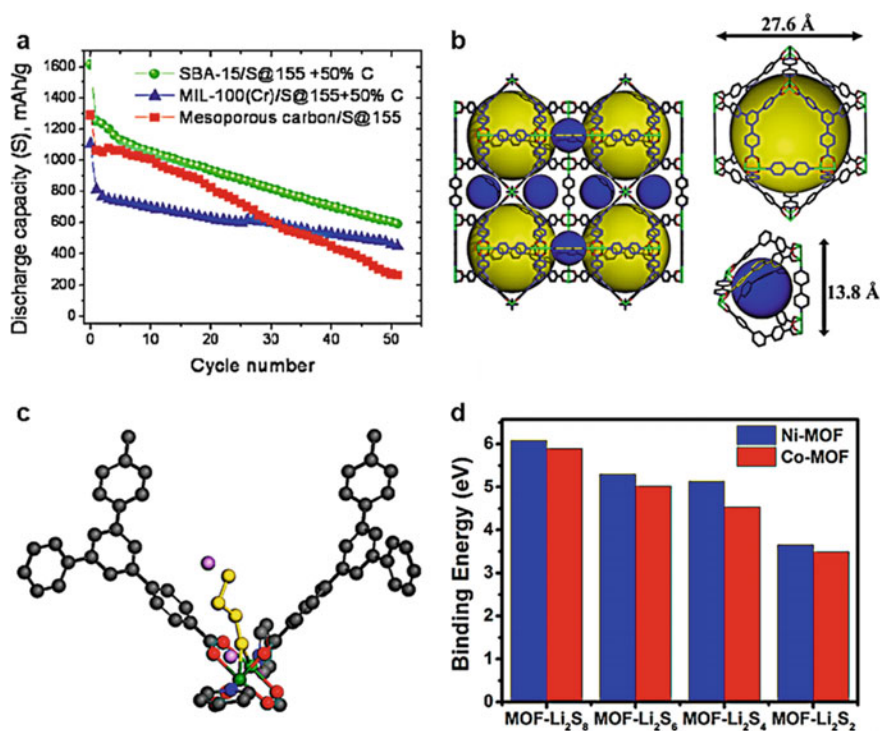


Fig. 4.28 **a** Cycle performance of various sulfur cathodes (i.e., SBA-15/S, MIL-100(Cr)/S and mesoporous carbon/S) at C/10 in the voltage range of 1.0 and 3.0 V. **b** Structure of Ni-MOF, which contains two different types of pores represented by dark yellow sphere (mesopore) and blue sphere (micropore) (gray, carbon (C); red, oxygen (O); green, nickel (Ni); blue, nitrogen (N)). **c** Schematic showing the interaction between polysulfides (Li_2S_4) and the paddle-wheel unit in Ni-MOF. **d** Comparison of the bond strength of various lithium polysulfides with Ni-MOF and Co-MOF. Panels adapted with permission from: **a** Ref. [53], ACS; **b, c, d** Ref. [55], ACS

physical and chemical interactions remarkably [55]. Specifically, the soluble lithium polysulfides could be effectively confined via the axial ligand formed by the coordination between the soluble polysulfides anion (soft Lewis base) and Ni (II) center (Lewis acid) of Ni-MOF. According to the DFT calculations, the $\text{Li}_2\text{S}_8/\text{Li}_2\text{S}_6/\text{Li}_2\text{S}_4/\text{Li}_2\text{S}_2$ could be stably retained within the pores of Ni-MOF (Fig. 4.28c, d). In addition, the strength of the Lewis acid–base interaction would increase with the increasing of the chain length of lithium polysulfides. After changing the center metal ions to Co^{2+} , the final S@Co-MOF composite cathode exhibits inferior cycling performance than the Ni (II) counterpart, even though it possesses better electronic conductivity (high electronic conductivity of Co-MOFs). The Irving-Williams Series governs the performance of S@MOFs composite. According to this principle, as to the high-spin complexes of divalent ions (sp^3d^2 hybridization) of first-row transition metals, the stability constant for the complex formation follows the order of $\text{Mn(II)} < \text{Fe(II)} < \text{Co(II)} < \text{Ni(II)} < \text{Cu(II)}$. Based on this, Cu(II)-embedded zirconium-metalloporphyrin framework MOF-525(Cu) was fabricated as a sulfur scaffold, and it accomplished excellent cycling and rate performances simultaneously (Fig. 4.29) [56].

Some useful guidelines can be concluded to prepare high-performance S@MOFs composite cathode. Decreasing the particle size of MOFs is helpful in boosting the ion and electron transportation and result in a high discharge capacity. In addition, the relatively smaller apertures coupling with Lewis acidic center that has an affinity with the polysulfide anions can help realize a stable yet long-term cycling. Based on this, future direction for S@MOFs cathode can be categorized as follows: (i) wrap the S@MOFs particles with materials has high electronic conductivity such as carbon nanotubes or graphene, to enhance the redox kinetics of sulfur transformation, (ii) reduce the dimensions of MOFs to increase sulfur utilization and ion transportation, (iii) enlarge the cages and reduce the windows of MOFs and (iv) develop advanced MOFs with stronger affinity with soluble lithium polysulfides [57].

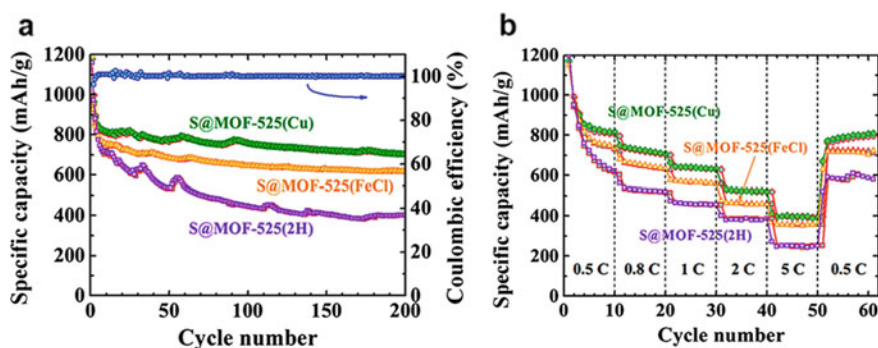


Fig. 4.29 **a** Cycle performance of S@MOF-525(2H), S@MOF-525(FeCl) and S@MOF(Cu) composite cathode with the Coulombic efficiency of S@MOF(Cu). **b** Rate capability of S@MOF-525(2H), S@MOF-525(FeCl) and S@MOF(Cu) composite cathode. Panels adapted with permission from Ref. [56], ACS

Since Gogotsi et al. fabricated MXenes by selective etching of the A element of MAX phases in aqueous HF solution, it has caught the attention of researchers all over the world [58]. The introduction of functional oxygen groups on Ti_2C nanosheets happened during the exfoliation and delamination of MXenes. In addition, the surficial Ti atom on Ti_2C nanosheets has unoccupied orbitals and an underlying delocalized band structure, which give it a metallic conductivity. Moreover, the electronegative S atoms in polysulfides can lower the electron density of the surface Ti atoms, resulting in a higher binding energy than Ti-C bond (Fig. 4.30a). Actually, a coordination existed between the unoccupied orbitals of the surface Ti atoms of MXenes and an electron-donating host (lithium polysulfide species), forming a Lewis acid–base interaction [59]. The MXene phases with hydroxyl functionalization have low resistivity ($0.03 \mu\Omega \text{ m}$), behaving as semiconductors with a very small band gap of 0.05 eV. On top of these merits, the final $\text{S@Ti}_2\text{C}$ cathode can retain a discharge capacity of 723 mAh g^{-1} after 650 cycles.

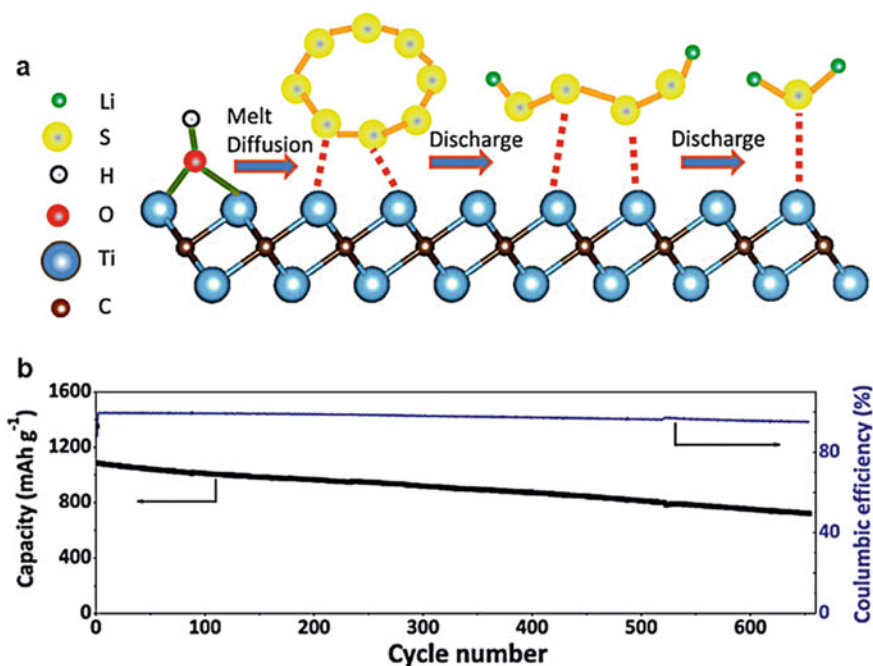
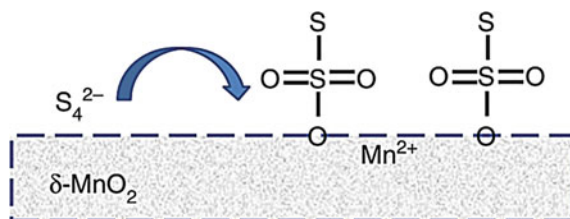


Fig. 4.30 **a** Schematic showing the S–Ti–C bond to replace the Ti–OH bond on the MXene surface during heat treatment or touched with polysulfides. **b** Long-term cycle performance of $\text{S/Ti}_2\text{C}$ composite cathode cells were conditioned at small current density ($C/20$) for one cycle before cycling at $C/2$. Panels adapted with permission from Ref. [59], Wiley-VCH

Fig. 4.31 Schematic showing the redox interactions induced by δ - MnO_2 substrate. Panel adapted with permission from Ref. [8], NPG



4.4.3 Redox Interactions

Redox mediators have long been utilized as catalysts for the chemical reaction which is difficult to take place, and it can be utilized to adjust the sulfur transformation either. Once the soluble lithium polysulfides react with the redox mediators, it would inhibit its shuttling. MnO_2 nanosheets were initially chosen as the prototype to act as redox mediators for sulfur cathode [8]. As shown in Fig. 4.31, during the discharging, the initially generated polysulfides would react with MnO_2 to form thiosulfate groups. With further discharging, the newly formed polysulfides would react with the thiosulfate groups to generate polythionate complexes and shorter-chain polysulfides simultaneously. Benefiting from the relatively poor solubility of the polythionate complex, the shuttling of polysulfides can be dramatically suppressed. Materials having a redox window higher than sulfur (2.4–3.05 V) were able to initiate the redox interaction to chemically anchor polysulfides [60].

4.4.4 Summary

Chemical adsorption of polysulfides is important for sulfur transformation. Three kinds of binding energies: (1) polar–polar interactions; (2) Lewis acid–base interactions; (3) redox interactions are discussed in this section. Carbon materials with doped heteroatoms such as nitrogen, oxygen, sulfur and so on deliver polarized electron distribution, and tend to bind with soluble lithium polysulfides. By adjusting the species of dopant atoms, the binding energy could be regulated. In addition, polymers always have multiple kinds of heteroatoms and can alleviate the shuttling effect either. In this regard, conductive polymers may be good choices to construct sulfur cathode for its excellent electronic conductivity. Moreover, metal compounds with high polarization could be utilized as scaffold or additive for sulfur cathode, for their superior binding energies with polar polysulfides. MOFs have Lewis acidic metal ions and hierarchical porous structure can confine polysulfides through Lewis acid–base interactions with soluble lithium polysulfides. Redox adjustment of sulfur transformation is more like catalytic conversion of sulfur cathode. In all, the chemical adsorption of soluble lithium polysulfides can restrain the shuttling effect efficiently. But only with the help of high electronic conductivity, the chemical adsorption can maximize its function for sulfur transformation.

4.5 Interlayer

Originating from the severe shuttling of lithium polysulfides, Li-S batteries suffer from rapid Coulombic efficiency declining and irreversible capacity fading. Apart from the modification of sulfur electrode directly, a novel interlayer was designed by Manthiram et al. to tackle these problems [61]. Specifically, just as its name implies, the interlayer, a conductive and porous paper comprised of multiwalled carbon nanotube (MWCNT), was inserted between the cathode and separator, as schematic in Fig. 4.32. Through this insertion, the shuttling effect could be largely suppressed. Therefore, upon incorporation of interlayer, the sulfur utilization and cycle life of cathode would be significantly improved. This carbon interlayer can reduce the interfacial resistance and confine the polysulfides within the cathode, avoiding the harmful polysulfides diffusion to the anode surface. Therefore, the final Li-S batteries with interlayer deliver excellent performance at both $C/2$ and $1C$ current density (Fig. 4.33a). Starting from this research, many interlayer configurations have been composed to alleviate the shuttling of polysulfides, and we will only introduce some representative ones in this section.

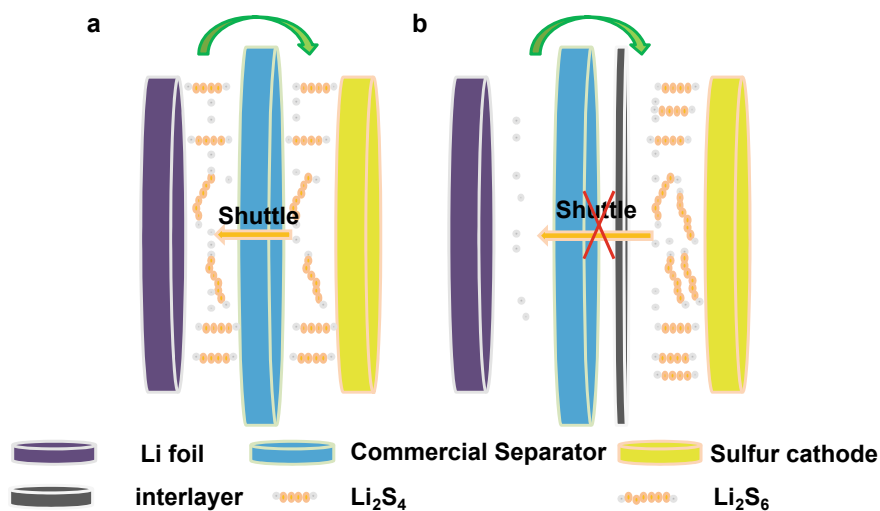


Fig. 4.32 Schematic showing rechargeable Li-S batteries: **a** without and **b** with interlayer



Fig. 4.33 **a** Cycle performance of high-rate Li-S batteries armed with and without the MWCNT insertion between separator and cathode, respectively. **b, c** Digital photos of the CNF-TiO₂ (CNF-T) interlayer under mechanical bending conditions. Panels adapted with permission from: **a** Ref. [61], RSC; **b, c, d** Ref. [62], ACS

4.5.1 Representative Configurations of Interlayer

4.5.1.1 Independent Flexible Carbon-Based Interlayer

The foremost interlayer is an MWCNT film fabricated by first vacuum-filtration and further peeling. Electrospinning is also an effective method to produce free-standing carbon film, as shown in Fig. 4.33b, c. For example, an interlayer constructed by TiO₂ decorated CNF (named CNF-T) was fabricated to suppress the shuttling of lithium polysulfides [62]. The superior 1D electronic conductivity of CNF can enhance the sulfur redox kinetics. Meanwhile, the decoration of TiO₂ NPs can adsorb soluble lithium polysulfides and confine them in between the cathode and CNF-T interlayer, improving the cycling and rate performance.

4.5.1.2 In Situ Formed Interlayer on Separator

When the pure carbon was used as interlayer, the utilization and kinetics for sulfur transformation can be greatly improved (Fig. 4.33a). As discussed in section “Sulfides”, metal sulfides such as TiS₂, Co₉S₈ and CoS₂ have ultrahigh electronic conductivity and deliver high binding energy with soluble lithium polysulfides simultaneously. Therefore, an in situ grown Co₉S₈ sheets were fabricated as interlayer on a Celgard separator (Co₉S₈-Celgard) to sequester the shuttling of soluble lithium polysulfides [9]. As shown in Fig. 4.34a, after a slight scratch, the Co₉S₈ arrays deliver a hollow framework and which is beneficial to the adsorption of soluble lithium polysulfides, since lithium polysulfides adsorption capability is proportional to the substrate’s surface area. In addition, the robust connection between the Co₉S₈ arrays and Celgard can be clearly observed from the cross-sectional morphologies of Co₉S₈-Celgard, showing its good mechanical stability (Fig. 4.34b, c). Moreover, the corresponding elemental mapping images can show the homogeneous elemental distribution of carbon, sulfur and cobalt elements (Fig. 4.34d-f). Therefore, the Co₉S₈-Celgard separator can empower Li-S batteries with long cycle life and high sulfur utilization even when the sulfur loading reaches 5.6 mg cm⁻².

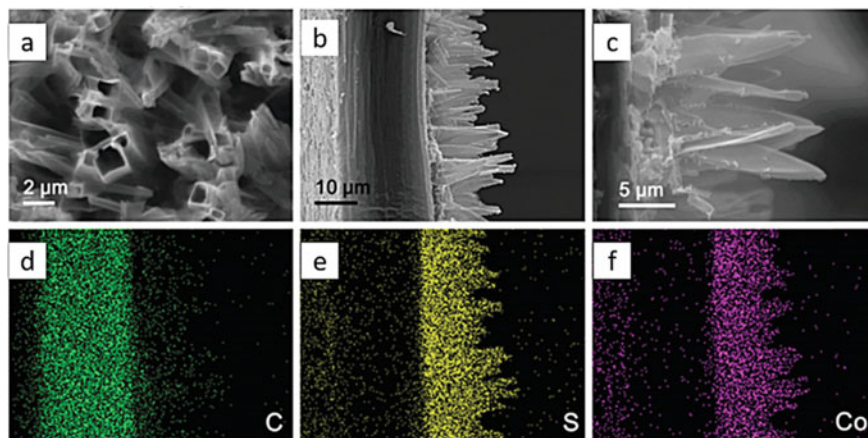


Fig. 4.34 **a** SEM image of Co_9S_8 -Celgard after slight scratching. **b, c** Cross-sectional morphologies of Co_9S_8 -Celgard. **d, e, f** Carbon, sulfur and cobalt elemental mapping of image (**b**), respectively. Panels adapted with permission from Ref. [9], RSC

4.5.1.3 Ex Situ-Coated Interlayer on Separator

Slurry coating is a universal method for the current anode and cathode fabrication industry. Therefore, a graphene/ TiO_2 interlayer was coated on top of sulfur cathode via this method directly [63], as shown in Fig. 4.35a, b. However, the interlayer obtained via slurry coating would be curly and quite open, delivering a much thicker, rougher structure [64], as shown in Fig. 4.35d. The vacuum filtration process would produce a densely packed interlayer (Fig. 4.35c).

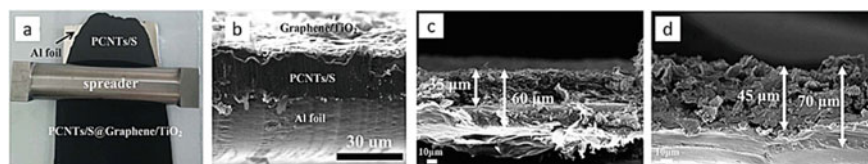


Fig. 4.35 **a** Digital photos showing the slurry coating process of graphene/ TiO_2 interlayer on top of sulfur cathode. **b** Cross-sectional SEM image of fresh cathode with graphene/ TiO_2 coating film. **c, d** Cross-sectional SEM images of fresh G-LTO@PP (vacuum filtration) and G-LTO + PP (slurry coating) separators, respectively. Panels adapted with permission from: **a, b** Ref. [63], Wiley-VCH; **c, d** Ref. [64], Elsevier

4.5.2 *Perspective of the Application of Interlayer Within Li-S Batteries*

Both the carbon and non-carbon interlayers show the capability to restrain the shuttling of soluble lithium polysulfides and boost the electrochemical performance of sulfur cathode. However, for future development, some crucial points must be taken into consideration:

- (i) The preparation process of interlayer should be simple enough. As a matter of fact, commercialization is the ultimate goal for suggesting interlayer into Li-S batteries. Therefore, the fabrication methods should be delicate enough to control the thickness/weight of interlayer precisely;
- (ii) Bare carbon interlayer can act as a physical barrier only, and its non-polar nature may lead to a weak interaction with polar polysulfides. Therefore, materials can chemically bind lithium polysulfides should be incorporated via suitable methods;
- (iii) The Li^+ ion transportation and wetting of electrolyte are very important for later battery operation, especially under large current density [65]. Therefore, the appropriate porosity is necessary for the interlayer.

4.6 Outlooks

Physical and chemical restraining of the polysulfides shuttling is important to construct high-performance Li-S batteries. Since the first research invented the melt-infusion method to incorporate sulfur on a carbon substrate, large amounts of carbon materials have been developed to host sulfur. However, the physical interactions between carbon materials and soluble lithium polysulfides are weak, and cannot restrain the shuttling of soluble intermediates efficiently. Chemical interaction can alleviate this problem to a large extent. While bare chemical bonding is not able to facilitate the redox kinetics for its common low electronic conductivity. To this end, the combination of physical and chemical interaction is the best choice. Many methods have been developed to realize this objective such as mechanical mixing, in situ growing, thermal processing and so on.

The sulfur transformation in ether electrolyte is a solid-liquid-solid process, which is different from current commercialized Li-ion batteries. Incorporating the physical and chemical interaction in sulfur cathode can slow down the capacity decay to some extent, but which is still not enough for practical application. The problems of Li metal anode can seriously damage the performance either. Therefore, future research should take the whole reaction process of Li-S batteries into consideration, including the Li metal anode modification, electrolyte optimization and cathode construction.

Acknowledgments The authors thank all the other members of Li's group for their valuable advice.

References

1. Wang Q et al (2015) Direct observation of sulfur radicals as reaction media in lithium sulfur batteries. *J Electrochem Soc* 162:A474–A478. <https://doi.org/10.1149/2.0851503jes>
2. Gao J, Lowe MA, Kiya Y, Abruña HD (2011) Effects of liquid electrolytes on the charge-discharge performance of rechargeable lithium/sulfur batteries: electrochemical and in-situ X-ray absorption spectroscopic studies. *J Phys Chem C* 115:25132–25137. <https://doi.org/10.1021/jp207714c>
3. Rauh RD (1979) A lithium/dissolved sulfur battery with an organic electrolyte. *J Electrochem Soc* 126:523. <https://doi.org/10.1149/1.2129079>
4. Peled E (1989) Lithium-sulfur battery: evaluation of dioxolane-based electrolytes. *J Electrochem Soc* 136:1621. <https://doi.org/10.1149/1.2096981>
5. Mikhaylik YV, Akridge JR (2004) Polysulfide shuttle study in the Li/S battery system. *J Electrochem Soc* 151:A1969. <https://doi.org/10.1149/1.1806394>
6. Yao H et al (2014) Improving lithium-sulphur batteries through spatial control of sulphur species deposition on a hybrid electrode surface. *Nat Commun* 5:3943. <https://doi.org/10.1038/ncomms4943>
7. Liu N et al (2019) Direct electrochemical generation of supercooled sulfur microdroplets well below their melting temperature. *Proc Natl Acad Sci* 116:765. <https://doi.org/10.1073/pnas.1817286116>
8. Liang X et al (2015) A highly efficient polysulfide mediator for lithium-sulfur batteries. *Nat Commun* 6:5682. <https://doi.org/10.1038/ncomms6682>
9. He J, Chen Y, Manthiram A (2018) Vertical Co₉S₈ hollow nanowall arrays grown on a celgard separator as a multifunctional polysulfide barrier for high-performance Li–S batteries. *Energy Environ Sci* 11:2560–2568. <https://doi.org/10.1039/C8EE00893K>
10. Pang Q, Kundu D, Cuisinier M, Nazar LF (2014) Surface-enhanced redox chemistry of polysulfides on a metallic and polar host for lithium-sulphur batteries. *Nat Commun* 5:4759. <https://doi.org/10.1038/ncomms5759>
11. Hart CJ et al (2015) Rational design of sulphur host materials for Li–S batteries: correlating lithium polysulphide adsorptivity and self-discharge capacity loss. *Chem Commun* 51:2308–2311. <https://doi.org/10.1039/C4CC08980D>
12. Ji X, Lee KT, Nazar LF (2009) A highly ordered nanostructured carbon-sulphur cathode for lithium-sulphur batteries. *Nat Mater* 8:500–506. <https://doi.org/10.1038/nmat2460>
13. Tachikawa N et al (2011) Reversibility of electrochemical reactions of sulfur supported on inverse opal carbon in glyme–Li salt molten complex electrolytes. *Chem Commun* 47:8157–8159. <https://doi.org/10.1039/C1CC12415C>
14. Li X et al (2011) Optimization of mesoporous carbon structures for lithium-sulfur battery applications. *J Mater Chem* 21:16603–16610. <https://doi.org/10.1039/C1JM12979A>
15. Zhang B, Qin X, Li GR, Gao XP (2010) Enhancement of long stability of sulfur cathode by encapsulating sulfur into micropores of carbon spheres. *Energy Environ Sci* 3:1531–1537. <https://doi.org/10.1039/C002639E>
16. Wang H et al (2011) Graphene-wrapped sulfur particles as a rechargeable lithium-sulfur battery cathode material with high capacity and cycling stability. *Nano Lett* 11:2644–2647. <https://doi.org/10.1021/nl200658a>
17. Evers S, Nazar LF (2012) Graphene-enveloped sulfur in a one pot reaction: a cathode with good coulombic efficiency and high practical sulfur content. *Chem Commun* 48:1233–1235. <https://doi.org/10.1039/C2CC16726C>
18. Ahn W, Kim K-B, Jung K-N, Shin K-H, Jin C-S (2012) Synthesis and electrochemical properties of a sulfur-multi walled carbon nanotubes composite as a cathode material for lithium sulfur batteries. *J Power Sources* 202:394–399. <https://doi.org/10.1016/j.jpowsour.2011.11.074>
19. Ji L et al (2011) Porous carbon nanofiber-sulfur composite electrodes for lithium/sulfur cells. *Energy Environ Sci* 4:5053–5059. <https://doi.org/10.1039/C1EE02256C>

20. Zheng G, Yang Y, Cha JJ, Hong SS, Cui Y (2011) Hollow carbon nanofiber-encapsulated sulfur cathodes for high specific capacity rechargeable lithium batteries. *Nano Lett* 11:4462–4467. <https://doi.org/10.1021/nl2027684>
21. Bucur CB et al (2013) Ultrathin tunable ion conducting nanomembranes for encapsulation of sulfur cathodes. *Energy Environ Sci* 6:3286–3290. <https://doi.org/10.1039/C3EE42739K>
22. Miller MD, Bruening ML (2004) Controlling the nanofiltration properties of multilayer poly-electrolyte membranes through variation of film composition. *Langmuir* 20:11545–11551. <https://doi.org/10.1021/la0479859>
23. Bucur CB, Muldoon J, Lita A (2016) A layer-by-layer supramolecular structure for a sulfur cathode. *Energy Environ Sci* 9:992–998. <https://doi.org/10.1039/C5EE02367J>
24. Ji L et al (2011) Graphene oxide as a sulfur immobilizer in high performance lithium/sulfur cells. *J Am Chem Soc* 133:18522–18525. <https://doi.org/10.1021/ja206955k>
25. Zhang L et al (2012) Electronic structure and chemical bonding of a graphene oxide-sulfur nanocomposite for use in superior performance lithium-sulfur cells. *Phys Chem Chem Phys* 14:13670–13675. <https://doi.org/10.1039/C2CP42866K>
26. Qiu Y et al (2014) High-rate, ultralong cycle-life lithium/sulfur batteries enabled by nitrogen-doped graphene. *Nano Lett* 14:4821–4827. <https://doi.org/10.1021/nl5020475>
27. Liu J et al (2015) A graphene-like oxygenated carbon nitride material for improved cycle-life lithium/sulfur batteries. *Nano Lett* 15:5137–5142. <https://doi.org/10.1021/acs.nanolett.5b01919>
28. Pang Q, Nazar LF (2016) Long-life and high-areal-capacity Li–S batteries enabled by a light-weight polar host with intrinsic polysulfide adsorption. *ACS Nano* 10:4111–4118. <https://doi.org/10.1021/acsnano.5b07347>
29. Song J et al (2014) Nitrogen-doped mesoporous carbon promoted chemical adsorption of sulfur and fabrication of high-areal-capacity sulfur cathode with exceptional cycling stability for lithium-sulfur batteries. *Adv Func Mater* 24:1243–1250. <https://doi.org/10.1002/adfm.201302631>
30. Pang Q et al (2015) A nitrogen and sulfur dual-doped carbon derived from polyrhodanine@cellulose for advanced lithium-sulfur batteries. *Adv Mater* 27:6021–6028. <https://doi.org/10.1002/adma.201502467>
31. Zhou W et al (2015) Tailoring pore size of nitrogen-doped hollow carbon nanospheres for confining sulfur in lithium-sulfur batteries. *Adv Energy Mater* 5:1401752. <https://doi.org/10.1002/aenm.201401752>
32. Zhou G, Zhao Y, Manthiram A (2015) Dual-confined flexible sulfur cathodes encapsulated in nitrogen-doped double-shelled hollow carbon spheres and wrapped with graphene for Li–S batteries. *Adv Energy Mater* 5:1402263. <https://doi.org/10.1002/aenm.201402263>
33. Song J et al (2015) Strong lithium polysulfide chemisorption on electroactive sites of nitrogen-doped carbon composites for high-performance lithium-sulfur battery cathodes. *Angew Chem Int Ed* 54:4325–4329. <https://doi.org/10.1002/anie.201411109>
34. Zhang S, Tsuzuki S, Ueno K, Dokko K, Watanabe M (2015) Upper limit of nitrogen content in carbon materials. *Angew Chem Int Ed* 54:1302–1306. <https://doi.org/10.1002/anie.201410234>
35. Fu Y, Manthiram A (2012) Core-shell structured sulfur-polypyrrole composite cathodes for lithium-sulfur batteries. *RSC Adv* 2:5927–5929. <https://doi.org/10.1039/C2RA20393F>
36. Fu Y, Manthiram A (2012) Enhanced cyclability of lithium-sulfur batteries by a polymer acid-doped polypyrrole mixed ionic-electronic conductor. *Chem Mater* 24:3081–3087. <https://doi.org/10.1021/cm301661y>
37. Zheng G et al (2013) Amphiphilic surface modification of hollow carbon nanofibers for improved cycle life of lithium sulfur batteries. *Nano Lett* 13:1265–1270. <https://doi.org/10.1021/nl304795g>
38. Seh ZW et al (2013) Stable cycling of lithium sulfide cathodes through strong affinity with a bifunctional binder. *Chem Sci* 4:3673–3677. <https://doi.org/10.1039/C3SC51476E>
39. Chen H et al (2015) Rational design of cathode structure for high rate performance lithium-sulfur batteries. *Nano Lett* 15:5443–5448. <https://doi.org/10.1021/acs.nanolett.5b01837>

40. Park K et al (2015) Trapping lithium polysulfides of a Li–S battery by forming lithium bonds in a polymer matrix. *Energy Environ Sci* 8:2389–2395. <https://doi.org/10.1039/C5EE01809A>
41. Seh ZW et al (2014) Facile synthesis of Li₂S–polypyrrole composite structures for high-performance Li₂S cathodes. *Energy Environ Sci* 7:672–676. <https://doi.org/10.1039/C3EE43395A>
42. Ma L et al (2014) Tethered molecular sorbents: enabling metal-sulfur battery cathodes. *Adv Energy Mater* 4:1400390. <https://doi.org/10.1002/aenm.201400390>
43. Li W et al (2013) Understanding the role of different conductive polymers in improving the nanostructured sulfur cathode performance. *Nano Lett* 13:5534–5540. <https://doi.org/10.1021/nl403130h>
44. Song M-S et al (2004) Effects of nanosized adsorbing material on electrochemical properties of sulfur cathodes for Li/S secondary batteries. *J Electrochem Soc* 151:A791. <https://doi.org/10.1149/1.1710895>
45. Choi YJ et al (2007) Electrochemical properties of sulfur electrode containing nano Al₂O₃ for lithium/sulfur cell. *Phys Scr T129*:62–65. <https://doi.org/10.1088/0031-8949/2007/t129/014>
46. Kim H et al (2013) Plasma-enhanced atomic layer deposition of ultrathin oxide coatings for stabilized lithium-sulfur batteries. *Adv Energy Mater* 3:1308–1315. <https://doi.org/10.1002/aenm.201300253>
47. Ji X, Evers S, Black R, Nazar LF (2011) Stabilizing lithium-sulphur cathodes using polysulphide reservoirs. *Nat Commun* 2:325. <https://doi.org/10.1038/ncomms1293>
48. Evers S, Yim T, Nazar LF (2012) Understanding the nature of absorption/adsorption in nanoporous polysulfide sorbents for the Li–S battery. *J Phys Chem C* 116:19653–19658. <https://doi.org/10.1021/jp304380j>
49. Wei Seh Z et al (2013) Sulphur–TiO₂ yolk-shell nanoarchitecture with internal void space for long-cycle lithium-sulphur batteries. *Nat Commun* 4:1331. <https://doi.org/10.1038/ncomms2327>
50. Seh ZW et al (2014) Two-dimensional layered transition metal disulphides for effective encapsulation of high-capacity lithium sulphide cathodes. *Nat Commun* 5:5017. <https://doi.org/10.1038/ncomms6017>
51. Pang Q, Kundu D, Nazar LF (2016) A graphene-like metallic cathode host for long-life and high-loading lithium-sulfur batteries. *Mater Horiz* 3:130–136. <https://doi.org/10.1039/C5MH00246J>
52. Yuan Z et al (2016) Powering lithium-sulfur battery performance by propelling polysulfide redox at sulfiphilic hosts. *Nano Lett* 16:519–527. <https://doi.org/10.1021/acs.nanolett.5b04166>
53. Demir-Cakan R et al (2011) Cathode composites for Li–S batteries via the use of oxygenated porous architectures. *J Am Chem Soc* 133:16154–16160. <https://doi.org/10.1021/ja2062659>
54. Zhao Z et al (2014) Graphene-wrapped chromium-MOF(MIL-101)/sulfur composite for performance improvement of high-rate rechargeable Li–S batteries. *J Mater Chem A* 2:13509–13512. <https://doi.org/10.1039/C4TA01241K>
55. Zheng J et al (2014) Lewis acid-base interactions between polysulfides and metal organic framework in lithium sulfur batteries. *Nano Lett* 14:2345–2352. <https://doi.org/10.1021/nl404721h>
56. Wang Z et al (2015) Mixed-metal–organic framework with effective lewis acidic sites for sulfur confinement in high-performance lithium-sulfur batteries. *ACS Appl Mater Interfaces* 7:20999–21004. <https://doi.org/10.1021/acsami.5b07024>
57. Zhou J et al (2014) Rational design of a metal-organic framework host for sulfur storage in fast, long-cycle Li–S batteries. *Energy Environ Sci* 7:2715–2724. <https://doi.org/10.1039/C4EE01382D>
58. Naguib M et al (2011) Two-dimensional nanocrystals produced by exfoliation of Ti₃AlC₂. *Adv Mater* 23:4248–4253. <https://doi.org/10.1002/adma.201102306>
59. Liang X, Garsuch A, Nazar LF (2015) Sulfur cathodes based on conductive MXene nanosheets for high-performance lithium-sulfur batteries. *Angew Chem Int Ed* 54:3907–3911. <https://doi.org/10.1002/anie.201410174>

60. Liang X et al (2016) Tuning transition metal oxide-sulfur interactions for long life lithium sulfur batteries: the “goldilocks” principle. *Adv Energy Mater* 6:1501636. <https://doi.org/10.1002/aenm.201501636>
61. Su Y-S, Manthiram A (2012) A new approach to improve cycle performance of rechargeable lithium-sulfur batteries by inserting a free-standing MWCNT interlayer. *Chem Commun* 48:8817–8819. <https://doi.org/10.1039/C2CC33945E>
62. Liang G et al (2016) Ultrafine TiO₂ decorated carbon nanofibers as multifunctional interlayer for high-performance lithium-sulfur battery. *ACS Appl Mater Interfaces* 8:23105–23113. <https://doi.org/10.1021/acsami.6b07487>
63. Xiao Z et al (2015) A lightweight TiO₂/graphene interlayer, applied as a highly effective polysulfide absorbent for fast, long-life lithium-sulfur batteries. *Adv Mater* 27:2891–2898. <https://doi.org/10.1002/adma.201405637>
64. Zhao Y et al (2016) Dense coating of Li₄Ti₅O₁₂ and graphene mixture on the separator to produce long cycle life of lithium-sulfur battery. *Nano Energy* 30:1–8. <https://doi.org/10.1016/j.nanoen.2016.09.030>
65. Liu Y et al (2018) Fe₃O₄-decorated porous graphene interlayer for high-performance lithium-sulfur batteries. *ACS Appl Mater Interfaces* 10:26264–26273. <https://doi.org/10.1021/acsami.8b07316>

Chapter 5

Catalytic Conversion of Polysulfides in Li–S Batteries



Wenjia Qu, Chuannan Geng, Jingyi Xia, Wuxing Hua, Guowei Ling, Chen Zhang, and Quan-Hong Yang

Abstract The shuttling of polysulfides is a major issue that tackles the practical use of Li–S battery. Recently, the catalysis of polysulfides has been developed as an effective solution to accelerate the polysulfide conversion and reduce the shuttle effect fundamentally. In this chapter, the origin and the research progress of catalysis in Li–S batteries are presented systematically. We start with the redox chemistry of polysulfides and introduce the importance of catalysis in Li–S battery. Subsequently, promising catalytic materials are categorized according to their composition and functions. Moreover, key parameters that can precisely describe the catalytic mechanisms are proposed following by the summary of advanced characterization techniques for better demystifying the catalysis process, which is urgently needed for establishing a systematic research protocol for the catalysis in Li–S battery. Finally, perspectives are given for the rational design of high-efficiency catalytic materials and promoting the practice use of Li–S battery.

Keywords Catalysis · Polysulfide conversion · Material design · Characterization

5.1 Introduction

In Li–S battery, the sulfur reduction reaction (SRR) and its reversible process dominate the output performance, such as the voltage, energy density, cycling stability and rate capability. Polysulfides as the intermediates of the transformation from S to $\text{Li}_2\text{S}_2/\text{Li}_2\text{S}$, directly influence the kinetics of the SRR and further have an impact

W. Qu · C. Geng · J. Xia · W. Hua · Q.-H. Yang (✉)

State Key Laboratory of Chemical Engineering, Nanoyang Group, School of Chemical Engineering and Technology, Tianjin University and Collaborative Innovation Center of Chemical Science and Engineering, Tianjin 300350, China
e-mail: qhyangcn@tju.edu.cn

G. Ling · C. Zhang

School of Marine Science and Technology, Tianjin University, Tianjin 300072, China

Q.-H. Yang

Joint School of National University of Singapore and Tianjin University, International Campus of Tianjin University, Fuzhou 350207, China

on the battery performance. Physical and chemical adsorption of polysulfides has been introduced in Chap. 4, and the interaction between polysulfides and adsorbents can significantly retard the shuttling of polysulfides, while the severe sulfur loss and incomplete sulfur reduction can be avoided to some extent. However, the dissolution and sluggish transformation of polysulfides accomplished with the SRR is inevitable, thus the abuse of electrolyte usually occurs and further lowers the energy density. Therefore, accelerating the transformation of the polysulfides is vital to decrease their dissolution possibility in electrolyte to eliminate the shuttling, and the lean electrolyte condition can be realized to deliver a much higher energy density.

Catalysis is a common method to accelerate the chemical reaction in the chemical engineering industry, thermal catalysis and electrochemical catalysis have been developed for decades, and theory systems have been established to guide their usage. In case of Li-S batteries, some materials serving as the cathode materials or interlayer additives have shown a significant impact on the performance, and the role of these materials is beyond chemical adsorption. Thus, catalysis is attracting more and more attentions all around the world. Different catalysis materials have been emerging, and the catalysis process is under investigation by some world-class groups to demonstrate the role of catalysis in Li-S batteries (Fig. 5.1a). According to the index results from Web of Science (keyword: Li-S and catalysis), the number of publications on the topic of “Li-S and catalysis” increase almost twice per year since 2016 (Fig. 5.1b), indicating the catalysis of polysulfides is the hotspot in the R&D of Li-S battery. Hence, it is highly necessary to give some insightful inputs on this field for the readers and help them better understand the significance of the use of catalysis in Li-S battery. In this Chapter, we start with the generation and the transformation of polysulfides and briefly introduce the catalysis in Li-S battery. Subsequently, different catalytic materials are categorized according to their composition and functions. To better illustrate the catalysis process, some key parameters and potential mechanisms are highlighted following by the summary of the advanced characterization techniques. Some perspectives are also given to realize the rational design of catalytic materials and promote the practice use of Li-S battery.

5.2 Polysulfides in Li-S Battery

5.2.1 Redox Chemistry

Conventional Li-S batteries consist of a sulfur cathode, an organic liquid electrolyte, and a lithium metal anode as shown in Fig. 5.2a. During discharge, Li^+ ions are produced at the lithium-metal anode and move through the electrolyte to the sulfur cathode, while the electrons flow through the external circuit, producing Li_2S as the final discharge product at the cathode. The electrochemical reactions during charge are reversed compared to that during discharge [1]. A discharge/charge current can

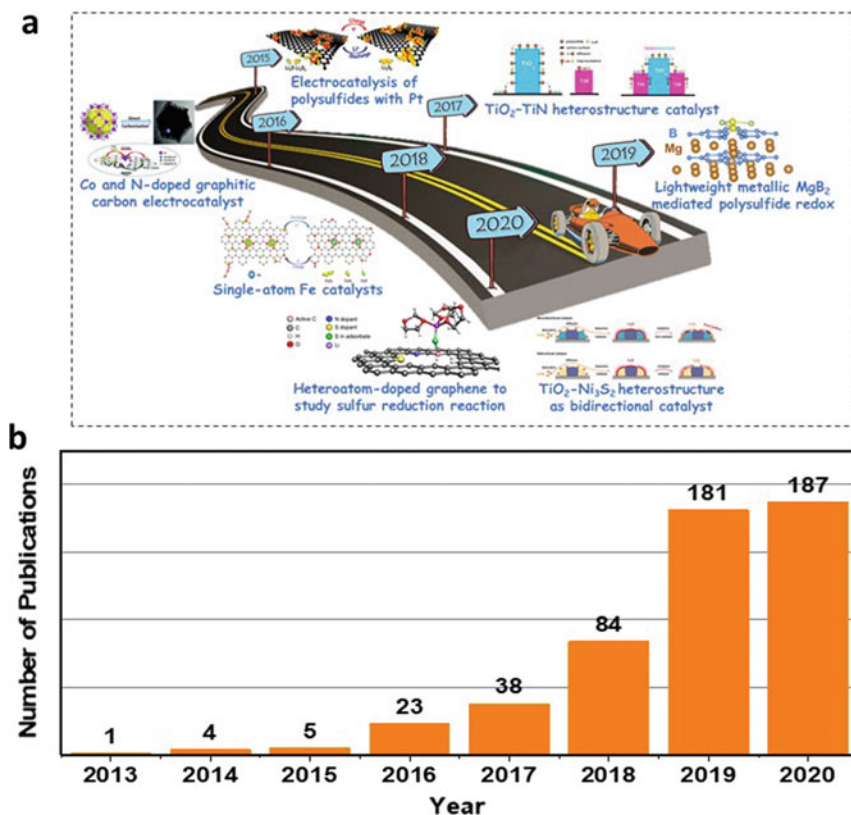


Fig. 5.1 **a** Schematic illustration of materials for Li-S batteries; **b** the number of publications of catalytic materials in Li-S batteries

be applied to the battery resulting in reduction/oxidation at the positive electrode and the oxidation/reduction at the negative electrode.

The multi-electron-transfer cathode reaction offers an extremely high theoretical capacity of 1672 mAh g^{-1} , while the lithium anode provides a theoretical capacity of 3860 mAh g^{-1} , thus offsetting the deficiency in average working voltage (*ca.* 2.1 V) and accounting for an attractively high specific energy of the battery [4, 5]. These electrochemical reactions occur in an ideal battery without considering the impact of lithium polysulfide dissolution, which hinders the practical application of the battery. As shown in Fig. 5.2b, the discharge profile can be divided into three parts based on the phase changes of sulfur species [3]. At the initial stage of the discharge process, sulfur reacts with lithium and then transforms into Li_2S_8 , which keeps dissolving in the electrolyte, facilitating the utilization of inner sulfur due to its exposure to the electrolyte. Continuing discharge creates more long-chain polysulfides (Li_2S_6 , Li_2S_4), accounting for a quarter of the profile, which is a solid-liquid phase reduction. The second part also accounts for a quarter of the profile

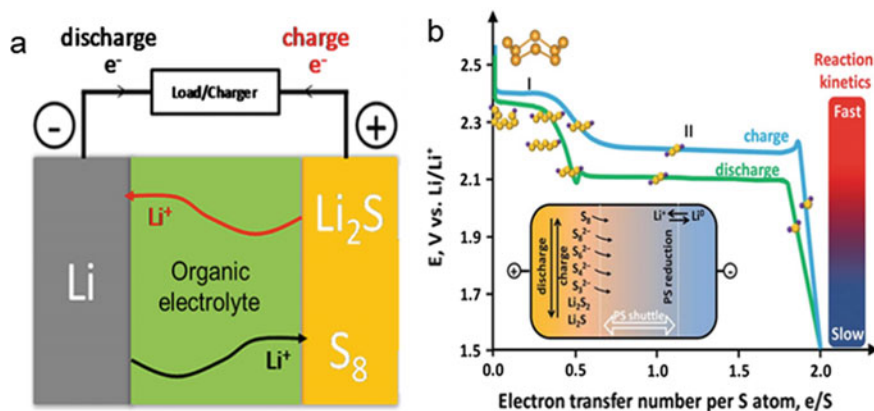


Fig. 5.2 **a** Illustration of the charge (red)/discharge (black) process in an ideal Li–S battery [2]; Reused with permission from Ref. [2] Copyright 2013 American Chemical Society. **b** Electrochemistry of sulfur showing an ideal charge–discharge profile. Inset: polysulfide shuttling [3]. Reused with permission from Ref. [3] Copyright 2013 The Royal Society of Chemistry

(plateau at *ca.* 2.0 V), corresponding to the reduction from Li_2S_4 to Li_2S_2 , which is a liquid–solid phase reduction. In this stage, the conversions of LiPSs become slow, resulting in their accumulation in the electrolytes, which thereby increase the viscosity of the electrolytes. When the electrolyte viscosity rises to a certain level, the lithium-ion transport will encounter some difficulties. Thus, the voltage drop in the sloping region reflects the concentration polarization (diffusion overpotential) in accordance with the increase in impedance. The third part is ascribed to the solid-state region, matching with the further reduction from Li_2S_2 to Li_2S , which contributes to the major portion of the capacity with a fixed voltage. In the reverse reaction, the oxidation of Li_2S back to LiPSs needs a large activation energy, which is made worse by their aggregation during their formation process, leading to slow reaction kinetics and low energy efficiency. Continuing charge corresponds to the upper charge plateau, representing the oxidation reactions in the dissolution region. At the end of recharge process, crystalline sulfur is recovered, completing the redox process [1].

5.2.2 Shuttling Phenomenon

As discussed above, the cathode reactions in Li–S batteries create a series of polysulfide ions (LiPSs), which are soluble in the organic ether-based electrolyte [6–8]. These dissolved PS bring numerous drawbacks. When the soluble polysulfides migrate out of the cathode region, they might not be re-utilizable, resulting in slow capacity fade during cycling. These highly active LiPSs can further react with the electrolyte, depleting both active materials and solvent molecules [9, 10]. Furthermore, they diffuse from cathode to anode easily driven by a concentration gradient, as

the polymeric separator cannot block their transport [11]. Once the LiPSs migrate to the anode side, they would be reduced by lithium metal to form insoluble short-chain $\text{Li}_2\text{S}_2/\text{Li}_2\text{S}$, causing severe irreversible capacity loss. The $\text{Li}_2\text{S}_2/\text{Li}_2\text{S}$ depositing on the Li anode can react with LiPSs, yielding soluble medium-chain ions, which diffuse back to the sulfur cathode. This mechanism can go round and round, even until the cell is reaching over its theoretical capacity. The whole process is known as the “shuttle effect” [1].

The LiPSs shuttling process can be detected by in-situ optical spectroscopy characterization techniques. As one of the most popular applied optical spectroscopic techniques, in-situ Raman can qualitatively or semi-quantitatively monitor the LiPSs dissolved in an ether-based electrolyte during cycling. Duan and co-workers [12] created a hole on both negative case and lithium metal foil to allow direct laser illumination on the separator and collection of the Raman signal from the separator at the side next to the lithium foil. The confocal Raman signal was taken from the separator/lithium interface, the signal accurately reflecting the LiPSs deposited on the separator. As shown in Fig. 5.3, the Raman signals of LiPSs were detected during the discharge–charge process, and the dissolved polysulfides shuttle severely especially at the upper plateau region of the charge curve.

The shuttle effect causes a series of issues that hinders the practical use of Li-S batteries. Such as the low Coulombic efficiency and unsatisfactory cycle life, and the origin of a self-discharge problem in on-shelf batteries during stocking or delivery. By increasing the percentage and total amount of sulfur in the whole cell, one would expect a multiplied LiPS shuttling due to a larger sulfur concentration gradient, which

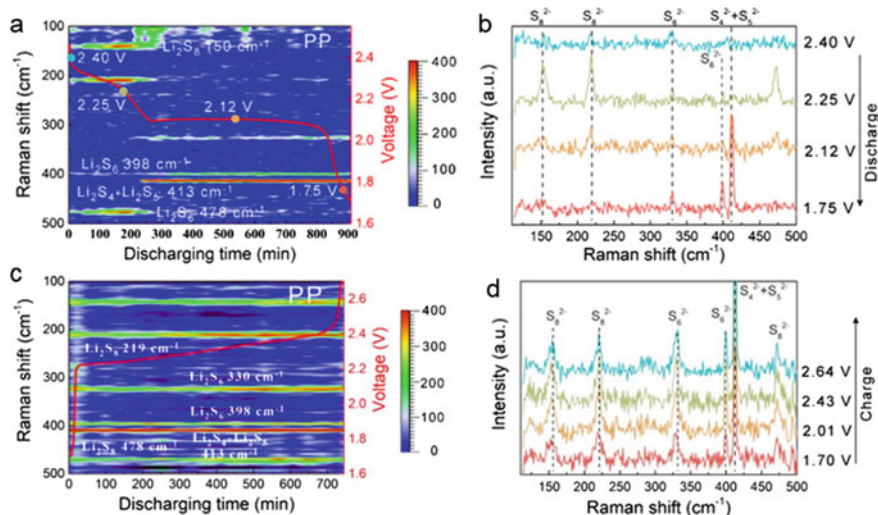


Fig. 5.3 a, c Time-resolved Raman spectra obtained during the discharge–charge processes of the battery with PP separator; b, d Selected original Raman spectra without background subtraction for the discharge–charge processes [12]. Reused with permission from Ref. [12] Copyright 2018 Elsevier Ltd.

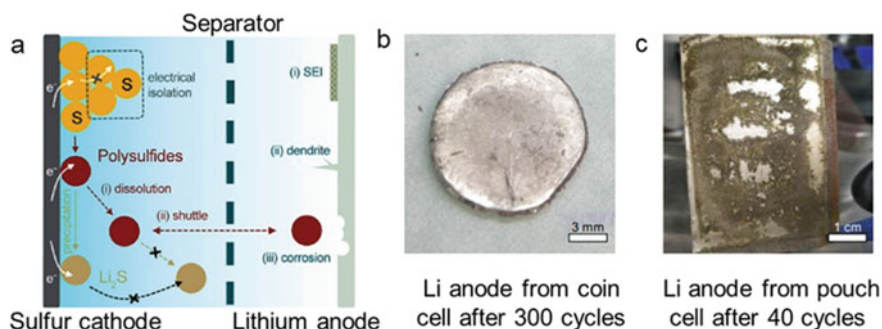


Fig. 5.4 **a** Schematic of a typical Li-S battery [13]; Reused with permission from Ref. [13] Copyright 2017 Wiley-VCH, **b** coin cell after 300 cycles, and **c** pouch cell after 40 cycles, showing vastly different Li deposition morphologies [14]. Reused with permission from Ref. [14] Copyright 2020 Elsevier Ltd.

makes it more difficult to inhibit the hazardous LiPSs crossover (Fig. 5.4a) [13]. The shuttle effect also results in severe corrosion of lithium anode, leading to the uncontrolled growth of lithium dendrites and raising severe safety hazards (Fig. 5.4b, c). In addition, due to the high reactivity of Li metal, the growth of Li dendrites exacerbates the reaction between the electrolyte and fresh Li metal. The resulting continuous consumption of electrolyte imposes a significant burden on lean-electrolyte Li-S batteries for the uncontrolled consumption of limited electrolyte, which eventually causes early termination of batteries due to the electrolyte depletion [14].

5.2.3 Remedies for Shuttling of LiPSs

To tackle these challenges, Nazar et al. reported a conductive mesoporous carbon framework to precisely constrain sulfur nanofiller growth within its channels in 2009 [15]. The structure provided access to Li^+ ingress/egress for reactivity with the sulfur. The sorption properties of the carbon aid in trapping the polysulfides formed during redox, thus achieving a reversible capacity up to $1,320 \text{ mAh g}^{-1}$ (Fig. 5.5). Since then, the Li-S battery has drawn overwhelming research attention due to the thirst for high energy storage systems, and employing sulfur-carbon composites is the most common and effective way to improve the cathode performance. Various carbonaceous materials, like Carbon black, microporous carbon, mesoporous carbon, hierarchical porous carbon, hollow carbon spheres, carbon nanotubes, carbon nanofibers, and graphene, have been employed as the host to confine active sulfur [16]. However, it was recognized by Zheng et al. that the weak interaction between nonpolar carbon-based materials and polar LiPSs/ Li_2S species leads to weak confinement and easy detachment of LiPSs from the carbon surface, with further diffusion into the electrolyte causing capacity decay and poor rate performance [17]. It is found that the capacity fading mechanism can be overcome by introducing amphiphilic polymers to

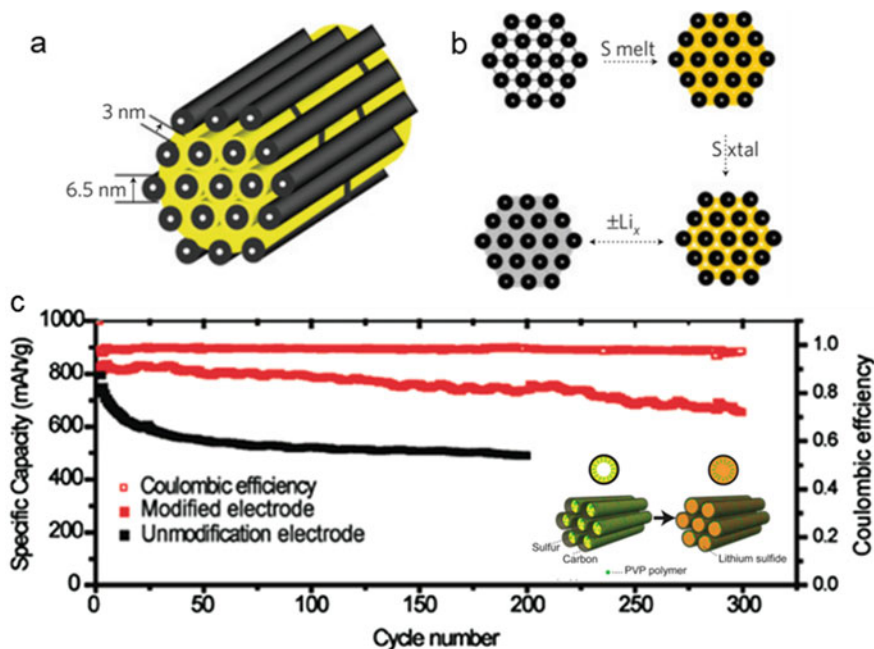


Fig. 5.5 **a** A schematic diagram of the sulfur (yellow) confined in the interconnected pore structure of mesoporous carbon, CMK-3 [15]; **b** schematic diagram of composite synthesis by impregnation of molten sulfur, followed by its densification on crystallization. The lower diagram represents subsequent discharging–charging with Li, illustrating the strategy of pore-filling to tune for volume expansion/contraction; **c** comparison of cycling performance at C/2 with and without the PVP modification. Inset: Schematics of the polymer modified sulfur cathode before (left) and after discharge (right) [15]. Reused with permission from Ref. [15] Copyright 2013 Springer Nature

modify the carbon surface, rendering strong interactions between the nonpolar carbon and the polar LiPSs. Afterwards, carbonaceous materials with heteroatoms (such as nitrogen, oxygen, boron, phosphorous, sulfur, or co-doping) for the generation of polar functional groups were adopted to enhance the interaction and immobilization of LiPSs species in the electrode and this strategy has shown great promise in trapping LiPSs [16, 18].

In addition to carbon, a wide variety of anchoring materials, such as metal oxides/sulfides/nitrides, have been introduced with polysulfide binding and trapping abilities [11, 19, 20]. It is proved that polysulfide binding and trapping can improve Li-S battery performance to some extent. However, the conductivity of these materials is relatively low, which inevitably compromises the rate capability and even the specific capacity. Therefore, it is still a great challenge to effectively restrict the electrochemical redox reactions of LiPSs in the cathode and at the same time achieve high sulfur utilization even at high current densities [21].

Another effective solution to the “shuttle effect” is proposed by Manthiram et al. They conceived an idea of inserting a bi-functional interlayer between the separator

and cathode, and the pores/carbon network can effectively capture the polysulfide intermediates (Fig. 5.6a) [22]. The interlayer not only serves as a polysulfide stock-room, but also offers additional electron paths covering the top surface of the cathode, leading to superior battery performance. Here the carbon interlayer can be regarded as another kind of separator to block the penetration of soluble polysulfides, resulting in less shuttle effect and better capacity retention. Afterwards, integrated separators are specially designed for Li–S cells to allow lithium ion flow but hinder polysulfide migration. For example, Zhou et al. presented a metal–organic framework (MOF)-based battery separator to mitigate the shuttling problem (Fig. 5.6b–d). The MOF-based separator acted as an ionic sieve in lithium-sulfur batteries, which selectively sieved Li^+ ions while efficiently suppressing undesired polysulfides migrating to the anode side. Therefore, a Li–S battery with a MOF-based separator exhibited a low capacity decay rate (0.019% per cycle over 1,500 cycles) [23].

In these strategies, LiPSs are trapped by the physical adsorption or by the chemical interaction onto the polar surfaces. However, these schemes are not able to provide enough active sites to immobilize such a large amount of LiPSs in the cathode, especially with high sulfur loadings. Furthermore, both these physical and chemical strategies are intrinsically the passive solutions, by which LiPSs are “confined” in

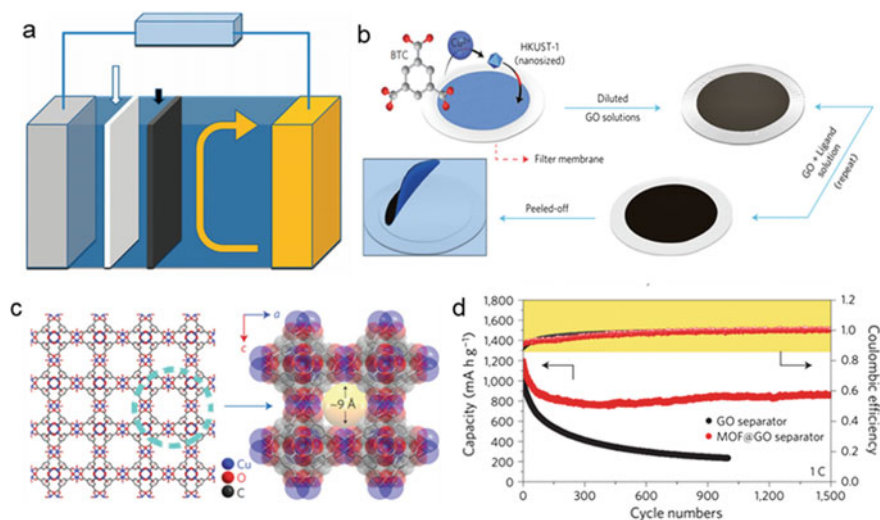


Fig. 5.6 **a** Schematic configuration of a Li–S cell with a bifunctional microporous carbon interlayer inserted between the sulphur cathode and the separator [22]; Reused with permission from Ref. [22] Copyright 2012 Springer Nature. **b** Schematic of the fabrication process to produce MOF@GO separators. The MOF nanoparticles and introduced GO laminates synergistically comprise a MOF@GO separator; **c** an illustration of the microporous crystalline structures (HKUST-1). The homogeneous coordinated structures are depicted as sticks, whereas the pores are highlighted in a space-filling representation; **d** cycling performance at a rate of 1 C over 1,500 cycles with MOF@GO separators and over 1,000 cycles with GO separators [23]. Reused with permission from Ref. [23] Copyright 2016 Springer Nature

the cathode region and “blocked” before they shuttle through the membrane. Hence, they are not the root solution to the shuttling problem. Therefore, a more positive strategy is required that accelerating the conversion of LiPSs during the sulfur redox to decrease the local concentration of LiPSs in the electrolyte, which can reducing the opportunities of the LiPSs shuttling.

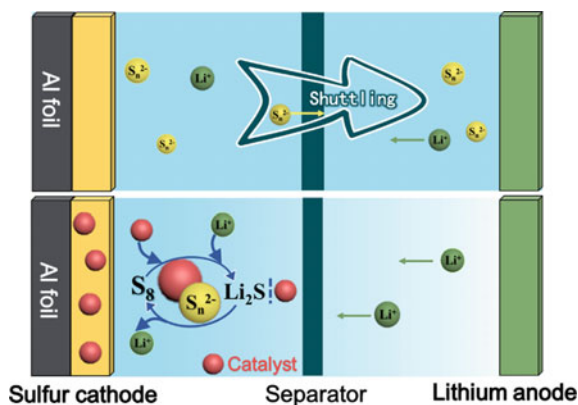
5.2.4 Introduction of Catalysis in Li-S Battery

Catalysis allows us to convert raw materials into valuable chemicals and fuels in an economical, efficient, and environmentally benign manner, which has numerous industrial applications in the chemical, food, pharmaceutical, automobile, and petrochemical industries. In the field of conventional chemical production, the catalyst is widely used to reduce the activation energy and increase the reaction rate. During an overall catalytic reaction, the reactants and products undergo a series of steps over the catalyst, including

- (i) diffusion of the reactants to the catalyst,
- (ii) formation of the adsorption complex (reactant surface),
- (iii) the chemical change on the surface,
- (iv) decomposition of the adsorption complex (product surface), and
- (v) diffusion of the reaction products from the catalyst.

Similarly, introducing the catalysis into the Li-S batteries also undergoes these steps as shown in Fig. 5.7. The redox of the sulfur species in Li-S batteries includes solid-liquid (elemental sulfur is reduced and adsorbed by the catalyst), liquid-liquid (the LiPSs accept electrons and continue to be reduced on the surface of the catalyst), liquid-solid (desorption of products from catalyst sites; Li_2S grows and nucleates on the surface of the catalyst), and solid-liquid (Li_2S loses electrons to form LiPSs and is adsorbed again by the catalyst) phase-conversion process during cycling.

Fig. 5.7 Schematic configuration of catalysis in accelerating the conversion of LiPSs and inhibiting the shuttle effect in Li-S batteries



The catalysis in the multi-step reaction reduces the reaction barrier and accelerates the liquid–solid process of LiPSs to $\text{Li}_2\text{S}_2/\text{Li}_2\text{S}$, thereby reducing the cumulative concentration of LiPSs in the electrolyte, which may be the proactive strategy to solve the shuttling problem.

Catalysis plays an important role in accelerating the conversion from long-chain LiPSs to insoluble discharge and charge products ($\text{Li}_2\text{S}/\text{S}_8$), inhibiting the shuttle effect. Until now, studies have proved that using well-designed catalytic materials, such as metal oxides, metal sulfides, metal nitrides, single atom catalysts, heterostructures, can facilitate polysulfide conversion, lowering the energy barriers in the reaction pathway. Unlike physical or chemical adsorbents, catalysts can be used in much smaller quantities to bring the battery capacity a big rise [24]. Recently, an article named a fundamental look at electrocatalytic sulfur reduction reaction was published in *Nature catalysis* to explore the reduction kinetics, activation energies and reduction mechanisms in Li–S batteries, which took a big step to the study of catalysis mechanism [25]. We believe that catalysis is a fundamental strategy to make Li–S batteries practical.

5.3 Catalytic Materials

5.3.1 Introduction

Li–S battery has extremely high energy density, but in the actual process, Li–S battery has some problems, such as low utilization of active substances, poor rate performance, short battery cycle life, and so on, which greatly restrict its practical use. Recently, unprecedented researches have focused on the development of catalytic materials to overcome the problems mentioned above. These materials significantly accelerate the conversion of lithium polysulfides (LiPSs), suppress the shuttle effect, and increase sulfur utilization. We aim to present a comprehensive and insightful overview of catalytic materials which can speed up the conversion of LiPSs and lower the barrier of sulfur redox. As presented in Fig. 5.8a, catalytic materials can be classified into two types. The first type is defined as metal-based catalysts, including metal oxides (e.g., MoO_2 , Nb_2O_5 , and VO_2), metal sulfides (e.g., CoS_2 , MoS_2 , and ZnS), metal nitrides (e.g., TiN , VN , and InV), single-atom catalysts (e.g., SA-Fe, SA-Co, and SA-Ni), and heterostructures (e.g., TiN-TiO_2 , MoN-VN , and $\text{TiO}_2\text{-Ni}_3\text{S}_2$). The second type, metal-free catalysts, including carbon materials and organic materials, can mediate the redox reaction of sulfur species. The number of publications of catalytic materials in Li–S batteries increases sharply by the year, as shown in Fig. 5.8b. Lastly, we put forward some possible measures for developing advanced catalytic materials of Li–S batteries with long cycle life and high-rate capacity.

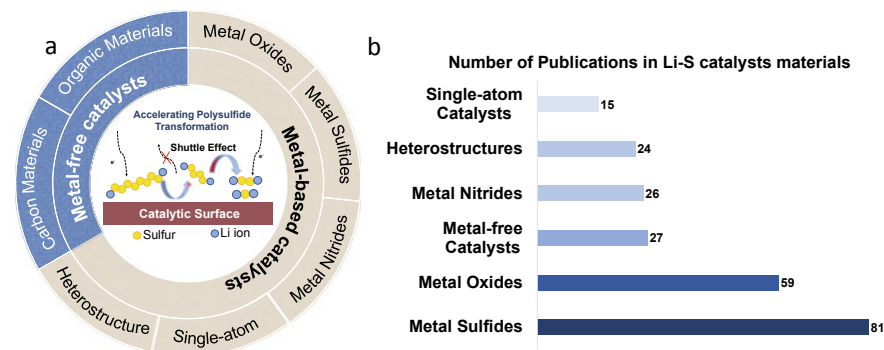


Fig. 5.8 a Schematic illustration of materials for Li-S batteries; b the number of publications of catalytic materials in Li-S batteries

5.3.2 Metal-Based Catalysts

Metal-based catalysts are the most important component for catalysis in Li-S batteries owing to their special electronic properties. Most metal compounds have polar surfaces suitable for chemical reactions with polysulfides. Recent works confirmed that metal-based catalysts can restrain the shuttle effect in Li-S batteries. In this section, some researches about metal-based catalysts are reviewed.

5.3.2.1 Metal Oxides

Metal oxides have strong catalytic activity for the reaction of LiPSs which are the first catalysts materials to be found. In 2014, Nazar et al. investigated Ti_4O_7 nanocrystals (with the highest conductivity) and confirmed that Ti_4O_7 showed a strong affinity for LiPSs and promoted the reduction of LiPSs than those on the carbon surface. X-ray photoelectron spectroscopy (XPS) analyses verified that O-Ti-O unites of Ti_4O_7 strongly interacted with Li_2S_4 and decreased shuttle effect by avoiding their dissolution in the electrolyte as shown in Fig. 5.9a [26]. The $\text{Ti}_4\text{O}_7/\text{S}$ electrode exhibited a low capacity decay of 0.08% per cycle at 0.5 C after 250 cycles. Lately, they reported the conversion of polysulfides to discharge product Li_2S can be promoted on an ultrathin MnO_2 nanosheet surface [27]. They proposed that the insoluble thiosulfate group was created on the surface of MnO_2 by the oxidation of initially formed LiPSs and the reduction of Mn^{4+} . And the active polythionate complex serves as an anchor to inhibit polysulfide dissolution into the electrolyte and control the deposition of Li_2S . The existence of thiosulfate and polythionate is confirmed by XPS. The oxidation of LiPSs followed by thiosulfate formation has also been observed on the surface of other metal oxides in the range of 2.4–3.05 V as shown in Fig. 5.9b. The metal oxides with slightly higher redox potentials facilitated LiPSs oxidation and the formation of thiosulfate, for example, CuO , VO_2 , and MnO_2 [28].

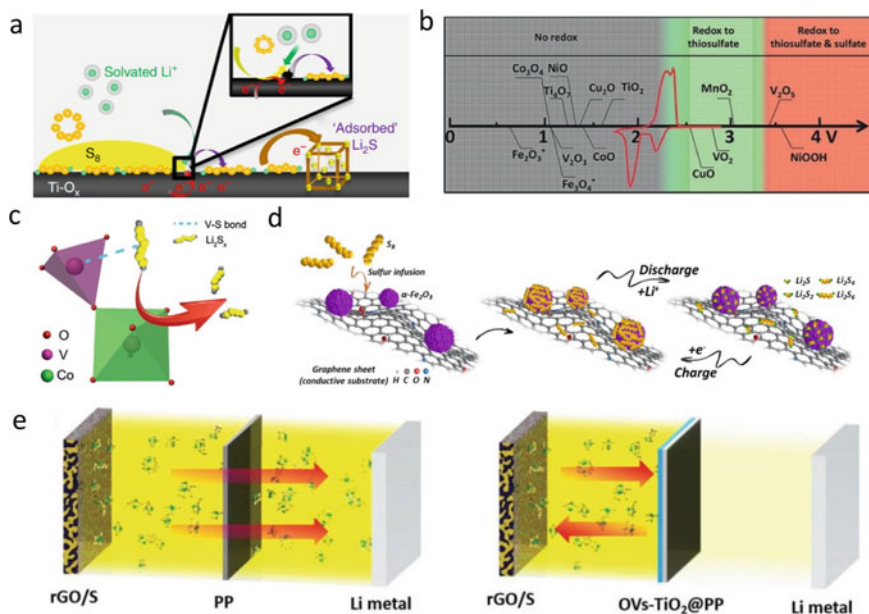


Fig. 5.9 **a** Diagram illustrating surface-mediated reduction of Li_2S from LiPSs on Ti_4O_7 [26]. Reused with permission from Ref. [26] Copyright 2014 Springer Nature. **b** Chemical reactivity of different metal oxides with LiPSs as a function of redox potential versus Li^+/Li , superimposed with a typical Li-S cyclic voltammety curve (shown in red) [28]. Reused with permission from Ref. [28] Copyright 2016 Wiley-VCH. **c** Schematic illustration of the synergistic mechanism between the LiPSs and the CVO [32]. Reused with permission from Ref. [29] Copyright 2019 Wiley-VCH. **d** Schematic of the conversion process of sulfur on a graphene surface with Fe_2O_3 NPs [38]. Reused with permission from Ref. [38] Copyright 2017, Elsevier Ltd. **e** Mechanism for inhibiting the shuttle effect of the PP separator and $\text{OVs-TiO}_2/\text{PP}$ separator [40]. Reused with permission from Ref. [40] Copyright 2020 Wiley-VCH

Recently, bi-metal based oxides are reported to show promising electrocatalysis for the conversion of LiPSs , including NiFe_2O_4 [29], $\text{Bi}_3\text{Ti}_4\text{O}_2$ [30], NiCo_2O_4 [31], and so on. Niu et al. proposed the “binary active sites” concept via the design of a flake-like cobalt vanadium oxide (CVO) modified separator, in Fig. 5.9c. Active vanadium sites anchored the LiPSs and active cobalt sites expedited the kinetic conversion of LiPSs , improving the sulfur utilization with the synergistic effect. The battery with CVO-based separator exhibits a high capacity of $1,253 \text{ mAh g}^{-1}$ at 0.1 C with the sulfur loading of 1.5 mg cm^{-2} . When the current density increases to 5 C, it remains a capacity of 505.6 mAh g^{-1} [32].

However, the poor conductivity of metal oxides limited the sulfur utilization and high-rate performance. Therefore, the incorporation of highly conductive materials is a key method to solve the problems, including $\text{Nb}_2\text{O}_5/\text{rGO}$ [33], VO_2 -Graphene [34], yolk-shelled $\text{C}/\text{Fe}_3\text{O}_4$ [35], $\text{Co}_3\text{O}_4/\text{acidified multiwall carbon nanotubes}$ [36], and so on. Yang et al. utilized ternary $\text{Fe}_3\text{O}_4/\text{porous carbon/graphene aerogel}$ to anchor polysulfide strongly and provide a fast conversion rate of LiPSs . The ordered

microchannel structure not only provides electron and lithium-ion transportation but also enhances the robustness of the aerogel structure. The composite cathode as the “catalytic center” can achieve an ultrahigh rate performance of 755 mAh g^{-1} at the rate of 3 C with a high sulfur loading of 7.7 mg cm^{-2} . Using in-situ XRD and DFT calculations revealed the mechanism of the reaction and the role of Fe_3O_4 in the anchoring and catalysis of LiPSs [37]. Yang et al. reported that Fe_2O_3 nanoparticles (NPs) increasingly promote the conversion of LiPSs to suppress shuttle effect [38]. Comparing with a pure graphene foam (PGM), a graphene foam containing Fe_2O_3 NPs (Fe-PGM) shows greater adsorption ability and stronger interaction with LiPSs (Fig. 5.9d). The composite cathodes deliver a capacity fade of 0.049% per cycle (over 1,000 cycles) at 5 C.

Oxygen-deficient sites have higher catalytic activity because oxygen vacancies facilitate electron transfer and the binding ability to polysulfides. The study of Zhang et al. revealed that oxygen vacancies catalyze the redox kinetics of polysulfides during cycling by propelling the electron/ Li^+ transport on the vacancy-enriched surface. Because the vacancies enhanced the affinity of TiO_2 toward LiPSs, the TiO_2/S composite cathode manifests high-rate performance (572 mAh g^{-1} at 2 C) and excellent cycling properties ($1,472 \text{ mAh g}^{-1}$ at 0.2 C) [39]. Besides, Mai et al. used DFT calculations to verify that the oxygen vacancies in TiO_2 decorated polypropylene ($\text{OVs-TiO}_2/\text{PP}$) greatly enhances the catalytic ability and the ion and electron conductivities (Fig. 5.9e). The oxygen vacancy generation increased OVs-TiO_2 polarity. Under a high sulfur loading (7.1 mg cm^{-2}), the electrode with OVs-TiO_2 -modified separator exhibited a stable electrochemical performance at 2 C after 500 cycles (an aerial capacity of 5.83 mg cm^{-2}) [40].

5.3.2.2 Metal Sulfides

Transition-metal sulfides (MSs, $\text{M} = \text{Co}, \text{Ti}, \text{Ni}, \text{Fe}, \text{Cu}, \text{V}, \text{Mn}, \text{W}, \text{and Mo}$) have shown great advantages due to their strong chemical interaction with LiPSs, triggering widespread attention for Li-S batteries. The large polar surface of transition-metal sulfides promotes high catalytic activity on the redox of sulfur species. What's more, transition-metal sulfides have high tap density, which is beneficial to the volumetric energy density of LSBs. Comparing with the transition-metal oxides, metal-sulfides possess high conductivity and enhance the electronic transmission capability of cathodes owing to the delocalized electronic structures [41].

Metal sulfides with 2-dimension (2D) layered structures contain two atomic configurations (basal plane and edge sites). The catalytic active sites are mainly edge sites. Cui et al. supposed that on the edge sides of MoS_2 , the conversion of LiPSs to insoluble Li_2S occurred selectively. The edge sites have stronger binding energies with Li_2S than the basal plane does [42]. Lately, they used a self-assembled ultrathin MoS_2 (only increasing 1% of cathode weight) as an interlayer to provide high density of catalytic active flake edges effectively mitigating the LiPSs diffusion, in Fig. 5.10a [43]. Besides, Arava et al. investigated the edge sites of WS_2 and MoS_2 and also confirm the edge sites were beneficial for adsorption of LiPSs [44]. Recently,

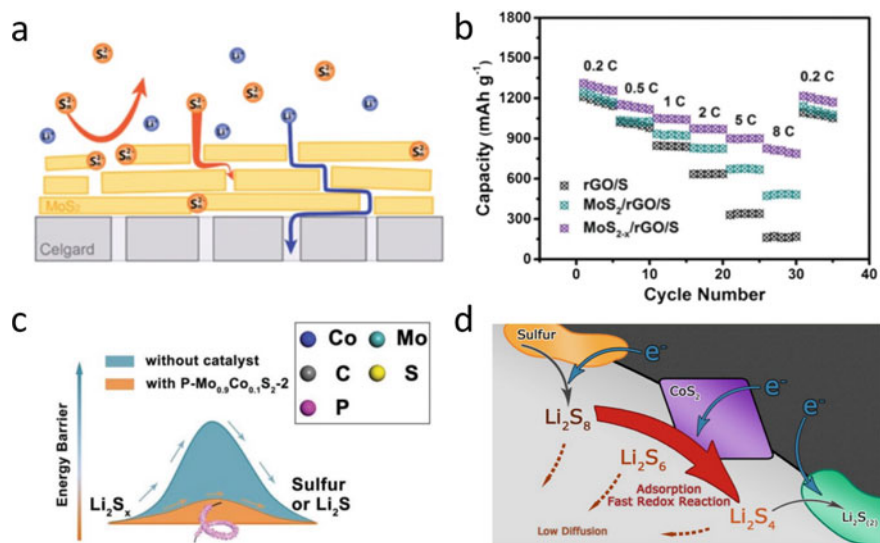


Fig. 5.10 **a** Illustrates the ion-transport processes at MoS₂-coated separator and the polysulfide anion adsorption at MoS₂ flakes. Reused with permission from Ref. [43] Copyright 2019 American Chemical Society. **b** Galvanostatic discharge–charge of rGO/S, MoS₂/rGO/S and MoS_{2-x}/rGO/S cells in the 1.8–2.6 V voltage range at 0.5 C (1 C = 1675 mA g⁻¹ based on the mass of sulfur) [45]. Reused with permission from [45] Copyright 2017 The Royal Society of Chemistry. **c** CoS₂-incorporated carbon/sulfur cathode where polysulfide reduction is accelerated and polysulfide diffusion is weakened [11]. Reused with permission from Ref. [11] Copyright 2016 American Chemical Society. **d** The energy barrier in Li₂S_x conversion reactions with and without P-Mo_{0.9}Co_{0.1}S₂₋₂ catalyst [46]. Reused with permission from Ref. [46] Copyright 2019 Wiley–VCH

more researches have been carried out around 2D-layered MoS₂. Lee et al. designed MoS_{2-x}/reduced graphene oxide (MoS_{2-x}/rGO) to catalyze the polysulfide reactions and accelerate the conversion of LiPSs. The deficiencies in MoS₂ edge sites have shown great electrochemical activity for Li₂S deposition. After adding MoS_{2-x}/rGO, the cathode exhibited better high-rate performance (capacity of 826.5 mAh g⁻¹ at 8 C) and stable cycle life (Fig. 5.10b) [45].

Aside from 2D-layered MoS₂, pyrite-type CoS₂ has also been investigated. Zhang et al. firstly found that CoS₂ can enhance the LiPSs redox owing to its electrical conductivity and strong sulfiphilic affinity (Fig. 5.10c) [11]. The electrodes with the mixing of graphene and CoS₂ microparticles deliver a high initial capacity of 1,368 mAh g⁻¹ at 0.5 C. With the CoS₂ content increasing from 0 to 30 wt%, the current density of cyclic voltammograms test for symmetrical cells also increased, which points out that charge transfer at a CoS₂-LiPSs interface is faster than a graphene-LiPSs interface. A subsequent study of this team proved that simultaneous cobalt and phosphorus doping of MoS₂ nanotubes can improve the electrical conductivity of MoS₂ and also provide a catalyst surface with the Co-P coordinated sites for the conversion reactions of polysulfide as shown in Fig. 5.10d [46]. The experimental results confirmed that the cobalt doping activates the transformation of MoS₂ from

2 H to metallic 1 T phase. The Co-P doping MoS₂-based cathode can reduce the capacity fade from 0.28% per cycle to 0.046% per cycle. The high-rate performance can achieve 931 mAh g⁻¹ at 6 C.

5.3.2.3 Metal Nitrides

The conductivity of transition metal nitrides is higher than those of metal oxides and sulfides [47, 48]. Electron-rich nitrogen can restrict shuttling of polysulfide ions to some extent because the electron transfer between the polar metal nitride and can accelerate the conversion of the intermediate products [49]. In recent years, metal nitrides have been extensively studied [50–55]. Zhang et al. provided that the introduction of a monometallic compound, similar to the alloying strategy for metal catalyst design. Using in situ extrinsic-metal etching strategy, an inert monometal nitride of hexagonal Ni₃N through iron incorporated cubic Ni₃FeN (Fig. 5.11a), rendering a highly active vacancy-rich phase to promote the high-speed conversion of polysulfides. The Li-S batteries modified with Ni₃FeN exhibited superb rate ability (a capacity of 822 mAh g⁻¹ at 3 C) and cycling stability (89% capacity retention after 150 cycles at a sulfur loading of 4.8 mg cm⁻²). This work broadens the exploration of elucidates catalytic surface reactions and the role of defect chemistry [56].

The sluggish reduction reaction of long chain sulfur species to short-chain polysulfides critically impedes the complete use of active sulfur. Abundant exposed active sites for sulfur species enhance the decomposition of Li₂S and the sulfur species

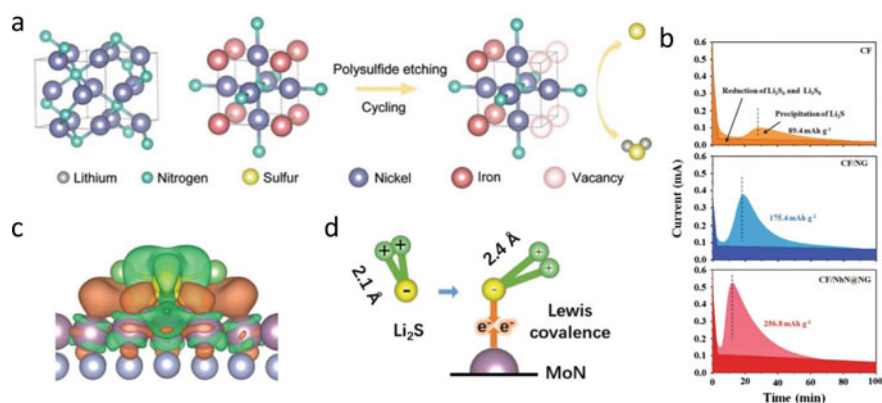


Fig. 5.11 **a** Atomic structure model of hexagonal Ni₃N and cubic Ni₃FeN and illustration of the polysulfide etching process toward an active Ni₃FeN phase [56]; Reused with permission from Ref. [56] Copyright 2018 Wiley-VCH. **b** Potentiostatic discharge curves of a Li₂S₆ solution employing CF, CF/NG, and CF/NbN@NG as current collectors at 2.08 V on different surfaces [58]; reused with permission from Ref. [58] Copyright 2019 American Chemical Society. **c**, **d** Charge density difference plot for Li₂S interacting with MoN. The orange (green) distribution corresponds to charge accumulation (depletion); Representation of the covalence-activation mechanism on MoN [59]. Reused with permission from Ref. [59] Copyright 2019 Wiley-VCH

utilization [57]. Yang et al. designed a multifunctional catalytic separator composed of niobium nitride/N-doped graphene (NbN/NG) along the polysulfides/electrolyte. The catalytic interface enabled by NbN anchored on NG is tailoring the Li_2S nucleation-growth-decomposition process (Fig. 5.11b) [58]. Firstly, the NbN/NG interface can govern the uniform growth of Li_2S . Secondly, the graphene support with N dopant can afford a stable interconnected network to boost Li-ion transport. With these advantages, the Li-S batteries can remain 621.2 mAh g^{-1} at 3 C and 81.5% capacity retention after 400 cycles. Zhang et al. developed a MoN-based interlayer sandwiched between the C-S cathode and the separator, which efficiently accelerates the decomposition of Li_2S . MoN efficiently catalyzes the cleavage of Li-S band in Li_2S and facilitates the migration of the produced Li^+ , as shown in Fig. 5.11c, d. As a result, the cathodes with the MoN-modified interlayer provided super cycling stability with a low capacity fading rate of 0.023% per cycle during 1,500 cycles at 1 C. With the high sulfur loading (7.0 mg cm^{-2}), the electrodes can achieve a high areal capacity of 6.02 mAh cm^{-2} at 1 C [59].

5.3.2.4 Single-Atom Catalysts

Normally metal- or metal oxide-based catalysts would add extra weight to the batteries and sacrifice the energy density. The single-atomic catalysts (SACs) with maximal atom utilization and large surface coverage combine the merit of heterogeneous and homogeneous catalysts. The unique electronic structure and unsaturated coordination environments of the active centers in SACs have been demonstrated to improve catalytic activity in Li-S batteries.

It is known that iron cobalt and nickel are both effective SACs and have been widely used for the design of Li-S batteries. Yang et al. for the first time reported the use of SACs to accelerate the LiPSs redox conversion in Li-S battery. They designed rich single-atom Fe sites with a matrix of porous carbon (Fe-PNC) through polymerization and pyrolysis of diphenylamine with iron phthalocyanine and a hard template. The Fe-PNC/S electrode not only remained a high capacity (557.4 mAh g^{-1}) at 0.5 C after 300 cycles, but also enhanced discharge capacity at high rates due to the strong Fe-LiPSs interactions, as shown in Fig. 5.12a, which paves an effective method for the conversion of soluble LiPSs to the insoluble Li_2S particles [60]. Zhang et al. prepared a Li_2S cathode with distributed Fe SACs supported on porous nitrogen-rich carbon matrices. The cathodes using Fe SACs showed a superior high-rate performance (a high specific capacity of 589 mAh g^{-1} at 12 C) and a long cycle at 5 C. In-situ and ex-situ X-ray absorption spectroscopy, theoretical simulations confirmed that Fe center first coordinates with Li_2S and dramatically decreases the energy barriers for breaking Li-S band, revealing the catalytic effect of Fe SACs (Fig. 5.12b) [61].

More complete works explain the great prospects of Co SACs for the design of high-performance Li-S batteries. Wan et al. proposed a structure that cobalt atoms embedded in nitrogen-doped graphene (Co-N/G) as a bifunctional electrocatalyst. Co-N/G could not only facilitate the electrochemical kinetics during the change

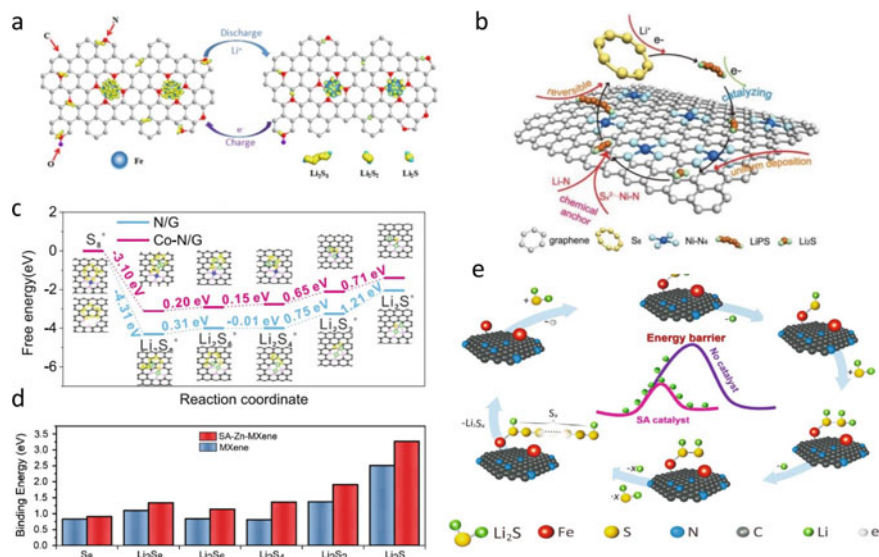


Fig. 5.12 **a** Schematic illustration of the conversion process of LiPSs on the Fe-PNC surface with single-atomic iron catalytic sites [60]; Reused with permission from Ref. [60] Copyright 2018 American Chemical Society. **b** A proposed mechanism for SAFe catalyzed Li₂S delithiation reaction [61]; Reused with permission from Ref. [61] Copyright 2018 Elsevier Ltd. **c** Energy profiles for the reduction of LiPSs on N/G and Co-N/G substrates. (insets) The optimized adsorption conformations of intermediate species on N/G and Co-N/G substrate [62]; Reused with permission from Ref. [62] Copyright 2019 American Chemical Society. **d** Binding energies between lithium polysulfides and SA-Zn-MXene layers and between lithium polysulfides and MXene layers [64]; Reused with permission from Ref. [64] Copyright 2020 Wiley-VCH. **e** The catalytic mechanism of the LiPSs on the surface of Ni@NG in electrochemical process [65]. Reused with permission from Ref. [65] Copyright 2019 Wiley-VCH

between LiPSs and insoluble Li₂S but also accelerate the decomposition of Li₂S (Fig. 5.12c). The composite cathode can deliver a capacity of 5.1 mAh cm⁻² at 0.2 C over 100 cycles [62]. Besides, Zhang et al. implanted atomic cobalt within the skeleton of mesoporous carbon (SC-Co) via a supramolecular self-templating strategy. The atomic cobalt dopants as active sites improve the kinetics of the sulfur redox reactions. The Li-S batteries with the SA-Co functional interlayer demonstrate high discharge capacity (837 mAh g⁻¹ at 0.5 C) for 300 cycles [63].

Yang et al. confirmed that single atom zinc implanted MXene (SA-Zn-MXene) can decrease the energy barriers from Li₂S₄ to Li₂S₂ and achieve strong interaction with LiPSs because of the high electronegativity of atomic zinc atoms as shown in Fig. 5.12d. Moreover, the zinc atoms homogeneously dispersed on MXene layers can also accelerate the nucleation of Li₂S. The SA-Zn-MXene-based sulfur cathode exhibits a high rate capability (640 mAh g⁻¹ at 6 C) and 80% capacity retention after 200 cycles at 4 C [64].

In fact, the cathode requires a large number of SACs to catalyze the conversion of LiPSs, whereas the separator demands only a low SACs loading due to the planar

architecture. So the incorporation of SACs on the separator seems to be a better option [66]. Xie et al. firstly coated graphene foams with Fe SACs at an extremely low metal loading of 20 mg onto a polypropylene to obtain a SACs-modified separator, which provided the strong adsorb ability of Li_2S_6 compared with Co and Ni SACs. They also found that the Fe SACs-modified separator reduced the voltage gap between the second discharge plateau and charge plateau from 0.48 to 0.24 V and enhance the redox kinetics of LiPSs [67]. Niu et al. also introduced Ni SACs to modify the commercial separators in Li-S batteries. The Ni-SACs modified separator delivered a better rate performance (a specific capacity of 612 mAh g^{-1} at 10 C), which demonstrated that the effective catalysis of LiPSs conversion due to the high activity of Ni SAC (Fig. 5.12e). Spectroscopic characterizations confirmed the formation of Ni-S bond through housing the electrons of polysulfide anions into the unfilled d orbitals of Ni centers. This work affords Ni atom as a new metal option of SACs to accelerate the conversion of LiPSs [65].

Despite some recent researches about SACs catalysis [68–71], there are still some confusions about the use of SACs with high catalytic activity for polysulfides. How do we select the ideal metal atoms for SACs in S cathode? And how to design more effective SACs support? If SACs are anchored on oxides, nitrides, and sulfides, they might show much higher catalytic activity due to the different coordination environments. And defect engineering should be introduced to provide sufficient active sites for SACs [72]. Besides, a deep understanding of the catalytic mechanism of SACs should be obtained at the atomic level through *in-situ* techniques.

5.3.2.5 Heterostructures

It is important to design a series of catalytic materials simultaneously with strong adsorption capacity for LiPSs and good electron conductivity facilitating charge transport. Therefore, some heterostructured catalytic materials attract researchers' attention due to their synergistic effects. Most metal oxides provide stronger adsorption of LiPSs due to the large surface but have low conductivity and poor electrocatalytic activity. The metal sulfides, metal nitrides, metal carbides, and metal phosphides have been demonstrated to show highly electrocatalytic activity but poor adsorption ability. As a result, it is a promising strategy to combine metal oxides and metal sulfides to construct heterostructures for achieving both excellent adsorption and electrocatalytic activity.

A twinborn heterostructure of TiO_2 -TiN loading onto graphene was firstly synthesized by Yang et al. [73]. The trapping of TiO_2 and the quick electron transfer of TiN have a great effect on the fast diffusion of LiPSs as shown in Fig. 5.13a. The contacted interface between TiN and TiO_2 efficiently avoided the accumulation of LiPSs and improved their utilization. Therefore, the TiO_2 -TiN-based electrodes show long cycle life with high sulfur loadings of 3.1 and 4.3 mg cm^{-2} compared to TiO_2 - and TiN-based electrodes. Following this study, some works about the heterostructure of metal oxide-metal nitrides have been published. Liu et al. designed an in situ VO_2 -VN binary host which combines the facile ionic diffusion properties of VO_2 and

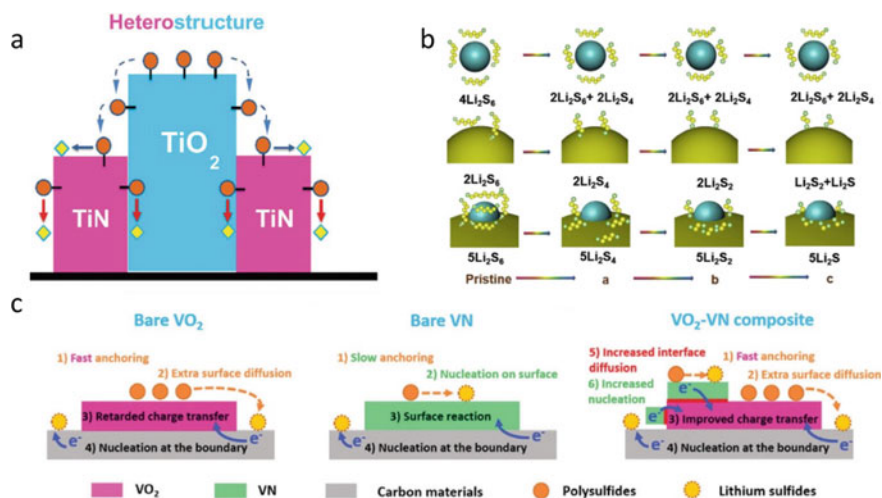


Fig. 5.13 **a** Schematic of the conversion process of LiPSs on the TiO₂-TiN heterostructure [73]; Reused with permission from Ref. [74] Copyright 2017 The Royal Society of Chemistry. **b** Schematics of LiPS anchoring-diffusion-conversion processes on VO₂, VN and VO₂-VN binary host surfaces [88]; Reused with permission from Ref. [88] Copyright 2018 The Royal Society of Chemistry. **c** Schematic illustration of polysulfide redox reaction on the surfaces of CoO, Co₉S₈, and Co₉S₈/CoO [79]. Reused with permission from Ref. [79] Copyright 2019 Elsevier Ltd.

high electrical conductivity of VN to accomplish smooth immobilization-diffusion-conversion of LiPSs in Fig. 5.13b. The VO₂-VN binary host-based cathodes show a high rate capability with 1105 and 935 mAh g⁻¹ at 1 C and 2 C. After 800 cycles at 2 C, the cathodes remained a better performance even with a high sulfur loading of 4.2 mg cm⁻².

On the other hand, metal sulfides, like CoS₂, MoS₂, and WS₂, show good catalytic performance during the redox reaction of LiPSs [74–76]. In this regard, Yang et al. reported the WS₂-WO₃ heterostructures which keep a balance of trapping ability and catalytic ability toward LiPSs [77]. The cathode with 5 wt% WS₂-WO₃ heterostructures shows a high capacity retention of 86.1% after 300 cycles at 0.5 C and 864 mAh g⁻¹ at 3 C. Subsequently, they designed a bidirectional TiO₂-Ni₃S₂ heterostructure. This heterostructure can accelerate both reduction of soluble LiPSs and the oxidation of insoluble discharge products. The intimately bonded interfaces between TiO₂ nanoparticles on Ni₃S₂ surfaces play a good role in the conversion of LiPSs and the dissolution of Li₂S. The composite cathodes with TiO₂-Ni₃S₂ deliver the capacity of 504 mAh g⁻¹ with sulfur loadings of 3.92 mg cm⁻² after 500 cycles [78]. Zhao et al. synthesized the CoO nanoparticles decorated Co₉S₈ heterostructures with well-defined interfaces (Fig. 5.13c) [79]. CoO provides a high surface area to adsorb LiPSs; simultaneously, Co₉S₈ has excellent electrocatalysis function in the conversion to Li₂S. The multifunctional separator with Co₉S₈/CoO heterostructure can prevent the diffusion of LiPSs by both physical and chemical blocking.

With the synergistic adsorption-electrocatalysis function, $\text{Co}_9\text{S}_8/\text{CoO}$ heterostructure exhibits a Coulombic Efficiency of approximately 100%. When the sulfur loading is 2.5 mg cm^{-2} , the composite electrode shows a specific capacity of 925 mAh g^{-1} at 1 C. Other heterostructured catalytic materials, including $\text{TiO}_2\text{-MXene}$ [80], MoC-MoO_x [81], $\text{MoS}_2@\text{GO}$ [82], $\text{VO}_2\text{-V}_2\text{C}$ [83], and TiC-graphene [84] also exhibited synergistic effects and promote the development of catalytic materials in Li-S batteries [85–87].

5.3.3 Metal-Free Catalysts

Metal-free catalysts are promising to increase the energy density due to their lightness, which can be divided into two classes: inorganic and organic materials. Most of the inorganic catalysts are carbon materials. Mai et al. prepared the N-doped porous carbon cages (NHSC) as sulfur host, which showed a good catalytic activity to facilitate the reduction of low-order polysulfides owing to a high pore volume and continuous electron and ion transport paths. A Li-S cell with the S@NHSC cathode achieved a high initial capacity of $1280.7 \text{ mAh g}^{-1}$ [89]. The microporous organic polymers with strong chemical adsorption sites and definite molecular composition have attracted considerable attention in Li-S batteries. Zhang et al. synthesized porphyrin organic framework hollow spheres (POF-HSs). Due to the polar chemical structures and hollow spherical morphology, POF-HSs efficiently mitigate the shuttling of LiPSs and speed up the reaction of polysulfides in Li-S batteries.

The development of various carbon frameworks and adsorbents has made great progress on Li-S batteries. However, non-polar carbon interacts weakly with the polar LiPSs in solution resulting in poor binding and the sluggish transfer of electron. Catalytic materials, for example metal oxides, metal sulfides, metal nitrides, SACs, and so on, speed up the redox kinetics of conversion reactions and decrease the kinetic energy barrier for the nucleation of Li_2S . Although a lot of achievements of high catalytic activity materials in Li-S batteries have been realized, several challenges and a lot of room for investigations in catalysis design still remain. Rational design of the structure is a key factor in catalytic materials. Both 2D materials with a large area surface and 3D materials with network structures help improve the catalytic activity. Besides, the effective catalysts should have high conductivity to allow the easy contact between the electron and lithium-ion because the migration and coupling of ions and electrons are significant to realize the fast conversion of LiPSs.

5.4 Catalysis Mechanism

5.4.1 *Bottlenecks of Catalysis in Li-S Batteries*

To solve the problem of sluggish kinetics of sulfur species conversion, it is a good way to borrow ideas from chemical industry. Many chemical reactions are thermodynamically feasible, but they cannot occur at a significant rate on their own; therefore, catalysts are widely used to reduce the activation energy of the reaction and increase the conversion rate. Since the reaction process of sulfur species in Li-S batteries is an electrochemical process, similar to catalysis for chemical reactions, it is one of the most effective approaches to introduce electrocatalysts to the electrodes to improve the reaction kinetics, thus can solve the shuttle effect fundamentally.

In the past few years, the design of electrocatalysts in Li-S batteries and the exploration of their catalysis mechanism have gradually become the research hotspots. However, the catalysis mechanism in Li-S batteries is still in its infancy and its theoretical system is not well-developed yet. While the field of electrocatalysis and traditional chemical industry have relatively mature theoretical system after a long period of development, which is just like a treasure trove of knowledge offering Li-S batteries researchers ideas that could be applied to Li-S batteries. Inspired by the enhancement to the reaction kinetics of electrocatalytic electrodes in aqueous polysulfides in photoelectrochemical solar cells and redox flow cells, Babu et al. first introduced the electrocatalysis concept of LiPSs conversion in Li-S batteries in 2015 [90]. Use of electrocatalytic current collectors such as Pt or Ni when coated on Al foil has shown to improve the reaction kinetics of the Li-S battery. Fe_2O_3 is a kind of common desulfurizer in chemical industry. Zheng et al. used the idea of traditional desulfurization catalyst, introducing Fe_2O_3 loaded on graphene as the sulfur host for Li-S batteries [38]. Such cathode exhibits good electrocatalytic performance, which can restrain shuttle effect by chemically adsorbing LiPSs thermodynamically and accelerate the transformation of the soluble LiPSs to insoluble products.

In order to get a further understanding of the catalysis mechanism of sulfur species reaction in Li-S batteries, researchers have devoted great efforts in selecting catalyst activity parameters to evaluate the catalytic performance of catalysts and exploring the nature of catalytic activity. This will be discussed in more detail in the next two sections.

5.4.2 *Parameters of Catalytic Activity*

In the study of electrocatalysis, some parameters are usually used to evaluate the electrocatalytic activity of electrocatalysts. To date, extensive investigations have referred to the electrocatalytic parameters to describe the improvement of electrochemical reaction kinetics so as to measure the electrocatalysts performance in Li-S batteries.

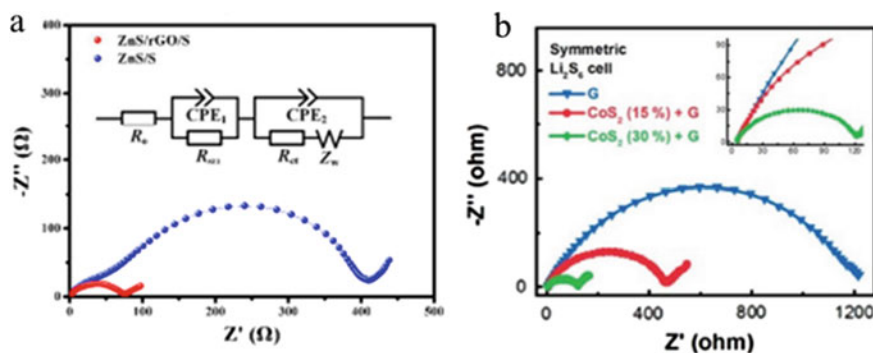


Fig. 5.14 **a** EIS plots of Li-S cells (inset shows the fitting equivalent circuit) [92], Reused with permission from Ref. [92] Copyright 2020 Elsevier Ltd. **b** EIS plots of symmetrical Li_2S_6 - Li_2S_6 cells [11], Reused with permission from Ref. [11] Copyright 2016 American Chemical Society

5.4.2.1 Resistance of Electrochemical Impedance Spectroscopy (EIS)

Electrochemical impedance spectroscopy (EIS), as one of the most powerful electroanalytical tools, has been widely used for investigating kinetics in different electrochemical systems. A typical EIS spectrum consists of two semicircles in high and middle frequency and a sloping line in low frequency. The semicircles represent the resistance of charge transfer (R_{ct}) and SEI (R_{SEI}), and the intercept reflects the resistance of bulk electrolyte (R_e). The sloping line represents the Warburg impedance (W_0) associated with the Li^+ diffusion in the electrode [91]. A conformal zinc sulfide/reduced graphene oxide/elemental sulfur ($\text{ZnS}/\text{rGO}/\text{S}$) composite is synthesized by Peng et al. and utilized as sulfur host in Li-S batteries (Fig. 5.14a) [92]. R_{ct} and R_{SEI} of the $\text{Li}||\text{ZnS}/\text{rGO}/\text{S}$ cell (61.71 and 10.49 Ω) are smaller than those of the $\text{Li}||\text{ZnS}/\text{S}$ cell (349.3 and 52.71 Ω), indicating the fast charge transfer and suppressed electrochemical polarization of the $\text{ZnS}/\text{rGO}/\text{S}$ electrode. Yuan et al. added CoS_2 to a carbon/sulfur cathode in Li-S batteries [11]. EIS plots of the symmetrical Li_2S_6 - Li_2S_6 cells (Fig. 5.14b) indicate that charge transfer at a CoS_2 -LiPSs interface is much faster than that at a graphene-LiPSs interface, suggesting an increase of the electrochemical reaction kinetics with the help of CoS_2 .

5.4.2.2 Shift Peak and Current Density of Cyclic Voltammetry (CV) Curves

Cyclic voltammetry (CV) is operated based on the Nernst equation which displays a peaked current-potential curve. During the CV test, a linearly swept potential (incentive) at a scan rate of v is applied to the electrode, and the redox reactions at the interface between electrode and electrolyte could be detected by measuring the response current (Fig. 5.15a). The peak potentials of the CV curves are related to the charge transfer barrier in a same system. Therefore it could be used for qualitative

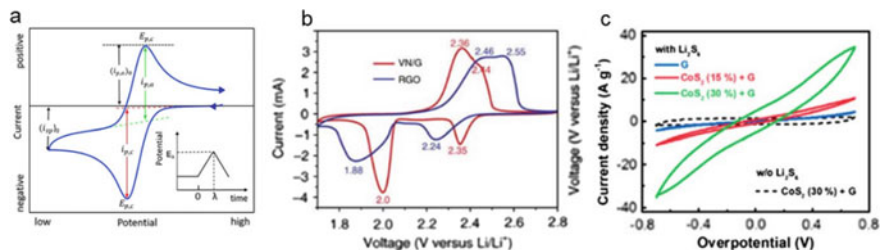


Fig. 5.15 **a** Schematic CV curve of a simple reversible reaction (inset shows the voltage change during the CV scan) [93]. Reused with permission from Ref. [93] Copyright 2019 Wiley-VCH. **b** CV curves of Li-S cells with VN/G and RGO cathodes at a scan rate of 0.1 mV s^{-1} [94]. Reused with permission from Ref. [94] Copyright 2017 Springer Nature. **c** CV curves of symmetrical Li_2S_6 - Li_2S_6 cells [11]. Reused with permission from Ref. [11] Copyright 2016 American Chemical Society

comparison of the reaction kinetic [93]. Sun et al. proposed a conductive porous vanadium nitride/graphene (VN/G) composite as cathode and used Li_2S_6 catholyte as the active material (Fig. 5.15b) [94]. The CV profile shows that the introduction of VN leads to higher reduction potentials and lower oxidation potentials than that of the reduced graphene (RGO) cathode, suggesting improved redox kinetics. To investigate the kinetics of reaction transformation between LiPSs, the CV test based on symmetrical cells is considered as a more straightforward approach (Fig. 5.15c) [95]. It consists of two identical electrodes with lithium polysulfide (Li_2S_8 , Li_2S_6 , or Li_2S_4) as the active material, showing an OCV of 0 V. The polarization curves can be directly related to the redox current of lithium polysulfide, thus a higher current density indicates faster reaction kinetics [11]. Using graphene combining CoS_2 as the electrode, an order of magnitude higher current density is obtained than that with the graphene-only electrode, indicating that CoS_2 dynamically accelerates the sulfur species conversion.

5.4.2.3 Li Ion Diffusion Coefficient

The kinetics of ion diffusion can be compared by cyclic voltammetry with different scan rates. With the increasing scan rates, the cathodic peaks shift to lower potential and the anodic peaks shift to higher potential, while all the peak current density levels up. The cathodic and anodic current peaks are linearly correlated with the square root of scanning rates reflecting the diffusion-controlled process. The Li^+ diffusion coefficients can be estimated from the Randles-Sevcik equation [96].

$$I_p = (2.69 \times 10^5) n^{3/2} A D_{\text{Li}}^{1/2} C_{\text{Li}} v^{1/2}, \quad (5.1)$$

where I_p is the peak current, n is the number of electrons per reaction, D_{Li} is the Li^+ diffusion coefficient, C_{Li} is the concentration of Li^+ in cathode, A is the geometric

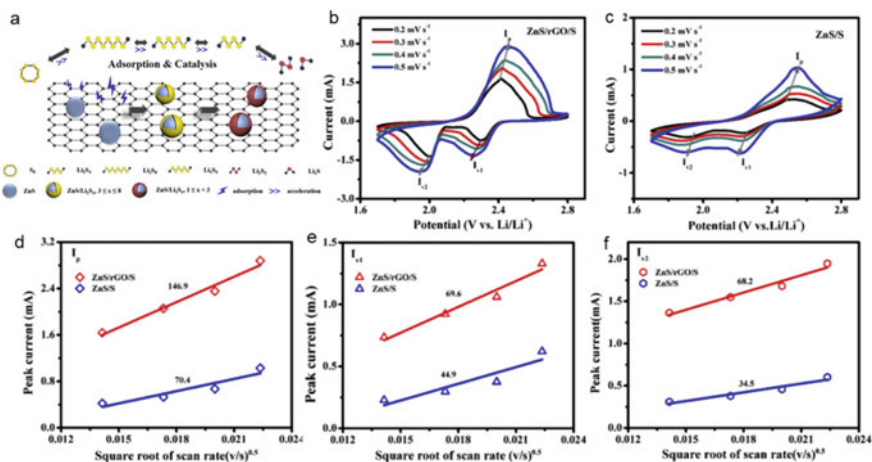


Fig. 5.16 a Conversion process of S_8 to Li_2S on the surface of ZnS/rGO/S electrode, CV curves of Li–S cells with ZnS/rGO/S (b) and ZnS/S (c) cathodes at various scan rates, plots of peak current vs. square root of scan rates for anodic oxidation process (d), first cathodic reduction process (e) and second reduction process (f) [92]. Reused with permission from Ref. [92] Copyright 2020 Elsevier Ltd.

surface area of electrode, and v is the scan rate. The Li^+ diffusion coefficients are calculated based on the anodic peaks at ~ 2.45 V and the cathodic peaks at ~ 2.30 and 1.90 V. Compared with the cathode without ZnS, the ZnS/rGO composite cathode exhibits the highest Li^+ diffusion coefficients at all peaks, suggesting the reduced concentration polarization of the ZnS/rGO composite cathode and the enhanced reaction transformation kinetics of sulfur species (Fig. 5.16) [92].

5.4.2.4 Tafel Slope

Tafel slope is an important kinetic parameter to reveal the reaction mechanism. The Tafel equation is expressed as follows:

$$\eta = a + b \cdot \log i, \quad (5.2)$$

where η is the overpotential, and i is the current density. In the field of electrocatalysis, it is generally believed that the smaller the Tafel slope (parameter b in the Tafel equation) is, the faster the current density grows in the same potential interval, indicating the larger reaction rate constant and the better electrocatalytic performance [97].

Linear sweep voltammetry (LSV) is a widely used electrochemical measurement in electrocatalysis to probe kinetic behaviors of targeted electrocatalysts. Li et al. developed a porphyrin derived atomic electrocatalyst (marked as atomic Co-N-C

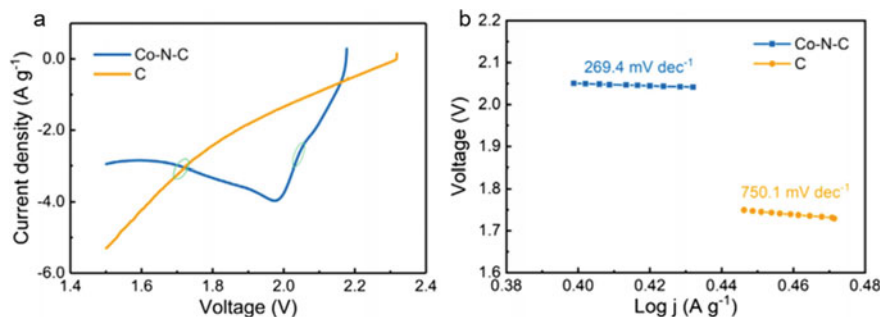


Fig. 5.17 LSV curves of Li-S cells with Co-N-C and C cathodes (a) and the corresponding Tafel plots (b) [98]. Reused with permission from Ref. [98] Copyright 2019 Wiley-VCH

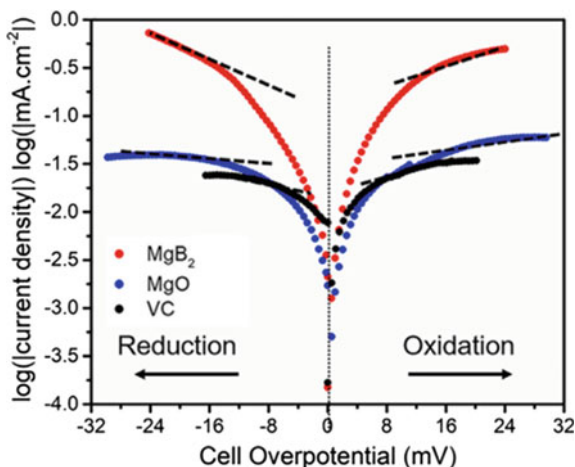
electrocatalysts) to exert atomic-efficient electrocatalytic effects on polysulfide intermediates [98]. In their study, the polarization curve was obtained by LSV measurement. They selected the region of strong polarization in the curve and obtained the Tafel curve (Fig. 5.17). Tafel plots exhibit a profoundly enhanced conversion reaction kinetics by the Co-N-C electrocatalyst ($269.4 \text{ mV dec}^{-1}$) in contrast of $750.1 \text{ mV dec}^{-1}$ over the C electrocatalyst. In a word, the atomic Co-N-C electrocatalysts impart significant kinetic merits to accelerate the conversion of sulfur species.

5.4.2.5 The Exchange Current Density

When the current density of the cathode reaction and the anode reaction are equal, the corresponding current density is the exchange current density of the electrode. Exchange current density can be used to describe the ability of an electrode to gain and loss electrons, that is, it can reflect the difficulty degree of an electrode reaction. The exchange current density is usually obtained by extrapolating the Tafel plot to zero overpotential.

After several years of research [25, 99–101], exchange current density has become an important index for evaluating the cathode electrocatalysts in Li-S batteries. Pang et al. investigated the electrochemical kinetics of LiPSs redox reactions on the surfaces of MgB₂, MgO, and VC as cathode electrocatalyst through LSV measurement on a three-electrode Swagelok cell [101]. They used Li₂S₄ solution as active material and focused on the reaction of liquid–solid (Li₂S₄ → Li₂S). The superior conversion kinetics afforded by the MgB₂ surface is clearly demonstrated by its high exchange current density (0.41 mA cm^{-2}), compared with 0.22 and 0.19 mA cm^{-2} for MgO and VC, as obtained from the Tafel plots (Fig. 5.18).

Fig. 5.18 Tafel plots of the Li_2S_4 solution redox with different cathodes [101]. Reused with permission from Ref. [101] Copyright 2018 Elsevier Ltd.



5.4.2.6 Activation Energy

Activation energy (E_a) refers to the minimum energy required by the reactants to reach the activated molecules in a chemical reaction. E_a is a parameter closely related to the rate of chemical reaction. The lower E_a is, the faster the reaction rate will be. Therefore, reducing E_a is the ultimate goal of catalyst design.

In order to further study the catalysis of Li-S batteries, many attempts have been made to obtain the parameter E_a by different methods [24, 25, 102, 103]. At present, the most common way to calculate E_a is to choose an experimental parameter and associate it with Arrhenius equation. Tao et al. systematically studied the catalysis of Nb_2O_5 on the redox reaction kinetics by scanning rate-dependent and temperature-dependent CV tests, as shown in Fig. 5.19a–c [102]. They combined the Li ion diffusion coefficient (D_{Li}) with Arrhenius equation and used Randles-Sevick equation to evaluate the catalytic activity of the Nb_2O_5 electrocatalyst for sulfur reduction process. Shen et al. fitted the relation of peak currents and temperatures to the Arrhenius equation, as shown in Fig. 5.19d–f [103]. E_a of LiPSs conversion is obtained by calculating the slope of $1/T \cdot \ln(|j|)$ plot. The calculation results indicates that $\text{Ni}_2\text{Co}_4\text{P}_3$ electrocatalyst has an ultralow barrier of only 3.97 kJ mol^{-1} , strongly proving the rapid conversion rate with its help. Peng et al. selected the parameter charge transfer resistance and related to Arrhenius equation to calculate E_a (Fig. 5.19g–i), comparing the catalytic performance of different heteroatom-doped graphene electrocatalysts for sulfur reduction reaction (SRR) [25]. While, there is another method for calculating E_a [24]. Luo et al. proposed that E_a could be calculated according to the slope of Tafel plot and the following equation:

$$E_{a,\text{Red}} = E_{a,\text{Red}}^0 - \frac{RT}{b} \varphi_{\text{cathode}} \left(\frac{Ox}{Red} \right)_{IR}, \quad (5.3)$$

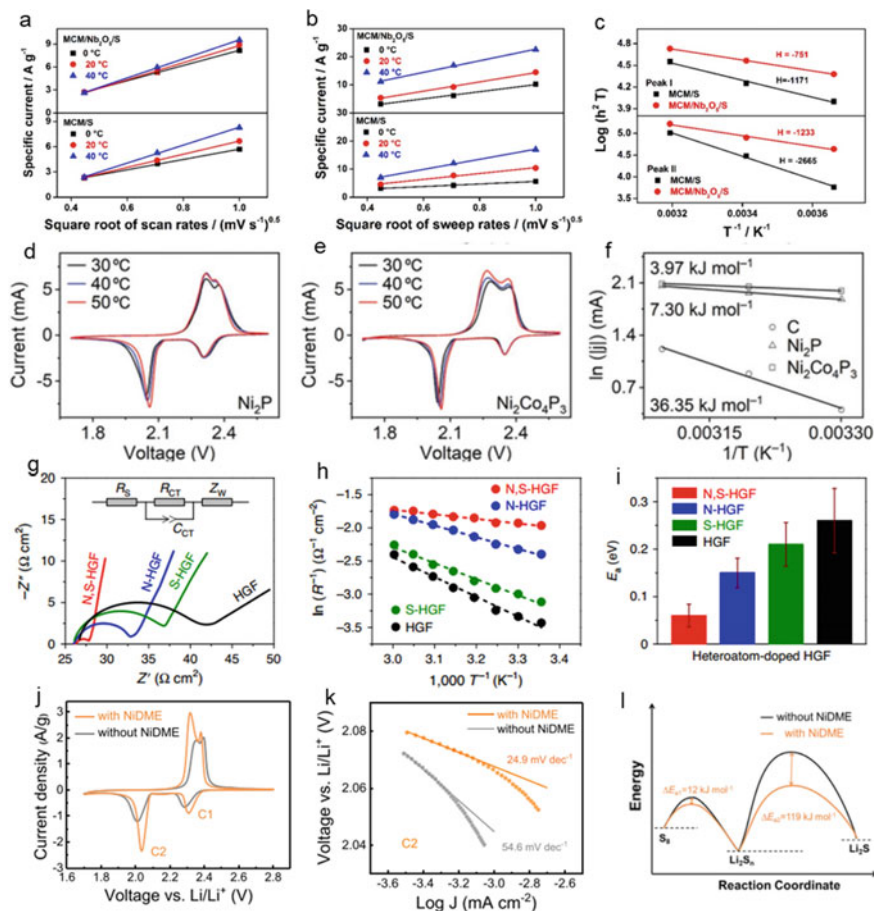


Fig. 5.19 The calculation method of activation energy (E_a) [24, 25, 102, 104]. Reused with permission from Ref. [102] Copyright 2016 The Royal Society of Chemistry, Ref. [25] Copyright 2019 Wiley-VCH, Ref. [24] Copyright 2020 Springer Nature, and Ref. [104] Copyright 2020 Elsevier Ltd.

where $E_{a,Red}$ is the activation energy of the reduction process, $E_{0a,Red}$ is the intrinsic activation energy, b is the slope of Tafel plot, and $\varphi_{cathode}$ is the irreversible potential in the reduction process. After adding homogeneous catalyst nickel chloride dimethoxyethane adduct (NiDME), a largely decreased E_a of the sulfur species redox reaction is achieved (Fig. 5.19j–l).

5.4.2.7 Electron Transfer Number

The parameter electron transfer number (n) is one of the most key characteristics of the electrocatalytic process. Take oxygen reduction reaction (ORR) for example,

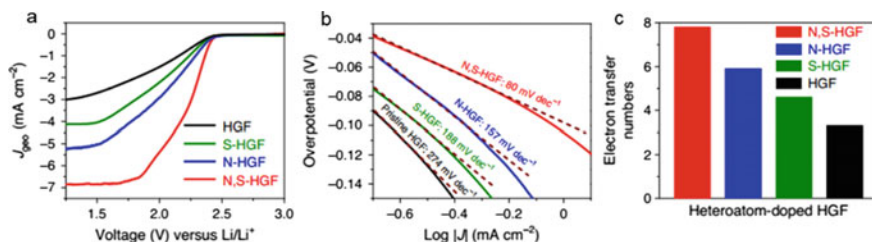


Fig. 5.20 **a** LSV curves of heteroatom-doped HGFs of sulfur reduction process, **b** Tafel plots of heteroatom-doped HGFs, **c** electron transfer number comparison among heteroatom-doped HGFs [25], Reused with permission from Ref. [25] Copyright 2020 Springer Nature

the parameter n not only reflects the efficiency of oxygen conversion but also provides information on the ORR mechanism [105]. To understand the sulfur reduction reaction (SRR) mechanism with the presence of catalysts, Peng et al. calculated the parameter n in the SRR process by using j_D according to the following Koutecky-Levich equation [25]:

$$\frac{1}{j} = \frac{1}{j_K} + \frac{1}{j_D} = B\omega^{-1/2} + \frac{1}{j_K}, \quad (5.4)$$

where j , j_K , and j_D represent the measured, kinetic-limited, and diffusion-limited current densities, respectively. The proportionality coefficient (B) can be written in the following equation:

$$B = 0.62D^{2/3}\nu^{-1/6}nFC, \quad (5.5)$$

where D is the diffusion coefficient of the reactant, ν is the kinematic viscosity of the electrolyte, F is the Faraday constant, and C is the concentration of the reactant in the bulk electrolyte. n can be deduced from the slope of the linear plot of j^{-1} versus $\omega^{-1/2}$ (K-L plot).

The dual heteroatom-doped graphene exhibits much higher n than the single heteroatom-doped graphene and pristine graphene, suggesting that it can promote more complete sulfur reduction and more rapid conversion of soluble LiPSs to the insoluble products (Fig. 5.20).

5.4.2.8 Parameters in Li₂S Deposition

About three quarters of the theoretical capacity (1,675 mAh g⁻¹) originates from the Li₂S₄ reduction, indicating the key role of the Li₂S deposition in enhancing the reaction kinetics in Li-S batteries [106, 107]. The kinetics of Li₂S nucleation from LiPSs on mediators can be characterized as a function of overpotential under potentiostatic conditions, and a function of current rate under galvanostatic conditions. The

characteristic curve reveals the time dependence of reduction current in the electrodeposition of Li_2S . Fan et al. investigated the kinetic analysis of Li_2S nucleation and growth process (Fig. 5.21a–c) [108]. The current peak has a sigmoidal cumulative distribution function, which follows the Avrami form:

$$Y = 1 - \exp(-Bt^n), \quad (5.6)$$

$$B = \left(\frac{\pi}{3}\right)Ak^2, \quad (5.7)$$

where Y , B , and n represent the portion that has been transformed, a kinetic constant, and the Avrami exponent, respectively. B is given by Eq. (5.2), where A and k are the nucleation and growth rates, respectively.

Fan et al. investigated the role of NbN@NG interface in regulating the Li_2S deposition (Fig. 5.21d–f) [109]. The quantity of the Li_2S precipitation on CF, CF/NG, and CF/NbN@NG are calculated to be 89.4, 175.4, and 256.8 mAh g^{-1} , respectively. This result suggests that the CF/NbN@NG electrocatalyst lowers down the Li_2S nucleation energy effectively thus accelerates the conversion of liquid LiPSs to solid Li_2S .

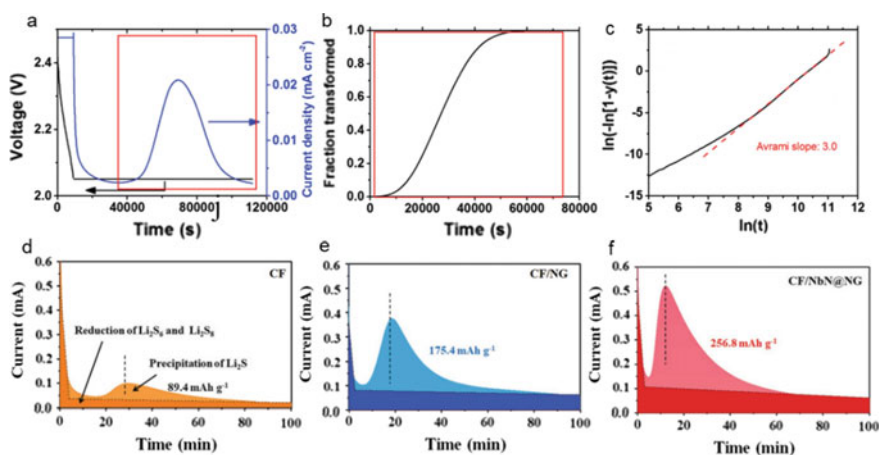


Fig. 5.21 **a** Plots of voltage and current versus time for a LiPSs-porous carbon cell, which was galvanostatically discharged to 2.05 V then potentiostatically discharged at 2.05 V, **b** plot of transformation versus time for potentiostatic current peak, **c** Avrami plot derived from the boxed portion of **(b)** [108], Reused with permission from Ref. [108] Copyright 2015 Wiley-VCH. **d–f** Potentiostatic discharge curves of the Li_2S deposition tests on CF, CF/NG, and CF/NbN@NG substrates [109], Reused with permission from Ref. [109] Copyright 2019 Wiley-VCH

5.4.2.9 Energy Barriers for the Formation and Decomposition of Li_2S

To understand the reason for the improved reactions kinetics of charge/discharge of the electrocatalyst in Li-S batteries, theoretical calculation represents a powerful tool for in-depth investigation at the molecular level. Du et al. first introduced single-atom cobalt as electrocatalyst to Li-S batteries and performed first-principles calculations [62]. They investigated the different possible reactions of LiPSs on Co-N/G and compared them to similar reactions N/G. The conversion of Li_2S_2 to Li_2S has the largest positive Gibbs free energy, which indicates that this is the rate-limiting step in the whole sulfur species reduction process. Compared with the N/G substrate, the lower Gibbs free energy on Co-N/G for the reduction of Li_2S_2 was achieved, which clearly confirms that the reduction of sulfur is thermodynamically more favorable on Co-N/G than N/G (Fig. 5.22a). In addition, they also evaluated the Li_2S oxidation reaction kinetics on the surfaces of N/G and Co-N/G by calculating the Li_2S decomposition energy barrier (Fig. 5.22b, c). The calculated value on Co-N/G and N/G are 1.43 eV and 2.29 eV respectively, indicating that the Co-N-C centers serve as active sites to accelerate the oxidation process of Li_2S . Zhou et al. synthesized a series of various single-atom materials and selected the most promising electrocatalyst for Li-S batteries by combing the theoretical calculations and experiments (Fig. 5.22d-g) [110].

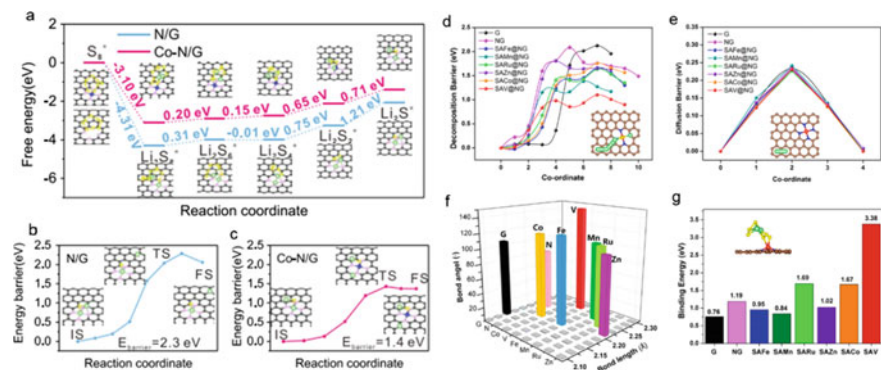


Fig. 5.22 a Energy profiles for the LiPSs reduction process on N/G and Co-N/G substrates, b, c energy profiles for Li_2S deposition on N/G and Co-N/G substrates [62], Reused with permission from Ref. [62] Copyright 2019 American Chemical Society. d-g Li_2S decomposition barriers, lithium ion diffusion barriers, bond angle and bond length of Li_2S , and binding energy of Li_2S_6 on different substrates [110], Reused with permission from Ref. [110] Copyright 2019 American Chemical Society

5.4.3 Exploration of Catalytic Mechanism

The whole traditional catalytic reaction process mainly consists of three steps: the adsorption of reactants on the catalyst, transformation of electron, and the desorption of the products from the catalyst. Differing from the traditional chemical catalytic reactions and electrocatalytic reactions, since Li-S battery is an energy storage system, the discharge product Li_2S is also the reactant in the charging process. In this regard, not only the adsorption step and electron transfer step should be paid attention, the relationship between the Li_2S deposition and the catalytic performance of catalyst also needs further investigation.

5.4.3.1 Adsorption Process

Chemical adsorption of LiPSs on sulfur host materials mainly consists of two forms: polar-polar interactions and lewis-base interactions.

Polar-polar interactions

The polar-polar interaction is a strong chemical interaction between polar LiPSs and polar sulfur host materials that can be tuned to adsorb LiPSs (Fig. 5.23a). Various materials have been developed to chemically interact with LiPSs in recent years, mainly including three types: modified carbonaceous materials, functional polymeric materials, and metal chalcogenides (oxides and sulfides). Doping heteroatoms and modifying functional groups on the matrix material to chemically adsorb the LiPSs stems from the polar-polar interaction of electron-rich groups with Li^+ [111, 112]. Beyond carbonaceous materials, metal chalcogenides possess intrinsic network polarity, where the surface metal chalcogen ions synergistically interact with the S_x^{2-} and Li^+ [113].

Lewis acid-base interactions

Polysulfide anions (S_x^{2-}) are soft Lewis bases owing to the sulfur lone electron pairs. Hence, host materials that exhibit Lewis acid characteristics are able to interact with LiPSs strongly and trap them within or on the host surface (Fig. 5.23b). Examples of such kind of materials are metal organic frameworks (MOFs), MXenes, and metal compounds. Take Ti_2C for example, a strong Lewis acid-based interaction of the LiPSs with its surface is demonstrated by metal-sulfur (S-Ti-C) binding at the surface [114].

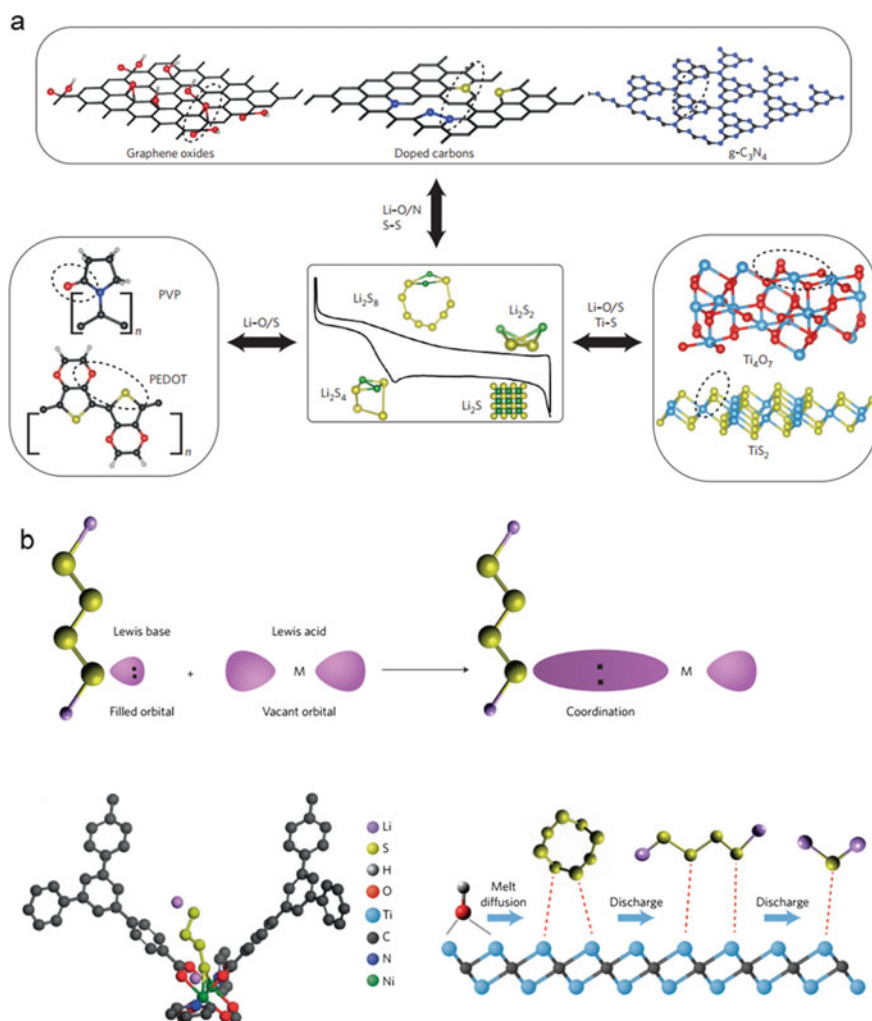


Fig. 5.23 Schematic of polar-polar interaction **a** and lewis-base interaction **b** between LiPSs and polar sulfur hosts [115]. Reused with permission from Ref. [115] Copyright 2016 Springer Nature

5.4.3.2 Electron Transfer Process

Since electron transfer process is the most important step in the whole electrocatalytic reaction, many researchers have devoted tremendous efforts on how electrocatalysts promote the electron transfer to make the electrocatalytic mechanism of Li-S batteries clearer.

Zhou et al. studied Co-based compounds on the catalytic process of sulfur species and reported that the p-band center modulated the interfacial electron transfer dynamics (Fig. 5.24a) [116]. They investigated the kinetic behavior of a series of

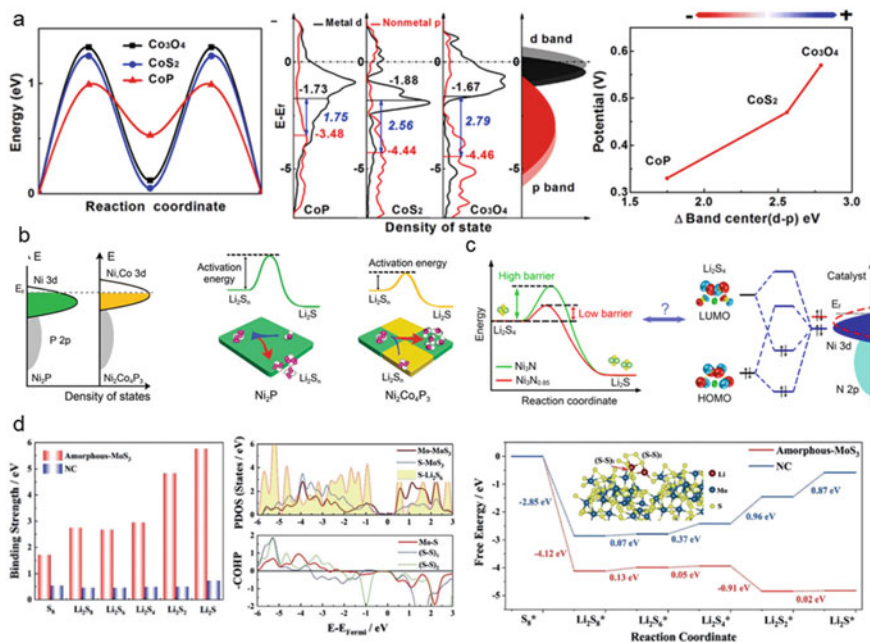


Fig. 5.24 Schematic of catalytic mechanism for electron transfer process [103, 104, 116, 118]. Reused with permission from Ref. [116] Copyright 2018 Elsevier Ltd., Ref. [103] Copyright 2020 American Chemical Society, Ref. [118] Copyright 2019 Wiley-VCH, and Ref. [104] Copyright 2020 Wiley-VCH

cobalt-based compounds containing different nonmetal anions in Li-S chemistry systematically. As a result, CoP exhibited superior electrochemical performance due to its moderate adsorption ability. The p band center in CoP shifts up distinctly with respect to Fermi level, reducing energy gap between the cobalt $3d$ and anion $2p$ band centers. The P anion was softer and less electron-pulling as compared to the S and O anions, which leads to an increased energy of bonding states and a decreased energy gap between the bonding and antibonding orbitals. This gives rise to a higher electron energy, due to anions with more hybridization and a contribution to the valence band electrons, which thus facilitates the electron exchange to promote interfacial S_6^{2-}/S^{2-} redox dynamics.

Inspired by the d -band theory proposed by Norskov et al., Shen et al. introduced the concept of d -band engineering into Li-S batteries (Fig. 5.24b) [103, 117]. They used Ni_2P as a model catalyst and substituted Ni with Co to tune and understand its catalysis activity for Li-S conversion reactions. The Co dopants in $Ni_2Co_4P_3$ raise the d -band of metal sites and further strengthen the interaction between polysulfides and catalysts. The terminal S atoms were adsorbed to the triply bridged metal sites through a strong metal-S bond. The S-S bonds of LiPSs were weakened due to the redistributed electron population, resulting in the reduced lower activation energy of LiPSs conversion. In addition, they found that introducing vacancies is also a

way to tune d-band center. They developed a $\text{Ni}_3\text{N}_{0.85}$ electrocatalyst by engineering N vacancies in a hexagonal Ni_3N (space group P6322). $\text{Ni}_3\text{N}_{0.85}$ interacts strongly with Li_2S_4 and charge transfer from the surface to the adsorbed Li_2S_4 molecules due to the rise of d-bands of Ni atoms. The strong interaction caused by N vacancies results in the high filling fraction of the lowest occupied molecular orbital (LUMO) of Li_2S_4 . Therefore the weakened S–S bond of the Li_2S_4 backbone facilitates the bond breaking.

Yu et al. proposed that amorphous MoS_3 has superior binding ability in anchoring Li_2S_6 , attributing to that the surface sulfur with negative charge can induce the conventional Li-binding, while unsaturated molybdenum has strong affinity toward the sulfur in Li_2S_6 [118]. They further clarified the electron transfer between the LiPSs and MoS_3 by projected density of states (PDOS) and crystal occupation Hamilton population (COHP) (Fig. 5.24c). For the (S–S)₁ bond that interacts with molybdenum, the anti-bonding states are significantly reduced compared to the original non-interacting (S–S)₂ bond, since electrons in sulfur chain can be transferred to the MoS bonding states. Besides, the loss of electrons in the sulfur chain of Li_2S_6 also reduces energy intervals between the highest occupied molecular orbitals (HOMO) and lowest unoccupied molecular orbitals (LUMO) from 1.88 to 0.56 eV. Therefore, the electron migration between LUMO and HOMO in Li_2S_6 can be benefited, thus promoting the redox process of polysulfides.

In Li-O₂ batteries and redox flow batteries, it is a very common and effective way to accelerate the reaction rate by introducing redox mediator. In Li–S batteries, mediators can facilitate LiPSs conversion through their reactions with LiPSs. In general, the mediators for Li–S batteries can be divided into two categories based on their physical form: one is the homogeneous mediators which are redox active species soluble in the electrolyte and are often referred to as redox mediators (RMs) (Fig. 5.25a), the other one is heterogeneous mediators which are distributed solid in the sulfur cathode (Fig. 5.25b) [119].

The RMs undergo charge-transfer reactions with sulfur species directly and transport the charge transferred to the current collector. They substitute charge conduction through solid materials in the electrode with the more effective charge conduction in the electrolyte [120]. Tsao et al. employed the redox chemistry of quinone to realize efficient, fast, and stable operation of Li–S batteries (Fig. 5.25c). The RM with appropriate redox potential was first electrochemically oxidized to RM^+ , which can chemically oxidize Li_2S over the whole surface and further electrochemically reoxidized after diffusing to the surface of conductive host. Therefore, the ideal redox potential of RM stayed slightly higher than the equilibrium voltage of Li_2S (≈ 2.15 V vs. Li^+/Li), enabling reduced overpotential and maximized energy efficiency.

As for the heterogeneous mediators, a good example is the MnO_2 mediator proposed by Liang et al. (Fig. 5.25d) [27]. They theorized that polysulfides are oxidized to surface-bound thiosulfates on MnO_2 . The reaction between thiosulfates and long-chain polysulfides thereafter forms polythionate complexes $[\text{O}_3\text{S}_2\text{-(S)}_{x-2}\text{-S}_2\text{O}_3]^{2-}$ and short-chain polysulfides immobilized on the MnO_2 surface. This thiosulfate-mediated conversion of long-chain polysulfides to short-chain polysulfides bypasses the normal long-chain to short-chain polysulfide conversion in the

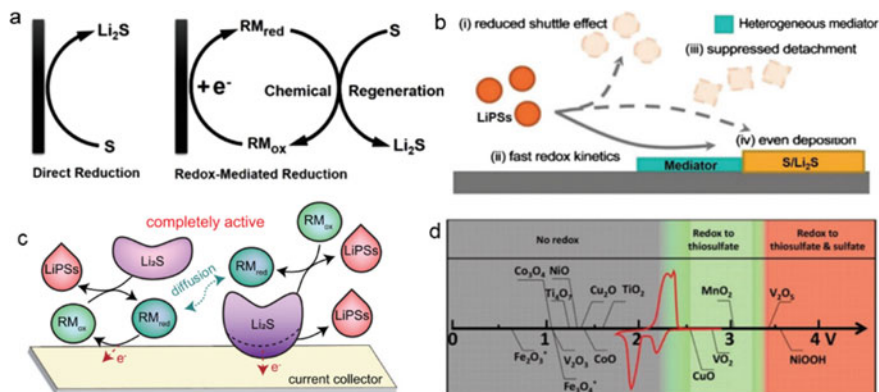


Fig. 5.25 Schematic of working mechanism of homogeneous mediators (a) and heterogeneous mediators (b) for Li–S batteries [119], Reused with permission from Ref. [119] Copyright 2020 Wiley-VCH. c schematic of redox mediator assisting Li₂S oxidation process [120], Reused with permission from Ref. [120] Copyright 2018 Elsevier Ltd. d Chemical reactivity and redox potentials of various metal oxides [121], Reused with permission from Ref. [121] Copyright 2015 Wiley-VCH

solution phase. Furthermore, Nazar’s group investigated this alternate polysulfide conversion pathway on other metal oxides and reported a “Goldilocks” principle in metal oxide–polysulfides interaction [121].

5.4.3.3 Li₂S Deposition Process

Li₂S is not only the product of the discharging process of Li–S batteries but also the reactant of the charging process. The deposition of Li₂S has a profound influence on the performance of Li–S batteries, especially the cycling performance is a key index to evaluate a secondary energy storage system.

Although plenty of electrocatalysts have been reported to improve the reaction kinetics of LiPSs, it is difficult to achieve an effective collaborative interface with strong adsorption, high electrical conductivity, and high reactive sites simultaneously, leading to a feeble regulation of Li₂S deposition. In this regard, Yuan et al. proposed a triple-phase interface among electrolyte/CoSe₂/G to afford strong chemisorption, high electrical conductivity, and superb electrocatalysis of LiPSs redox reactions in Li–S batteries (Fig. 5.26a, b) [122]. In details, the trogtalite CoSe₂ nanodots provide abundant exposed sites for intimate adsorption of liquid-phase lithium polysulfides and regulate the nucleation density, while the intrinsic metallic attribute of CoSe₂ facilitates the rapid electron transfer. More importantly, the uniformly dispersed CoSe₂ nanodots with an average size of 5 nm lead to densely and uniformly distributed sulfphilic active sites. It guides effective equilibrium to nucleation and growth of Li₂S. Therefore, the well-designed triple-phase interface realizes the uniform precipitation of Li₂S at nanoscale and inhibits their blocky growth and aggregation.

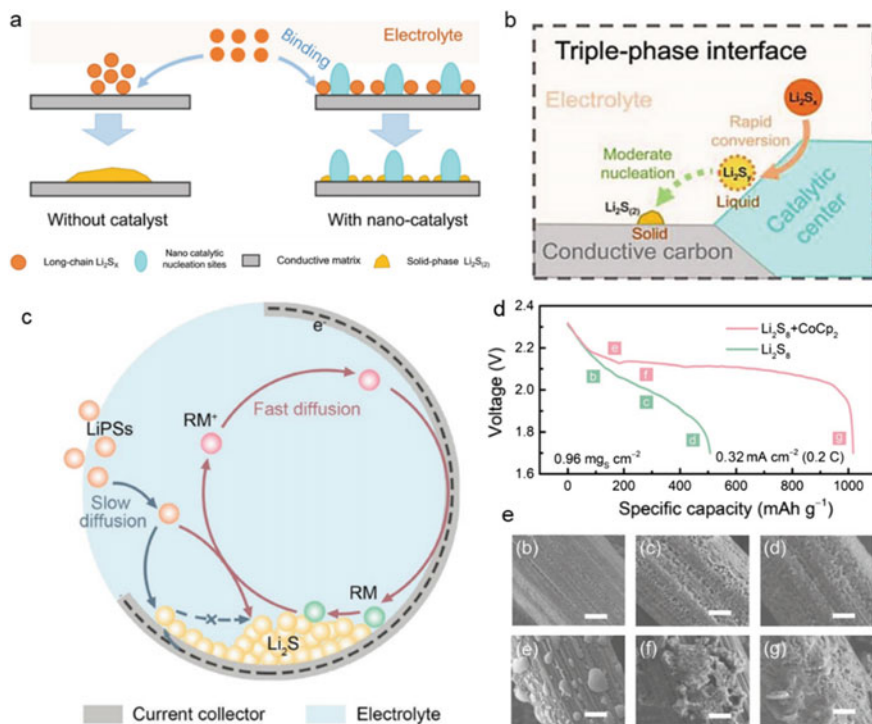


Fig. 5.26 Schematic of Li_2S deposition on conductive surface (a) and nanotriple-phase interface with uniformly distributed nucleation sites (b) [122], Reused with permission from Ref. [122] Copyright 2018 Wiley-VCH. c schematic of growing path of Li_2S with the assistance of CoCP_2 , d the first charge profile at 0.2 C, e SEM images of Li_2S deposition with CoCP_2 absent [123], Reused with permission from Ref. [123] Copyright 2019 Wiley-VCH

Redox mediators have a great potential in regulating Li_2S deposition due to their special form in existence. Zhao et al. introduced cobaltocene (CoCp_2) as a persistent extrinsic RM to dictate an alternative growing pathway toward three-dimensional Li_2S growth (Fig. 5.26c–e) [123]. $\text{CoCp}_2/\text{CoCp}_2^+$ maintains a soluble state across the whole discharge process. The persisted presence of extrinsic redox mediator ensures the integrity of redox-mediated Li_2S growth cycle toward full utilization of sulfur on the finite conductive surface. There are two main reasons that could explain why CoCp_2 helps the 3D growth of Li_2S : (1) CoCp_2^+ has easier access to the conductive surface than Li_2S_4 , especially at the end of discharge, to break the diffusion limitation on Li_2S_4 for further discharge; (2) CoCp_2 , once formed through on-surface electroreduction, can diffuse to external surface of existing Li_2S nuclei and build new mass upon these nuclei while polysulfides like Li_2S_4 can only mediate the Li_2S growth at the electrolyte/conductive substrate/ Li_2S triple-phase boundaries.

In recent years, researchers have conducted more in-depth research of the catalysis in Li–S batteries. Great progress has been made in the parameter research of catalyst

performance evaluation and catalyst design. (1) More and more parameters used to evaluate catalysis in other catalytic systems have been introduced into Li-S batteries. However, the accuracy of the methods that obtain the parameters needs to be further enhanced. (2) As for catalyst design for Li-S batteries, there are many kinds of catalysts introduced into Li-S batteries at present. Therefore, the catalytic mechanism of each catalyst in essence needs to be further studied at the molecular level.

5.5 Characterizations

Accurate characterization of the catalytic process in Li-S batteries is a prerequisite for studying the mechanism. We have previously summarized the characterization methods of catalysis in Li-S batteries [124]. Many mature characterization and analysis methods have been proposed in traditional catalysis and electrocatalysis, which can provide many ideas for researches of Li-S batteries. Some common parameters in studies of thermal catalysis and electrocatalysis like activation energy, number of electrons transferred, faraday efficiency, energetic efficiency, etc. have similar application values in Li-S batteries. Herein, we will introduce the application of electrochemical techniques, microscopic techniques optical techniques and in-situ characterization techniques in catalysis research from the perspective of characterization technique.

5.5.1 *Electrochemical Techniques*

Electrochemical technique is a kind of characterization technique that uses the specific response of tested system to various modes of current or voltage signals to characterize the electrochemical performance of the system. It includes many mature test techniques such as CV [11, 125], EIS [126, 127], and polarographic analysis. At present, electrochemical technique is widely used in the field of energy storage materials including Li-S batteries research. In the past few years when lithium-sulfur catalysis has been extensively studied, electrochemical technique is also the most important method for characterizing the catalytic performance of materials: shift of the peak position in the CV curve as evidence of the existence of catalysis; comparing the Tafel slope fitted by CV curve to evaluate the catalytic ability of the material; description of the improvement effect of the catalyst on the utilization rate of the active material by calculating of the dissolution/deposition amount of lithium sulfide using potentiostatic electrolysis technique; shortening of the diameter of the semicircular area of the EIS curve to prove that the catalyst improves the reaction kinetics. These characterizations can only solve the problem of whether lithium-sulfur catalysis exists and cannot completely explain the mechanism of catalysis. And they also have the problem of not being rigorous enough, and using electrochemical techniques to characterize the reaction mechanism has been proved to be

feasible in the field of electrocatalysis research, but these characterization techniques have not been fully applied in lithium-sulfur systems. In this section, we will introduce the application of electrochemical technology in lithium-sulfur catalysis and propose rigorous electrochemical test methods for lithium-sulfur systems.

- Traditional electrochemical techniques

Traditional electrochemical characterization techniques like CV and EIS are the most effective and simplest means to prove the existence of catalytic phenomena in Li-S batteries. Yang et al. [128] used CV to characterize the catalytic ability of TiO₂-heterostructures in Li-S batteries. To avoid adverse effects of lithium metal anodes and further reveal the conversion process of LiPSs on heterostructure surface, they assembled symmetrical cells using TiO₂-MXene heterostructure mixed with GN as the electrode. The CV profiles in a voltage window of -0.7 to 0.7 V at 10 mV s⁻¹ were shown in Fig. 5.27a. It could be clearly observed that the symmetrical cell with the Ti₃C₂T_x (4 h) displayed more intensive redox peaks, demonstrating the well-tailored chemical components and surface properties enable rational balance between LiPSs adsorption and conversion on its surface, thus leading to the highest sulfur utilization. The CV curves

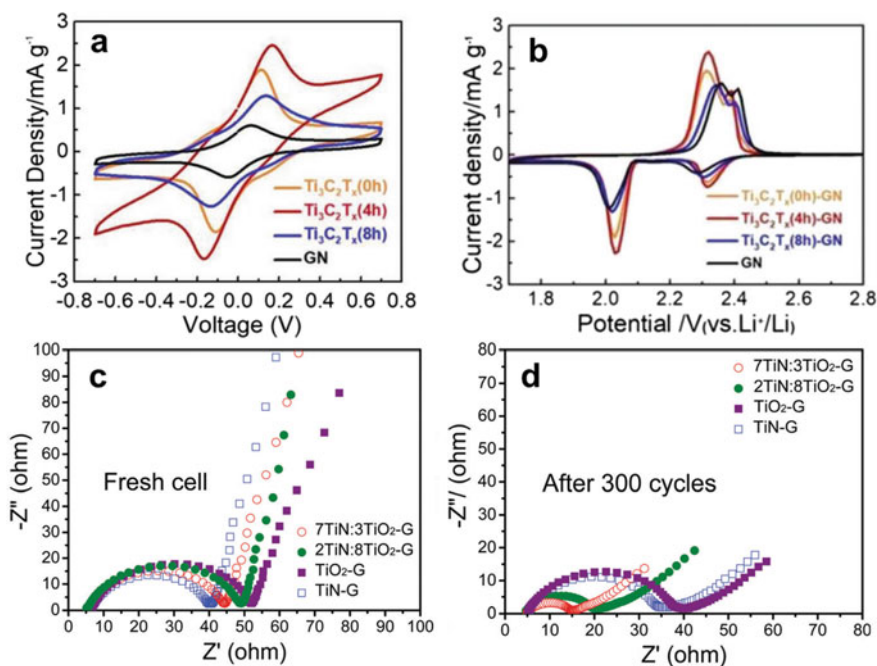


Fig. 5.27 CV profiles of **a** symmetrical Li₂S₆-Li₂S₆ cells and **b** Li-S batteries [128], Reused with permission from Ref. [128] Copyright 2019 Wiley-VCH. Nyquist plots of cells with the 7TiN:3TiO₂-G coating layer **c** before cycling and **d** after 300 cycles at 1 C from 100 kHz to 10 MHz at room temperature [73]. Reused with permission from Ref. [73] Copyright 2017 The Royal Society of Chemistry

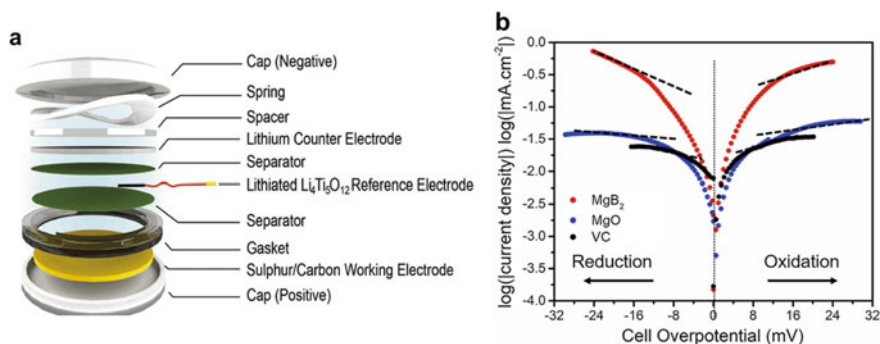


Fig. 5.28 **a** Three-electrode coin-cell configurations with a lithiated $\text{Li}_4\text{Ti}_5\text{O}_{12}$ reference electrode [129], Reused with permission from Ref. [130] Copyright 2018 Wiley-VCH. **b** The Tafel plots of the Li_2S_4 solution redox on different host materials, derived from linear sweep voltammetry scans in a three-electrode Swagelok cell [101]. Reused with permission from Ref. [101] Copyright 2019 Elsevier Ltd.

of Li-S batteries with TiO_2 -MXene interlayer were shown in Fig. 5.27b. The CV profile of the cell with heterostructure layer showed distinct positive shift for the two cathodic peaks and higher peak current, indicating the enhanced transformation of S_8 to soluble LiPSs and further to insoluble products (Li_2S). They had also used EIS to characterize the performance of heterostructure catalysts (Fig. 5.27c, d). The Li-S battery with the $7\text{TiN}:3\text{TiO}_2$ -G coating has the smallest R_{ct} , which is possibly because of the higher conductivity because of it containing more TiN and the strong affinity of the heterostructures for LiPSs [73].

- Three-electrode system
- The three-electrode system, as a commonly used electrochemical analysis method, consists of working electrode, reference electrode, counter electrode, and two electrical circuits formed by these electrodes. The three-electrode battery can accurately measure the potential of the working electrode by separating the measurement circuit for measuring the potential and the polarization circuit for applying current to eliminate errors caused by electrode polarization. Most of the tests currently used to characterize the electrochemical performance of lithium-sulfur catalysis are carried out with two-electrode batteries. In this case, the polarization current is usually not negligible ($>1 \text{ A g}_{\text{sulfur}}^{-1}$), and the polarization of the lithium electrode will affect the accuracy of the potential measurement. Therefore, the use of a three-electrode battery to eliminate the effects of other electrodes is an important and promising method to study sulfur cathodes with catalysts.
- There have been many works in the field of Li-S batteries that have used a variety of different types of three-electrode systems to eliminate the influence of the polarization of the lithium metal negative electrode on the measurement. Zhang et al. [129] constructed a three-electrode coin-cell by inserting a lithiated $\text{Li}_4\text{Ti}_5\text{O}_{12}$ electrode as a reference electrode. The battery is stable to the production of LiPSs

in the bulk electrolyte during the cycle, as shown in Fig. 5.28a. This special coin-cell can be used to accurately monitor the real-time evolution of impedance and explain the influence of LiPS dissolution on electrolyte viscosity and conductivity and was used to monitor real-time impedance evolution and explain the influence of LiPS dissolution on electrolyte viscosity and conductivity. However, in this simple test method, the additional potential consumption between the reference electrode and the working electrode due to the presence of the separator cannot be ignored for catalytic characterization. Therefore, the reference electrode of a three-electrode system should be built in free electrolyte to avoid the use of separators. Nazar et al. [101] constructed a three-electrode Swagelok cell for LSV testing to examine the redox kinetics of polysulfides on the surface of MgB_2 , MgO , and VC. The overpotential and the current response from the LSV experiment were used to construct the Tafel plot (Fig. 5.28b). The linear region of the semi-logarithmic Tafel plot was manually fitted and extrapolated to obtain the exchange current density according to the Butler-Volmer equation. At present, most three-electrode batteries in lithium-sulfur system use lithium metal as the reference electrode, which is unfavorable for the accurate measurement of potential, because lithium metal has poor stability in LiPSs, and it is not an unpolarized electrode. Therefore, the electrode that maintains electrochemical stability in electrolyte in which LiPSs are dissolved, should be selected as a reference electrode, such as a platinum electrode. Manthiram et al. [82] used a three-electrode system with Pt foil as a reference electrode to demonstrate the advantages of three-dimensional graphene/1 T MoS_2 heterostructures as an electrocatalyst toward LiPSs conversion.

- Calculation of activation energy

Activation energy is one of the main parameters that characterizes catalytic activity in traditional catalysis studies. The essence of the catalytic reaction is to reduce the activation energy of the target reaction. In the researches of thermal catalysis, the apparent activation energy is calculated by the Arrhenius equation. The reaction rate is an important parameter in the Arrhenius equation. In the lithium-sulfur system, the concentration of various polysulfides is difficult to measure due to the complex reaction process, so it is almost impossible to calculate the reaction rate accurately. However, many other electrochemical parameters, such as the peak current density in the CV curve, the diffusion rate, and the charge transfer resistance derived from the EIS, also reflect the reaction rate to a certain extent, showing a temperature-dependent Arrhenius behavior. The reaction activation energy calculated by this relationship can also reflect the strength of the catalytic ability to a certain extent.

Haart et al. [130] used EIS to obtain the impedance data of manufactured lithium-ion pouch cells to calculate the charge transfer resistance and diffusion rate. Both processes follow an Arrhenius law, allowing the determination of activation energies with small variance. Figure 5.29a, b shows the impedance data at different temperatures and Arrhenius plots obtained from battery model measured at different temperatures. This study provided a new idea for the researches of lithium-sulfur catalysis. The information contained in the more easily measured electrochemical

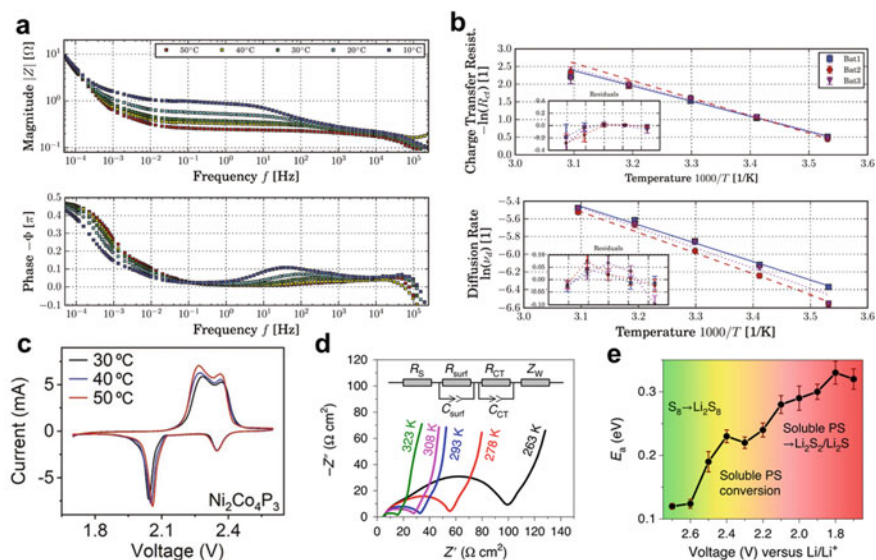


Fig. 5.29 **a** Impedance data measured by EIS from manufactured lithium-ion pouch cells, **b** Arrhenius plots of charge transfer resistance (top) and solid-state diffusion rate (bottom) obtained from battery model fit of impedance data measured at different temperatures [130], Reused with permission from Ref. [130] Copyright 2016 The Electrochemical Society. CV curves of the Li-S cells using **c** $\text{Ni}_2\text{Co}_4\text{P}_3$ as catalysts at varied temperatures [131], Reused with permission from Ref. [131] Copyright 2019 Wiley-VCH. **d** EIS measurements at various temperatures at 2.7 V. **e** Activation energy profiles at various voltages [132], Reused with permission from Ref. [132] Copyright 2020 Springer Nature

techniques can be used to obtain activation energy data to evaluate and select the catalyst, which can avoid the difficult measurement of polysulfide concentration. Zhang et al. [131] fitted the relation of CV peak currents and temperatures to the Arrhenius equation and obtained the activation energy of polysulfide conversion by calculating the slope. In this way, they evaluated the performance of $\text{Ni}_2\text{Co}_4\text{P}_3$ as a catalyst for Li-S batteries (Fig. 5.28c).

Duan et al. [132] also used this idea to determine the activation energy for each step of the LiPSs conversion process by fitting the charge transfer resistance of EIS tests under different voltages at different temperatures in a standard Ketjen carbon black/sulfur (KCB/S) composite cathode (1 mg cm^{-2}). Figure 5.29d shows the EIS variable temperature curves in a frequency range from 10 MHz to 100 kHz with an alternating current amplitude of 5 mV. In EIS plots, the first semicircle is attributed to the deposition of insoluble solid sulfide ($\text{Li}_2\text{S}_2/\text{Li}_2\text{S}$) on the surface (R_{surf}), the second semicircle represents the charge transfer (R_{CT}), and the tail line is attributed to the Warburg resistance (Z_W). Using the charge transfer resistance at different temperatures, the activation energy of the electrochemical reaction at the test potential can be calculated by Arrhenius equation. Figure 5.29e shows the activation energy of the SRR at different potentials calculated by EIS in the voltage range of 2.7–1.7 V. At

a high voltage of about 2.7 V (corresponding to the conversion from S_8 to Li_2S_8), E_a is as low as 0.12 eV, proving a high-speed conversion of LiPSs. The activation energy increases to 0.24 eV at 2.4–2.1 V and then reaches a maximum value of 0.33 eV at 1.8 V. This shows that the conversion process of low-order polysulfides and solid lithium sulfide is very slow.

5.5.2 Microscopic Techniques

In order to ensure a high degree contact with the active material, the catalyst usually has a fine nanoscale structure. This requires advanced electron microscopic techniques to characterize the microscopic changes in catalysts and reactants. Scanning electron microscopy (SEM) and transmission electron microscopy (TEM) are the two most used morphological characterization methods in the study of lithium-sulfur catalysis. Electron microscopy combined with X-ray energy dispersive spectroscopy (XEDS) can intuitively observe the basic morphology and element distribution of the material. High-resolution transmission electron microscopy (HR-TEM) combined with selected area electron diffraction (SAFD) or electron energy loss spectroscopy (EELS) can even characterize the crystal structure of the material [133–136]. Yang et al. [73] used HR-TEM to characterize the TiO_2 -TiN heterostructure added to the sulfur cathode. The TEM image in Fig. 5.30a confirmed the generation of heterostructures. Among them, TiO_2 and TiN grow together in a large particle, which can be confirmed by the lattice fringes of HR-TEM. And the interface between these two components can be clearly observed through the electron microscope images. This interface is the key to catalyze the conversion of LiPSs. The heterogeneous interface not only improves the adsorption capacity of LiPSs but also provides a fast electron transfer pathway for the conversion through the synergistic effect of the two components.

In order to ensure the reliability of the electron microscopy characterization of the material morphology, it must be ensured that the sample will not be changed due to changes in the physical conditions in the microscope sample compartment [137]. However, the vapor pressure of elemental sulfur is very low, and sulfur sublimation easily occurs in the high vacuum environment in the sample chamber of the electron microscope [138]. This phenomenon is an important challenge for the characterization of high-resolution sulfur electrodes [139]. To illustrate this problem, Fig. 5.30b shows the vapor pressure curve of sulfur, with the conditions of an FEI Tecnai F20 transmission electron microscopy (TEM) sample chamber (8.8×10^{-8} Torr at $\sim 18^\circ C$) indicated. Figure 5.30c shows the TEM images of sulfur under this condition. It can be observed that sulfur sublimates at a rate of about 1 single layer of sulfur per second, and finally only a small portion of “super-sublimated” polymerized sulfur remains, which remains relatively stable under vacuum.

Cryo-TEM is a well-established method for imaging hydrated biological samples that cannot be exposed to vacuum at room temperature. Cryo-TEM can authentically characterize the distribution of S in the composites by suppressing the sublimation

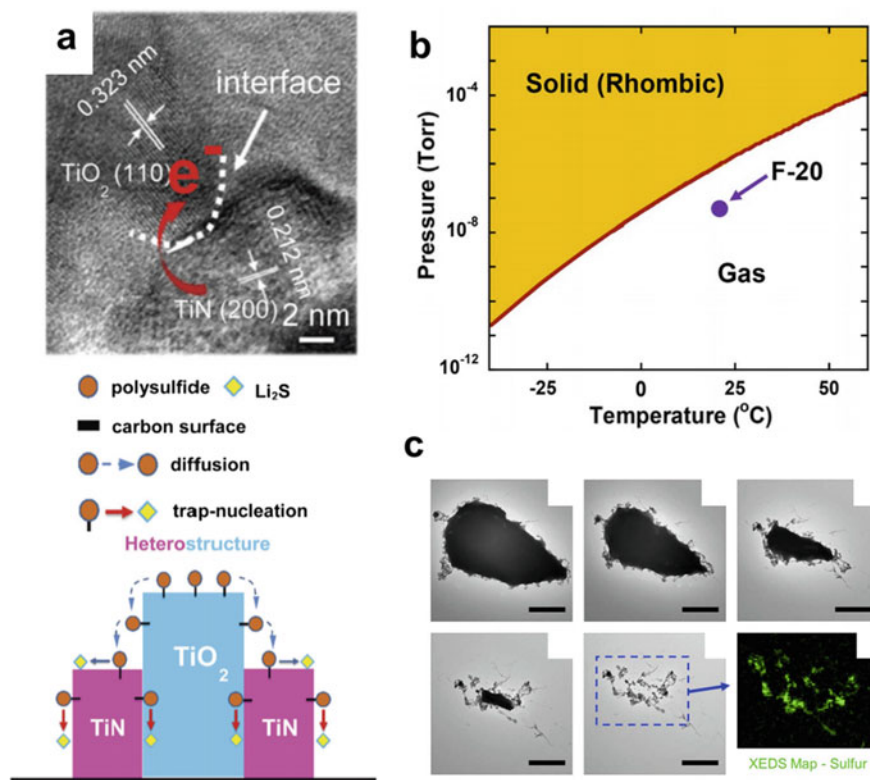


Fig. 5.30 a TEM image of TiO₂-TiN structure and schematic of LiPS conversion processes on TiO₂-TiN heterostructure surface [73], Reused with permission from Ref. [73] Copyright 2017 The Royal Society of Chemistry. b Vapor pressure versus temperature for elemental sulfur. c Sulfur particle sublimating in TEM vacuum chamber at 18 °C, at a pressure of 8.8×10^{-8} Torr [137]. Reused with permission from Ref. [137] Copyright 2017 Cambridge University Press

of S and further avoid the potential damages of electron microscopy. Levin et al. [137] enabled the reliable distribution of S in various types of carbon/S composites through cryo-STEM and demonstrated that uniform S infiltration and dispersion through the melt infusion method was easier in activated porous carbon hosts than in nonactivated porous carbon, hollow carbon spheres, and carbon nanotubes. In order to study whether the sublimation effect was still apparent at low temperatures, sulfur particles were prepared and imaged by cryo-TEM at a cryogenic temperature of -173 °C. A time series of cryo-TEM images from a sulfur particle is shown in Fig. 5.31. Figure 5.31a–c shows that the sulfur particles did not change within 5 h, which is in sharp contrast with the sulfur particles that sublime and disappear within 40 min at room temperature. The cryogenically cooled sulfur remained stable enough under the electron beam to allow imaging in annular dark field (ADF) cryo-scanning TEM (Fig. 5.31d) and XEDS (Fig. 5.31e) mapping. The suppression of

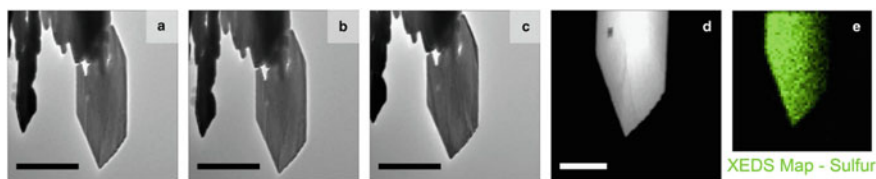


Fig. 5.31 a–c Time series of images of a cryogenically cooled sulfur particle at ~ 173 °C after **a** 86 min, **b** 170 min, and **c** 311 min under 8.8×10^{-8} Torr vacuum. After 4 h under vacuum, a high angle annular dark field (HAADF) scanning transmission electron microscopy (STEM) image (**d**) and STEM X-ray energy dispersive spectroscopy (XEDS) map (**e**) were taken from the tip of the particle. Scale bar: (**a–c**) 1 μm and (**d**) 500 nm+ [137]. Reused with permission from Ref. [137] Copyright 2017 Cambridge University Press

sulfur sublimation by cryogenic sample cooling demonstrates that cryo-TEM is a viable method for both imaging and spectroscopic characterization of composites containing elemental sulfur such as catalyst-sulfur composites in Li–S batteries.

5.5.3 Optical Techniques

- Spectroscopic techniques

Optical spectroscopic techniques, including Raman [140], FT-IR [141, 142], and UV–vis [94, 102, 143], have gained much attention and have been widely adopted, owing to their ease of operation, non-destructive nature, high time and spatial resolutions, ample information, etc. Raman spectroscopy is commonly utilized to distinguish between different molecules by providing their structural fingerprints, which are used to survey the vibrational, rotational, and other low-frequency modes in a studied system. In a Raman spectrum, individual bands are characteristic of specific molecular motions and can, therefore, be used to identify and quantify specific molecules. For Li–S battery, Raman spectroscopy can gather information from both the polarizable electrode surface and liquid organic electrolyte. Chen et al. [144] used Raman spectroscopy to characterize sulfur host materials. As elucidated in Fig. 5.32a, Raman spectra displays two prominent peaks of carbon at around 1368 cm^{-1} (D band) and 1585 cm^{-1} (G band) corresponding to disordered/defective carbon and graphite carbon, respectively. Moreover, the spectra all show a G peak at 2696 cm^{-1} referring to an overtone of the G band, which appears commonly in graphitic carbon. Compared with the CoP@HPCN, three characteristic peaks of sulfur at 155, 219, and 475 cm^{-1} demonstrate the confinement of sulfur in the CoP@HPCN/S.

Infrared spectroscopy (IR) is a kind of absorption spectroscopy, which analyzes and identifies the molecular structure of substances by detecting the vibration and rotation of molecular bonds when absorbing specific infrared light. Infrared spectroscopy has a wide range of applicability to samples and has been maturely used in

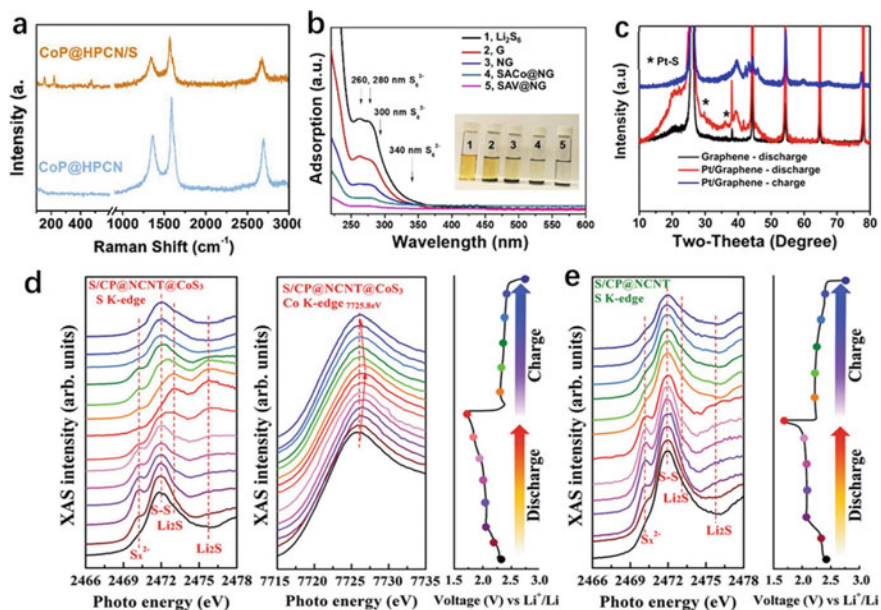


Fig. 5.32 **a** Raman spectra of as synthesized CoP@HPCN, and CoP@HPCN/S composites (with 70 wt% of S) [144], Reused with permission from Ref. [144] Copyright 2019 Elsevier Ltd. **b** UV-vis spectra of the Li_2S_6 solution after exposure to graphene (G), NG, SACo@NG, and SAV@NG and the inserted digital image of Li_2S_6 absorption test [145], Reused with permission from Ref. [145] Copyright 2019 American Chemical Society. **c** XRD patterns of pristine and Pt anchored graphene electrode [150], Reused with permission from Ref. [150] Copyright 2015 American Chemical Society. **d** Sulfur K-edge and cobalt K-edge XANES of S/CP@NCNT@CoS₃ electrode at different depth of discharge/charge. **e** Sulfur K-edge of S/CP@NCNT electrode at different depth of discharge/charge [151]. Reused with permission from Ref. [151] Copyright 2019 Wiley-VCH

the fields of chemical substance structure analysis and chemical imaging. In particular, Fourier Transform Infrared Spectroscopy (FT-IR) has the advantages of rapid testing, convenient operation, good repeatability, and high sensitivity for the testing of LSB electrochemical reaction products. FT-IR can distinguish different lithium polysulfide species through the infrared spectrum of the standard solution and theoretical calculations.

Ultraviolet-visible (UV-vis) spectroscopy is another widely used absorption spectrum. The UV-vis spectrum and absorption of ultraviolet and visible light by the molecules or ions of the substance can be used to analyze, determine, and infer the composition, content, and structure of the substance. UV-vis spectroscopy has the advantages of fast analysis speed, wide detection range, strong stability, and high accuracy. It has become an important means for the characterization of electrochemical reactions in a solution system. Lithium polysulfide compounds absorb ultraviolet-visible radiation, so UV-vis spectroscopy has been widely used in the qualitative and quantitative analysis of lithium polysulfide substances in LSB. Cui et al. [145] used UV-vis spectroscopy to study the adsorption capacity of single-atom

vanadium-cobalt catalysts for polysulfides in Li–S batteries. As shown in Fig. 5.32b, the characteristic peak of polysulfide appears at 260, 280, 300, and 340 nm, and the absorption intensity will change with the concentration decrease of polysulfides.

- Other optical techniques

In addition to various spectroscopic techniques, there are many other optical techniques such as XRD [20, 146, 147], XPS [148, 149], and XANES that play a huge role in the characterization of catalysis in Li–S battery. Arava et al. [150] introduced metal catalyst Pt to Li–S batteries and they used XRD to prove reversible catalytic process. From XRD (Fig. 5.32c) patterns, formation of platinum sulfide on the discharged state ($2\theta = 29.2^\circ$ and 36.4°) and further its fading on charging was observed. Hence, it is confirmed that the nature of interactions between Pt and sulfur is reversible and accountable for stable electrochemical performance. Sun et al. [151] prepared a special material that nitrogen-doped carbon nanotube loaded with CoS_3 catalyst growing on carbon paper. To further understand the catalytic mechanism of CoS_3 , in-situ synchrotron-based XANES measurements are conducted in an ether-based electrolyte with LiClO_4 as lithium salt within a custom-designed in-situ testing cell. The results from the sulfur K-edge and cobalt K-edge XANES are displayed in Fig. 5.32d–e. Before charging/discharging processes, a feature at 2472.0 eV is presented for both sulfur K-edge XANES of S/CP@NCNT@ CoS_3 and S/CP@NCNT electrodes, which is attributed to the S 1s to S–S π^* state transition of elemental sulfur. With the depth of discharge, a weak pre-edge feature at 2470.1 eV emerges, which can be assigned to the S 1s to π^* state transition associated with linear polysulfides. Moreover, the pre-edge at 2470.1 eV gradually picks up the intensity at the expense of the feature at 2472.0 eV which becomes weaker, suggesting decreasing chain length with the depth of discharge. At the inflection point of second discharge plateau (the light pink point in the discharge profile), the intensity of the pre-edge is the highest, indicating the formation of Li_2S_2 with the lowest chain length. After that, two features at 2473.0 and 2475.3 eV, assigned to Li_2S appear with decreasing intensity of the pre-edge feature at 2470.1 eV, indicating the transformation from Li_2S_2 to Li_2S . However, for the S/CP@NCNT electrode, due to the polarization increase at the inflection point, the discharging process terminates within a few seconds, resulting in the incomplete transformation from Li_2S_2 to Li_2S . In contrast, for the S/CP@NCNT@ CoS_3 electrode, the feature associated with polysulfides disappears and only two Li_2S features remain at the end of discharge, further demonstrating the contribution of CoS_3 in increasing the sulfur utilization.

5.5.4 In-Situ Characterization Techniques

At present, the characterization of the catalysis in Li–S battery is mainly reflected in the evaluation of the macroscopic electrochemical performance, such as cycling stability, rate capability, and electrochemical impedance spectroscopy (EIS) and

the structure and composition changes within the Li-S batteries. It is a common idea to link the electrochemical performance with changes in the internal structure and composition of the battery to evaluate the optimization effect of the catalyst. However, none of these evaluation methods can describe the real-time changes in the chemical/physical state of the electrode material during cycling (i.e., electrochemical transients at certain potential values). In other words, ordinary characterization techniques can hardly figure out how changes in the microscopic state of the catalyst affect these steps during the charge/discharge process. Considering the high complexity of the catalytic reaction routes of Li-S batteries, it is imperative to develop novel in situ characterization techniques to monitor the cell components/environment, especially the electrode states at different depths of discharges (DODs) and states of charges (SOCs), and therefore, setting up a bridge linking the macroscopic electrochemical performance and microscopic architectures of the catalyst. This section will introduce the application of in-situ characterization techniques in catalysis. Figure 5.33 show the in situ electrochemical spectroscopy coupling setups [152].

Huang et al. [153] used the in-situ Raman test to monitor the charging-discharging reaction process of LSBs to study the effects of catalysts. The sulfur host material is a multifunctional iron phosphide (FeP) nanocrystal bonded to a 3D porous rGO/CNT scaffold. As shown in Fig. 5.34a, the left side shows the discharge-charge curve of the LSBs, and the right side shows the Raman signal collected of the corresponding voltage. The alternating appearance of Raman peaks explains the conversion of S_8 to polysulfide (Li_2S_x , $x = 4-8$) during discharge and the conversion of polysulfide back to solid sulfur when charged to 2.32 V. The author claims that the test results can verify the idea that FeP nanocrystalline catalyst shows strong adsorption ability toward LiPS and effectively accelerates its conversion.

Yan et al. [88] applied the in-situ Raman spectroscopy to investigate the enhanced polysulfide redox at a VN/VO₂ hybrid host. The heterostructure catalyst has the advantages of ultra-fast anchoring (VO₂) of LiPSs and high-efficiency electrical conductivity (VN) and realized the smooth immobilization, diffusion, and conversion

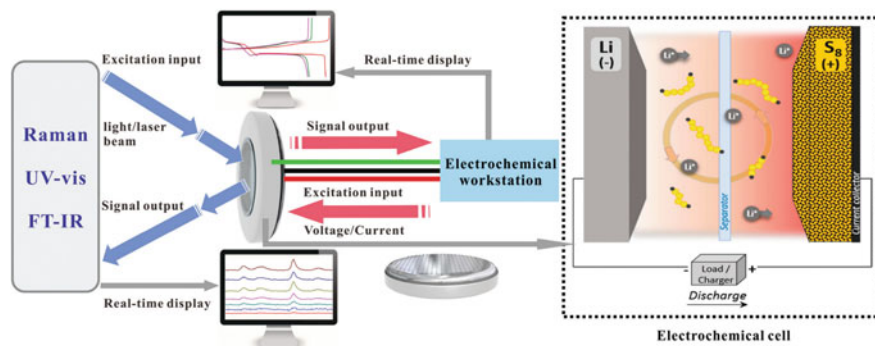


Fig. 5.33 Schematic of the basic configuration of the in situ electrochemical spectroscopy coupling setups [152]. Reused with permission from Ref. [152] Copyright 2017 The Royal Society of Chemistry

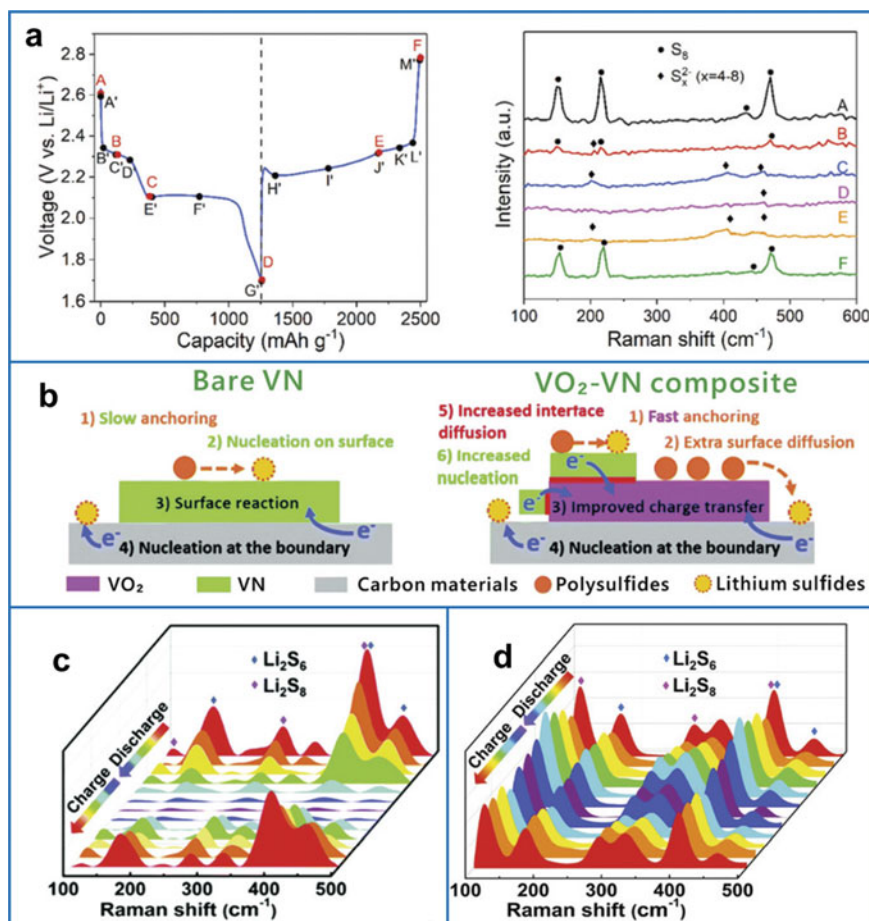


Fig. 5.34 **a** In-situ Raman spectra collected on FeP/rGO/CNTs-S cathode [153]. Reused with permission from Ref. [153] Copyright 2018 Elsevier Ltd. **b** Schematic drawing and comparison of the different anchoring–diffusion–conversion processes on bare VN and VO₂-VN binary host surfaces, respectively. **c** In situ Raman spectra collected upon the first cycle at 0.2 C on the S@₃VO₂-1VN/G cathode. **d** In situ Raman spectra based on the bare S@G cathode collected upon the first cycle at 0.2 C [88]. Reused with permission from Ref. [88] Copyright 2018 The Royal Society of Chemistry

of LiPSs on the interface (Fig. 5.34b). Figure 5.34c, d displayed the in-situ Raman spectra of the electrolyte during charge and discharge process, demonstrating that the VO₂-VN catalyst can accelerate the conversion of polysulfides and suppress the shuttling phenomenon.

Recent years have witnessed a burgeoning interest in introducing catalytic components to accelerate the conversion of polysulfides for development of high-energy and long-life LSBs. The existence of catalysis and its performance improvement in

LSBs have been confirmed by common characterization technology, but the catalytic mechanism has not been fully explained. It is of great significance for explaining the catalytic mechanism to screen catalytic characterization methods suitable for lithium-sulfur systems. This chapter, based on traditional catalytic characterization and characteristics of lithium-sulfur system, has discussed the current problems in catalytic characterization from for aspects: electrochemical techniques, electron microscopy techniques, optical techniques, and in-situ characterization techniques.

5.6 Summary and Perspective

Physical confinement and chemical anchoring of the LiPSs in the cathode region are intrinsically the passive solutions to the “shuttle effect” problem. Catalysis is recently proposed as a fundamental strategy that accelerates the conversion from soluble LiPSs to the solid discharge/charge products ($\text{Li}_2\text{S}/\text{S}_8$) and reduces their accumulation in the electrolyte. Tracing the evolution of various polysulfides to obtain their conversion mechanisms with advanced characterization techniques is important to rational design catalysts. In-situ optical spectroscopy (XAS, XPS, Raman, UV–vis, etc.) are developed for real time monitoring of polysulfides variation and built the bridge that links the macroscopic electrochemical behaviors and microscopic structure and component changes in the operation Li–S batteries. Besides, catalytic materials, including metal oxides, metal sulfides, metal nitrides, single atom catalysts, heterostructures, etc., are summarized to give a cognitive competence about how to construct an ideal catalyst that should have high surface area to facilitate uniform deposition of active sulfur and offer sufficient trapping and catalytic sites for immobilizing and transforming LiPSs. First-principles calculations indicate efficient catalyst should have appropriate polysulfide binding energies—neither too low nor too high for polysulfide adsorption and desorption.

The reactants and products undergo a series of steps on the catalyst. The surface of the catalyst may change as the catalytic reaction proceeds. It is vital to explore the evolution of a catalyst for further understanding the mechanism in Li–S batteries. The identical location TEM (IL-TEM) method shows great potential to enable multiple analyses of one catalyst at identical locations before and after reaction without any changes to the TEM equipment and allows one to track the catalysts of different reaction stages at the same location on an atomic scale to further explore the detailed structure evolution process of catalyst during operation conditions.

In summary, the practical use of Li–S batteries would require more efforts on the exploration of catalysts with high catalytic activity and more exposed active sites in the sulfur redox. Revealing the mechanism of catalysis requires a more complete characterization techniques of the Li–S chemistry than what is available today.

References

1. Yin YX, Xin S, Guo YG, Wan LJ (2013) Lithium-sulfur batteries: electrochemistry, materials, and prospects. *Angew Chem* 52(50):13186–13200. <https://doi.org/10.1002/anie.201304762>
2. Manthiram A, Fu Y, Su Y-S (2013) Challenges and prospects of lithium-sulfur batteries. *Acc Chem Res* 46(5):1125–1134. <https://doi.org/10.1021/ar300179v>
3. Wang D-W, Zeng Q, Zhou G, Yin L, Li F, Cheng H-M, Gentle IR, Lu GQM (2013) Carbon-sulfur composites for Li-S batteries: status and prospects. *J Mater Chem A* 1(33):9382–9394. <https://doi.org/10.1039/c3ta11045a>
4. Manthiram A, Chung SH, Zu C (2015) Lithium-sulfur batteries: progress and prospects. *Adv Mater* 27(12):1980–2006. <https://doi.org/10.1002/adma.201405115>
5. Chen X, Hou T, Persson KA, Zhang Q (2018) Combining theory and experiment in lithium-sulfur batteries: current progress and future perspectives. *Mater Today*. <https://doi.org/10.1016/j.mattod.2018.04.007>
6. Bruce PG, Freunberger SA, Hardwick LJ, Tarascon JM (2011) Li-O₂ and Li-S batteries with high energy storage. *Nat Mater* 11(1):19–29. <https://doi.org/10.1038/nmat3191>
7. Chung S-H, Chang C-H, Manthiram A (2018) Progress on the critical parameters for lithium-sulfur batteries to be practically viable. *Adv Func Mater* 28(28):1801188. <https://doi.org/10.1002/adfm.201801188>
8. Rauh R, Abraham K, Pearson G, Surprenant J, Brummer S (1979) A lithium/dissolved sulfur battery with an organic electrolyte. *J Electrochem Soc* 126(4):523
9. Li G, Lu F, Dou X, Wang X, Luo D, Sun H, Yu A, Chen Z (2020) Polysulfide regulation by the zwitterionic barrier toward durable lithium-sulfur batteries. *J Am Chem Soc* 142(7):3583–3592. <https://doi.org/10.1021/jacs.9b13303>
10. Zhang SS (2013) Liquid electrolyte lithium/sulfur battery: fundamental chemistry, problems, and solutions. *J Power Sources* 231:153–162. <https://doi.org/10.1016/j.jpowsour.2012.12.102>
11. Yuan Z, Peng HJ, Hou TZ, Huang JQ, Chen CM, Wang DW, Cheng XB, Wei F, Zhang Q (2016) Powering lithium-sulfur battery performance by propelling polysulfide redox at sulfiphilic hosts. *Nano Lett* 16(1):519–527. <https://doi.org/10.1021/acs.nanolett.5b04166>
12. Lei T, Chen W, Lv W, Huang J, Zhu J, Chu J, Yan C, Wu C, Yan Y, He W, Xiong J, Li Y, Yan C, Goodenough JB, Duan X (2018) Inhibiting polysulfide shuttling with a graphene composite separator for highly robust lithium-sulfur batteries. *Joule* 2(10):2091–2104. <https://doi.org/10.1016/j.joule.2018.07.022>
13. Peng H-J, Huang J-Q, Cheng X-B, Zhang Q (2017) Review on high-loading and high-energy lithium-sulfur batteries. *Adv Energy Mater* 7(24):1700260. <https://doi.org/10.1002/aenm.201700260>
14. Bhargava A, He J, Gupta A, Manthiram A (2020) Lithium-sulfur batteries: attaining the critical metrics. *Joule* 4(2):285–291. <https://doi.org/10.1016/j.joule.2020.01.001>
15. Ji X, Lee KT, Nazar LF (2009) A highly ordered nanostructured carbon-sulphur cathode for lithium-sulphur batteries. *Nat Mater* 8(6):500–506. <https://doi.org/10.1038/nmat2460>
16. Zhou G, Tian H, Jin Y, Tao X, Liu B, Zhang R, Seh ZW, Zhuo D, Liu Y, Sun J, Zhao J, Zu C, Wu DS, Zhang Q, Cui Y (2017) Catalytic oxidation of Li₂S on the surface of metal sulfides for Li-S batteries. *Proc Natl Acad Sci USA* 114(5):840–845. <https://doi.org/10.1073/pnas.1615837114>

17. Zheng G, Zhang Q, Cha JJ, Yang Y, Li W, Seh ZW, Cui Y (2013) Amphiphilic surface modification of hollow carbon nanofibers for improved cycle life of lithium sulfur batteries. *Nano Lett* 13(3):1265–1270. <https://doi.org/10.1021/nl304795g>
18. Pang Q, Liang X, Kwok CY, Nazar LF (2016) Advances in lithium-sulfur batteries based on multifunctional cathodes and electrolytes. *Nat Energy* 1. <https://doi.org/10.1038/nenergy.2016.132>
19. Wu DS, Shi F, Zhou G, Zu C, Liu C, Liu K, Liu Y, Wang J, Peng Y, Cui Y (2018) Quantitative investigation of polysulfide adsorption capability of candidate materials for Li-S batteries. *Energy Storage Mater* 13:241–246. <https://doi.org/10.1016/j.ensm.2018.01.020>
20. Ma L, Yuan H, Zhang W, Zhu G, Wang Y, Hu Y, Zhao P, Chen R, Chen T, Liu J, Hu Z, Jin Z (2017) Porous-shell vanadium nitride nanobubbles with ultrahigh areal sulfur loading for high-capacity and long-life lithium-sulfur batteries. *Nano Lett* 17(12):7839–7846. <https://doi.org/10.1021/acs.nanolett.7b04084>
21. Zhang J, Hu H, Li Z, Lou XW (2016) Double-shelled nanocages with cobalt hydroxide inner shell and layered double hydroxides outer shell as high-efficiency polysulfide mediator for lithium-sulfur batteries. *Angew Chem* 55(12):3982–3986. <https://doi.org/10.1002/anie.201511632>
22. Su YS, Manthiram A (2012) Lithium-sulphur batteries with a microporous carbon paper as a bifunctional interlayer. *Nat Commun* 3:1166. <https://doi.org/10.1038/ncomms2163>
23. Bai S, Liu X, Zhu K, Wu S, Zhou H (2016) Metal-organic framework-based separator for lithium-sulfur batteries. *Nat Energy* 1(7). <https://doi.org/10.1038/nenergy.2016.94>
24. Luo C, Liang X, Sun Y, Lv W, Sun Y, Lu Z, Hua W, Yang H, Wang R, Yan C, Li J, Wan Y, Yang Q-H (2020) An organic nickel salt-based electrolyte additive boosts homogeneous catalysis for lithium-sulfur batteries. *Energy Storage Mater* 33:290–297. <https://doi.org/10.1016/j.ensm.2020.08.033>
25. Peng L, Wei Z, Wan C, Li J, Chen Z, Zhu D, Baumann D, Liu H, Allen CS, Xu X, Kirkland AI, Shakir I, Almutairi Z, Tolbert S, Dunn B, Huang Y, Sautet P, Duan X (2020) A fundamental look at electrocatalytic sulfur reduction reaction. *Nat Catal* 3(9):762–770. <https://doi.org/10.1038/s41929-020-0498-x>
26. Pang Q, Kundu D, Cuisinier M, Nazar LF (2014) Surface-enhanced redox chemistry of polysulfides on a metallic and polar host for lithium-sulphur batteries. *Nat Commun* 5:4759. <https://doi.org/10.1038/ncomms5759>
27. Liang X, Hart C, Pang Q, Garsuch A, Weiss T, Nazar LF (2015) A highly efficient polysulfide mediator for lithium-sulfur batteries. *Nat Commun* 6:5682. <https://doi.org/10.1038/ncomms6682>
28. Liang X, Kwok CY, Lodi-Marzano F, Pang Q, Cuisinier M, Huang H, Hart CJ, Houtarde D, Kaup K, Sommer H, Brezesinski T, Janek J, Nazar LF (2016) Tuning transition metal oxide-sulfur interactions for long life lithium sulfur batteries: the “goldilocks” principle. *Adv Energy Mater* 6(6). <https://doi.org/10.1002/aenm.201501636>
29. Wang H, Zhang N, Li Y, Zhang P, Chen Z, Zhang C, Qiao X, Dai Y, Wang Q, Liu S (2019) Unique flexible NiFe₂O₄@S/rGO-CNT electrode via the synergistic adsorption/electrocatalysis effect toward high-performance lithium-sulfur batteries. *J Phys Chem Lett* 10(21):6518–6524. <https://doi.org/10.1021/acs.jpcclett.9b02649>
30. Zhou Y, Shu H, Zhou Y, Sun T, Han M, Chen Y, Chen M, Chen Z, Yang X, Wang X (2020) Flower-like Bi₄Ti₃O₁₂/carbon nanotubes as reservoir and promoter of polysulfide for lithium sulfur battery. *J Power Sources* 453. <https://doi.org/10.1016/j.jpowsour.2020.227896>
31. Liu YT, Han DD, Wang L, Li GR, Liu S, Gao XP (2019) NiCo₂O₄ nanofibers as carbon-free sulfur immobilizer to fabricate sulfur-based composite with high volumetric capacity for lithium-sulfur battery. *Adv Energy Mater* 9(11). <https://doi.org/10.1002/aenm.201803477>
32. Zhang L, Wan F, Cao H, Liu L, Wang Y, Niu Z (2020) Integration of binary active sites: Co₃V₂O₈ as polysulfide traps and catalysts for lithium-sulfur battery with superior cycling stability. *Small* 16(18):e1907153. <https://doi.org/10.1002/smll.201907153>
33. Guo P, Sun K, Shang X, Liu D, Wang Y, Liu Q, Fu Y, He D (2019) Nb₂O₅/RGO nanocomposite modified separators with robust polysulfide traps and catalytic centers for boosting

- performance of lithium-sulfur batteries. *Small* 15(40):1902363. <https://doi.org/10.1002/smll.201902363>
34. Song YZ, Zhao W, Zhu XY, Zhang L, Li QC, Ding F, Liu ZF, Sun JY (2018) Vanadium dioxide-graphene composite with ultrafast anchoring behavior of polysulfides for lithium-sulfur batteries. *Acs Appl Mater Inter* 10(18):15733–15741. <https://doi.org/10.1021/acsami.8b02920>
 35. He J, Luo L, Chen Y, Manthiram A (2017) Yolk-shelled C@Fe₃O₄ nanoboxes as efficient sulfur hosts for high-performance lithium-sulfur batteries. *Adv Mater* 29(34):1702707–1702712. <https://doi.org/10.1002/adma.201702707>
 36. Liu R, Guo F, Zhang X, Yang J, Li M, Miaomiao W, Liu H, Feng M, Zhang L (2019) Novel “bird-nest” structured Co₃O₄/acidified multiwall carbon nanotube (ACNT) hosting materials for lithium-sulfur batteries. *Acs Appl Energy Mater* 2(2):1348–1356. <https://doi.org/10.1021/acsaem.8b01914>
 37. Ding M, Huang S, Wang Y, Hu J, Pam ME, Fan S, Shi Y, Ge Q, Yang HY (2019) Promoting polysulfide conversion by catalytic ternary Fe₃O₄/carbon/graphene composites with ordered microchannels for ultrahigh-rate lithium-sulfur batteries. *J Mater Chem A* 7(43):25078–25087. <https://doi.org/10.1039/c9ta06489c>
 38. Zheng C, Niu S, Lv W, Zhou G, Li J, Fan S, Deng Y, Pan Z, Li B, Kang F, Yang Q-H (2017) Propelling polysulfides transformation for high-rate and long-life lithium-sulfur batteries. *Nano Energy* 33:306–312. <https://doi.org/10.1016/j.nanoen.2017.01.040>
 39. Wang H-E, Yin K, Qin N, Zhao X, Xia F-J, Hu Z-Y, Guo G, Cao G, Zhang W (2019) Oxygen-deficient titanium dioxide as a functional host for lithium-sulfur batteries. *J Mater Chem A* 7(17):10346–10353. <https://doi.org/10.1039/c9ta01598a>
 40. Li Z, Zhou C, Hua J, Hong X, Sun C, Li HW, Xu X, Mai L (2020) Engineering oxygen vacancies in a polysulfide-blocking layer with enhanced catalytic ability. *Adv Mater* 32(10):e1907444. <https://doi.org/10.1002/adma.201907444>
 41. Pu J, Shen Z, Zheng J, Wu W, Zhu C, Zhou Q, Zhang H, Pan F (2017) Multifunctional Co₃S₄@sulfur nanotubes for enhanced lithium-sulfur battery performance. *Nano Energy* 37:7–14. <https://doi.org/10.1016/j.nanoen.2017.05.009>
 42. Wang H, Zhang Q, Yao H, Liang Z, Lee HW, Hsu PC, Zheng G, Cui Y (2014) High electrochemical selectivity of edge versus terrace sites in two-dimensional layered MoS₂ materials. *Nano Lett* 14(12):7138–7144. <https://doi.org/10.1021/nl503730c>
 43. Yu X, Zhou G, Cui Y (2019) Mitigation of shuttle effect in Li-S battery using a self-assembled ultrathin molybdenum disulfide interlayer. *ACS Appl Mater Inter* 11(3):3080–3086. <https://doi.org/10.1021/acsami.8b19354>
 44. Babu G, Masurkar N, Al Salem H, Arava LM (2017) Transition Metal Dichalcogenide atomic layers for lithium polysulfides electrocatalysis. *J Am Chem Soc* 139(1):171–178. <https://doi.org/10.1021/jacs.6b08681>
 45. Lin HB, Yang LQ, Jiang X, Li GC, Zhang TR, Yao QF, Zheng GW, Lee JY (2017) Electrocatalysis of polysulfide conversion by sulfur-deficient MoS₂ nanoflakes for lithium-sulfur batteries. *Energy Environ Sci* 10(6):1476–1486. <https://doi.org/10.1039/c7ee01047h>
 46. Lin HB, Zhang SL, Zhang TR, Ye HL, Yao QF, Zheng GW, Lee JY (2019) Simultaneous cobalt and phosphorous doping of MoS₂ for improved catalytic performance on polysulfide conversion in lithium-sulfur batteries. *Adv Energy Mater* 9(38). <https://doi.org/10.1002/aenm.201902096>
 47. Li Z, He Q, Xu X, Zhao Y, Liu X, Zhou C, Ai D, Xia L, Mai L (2018) A 3D nitrogen-doped graphene/TiN nanowires composite as a strong polysulfide anchor for lithium-sulfur batteries with enhanced rate performance and high areal capacity. *Adv Mater* 30(45):1804089. <https://doi.org/10.1002/adma.201804089>
 48. Cui Z, Zu C, Zhou W, Manthiram A, Goodenough JB (2016) Mesoporous titanium nitride-enabled highly stable lithium-sulfur batteries. *Adv Mater* 28(32):6926–6931. <https://doi.org/10.1002/adma.201601382>
 49. Sun ZH, Zhang JQ, Yin LC, Hu GJ, Fang RP, Cheng HM, Li F (2017) Conductive porous vanadium nitride/graphene composite as chemical anchor of polysulfides for lithium-sulfur batteries. *Nat Commun* 8:8. <https://doi.org/10.1038/ncomms14627>

50. Characterization and electrochemical actives of nanostructured transition metal nitrides as cathode materials for lithium sulfur batteries
51. Chen G, Song X, Wang S, Chen X, Wang H (2018) Two-dimensional molybdenum nitride nanosheets modified Celgard separator with multifunction for Li-S batteries. *J Power Sources* 408:58–64. <https://doi.org/10.1016/j.jpowsour.2018.10.078>
52. Deng D-R, An T-H, Li Y-J, Wu Q-H, Zheng M-S, Dong Q-F (2016) Hollow porous titanium nitride tubes as a cathode electrode for extremely stable Li-S batteries. *J Mater Chem A* 4(41):16184–16190. <https://doi.org/10.1039/c6ta07221f>
53. Deng DR, Xue F, Jia YJ, Ye JC, Bai CD, Zheng MS, Dong QF (2017) Co₄N nanosheet assembled mesoporous sphere as a matrix for ultrahigh sulfur content lithium-sulfur batteries. *ACS Nano* 11(6):6031–6039. <https://doi.org/10.1021/acsnano.7b01945>
54. Li Z, Wang X, Liu J, Gao C, Jiang L, Lin Y, Meng A (2020) 3D honeycomb nanostructure comprised of mesoporous N-doped carbon nanosheets encapsulating isolated cobalt and vanadium nitride nanoparticles as a highly efficient electrocatalyst for the oxygen reduction reaction. *ACS Sustain Chem Eng* 8(8):3291–3301. <https://doi.org/10.1021/acssuschemeng.9b06934>
55. Wang Y, Zhang R, Pang Y-c, Chen X, Lang J, Xu J, Xiao C, Li H, Xi K, Ding S (2019) Carbon@titanium nitride dual shell nanospheres as multi-functional hosts for lithium sulfur batteries. *Energy Storage Mater* 16:228–235. <https://doi.org/10.1016/j.ensm.2018.05.019>
56. Zhao M, Peng HJ, Zhang ZW, Li BQ, Chen X, Xie J, Chen X, Wei JY, Zhang Q, Huang JQ (2019) Activating inert metallic compounds for high-rate lithium-sulfur batteries through in situ etching of extrinsic metal. *Angew Chem Int Edit* 58(12):3779–3783. <https://doi.org/10.1002/anie.201812062>
57. Li X, Gao B, Huang X, Guo Z, Li Q, Zhang X, Chu PK, Huo K (2019) Conductive mesoporous niobium nitride microspheres/nitrogen-doped graphene hybrid with efficient polysulfide anchoring and catalytic conversion for high-performance lithium-sulfur batteries. *ACS Appl Mater Interfaces* 11(3):2961–2969. <https://doi.org/10.1021/acsmi.8b17376>
58. Fan S, Huang SZ, Pam ME, Chen S, Wu QY, Hu JP, Wang Y, Ang LK, Yan CC, Shi YM, Yang HY (2019) Design multifunctional catalytic interface: toward regulation of polysulfide and Li₂S redox conversion in Li-S batteries. *Small* 15(51). <https://doi.org/10.1002/sml.201906132>
59. Tian D, Song XQ, Wang MX, Wu X, Qiu Y, Guan B, Xu XZ, Fan LS, Zhang NQ, Sun KN (2019) MoN supported on graphene as a bifunctional interlayer for advanced Li-S batteries. *Adv Energy Mater* 9(46). <https://doi.org/10.1002/aenm.201901940>
60. Liu Z, Zhou L, Ge Q, Chen R, Ni M, Utetiwo W, Zhang X, Yang W (2018) Atomic iron catalysis of polysulfide conversion in lithium-sulfur batteries. *ACS Appl Mater Interfaces* 10(23):19311–19317. <https://doi.org/10.1021/acsmi.8b03830>
61. Wang J, Jia L, Zhong J, Xiao Q, Wang C, Zang K, Liu H, Zheng H, Luo J, Yang J, Fan H, Duan W, Wu Y, Lin H, Zhang Y (2019) Single-atom catalyst boosts electrochemical conversion reactions in batteries. *Energy Storage Mater* 18:246–252. <https://doi.org/10.1016/j.ensm.2018.09.006>
62. Du Z, Chen X, Hu W, Chuang C, Xie S, Hu A, Yan W, Kong X, Wu X, Ji H, Wan LJ (2019) Cobalt in nitrogen-doped graphene as single-atom catalyst for high-sulfur content lithium-sulfur batteries. *J Am Chem Soc* 141(9):3977–3985. <https://doi.org/10.1021/jacs.8b12973>
63. Xie J, Li BQ, Peng HJ, Song YW, Zhao M, Chen X, Zhang Q, Huang JQ (2019) Implanting atomic cobalt within mesoporous carbon toward highly stable lithium-sulfur batteries. *Adv Mater* 31(43):e1903813. <https://doi.org/10.1002/adma.201903813>
64. Zhang D, Wang S, Hu R, Gu J, Cui Y, Li B, Chen W, Liu C, Shang J, Yang S (2020) Catalytic conversion of polysulfides on single atom zinc implanted MXene toward high-rate lithium-sulfur batteries. *Adv Func Mater*. <https://doi.org/10.1002/adfm.202002471>
65. Zhang L, Liu D, Muhammad Z, Wan F, Xie W, Wang Y, Song L, Niu Z, Chen J (2019) Single nickel atoms on nitrogen-doped graphene enabling enhanced kinetics of lithium-sulfur batteries. *Adv Mater* 31(40):e1903955. <https://doi.org/10.1002/adma.201903955>

66. Li S, Zhang W, Zheng J, Lv M, Song H, Du L (2020) Inhibition of polysulfide shuttles in Li-S batteries: modified separators and solid-state electrolytes. *Adv Energy Mater* 202000779–220200803. <https://doi.org/10.1002/aenm.202000779>
67. Zhang K, Chen Z, Ning R, Xi S, Tang W, Du Y, Liu C, Ren Z, Chi X, Bai M, Shen C, Li X, Wang X, Zhao X, Leng K, Pennycook SJ, Li H, Xu H, Loh KP, Xie K (2019) Single-atom coated separator for robust lithium-sulfur batteries. *ACS Appl Mater Interfaces* 11(28):25147–25154. <https://doi.org/10.1021/acsami.9b05628>
68. Lu C, Chen Y, Yang Y, Chen X (2020) Single-atom catalytic materials for lean-electrolyte ultrastable lithium-sulfur batteries. *Nano Lett* 20(7):5522–5530. <https://doi.org/10.1021/acs.nanolett.0c02167>
69. Wang C, Song H, Yu C, Ullah Z, Guan Z, Chu R, Zhang Y, Zhao L, Li Q, Liu L (2020) Iron single-atom catalyst anchored on nitrogen-rich MOF-derived carbon nanocage to accelerate polysulfide redox conversion for lithium sulfur batteries. *J Mater Chem A* 8(6):3421–3430. <https://doi.org/10.1039/c9ta11680j>
70. Li Y, Wu J, Zhang B, Wang W, Zhang G, Seh ZW, Zhang N, Sun J, Huang L, Jiang J, Zhou J, Sun Y (2020) Fast conversion and controlled deposition of lithium (poly)sulfides in lithium-sulfur batteries using high-loading cobalt single atoms. *Energy Storage Mater* 30:250–259. <https://doi.org/10.1016/j.ensm.2020.05.022>
71. Wu J, Chen J, Huang Y, Feng K, Deng J, Huang W, Wu Y, Zhong J, Li Y (2019) Cobalt atoms dispersed on hierarchical carbon nitride support as the cathode electrocatalyst for high-performance lithium-polysulfide batteries. *Sci Bull* 64(24):1875–1880. <https://doi.org/10.1016/j.scib.2019.08.016>
72. Fang L, Feng Z, Cheng L, Winans RE, Li T (2020) Design principles of single atoms on carbons for lithium-sulfur batteries. *Small Methods* 2000315. <https://doi.org/10.1002/smtd.202000315>
73. Zhou TH, Lv W, Li J, Zhou GM, Zhao Y, Fan SX, Liu BL, Li BH, Kang FY, Yang QH (2017) Twinborn TiO₂-TiN heterostructures enabling smooth trapping-diffusion-conversion of polysulfides towards ultralong life lithium-sulfur batteries. *Energy Environ Sci* 10(7):1694–1703. <https://doi.org/10.1039/c7ee01430a>
74. Wang M, Fan L, Wu X, Qiu Y, Wang Y, Zhang N, Sun K (2019) SnS₂/SnO₂ heterostructures towards enhanced electrochemical performance of lithium-sulfur batteries. *Chemistry* 25(21):5416–5421. <https://doi.org/10.1002/chem.201806231>
75. Jin Z, Lin T, Jia H, Liu B, Zhang Q, Chen L, Zhang L, Li L, Su Z, Wang C (2020) In situ engineered ultrafine NiS₂-ZnS heterostructures in micro-mesoporous carbon spheres accelerating polysulfide redox kinetics for high-performance lithium-sulfur batteries. *Nanoscale* 12(30):16201–16207. <https://doi.org/10.1039/d0nr04189k>
76. Hao B, Li H, Lv W, Zhang Y, Niu S, Qi Q, Xiao S, Li J, Kang F, Yang Q-H (2019) Reviving catalytic activity of nitrides by the doping of the inert surface layer to promote polysulfide conversion in lithium-sulfur batteries. *Nano Energy* 60:305–311. <https://doi.org/10.1016/j.nanoen.2019.03.064>
77. Zhang B, Luo C, Deng Y, Huang Z, Zhou G, Lv W, He YB, Wan Y, Kang F, Yang QH (2020) Optimized catalytic WS₂-WO₃ heterostructure design for accelerated polysulfide conversion in lithium-sulfur batteries. *Adv Energy Mater* 10(15):2000091. <https://doi.org/10.1002/aenm.202000091>
78. Wang R, Luo C, Wang T, Zhou G, Deng Y, He Y, Zhang Q, Kang F, Lv W, Yang QH (2020) Bidirectional catalysts for liquid-solid redox conversion in lithium-sulfur batteries. *Adv Mater* e2000315. <https://doi.org/10.1002/adma.202000315>
79. Wang N, Chen B, Qin K, Liu E, Shi C, He C, Zhao N (2019) Rational design of Co₉S₈/CoO heterostructures with well-defined interfaces for lithium sulfur batteries: A study of synergistic adsorption-electrocatalysis function. *Nano Energy* 60:332–339. <https://doi.org/10.1016/j.nanoen.2019.03.060>
80. Jiao L, Zhang C, Geng C, Wu S, Li H, Lv W, Tao Y, Chen Z, Zhou G, Li J, Ling G, Wan Y, Yang QH (2019) Capture and catalytic conversion of polysulfides by in situ built TiO₂-MXene heterostructures for lithium-sulfur batteries. *Adv Energy Mater* 9(19):1900219–1900228. <https://doi.org/10.1002/aenm.201900219>

81. Fang R, Zhao S, Sun Z, Wang D-W, Amal R, Wang S, Cheng H-M, Li F (2018) Polysulfide immobilization and conversion on a conductive polar MoC@MoO_x material for lithium-sulfur batteries. *Energy Storage Mater* 10:56–61. <https://doi.org/10.1016/j.ensm.2017.08.005>
82. He J, Hartmann G, Lee M, Hwang GS, Chen Y, Manthiram A (2019) Freestanding 1T MoS₂/graphene heterostructures as a highly efficient electrocatalyst for lithium polysulfides in Li-S batteries. *Energy Environ Sci* 12(1):344–350. <https://doi.org/10.1039/c8ee03252a>
83. Wang Z, Yu K, Feng Y, Qi R, Ren J, Zhu Z (2019) VO₂(p)-V₂C(MXene) grid structure as a lithium polysulfide catalytic host for high-performance Li-S battery. *ACS Appl Mater Interfaces* 11(47):44282–44292. <https://doi.org/10.1021/acsami.9b15586>
84. Zhou T, Zhao Y, Zhou G, Lv W, Sun P, Kang F, Li B, Yang QH (2017) An in-plane heterostructure of graphene and titanium carbide for efficient polysulfide confinement. *Nano Energy* 39:291–296. <https://doi.org/10.1016/j.nanoen.2017.07.012>
85. Wu J, You N, Li X, Zeng H, Li S, Xue Z, Ye Y, Xie X (2019) SiO₂@MoS₂ core-shell nanocomposite layers with high lithium ion diffusion as a triple polysulfide shield for high performance lithium-sulfur batteries. *J Mater Chem A* 7(13):7644–7653. <https://doi.org/10.1039/c9ta00982e>
86. Zhang L, Liu Y, Zhao Z, Jiang P, Zhang T, Li M, Pan S, Tang T, Wu T, Liu P, Hou Y, Lu H (2020) Enhanced polysulfide regulation via porous catalytic V₂O₃/V₈C₇ heterostructures derived from metal-organic frameworks toward high-performance Li-S batteries. *ACS Nano* 14(7):8495–8507. <https://doi.org/10.1021/acsnano.0c02762>
87. Ye C, Jiao Y, Jin H, Slattey AD, Davey K, Wang H, Qiao SZ (2018) 2D MoN-VN heterostructure to regulate polysulfides for highly efficient lithium-sulfur batteries. *Angew Chem Int Ed Engl* 57(51):16703–16707. <https://doi.org/10.1002/anie.201810579>
88. Song Y, Zhao W, Kong L, Zhang L, Zhu X, Shao Y, Ding F, Zhang Q, Sun J, Liu Z (2018) Synchronous immobilization and conversion of polysulfides on a VO₂-VN binary host targeting high sulfur load Li-S batteries. *Energy Environ Sci* 11(9):2620–2630. <https://doi.org/10.1039/c8ee01402g>
89. Zeng S, Arumugam GM, Liu X, Yang Y, Li X, Zhong H, Guo F, Mai Y (2020) Encapsulation of sulfur into N-doped porous carbon cages by a facile, template-free method for stable lithium-sulfur cathode. *Small*:e2001027. <https://doi.org/10.1002/sml.202001027>
90. Babu G, Ababtain K, Ng KY, Arava LM (2015) Electrocatalysis of lithium polysulfides: current collectors as electrodes in Li/S battery configuration. *Sci Rep* 5:8763. <https://doi.org/10.1038/srep08763>
91. Bisquert J (2002) Theory of the impedance of electron diffusion and recombination in a thin layer. *J Phys Chem B* 106:325–333
92. Peng H, Zhang Y, Chen Y, Zhang J, Jiang H, Chen X, Zhang Z, Zeng Y, Sa B, Wei Q, Lin J, Guo H (2020) Reducing polarization of lithium-sulfur batteries via ZnS/reduced graphene oxide accelerated lithium polysulfide conversion. *Mater Today Energy* 18:100519. <https://doi.org/10.1016/j.mtener.2020.100519>
93. Huang X, Wang Z, Knibbe R, Luo B, Ahad SA, Sun D, Wang L (2019) Cyclic voltammetry in lithium-sulfur batteries—challenges and opportunities. *Energy Technol*. <https://doi.org/10.1002/ente.201801001>
94. Sun Z, Zhang J, Yin L, Hu G, Fang R, Cheng HM, Li F (2017) Conductive porous vanadium nitride/graphene composite as chemical anchor of polysulfides for lithium-sulfur batteries. *Nat Commun* 8:14627. <https://doi.org/10.1038/ncomms14627>
95. Zhang G, Zhang Z-W, Peng H-J, Huang J-Q, Zhang Q (2017) A toolbox for lithium-sulfur battery research: methods and protocols. *Small Methods* 1(7):1700134. <https://doi.org/10.1002/smt.201700134>
96. Tang K, Yu X, Sun J, Li H, Huang X (2011) Kinetic analysis on LiFePO₄ thin films by CV, GITT, and EIS. *Electrochim Acta* 56(13):4869–4875. <https://doi.org/10.1016/j.electacta.2011.02.119>
97. Chauhan M, Reddy KP, Gopinath CS, Deka S (2017) Copper cobalt sulfide nanosheets realizing a promising electrocatalytic oxygen evolution reaction. *ACS Catal* 7(9):5871–5879. <https://doi.org/10.1021/acscatal.7b01831>

98. Li BQ, Kong L, Zhao CX, Jin Q, Chen X, Peng HJ, Qin JL, Chen JX, Yuan H, Zhang Q, Huang JQ (2019) Expediting redox kinetics of sulfur species by atomic-scale electrocatalysts in lithium–sulfur batteries. *InfoMat* 1(4):533–541. <https://doi.org/10.1002/inf2.12056>
99. Al Salem H, Babu G, Rao CV, Arava LM (2015) Electrocatalytic polysulfide traps for controlling redox shuttle process of Li-S batteries. *J Am Chem Soc* 137(36):11542–11545. <https://doi.org/10.1021/jacs.5b04472>
100. Yu M, Zhou S, Wang Z, Wang Y, Zhang N, Wang S, Zhao J, Qiu J (2019) Accelerating polysulfide redox conversion on bifunctional electrocatalytic electrode for stable Li-S batteries. *Energy Storage Mater* 20:98–107. <https://doi.org/10.1016/j.ensm.2018.11.028>
101. Pang Q, Kwok CY, Kundu D, Liang X, Nazar LF (2019) Lightweight metallic MgB₂ mediates polysulfide redox and promises high-energy-density lithium-sulfur batteries. *Joule* 3(1):136–148. <https://doi.org/10.1016/j.joule.2018.09.024>
102. Tao Y, Wei Y, Liu Y, Wang J, Qiao W, Ling L, Long D (2016) Kinetically-enhanced polysulfide redox reactions by Nb₂O₅ nanocrystals for high-rate lithium–sulfur battery. *Energy Environ Sci* 9(10):3230–3239. <https://doi.org/10.1039/c6ee01662f>
103. Shen Z, Zhang Z, Li M, Yuan Y, Zhao Y, Zhang S, Zhong C, Zhu J, Lu J, Zhang H (2020) Rational design of a Ni₃N_{0.85} electrocatalyst to accelerate polysulfide conversion in lithium-sulfur batteries. *ACS Nano* 14(6):6673–6682. <https://doi.org/10.1021/acsnano.9b09371>
104. Shen Z, Cao M, Zhang Z, Pu J, Zhong C, Li J, Ma H, Li F, Zhu J, Pan F, Zhang H (2019) Efficient Ni₂Co₄P₃ nanowires catalysts enhance ultrahigh-loading lithium-sulfur conversion in a microreactor-like battery. *Adv Func Mater* 30(3):1906661. <https://doi.org/10.1002/adfm.201906661>
105. Zhou R, Zheng Y, Jaroniec M, Qiao S-Z (2016) Determination of the electron transfer number for the oxygen reduction reaction: from theory to experiment. *ACS Catal* 6(7):4720–4728. <https://doi.org/10.1021/acscatal.6b01581>
106. Du L, Wu Q, Yang L, Wang X, Che R, Lyu Z, Chen W, Wang X, Hu Z (2019) Efficient synergism of electrocatalysis and physical confinement leading to durable high-power lithium-sulfur batteries. *Nano Energy* 57:34–40. <https://doi.org/10.1016/j.nanoen.2018.12.019>
107. Song Y, Cai W, Kong L, Cai J, Zhang Q, Sun J (2019) Rationalizing electrocatalysis of Li–S chemistry by mediator design: progress and prospects. *Adv Energy Mater* 10(11):1901075. <https://doi.org/10.1002/aenm.201901075>
108. Fan FY, Carter WC, Chiang YM (2015) Mechanism and kinetics of Li₂S precipitation in lithium-sulfur batteries. *Adv Mater* 27(35):5203–5209. <https://doi.org/10.1002/adma.201501559>
109. Fan S, Huang S, Pam ME, Chen S, Wu Q, Hu J, Wang Y, Ang LK, Yan C, Shi Y, Yang HY (2019) Design multifunctional catalytic interface: toward regulation of polysulfide and Li₂S redox conversion in Li-S batteries. *Small* 15(51):e1906132. <https://doi.org/10.1002/smll.201906132>
110. Zhou G, Zhao S, Wang T, Yang SZ, Johannessen B, Chen H, Liu C, Ye Y, Wu Y, Peng Y, Liu C, Jiang SP, Zhang Q, Cui Y (2020) Theoretical calculation guided design of single-atom catalysts toward fast kinetic and long-life Li-S batteries. *Nano Lett* 20(2):1252–1261. <https://doi.org/10.1021/acs.nanolett.9b04719>
111. Guangmin Zhou L-CY, Lu, Da-Wei Wang, Li SP, Gentle IR, Li F, Cheng H-M (2013) Fibrous hybrid of graphene and sulfur nanocrystals for high-performance lithium-sulfur batteries. *ASC Nano* 7:5367–5375
112. Ma L, Zhuang H, Lu Y, Moganty SS, Hennig RG, Archer LA (2014) Tethered molecular sorbents: enabling metal-sulfur battery cathodes. *Adv Energy Mater* 4(17):1400390. <https://doi.org/10.1002/aenm.201400390>
113. Xiao Z, Yang Z, Wang L, Nie H, Zhong M, Lai Q, Xu X, Zhang L, Huang S (2015) A lightweight TiO₍₂₎/graphene interlayer, applied as a highly effective polysulfide absorbent for fast, Long-Life Lithium-Sulfur Batteries. *Adv Mater* 27(18):2891–2898. <https://doi.org/10.1002/adma.201405637>
114. Liang X, Garsuch A, Nazar LF (2015) Sulfur cathodes based on conductive MXene nanosheets for high-performance lithium-sulfur batteries. *Angew Chem Int Ed Engl* 54(13):3907–3911. <https://doi.org/10.1002/anie.201410174>

115. Pang Q, Liang X, Kwok CY, Nazar LF (2016) Advances in lithium-sulfur batteries based on multifunctional cathodes and electrolytes. *Nat Energy* 1(9). <https://doi.org/10.1038/nenergy.2016.132>
116. Zhou J, Liu X, Zhu L, Zhou J, Guan Y, Chen L, Niu S, Cai J, Sun D, Zhu Y, Du J, Wang G, Qian Y (2018) Deciphering the modulation essence of p bands in co-based compounds on Li-S chemistry. *Joule* 2(12):2681–2693. <https://doi.org/10.1016/j.joule.2018.08.010>
117. Song Y, Cai W, Kong L, Cai J, Zhang Q, Sun J (2019) Rationalizing electrocatalysis of Li-S chemistry by mediator design: progress and prospects. *Adv Energy Mater* 10(11). <https://doi.org/10.1002/aenm.201901075>
118. Yu J, Xiao J, Li A, Yang Z, Zeng L, Zhang Q, Zhu Y, Guo L (2020) Enhanced multiple anchoring and catalytic conversion of polysulfides by amorphous MoS₃ nanoboxes for high-performance Li-S batteries. *Angew Chem Int Ed Engl* 59(31):13071–13078. <https://doi.org/10.1002/anie.202004914>
119. Ye H, Lee JY (2020) Solid additives for improving the performance of sulfur cathodes in lithium-sulfur batteries—adsorbents, mediators, and catalysts. *Small Methods* 4(6):1900864. <https://doi.org/10.1002/smt.201900864>
120. Tsao Y, Lee M, Miller EC, Gao G, Park J, Chen S, Katsumata T, Tran H, Wang L-W, Toney MF, Cui Y, Bao Z (2019) Designing a quinone-based redox mediator to facilitate Li₂S oxidation in Li-S batteries. *Joule* 3(3):872–884. <https://doi.org/10.1016/j.joule.2018.12.018>
121. Liang X, Kwok CY, Lodi-Marzano F, Pang Q, Cuisinier M, Huang H, Hart CJ, Houtarde D, Kaup K, Sommer H, Brezesinski T, Janek J, Nazar LF (2016) Tuning transition metal oxide-sulfur interactions for long life lithium sulfur batteries: the “goldilocks” principle. *Adv Energy Mater* 6(6):1501636. <https://doi.org/10.1002/aenm.201501636>
122. Yuan H, Peng H-J, Li B-Q, Xie J, Kong L, Zhao M, Chen X, Huang J-Q, Zhang Q (2019) Conductive and catalytic triple-phase interfaces enabling uniform nucleation in high-rate lithium-sulfur batteries. *Adv Energy Mater* 9(1):1802768. <https://doi.org/10.1002/aenm.201802768>
123. Zhao M, Peng HJ, Wei JY, Huang JQ, Li BQ, Yuan H, Zhang Q (2019) Dictating high-capacity lithium-sulfur batteries through redox-mediated lithium sulfide growth. *Small Methods* 4(6):1900344. <https://doi.org/10.1002/smt.201900344>
124. Geng C, Hua W, Wang D, Ling G, Zhang C, Yang QH (2021) Demystifying the catalysis in lithium-sulfur batteries: characterization methods and techniques. *SusMat*. <https://doi.org/10.1002/sus2.5>
125. Dai C, Lim J-M, Wang M, Hu L, Chen Y, Chen Z, Chen H, Bao S-J, Shen B, Li Y, Henkelman G, Xu M (2018) Honeycomb-like spherical cathode host constructed from hollow metallic and polar Co₉S₈ tubules for advanced lithium-sulfur batteries. *Adv Funct Mater* 28(14). <https://doi.org/10.1002/adfm.201704443>
126. Zhou F, Li Z, Luo X, Wu T, Jiang B, Lu L-L, Yao H-B, Antonietti M, Yu S-H (2018) Low cost metal carbide nanocrystals as binding and electrocatalytic sites for high performance Li-S batteries. *Nano Lett* 18(2):1035–1043. <https://doi.org/10.1021/acs.nanolett.7b04505>
127. Li Z, Zhang J, Guan B, Wang D, Liu L-M, Lou XW (2016) A sulfur host based on titanium monoxide@carbon hollow spheres for advanced lithium-sulfur batteries. *Nat Commun* 7(1). <https://doi.org/10.1038/ncomms13065>
128. Jiao L, Zhang C, Geng C, Wu S, Li H, Lv W, Tao Y, Chen Z, Zhou G, Li J, Ling G, Wan Y, Yang QH (2019) Capture and catalytic conversion of polysulfides by in situ built TiO₂-MXene heterostructures for lithium-sulfur batteries. *Adv Energy Mater* 9(19). <https://doi.org/10.1002/aenm.201900219>
129. Wang H, Adams BD, Pan H, Zhang L, Han KS, Estevez L, Lu D, Jia H, Feng J, Guo J, Zavadil KR, Shao Y, Zhang J-G (2018) Tailored reaction route by micropore confinement for Li-S batteries operating under lean electrolyte conditions. *Adv Energy Mater* 8(21). <https://doi.org/10.1002/aenm.201800590>
130. Mertens A, Vinke IC, Tempel H, Kungl H, de Haart LGJ, Eichel R-A, Granwehr J (2016) Quantitative analysis of time-domain supported electrochemical impedance spectroscopy data of Li-ion batteries: reliable activation energy determination at low frequencies. *J Electrochem Soc* 163(7):H521–H527. <https://doi.org/10.1149/2.0511607jes>

131. Shen Z, Cao M, Zhang Z, Pu J, Zhong C, Li J, Ma H, Li F, Zhu J, Pan F, Zhang H (2019) Efficient Ni₂Co₄P₃ nanowires catalyze ultrahigh-loading lithium–sulfur conversion in a microreactor-like battery. *Adv Funct Mater* 30(3). <https://doi.org/10.1002/adfm.201906661>
132. Peng L, Wei Z, Wan C, Li J, Chen Z, Zhu D, Baumann D, Liu H, Allen CS, Xu X, Kirkland AI, Shakir I, Almutairi Z, Tolbert S, Dunn B, Huang Y, Sautet P, Duan X (2020) A fundamental look at electrocatalytic sulfur reduction reaction. *Nat Catal*. <https://doi.org/10.1038/s41929-020-0498-x>
133. Lei T, Chen W, Huang J, Yan C, Sun H, Wang C, Zhang W, Li Y, Xiong J (2017) Multi-functional layered WS₂ nanosheets for enhancing the performance of lithium-sulfur batteries. *Adv Energy Mater* 7(4). <https://doi.org/10.1002/aenm.201601843>
134. Xu Z-L, Kim SJ, Chang D, Park K-Y, Dae KS, Dao KP, Yuk JM, Kang K (2019) Visualization of regulated nucleation and growth of lithium sulfides for high energy lithium sulfur batteries. *Energy Environ Sci* 12(10):3144–3155. <https://doi.org/10.1039/c9ee01338e>
135. Su D, Cortie M, Fan H, Wang G (2017) Prussian blue nanocubes with an open framework structure coated with PEDOT as high-capacity cathodes for lithium-sulfur batteries. *Adv Mater* 29(48). <https://doi.org/10.1002/adma.201700587>
136. Li L, Chen L, Mukherjee S, Gao J, Sun H, Liu Z, Ma X, Gupta T, Singh CV, Ren W, Cheng H-M, Koratkar N (2017) Phosphorene as a polysulfide immobilizer and catalyst in high-performance lithium-sulfur batteries. *Adv Mater* 29(2). <https://doi.org/10.1002/adma.201602734>
137. Levin BDA, Zachman MJ, Werner JG, Sahore R, Nguyen KX, Han Y, Xie B, Ma L, Archer LA, Giannelis EP, Wiesner U, Kourkoutis LF, Muller DA (2017) Characterization of sulfur and nanostructured sulfur battery cathodes in electron microscopy without sublimation artifacts. *Microsc Microanal* 23(1):155–162. <https://doi.org/10.1017/s1431927617000058>
138. Ferreira AGM, Lobo LQ (2011) The low-pressure phase diagram of sulfur. *J Chem Thermodyn* 43(2):95–104. <https://doi.org/10.1016/j.jct.2010.07.007>
139. Raib C, Peppler K, Janek J, Adelhelm P (2014) Pitfalls in the characterization of sulfur/carbon nanocomposite materials for lithium–sulfur batteries. *Carbon* 79:245–255. <https://doi.org/10.1016/j.carbon.2014.07.065>
140. Zhang J, Huang M, Xi B, Mi K, Yuan A, Xiong S (2018) Systematic study of effect on enhancing specific capacity and electrochemical behaviors of lithium-sulfur batteries. *Adv Energy Mater* 8(2). <https://doi.org/10.1002/aenm.201701330>
141. Cheng Z, Xiao Z, Pan H, Wang S, Wang R (2018) Elastic sandwich-type rGO-VS₂/S composites with high tap density: structural and chemical cooperativity enabling lithium-sulfur batteries with high energy density. *Adv Energy Mater* 8(10). <https://doi.org/10.1002/aenm.201702337>
142. Pang Y, Wei J, Wang Y, Xia Y (2018) Synergetic protective effect of the ultralight MWCNTs/NCQDs modified separator for highly stable lithium-sulfur batteries. *Adv Energy Mater* 8(10). <https://doi.org/10.1002/aenm.201702288>
143. Wang X, Yang C, Xiong X, Chen G, Huang M, Wang J-H, Liu Y, Liu M, Huang K (2019) A robust sulfur host with dual lithium polysulfide immobilization mechanism for long cycle life and high capacity Li-S batteries. *Energy Storage Mater* 16:344–353. <https://doi.org/10.1016/j.ensm.2018.06.015>
144. Ye Z, Jiang Y, Qian J, Li W, Feng T, Li L, Wu F, Chen R (2019) Exceptional adsorption and catalysis effects of hollow polyhedra/carbon nanotube confined CoP nanoparticles superstructures for enhanced lithium–sulfur batteries. *Nano Energy* 64. <https://doi.org/10.1016/j.nanoen.2019.103965>
145. Zhou G, Zhao S, Wang T, Yang S-Z, Johannessen B, Chen H, Liu C, Ye Y, Wu Y, Peng Y, Liu C, Jiang SP, Zhang Q, Cui Y (2019) Theoretical calculation guided design of single-atom catalysts toward fast kinetic and long-life Li–S batteries. *Nano Lett* 20(2):1252–1261. <https://doi.org/10.1021/acs.nanolett.9b04719>
146. Hong X-J, Tan T-X, Guo Y-K, Tang X-Y, Wang J-Y, Qin W, Cai Y-P (2018) Confinement of polysulfides within bi-functional metal–organic frameworks for high performance lithium–sulfur batteries. *Nanoscale* 10(6):2774–2780. <https://doi.org/10.1039/c7nr07118c>

147. Xue W, Shi Z, Suo L, Wang C, Wang Z, Wang H, So KP, Maurano A, Yu D, Chen Y, Qie L, Zhu Z, Xu G, Kong J, Li J (2019) Intercalation-conversion hybrid cathodes enabling Li–S full-cell architectures with jointly superior gravimetric and volumetric energy densities. *Nat Energy* 4(5):374–382. <https://doi.org/10.1038/s41560-019-0351-0>
148. Sun Q, Xi B, Li J-Y, Mao H, Ma X, Liang J, Feng J, Xiong S (2018) Nitrogen-doped graphene-supported mixed transition-metal oxide porous particles to confine polysulfides for lithium-sulfur batteries. *Adv Energy Mater* 8(22). <https://doi.org/10.1002/aenm.201800595>
149. Liang X, Garsuch A, Nazar LF (2015) Sulfur cathodes based on conductive MXene nanosheets for high-performance lithium-sulfur batteries. *Angew Chem Int Ed* 54(13):3907–3911. <https://doi.org/10.1002/anie.201410174>
150. Al Salem H, Babu G, Rao VC, Arava LMR (2015) Electrocatalytic polysulfide traps for controlling redox shuttle process of Li–S batteries. *J Am Chem Soc* 137(36):11542–11545. <https://doi.org/10.1021/jacs.5b04472>
151. Yang X, Gao X, Sun Q, Jand SP, Yu Y, Zhao Y, Li X, Adair K, Kuo LY, Rohrer J, Liang J, Lin X, Banis MN, Hu Y, Zhang H, Li X, Li R, Zhang H, Kaghazchi P, Sham TK, Sun X (2019) Promoting the transformation of Li_2S_2 to Li_2S : significantly increasing utilization of active materials for high-sulfur-loading Li–S batteries. *Adv Mater* 31(25). <https://doi.org/10.1002/adma.201901220>
152. Zhang L, Qian T, Zhu X, Hu Z, Wang M, Zhang L, Jiang T, Tian JH, Yan C (2019) In situ optical spectroscopy characterization for optimal design of lithium-sulfur batteries. *Chem Soc Rev* 48(22):5432–5453. <https://doi.org/10.1039/c9cs00381a>
153. Huang S, Lim YV, Zhang X, Wang Y, Zheng Y, Kong D, Ding M, Yang SA, Yang HY (2018) Regulating the polysulfide redox conversion by iron phosphide nanocrystals for high-rate and ultrastable lithium-sulfur battery. *Nano Energy* 51:340–348. <https://doi.org/10.1016/j.nanoen.2018.06.052>

Chapter 6

Lithium Metal and Other Anodes



Li-Peng Hou, Xue-Qiang Zhang, and Qiang Zhang

Abstract The lithium (Li) metal anode enables the lithium–sulfur (Li–S) battery to a promising high-energy-density battery system. However, the dissolution–precipitation conversion in Li–S batteries complicates the stability of Li metal anodes. Generally, non-uniform Li deposition induced by the heterogeneous solid electrolyte interphase on Li metal anodes gives rise to a short lifespan and even safety hazards. Li polysulfides (LiPSs) dissolve into electrolyte in Li–S batteries due to the dissolution–precipitation conversion of S. Li metal anodes thereby immerse in an electrolyte with highly reactive LiPSs, inducing parasitic reactions inevitably. The tough challenges of Li metal anodes severely hamper the practical applications of Li–S batteries. Both fundamental understanding of Li metal anodes and targeted protection strategies in Li–S batteries are crucial. In this chapter, the general issues of Li metal anodes and specific challenges in Li–S batteries induced by LiPSs are synthetically analyzed. Then, the recent advances in Li metal anodes protection in Li–S batteries are summarized, as well as a comparison with other metal anodes. Finally, an outlook is put forward to further promote the progress of Li–S batteries.

Keywords Lithium metal anodes · Lithium polysulfides · Lithium–sulfur batteries · Electrolytes · Solid electrolyte interphase

6.1 Introduction

The lithium (Li) metal anode is regarded as one of the most promising anode candidates in constructing high-energy-density secondary batteries due to its ultra-high theoretical specific capacity (3860 mAh g^{-1}) and ultralow reduction potential (-3.04 V vs. standard hydrogen electrode). When the Li metal anode is coupled with cathodes with conversion mechanism, such as sulfur (S) and oxygen (O), theoretically high-energy-density over 2000 Wh kg^{-1} at material level is facile, which is twice

L.-P. Hou · X.-Q. Zhang · Q. Zhang (✉)

Beijing Key Laboratory of Green Chemical Reaction Engineering and Technology,
Department of Chemical Engineering, Tsinghua University, Beijing 100084, China
e-mail: zhang-qiang@mails.tsinghua.edu.cn

higher than the current intercalation cathode of 1000 Wh kg^{-1} , such as layered transition metal oxides [1]. In particular, Li–S batteries with a theoretical specific energy over 2600 Wh kg^{-1} and a practical specific energy over 500 Wh kg^{-1} have received tremendous attention. Diverse S cathodes have been investigated from 1960s, and recently S/carbon (S/C) composite cathode stands out as a promising configuration to pursue the high energy density of Li–S batteries after a tortuous development in decades [2–4]. Nowadays, S/C composite cathode with stable cycles gradually become possible under conditions with high S content ($>60\%$) and high S loading ($>4.0 \text{ mg cm}^{-2}$), which is the footstone in constructing Li–S batteries with high specific energy. Nevertheless, the lifespan of practical Li–S batteries is still unsatisfactory while combining limited excessive Li metal anodes and lean electrolytes, hindering the practical application of Li–S batteries. The biggest obstacle is the Li metal anode, an old but challenged task originating from 1950s [5]. Therefore, the fundamental understanding and regulation strategies in stabilizing Li metal anodes in Li–S batteries are strongly required and attract much interest from all over the world. It is worth mentioning that, in this chapter, Li–S batteries with liquid electrolyte are focused on and solid-state Li–S batteries beyond the scope of this chapter can be referenced in other impactful reviews and books [6–8].

In a typical Li–S battery, S/C cathode falls into a dissolution–precipitation conversion mechanism. S_8 is firstly reduced to a series of long-chain lithium polysulfide intermediates (LiPSs, e.g., Li_2S_x , $4 \leq x \leq 8$) at the first plateau during discharge. Then, long-chain LiPSs are reduced to solid Li_2S_2 and Li_2S at the second plateau. Long-chain LiPSs can accelerate the conversion kinetics of S cathode as inherent redox mediators. Meanwhile, dissolved LiPSs inevitably diffuse to the surface of Li metal anodes under concentration gradients. At anode side, Li metal is highly reactive and the decomposition of LiPSs which are in high oxidation states is logically inevitable. Consequently, on the one hand, fresh Li and active LiPSs are constantly depleted to form inactive materials by parasitic reactions, inducing the loss of active materials and then the rapid decay of batteries. On the other hand, the decomposition products of LiPSs can involve into the generation of solid electrolyte interphase (SEI) on Li metal anodes, becoming the building blocks of SEI. Generally, the stability of Li anodes highly depends on the uniformity of SEI, which will be discussed in the following sections. The decomposition products of LiPSs in SEI can deteriorate the uniformity of SEI and then the stability of Li metal anodes. The challenges of Li metal anodes induced by soluble LiPSs in a practical Li–S battery are summarized in Table 6.1. Therefore, the stabilization of Li metal anodes is more challenged than that in common Li metal batteries. Much attention is deserved to the strong coupling between the cathode and anode, which is not encountered in the state-of-the-art Li-ion and lead acid batteries.

Furthermore, at initial research stage, the fundamental understanding of physicochemical features of Li–S batteries are mainly investigated under undemanding conditions including low S loading ($<2.0 \text{ mg cm}^{-2}$), high electrolyte/sulfur (E/S) ratio ($>10.0 \mu\text{L mg}_\text{S}^{-1}$), and much excess Li anodes ($>500 \mu\text{m}$). The employment of

Table 6.1 Challenges of Li metal anodes in Li–S batteries

Contents	Challenges
Electrolyte	(a) Concentrated and dynamic LiPSs under lean electrolytes (b) Complex electrolyte structure of Li-ions and LiPSs (c) Limitation in choice of solvents, Li salts, and additives to balance cathode conversion and stability of Li anodes
Li metal anode	(a) Li dendrite growth (b) Low Coulombic efficiency and dead Li (c) Corrosion of LiPSs on Li
SEI	(a) Spatial heterogeneity, long-term instability, and LiPS-intolerance (b) Participation of LiPSs into SEI evolution

undemanding conditions supports the exploitation of various materials with distinctive physico-chemical properties at material level. However, the undemanding conditions cannot achieve practically high energy density of Li–S batteries at cell level. To meet the demand of high-energy-density Li–S batteries over 500 Wh kg^{-1} , practical conditions of limited Li anodes ($<50 \mu\text{m}$), high S loading ($>4.0 \text{ mg cm}^{-2}$), and low E/S ratio ($<3.0 \mu\text{L mg}_\text{S}^{-1}$) are prerequisites [2–4, 9, 10]. A low E/S ratio means that a high concentration of soluble LiPSs ($>6.0 \text{ M [S]}$ species) is produced in electrolyte under practical conditions, which may aggravate the degradation of Li anodes. The low negative/positive capacity (N/P) ratio (<1.5) further signifies that limited Li metal anode cannot be a sufficient lithium reservoir to ensure the long-term cycle stability of Li–S batteries. Disclosing the gap of Li anodes under undemanding and harsh conditions is also necessary to push forward the application process of Li–S batteries [11, 12].

In this chapter, the challenges of Li metal anodes confronting soluble LiPS intermediates in practical Li–S batteries are analyzed firstly. Recent advances in Li metal anode protection in Li–S batteries are then summarized. Other anodes are also briefly discussed. Finally, an outlook is presented to promote the fundamental understanding and practical application of Li metal anodes in Li–S batteries.

6.2 Challenges of Li Metal Anodes

6.2.1 General Issues of Li Metal Anodes

Li metal is still mysterious although it has been proposed to be as a promising anode material since 1950s. Moli Energy explored the commercialization of rechargeable Li metal batteries (Li–MoS₂) in the late 1980s. However, due to the safety issues, these batteries were withdrawn from the market [5]. The safety issues hindering the practical applications of Li metal anodes are owing to its high reactivity and large volume change.

- (1) **Unstable SEI.** Metallic Li is chemically/electrochemically unstable with most electrolyte components (e.g., Li salt anions, solvents, and additives) due to the low reduction potential. The decomposition products of electrolyte, inorganic and organic species, will precipitate on the surface of Li metal anodes in a mosaic or multi-layered pattern to form a passivation film, i.e., SEI. In fact, mosaic or multi-layered model is simplified. Generally, the formed SEI is multicomponent with complicated structure due to the coupled chemical/electrochemical reactions, the complex electrolyte components with different chemical/electrochemical kinetics, and the multiple reaction processes. Moreover, the formation of SEI can be strongly influenced by current density, operation temperature, and other external test conditions. The typical multi-layered model of SEI (inner layer dominated by inorganic species and outer layer dominated by organic species) indicates that the SEI is spatially heterogeneous [13]. The chemical stability, mechanical stability, and Li-ion conductivity of SEI play vital roles in regulating the behaviors of Li deposition. The fracture of SEI is inescapable during the repeated Li plating and stripping, especially under a huge utilization depth of Li anodes. This results in repeated repair and regeneration of SEI, gradually consuming active Li and electrolyte. The accumulation of new formed SEI further increases the internal resistance of a battery.
- (2) **Li dendrite growth.** Metallic Li will deposit into an irregular morphology due to the heterogeneity of SEI. Li dendrite growth may break through SEI and expose in electrolyte, resulting in reactions between Li metal and electrolyte, i.e., SEI regeneration mentioned above. Vimineous dendrites may even pierce separator and cause short circuit, especially under a high current density above 3.0 mA cm^{-2} [14]. In a pouch cell, the inhomogeneity of current density is magnifying due to significantly increased area.
- (3) **Low Coulombic efficiency and dead Li.** The stripping process of Li anodes is as important as Li deposition. For an electrode, the capacity of deposited Li divided by the stripped Li is defined as Coulombic efficiency. A Coulombic efficiency above 99.9% of Li anodes is necessary to maintain a 60% capacity retention after 500 cycles when no excess Li is used and assuming the Coulombic efficiency of the cathode is 100%. However, this is a huge challenge for Li metal anodes in almost all electrolytes till now and excess Li is necessary to extend the cycle performance of a practical battery [15, 16]. The formation of SEI contributes to partial consumption of active Li. Another critical reason for the low Coulombic efficiency of Li anodes is the incomplete stripping [17]. A Li dendrite may lose electron pathways once its contact with current collector or bulk Li is broken due to the inhomogeneous stripping, thus forming “dead” Li and causing low Coulombic efficiency. Dead Li, which loses electron pathways and is packaged by SEI, continuously accumulates and hardly be reused, leading to a large polarization and a short lifespan of a battery.

The general challenges of Li metal anodes suppress its practical application. Progress has been made to address these challenges, including optimization of electrolyte, introduction of artificial SEI, design of anode host or composite anodes, and combination of approaches [18]. Persistent efforts bring Li metal anodes from dream to reality closer than decades ago.

6.2.2 *Specific Challenges of Li Metal Anodes in Li–S Batteries*

In addition to the general challenges, Li metal anodes in Li–S batteries suffer specific issues. In common Li metal batteries, such as Li–LiFePO₄ batteries, the effect of cathode reaction intermediates has little effect on the stability of Li metal anodes. The stability of the anode is hardly coupled with the cathode. However, in Li–S batteries, the formation of soluble LiPS intermediates will dissolve into electrolyte and diffuse to the surface of Li metal anodes. Reactive LiPSs easily react with Li metal anodes. The corrosion on Li metal is aggravated due to the exposure of active Li in LiPS electrolyte. SEI components are also influenced by LiPSs due to the formation of insoluble Li₂S/Li₂S₂ on Li surface, further impacting Li-ion transport. Understanding of the solution chemistry induced by LiPSs in electrolyte is the precondition to construct a stable Li metal anode for a Li–S battery.

6.2.2.1 LiPSs in Electrolyte

The type and concentration of electrolyte components impact the existence states of LiPSs in electrolyte (Fig. 6.1a). Polysulfide dianions (e.g., S₄²⁻, S₆²⁻, and S₈²⁻) are dominant in low donor number solvents, such as 1,3-dioxolane (DOL) and 1,2-dimethoxyethane (DME) [19]. In contrast, high donor number solvents (e.g., dimethyl sulfoxide (DMSO), dimethylformamide (DMF), and dimethylacetamide (DMA)) can stabilize radical monoanions (e.g., S₃^{•-}) [19–22]. High donor number solvents usually have high solubility of LiPSs over 10.0 M [S] species yet poor stability with Li metal due to the high reactivity of solvents. Specifically, the applicable solvents for Li–S batteries are much limited due to the nucleophilicity of LiPSs [23, 24]. Till now, DOL and DME are the most common solvents in Li–S batteries because of the capability to protect Li metal anodes and to maintain an appropriate LiPS conversion kinetics.

There are three aspects that should be clearly analyzed about LiPSs before the investigation of Li anodes in LiPS electrolyte. Firstly, the species of LiPSs are continuously changed during the cycling of a Li–S battery. Active materials of the cathode undergo a solid S₈–liquid LiPSs (Li₂S_{8–4})–solid Li₂S₂/Li₂S conversion

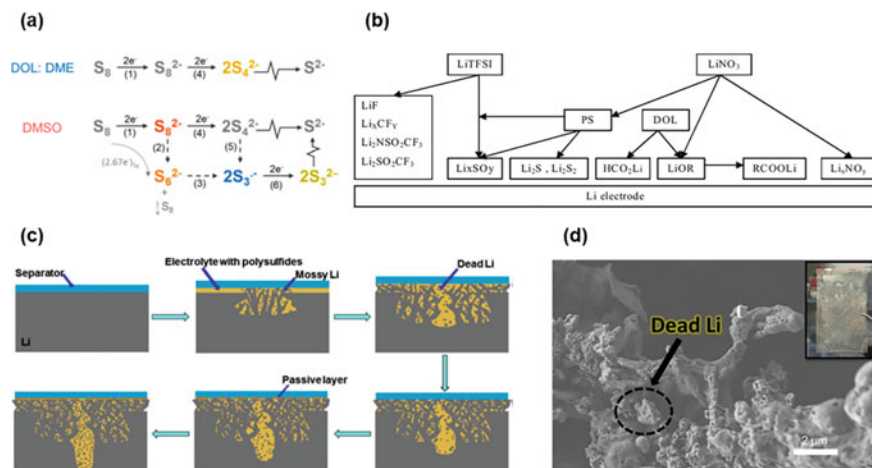


Fig. 6.1 Challenges of Li metal anodes in Li-S batteries. **a** Complex LiPS species in electrolyte. (Reprinted with permission from [19], 2016, American Chemical Society.) **b** LiPSs involve into SEI formation. (Reprinted with permission from [25], 2009, The Electrochemical Society.) **c** Schemes of the formation of mossy Li and dead Li during cycling in Li-S batteries. (Reprinted with permission from [26], 2017, American Chemical Society.) **d** Inhomogeneous Li deposition and accumulation of dead Li in a Li-S pouch cell. (Reprinted with permission from [27], 2017, Elsevier.)

process during discharge. The conversion of LiPSs reverses during charge from low-order polysulfides to high-order ones. The conversion of LiPSs implies that the Li metal anode is immersed in a variable electrolyte environment.

Secondly, LiPSs have complicated physical, chemical, and electrochemical properties, as well as interactions with other electrolyte components. LiPSs are usually regarded as a series of neutral molecules (e.g., Li_2S_x). The solubility of LiPSs decreases with the shortening of chain length of polysulfides. For instance, DOL and DME mixed solvents (1:1, by vol.) can dissolve above 0.5 M Li_2S_8 yet only 0.06 M Li_2S_4 [28–30]. The low dissolubility of Li_2S_4 might be ascribed to the strong interaction between Li-ions and S_x^{2-} . Dissolved LiPSs can further dissociate to form LiS_x^- or S_x^{2-} . Due to the stronger binding of $Li^+-S_x^{2-}$, low-order LiPSs generally have a lower dissociation degree in electrolyte than high-order ones. Moreover, low-order LiPSs prefer to form larger clusters compared to high-order ones [31, 32]. The dissolubility and dissociation capability have a direct relationship with ionic conductivity. For example, a lower ionic conductivity about 1.0 mS cm^{-1} is recorded of Li_2S_4 than that of Li_2S_8 ($\sim 3.0 \text{ mS cm}^{-1}$) based on 0.5 M LiPSs in DOL/DME theoretically [31]. Furthermore, low-order S_4^{2-} usually has a higher diffusion coefficient than that of high-order S_6^{2-} and S_8^{2-} due to particle's effective size [31, 33]. Therefore, the complicated properties of LiPSs, such as solubility, dissociation, and diffusion coefficient, trap Li metal anodes into complex electrolyte circumstances.

Thirdly, electrolyte structure changes dramatically under lean electrolytes (E/S ratio $< 3.0 \mu\text{L mg}^{-1}$) compared to flooded electrolytes (E/S ratio $> 10.0 \mu\text{L mg}^{-1}$).

For example, a high concentration of LiPSs about 10.4 M [S] is produced at an E/S ratio of $3.0 \mu\text{L mg}_\text{S}^{-1}$ if a theoretical specific capacity of 1672 mAh g^{-1} is delivered. This means that the concentration of LiPSs easily approaches saturation point. LiPSs are precipitated prematurely and a coupled solid–solid conversion is delivered [34, 35]. The high concentration of LiPSs above 1.0 M extremely increases the viscosity [31, 36, 37] and decreases the ionic conductivity of electrolyte [37]. More worse, the electrolyte may be even gelled. Additionally, the concentration of LiPSs changes as the electrochemical reaction proceeds, which entangles the investigation of electrolyte structure.

6.2.2.2 Li Metal Anodes in LiPS Electrolyte

Li metal anodes can react with LiPSs, inducing the corrosion of Li metal anodes. The corrosion degree is impacted by three aspects, including the reactivity of LiPSs, the concentration of LiPSs, and the exposed area of Li metal in LiPS electrolyte. Firstly, various LiPSs have different reactive activity due to the distinction in molecular structure. High-order LiPSs are usually easier to be reduced than low-order ones [38]. The reaction kinetics between LiPSs and Li metal are generally faster than that between solvents (e.g., DOL/DME) or Li salts (e.g., lithium bis(trifluoromethanesulfonyl)imide (LiTFSI)) and Li metal [38, 39]. Secondly, a high concentration of LiPSs produced at the cathode side under a low E/S ratio generates a large concentration gradient compared to that under flooded electrolytes. The highly concentrated LiPSs may intensify the corrosion on Li anodes. Thirdly, Li dendrites or filaments are generally formed due to the inhomogeneous Li-ion transport on Li metal surface. Dendritic Li can crack SEI, exposing fresh Li to electrolyte. More exposed fresh Li there is, more severe corrosion of LiPSs on Li anodes occurs. When it comes to practical conditions with a high S loading ($>4.0 \text{ mg cm}^{-2}$), a large amount of Li metal above $20 \mu\text{m}$ is utilized during each plating/stripping process assuming a practical discharge specific capacity of 1000 mAh g^{-1} . The huge utilization of Li metal anodes results in a large volume change and propagation of Li dendrites, exacerbating the erosion of LiPSs on Li anodes [27, 40, 41].

A series of problems are induced by the parasitic reactions between LiPSs and Li anodes. Firstly, the loss of active materials and low energy efficiency are obvious due to the notorious shuttle effect. High-order polysulfides produced at the cathode side diffuse to the anode side and react with Li anodes. Then, low-order polysulfides or $\text{Li}_2\text{S}/\text{Li}_2\text{S}_2$ are formed on the surface of Li metal anodes, causing the loss of active S and the decrease of discharge capacity [42–44]. Secondly, the behaviors of Li deposition/stripping are deteriorated due to the corrosion of LiPSs on Li anodes (Fig. 6.1c). Li dendrites are always vimineous and fragile. If the root of Li dendrites where they connect with the bulk Li is corroded by LiPSs, Li whiskers will lose connection to the electrode and thus dead Li forms [26, 45]. The corrosion on Li metal accelerates the depletion of electrolyte/Li anodes and capacity decay. The dead Li accumulates on the surface of Li metal anodes, consequently increasing the internal resistance and polarization and shortening the lifespan of a Li–S battery.

Thirdly, safety concerns arising from Li metal and LiPSs should be paid attention to, especially in Li–S pouch cells. Li dendrite growth is much severe in a pouch cell due to the amplifying effect of inhomogeneous current density and huge utilization depth of Li metal anodes (Fig. 6.1d) [27]. Dendritic Li may pierce separator and cause short circuit. Fires and explosions are at high risks due to the accumulation of dead and pulverized Li if a pouch cell is pressed or broken. Gassing problem should be considered equally. CH₄ and H₂ are produced by the reduction of solvents (DOL/DME) on Li metal surface [46, 47]. LiNO₃ which is employed as a requisite additive to inhibit the shuttle of LiPSs also may result in gassing problem [48].

6.2.2.3 SEI Chemistry in LiPS Electrolyte

SEI can hardly be ignored when talking about Li metal anodes. SEI, the reaction products between Li metal and electrolyte components, is a Li-ion conductor but electron insulator. The components and structure of SEI dictate Li-ion transport and subsequent Li plating/stripping [49]. In Li–S batteries, Li₂S₂/Li₂S are usually main components in the bottom layer of SEI from the decomposition of LiPSs (Fig. 6.1b) [25, 43, 50]. Generally, Li₂S is not a fast Li-ion conductor with a conductivity about 10⁻⁵ S cm⁻¹. A high concentration and inhomogeneous spatial distribution of LiPSs may result in a much heterogeneous SEI [51]. The irregular distribution of Li₂S in SEI results in a spatial inhomogeneity of Li-ion transport [52, 53]. An inhomogeneous utilization of Li anodes is therefore predictable. Moreover, the stripping of Li occurs firstly in a Li–S battery, and hence, discrete pits are formed on Li surface [54]. During the following charge process, freshly plated Li tends to deposit in the pits due to the new formed thin SEI in these areas with relatively high Li-ion transport capability [55, 56]. Finally, the heterogeneous SEI involved by soluble LiPSs will intensify the inhomogeneous utilization and fast degradation of Li metal anodes.

6.3 Advances of Li Metal Anodes in Li–S Batteries

Improving the stability of Li metal anodes is necessary for practical Li–S batteries. In addition to external factors (e.g., current density, pressure, and temperature), the behaviors of Li deposition and stripping are strongly affected by electrolyte, SEI, and intrinsic properties of Li anodes. The effect of external factors is not included in this chapter. Three principles to protect Li metal anodes under LiPS intermediates are under investigation, including inhibition of the dissolution of LiPSs in electrolyte, optimization of SEI, and reinforcement of bulk Li metal. Specifically, other general protective strategies for Li anodes under conditions without LiPSs have been summarized in previous reviews [57–60] and are no longer listed in this chapter.

6.3.1 Inhibition of the Dissolution of LiPSs

Soluble LiPSs are the main sources to disturb SEI formation and corrode Li in Li-S batteries. Reducing the concentration of LiPSs in electrolyte is a direct approach to alleviate the corrosion of LiPSs on Li anodes. The dissolution of LiPSs is essentially related to the solvation capability of solvents. On the one hand, a solvent which has a weak solvation interaction with the Li-ion in LiPSs can alleviate the dissolution of LiPSs. On the other hand, the absolute concentration of LiPSs that an electrolyte can dissolve is related to the amount of free solvent molecules. Therefore, reducing the content of free solvents in electrolyte and employing low polar solvents are two basic conceptions to inhibit the dissolution of LiPSs.

Li salts are essential components to support Li-ion conduction. The dissolution and dissociation of Li salts require free solvent molecules to solvate Li-ions. Increasing the concentration of Li salts enables less free solvent molecules left to dissolve LiPSs [61–63]. Hu and co-workers designed a new class of “solvent-in-salt” electrolyte in 2013 [64]. The dissolution of LiPSs in the electrolyte of 7 M LiTFSI in DOL/DME is significantly inhibited. Nazar and co-workers further demonstrated that Li-ions and anions form contact ion pairs (CIP) and aggregates (AGG) in a high-concentrated electrolyte consisted of diethylene glycol dimethyl ether (G2) and LiTFSI (0.8:1, by mol, Fig. 6.2a) [65]. The participation of anions into Li-ion solvation sheaths indicates that insufficient solvents to dissolve Li salts, let alone LiPSs. Watanabe and co-workers illustrated that when long-chain glyme (e.g., triglyme (G3) or tetraglyme (G4)) is used and equimolar to LiTFSI, a large cation of $[\text{Li}(\text{G3} \text{ or } \text{G4})_1]^+$ is formed and few free solvents remain (Fig. 6.2b) [66–68]. Only *ca.* 4 and 8 mM Li_2S_8 can be dissolved in $[\text{Li}(\text{G3})_1][\text{TFSI}]$ and $[\text{Li}(\text{G4})_1][\text{TFSI}]$, respectively [67]. The unique electrolyte structure is named as solvate ionic liquid. However, high-concentrated electrolytes and solvate ionic liquids lead to high viscosity and low Li-ion conductivity.

In terms of the solvation capability of a specific solvent, a lower polarity generally contributes to a lower dissolubility of LiPSs. Dielectric constant and donor number are usually employed to infer the polarity and solvation capability of a solvent. However, the measurement of donor number is a fussy work. Instead, carbon/oxygen (C/O) ratio for ethers and steric hindrance of a solvent molecule can simply reflect the polarity. The O atoms in ethers with high C/O ratio have a weak dipole-ion interaction with the Li-ion in LiPSs, reducing the solubility of LiPSs [70]. A strong steric hindrance also contributes to a reduced coordination ability of a solvent. For instance, diisopropyl ether (DIPE) has a high C/O ratio of 6 and high steric hindrance with two isopropyls, which hardly dissolves LiPSs. The DIPE/DOL/DME mixed solvent (50:25:25, by vol.) also only can dissolve about 0.1 M Li_2S_8 , much lower than the traditional DOL/DME mixed solvents [71]. Additionally, ethers with high C/O ratio and steric hindrance are more stable with Li metal anodes compared to the relatively highly reactive DOL/DME.

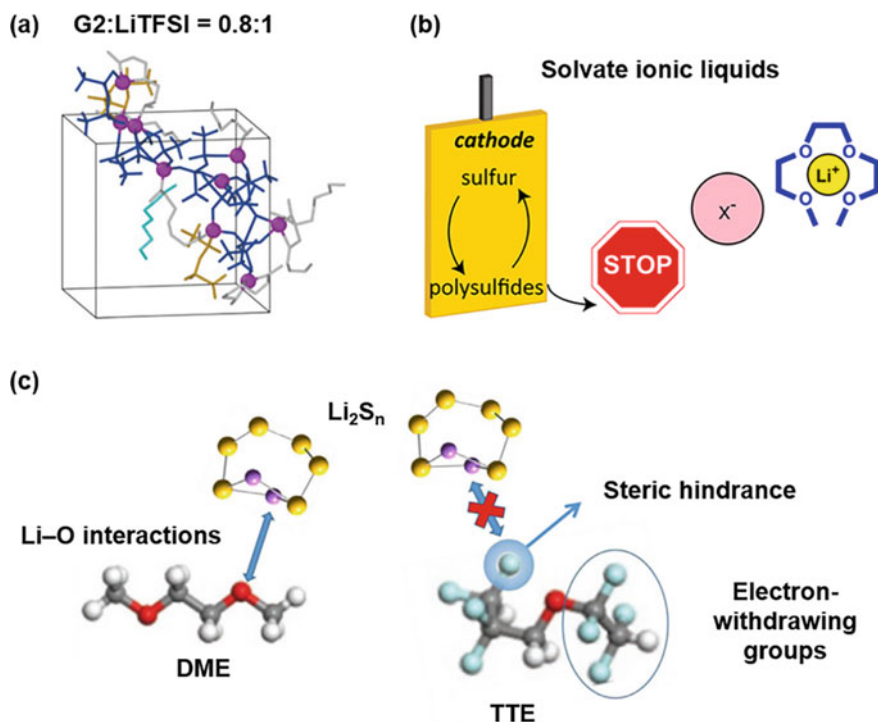


Fig. 6.2 Inhibition of the dissolution of LiPSs in electrolyte. **a** High-concentrated electrolytes. (Reprinted with permission from [65], 2018, Nature.) **b** Solvate ionic liquids. (Reprinted with permission from [68], 2013, Elsevier. American Chemical Society.) **c** Localized high concentration electrolytes. (Reprinted with permission from [69], 2020, Elsevier.)

Introducing highly electron-withdrawing groups into molecules can decrease the solvation capability. The hydrofluoroether (HFE) is one of the most significant successes. Abundant fluorine atoms enable HFES to have a weak affinity to Li-ions (Fig. 6.2c) [69]. The degree of fluorination and the position of fluoroalkyl groups determine the solvation ability [72–74]. For example, HFES with α - and β' -substituted fluoroalkyl groups usually have the lowest solvation capability with Li-ions [74]. HFES can hardly dissolve Li salts, indicating that HFES can never be used as electrolyte solvents alone. On the contrast, the low viscosity enables HFES to be employed as diluents in high-concentrated electrolytes. Manifold HFES, such as 1,1,2,2-tetra-fluoroethyl 2,2,3,3-tetrafluoropropyl ether (TTE) [65, 75–78], bis(2,2,2-trifluoroethyl) ether (BTFE) [79, 80], and 1,1,2,2-tetrafluoroethyl 2,2,2-trifluoroethyl ether (TFTFE) [81, 82], are developed during decades. The high-concentrated electrolyte which introduces HFES as diluents is named as the localized high concentration electrolyte (LHCE). Not only the viscosity and wettability are ameliorative, but also the corrosion of LiPSs on Li metal is restrained in LHCE.

All in all, no matter reducing the content of free solvents in electrolyte or employing low polar solvents, the reduced LiPS solubility inevitably delays conversion kinetics of $S/\text{Li}_2\text{S}$, and thus, a large voltage hysteresis is always observed. Low current density and elevated operation temperature are sometimes required to maintain the normal conversion kinetics of cathodes.

6.3.2 Optimization of SEI

In Li-S batteries, there are basic requirements of SEI, including fast and homogeneous Li-ion diffusion, certain mechanical strength, and long-term stability [83, 84]. Besides, shielding the corrosion of LiPSs on Li anodes is a special requirement for SEI. *In situ* SEI and artificial SEI are classified to protect Li anodes.

6.3.2.1 In Situ SEI

In situ SEI can be directly regulated by electrolyte components (e.g., solvents, Li salts, and additives). Till now, LiN_xO_y and $\text{Li}_2\text{S}_x\text{O}_y$ are regarded as important components in SEI to inhibit the shuttle of LiPSs. The function of LiF, which is a most effective SEI component to improve the homogeneity of Li deposition in other Li metal batteries, is controversial in Li-S batteries.

LiNO_3 is considered as the most effective additive to protect Li metal anodes away from the attack of LiPSs ascribed to the formation of LiN_xO_y in SEI (Fig. 6.3a) [25, 85–88]. Inspired by the success of LiNO_3 , other additives containing NO_3^- are demonstrated to improve the stability of Li anodes, including CsNO_3 [89], $\text{La}(\text{NO}_3)_3$ [90], $\text{ZrO}(\text{NO}_3)_2$ [91], and KNO_3 [92]. When it comes to Li-S pouch cells, a huge utilization depth of Li metal anodes ($>20\ \mu\text{m}$) during each plating and

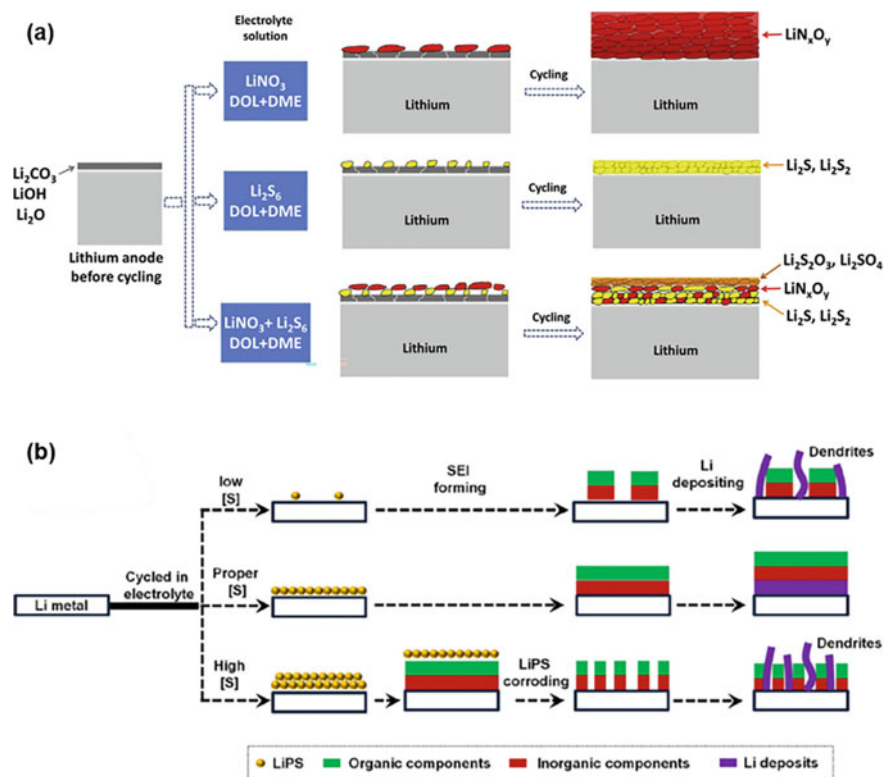


Fig. 6.3 Strategies to optimize in situ SEI. **a** The synergistic effect of LiNO_3 and LiPSs in the formation of SEI. (Reprinted with permission from [87], 2014, Elsevier.) **b** A suitable LiPS concentration is necessary for a stable SEI. (Reprinted with permission from [94], 2016, Elsevier.)

stripping results in a large amount of LiNO_3 to consume to construct SEI. However, a too high concentration of LiNO_3 over 0.5 M results in irreversible reaction with element S_8 [93]. The safety hazards also should be considered as mentioned above.

Generally, the reaction between LiPSs and Li metal is a catastrophe. However, when introducing LiNO_3 into electrolyte, LiPSs can serve as assistant additives [88, 95, 96]. The formed $\text{Li}_2\text{S}/\text{Li}_2\text{S}_2$ due to the reaction between LiPSs and Li metal can be oxidized by LiNO_3 to $\text{Li}_2\text{S}_x\text{O}_y$. The synergistic effect of LiN_xO_y and $\text{Li}_2\text{S}_x\text{O}_y$ can further improve the homogeneity of Li deposition and inhibit the subsequent LiPS corrosion. It should be noted that the concentration and species of LiPSs play a role in the function of SEI (Fig. 6.3b) [94, 97, 98]. For example, Li_2S_5 enables better SEI compared with other LiPSs when 0.10 M LiPSs and 1.0 wt.% LiNO_3 additive are used [97]. In a pouch cell under practical conditions, a high and dynamic concentration of LiPSs is expected. Therefore, whether LiPSs can synergistically protect Li anodes with LiNO_3 is unclear.

LiF is always regarded as a necessary component in SEI to achieve homogeneous Li deposition in other Li metal batteries. However, the role of LiF in SEI for Li-S batteries is under controversy. Some publications demonstrated that SEI consisted of LiF could improve Li-ion diffusion and inhibit LiPS shuttle [99–101]. The introduction of LiF in SEI can be regulated by Li salts [101–104]. However, others hold the opinion that LiF may be not a critical component in SEI for Li-S batteries, because lithium bis(fluorosulfonyl)imide (LiFSI), which can deposit to abundant LiF, on the contrary, induces a too loose SEI to shield LiPSs compared to LiTFSI [88, 105].

In a word, most additives to improve Li deposition and resist LiPS corrosion on Li anodes are sacrifices. The fast consumption under practical conditions extremely limits the lifespan of Li metal anodes. Other safe and effective additives are in urgent demand.

6.3.2.2 Artificial SEI

Artificial SEI can be employed as an external protective layer for Li metal designed before battery assembly. Inorganic protection layer with a high mechanical strength and fast ion conduction is expected to inhibit Li dendrites and shield LiPSs. Pretreatment of Li anodes with sulfide-solid-electrolyte (e.g., Li_3PS_4) can form a robust SEI with high Li-ion conductivity about $10^{-3} \text{ S cm}^{-1}$ to promote smooth Li deposition [106–108]. A porous Al_2O_3 layer through spin-coating method [109] and a 250 nm lithium phosphorus oxynitride (LPON) coating can serve as electrochemically and mechanically robust layers to resist Li dendrite growth and minimize corrosive reactions of LiPSs on Li anodes (Fig. 6.4a) [110]. Compared with inorganic protection layers, an inorganic/organic hybrid SEI can combine the flexibility of organic materials and the hardness of inorganic materials. A polyvinylidene fluoride (PVDF)- $\text{Li}_{1.5}\text{Al}_{0.5}\text{Ge}_{1.5}(\text{PO}_4)_3$ composite protective layer effectively resists the corrosion of LiPSs on Li metal anodes and an average coulombic efficiency of 92% is

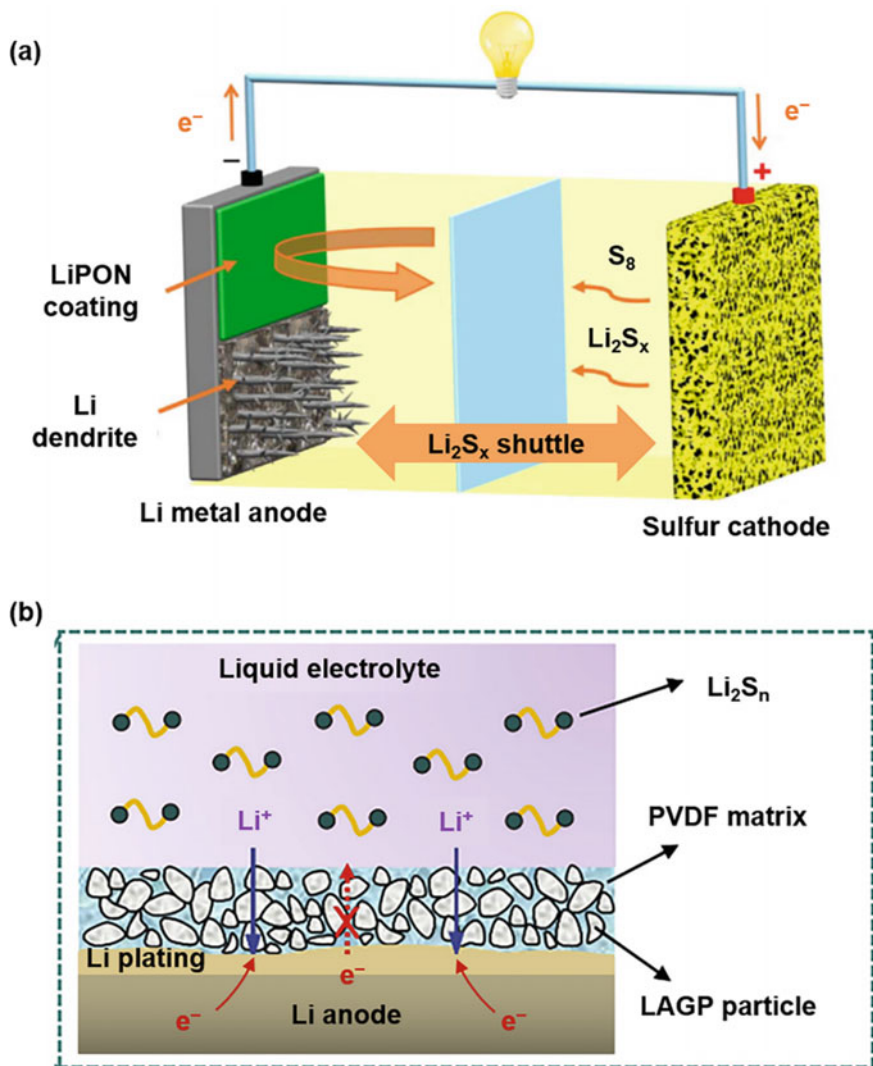


Fig. 6.4 Artificial SEI to protect Li metal anodes. **a** Scheme of an inorganic LPON layer to shield LiPSs and inhibit Li dendrites. (Reprinted with permission from [110], 2019, Elsevier.) **b** Scheme of an organic/inorganic hybrid PVDF-Li_{1.5}Al_{0.5}Ge_{1.5}(PO₄)₃ composite layer to protect Li anodes from the attack of LiPSs. (Reprinted with permission from [111], 2018, Elsevier.)

achieved without LiNO₃ as additive (Fig. 6.4b) [111]. Besides, other hybrid coatings such as PVDF-graphitic carbon nitride (g-C₃N₄) [112] and Nafion-Li_xSi_y [113] are demonstrated to withstand the corrosive LiPSs.

However, some problems should be overcome for the practical application of artificial SEI in Li–S batteries. Firstly, artificial SEI cannot be self-repaired once broken in a battery. Secondly, a large amount of dead Li may accumulate between the artificial SEI and bulk Li during repeated Li plating/stripping, and hence, the artificial SEI is out of action. Thirdly, the introduction of artificial SEI will reduce the energy density of the whole battery. Fourthly, the compatibility among Li anodes, artificial SEI, LiPSs, and other electrolyte components should be carefully balanced.

6.3.3 Reinforcement of Bulk Li Metal and Other Anodes

Once SEI is broken, active Li immerses in electrolyte with LiPS intermediates. Improvement of the stability of bulk Li can relieve parasitic reactions even if the Li anode pierces SEI and exposes to LiPSs. Alloy is a facile way to improve the comprehensive stability of Li anodes. Various elements (e.g., B, Mg, Al, Si, and Sn) have been designed as Li alloy in Li–S batteries. Li–B alloy can act as a stable matrix to resist the corrosion of LiPSs due to the improved electrochemical potential (>0.4 V vs. Li/Li⁺) [114–117]. Li–Al alloy (Li₉Al₄) with a 0.3 V potential vs. Li/Li⁺ also can reduce the activity of anodes in LiPS electrolyte (Fig. 6.5a) [118–120]. Al matrix can further enhance uniform lithiation due to the high Vickers hardness [121]. However, the elevated electrochemical potential of Li–B and Li–Al alloy causes the loss of energy density of Li–S batteries. Other heavy elements such as Sn [122, 123], Sb [124], and Bi [125] are also unsuitable to be employed as bulk anode materials but can be designed as functional protective layers on Li surface to balance the stability of anodes and demand of energy density. Li–Mg alloy has a high theoretical specific capacity of 3151 mAh g⁻¹ and a low electrode potential about 0 V versus Li/Li⁺, which seems to be an alternative anode material. It is demonstrated that Li–Mg alloy is stable in LiPS electrolyte compared to pure Li metal due to a robust SEI formation (Fig. 6.5b) [126]. A *bcc* β -phase during the range of Li content from 30 to 100 at.% further maintains a structure stability of the anode during charge and discharge [127]. The merits of Li–Mg alloy indicate that it has the potential to be verified in pouch cells under practical conditions.

When referring to other metal anodes, such as sodium (Na), potassium (K), magnesium (Mg), calcium (Ca), and aluminum (Al) having a potential to compete with the Li metal anode, it is apparent that Li metal is the most competitive material to meet the demand of high mass energy density over 500 Wh kg⁻¹. Some metal–sulfur batteries (e.g., Mg–S, Ca–S, and Al–S systems) have the potential to improve the volumetric energy density of sulfur-based batteries. For example, volumetric capacities of Mg, Ca, and Al are 3882, 2064, and 8040 mAh cm⁻³, respectively, higher than that of Li (2045 mAh cm⁻³) [128]. However, advances on these metal–sulfur batteries are far behind Li–S batteries due to numerous critical challenges. Firstly, the fundamental electrochemical mechanism is unclear. For instance, the electrochemical mechanism of K–S batteries is less well established due to the difficulty in analyzing potassium polysulfide species (K₂S₈, K₂S₅, and K₂S₃) [129]. Al–S batteries usually work with

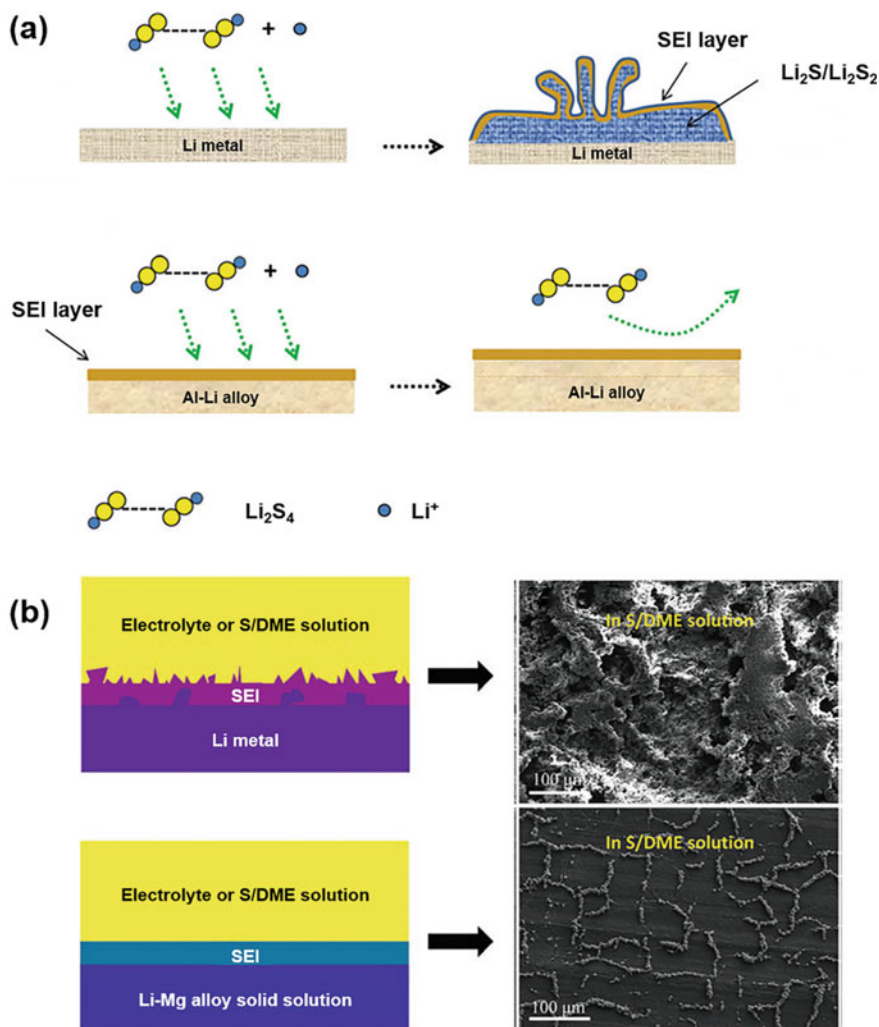


Fig. 6.5 Reinforcement of bulk Li by Li alloy. **a** Schematic of the stability of Li–Al alloy and Li metal in LiPS electrolyte. (Reprinted with permission from [120], 2018, The Royal Society of Chemistry.) **b** The stability of Li–Mg alloy and Li metal in S/DME solution. (Reprinted with permission from [126], 2019, Wiley-VCH.)

ionic liquid electrolytes and have more complex electrochemical mechanism than other metal–sulfur cell systems [130]. Secondly, the stability of metal anodes and SEI is challenged. Na and K are more chemically active than Li metal. The nucleation and growth of Na and K are inhomogeneous, also inducing severe dendrite propagation. Ca cannot form a fast ion conductive SEI in organic electrolyte. Hence, Ca–S batteries have trouble in serving as a rechargeable battery and the electrochemical mechanism has been only demonstrated with a Li-ion mediated electrolyte prelim-

inarily [131, 132]. Thirdly, the shuttle of soluble high-order metal polysulfides is also severe in these metal–sulfur batteries. Therefore, vast problems are required to be addressed for these metal–sulfur battery systems as an alternative energy-storage technology.

6.4 Conclusions and Outlook

The issues of the Li metal anode in Li–S batteries are complex but representative, which include the typical challenges of Li metal anodes, such as the formation of Li dendrites, the heterogeneity of SEI, and the large volume change. In Li–S batteries, the above issues are coupled with the parasitic reactions of the reactive intermediates from the cathode. Although tremendous strategies are designed in the last decades to protect Li metal anodes by decreasing the dissolution of LiPSs, optimizing the components and structure of SEI, and enhancing the stability of bulk Li to prolong the lifespan of Li–S batteries, the development of Li–S batteries under practical conditions is still in the infancy. Further investigations are deserved to stabilize Li metal anodes for practical Li–S batteries, especially the challenges induced by LiPSs.

- (1) Fundamental understanding of LiPSs. The basic properties of LiPSs, e.g., the behaviors of dissolution, dissociation, diffusion, and electric mobility, and chemical/electrochemical activity, have not been clearly investigated under a high concentration of LiPSs. A low E/S ratio ($<3.0 \mu\text{L mg}_\text{S}^{-1}$) will result in quite different features of LiPSs compared to that in flooded electrolytes, which is necessary to be disclosed to guide the exploitation of high-energy-density Li–S batteries.
- (2) Electrolyte structure and properties. The dissolution of a series of LiPSs complicates the electrolyte structure where there are only Li salts and solvents in common electrolyte. Not only the solvation structure of Li-ions, but also the electrolyte structure of polysulfides are important. Interactions among Li-ions, S_x^{2-} , anions, solvents, and even additives, influence the physicochemical properties of LiPS electrolyte, such as ionic conductivity, transfer number, viscosity, and wettability.
- (3) SEI and Li metal in LiPS electrolyte. The decomposition mechanism of solvents, Li salts, additives, and LiPSs on Li metal surface to form SEI may change dramatically under lean electrolytes with a high concentration of LiPSs due to the changed electrolyte structure and features compared with that in flooded electrolytes. The induced components, structure, and properties of SEI will be also altered yet investigations are much lacking. The behaviors of Li plating/stripping which are affected directly by SEI may be also disturbed and deserve to be further investigated.
- (4) Design of electrolyte. The routine electrolyte, 1.0 M LiTFSI in DOL/DME (1:1, by vol.) with LiNO_3 as the additive, is unsatisfactory to support a long-term stability of Li anodes under practical conditions. Novel electrolyte formulations

are highly required to keep a delicate balance between cathode conversion and anode protection for a practical Li–S battery. For example, solvents with high stability with Li metal and moderate dissolubility of LiPSs are needed. It is necessary to design effective additives to form stable SEI to inhibit the shuttle of LiPSs and improve the utilization efficiency of Li anodes. The concentration and species of Li salts can also be regulated to improve ionic conductivity and decrease viscosity of electrolyte under a low E/S ratio.

- (5) Advanced characterizations to disclose the underlying mechanism. Characterizations such as Raman spectroscopy, ultraviolet–visible light spectroscopy, and mass spectrometry have been widely employed to disclose the existence of various LiPSs under a low concentration, while circumstances under a high concentration of LiPSs can exceed their detection capacity due to range and accuracy. More precise characterizations are highly demanded to reveal the LiPS species, solvation structure of Li-ions and LiPSs, diffusion or electron migration of LiPSs, and so on, under a high-concentrated LiPS electrolyte instead of a dilute LiPS solution. Advanced characterizations, such as electrochemical quartz crystal microbalance and cryogenic electron microscopy may provide a new perspective for the understanding of LiPSs, SEI, and Li anodes. Moreover, soluble LiPSs, electrolyte structure, components and structure of SEI, and conditions of Li anodes, are dynamically changing during charge and discharge. Development of advanced in situ characterizations is beneficial to capture the subtle changes and underlying evolution mechanism in dynamically electrochemical processes which cannot be observed under ex-situ characterizations.

Li–S batteries have experienced a tortuous development during decades. However, there is still a long way to achieve a practical Li–S battery with both high energy density and long-term cycle stability. The Li metal anode plays a vital role in hindering the practical applications of Li–S batteries. Conditions with less excess Li anodes, high loading S cathodes, and lean electrolytes bring fresh challenges to Li metal anodes, which requires both new fundamental understanding and practical exploitations. Persistent investigations on Li metal anodes in Li–S batteries can also be used as references for other advanced batteries for energy storage scenarios.

Acknowledgements Financial support by the National Natural Science Foundation of China (21825501 and U1801257), National Key Research and Development Program (2016YFA0202500), Scientific and Technological Key Project of Shanxi Province (20191102003), and the Tsinghua University Initiative Scientific Research Program.

References

1. Bruce PG, Freunberger SA, Hardwick LJ, Tarascon J-M (2012) *Nat Mater* 11:19–29
2. Bhargav A, He JR, Gupta A, Manthiram A (2020) *Joule* 4:285–291
3. Dörfler S, Althues H, Härtel P, Abendroth T, Schumm B, Kaskel S (2020) *Joule* 4:539–554

4. Zhao M, Li BQ, Zhang XQ, Huang JQ, Zhang Q (2020) *ACS Cent Sci* 6:1095–1104
5. Winter M, Barnett B, Xu K (2018) *Chem Rev* 118:11433–11456
6. Yang X, Luo J, Sun X (2020) *Chem Soc Rev* 49:2140–2195
7. Wu J, Liu S, Han F, Yao X, Wang C (2020) *Adv Mater* 32:2000751
8. Krauskopf T, Richter FH, Zeier WG, Janek J (2020) *Chem Rev* 120:7745–7794
9. Chung SH, Manthiram A (2019) *Adv Mater* 31:1901125
10. Zhao M, Li B-Q, Peng H-J, Yuan H, Wei J-Y, Huang J-Q (2019) *Angew Chem Int Ed* 59:12636–12652
11. Yan C, Zhang X-Q, Huang J-Q, Liu Q, Zhang Q (2019) *Trends in Chem* 1:693–704
12. Zhao Y, Ye Y, Wu F, Li Y, Li L, Chen R (2019) *Adv Mater* 31:1806532
13. Zhang JG, Xu W, Xiao J, Cao X, Liu J (2020) *Chem Rev* 120:13312–13348
14. Shi P, Cheng XB, Li T, Zhang R, Liu H, Yan C, Zhang XQ, Huang JQ, Zhang Q (2019) *Adv Mater* 31:1902785
15. Xiao J, Li QY, Bi YJ, Cai M, Dunn B, Glossmann T, Liu J, Osaka T, Sugiura R, Wu BB, Yang JH, Zhang JG, Whittingham MS (2020) *Nat Energy* 5:561–568
16. Zhu Y, Pande V, Li L, Wen B, Pan MS, Wang D, Ma Z-F, Viswanathan V, Chiang Y-M (2020) *Proc Natl Acad Sci USA* 117:27195–27203
17. Fang C, Li J, Zhang M, Zhang Y, Yang F, Lee JZ, Lee M-H, Alvarado J, Schroeder MA, Yang Y, Lu B, Williams N, Ceja M, Yang L, Cai M, Gu J, Xu K, Wang X, Meng YS (2019) *Nature* 572:511–515
18. Cheng X-B, Zhang R, Zhao C-Z, Zhang Q (2017) *Chem Rev* 117:10403–10473
19. Zou Q, Lu Y-C (2016) *J Phys Chem Lett* 7:1518–1525
20. Vijayakumar M, Govind N, Walter E, Burton SD, Shukla A, Devaraj A, Xiao J, Liu J, Wang C, Karim A, Thevuthasan S (2014) *Phys Chem Chem Phys* 16:10923–10932
21. Cuisinier M, Hart C, Balasubramanian M, Garsuch A, Nazar LF (2015) *Adv Energy Mater* 5:1401801
22. Zhang G, Peng H-J, Zhao C-Z, Chen X, Zhao L-D, Li P, Huang J-Q, Zhang Q (2018) *Angew Chem Int Ed* 57:16732–16736
23. Gao J, Lowe MA, Kiya Y, Abruna HD (2011) *J Phys Chem C* 115:25132–25137
24. Yim T, Park M-S, Yu J-S, Kim KJ, Im KY, Kim J-H, Jeong G, Jo YN, Woo S-G, Kang KS, Lee I, Kim Y-J (2013) *Electrochim Acta* 107:454–460
25. Aurbach D, Pollak E, Elazari R, Salitra G, Kelley CS, Affinito J (2009) *J Electrochem Soc* 156:A694–A702
26. Zhang Y, Heim FM, Song N, Bartlett JL, Li X (2017) *ACS Energy Lett* 2:2696–2705
27. Cheng X-B, Yan C, Huang J-Q, Li P, Zhu L, Zhao L, Zhang Y, Zhu W, Yang S-T, Zhang Q (2017) *Energy Storage Mater* 6:18–25
28. Gupta A, Bhargava A, Manthiram A (2018) *Adv Energy Mater* 9:1803096
29. Dibden JW, Smith JW, Zhou N, Garcia-Araez N, Owen JR (2016) *Chem Commun* 52:12885–12888
30. Wang H, Shao YY, Pan HL, Feng XF, Chen Y, Liu YS, Walter ED, Engelhard MH, Han KS, Deng T, Ren GX, Lu DP, Lu XC, Xu W, Wang CS, Feng J, Mueller KT, Guo JH, Zavadil KR, Zhang JG (2020) *Nano Energy* 76:105041
31. Park C, Ronneburg A, Risse S, Ballauff M, Kanduc M, Dzubiella J (2019) *J Phys Chem C* 123:10167–10177
32. Andersen A, Rajput NN, Han KS, Pan H, Govind N, Persson KA, Mueller KT, Murugesan V (2019) *Chem Mater* 31:2308–2319
33. Rajput NN, Murugesan V, Shin Y, Han KS, Lau KC, Chen J, Liu J, Curtiss LA, Mueller KT, Persson KA (2017) *Chem Mater* 29:3375–3379
34. Shen C, Xie J, Zhang M, Andrei P, Hendrickson M, Plichta EJ, Zheng JP (2017) *Electrochim Acta* 248:90–97
35. Shen C, Xie J, Zhang M, Andrei P, Zheng JP, Hendrickson M, Plichta EJ (2019) *J Power Sources* 414:412–419
36. Fan FY, Pan MS, Lau KC, Assary RS, Woodford WH, Curtiss LA, Carter WC, Chiang Y-M (2016) *J Electrochem Soc* 163:A3111–A3116

37. Xu R, Belharouak I, Li JCM, Zhang X, Bloom I, Bareño J (2013) *Adv Energy Mater* 3:833–838
38. Zheng D, Yang X-Q, Qu D (2016) *Chemsuschem* 9:2348–2350
39. Camacho-Forero LE, Smith TW, Bertolini S, Balbuena PB (2015) *J Phys Chem C* 119:26828–26839
40. Salihoglu O, Demir-Cakan R (2017) *J Electrochem Soc* 164:A2948–A2955
41. Kong L, Jin Q, Huang J-Q, Zhao L-D, Li P, Li B-Q, Peng H-J, Zhang X, Zhang Q (2019) *Energy Technol* 7:1900111
42. Xiong S, Xie K, Diao Y, Hong X (2013) *J Power Sources* 236:181–187
43. Akridge JR, Mikhaylik YV, White N (2004) *Solid State Ionics* 175:243–245
44. Mikhaylik YV, Akridge JR (2004) *J Electrochem Soc* 151:A1969–A1976
45. Rong G, Zhang X, Zhao W, Qiu Y, Liu M, Ye F, Xu Y, Chen J, Hou Y, Li W, Duan W, Zhang Y (2017) *Adv Mater* 29:1606187
46. Jozwiuk A, Berkes BB, Weiss T, Sommer H, Janek J, Brezesinski T (2016) *Energy Environ Sci* 9:2603–2608
47. Chen X, Hou T-Z, Li B, Yan C, Zhu L, Guan C, Cheng X-B, Peng H-J, Huang J-Q, Zhang Q (2017) *Energy Storage Mater* 8:194–201
48. Weller C, Thieme S, Haertel P, Althues H, Kaskel S (2017) *J Electrochem Soc* 164:A3766–A3771
49. Goodenough JB, Kim Y (2010) *Chem Mater* 22:587–603
50. Liu Z, Bertolin S, Balbuena PB, Mukherjee PP (2016) *ACS Appl Mater Interfaces* 8:4700–4708
51. Yemini R, Rosy, Noked M (2019) *J Electrochem Soc* 166:A3098–A3101
52. Tikekar MD, Choudhury S, Tu Z, Archer LA (2016) *Nat Energy* 1:16114
53. Bai P, Li J, Brushett FR, Bazant MZ (2016) *Energy Environ Sci* 9:3221–3229
54. Huang F, Wang S, Jie Y, Hansen E, Wang S, Lei Z, Liu J, Cao R, Zhang G, Jiao S (2020) *J Energy Chem* 49:257–261
55. Liu H, Cheng X-B, Xu R, Zhang X-Q, Yan C, Huang J-Q, Zhang Q (2019) *Adv Energy Mater* 9:1902254
56. Koo D, Kwon B, Lee J, Lee KT (2019) *Chem Commun* 55:9637–9640
57. Lin D, Liu Y, Cui Y (2017) *Nat Nanotechnol* 12:194–206
58. Zhang H, Gebresilassie Eshetu G, Judez X, Li C, Rodriguez-Martinez LM, Armand M (2018) *Angew Chem Int Ed* 57:15002–15027
59. Li T, Zhang X-Q, Shi P, Zhang Q (2019) *Joule* 3:2647–2661
60. Zhang X, Yang Y, Zhou Z (2020) *Chem Soc Rev* 49:3040–3071
61. Shin ES, Kim K, Oh SH, Il Cho W (2013) *Chem Commun* 49:2004–2006
62. Kim H, Wu F, Lee JT, Nitta N, Lin H-T, Oschatz M, Cho WI, Kaskel S, Borodin O, Yushin G (2015) *Adv Energy Mater* 5:1401792
63. Zheng J, Fan X, Ji G, Wang H, Hou S, DeMella KC, Raghavan SR, Wang J, Xu K, Wang C (2018) *Nano Energy* 50:431–440
64. Suo L, Hu YS, Li H, Armand M, Chen L (2013) *Nat Commun* 4:1481
65. Pang Q, Shyamsunder A, Narayanan B, Kwok CY, Curtiss LA, Nazar LF (2018) *Nat Energy* 3:783–791
66. Yoshida K, Nakamura M, Kazue Y, Tachikawa N, Tsuzuki S, Seki S, Dokko K, Watanabe M (2011) *J Am Chem Soc* 133:13121–13129
67. Dokko K, Tachikawa N, Yamauchi K, Tsuchiya M, Yamazaki A, Takashima E, Park J-W, Ueno K, Seki S, Serizawa N, Watanabe M (2013) *J Electrochem Soc* 160:A1304–A1310
68. Ueno K, Park J-W, Yamazaki A, Mandai T, Tachikawa N, Dokko K, Watanabe M (2013) *J Phys Chem C* 117:20509–20516
69. Wang X, Tan Y, Shen G, Zhang S (2020) *J Energy Chem* 41:149–170
70. Weller C, Pempel J, Dörfler S, Althues H, Kaskel S (2019) *Energy Technol* 7:1900625
71. Sun K, Wu Q, Tong X, Gan H (2018) *ACS Appl Energy Mater* 1:2608–2618
72. Shin M, Wu H-L, Narayanan B, See KA, Assary RS, Zhu L, Haasch RT, Zhang S, Zhang Z, Curtiss LA, Gewirth AA (2017) *ACS Appl Mater Interfaces* 9:39357–39370
73. Su C-C, He M, Amine R, Chen Z, Amine K (2018) *Angew Chem Int Ed* 57:12033–12036

74. Su C-C, He M, Amine R, Amine K (2019) *Angew Chem Int Ed* 58:10591–10595
75. Weng W, Pol VG, Amine K (2013) *Adv Mater* 25:1608–1615
76. Azimi N, Weng W, Takoudis C, Zhang Z (2013) *Electrochem Commun* 37:96–99
77. Azimi N, Xue Z, Bloom I, Gordin ML, Wang D, Daniel T, Takoudis C, Zhang Z (2015) *ACS Appl Mater Interfaces* 7:9169–9177
78. Azimi N, Xue Z, Rago ND, Takoudis C, Gordin ML, Song J, Wang D, Zhang Z (2015) *J Electrochem Soc* 162:A64–A68
79. Gordin ML, Dai F, Chen S, Xu T, Song J, Tang D, Azimi N, Zhang Z, Wang D (2014) *ACS Appl Mater Interfaces* 6:8006–8010
80. Chen S, Yu Z, Gordin ML, Yi R, Song J, Wang D (2017) *ACS Appl Mater Interfaces* 9:6959–6966
81. Lu H, Yuan Y, Zhang K, Qin F, Lai Y, Liu Y (2015) *J Electrochem Soc* 162:A1460–A1465
82. Gao M, Su C, He M, Glossmann T, Hintennach A, Feng Z, Huang Y, Zhang Z (2017) *J Mater Chem A* 5:6725–6733
83. Zhang X-Q, Cheng X-B, Zhang Q (2018) *Adv Mater Interfaces* 5:1701097
84. Bai SY, Sun Y, Yi J, He YB, Qiao Y, Zhou HS (2018) *Joule* 2:2117–2132
85. Mikhaylik YV (2008) U.S. Patent 7352680
86. Zhang SS (2012) *Electrochim Acta* 70:344–348
87. Xiong S, Xie K, Diao Y, Hong X (2014) *J Power Sources* 246:840–845
88. Li W, Yao H, Yan K, Zheng G, Liang Z, Chiang Y-M, Cui Y (2015) *Nat Commun* 6:7436
89. Kim J-S, Yoo D-J, Min J, Shakoor RA, Kahraman R, Choi JW (2015) *ChemNanoMater* 1:240–245
90. Liu S, Li G-R, Gao X-P (2016) *ACS Appl Mater Interfaces* 8:7783–7789
91. Li J, Zhang L, Qin F, Hong B, Xiang Q, Zhang K, Fang J, Lai Y (2019) *J Power Sources* 442:227232
92. Jia W, Fan C, Wang L, Wang Q, Zhao M, Zhou A, Li J (2016) *ACS Appl Mater Interfaces* 8:15399–15405
93. Ye Y, Song M-K, Xu Y, Nie K, Liu Y-S, Feng J, Sun X, Cairns EJ, Zhang Y, Guo J (2019) *Energy Storage Mater* 16:498–504
94. Yan C, Cheng X-B, Zhao C-Z, Huang J-Q, Yang S-T, Zhang Q (2016) *J Power Sources* 327:212–220
95. Cheng XB, Yan C, Chen X, Guan C, Huang JQ, Peng HJ, Zhang R, Yang ST, Zhang Q (2017) *Chem* 2:258–270
96. Zhang L, Ling M, Feng J, Mai L, Liu G, Guo J (2018) *Energy Storage Mater* 11:24–29
97. Zhao C-Z, Cheng X-B, Zhang R, Peng H-J, Huang J-Q, Ran R, Huang Z-H, Wei F, Zhang Q (2016) *Energy Storage Mater* 3:77–84
98. Cheng X-B, Yan C, Peng H-J, Huang J-Q, Yang S-T, Zhang Q (2018) *Energy Storage Mater* 10:199–205
99. Lin D, Liu Y, Chen W, Zhou G, Liu K, Dunn B, Cui Y (2017) *Nano Lett* 17:3731–3737
100. Tang B, Wu H, Du X, Cheng X, Liu X, Yu Z, Yang J, Zhang M, Zhang J, Cui G (2020) *Small* 16:1905737
101. Xiao Y, Han B, Zeng Y, Chi S-S, Zeng X, Zheng Z, Xu K, Deng Y (2020) *Adv Energy Mater* 10:1903937
102. Wu F, Qian J, Chen R, Lu J, Li L, Wu H, Chen J, Zhao T, Ye Y, Amine K (2014) *ACS Appl Mater Interfaces* 6:15542–15549
103. Azimi N, Xue Z, Hua L, Takoudis C, Zhang S, Zhang Z (2015) *Electrochim Acta* 154:205–210
104. Wu F, Zhu Q, Chen R, Chen N, Chen Y, Ye Y, Qian J, Li L (2015) *J Power Sources* 296:10–17
105. Cao R, Chen J, Han KS, Xu W, Mei D, Bhattacharya P, Engelhard MH, Mueller KT, Liu J, Zhang J-G (2016) *Adv Funct Mater* 26:3059–3066
106. Pang Q, Liang X, Shyamsunder A, Nazar LF (2017) *Joule* 1:871–886
107. Lu Y, Gu S, Hong X, Rui K, Huang X, Jin J, Chen C, Yang J, Wen Z (2018) *Energy Storage Mater* 11:16–23
108. Liang J, Li X, Zhao Y, Goncharova LV, Wang G, Adair KR, Wang C, Li R, Zhu Y, Qian Y, Zhang L, Yang R, Lu S, Sun X (2018) *Adv Mater* 30:1804684

109. Jing H-K, Kong L-L, Liu S, Li G-R, Gao X-P (2015) *J Mater Chem A* 3:12213–12219
110. Wang W, Yue X, Meng J, Wang J, Wang X, Chen H, Shi D, Fu J, Zhou Y, Chen J, Fu Z (2019) *Energy Storage Mater* 18:414–422
111. Sun C, Huang X, Jin J, Lu Y, Wang Q, Yang J, Wen Z (2018) *J Power Sources* 377:36–43
112. Xiong C, Ren YX, Jiang HR, Wu MC, Zhao TS (2019) *J Energy Storage* 26:101006
113. Jin Q, Zhang X, Gao H, Li L, Zhang Z (2020) *J Mater Chem A* 8:8979–8988
114. Duan B, Wang W, Zhao H, Wang A, Wang M, Yuan K, Yu Z, Yang Y (2013) *ECS Electrochem Lett* 2:A47–A51
115. Zhou D, Liu Z, Lv X, Zhou G, Yin J (2006) *Electrochim Acta* 51:5731–5737
116. Cheng X-B, Peng H-J, Huang J-Q, Wei F, Zhang Q (2014) *Small* 10:4257–4263
117. Zhang X, Wang W, Wang A, Huang Y, Yuan K, Yu Z, Qiu J, Yang Y (2014) *J Mater Chem A* 2:11660–11665
118. Kim MS, Deepika, Lee SH, Kim M-S, Ryu J-H, Lee K-R, Archer LA, Cho WI (2019) *Sci Adv* 5:eaax5587
119. Markevych AV, Shembel E, Straková Fedorková A, Redko VI (2019) *ECS Trans* 95:9–17
120. Sun J, Liang J, Liu J, Shi W, Sharma N, Lv W, Lv R, Yang Q-H, Amal R, Wang D-W (2018) *Energy Environ Sci* 11:2509–2520
121. Li H, Yamaguchi T, Matsumoto S, Hoshikawa H, Kumagai T, Okamoto NL, Ichitsubo T (2020) *Nat Commun* 11:1584
122. Xia S, Zhang X, Liang C, Yu Y, Liu W (2020) *Energy Storage Mater* 24:329–335
123. Li C, Lan Q, Yang Y, Shao H, Zhan H (2019) *ACS Appl Mater Interfaces* 11:2479–2489
124. Chen T, Kong WH, Zhao PY, Lin HN, Hu Y, Chen RP, Yan W, Jin Z (2019) *Chem Mater* 31:7565–7573
125. Ren YX, Zeng L, Jiang HR, Ruan WQ, Chen Q, Zhao TS (2019) *Nat Commun* 10:3249
126. Kong L-L, Wang L, Ni Z-C, Liu S, Li G-R, Gao X-P (2019) *Adv Funct Mater* 29:1808756
127. Nayeb-Hashemi AA, Clark JB, Pelton AD (1984) *Bull Alloy Phase Diagrams* 5:365–374
128. Yu XW, Manthiram A (2020) *Adv Funct Mater* 30:2004084
129. Yu X, Manthiram A (2018) *Energy Storage Mater* 15:368–373
130. Yu X, Boyer MJ, Hwang GS, Manthiram A (2018) *Chem* 4:586–598
131. See KA, Gerbec JA, Jun Y-S, Wudl F, Stucky GD, Seshadri R (2013) *Adv Energy Mater* 3:1056–1061
132. Yu X, Boyer MJ, Hwang GS, Manthiram A (2019) *Adv Energy Mater* 9:1803794

Chapter 7

Organosulfide Cathodes



Pengfei Sang, Dan-Yang Wang, Wei Guo, and Yongzhu Fu

Abstract Lithium–sulfur (Li–S) batteries have been studied over the last decades. So far, significant progress and deep understanding have been made. However, lithium polysulfides have to be formed in ether electrolyte, causing shuttle effect and limited cycle life. Many strategies have been developed, which have moved the Li–S battery technology to an unprecedented frontier. Among them, organosulfides as cathode materials has shown unique advantages. In particular, they reduce the formation of lithium polysulfides and introduce organic functional groups. In this chapter, we first introduce the linear organosulfides with different organic functional groups, which contain sulfur chains of 2–6 atoms. They have precise redox sites which allow us to have a deep understanding of the electrochemical behavior of these molecules. Organosulfide polymers with multiple S–S bonds can provide high capacity and stable cycling performance and some can be elastic showing unique properties. In the following, cyclic organosulfides are briefly discussed. Then, organosulfides containing N-heterocycles are presented, which deliver the enhancement of discharge voltage because of the effect of electron-withdrawing groups. Finally, organosulfides containing S–Se bonds are discussed. The introduction of Se atoms not only increases the conductivity, but also improves the redox kinetics and reduces overpotential. At the end, some perspectives are provided to show the strategies to improve the properties and performance of organosulfide cathodes and the potential of organosulfide materials in lithium batteries and beyond.

Keywords Lithium–sulfur battery · Cathode · Organosulfide · Redox mechanism

7.1 Introduction

Polysulfide scaffolds, containing covalently linked sulfur atoms, are important molecular motifs and widely exist in biomolecules, natural products, and pharmaceutical molecules. Organosulfides as cathode materials for rechargeable lithium

P. Sang · D.-Y. Wang · W. Guo · Y. Fu (✉)
College of Chemistry, Zhengzhou University, Zhengzhou 450001, P. R. China
e-mail: yfu@zzu.edu.cn

batteries offer praiseworthy advantages owing to their high theoretical capacity, low cost, and abundant resources [1]. Regulations of functional groups are the incomparable advantage for improving battery performance. In fact, organic compounds have only been studied in three main areas including organosulfides, free radicals, and carbonyl compounds [2]. Organosulfides serve as alternative electrode materials that have been gradually applied for the energy storage field since the pioneering work of Visco et al. in 1988 (Fig. 7.1) [3, 4].

Redox reactions of organosulfides involve cleavage and reformation of S–S bonds. The S–S bonds break during the discharge of lithium batteries, lithium ions and electrons are ingested and stored [5]. Since a single S–S bond (R–S–S–R) can only take two lithium ions and electrons, compounds (R–S_n–R, n > 2) containing multiple S–S bonds can store more electrons, thus providing higher capacity. In addition, the organic framework of organosulfides can effectively inhibit the dissolution of polysulfides in the electrolyte and suppress the shuttle effect through the restriction of covalent bonds. Therefore, in recent years, organosulfides as cathode materials have been widely studied. Herein, we introduce a series of organosulfides cathode materials including linear and cyclic organosulfides, organosulfide polymers, heteroatoms-containing organosulfides, and selenium-doped organosulfides. Organosulfides as cathode materials would provide the alternatives for the exploration of high capacity and high energy batteries.

7.2 Linear Organosulfides

7.2.1 Small Organosulfide Molecules

Small organosulfide molecules have high capacity and structure diversity, making them potential cathode materials for lithium batteries. Dimethyl trisulfide (DMTS) used as cathode material was researched by Wu et al. [6]. In their research, DMTS was dissolved in ether-electrolyte to form catholyte, binder-free carbon nanotube (CNT) paper was used as a current collector and reservoir for holding charged–discharged products (Fig. 7.2a). The theoretical capacity of DMTS is 849 mAh g⁻¹ based on the transfer of 4e⁻ per molecule. Its charge–discharge process has been explored through X-ray diffraction (XRD), gas chromatography–mass spectroscopy (GC–MS), and X-ray photoelectron spectroscopy (XPS) characterization techniques. The redox mechanism of DMTS is shown in Fig. 7.2b. During discharge, one S–S bond in DMTS would be broken and react with Li⁺ and e⁻ to form LiSCH₃ and LiSSCH₃. Continually, the S–S bond in LiSSCH₃ would be broken and react with another Li⁺ and e⁻ to form the final discharge products of Li₂S and LiSCH₃. In the recharge process, LiSCH₃ and Li₂S are delithiated. The radicals ·SCH₃ and ·SSCH₃ could combine with each other to form CH₃SSCH₃ (DMDS), DMTS, and CH₃SSSSCH₃ (DMTtS). The cycling performance of the Li/DMTS cell with mass loading of 6.7 mg cm⁻² at 0.1 C rate is shown in Fig. 7.2c, the discharge capacity

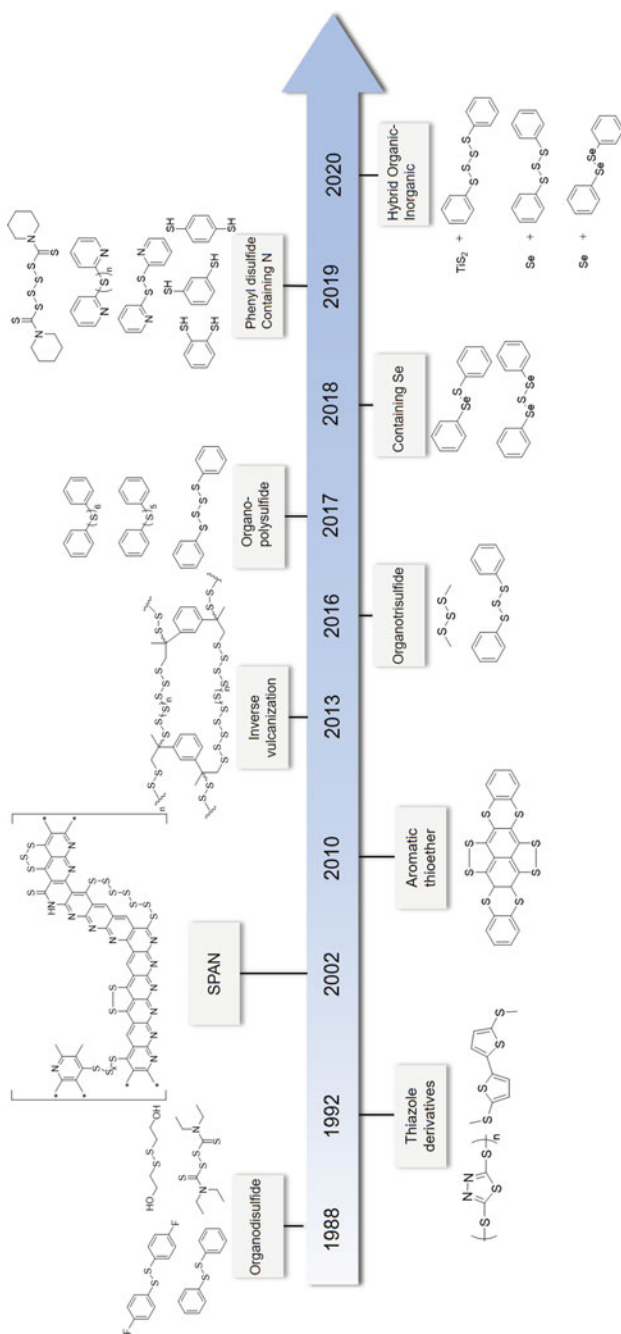


Fig. 7.1 The development timeline of selected organosulfides for batteries. The dates correspond to the first published reports of organosulfides

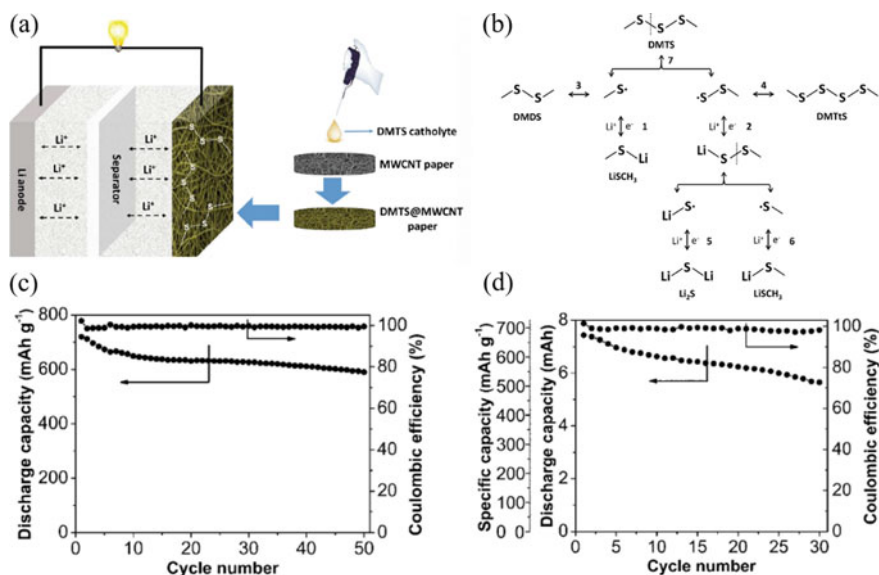


Fig. 7.2 **a** Schematic illustration of the cell configuration and the composition of the dimethyl trisulfide (DMTS) cathode. **b** The proposed redox reaction of DMTS in rechargeable lithium battery. The cycling performance and Coulombic efficiency of the cell cycled between 1.7–2.7 V at 0.1 C rate with DMTS loading of **c** 6.7 mg cm^{-2} and **d** 11.3 mg cm^{-2} . Reproduced with permission from Ref. [6]. Copyright 2016, Wiley-VCH

is 590 mAh g^{-1} after 50 cycles with capacity retention of 82%, and the Coulombic efficiencies for most cycles are more than 98%. Furthermore, the high mass loading of DMTS electrode was tested to realize a high energy density cell (229 Wh kg^{-1}), the Li/DMTS cell with mass loading of 11.3 mg cm^{-2} shows an initial discharge capacity of 675 mAh g^{-1} at 0.1 C rate, the capacity retention is 76% after 30 cycles (Fig. 7.2d).

The structure of organosulfide can be tuned by changing the organic functional groups. Changing the methyl group in DMTS to a phenyl group with stronger electron-withdrawing effect can improve the discharge voltage. Diphenyl trisulfide (DPTS) reported by Wu et al. was synthesized by heating the mixture solution with a stoichiometric ratio of diphenyl disulfide (DPDS) and sulfur in ether-electrolyte [7]. The solution was evaluated as catholyte in lithium battery using CNT paper as current collector. The theoretical specific capacity of organosulfide decreases with the increasement of relative molecular mass of molecules. DPTS can be involved in the conversion reaction of $4e^-$, having a theoretical specific capacity of 428 mAh g^{-1} . The cyclic voltammogram (CV) profile of a Li/DPTS cell is shown in Fig. 7.3a, an anodic peak at 2.4 V and two cathodic peaks at 2.0 and 2.2 V can be seen. The redox reaction is confirmed to be $\text{PhSSSPH} + 4\text{Li} \leftrightarrow 2\text{PhSLi} + \text{Li}_2\text{S}$. The cycling performance of the Li/DPTS cell at 0.5 C rate is shown in Fig. 7.3b, the discharge

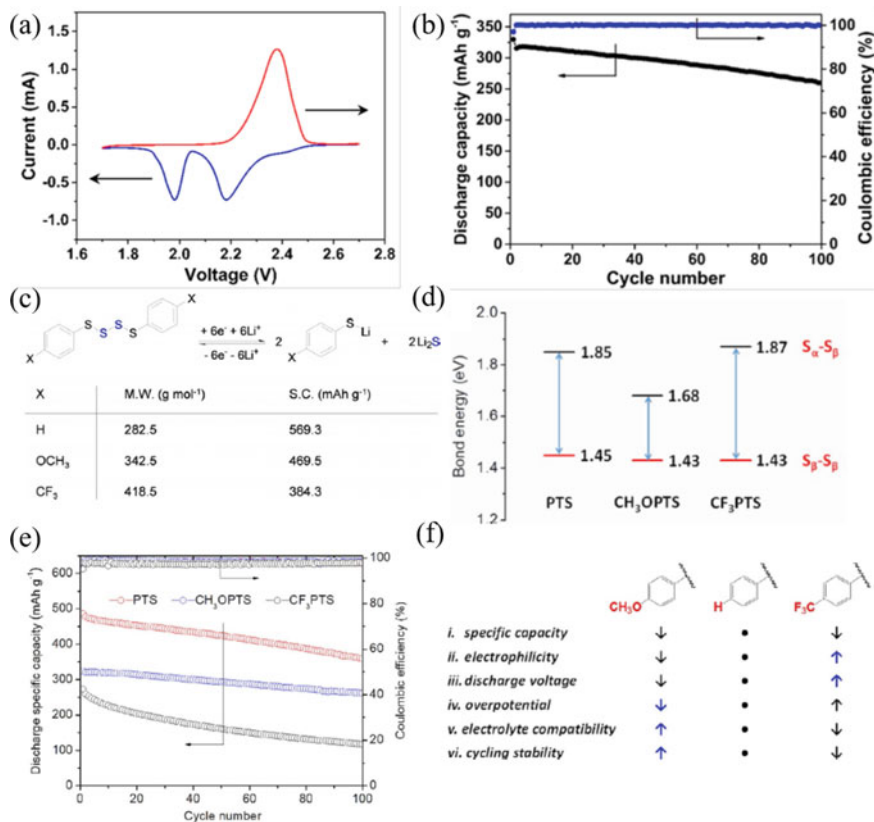


Fig. 7.3 **a** Cyclic voltammogram of the Li/DPTS cell at a scan rate of 0.05 mV s⁻¹. **b** The cycle performance and Coulombic efficiency of the Li/DPTS cell with mass loading of 3.9 mg cm⁻² at 0.5 C rate. Reproduced with permission from Ref. [7]. Copyright 2016, American Chemical Society. **c** The possible conversion reactions of phenyl tetrasulfides with different functional groups in rechargeable lithium batteries, and the molecular weights (M.W.) and theoretical specific capacity (S.C.) of these compounds. **d** S-S bond energies in these three tetrasulfides. **e** The cycling performance and Coulombic efficiency of PTS, CH₃OPTS, and CF₃PTS at 0.1 C rate. **f** Effects of the functional groups on the electrochemical characteristics of tetrasulfides, the upper arrow indicates an increase, and the lower arrow indicates a decrease. Reproduced with permission from Ref. [8]. Copyright 2017, Wiley-VCH

capacity is 260 mAh g⁻¹ after 100 cycles with high Coulombic efficiency of over 99.5%, the capacity retention is about 79%.

In order to increase the theoretical specific capacity of organosulfides, phenyl tetrasulfide (PTS) was studied by Guo et al. [8]. In addition, *p*-methoxyphenyl tetrasulfide (CH₃OPTS) containing electron-donating group and *p*-trifluoromethylphenyl tetrasulfide (CF₃PTS) containing electron-withdrawing group were also studied to compare their electrochemical performance. The possible chemical transformations

of these three tetrasulfides in lithium battery are shown in Fig. 7.3c, the molecular weights (M.W.) and theoretical specific capacity (S.C.) of these molecules are shown together. First-principles density functional theoretical (DFT) calculations were performed to investigate the discharge processes. The S–S bond energies were calculated to understand where the reduction reactions start, the related bond energies are summarized in Fig. 7.3d. The S directly connected to the benzene ring is named α -sulfur (S_α) and the S bonded to the α -sulfur is named β -sulfur (S_β). The S_β – S_β bond energy (1.43–1.45 eV) is much lower than the S_α – S_β bond energy (1.68–1.87 eV), indicating that the S_β – S_β bond will break first, the initial reaction formula should be $RS_4R + 2Li \rightarrow 2RS_2Li$. The RS_2Li molecules subsequently react with lithium through $2RS_2Li + 4Li \rightarrow 2RSLi + 2Li_2S$. Figure 7.3e shows the cycling performance of the three tetrasulfides at 0.1 C rate. PTS with a small molecular mass has a high specific capacity. The initial discharge capacities are 486 mAh g^{-1} (PTS), 324 mAh g^{-1} (CH_3OPTS), and 272 mAh g^{-1} (CF_3PTS), and the capacity retentions are 74%, 81%, and 43% after 100 cycles, respectively. The influence of the functional groups on the phenyl tetrasulfides is summarized in Fig. 7.3f.

Phenyl polysulfides can be generated by the direct reaction of benzenethiol (PhSH) and element sulfur (Fig. 7.4a). Phenyl tetrasulfide (PTS, PhS_4Ph), phenyl pentasulfide (PPS, PhS_5Ph), and phenyl hexasulfide (PHS, PhS_6Ph) reported by Bhargav et al. were synthesized by the reaction of 2 equiv. of PhSH and 3, 4, and 5 equiv. of sulfur, respectively [9]. The generated H_2S gas can be detected by a lead acetate test strip. A variety of spectroscopic techniques were performed to prove the successful

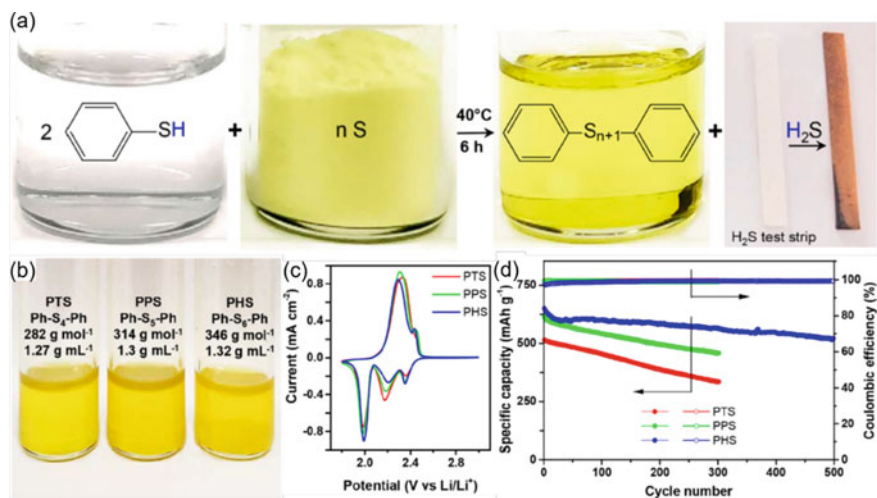


Fig. 7.4 a Images of reactants and products, as well as reaction equations for the synthesis of phenyl polysulfides. Lead acetate test paper was used to detect the production of H_2S gas. b Optical images and properties of the obtained liquid polysulfides. c Cyclic voltammetry profiles of the phenyl polysulfide cathodes was performed at a scan rate of 0.05 mV s^{-1} . d Cycling performance and Coulombic efficiency of the phenyl polysulfides at 1 C rate. Reproduced with permission from Ref. [9]. Copyright 2018, American Chemical Society

synthesis of PTS, PPS, and PHS. The relative molecular mass and density of these three phenyl polysulfides are shown in Fig. 7.4b, the density of phenyl polysulfide increases with the number of sulfur atoms increased in the molecules. When they are used as cathode materials, the theoretical specific capacities are 570.2 (PTS), 682.8 (PPS), and 774.5 mAh g⁻¹ (PHS), respectively. Li half cells were assembled to study the electrochemical performance of these phenyl polysulfides. The CV plots are shown in Fig. 7.4c. PTS, PPS, and PHS all show similar reduction and oxidation peaks. The first reduction peak at 2.4 V is related to the breakage of the central S–S bonds, the second peak at 2.2 V corresponds to the reduction of the lithium polysulfides to form phenyl sulfide radicals and phenyl persulfides. Finally, lithium sulfide is formed from lithium polysulfides (Li₂S_x, 2 ≤ x ≤ 4) and PhSLi is formed at 2 V simultaneously. The oxidation process occurs in two steps, the reduced products are completely converted to phenyl polysulfides at approximately 2.43 V. The cycling performance of PTS, PPS, and PHS are shown in Fig. 7.4d, the initial discharge specific capacities are 514, 612, 650 mAh g⁻¹, and the capacity retentions are 65% after 300 cycles (PTS), 75% after 300 cycles (PPS), and 80% after 500 cycles (PHS), respectively. The average Coulombic efficiencies of all of the phenyl polysulfides are over 99.5%.

PTS can also be prepared by heating phenyl disulfide (PDS) and sulfur with a molar ratio of 1:2 at 170 °C under vacuum for 8 h (Fig. 7.5a) [10]. The reaction reported by Fan et al. does not require any catalyst or solvent. The product is a clear yellow liquid. In order to improve the performance of PTS, TiS₂ nanosheets with high lithium diffusion rate, high specific surface area, and high catalytic performance were used as the mediator in the PTS cathode. TiS₂ and multi-walled carbon nanotubes (MWCNTs) were self-woven together by vacuum filtration and the composited carbon paper (named TiS₂ NSs@MWCNT) was used as a binder-free current collector. The ultraviolet–visible (UV–vis) analysis and visual adsorption experiments were performed to verify the chemisorption ability of TiS₂. From Fig. 7.5b, it can be seen that the color of the 1,3-dioxolane (DOL)/1,2-dimethoxyethane (DME) (1:1 v/v) solution dissolved with PhSLi became lighter after TiS₂ NSs was added, while there was no significant change with the addition of MWCNT and the color of the solution still was yellow, like the blank solution. Additionally, the UV absorbance of PhSLi solution exposed to TiS₂ becomes much lower than the solution exposed to MWCNT, which indicates that TiS₂ has strong adsorption ability to PhSLi. Subsequently, in order to prove the electrocatalytic properties of TiS₂ for the redox process of PhSLi, the CV of the symmetric cell with 0.2 M PhSLi electrolyte was measured. Figure 7.5c shows that TiS₂ NSs@MWCNT has a pair of obvious redox peaks at -0.55 and 0.55 V, which are more obvious than pure MWCNT, indicating that TiS₂ NSs are conducive to accelerate the conversion reaction of PhSLi. Charge–discharge profiles of pure PTS and PTS/TiS₂ NSs electrodes are displayed in Fig. 7.5d, PTS/TiS₂ NSs electrode shows similar charge and discharge profiles but with smaller polarization. The batteries were charged and discharged at 0.5 C rate with PTS loading of 1.4 mg cm⁻² (Fig. 7.5e). The PTS/TiS₂ NSs electrode could deliver a discharge specific capacity of 467.6 mAh g⁻¹ after 200 cycles with high Coulombic efficiency of 99.9%, and the capacity retention relative to the 5th cycle is 81.9%, which is higher than that

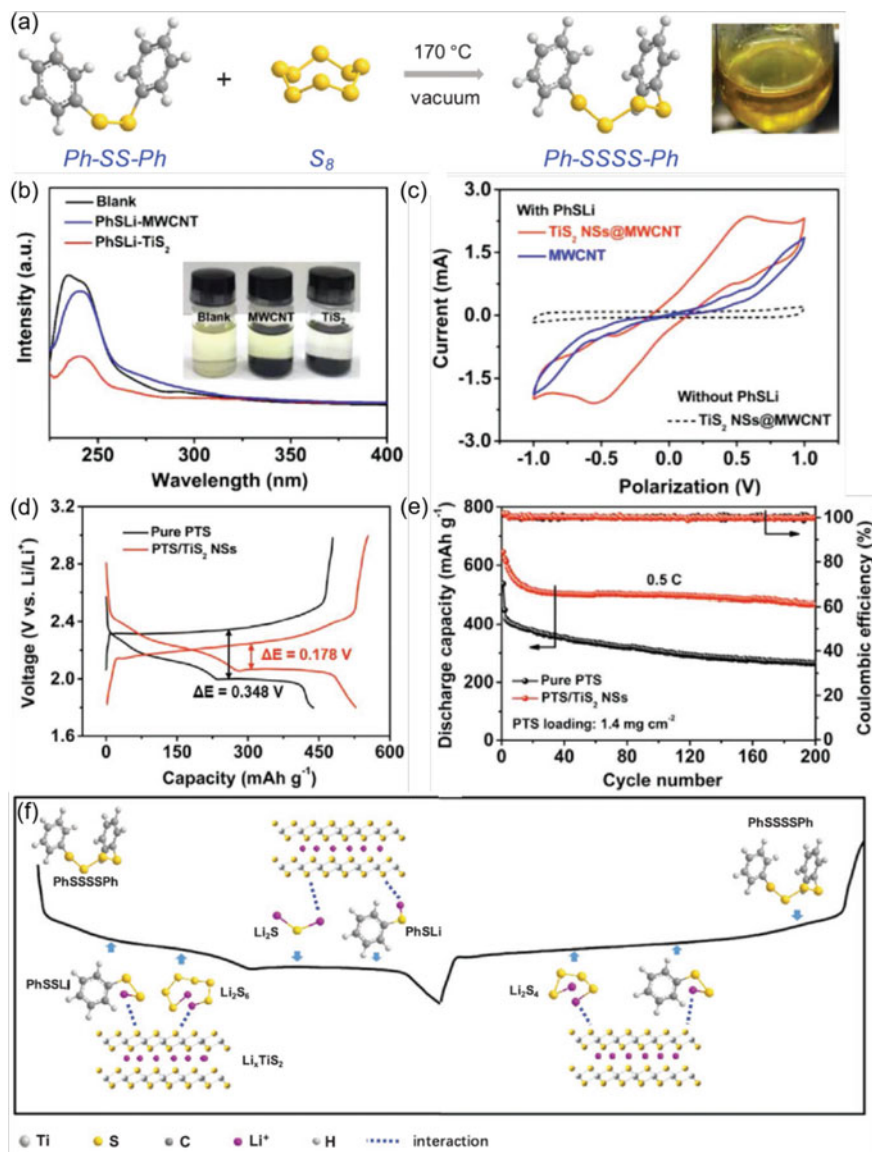


Fig. 7.5 a Synthesis process of PTS along with a visual image of the PTS liquid. b UV-vis absorption spectra of PhSLi solutions before and after the addition of MWCNT and TiS₂, the insets show the color changes of PhSLi solutions in the absorption tests. c CV curves of the symmetric cells with TiS₂ NSs@MWCNT or pure MWCNT as electrodes in 0.2 M PhSLi electrolyte at 3 mV s⁻¹. d Charge-discharge profiles of PTS/TiS₂ NSs and pure PTS electrodes of the 10th cycle at 0.2 C rate. e Cycling performance and Coulombic efficiency of PTS/TiS₂ NSs and pure PTS electrodes with PTS areal loading of 1.4 mg cm⁻² at 0.5 C rate. f The proposed redox process of PTS/TiS₂ NSs electrode in rechargeable lithium battery. Reproduced with permission from Ref. [10]. Copyright 2020, Wiley-VCH

of pure PTS electrode (66.1%). The redox reactions of PTS/TiS₂ NSs electrode in rechargeable lithium battery are shown in Fig. 7.5f. First, the middle S–S bond in PTS is broken and PhS_xLi (1 ≤ x) is formed, meanwhile, a small amount of LiPSs is formed because the high-order phenyl polysulfide (e.g., PPS and PHS) may exist in the starting material. These lithiation products are adsorbed on the surface of lithiated titanium disulfide (Li_xTiS₂, 0 < x < 1), and then they are converted to Li₂S and PhSLi in the following region, the final discharged products also can be adsorbed on the surface of Li_xTiS₂. In the charge process, the two regions are the formation of LiPSs and PhS_xLi and the formation of PTS. This study demonstrates TiS₂ has dual effects of adsorption and electrocatalysis on organosulfides.

In order to improve the performance of organosulfide cathode material, like phenyl disulfide, phase extraction technique reported by Bhargav et al. was used to prepare phenyl disulfide@carbon nanotubes (PDS@CNTs) composite with core-sheath structure [11]. This technique mainly uses the difference of PDS solubility in methanol and water, the fabrication process is schematically illustrated in Fig. 7.6a. Firstly, CNTs and PDS were added in a methanol solution, and the solution was then ultrasonicated so that CNTs were evenly dispersed. After ultrasonication, the water was added to the methanol solution. PDS was extracted from the methanol phase and deposited on the interwoven CNT fibers because PDS is insoluble in water. Following vacuum filtration and drying, the “phase-extracted” PDS@CNTs composite was obtained. This preparation method can effectively avoid the agglomeration of PDS to ensure that the active material can be fully utilized. CV was tested to understand the redox behavior of PDS (Fig. 7.6b). A reduction peak at about 2.0 V in the cathodic scan and an oxidation peak at about 2.4 V in the anodic scan are observed, which represent the homogeneous cleavage of S–S bonds and the combination of thiophenolate radicals (C₆H₅S·) to form PDS, respectively. The galvanostatic cycling performance of the PDS@CNTs cathode at 1 C is shown in Fig. 7.6c. The battery delivers an initial discharge capacity of 218 mAh g⁻¹ corresponding to 89% of the theoretical capacity. After 150 cycles, 70% of the initial capacity with high Coulombic efficiencies of over 99% through the cycles is achieved.

Diisopropyl xanthogen polysulfide (DIXPS) was selected to study the unique electrochemical properties of xanthogen polysulfide cathode materials in lithium battery [12]. DIXPS reported by Bhargav et al. was dissolved in ether-based electrolyte and used as catholyte. The free-standing CNT paper is used as a current collector to estimate the battery performance (Fig. 7.7a). The simplified process of the charge–discharge reaction is shown in Fig. 7.7a. DIXPS can provide a theoretical specific capacity of 973 mAh g⁻¹ based on the transfer reaction of 10e⁻. Figure 7.7b shows the charge and discharge profiles of DIXPS and diisopropyl xanthogen disulfide (DIXDS), DIXDS only shows one plateau at 2.61 V in the discharge process, which corresponds to the cleavage of S–S bond in DIXDS. DIXPS shows the same plateau but with two more plateaus at 2.30 and 2.08 V, respectively, the subsequent plateaus involve a further reduction from linear sulfur chain to Li₂S. During the charge process, the lithium isopropyl xanthate could combine with sulfur atoms to form organosulfide throughout the plateaus at 2.26 and 2.36 V, then to form DIXPS at 2.68 V. The DIXPS electrode in Li half cell can deliver an initial discharge specific

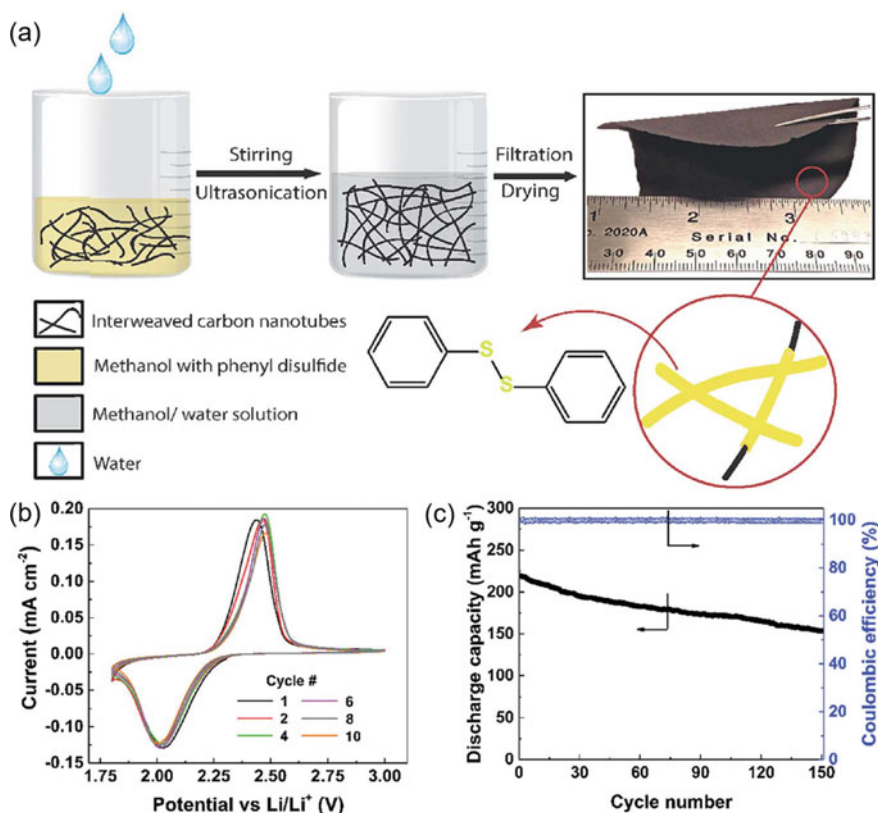


Fig. 7.6 **a** The schematic illustration of the preparation of the PDS@CNTs cathode. **b** Cyclic voltammogram of the PDS@CNTs cathode tested at a scan rate of 0.2 mV s⁻¹. **c** Cycle performance of PDS@CNTs cathode at 1 C with the mass loading of 5 mg cm⁻². Reproduced with permission from Ref. [11]. Copyright 2017, Royal Society of Chemistry

capacity of 467 mAh g⁻¹ with a capacity retention of 74% after 1000 cycles at 4 C rate (Fig. 7.7c). In order to measure the high-energy promise of the material, DIXPS cathode was tested under high loading and lean electrolyte conditions (Fig. 7.7d). The coin cell with a high areal loading of 13 mg cm⁻² was prepared, as well as a low electrolyte-to-DIXPS ratio of 2.7 μL mg⁻¹ was used. The cell delivers an initial capacity of 400 mAh g⁻¹ and retains nearly 83% of the initial capacity after 50 cycles. The pouch-cell electrode that has 40 times the area of the coin-cell electrode was prepared to study the battery performance in practical application (Fig. 7.7e). The pouch cell with an ultralow electrolyte-to-DIXPS ratio of 2.0 μL mg⁻¹ was tested at 0.05 C rate, which delivers a capacity of 365 mAh g⁻¹ and retains 93% capacity after 50 cycles.

The application of organosulfur acene compounds in lithium batteries has been explored. Two similar small organosulfur acene molecules tetrathiotetracene (TTT)

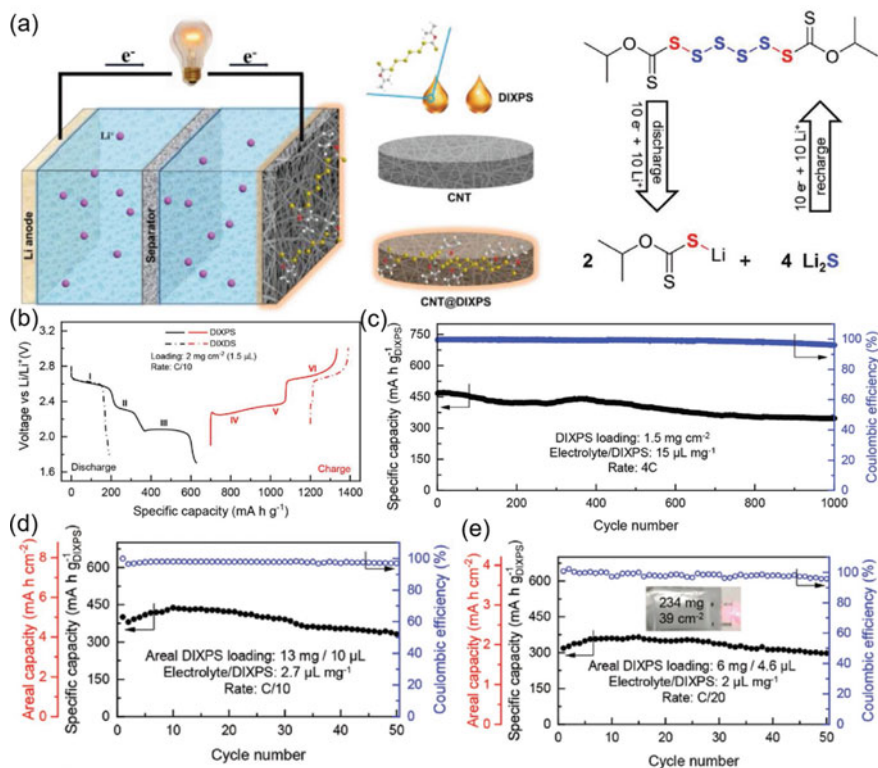


Fig. 7.7 a Schematic of the cell configuration and the cathode structure. On the right is the simplified scheme of the charge–discharge reaction. b Voltage profile for DIXPS and DIXDS when cycled at 0.1 C rate. c The cycling performance and Coulombic efficiency of the DIXPS cathode at 4 C rate. The battery performance of a high loading, lean electrolyte DIXPS cathode assembled in d coin cell and e pouch cell. Reproduced with permission from Ref. [12]. Copyright 2020, Wiley-VCH

and hexathiapentacene (HTP) reported by Hu et al. were fabricated by a zone-melting chemical vapor transport (ZM-CVT) method to investigate the structure–property relationship [13]. A schematic diagram for the synthesis of HTP and TTT is shown in Fig. 7.8a. The device consists of a vertical quartz tube (diameter = 19 mm) with a gas outlet and inlet at separated ends. The tube is equipped with a heater bearing a movement controller providing continuous conditions. The starting mixed raw materials were introduced into a one-end sealed quartz tube of a smaller diameter (10 mm). The inside quartz tube with a narrow open neck at the upper end minimizes sulfur leakage and allows gas evolution. Because the system does not require any solvents, the purity of the raw materials is not demanding, which is conducive to large-scale production. A Li half cell was assembled to research the electrochemical performance of HTP and TTT. The charge–discharge curves of HTP are shown in Fig. 7.8b, the lithiation/delithiation of HTP occurs in two main steps. The first reduction process at 1.87 V is assigned to the cleavage of trisulfide (S–S–S) bonds.

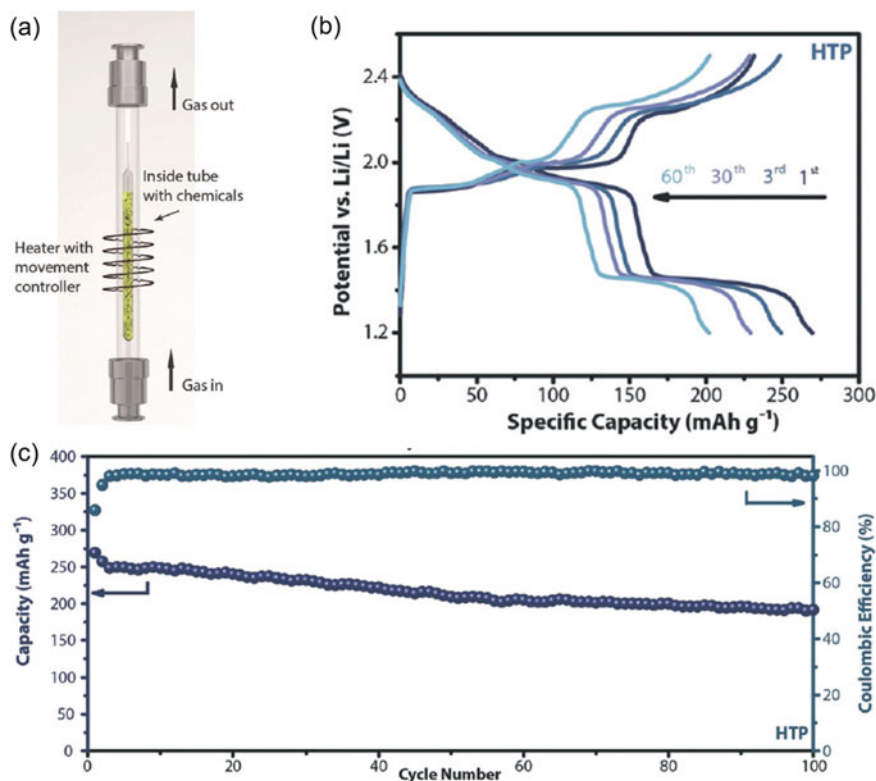


Fig. 7.8 a Schematic diagram of the device for zone-melting chemical vapor transport (ZM-CVT). Charge–discharge profile (b) and cycling performance (c) of HTP at 0.1 C rate. Reproduced with permission from Ref. [13]. Copyright 2019, Wiley-VCH

The remaining trisulfide bonds break at about 1.41 V while further discharged. The curves are similar at different cycle numbers, which indicate the high electrochemical reversibility of HTP molecule structure during cycles. The HTP cathode delivers an initial discharged capacity of 265 mAh g⁻¹ at 0.1 C rate, with a capacity retention of 72% after 100 cycles (Fig. 7.8c). However, the discharge specific capacity of TTT decays faster than HTP, remains only 51 mAh g⁻¹ after 30 cycles.

DFT modeling was used to explore the lithiation mechanism for HTP and TTT. According to the modeling results (Fig. 7.9), the lithium atoms favor reacting with sulfur atoms on the same side of S–S bonds or S–S–S bonds and then react with the S atoms on the other side instead of reacting with sulfur atoms on both sides at the same time. The reduction potentials (E_{red}) of HTP and TTT upon lithiation were calculated by using the lowest-energy structures, which are shown in Fig. 7.9. The E_{red} of HTP is lower than that of TTT, which is due to the breaking of stronger S–S bond in TTT.

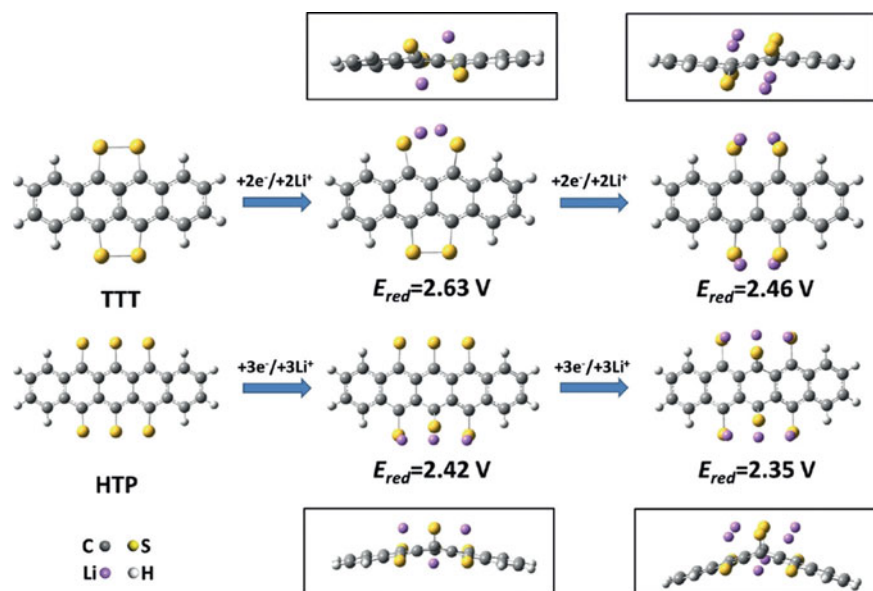


Fig. 7.9 Proposed lithiation mechanisms during the discharge process along with theoretical reduction potentials at each step according to the DFT calculations. Side views of the lithiated molecules are shown in the boxes. Reproduced with permission from Ref. [13]. Copyright 2019, Wiley-VCH

7.2.2 Organosulfide Polymers

Organosulfide polymers are chemically stable materials formed by copolymerizing sulfur with different organic linking monomers. The dissolution of long-chain polysulfides can be suppressed to a certain extent due to the strong bonds between sulfur and carbon framework. Therefore, the electrochemical performance of the battery with organosulfide polymer electrode has been improved compared with those with elemental sulfur electrode [14].

Polyphenylene tetrasulfide (PPTS) reported by Bhargav et al. was synthesized through the condensation reaction of elemental sulfur with 1,4-benzenedithiol (BDT) in the mixture solution of carbon disulfide and toluene for 12 h, and the formation of H_2S was tested by the lead acetate paper (Fig. 7.10a) [15]. The equation of the reaction is shown in Fig. 7.10a. A soft polymer membrane was obtained after coating the solution on the polytetrafluoroethylene (PTFE) dish and evaporating the solvent (Fig. 7.10b). As displayed in Fig. 7.10c, the battery cathode was prepared by injecting the PPTS solution into CNT paper, followed by drying to eliminate the solvent. At the same time, the PPTS-CNT composite cathode exhibits excellent flexibility and is easy to be folded. The microstructural details of the PPTS-CNT cathode were observed by scanning electron microscopy (SEM). From Fig. 7.10d, it can be seen that the PPTS interwoven in the depths of the network of porous CNT paper and

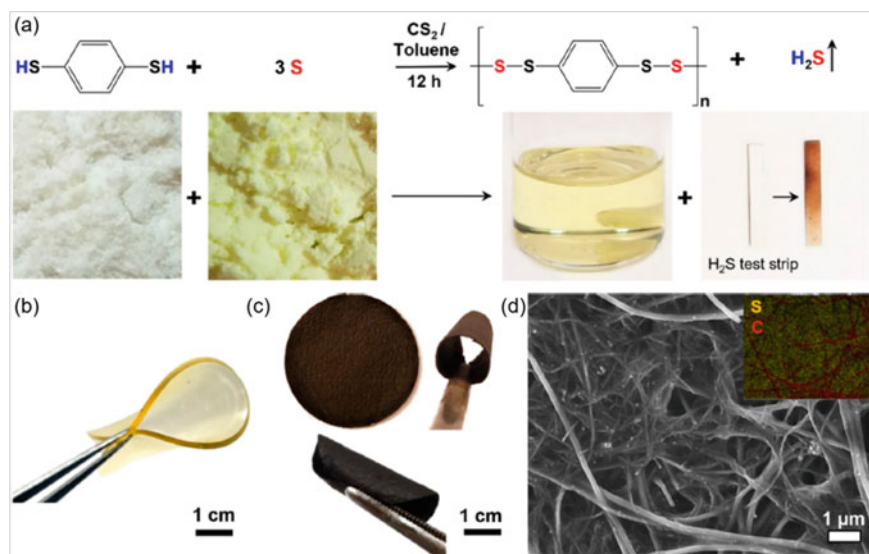


Fig. 7.10 **a** Reaction equation and visual representation of raw materials and products. **b** Optical images of the obtained PPTS membrane with flexibility and transparent property. **c** Optical images of PPTS-CNT cathode with flexible nature. **d** SEM image of the PPTS-CNT cathode, the inset EDS image shows details of the elemental distribution. Reproduced with permission from Ref. [15]. Copyright 2018, American Chemical Society

the energy dispersive spectroscopy (EDS) elemental mapping reveals that the sulfur element from PPTS is evenly distributed in the electrode.

A variety of material characterization techniques were used to validate the above-stated synthesis process. XRD characterization results show that both BDT and sulfur have strong crystallinity, while PPTS only has a broad feature between 20° and 35° region due to the non-crystalline nature of the polymer material (Fig. 7.11a). The PPTS-CNT shows similar but one more peak at $2\theta = 26.3^\circ$ than PPTS, the peak is associated with graphitic (002) peak of the CNT matrix. Next, Fourier transform infrared spectroscopy (FTIR) was used for further insight into the mechanism of the reaction (Fig. 7.11b). The characteristic absorption peak of the thiol group in BDT is at 2550 cm^{-1} , which disappears in the polymer, thus proving the occurrence of the polymerization reaction. Nuclear magnetic resonance (NMR) analysis was used to further exploring of the degree of polymerization. Figure 7.11c shows the ^1H NMR spectra of PPTS and BDT, wherein the peak corresponding to a chemical shift of 3.55 ppm belongs to the proton of the thiol group and it is obvious that the thiol intensity of BDT is 20-fold higher than that of PPTS, which indicates that the polymer chain is terminated by thiol group. Unsurprisingly, the proton peak intensity of the benzene ring of PPTS has no change compared to BDT, only a slight shift (PPTS: 7 ppm, BDT: 7.1 ppm). The voltage profiles of the cathode cycled at 0.05 C and 1 C-rates are shown in Fig. 7.11d. A four-step reduction process and a combinatorial oxidation process are observed at 0.05 C rate. However, the multistep reduction

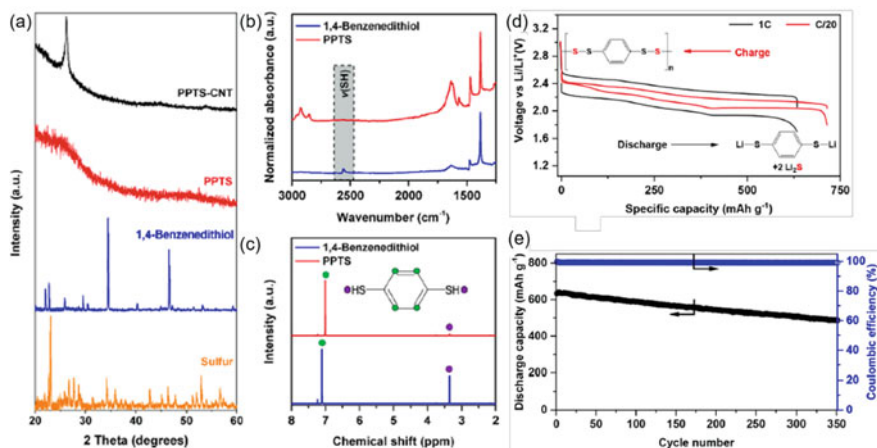


Fig. 7.11 **a** XRD patterns of sulfur, 1,4-benzenedithiol, PPTS polymer, and PPTS-CNT composite electrode. **b** FTIR and **c** ^1H NMR spectra of 1,4-benzenedithiol and PPTS polymer. **d** Voltage profile of the Li/PPTS cell cycled at 0.05 C and 1 C-rates. **e** Cycling performance and Coulombic efficiency of the Li/PPTS cell at 1 C rate. Reproduced with permission from Ref. [15]. Copyright 2018, American Chemical Society

occurs at 2.2 V overlap during fast rate cycling, which may be due to the very small free-energy changes. The Li/PPTS cell delivers an initial discharge specific capacity of 633 mAh g^{-1} at 1 C rate and retains 77% of the initial capacity after 350 cycles, with an average Coulombic efficiency of 99.2% over the 350 cycles (Fig. 7.11e).

The maximum range of tensile strain for the PPTS-CNT composite and the PPTS strip was determined by a tensile testing machine. The PPTS strip can stretch to 334% of its initial length (Fig. 7.12a). In comparison, the PPTS-CNT composite can stretch to 107%, while CNT alone can only afford a 12% tensile strain (Fig. 7.12b). The electrochemical performance was tested in a coin cell after 50 cycles of stretching or 50 cycles of blending. Figure 7.12c reveals the charge–discharge profiles for comparing the effect of mechanical strain on the electrode. Obviously, they all show similar discharge voltages at 2.0, 2.05, and 1.95 V for bent, stretched, and strain-free electrodes, respectively. Figure 7.12d compares the cycling performance of electrodes under three kinds of mechanical strains. Satisfactorily, all three electrodes deliver the same initial discharge capacity of about 625 mAh g^{-1} , the capacity retentions are 79, 86, and 86% after 200 cycles for the electrodes under bending, stretching, and no strain, respectively. The Coulombic efficiencies are 99.8, 99.3, and 99.5%, respectively. These results signify that there is not too much difference between the electrochemical performance. Consequently, the polymer has the potential to be used as a flexible battery electrode material.

A similar synthesis method as above was adopted by Sang et al. to synthesize a series of polyphenyl polysulfides through the polycondensation reaction of 4,4'-thiobisbenzenethiol (TBBT) and four ratios of sulfur, a small amount of diethylamine was used as catalyst (Fig. 7.13a) [16]. According to the different feed ratios of

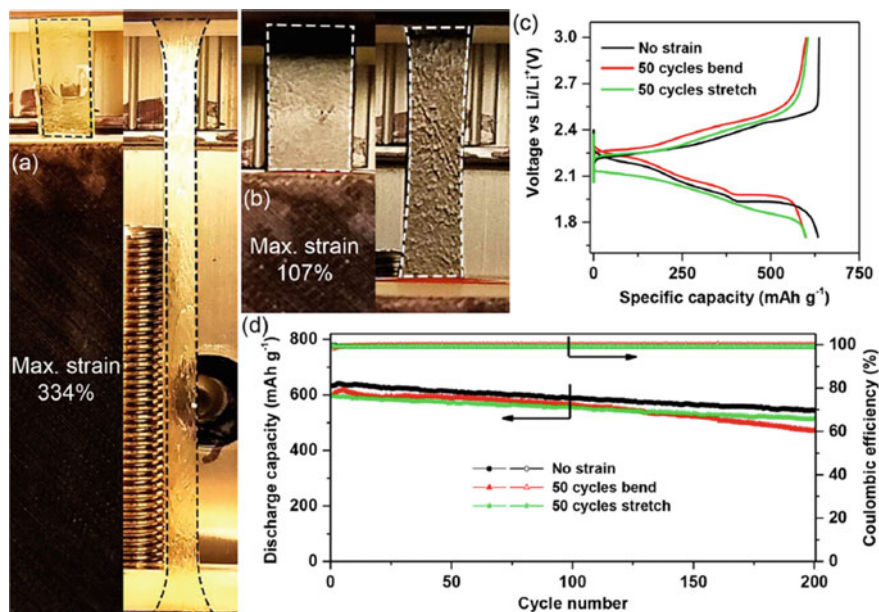


Fig. 7.12 Optical images at a maximum strain of **a** PPTS strip and **b** PPTS-CNT composite. **c** Voltage profile and **d** cycling performance of the three types of cathodes cycled at 1 C rate. Reproduced with permission from Ref. [15]. Copyright 2018, American Chemical Society

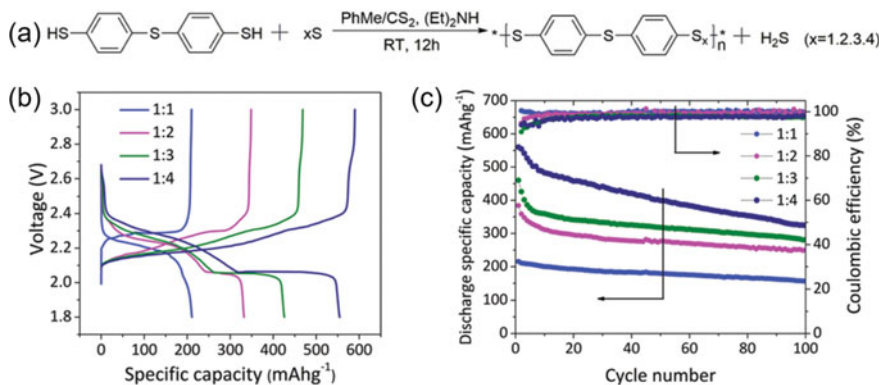


Fig. 7.13 **a** Reaction equation of 4,4'-thiobisbenzenethiol (TBBT) and sulfur. **b** Voltage profile and **c** cycling performance of these cathodes at 0.1 C rate. Reproduced with permission from Ref. [16]. Copyright 2019, Royal Society of Chemistry

reactants, the prepared polymers are named PPPS-11, PPPS-12, PPPS-13, and PPPS-14. The electrochemical performance was performed in Li half cells. Voltage profiles of the four polymer cathodes are shown in Fig. 7.13b. They all show the same discharge voltage plateau at around 2.20 V, which corresponds to the formation of Li-S-Ph-S-Ph-S-Li. In addition, PPPS-12, PPPS-13, and PPPS-14 show another voltage plateau at 2.05 V, which is caused by the formation of lithium polysulfides and the further transformation to Li_2S_2 and Li_2S . The cells deliver an initial discharge specific capacity of 215.6, 383.9, 460.1, and 559.9 mAh g^{-1} , respectively, and the capacity retentions are 72.5, 65.0, 61.0, and 57.9% after 100 cycles at 0.1 C rate, respectively (Fig. 7.13c).

Polyethylene hexasulfide (PEHS) studied by Bhargav et al. contains low-molecular-weight organic functional groups and as high as 87% sulfur content, which can provide a high theoretical specific capacity of up to 1217 mAh g^{-1} [17]. PEHS was synthesized by the condensation reaction of 1,2-ethanedithiol (EDT) and a certain ratio of sulfur in the 1:1 v/v mixture of toluene/ CS_2 solvents. A small amount of diethylamine was added to accelerate the reaction (Fig. 7.14a). PEHS solution was added dropwise to CNT paper, and the PEHS-CNT cathode can be obtained after evaporating the solvent. The SEM image of the cathode shows that PEHS is uniformly distributed around the porous CNT, and the elemental sulfur distribution

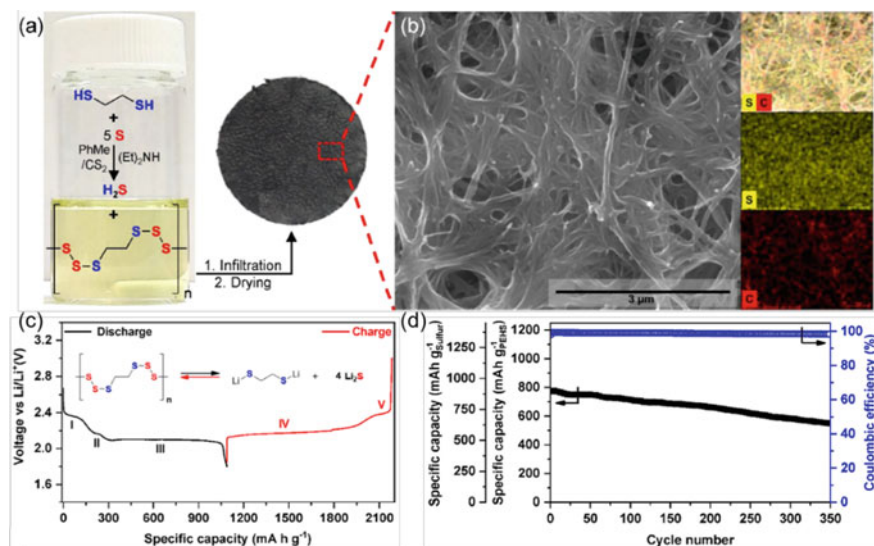


Fig. 7.14 **a** Optical image of the synthesized polyethylene hexasulfide (PEHS) polymer in the 1:1 v/v mixture of toluene/ CS_2 along with the reaction equation on the left. The obtained PEHS-CNT cathode is shown on the right. **b** SEM image of the cathode along with the EDX elemental mapping of carbon and sulfur in the inset. **c** Voltage profile of the PEHS-CNT cathode cycled at 0.05 C rate. The discharge/recharge reaction is also indicated. **d** Cycling performance of the cathode at 1 C rate. Capacities are respected to both the sulfur and polymer mass in the cathode. Reproduced with permission from Ref. [17]. Copyright 2019, American Chemical Society

in the EDS map further confirms this (Fig. 7.14b). The voltage profile clearly shows the charging and discharging process of the PEHS-CNT electrode (Fig. 7.14c), there are three plateaus in the discharge process and two plateaus in the charge process. Due to the low bond energy, plateau I and plateau II correspond to the scission between S atoms connected to the ethyl group and the S atoms in the polysulfide chain, leading to the formation of $\text{Li-SC}_2\text{H}_4\text{S-Li}$ and Li_2S_4 . Plateau III corresponds to the further reduction of Li_2S_4 to Li_2S at 2.0 V. The organic thiolate mediates the formation of Li_2S_4 at plateau IV which is followed by the reversal to the polymeric state at plateau V during the charge process. The PEHS-CNT cathode shows an initial discharge specific capacity of 774 mAh g^{-1} (889 mAh g^{-1} with respect to sulfur), and it retains 71% of the initial capacity after 350 cycles along with a Coulombic efficiency of 99.3% (Fig. 7.14d).

7.3 Cyclic Organosulfides

As an important component of organosulfides, cyclic organosulfides have also been explored for their electrochemical performance in rechargeable lithium batteries. The intermolecular cyclic polysulfide 2,3,4,6,7,8-hexathia-1,5(1,3)-dibenzenacyclooctaphane (HDBCO) was synthesized by Li et al. through the reaction of 1,3-benzenedithiol (1,3-BDT) and sulfur in a mixture of toluene/ CS_2 solvents (Fig. 7.15a) [18]. After evaporating the solvent, a green crystalline product was obtained (Fig. 7.15b). Ultrahigh performance liquid chromatography quadrupole time-of-flight mass spectrometry (UPLC-QToF-MS) was used to validate the composition of the products. UV absorption spectrum shows three peaks at retention times of 8.20, 9.35, and 12.25 min, which indicate that there were three compounds generated in the synthesis process (Fig. 7.15c). The results of the extract ion chromatogram (XIC) reveal that the UV absorption peaks at 8.20, 9.35, and 12.25 min correspond to the compounds of $\text{C}_{12}\text{H}_8\text{S}_6$, $\text{C}_{18}\text{H}_{12}\text{S}_6$, and $\text{C}_{18}\text{H}_{12}\text{S}_7$, respectively. The presumed structures are shown in the inset of Fig. 7.15c. As can be seen in the CV in Fig. 7.15d, four reduction peaks can be observed at 2.24, 2.08, 2.04, and 1.96 V during the cathodic scan. According to the speculation, the peak at 2.24 V corresponds to the lithiation of the S-S bonds in -Ph-S-S-S-Ph-, the peak at 2.08 V corresponds to the breakage of the S-S bonds in the intermediate -Ph-S-S-Li and -Ph-S-S-Ph-, the peak at 2.04 V and 1.96 V correspond to the formation of LiS-Ph-SLi and Li_2S , respectively. During the anodic scan, there are three oxidation peaks at 2.28, 2.32, and 2.34 V, which correspond to the transformation of Li_2S to sulfur radicals and the delithiation of LiS-Ph-SLi to form free radicals, and then they are combined with each other to form cyclic organosulfides. The cycling performance of the battery at 1 C rate is presented in Fig. 7.15e, the initial discharge specific capacity is 596.1 mAh g^{-1} along with a capacity retention of 63.4% after 500 cycles. The recharged cathode after the 50th and 100th cycles were examined by UPLC-QToF-MS. It can be seen that the content of HDBCO decreases over cycling (Fig. 7.15f, g), this is due

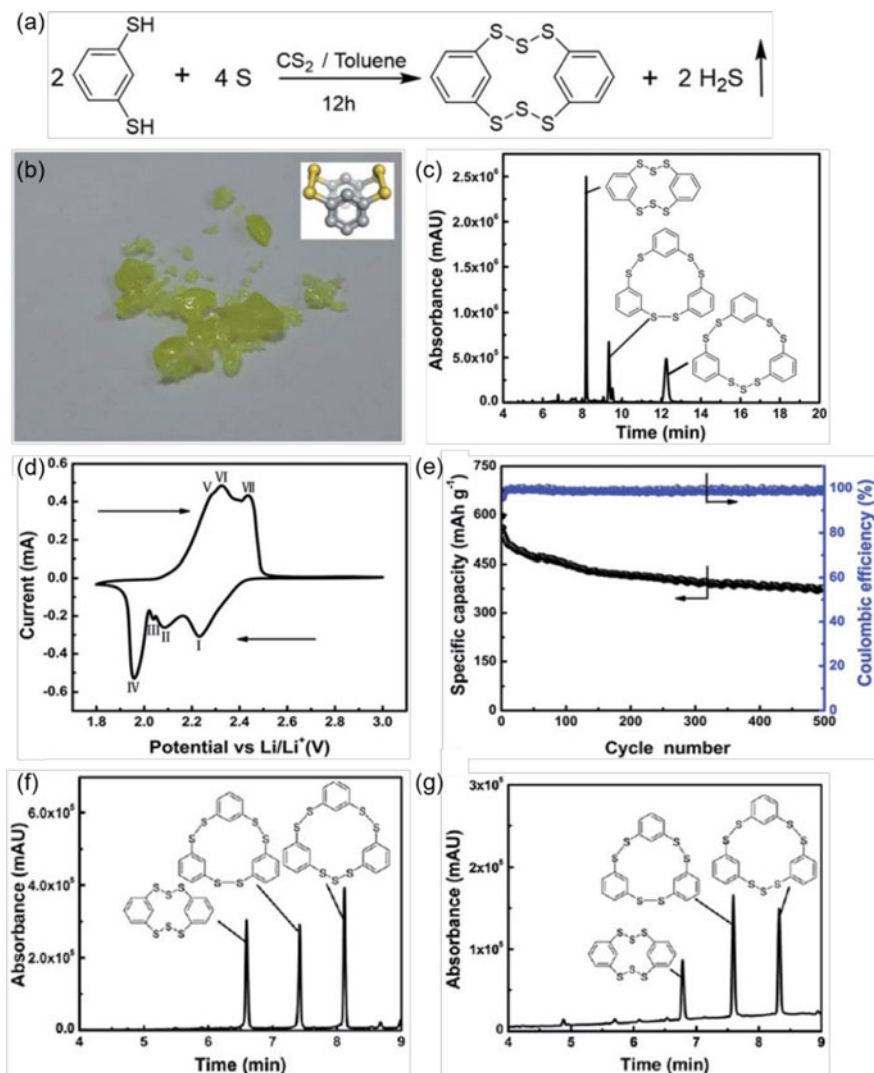


Fig. 7.15 a Reaction equation of the synthesis of 2,3,4,6,7,8-hexathia-1,5(1,3)-dibenzenacyclooctaphane (HDBCO). b Optical image of the synthesized product, the inset is the structure of HDBCO. c UV absorption of the synthesized products in UPLC-Qtof-MS. d CV plot of the cell at a scanning rate of 0.05 mV s^{-1} . e Cycling performance of the cell with mass loading of 1 mg cm^{-2} at 1 C rate. The UV absorption spectra of the recharged cathode samples in UPLC-QTof-MS after f 50th and g 100th cycle. Reproduced with permission from Ref. [18]. Copyright 2020, Royal Society of Chemistry

to the formation of insulating and insoluble Li_2S during the discharge process, which is difficult to convert S into the HDBCO structure during the recharge process.

Cyclic organosulfides can also be generated in the charged products of lithium batteries. Three lithium benzenedithiolates (LBDT) reported by Li et al. were used as catholyte in Li half cells, i.e., 1,2-LBDT, 1,3-LBDT, and 1,4-LBDT [19]. The three LBDTs were selected to study the effect of the location of the lithium thiolate on their electrochemical performance. The LBDTs were obtained by adding a piece of lithium metal in the ether-based electrolyte containing dissolved benzenedithiols (BDTs). The obtained catholytes are shown in Fig. 7.16a, the color is light yellow, yellow, and dark yellow for 1,2-, 1,3-, and 1,4-LBDT catholyte, respectively. The charge–discharge profiles of the LBDTs are shown in Fig. 7.16b, 1,3- and 1,4-LBDTs both exhibit one continuous plateau and 1,2-LBDT shows two charge plateaus during the oxidation process. During the reduction process, they all show two discharge plateaus while the first discharge voltage is in the order of 1,2-LBDT > 1,3-LBDT > 1,4-LBDT. It can be seen that there is a voltage raise in the second discharge plateau of 1,3-LBDT, which indicates the intrinsic kinetic bottleneck restricts its discharge process. UPLC-QToF-MS was used to identify the charge and discharge products of 1,2-LBDT. XIC and the corresponding MS of the peak of the charge product are shown in Fig. 7.16c, d. The retention time of the absorption peak appears at 5.598 min, the strongest intensity peak with mass/charge ratio (m/z) should be assigned to the protonated cyclic dimer. The XIC (Fig. 7.16e) and MS (Fig. 7.16f) of the discharge product are assigned to the deprotonated 1,2-BDT which corresponds to the form of 1,2-LBDT in MS analysis. Thus, the equation of the redox reaction process of 1,2-LBDT is described in Fig. 7.16g. The redox chemistry of 1,3-, and 1,4-LBDTs was explored through the same characterization techniques.

The XICs of the charged samples of 1,3-, and 1,4-LBDTs are shown in Fig. 7.17a and b. Two high-intensity peaks are found in Fig. 7.17a, which indicate the formation of two kinds of products. Further exploration shows that the structures can be assigned to cyclic trimer and tetramer. Similarly, the structure of the charged sample of 1,4-LBDT is confirmed to be a cyclic tetramer. Consequently, the redox reactions of 1,3- and 1,4-LBDTs in lithium battery are shown in Fig. 7.17c, d.

The cycling performance of the Li/LBDT cells at 0.5 C rate is shown in Fig. 7.18, the initial capacity of 1,2-LBDT is 340 mAh g^{-1} and the capacity retention is 84.1% after 100 cycles, while 1,3- and 1,4-LBDTs only show initial capacities of 182.9 and 201.9 mAh g^{-1} , respectively. After the mass loading is increased to 2.6 mg cm^{-2} , the initial capacity of 1,2-LBDT is 237.4 mAh g^{-1} , which is much higher than those of 1,3-LBDT (96.3 mAh g^{-1}) and 1,4-LBDT (120.5 mAh g^{-1}). In summary, 1,2-LBDT exhibits the best electrochemical performance among the three LBDTs.

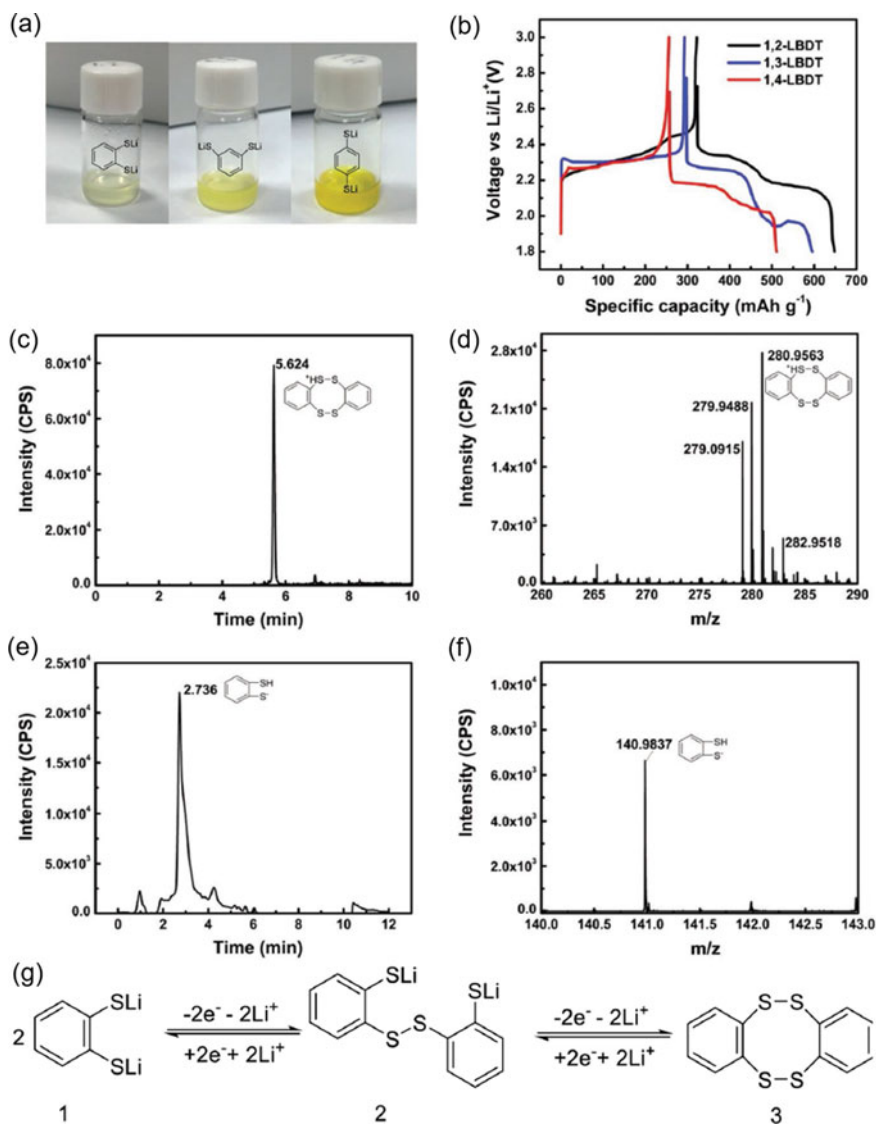


Fig. 7.16 **a** Photographs of the three LBDT catholytes. **b** Voltage profiles of the Li-LBDTs batteries at 0.1 C rate. **c** XIC of the charged product of 1,2-LBDT. **d** The MS data of the peak at 5.624 min in (c). **e** XIC of the discharged product of 1,2-LBDT. **f** Corresponding MS of the peak at 2.736 min in (e). **g** Equation reaction of 1,2-LBDT during Li-battery cycling. Reproduced with permission from Ref. [19]. Copyright 2019, Wiley-VCH

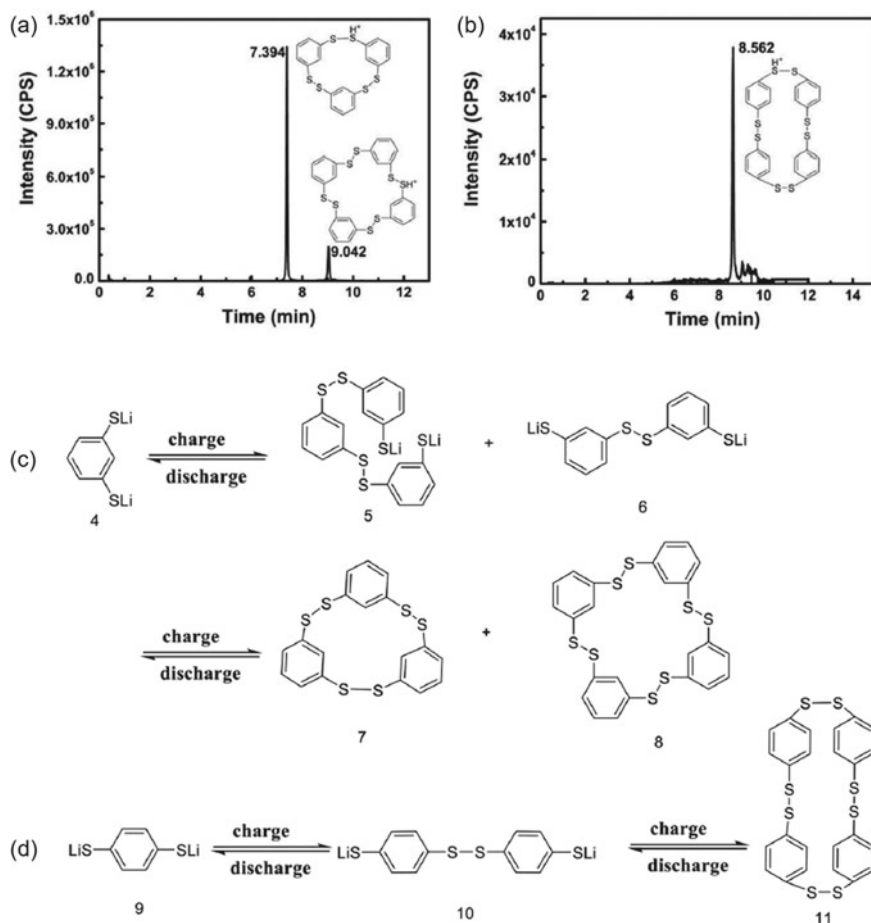


Fig. 7.17 XIC of the charged products of **a** 1,3-LBDT and **b** 1,4-LBDT. Redox reactions of **c** 1,3-LBDT and **d** 1,4-LBDT in rechargeable lithium battery. Reproduced with permission from Ref. [19]. Copyright 2019, Wiley-VCH

7.4 Oranosulfides Containing N-heterocycles

It is one of the feasible strategies to improve the battery performance of organosulfides by changing the organic functional groups. As we all know, organosulfides with electron-withdrawing groups generally have low lowest unoccupied molecular orbit (LUMO), which can deliver higher discharge voltage. Nitrogen is the most abundant element in the air. It exists widely in nature and has a great effect on living organisms. Meanwhile, the N-containing groups usually possess the electron-withdrawing capability, thus can be used to tune the electrochemical properties of organic electrode materials [20, 21].

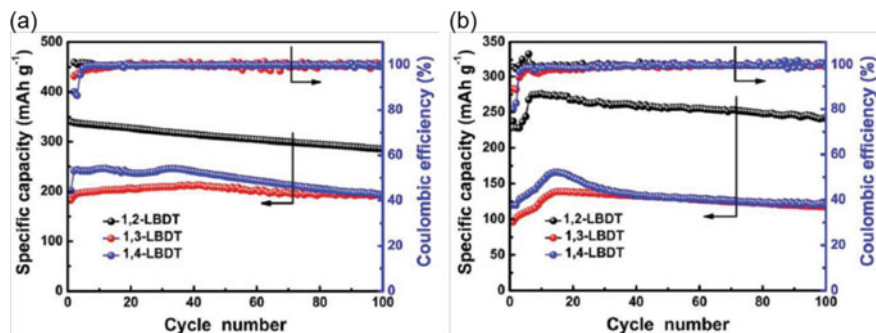


Fig. 7.18 Cycling performance of the three LBDTs with the mass loading of **a** 0.7 mg cm^{-2} and **b** 2.6 mg cm^{-2} at 0.5 C rate. Reproduced with permission from Ref. [19]. Copyright 2019, Wiley-VCH

Thiuram polysulfides containing N atoms such as dipentamethylene thiuram tetrasulfide (PMTT) and dipentamethylenethiuram hexasulfide (PMTH) are commonly used as vulcanization accelerators in the rubbery industry (Fig. 7.19a). This makes them easily available and cost-effective materials for battery application. Bhargav et al. researched their electrochemical properties in lithium batteries [22]. The structure of multiple S–S bonds endows them high theoretical specific capacities of 418 and 597 mAh g^{-1} , respectively. In addition, PMTT delivers three discharge voltage plateaus at 2.53 , 2.33 , and 2.1 V in lithium battery. The charge process shows a sloping plateau at 2.25 – 2.40 V followed by further oxidation at 2.65 V (Fig. 7.19b).

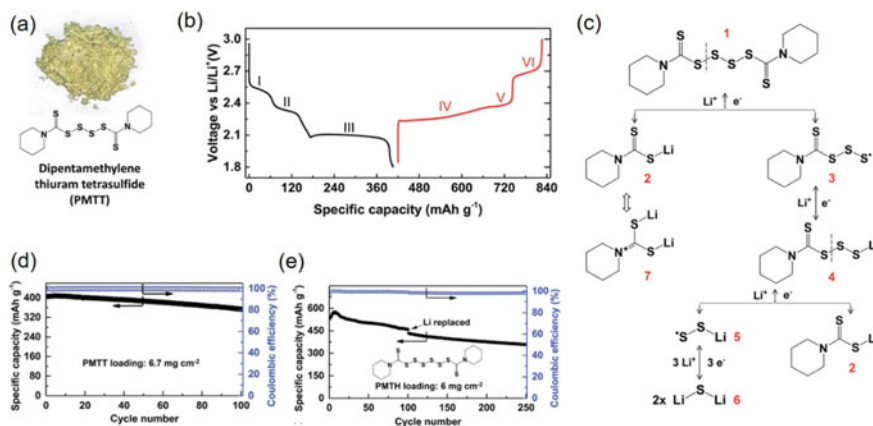


Fig. 7.19 **a** Commercial PMTT powder along with its chemical structure. **b** Voltage profile of the first cycle of PMTT at $C/5$ rate. **c** Reaction mechanism of PMTT during redox process. **d** Cycling performance of PMTT with the mass loading 6.7 mg cm^{-2} . **e** Cycling performance of PMTT with the mass loading 6 mg cm^{-2} . Reproduced with permission from Ref. [22]. Copyright 2017, Royal Society of Chemistry

The redox process is displayed in Fig. 7.19c. The marked S–S bond would break when PMTT accepts the first electron, forming LiPMDTC **2** and radical **3**. The following discharge leads to the cleavage of the marked bond in **4** and the formation of LiPMDTC **2** and lithium persulfide radical **5**. This radical upon further lithiation in the presence of excess Li^+ results in the formation of two Li_2S **6**. Importantly, LiPMDTC **2** can alternatively exist in its mesomeric form **7** ($\text{Li}_2\text{PMDTC}^+$) accompanied by N^+ center in the presence of excess Li^+ owing to the N-electron flow from nitrogen to sulfur through planar delocalized π -orbitals. PMTH also has a similar redox mechanism. The Li/PMTH cell delivers a high initial discharge specific capacity of 406 mAh g^{-1} corresponding to the 6e^- transfer process while maintaining 87% of the initial capacity after 100 cycles (Fig. 7.19d). The Li/PMTH cell can yield the first discharge capacity of 575 mAh g^{-1} and retain 85% of the initial capacity after 100 cycles (Fig. 7.19e).

To understand the effect of N-heterocycles on the electrochemical behavior of organosulfides, Wang et al. reported the research of three N-containing organodisulfide compounds including 2,2'-dipyridyl disulfide (2,2'-DpyDS), 4,4'-dipyridyl disulfide (4,4'-DpyDS), and 2,2'-dipyridyl disulfide-N,N'-dioxide (DpyDSDO) in lithium batteries (Fig. 7.20a) [23]. 2,2'-DpyDS and 4,4'-DpyDS have N atoms at ortho and para positions while DpyDSDO has strong electronegative nitro groups on the ortho position. All of them have similar theoretical specific capacities. Compared with diphenyl disulfide (DPDS), the former three compounds present high discharge voltages. The Li/2,2'-DpyDS and Li/4,4'-DpyDS cells exhibit high discharge voltage at 2.45 V, which is higher than that (2.2 V) of the Li/DPDS cell, attributing to the electron-withdrawing effect of N-heterocycles (Fig. 7.20b). In particular, DpyDSDO presents higher voltage at 2.80 V owing to the effect of stronger electron-withdrawing nitro groups (Fig. 7.20c). Meanwhile, the voltage hysteresis between discharge and recharge of the Li/2,2'-DpyDS cell is only 0.04 V which is significantly smaller than that (0.10 V) of the Li/DPDS cell, indicating the faster reaction kinetics of DpyDS. LC-MS was used to identify the discharged and charged products of these compounds. 2,2'-DpyDS is lithiated to form lithium pyridine-2-thiolate (**a** peak) in discharge (Fig. 7.20d). The recharged TIC has witnessed the m/z of 2,2'-DpyDS (**c** peak). Similarly, 4,4'-DpyDS is also converted to the lithiated pyridine-4-thiolate (**d** peak) and then back to 4,4'-DpyDS at charged state (Fig. 7.20e). Figure 7.20f also exhibits the emergence of the protonated 2-pyridinethiol N-oxide (**g** peak) and weakening of the **i** peak of DpyDSDO in the discharge process. Peak **i** becomes stronger again in the recharged chromatogram.

When these N-containing organosulfides are used as the cathode materials in lithium battery, they all deliver more stable cycling performance than DPDS (Fig. 7.21a). DPDS only displays an initial discharge capacity of 193 mAh g^{-1} and the capacity retention is only 54% after 100 cycles. DpyDS presents an initial discharge capacity of 237 mAh g^{-1} and the capacity retention is 69% after 500 cycles. The Coulombic efficiency is above 99.6% except for the first ten cycles. 4,4'-DpyDS shows an initial specific capacity of 208 mAh g^{-1} , while its capacity retention is only 57% after 100 cycles, which is just comparable with that of DPDS. DpyDSDO presents an initial specific capacity of 160 mAh g^{-1} and retains 82% of the initial

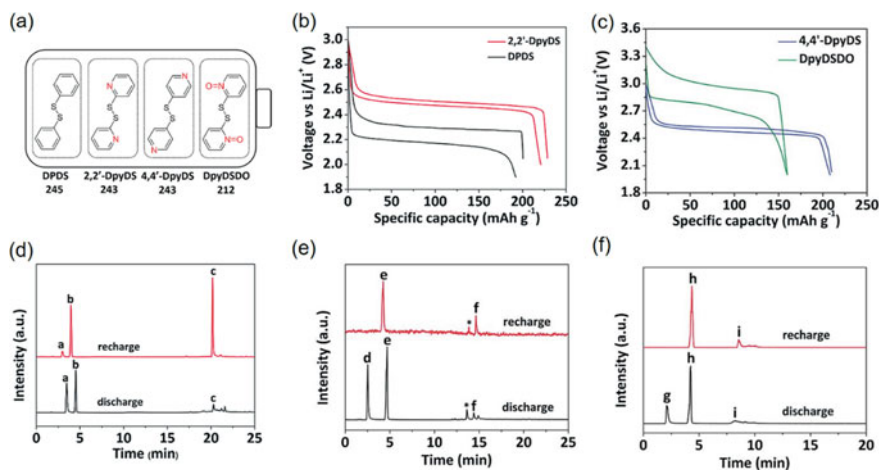


Fig. 7.20 **a** Chemical structures of diphenyl disulfide (DPDS), 2,2'-dipyridyl disulfide (2,2'-DpyDS), 4,4'-dipyridyl disulfide (4,4'-DpyDS), and 2,2'-dipyridyl disulfide-N,N'-dioxide (DpyDSDO); the values are their theoretical specific capacities in mAh g^{-1} . **b** Voltage–capacity profiles of the Li/2,2'-DpyDS and Li/DPDS cells in the first cycle at C/10 rate. **c** Voltage–capacity profile of the Li/4,4'-DpyDS and Li/DpyDSDO cells in the first cycle at C/10 rate. **d** Total ion chromatograms (TICs) of 2,2'-DpyDS electrodes after discharge and recharge: a, b, and c represent the protonated 2-pyridinethiol, LiTFSI, and 2,2'-DpyDS, respectively. **e** TICs of the 4,4'-DpyDS electrodes after discharge and recharge: d, e, f, and * represent the protonated 4-pyridinethiol, lithium salt, 4,4'-DpyDS, and impurity, respectively. **f** TICs of the DpyDSDO electrodes after discharge and recharge: g, h, and i represent the protonated 2-pyridinethiol N-oxide, lithium salt, and DpyDSDO, respectively. Reproduced with permission from Ref. [23]. Copyright 2019, Royal Society of Chemistry

capacity after 200 cycles. The charge–discharge curves of the 100th cycle are shown in Fig. 7.21b. The Li/DPDS cell shows significant capacity decay and a rise in overpotential. In contrast, the Li/DpyDS cells have no overpotential growth. However, the Li/2,2'-DpyDS cell shows better cycling stability than the Li/4,4'-DpyDS cell. To reveal the reason behind this phenomenon, DFT simulations of the stable configurations after discharge of 2,2'-DpyDS and 4,4'-DpyDS were performed as shown in Fig. 7.21c. The three atoms of $\text{N}\cdots\text{Li}\cdots\text{S}$ with weak coordination in the discharged product of 2,2'-DpyDS are tightly combined to form compact clusters. While the discharged product of 4,4'-DpyDS forms a loose structure. Thus, the compact structure is conducive to the reduced solubility in the electrolyte as confirmed by the HPLC-QToF-MS analysis, leading to the more stable cycling performance of 2,2'-DpyDS. Accordingly, the N atoms in the structure of organosulfides could lead to stable battery performance.

The theoretical capacities of the above-mentioned N-containing organosulfides are generally below 300 mAh g^{-1} , which limits the specific energy. Accordingly, similar to the linear organosulfides structure, pyridine polysulfides having multiple S–S bonds have been designed and synthesized to achieve the improvement in specific capacity by Wang et al. (Fig. 7.22) [24]. The dipyridyl disulfide (Py_2S_2) reacts with

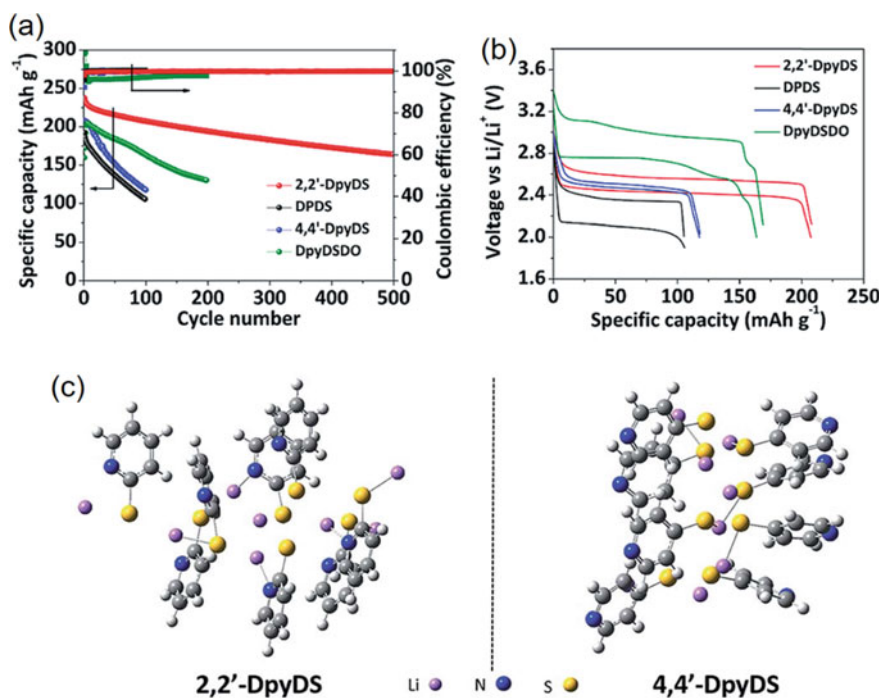


Fig. 7.21 **a** Cycling performance of the Li/2,2'-DpyDS, Li/DPDS, Li/4,4'-DpyDS, and Li/DpyDSDO cells at C/2 rate. **b** Voltage–capacity profiles of these cells in the 100th cycle. **c** Cluster structures of the discharge products of 2,2'-DpyDS and 4,4'-DpyDS. Reproduced with permission from Ref. [23]. Copyright 2019, Royal Society of Chemistry

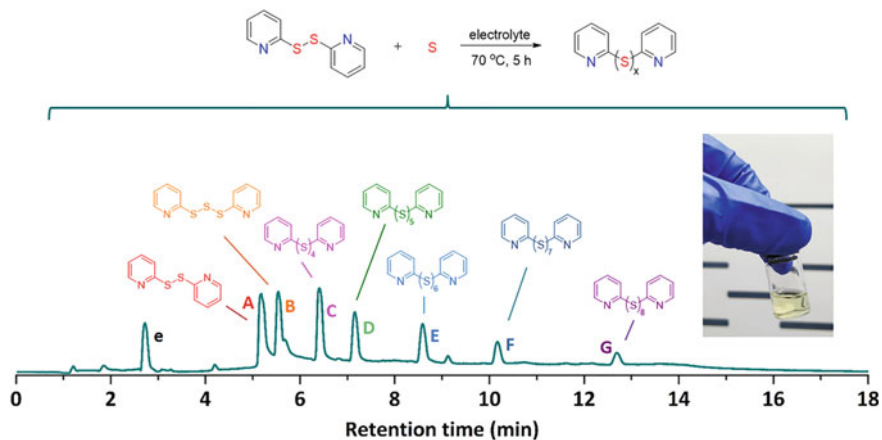


Fig. 7.22 The synthesis of a spectrum of Py_2S_x in electrolyte and TIC spectrum of the mixture catholyte; the inset is a photograph of the prepared Py_2S_x catholyte. Reproduced with permission from Ref. [24]. Copyright 2020, Wiley-VCH

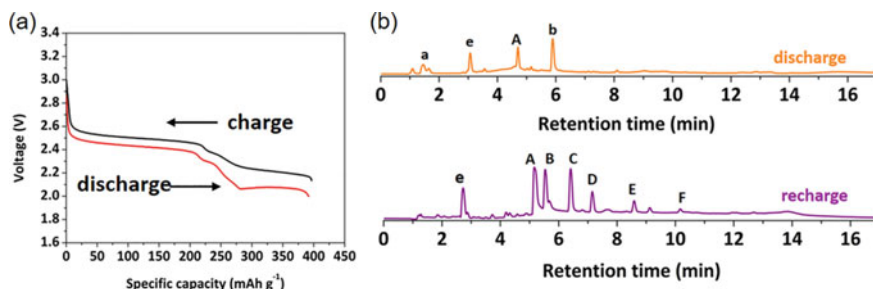


Fig. 7.23 **a** The first discharge and recharge voltage curves at $C/10$ rate. **b** TIC of the Py_2S_x electrode after discharge and recharge. Reproduced with permission from Ref. [24]. Copyright 2020, Wiley-VCH

one equiv. sulfur in the ether electrolyte at 70 °C to form dipyriddy polysulfides (Py_2S_x). Interestingly, the synthesized product contains a variety of dipyriddy polysulfides. Figure 7.22 exhibits the UPLC-QToF-MS analysis of the synthesized product, which presents the different components in corresponding retention times. The A peak represents the unreacted Py_2S_2 and B to G are Py_2S_2 to Py_2S_8 , respectively. The reaction mixture was used as a catholyte which was evaluated in Li half cells. If the average molecular structure is considered to be Py_2S_3 , its theoretical capacity is 425.4 mAh g^{-1} .

The charge–discharge voltage curves of the Li/ Py_2S_x cell are shown in (Fig. 7.23a), which exhibits the first discharge voltage plateau at 2.5 V and the following voltage plateaus at 2.3 and 2.1 V. The recharge has similar voltage plateaus with slight overpotential. The cell shows the initial specific capacity of 391.7 mAh g^{-1} , corresponding to 92.1% of its theoretical capacity. To identify the cycled products of Py_2S_x in lithium battery, UPLC-QToF-MS was employed (Fig. 7.23b). After discharge, the large amount of discharged product is the protonated 2-pyridinethiol corresponding to **a** peak. Peak **A** is the remaining incompletely reduced Py_2S_2 . Interestingly, through the analysis of **b** peak, the intermediate Py_2S_2 with two lithium atoms is confirmed, indicating the formation of facile coordination structure of $\text{N}\cdots\text{Li}\cdots\text{S}$ in the discharge process. In the recharge, dipyriddy polysulfides from Py_2S_2 to Py_2S_7 are identified, while Py_2S_8 can no longer be formed. In addition, even after 100 cycles, the recharged products still include $\text{Py}_2\text{S}_{2-5}$. This means that the formation of dipyriddy polysulfides are reversible in the electrochemical redox process in lithium battery.

Based on the above analysis, the electrochemical redox mechanism of Py_2S_x is proposed in Fig. 7.24. In the discharge process, the initial lithiation leads to the cleavage of the $\text{S}_\alpha\text{-S}_\beta$ bonds at 2.5 V. Then, the intermediate sulfur radicals are cleaved to form lithium polysulfides Li_2S_y . Due to the strong electron withdrawing of N atoms, some transiently stable intermediates can be captured by UPLC-QToF-MS. The 2-pyridinethiolate can coordinate Li_2S_x to form various cyclic complexes by $\text{N}\cdots\text{Li}\cdots\text{S}$ interactions. These conjectured structures also are verified by DFT simulations.

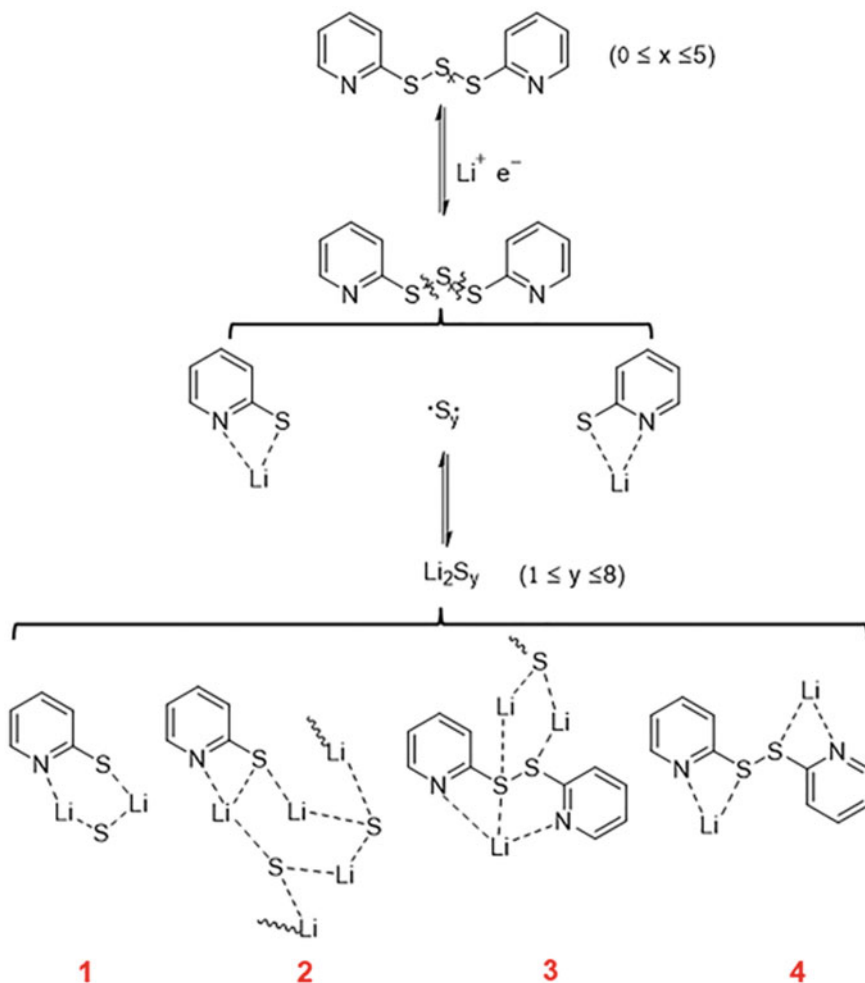


Fig. 7.24 The proposed lithiation process of Py_2S_x in lithium battery, complexes 1–4 are either simulated or detected by UPLC-QToF-MS. The dotted and solid lines represent non-covalent interactions and covalent bonds, respectively. Reproduced with permission from Ref. [24]. Copyright 2020, Wiley-VCH

The cycling performance Py_2S_x is evaluated in Li half cells at 1 C rate (Fig. 7.25a). The $\text{Li}/\text{Py}_2\text{S}_x$ cell exhibits the initial capacity of 388.4 mAh g^{-1} and remains 70.5% of the initial capacity even after 1200 cycles. Figure 7.25b shows the corresponding voltage profiles in the selected cycles. Even after 1200 cycles, this cell still has no obvious increase in overpotential. At 5 C rate, the cell still shows a stable performance of 1000 cycles (Fig. 7.25c). The study of Py_2S_x offers guidance for the development

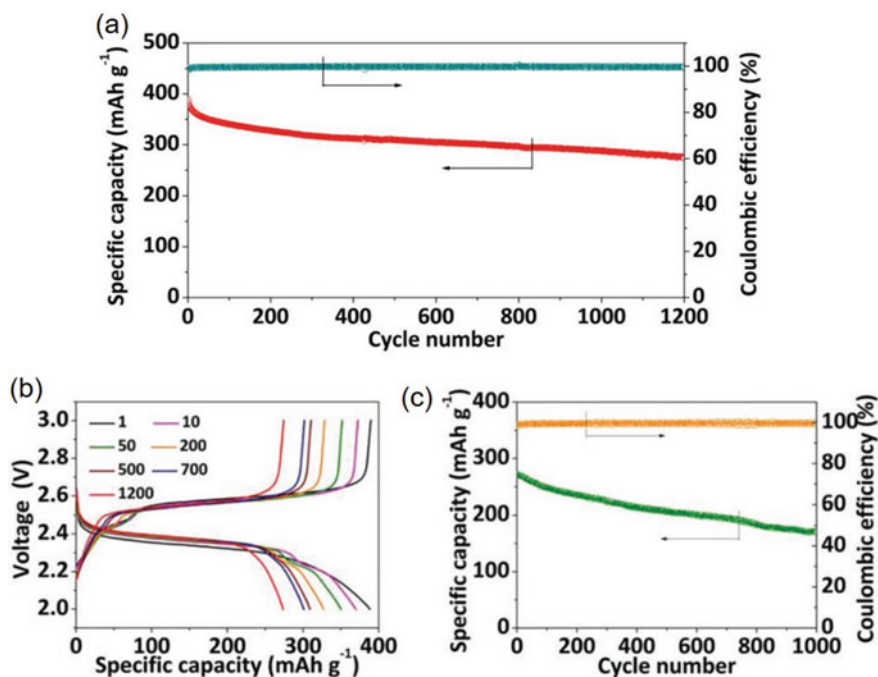


Fig. 7.25 **a** Long-term cycling performance of the Li/Py₂S_x cell at 1 C rate; **b** selected voltage–capacity profiles of the cell; **c** long-term cycling performance of the Li/Py₂S_x cell at 5 C rate. Reproduced with permission from Ref. [24]. Copyright 2020, Wiley-VCH

of high-capacity and long-cycle-life organosulfide cathode materials for rechargeable lithium batteries. Accordingly, the N-containing organosulfides have significant potential to enable superior battery performance.

7.5 Organosulfides Containing S–Se Bonds

7.5.1 Small Molecules

In addition to gravimetric capacities, volumetric and areal capacities of electrode materials are also important. Selenium (Se) has a high theoretical volumetric capacity of 3253 mAh cm⁻³, having the potential to enable dense and high energy batteries. Moreover, it has a high electronic conductivity of 1×10^{-3} S m⁻¹, which could help reduce carbon additives and improve the reaction kinetics of electrodes [25]. Therefore, introducing Se into organosulfides to form S–Se bonds is a promising strategy to enable high performance electrodes and introduce intriguing electrochemical properties of organosulfides in rechargeable lithium batteries.

A control study has been carried out by Guo et al. to compare the synthesized phenyl selenosulfide (PhS-SePh) and the two precursors of phenyl disulfide (PhS-SPh) and phenyl diselenide (PhSe-SePh) in lithium batteries (Fig. 7.26a) [26]. Although PhS-SePh possesses average LUMO and bond energy compared with PhS-SPh and PhSe-SePh, it exhibits higher onset potential of cathodic reaction (Fig. 7.26b) and higher discharge voltage plateau (Fig. 7.26c). More importantly, PhS-SePh shows much better cycling stability than the other two in lithium batteries as shown in Fig. 7.26d, e. This interesting difference reveals the potential of Se-doping in organosulfide materials, featuring mixture is better.

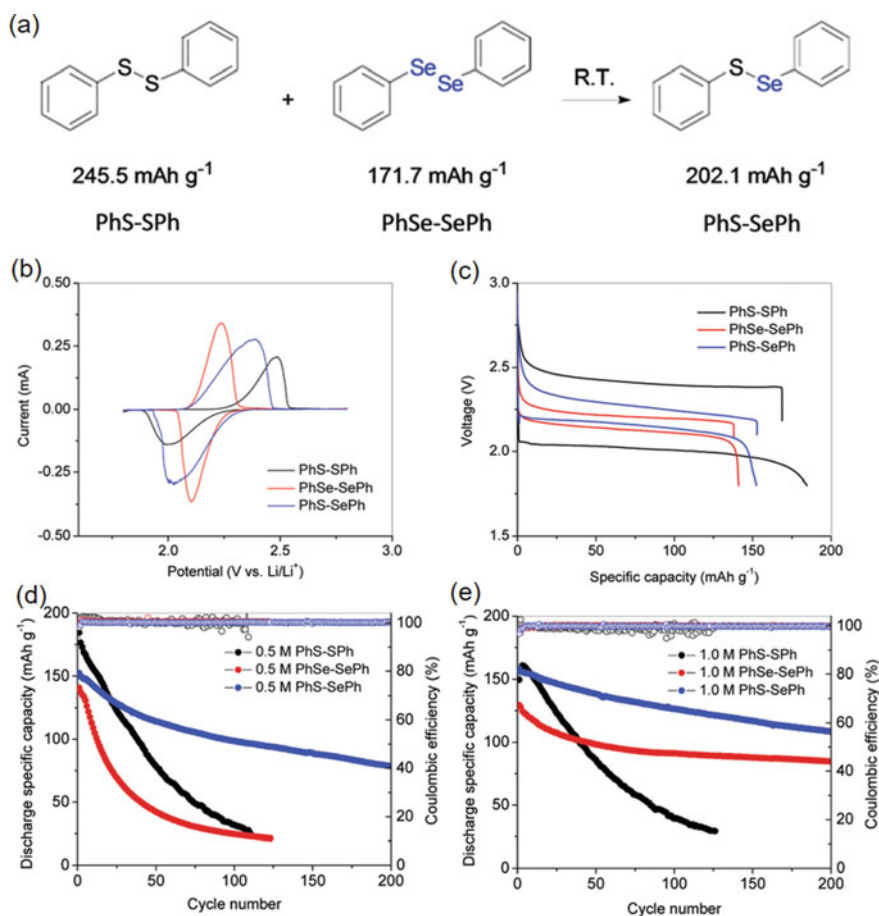


Fig. 7.26 a Reaction of phenyl disulfide (PhS-SPh) and phenyl diselenide (PhSe-SePh) to form phenyl selenosulfide (PhS-SePh) along with their specific capacities. b CVs, c voltage profiles, and d cycling performance of 0.5 M PhS-SPh, PhSe-SePh, and PhS-SePh catholytes at C/5 rate. e Cycling performance of 1.0 M catholytes of these compounds at C/5 rate. Reproduced with permission from Ref. [26]. Copyright 2018, Royal Society of Chemistry

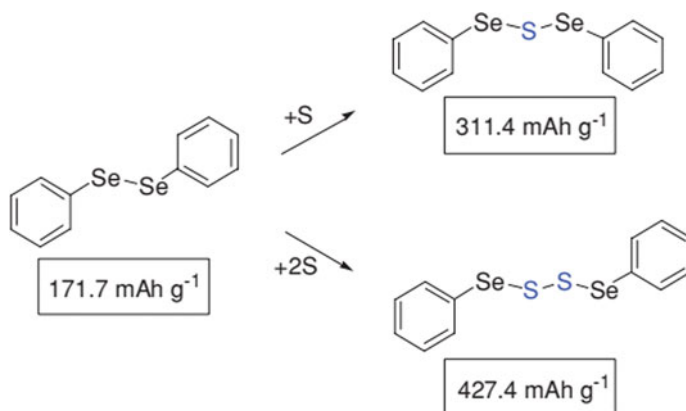


Fig. 7.27 Schematic of addition reactions of phenyl diselenide (PDSe) with one sulfur atom to form phenyl selenosulfide (PDSe-S) and phenyl selenodisulfide (PDSe-S₂). The values shown in the boxes are their theoretical specific capacities. Reproduced with permission from Ref. [27]. Copyright 2018, Wiley-VCH

In addition to organosulfides, organoselenides containing S–Se bonds also exhibit promising performance in lithium batteries. For example, Cui et al. reported that sulfur atoms can be added to the structure of phenyl diselenide (PDSe) to form phenyl selenosulfide (PDSe-S, PhSe-S-SePh) and phenyl selenodisulfide (PDSe-S₂, PhSe-SS-SePh), as shown in Fig. 7.27 [27]. The introduction of sulfur atoms can significantly increase the theoretical capacity of these compounds. For example, PDSe-S₂ has a theoretical specific capacity of 427.4 mAh g⁻¹, which is more than twice that of PDSe.

CV was performed to evaluate the electrochemical redox behavior of these compounds in lithium batteries (Fig. 7.28a). PDSe only shows one reduction peak at 2.1 V corresponding to the formation of PDSeLi, while PDSe-S and PDSe-S₂ exhibit three cathodic peaks and three discharge plateaus (Fig. 7.28b). DFT calculations were performed to understand the redox mechanism (Fig. 7.28c). For PDSe-S, the Li⁺ and e⁻ first attack the S atom leading to the cleavage of Se-S bonds at the discharge plateau of 2.4 V. Further discharge yields PhSeLi corresponding to the voltage at 2.2 V. The final discharge plateau indicates the formation process of Li₂S. For PDSe-S₂, the Li⁺ and e⁻ first attack the S atom of PDSe-S₂ resulting in the cleavage of S–S bonds and formation of PhSe-SLi molecules (Fig. 7.28d). In the following discharge, the S–Se bond in PhSe-SLi breaks leading to the formation of PhSeLi and Li₂S. The two redox processes are quite reversible, meaning the S atoms also can be inserted in the structure of PDSe in the electrochemical reactions.

The cycling performance of PDSe-S and PDSe-S₂ in lithium batteries was also studied (Fig. 7.29a). The Li/PDSe-S and Li/PDSe-S₂ cells show the initial discharge specific capacities of 252 and 330 mAh g⁻¹, respectively. They can retain 77% and 73% of the initial capacities after 200 cycles. It is believed that the formed insoluble Li₂S in the discharge of these compounds helps anchor soluble PhSeLi,

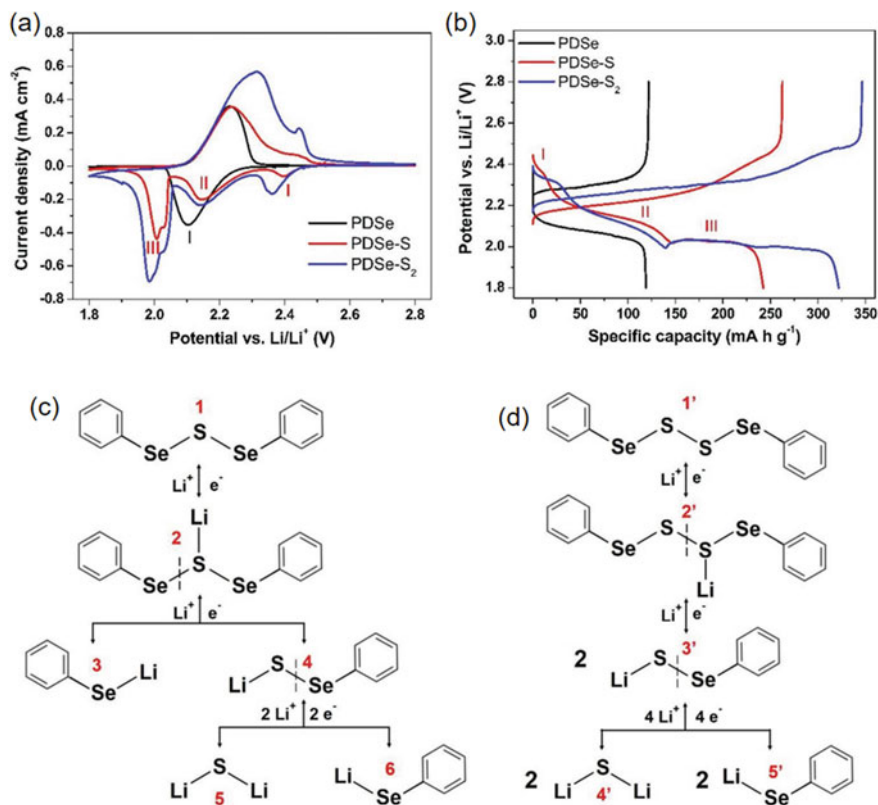


Fig. 7.28 **a** CVs and **b** voltage profiles of PDSe, PDSe-S, and PDSe-S₂. Redox reactions of **c** PDSe-S and **d** PDSe-S₂ in rechargeable lithium batteries. Reproduced with permission from Ref. [27]. Copyright 2018, Wiley-VCH

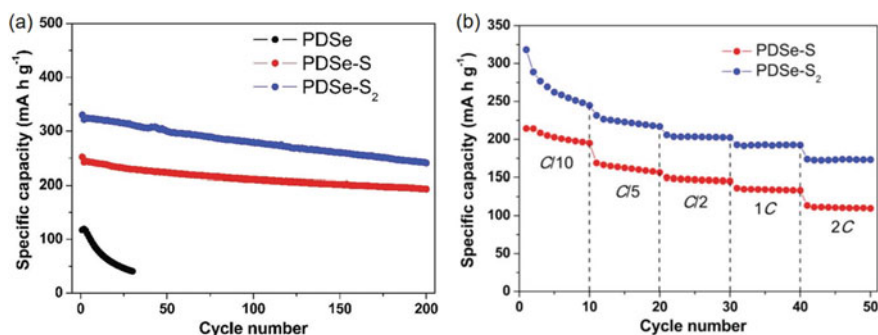


Fig. 7.29 **a** Cycling performance of PDSe, PDSe-S, and PDSe-S₂ at C/5 rate. **b** Rate performance of PDSe-S and PDSe-S₂ in rechargeable lithium batteries. Reproduced with permission from Ref. [27]. Copyright 2018, Wiley-VCH

therefore, improving cycling stability. The rate performance is shown in Fig. 7.29b. This study demonstrates that mixing S and Se atoms in the organoselenides can not only increase the specific capacity of these compounds, but also improve the cycling stability of batteries. The S–Se bonds present unique properties as redox active sites in rechargeable lithium batteries.

Previous studies reveal the crucial role of S–Se bonds in organosulfides. Therefore, it is easy to use this approach to improve the battery performance of selenium cathode in rechargeable lithium batteries. A recent study from Zhao et al. reported an organic–inorganic hybrid cathode including diphenyl trisulfide (DPTS) and the selenium nanowires (Fig. 7.30a), which shows alternative redox pathways and enhanced cycling performance [28]. Firstly, Se nanowires were mixed with CNTs to form a self-woven composite electrode (Fig. 7.30b). Then DPTS catholyte was introduced into the electrode to form DPTS–Se hybrid electrolyte. DPTS has a theoretical specific capacity of 428 mAh g^{-1} . Transmission electron microscopy (TEM) and XRD confirm the morphology and crystal structure of Se nanowires with a diameter of about 100 nm. Subsequently, the electrochemical performance of the DPTS–Se hybrid cathode in a Li half cell is evaluated and its discharge–charge voltage profile is shown in Fig. 7.30c, which exhibits the long slope at 2.3 V corresponding to the

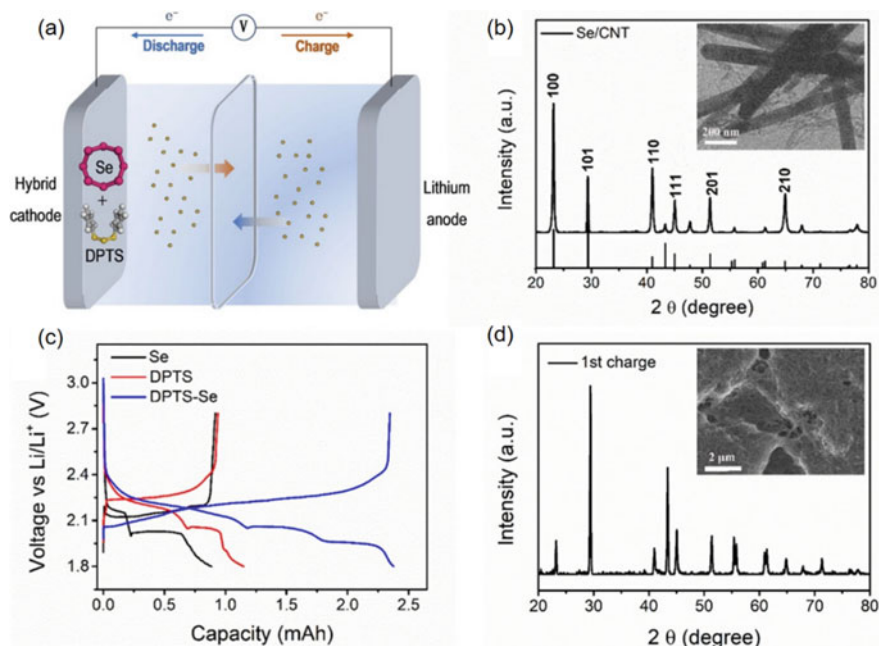


Fig. 7.30 a A lithium half cell with DPTS–Se hybrid cathode. b XRD pattern of the fresh Se/CNT composite; inset: TEM image of the composite. c The first discharge and recharge voltage profiles of Li/Se, Li/DPTS, and Li/DPTS–Se cells. d XRD pattern of the recharged DPTS–Se electrode; inset: SEM image of the electrode. Reproduced with permission from Ref. [28]. Copyright 2020, Wiley-VCH

formation of PhSSLi, PhSLi, and Li_2Se_8 . Further reduction leads to two plateaus at 2.05 and 1.95 V attributing to the formation of Li_2S and Li_2Se , respectively. Obviously, the DPTS-Se hybrid cathode shows higher initial discharge capacity than those of Se and DPTS control cathodes. In the following charge, crystalline Se is formed again, but its morphology changes significantly, as shown in Fig. 7.30d. Intimate contact between Se and CNTs is formed.

In order to understand the redox mechanism of DPTS-Se, UPLC-QToF-MS was used to characterize the charged products. Precise m/z values of these components are shown in Fig. 7.31. Interestingly, multiple new compounds are discovered, including PhSSeSPh, PhSSeSSPh, PhSSeSeSPh, and PhSSeSeSeSPh having the m/z of 298.973, 330.944, 377.317, and 458.772, respectively. This result indicates that Se atoms are continuously inserted into the molecular structure of DPTS during the charge process. It is known that lithium polyselenides are formed in the discharge-charge process of Li-Se battery, resulting in shuttle effect and short cycling life. When DPTS is present, it can capture some Se atoms altering the redox pathway of Se, inhibiting the formation of lithium polyselenides, and thus improving cycling stability of Li-Se battery.

Based on the above analysis, the redox process of DPTS-Se hybrid electrode in lithium batteries is illustrated in Fig. 7.32a. At the first discharge plateau of 2.3 V,

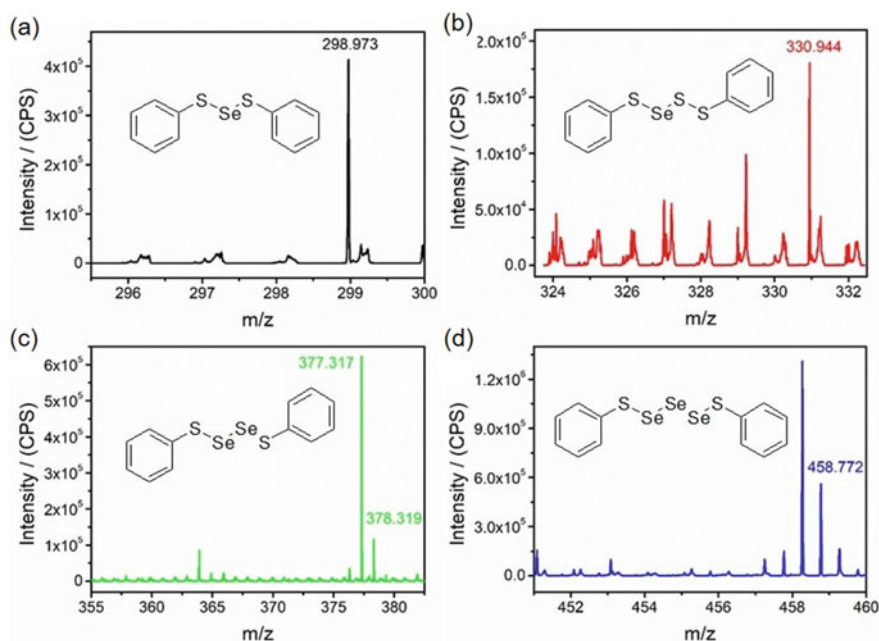


Fig. 7.31 Total ion chromatograms of a DPTS-Se electrode after charge. The mass spectra of the charged products: **a** PhSSeSPh, **b** PhSSeSSPh, **c** PhSSeSeSPh, and **d** PhSSeSeSeSPh. Reproduced with permission from Ref. [28]. Copyright 2020, Wiley-VCH

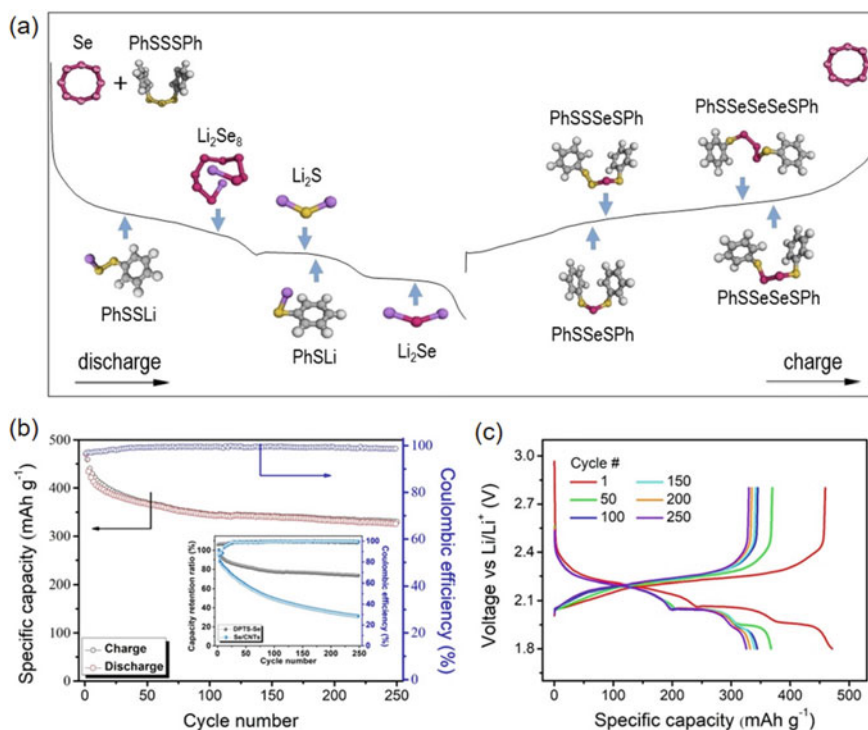


Fig. 7.32 a The redox reactions of the DPTS-Se cathode in a lithium cell. Cycling performance of the Li/DPTS-Se cell at C/10 rate; inset: cycling performance of the Li/Se cell for comparison. **b** The selected discharge and charge voltage profiles. Reproduced with permission from Ref. [28]. Copyright 2020, Wiley-VCH

the S–S bonds of DPTS firstly break to form $\text{PhSS}\cdot$ that reacts with Li^+ to yield PhSSLi . Meanwhile, the Se nanowires are transformed into Li_2Se_8 . In the following reduction steps at 2.1 and 2.0 V, PhSSLi is further lithiated to PhSLi and Li_2S . Finally, the Li_2Se_8 would be reduced to the Li_2Se . Upon the oxidation process, Li_2Se , Li_2S , and PhSLi are delithiated, which could form the $\cdot\text{Se}$ -, $\cdot\text{S}$ -, $\text{PhS}\cdot$ radicals. Then they are combined to form Se-doped organosulfides. Of course, some Se are converted to crystalline Se at the end of recharge.

The cycling performance of the Li/DPTS-Se cell is shown in Fig. 7.32b, which shows the initial capacity of 471.1 mAh g^{-1} . After 250 cycles, the DPTS-Se still can retain the capacity of 325.8 mAh g^{-1} . The capacity retention is 69.2%. In contrast, the Li/Se cell shows low capacity and poor cycling stability. The rapid capacity decay is caused by the dissolution of lithium polyselenides in electrolyte. The selected voltage profiles of the Li/DPTS-Se cell are shown in Fig. 7.32c. The plateau at 1.9 V corresponding to the formation of Li_2Se is gradually shortened, indicating that Se is continuously introduced into the structure of DPTS forming PhSSeSPH , PhSSeSeSPH , PhSSeSeSeSPH , and PhSSeSeSeSeSPH . Therefore, this strategy alters the redox pathway

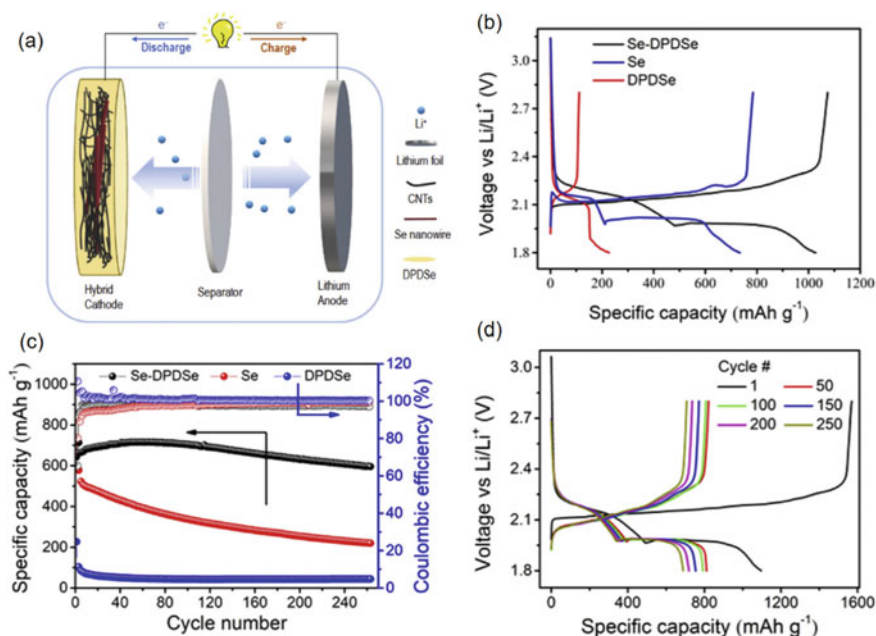


Fig. 7.33 **a** The scheme of a Li/Se-DPDSe cell. **b** Initial discharge–charge profiles of Li/DPDSe, Li/Se, and Li/Se-DPDSe cells. **c** Cycling performance of Li/DPDSe, Li/Se, and Li/Se-DPDSe cells at 0.3 C rate. **d** The charge and discharge profiles of the Li/Se-DPDSe cell at various cycles. Reproduced with permission from Ref. [29]. Copyright 2020, Elsevier

of Se in lithium battery, leading to reduced formation of lithium polyselenides and enhanced cycling stability.

Besides DPTS, Zhao et al. reported DPDSe is also effective in altering the redox pathways of Se in lithium battery (Fig. 7.33a) [29]. Similarly, the Se was prepared to nanowires and then fixed with CNTs as the composite electrode. The Li half cell is evaluated with the electrolyte containing DPDSe, which exhibits two major plateaus at 2.25 and 1.98 V with a slope between them (Fig. 7.33b). The two voltage plateaus represent the formation of lithium polyselenides and lithium phenyl selenide, respectively. The following reduction is assigned to the formation of insoluble Li₂Se. Compared to DPDSe and Se, the Se-DPDSe provides higher capacity. As shown in Fig. 7.33c, the Se-DPDSe composite cathode shows the initial capacity of 643 mAh g⁻¹ at 0.3 C rate and still retains 93.6% of the initial capacity after 250 cycles. The Li/DPDSe and Li/Se cells deliver poor battery performance due to the soluble PhSeLi and Li₂Se_x. It can be seen that the cycling performance of the Li/Se-DPDSe cell far exceeds those of the Li/DPDSe and Li/Se cells. Some selected voltage profiles are shown in Fig. 7.33d.

To investigate the redox mechanism of the Li/Se-DPDSe cell, in situ XRD was performed and the pattern of the composite electrode in the first two cycles is shown

in Fig. 7.34a. As the discharge progresses, the peak intensity of elemental selenium at 29.71° gradually decreases, indicating the transition to lithium polyselenides. During the first charge, the peak reappears at the end of the charge voltage plateau at 2.25 V. Its intensity gradually increases with charging. In the 2nd charge, this peak becomes weaker, meaning Se is continuously consumed and exists in another state in the following cycles. LC-MS was employed to verify the charged products of the cell. The TICs of the charged products are shown in Fig. 7.34b, which show two strong peaks at 6.785 and 6.770 min. The m/z values of 313.9157 and 391.8350 in the insets correspond to DPDSe and DPTSe, respectively. This result confirms the continuous conversion of Se into DPTSe leading to the disappearance of the Se peak in the XRD pattern. Accordingly, the redox process is proposed in Fig. 7.35. In the discharge process, the Se-Se bond in DPDSe is attacked by Li^+ and e^- to form PhSeLi. The

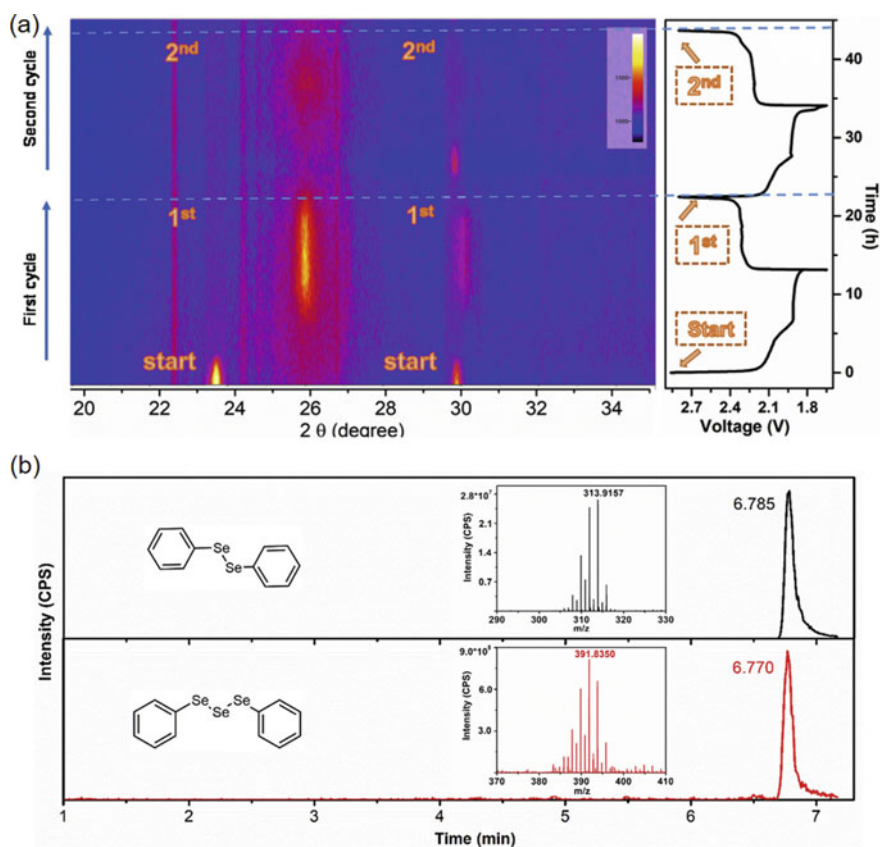


Fig. 7.34 **a** The in situ XRD pattern of the Se electrode in a Li/Se-DPDSe cell was collected during the first and second cycles at 0.1 C rate with a sampling interval of 30 min. **b** TICs of the Se-DPDSe electrode after 3 cycles at the charged state, representing the charge products of DPDSe and DPTSe, insets are corresponding MS of the peaks at 6.785 and 6.770 min. Reproduced with permission from Ref. [29]. Copyright 2020, Elsevier

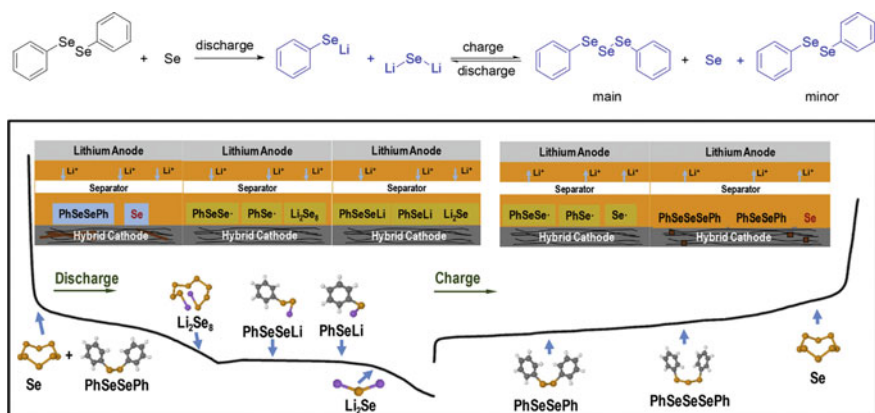


Fig. 7.35 The scheme of proposed redox reactions of the Li/Se-DPDS cell. Reproduced with permission from Ref. [29]. Copyright 2020, Elsevier

elemental Se would be lithiated to lithium polyselenides. In the recharge process, they are oxidized to PhSeSe \cdot , PhSeSe \cdot , and Se \cdot . The Se radical can insert into the structure of DPDS to form DPDS \cdot , which alleviates the formation and dissolution of lithium polyselenides, promoting the improvement of the cycling performance of the battery.

7.5.2 Polymers

The S–S bonds in the cyclic sulfur molecules can break and form sulfur radicals at 120 °C, which can react with unsaturated bonds leading to “inverse vulcanization” reported by Pyun and coworkers in 2013. Therefore, Gomez et al. reported the prepared hybrid poly(SeS-DIB) by using S powder, 1,3-diisopropenylbenzene (DIB), and element Se at 180 °C (Fig. 7.36a) [30]. Se was successfully added to the molecular structure of organosulfide polymer. In order to identify the electrochemical properties of the Se-doped polymer, CV measurement of the cells was performed. The Li/poly(S-DIB) cell shows the first cathodic peaks at 2.30–2.35 V due to the formation of high-order lithium polysulfides (Fig. 7.36b). The following second cathodic peak at 2.0 V represents the formation of low-order lithium polysulfides. While the Li/poly(Se_{0.1}S_{0.9}-DIB) cell possesses two distinguishable cathodic peaks at 2.2 and 1.9 V, corresponding to the formation of high-order Se-doped lithium polysulfides and low-order Se-doped lithium polysulfides, respectively.

Then these polymers with various Se contents are used as the cathode materials for lithium batteries. Firstly, the cells are performed at different C-rates including 0.2, 0.4, and 1 C rates (Fig. 7.37a). The cells with Se content of 2.5, 5, and 7.5 mol% have higher capacities than that of the Li/P(S-DIB) cell. Whereas the cell containing 10% Se provides a significant drop in the capacity. Figure 7.37b shows the voltage profiles

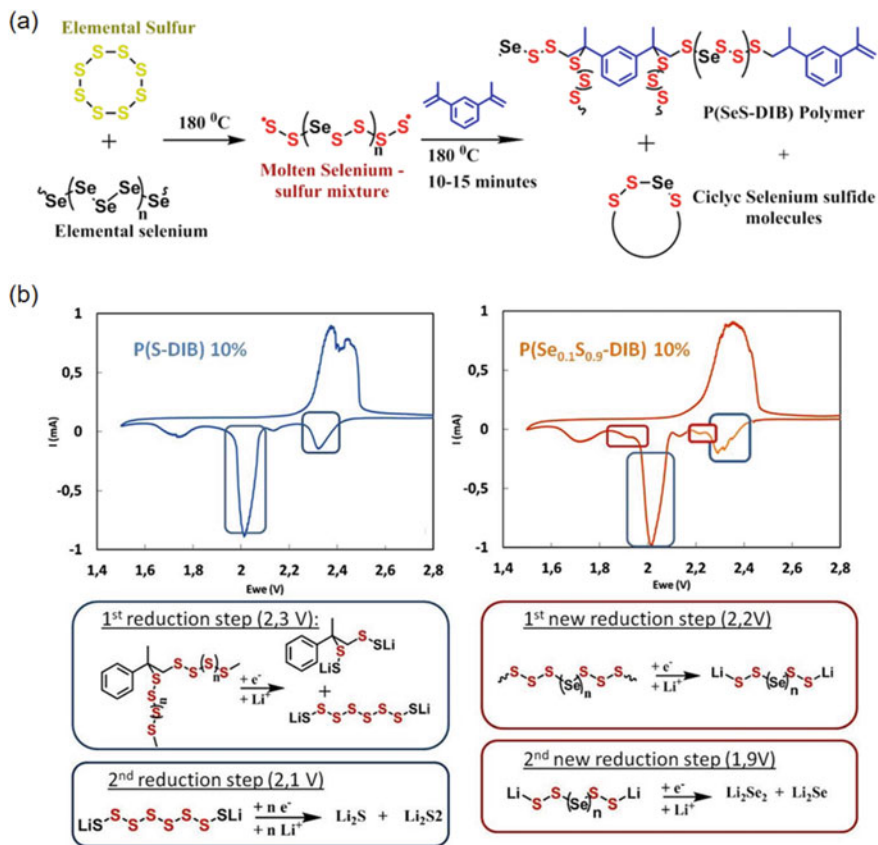


Fig. 7.36 a Schematic representation of the inverse vulcanization process of S-Se hybrids. b CVs of the Li/poly(S-DIB) 10% and Li/poly(Se_{0.1}S_{0.9}-DIB) 10% cells. The lower squares depict the schematic reduction reactions for each step. Reproduced with permission from Ref. [30]. Copyright 2018, Wiley-VCH

of the cells with Se-doped polymers at 0.2 C rate, which have two characteristic voltage plateaus corresponding to the reduction reactions of S at 2.3 and 2.05 V. However, due to the small contribution of Se, the redox activity of Se is unnoticed. Finally, the cycling performance of these polymers is shown in Fig. 7.37c. The polymers with Se contents of 5 and 7.5% possess the initial specific capacities of 860 and 880 mAh g⁻¹ at 0.2 C rate, respectively, and present the low capacity losses of 0.14 and 0.4% over 100 cycles. The cycling performance of Se-containing polymer cathodes is more superior than that without Se. Therefore, the hybrid S-Se copolymers as cathode materials possess unique advantages.

In order to improve the capacity and Coulombic efficiency, Zhou et al. reported the Se-doped poly(diallyl tetrasulfide) (PDATtSSe) with four S atoms and one Se atom in the repeating unit (Fig. 7.38a) [31]. Diallyl disulfide (DADS) and SeS₂ were used

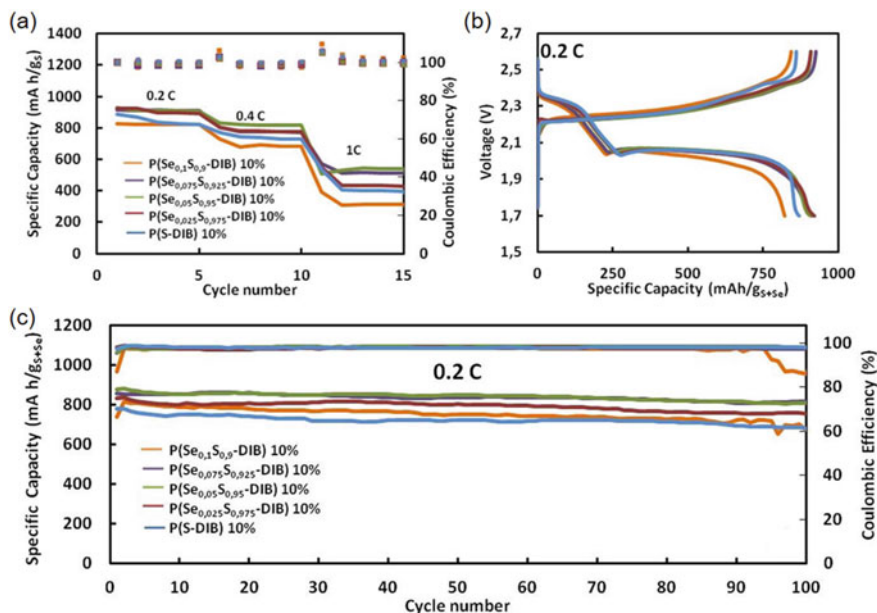


Fig. 7.37 **a** Effect of intensity current (C-units) for different poly($\text{Se}_x\text{S}_{1-x}$ -DIB) electrodes on discharge capacity and Coulombic efficiency. **b** Voltage profiles of the cells with poly($\text{Se}_x\text{S}_{1-x}$ -DIB) electrodes at C/5 rate. **c** Long-term cycling performance of the cells with P($\text{Se}_x\text{S}_{1-x}$ -DIB) polymer electrodes at C/5 rate. Reproduced with permission from Ref. [30]. Copyright 2018, Wiley-VCH

as precursors to prepare the Se-doped compound which is then polymerized to form PDATtSSe. The molecule weights containing different Se isotopes are delivered, which indicate the presence of $\text{CH}_2 = \text{CHCH}_2\text{SSeH}$ ($m/z = 182, 183, 184, 186,$ and 188). The ^1H NMR analysis also demonstrates the complete reaction of DADS and SeS_2 (Fig. 7.38b, c).

Then this polymer was used as the cathode material for lithium batteries. Firstly, the surface of the Li foil after cycles are shown in Fig. 7.39a to reveal the shuttle effect of PDATtSSe in the cathode. The smooth and uniform morphology is observed, indicating there are no high-order lithium polysulfides and polyselenides. Therefore, the shuttle effect of PDATtSSe is limited that would result in high Coulombic efficiency. The CV of the Li/PDATtSSe cell is shown in Fig. 7.39b. The two small reduction peaks at 2.25, 2.12 V and the strong peaks at 2.07, 1.98 V can be seen that are attributed to the cleavage of S–S and S–Se bonds. The followed oxidation peak at 2.3 V corresponds to the delithiation process. The voltage profile in Fig. 7.39c is consistent with the CV, showing the discharge capacity of 700 mAh g^{-1} at the current density of 200 mA g^{-1} . Meanwhile, the cell also has a high volumetric capacity of 2457 mAh cm^{-3} . The cycling performances of PDATtSSe are presented in Fig. 7.39d, which presents stable performance for 400 cycles at 600 mA g^{-1} with a high capacity retention of 92%. Accordingly, the PDATtSSe containing S–Se bonds shows improved performance.

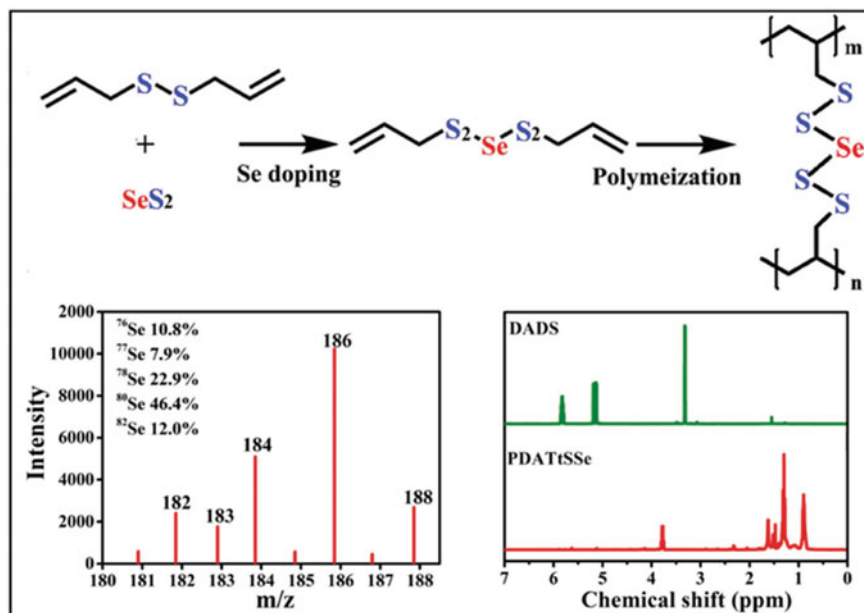


Fig. 7.38 a The synthetic mechanism of Se-doped PDATsSe polymer as cathode for lithium batteries, where m and n indicate the degree of polymerization. b The presence of molecule $\text{CH}_2\text{CHCH}_2\text{SSeH}$ ($m/z = 182, 183, 184, 186,$ and 188) was confirmed according to the abundance of Se isotopes. c ^1H NMR full spectra of the DADS monomer (green line) and PDATsSe polymer (red line). Reproduced with permission from Ref. [31]. Copyright 2017, Wiley-VCH

Se-doping has also been applied in sulfurized polyacrylonitrile. Chen et al. researched Se_xS and PAN with different ratios are heated at $300\text{ }^\circ\text{C}$ to prepare the composites Se_xSPAN ($x = 0.06, 0.09, 0.14$), which possess unique electrochemical properties and improved cycling performance in ether electrolytes [32]. The $\text{Se}_{0.06}\text{SPAN}$ containing a catalytic amount of Se is used as cathode material in ether electrolyte. The cycling performance of $\text{Se}_{0.06}\text{SPAN}$ is better than that of SPAN reported in the literature. The capacity of 1156 mAh g^{-1} based on the mass of S and Se in the composite is obtained in the 2nd cycle (Fig. 7.40a). Importantly, the 800 cycles with 0.029% loss per cycle hit the record in the reports on ether-based electrolyte. In addition, the cell can also deliver the specific capacity of 546 mAh g^{-1} based on the mass of the composite in the 2nd cycle and still retain 416 mAh g^{-1} even after 800 cycles. Because of the high conductivity of Se, it plays the role of a rate accelerator and capacity contributor in the SPAN polymeric framework. The Li^+ diffusion coefficients (D_{Li^+}) are calculated and shown in Fig. 7.40b. The D_{Li^+} for the reduction and oxidation peaks of the Li/SeSPAN cell are both higher than those of the Li/SPAN cell, indicating the advantage of Se-doping. In addition, the Li/SeSPAN cell has a smaller polarization voltage of 0.42 V than the 0.6 V of the Li/SPAN cell (Fig. 7.40c). The reasons behind these results are shown in Fig. 7.41, the Li/SPAN cell has a slow reaction process accompanied by the formation of lithium polysulfides.

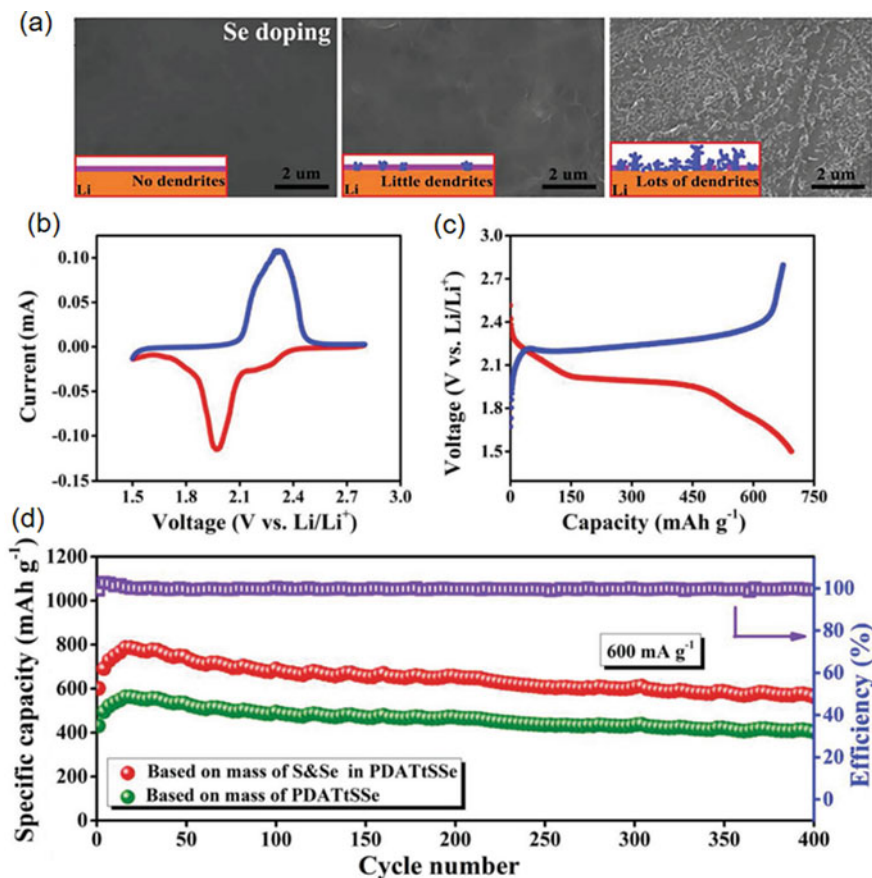


Fig. 7.39 **a** SEM images of the lithium anode surface of the Li/PDATtSSe, Li/PDAPtS, and Li/S cells with an electrolyte without LiNO_3 cycled at the current density of 600 mA g^{-1} after 100 cycles. **b** CV of the Li/PDATtSSe cell at a scan rate of 0.01 mV s^{-1} . **c** Voltage profile of the Li/PDATtSSe cell at a current density of 200 mA g^{-1} . **d** The cycling performance of the Li/PDATtSSe cell at a current density of 600 mA g^{-1} , the capacities are either based on the mass of PDATtSSe or the mass of S and Se in PDATtSSe. Reproduced with permission from Ref. [31]. Copyright 2017, Wiley-VCH

In contrast, the catalytic amount Se can enhance the redox conversion of polysulfides and reaction kinetics, thus leading to excellent electrochemical performance in ether-based electrolyte.

In addition to the above-mentioned preparation methods of Se-containing polymers, strategies of organic synthetic chemistry were also utilized to design and prepare short chain polyselenosulfide copolymers, which was reported by Park et al. (Fig. 7.42) [33]. This polymer was synthesized through the substitution ($\text{S}_{\text{N}}2$) reaction using the sodium poly(seleno)sulfide and 1,2,3-trichloropropane (TCP). In this reaction, the highly nucleophilic polysulfide anions S_n^{2-} would attack the $\alpha\text{-C}$ ($\text{C}_{\alpha}\text{-Cl}$)

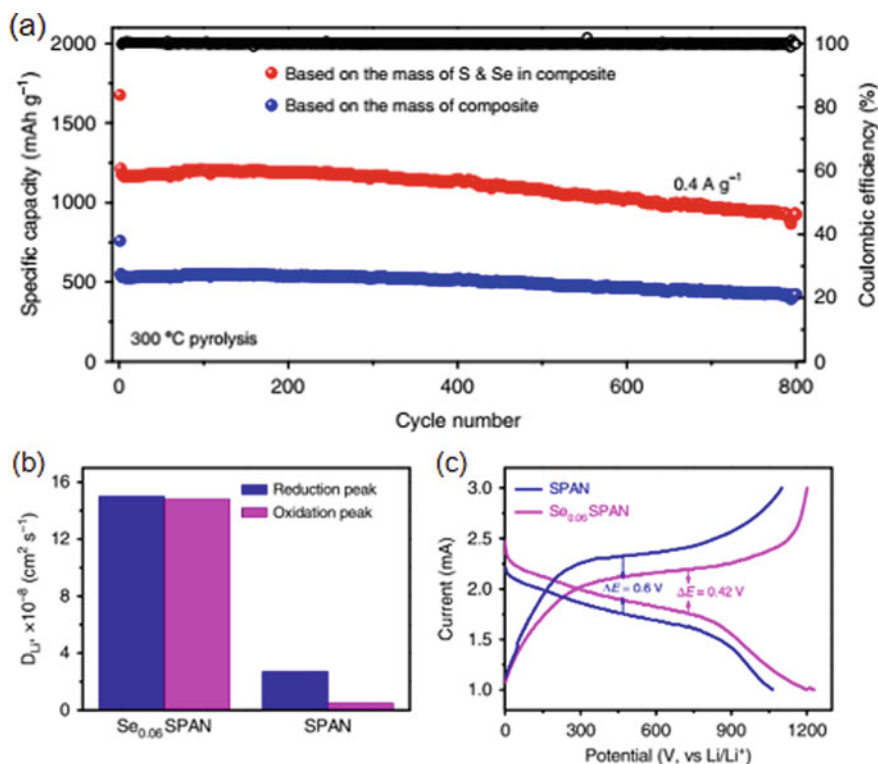


Fig. 7.40 **a** Cycling performance of the Li/Se_{0.06}SPAN cell. The red curve is relative to the weight of the S and Se in the composite, whereas the data represented by the blue curve are the corresponding capacities based on the overall composite mass. **b** Improved electrochemical reaction kinetics, Li⁺ diffusion coefficients of reduction peaks of Se_{0.06}SPAN and SPAN cathodes. **c** Discharge–charge voltage curves of the Li/SPAN and Li/Se_{0.06}SPAN cells. Reproduced with permission from Ref. [32]. Copyright 2019, Nature Publishing Group

of TCP at 60 °C to form the covalent C-S bonds, which have the highly cross-linked network structures and the theoretical capacity of the synthesized polymer is 1033 mAh g⁻¹. Additionally, the sodium polysulfides were modified by inserting Se atoms. Through the substitution reaction and polymerization, PTSeS nanoparticles were prepared.

Then the battery performances of these polymers were performed. As shown in Fig. 7.43a, the PTSeS and PTS deliver the obvious discharge plateaus at 2.4–2.1 V, showing the specific capacities of 701 and 755 mAh g⁻¹, respectively. In the CV of the Li/PTSeS and Li/PTS cells (Fig. 7.43b, c), the first reduction peak at 2.18–2.32 V represents the lithiation of middle S and Se. The following reduction steps at 1.8–2.18 V are attributed to the complete lithiation of S and Se to form Li₂S/Li₂Se. Figure 7.43d presents the cycling performance of the Li/PTSeS and Li/PTS cells at 0.5 C rate. The Li/PTSeS cell delivers the initial capacity of 635.6 mAh g⁻¹ and 387.2

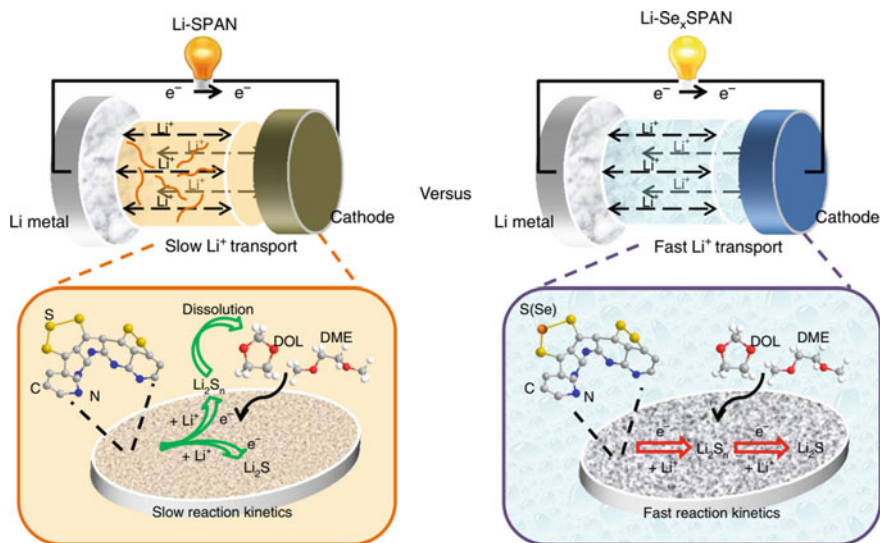


Fig. 7.41 The scheme of the proposed reaction process. Small amount of Se-doping significantly enhances the redox conversion of polysulfides and reaction kinetics, leading to ether compatibility and superior performance of Li/Se_{0.06}SPAN battery. Reproduced with permission from Ref. [32]. Copyright 2019, Nature Publishing Group

mAh g⁻¹ after 500 cycles, which are higher than those of PTS. In summary, the Se-doping with high conductivity could significantly improve the battery performance of organosulfides such as cycling stability, active material utilization, and rate capability.

7.6 Summary and Outlooks

Organosulfide is a kind of potential cathode material. In particular, organic functional groups have proven to have a profound impact on the properties and performance of these materials. In recent years, organosulfides with different structures and functional groups have been studied in lithium batteries. Although some progress on organosulfides has been made in recent years, there is still a long way to go before practicality. Future research should be focused on the following aspects (Fig. 7.44): (1) Capacity: improve the theoretical capacity of organosulfides by increasing the content of active sulfur in the molecular structure. (2) Output voltage: increase the discharge voltage by introducing electron-withdrawing heterocycles or regulating functional groups. (3) Tap density: the tap density of organosulfide should be lower than that of inorganic materials, which could be increased by the coordination of organosulfide with metal ions. (4) Shuttle effect: suppress the shuttle effect of organosulfides by using metal oxides or sulfides to adsorb the discharge products

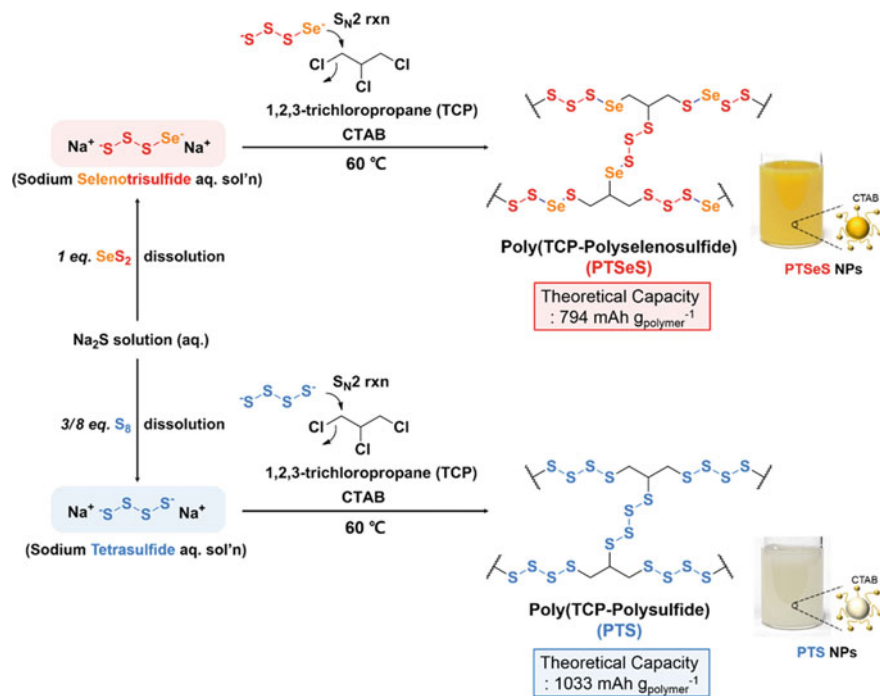


Fig. 7.42 Scheme for the preparation of aqueous sodium poly(seleno)sulfide precursor solution (Na_2S_4 and Na_2SeS_3) and following synthesis of PTSeS and PTS polymer nanoparticles via $\text{S}_\text{N}2$ -based polycondensation with 1,2,3-trichloropropane (TCP). Reproduced with permission from Ref. [33]. Copyright 2019, American Chemical Society

of organosulfides or using solid electrolytes. (5) Electrolyte additive: use organosulfides as electrolyte additives to improve battery performance of Li-S batteries. (6) Conductivity: use conductive materials such as graphene and carbon nanotubes in organosulfide electrodes. (7) Application: explore the application of organosulfides in other metal (e.g., Na, K, Mg, or Zn) batteries and flow battery systems. (8) Mechanism: investigate the redox mechanism of organosulfides through advanced characterization techniques and theoretical calculations. In summary, organosulfides are a class of promising electrode materials with high energy density. More in-depth and systematic research will promote the revival of organosulfides in several aspects of the battery fields.

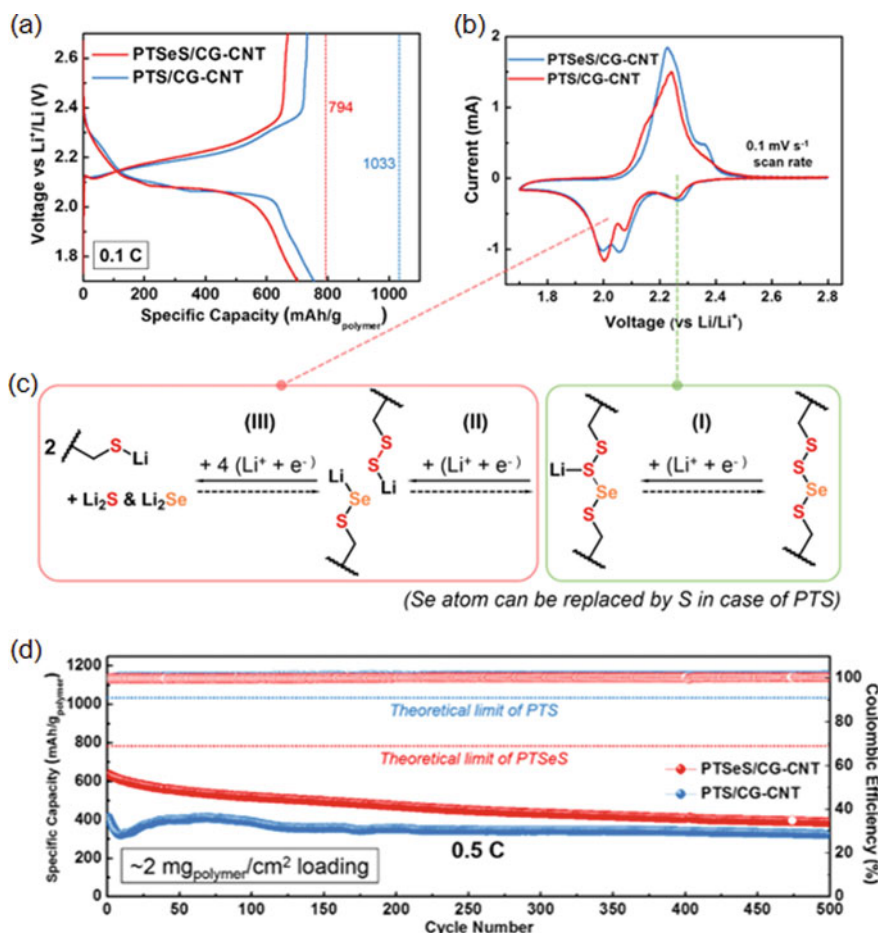


Fig. 7.43 **a** Galvanostatic charge/discharge voltage curves with the current density of C/10 rate in the voltage range of 1.7–2.7 V. **b** CV plots in the 2nd cycle at a scan rate of 0.1 mV s⁻¹ in the voltage range of 1.7–2.7 V and **c** the corresponding proposed electrochemical reaction mechanism of PTSeS and PTS in lithium battery. **d** Cycling performances of PTSeS/CG-CNT and PTS/CG-CNT in lithium batteries with high mass loading of ~2 mg cm⁻² at 0.5 C rate. Reproduced with permission from Ref. [33]. Copyright 2019, American Chemical Society

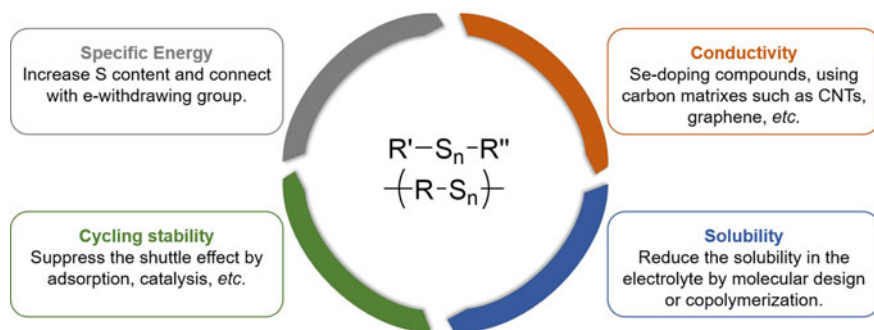


Fig. 7.44 Strategies to improve the performance of organosulfide cathode materials

Acknowledgements This work was supported by the National Natural Science Foundation of China (Grant Nos. 21975225, U2004214, and 51902293).

References

1. Wang D-Y, Guo W, Fu Y (2019) Organosulfides: an emerging class of cathode materials for rechargeable lithium batteries. *Acc Chem Res* 52:2290–2300
2. Liang Y, Tao Z, Chen J (2012) Organic electrode materials for rechargeable lithium batteries. *Adv Energy Mater* 2:742–769
3. Visco SJ, DeJonghe LC (1988) Ionic conductivity of organosulfur melts for advanced storage electrodes. *J Electrochem Soc* 135:2905–2909
4. Liu M, Visco SJ, Jonghe LCD (1989) Electrochemical properties of organic disulfide thiolate redox couples. *J Electrochem Soc* 136:2570–2575
5. Guo W, Fu Y (2018) A perspective on energy densities of rechargeable Li-S batteries and alternative sulfur-based cathode materials. *Energy Environ Mater* 1:20–27
6. Wu M, Cui Y, Bhargava A, Losovyj Y, Siegel A, Agarwal M, Ma Y, Fu Y (2016) Organotrисульфид: a high capacity cathode material for rechargeable lithium batteries. *Angew Chem Int Ed* 55:10027–10031
7. Wu M, Bhargava A, Cui Y, Siegel A, Agarwal M, Ma Y, Fu Y (2016) Highly reversible diphenyl trisulfide catholyte for rechargeable lithium batteries. *ACS Energy Lett* 1:1221–1226
8. Guo W, Wawrzyniakowski ZD, Cerda MM, Bhargava A, Pluth MD, Ma Y, Fu Y (2017) Bis(aryl) tetrasulfides as cathode materials for rechargeable lithium batteries. *Chem Eur J* 23:16941–16947
9. Bhargava A, Bell ME, Karty J, Cui Y, Fu Y (2018) A class of organopolysulfides as liquid cathode materials for high-energy-density lithium batteries. *ACS Appl Mater Interfaces* 10:21084–21090
10. Fan Q, Guo W, Si Y, Wang X, Wang B, Fu Y (2020) Inorganic mediator toward organosulfide active material: anchoring and electrocatalysis. *Adv Funct Mater* 2001493
11. Bhargava A, Patil SV, Fu Y (2017) A phenyl disulfide@CNT composite cathode for rechargeable lithium batteries. *Sustain Energy Fuels* 1:1007–1012
12. Bhargava A, Manthiram A (2020) Xanthogen polysulfides as a new class of electrode material for rechargeable batteries. *Adv Energy Mater* 10:2001658
13. Hu P, He X, Ng MF, Ye J, Zhao C, Wang S, Tan K, Chaturvedi A, Jiang H, Kloc C, Hu W, Long Y (2019) Trisulfide-bond acenes for organic batteries. *Angew Chem Int Ed* 58:13513–13521

14. Liu J, Wang M, Na X, Qian T, Yan C (2018) Progress and perspective of organosulfur polymers as cathode materials for advanced lithium-sulfur batteries. *Energy Storage Mater* 15:53–64
15. Bhargav A, Bell ME, Cui Y, Fu Y (2018) Polyphenylene tetrasulfide as an inherently flexible cathode material for rechargeable lithium batteries. *ACS Appl Energy Mater* 1:5859–5864
16. Sang P, Si Y, Fu Y (2019) Polyphenyl polysulfide: a new polymer cathode material for Li-S batteries. *Chem Commun* 55:4857–4860
17. Bhargav A, Chang CH, Fu Y, Manthiram A (2019) Rationally designed high-sulfur-content polymeric cathode material for lithium-sulfur batteries. *ACS Appl Mater Interfaces* 11:6136–6142
18. Li F, Si Y, Li Z, Guo W, Fu Y (2020) Intermolecular cyclic polysulfides as cathode materials for rechargeable lithium batteries. *J Mater Chem A* 8:87–90
19. Li F, Si Y, Liu B, Li Z, Fu Y (2019) Lithium benzenedithiolate catholytes for rechargeable lithium batteries. *Adv Funct Mater* 29:1902223
20. NuLi Y, Guo Z, Liu H, Yang J (2007) A new class of cathode materials for rechargeable magnesium batteries: organosulfur compounds based on sulfur–sulfur bonds. *Electrochem Commun* 9:1913–1917
21. Rodríguez-Calero GG, Conte S, Lowe MA, Gao J, Kiya Y, Henderson JC, Abruña HD (2015) Synthesis and characterization of poly-3,4-ethylenedioxythiophene/2,5-dimercapto-1,3,4-thiadiazole (PEDOT-DMcT) hybrids. *Electrochim Acta* 167:55–60
22. Bhargav A, Ma Y, Shashikala K, Cui Y, Losovyj Y, Fu Y (2017) The unique chemistry of thiuram polysulfides enables energy dense lithium batteries. *J Mater Chem A* 5:25005–25013
23. Wang D-Y, Si Y, Li J, Fu Y (2019) Tuning the electrochemical behavior of organodisulfides in rechargeable lithium batteries using N-containing heterocycles. *J Mater Chem A* 7:7423–7429
24. Wang DY, Si Y, Guo W, Fu Y (2020) Long cycle life organic polysulfide catholyte for rechargeable lithium batteries. *Adv Sci* 7:1902646
25. Guo W, Fu Y (2020) Electrochemistry of electrode materials containing S-Se bonds for rechargeable batteries. *Chem Eur J* 26:13322–13331
26. Guo W, Bhargav A, Ackerson JD, Cui Y, Ma Y, Fu Y (2018) Mixture is better: enhanced electrochemical performance of phenyl selenosulfide in rechargeable lithium batteries. *Chem Commun* 54:8873–8876
27. Cui Y, Ackerson JD, Ma Y, Bhargav A, Karty JA, Guo W, Zhu L, Fu Y (2018) Phenyl selenosulfides as cathode materials for rechargeable lithium batteries. *Adv Funct Mater* 28:1801791
28. Zhao J, Si Y, Han Z, Li J, Guo W, Fu Y (2020) An organic-inorganic hybrid cathode based on S-Se dynamic covalent bonds. *Angew Chem Int Ed* 59:2654–2658
29. Zhao J, Guo W, Fu Y (2020) Performance enhancement of Li–Se batteries by manipulating redox reactions pathway. *Mater Today Energy* 17:100442
30. Gomez I, Mantione D, Leonet O, Blazquez JA, Mecerreyes D (2018) Hybrid sulfur–selenium co-polymers as cathodic materials for lithium batteries. *ChemElectroChem* 5:260–265
31. Zhou J, Qian T, Xu N, Wang M, Ni X, Liu X, Shen X, Yan C (2017) Selenium-doped cathodes for lithium-organosulfur batteries with greatly improved volumetric capacity and coulombic efficiency. *Adv Mater* 29:1701294
32. Chen X, Peng L, Wang L, Yang J, Hao Z, Xiang J, Yuan K, Huang Y, Shan B, Yuan L, Xie J (2019) Ether-compatible sulfurized polyacrylonitrile cathode with excellent performance enabled by fast kinetics via selenium doping. *Nat Commun* 10:1021
33. Park S, Kim SJ, Sung YE, Char K, Son JG (2019) Short-Chain Polyselenosulfide copolymers as cathode materials for lithium-sulfur batteries. *ACS Appl Mater Interfaces* 11:45785–45795

Chapter 8

Sulfur-Containing Polymer Cathode Materials for Li–S Batteries



Yizhou Wang, Dong Zhou, and Guoxiu Wang

Abstract Due to high energy density and low cost of sulfur, lithium-sulfur batteries are of great promise to substitute for lithium-ion batteries in a variety of applications, ranging from electric vehicles to portable electronics. Unfortunately, while providing many advantages, sulfur also has several fatal problems, including poor electronic conductivity, huge volume variation upon charge/discharge, and shuttle effect of polysulfides. Utilizing sulfur-containing polymers rather than elemental sulfur as cathode materials for lithium-sulfur batteries received tremendous attention in recent years. Sulfur species are confined in sulfur-containing polymers via covalent bonds, which can greatly alleviate the shuttle effect and thus render lithium-sulfur batteries improved discharge capacity, enhanced rate capability, and high cycling stability. In this chapter, a comprehensive review on the recent development of sulfur-containing polymer cathodes is provided. Different electrochemical behaviors and different molecular structures of sulfur-containing polymer cathode materials are systematically summarized. Furthermore, the optimization strategies for sulfur-containing polymer cathodes are discussed in detail. Finally, the remaining problems and future prospects for sulfur-containing polymer cathodes are outlined.

Keywords Lithium-sulfur batteries · Sulfur-containing polymer cathodes · Polymeric sulfur · Shuttle effect

8.1 Introduction

As mentioned in above chapters, lithium-sulfur (Li–S) batteries using sulfur as cathode materials possess many merits (e.g., low cost, low toxicity, and high capacity), and received widespread attention in the recent decade. However, Li–S batteries have not achieved widespread applications yet due to huge intrinsic problems [1]. Most of these problems occur in the cathode of Li–S batteries. Specifically, (1) sulfur possesses extremely low electronic conductivity (5×10^{-30} S cm⁻¹); (2)

Y. Wang · D. Zhou · G. Wang (✉)

School of Mathematical and Physical Sciences, Research Centre for Clean Energy Technology,
University of Technology Sydney, Ultimo, Australia
e-mail: guoxiu.wang@uts.edu.au

sulfur experiences huge volume change (*ca.* 80%) while reducing to Li_2S during discharge; (3) the charge/discharge intermediates, Li polysulfides, are readily to dissolve in the electrolyte and shuttle to the anode side under electric field effect, which leads to the corrosion of Li metal anode and irreversible loss of battery capacity [2]. The above problems would deteriorate the electrochemical performances of Li–S batteries from various aspects, including battery capacity less than expected, high self-discharge, and rapid capacity decay [3]. Therefore, near half of the research on Li–S batteries is focused on the cathode materials in order to solve these problems. Commonly used modification methods for Li–S battery cathode materials include applying carbonaceous materials to encapsulate sulfur [4], using electrocatalysts to boost sulfur's redox kinetics [5], replacing elemental sulfur with Li_2S or Li polysulfides [6], and confining sulfur into organic molecules by covalent bonds. Among these strategies, confining sulfur into organic molecules by chemical bonds to form sulfur-containing polymer as cathode material is a promising strategy to boost the performances of Li–S batteries, since sulfur-containing polymer possess various advantages while being used as cathode material [7]. The formed covalent bonds between sulfur species and polymer chain can strongly limit polysulfides from dissolution, which can suppress the shuttle effect and hence improve the cycling performances of battery. The sulfur chains in the sulfur-containing polymers can achieve a uniform dispersity that is able to avoid the agglomeration of sulfur species. Moreover, the polymer chain can be designed with different functional groups to endow the polymer with special characteristics. However, generally the polymer chains in sulfur-containing polymers do not make any contribution to the battery discharge capacity. Thus, it is important to increase the sulfur content in sulfur-containing polymer cathodes. For now, the sulfur content in sulfur-containing polymers can reach a value higher than 95%, which enable them to obtain both high specific capacity and stable cycle performance [8].

In the past several decades, great progress has been made in research on sulfur-containing polymer cathodes. These sulfur-containing polymer cathodes played a huge role in promoting the research of Li–S batteries and even non-Li metal-sulfur batteries [9, 10]. Figures 8.1 and 8.2 show overviews of this chapter, including different sulfur-containing polymer cathodes and different strategies to further boost the performances of these polymer cathodes. In this chapter, we introduce the electrochemical mechanisms of different sulfur-containing polymer cathodes at first. Subsequently, according to the electrochemical mechanisms, we summarize sulfur-containing polymer cathodes by different types, including the polymers based on conventional redox chemistry or solid-phase conversion. Moreover, we systematically discuss the strategies to further optimize the electrochemical performances of sulfur-containing polymer cathodes, e.g., adding conductive additives, introducing reaction accelerators, and applying quasi-solid-state or solid-state electrolytes. In the end of this chapter, we provide the future perspectives on sulfur-containing polymer cathode research.

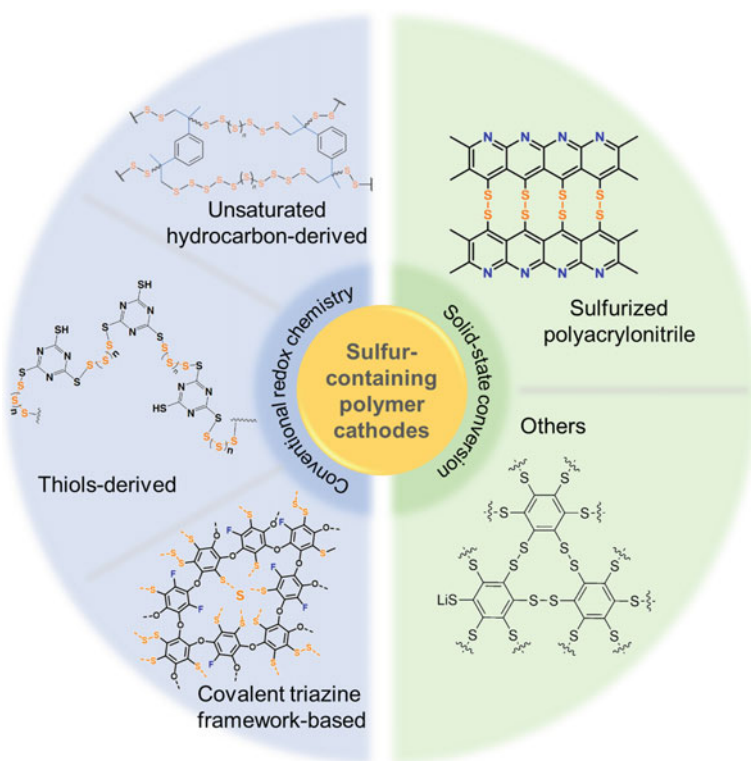


Fig. 8.1 An overview of different sulfur-containing polymer cathode materials for Li-S batteries. The content for unsaturated hydrocarbon-derived, thiol-derived, covalent triazine framework-based, sulfurized polyacrylonitrile, others was reprinted with permission from Ref. [11] (Copyright 2013 Nature Publishing Group), Ref. [12] (Copyright 2016 Nature Publishing Group), Ref. [13] (Copyright 2019 American Chemical Society), Ref. [14] (Copyright 2018 American Chemical Society), Ref. [15] (Copyright 2017 Wiley-VCH), respectively

8.2 Electrochemical Mechanisms of Different Sulfur-Containing Polymer Cathode Materials

Sulfur-containing polymers are composed of polymer molecular chains and sulfur segments. Generally, the number of sulfur atoms in sulfur bridge bonds can determine the sulfur content of the polymer, and also have a significant effect in the electrochemical behaviors of the sulfur-containing polymer cathodes [18]. In the current research, two typical electrochemical reaction processes can be observed in sulfur-containing polymer cathodes, e.g., conventional redox chemistry and solid-phase conversion.

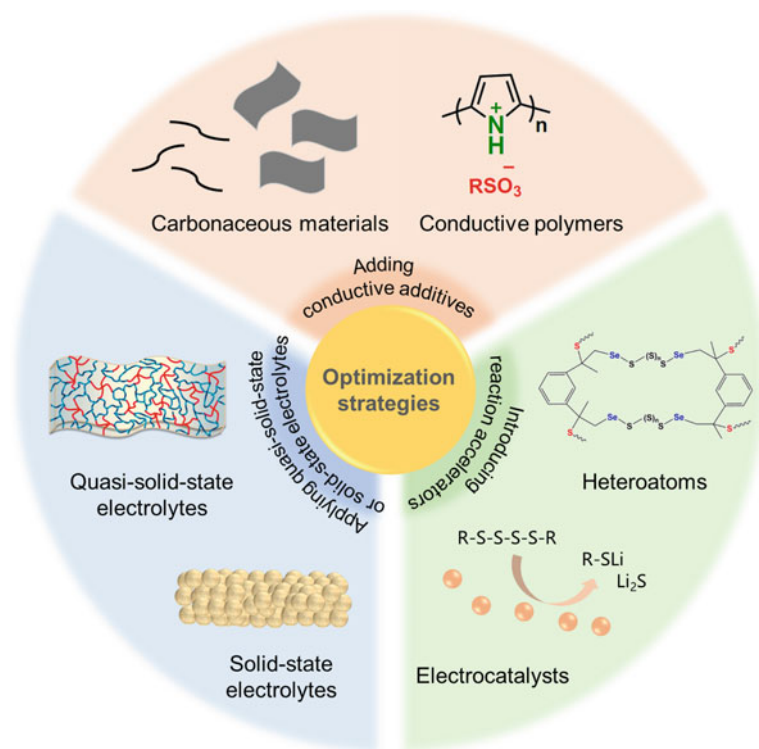


Fig. 8.2 An overview of different optimization strategies for Li-S batteries using sulfur-containing polymer cathode materials. The content for conductive polymers and heteroatoms was reprinted with permission from Ref. [16] (Copyright 2020 American Chemical Society) and Ref. [17] (Copyright 2018 American Chemical Society), respectively

Conventional redox chemistry. Sulfur-containing polymer cathodes with conventional redox chemistry deliver similar electrochemical behaviors as elemental sulfur cathodes. With generally greater than or equal to 6 sulfur atoms in the sulfur bridge bond, the polymers undergo the electrochemical reactions as shown in Fig. 8.3, e.g., sulfur chain within polymer backbone (solid phase) \rightarrow Li polysulfides (liquid phase) \rightarrow Li_2S (solid phase) [19]. Figure 8.3b exhibits the typical charge–discharge curves of a sulfur-containing polymer, poly(sulfur-random-1,3-diisopropenylbenzene) (poly(S-r-DIB)), with conventional redox chemistry mechanism [11]. The discharge curve showed two obvious discharge platforms around 2.2 V and 2 V, representing a solid–liquid transformation and a liquid–solid transformation, respectively. This is very similar to the electrochemical properties of elemental sulfur.

Solid-phase conversion. When the sulfur atoms in the sulfur bridge bond is less than or equal to 4, usually the formation of Li polysulfide is not involved in the

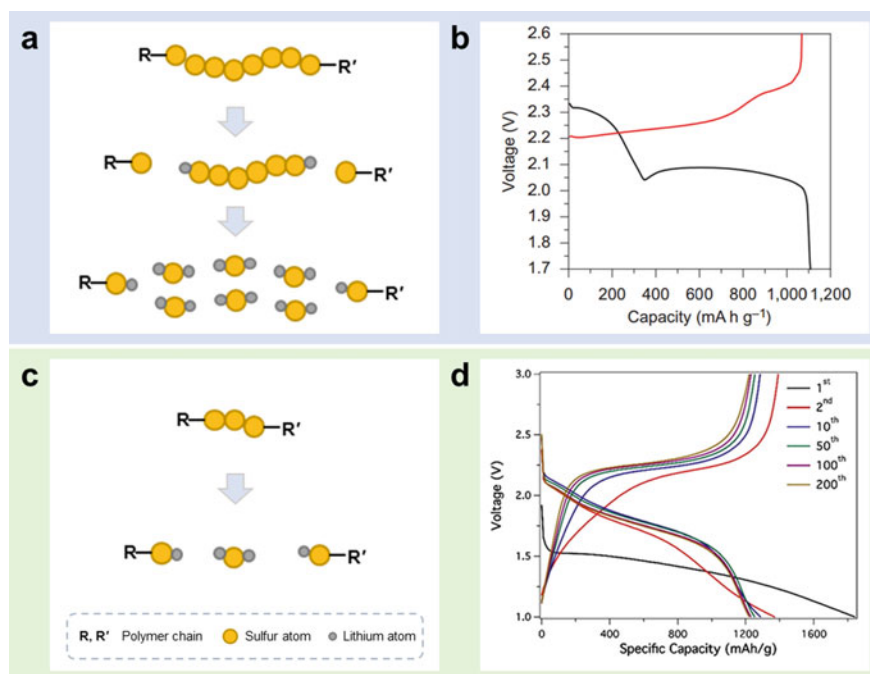


Fig. 8.3 **a** Schematics showing the electrochemical reaction process of sulfur-containing polymer cathodes with conventional redox chemistry. **b** Typical charge-discharge curves of Li-S batteries with poly(S-r-DIB) cathodes at 0.1 C. The electrolyte used for tests was 0.38 M lithium bis(trifluoromethane)sulfonimide (LiTFSI), 0.31 M LiNO₃ in 1,3-dioxolane (DOL)/1,2-dimethoxy ethane (DME) (1: 1 by volume). Reprinted with permission from Ref. [11]. Copyright 2013 Nature Publishing Group. **c** Schematics showing the electrochemical reaction process of sulfur-containing polymer cathodes with solid-phase conversion. **d** Typical charge-discharge curves of Li-S batteries with SPAN cathodes at 0.4 C. The electrolyte used for tests was 1 M LiPF₆ in ethylene carbonate (EC)/diethyl carbonate (DEC). Reprinted with permission from Ref. [20]. Copyright 2015 American Chemical Society

electrochemical reaction process, and the polymers experience solid-phase conversion and finally generate Li₂S (Fig. 8.3c) [19]. Figure 8.3d shows representative charge-discharge curves of a sulfur-containing polymer (sulfurized polyacrylonitrile (SPAN)) with solid-phase conversion mechanism [20]. In the first discharge, such polymers generally involve an activation process to generate a cathode electrolyte interphase (CEI) layer on sulfur surface, and the discharge voltage is lower than that in subsequent cycles. In subsequent cycles, unlike elemental sulfur possesses two obvious discharge plateaus, such polymers only deliver a slope within 2.2–1.5 V during the discharge curve, indicating a continuous solid-solid conversion process.

8.3 Sulfur-Containing Polymer Cathode Materials with Different Electrochemical Mechanisms in Li–S Batteries

8.3.1 Sulfur-Containing Polymers Based on Conventional Redox Chemistry

Sulfur-containing polymer cathodes with conventional redox chemistry are discussed by molecule structures (i.e., unsaturated hydrocarbon-derived, thiol-derived, and covalent triazine framework-based) in this section. Generally, these polymers have long sulfur molecular chains (usually >4 atoms) in the backbone, and can exhibit similar electrochemical behaviors like elemental sulfur. Meanwhile, due to the existence of these relatively long sulfur chains, such polymers are readily to achieve high sulfur content, which is beneficial for the energy density of Li–S batteries. Furthermore, since the molecular structure of sulfur-containing polymer has a huge impact on its chemical properties, sulfur-containing polymers with different molecule structures are discussed.

8.3.1.1 Unsaturated Hydrocarbon-Derived Polymers

Copolymerizing unsaturated hydrocarbon molecules with elemental sulfur is a very widely adopted strategy for synthesizing sulfur-containing polymers [21]. In this strategy, these unsaturated hydrocarbon molecules are worked as crosslinkers to bind sulfur chains. Specifically, at an elevated temperature, elemental sulfur experiences a ring-opening reaction and forms diradical segment, which can readily graft on the unsaturated bonds of unsaturated hydrocarbon molecules [22]. Such copolymerization reaction can obtain a highly crosslinked sulfur-organic molecule copolymer network. The sulfur-containing polymers synthesized using this method can achieve a high sulfur content (>95%) [8], and exhibit similar electrochemical behaviors as elemental sulfur. The copolymer network is able to effectively confine sulfur by covalent bonds, and thus limit the shuttle effect of Li polysulfides [23]. Regarding this strategy, a variety of olefinic molecules have been reported to be used as crosslinkers to synthesize sulfur-containing polymers [24]. Chung et al. reported poly(S-*r*-DIB) as cathode material for Li–S batteries [11]. As shown in Fig. 8.4a, poly(S-*r*-DIB) was synthesized via a free-radical copolymerization process between 1,3-diisopropenylbenzene (DIB) and diradical sulfur segments at 185 °C. This process required no additional initiator or organic solvents. By controlling the amount of DIB and elemental sulfur, sulfur content of the obtained copolymer could be readily controlled from 50 to 90%. While used as cathode materials for Li–S batteries, such copolymer (with a sulfur content of 90%) exhibited good electrochemical activity, and yielded a specific capacity of *ca.* 800 mAh g⁻¹ after 100 cycles at 0.1 C (Fig. 8.4b).

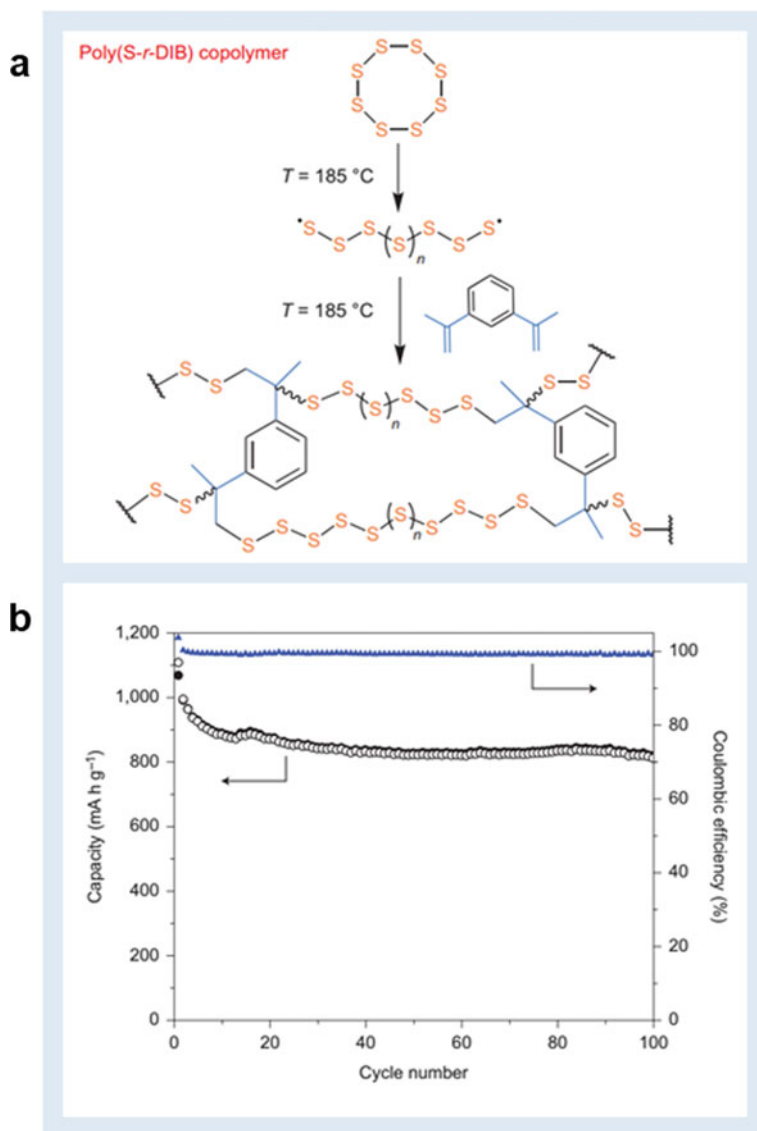


Fig. 8.4 **a** Schematic illustration of the process of poly(*S-r-DIB*). **b** Cycling performance of a Li-S battery using poly(*S-r-DIB*) (sulfur content: 90%) cathodes at 0.1 C. Reprinted with permission from Ref. [11]. Copyright 2013 Nature Publishing Group

After that, Hoefling et al. further researched the electrochemical reaction process of DIB-sulfur copolymers [25]. Figure 8.5a shows the ^{13}C solid-state nuclear magnetic resonance (NMR) spectra of DIB-sulfur copolymers with different contents

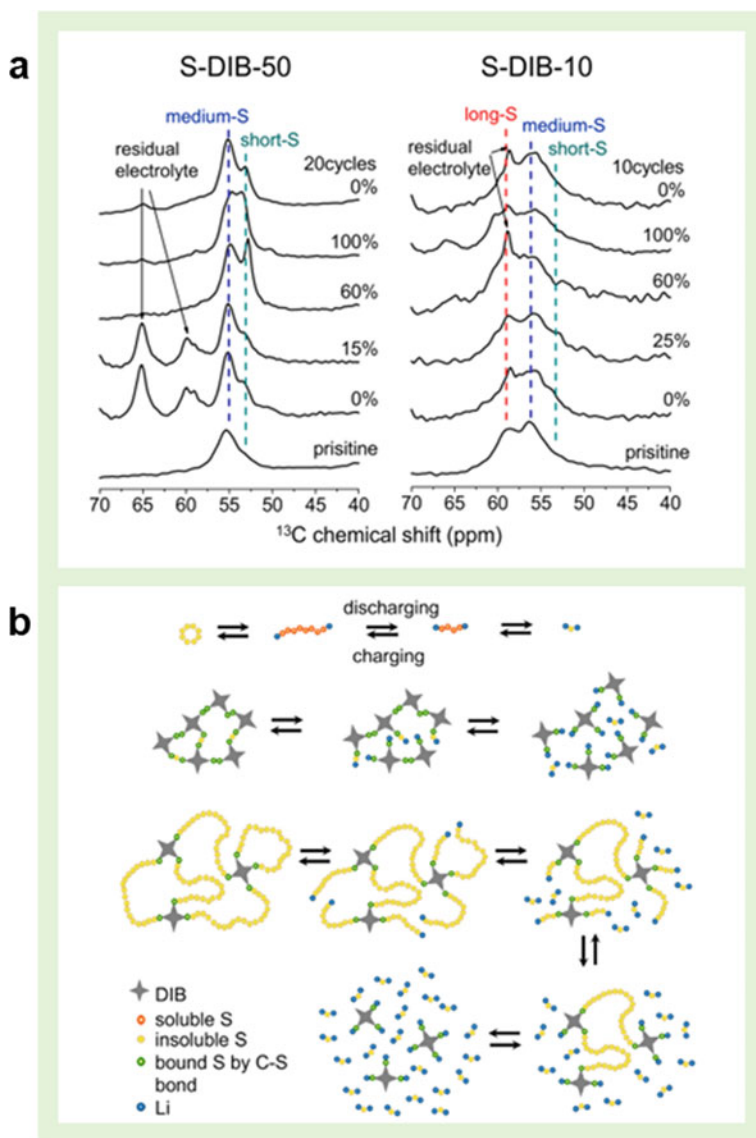


Fig. 8.5 **a** Ex-situ $^{13}\text{C}\{^1\text{H}\}$ cross polarization (CP)/magic angle spinning (MAS) NMR spectra of S-DIB-50 and S-DIB-10 cathodes discharged to various states. **b** Schematic illustration showing the reaction processes of DIB-sulfur copolymers with different sulfur content. Reprinted with permission from Ref. [25]. Copyright 2018 American Chemical Society

of DIB (50% DIB, denoted as DIB-S-50; 10% DIB, denoted as DIB-S-10) at different discharge state after one formation cycle. Long-chain sulfur segments ($C-S_x-C$, $x \geq \sim 5$, denoted as long-S), medium-chain sulfur segments ($C-S_x-C$, $x \approx 3-4$, denoted as mid-S), and short-chain sulfur segments ($C-S_x-C$, $x \approx 1-2$, denoted as short-S) can be clearly identified in the spectra. It can be observed that the signal of long-S only exhibited in the spectra of DIB-S-10, and the signal strength of short-S in DIB-S-50 is much higher than that in DIB-S-10. Thus, the reaction routes of different cathode materials were supposed to be as exhibited in Fig. 8.5b. The sulfur content had a great influence on electrochemical behaviors of DIB-sulfur copolymer, and a higher sulfur content would result in a larger proportion of Li_2S in discharge products.

In addition, special functional groups (e.g., thiophene groups [26]) can be introduced to render polymers with special properties, such as improved electronic conductivities and enhanced chemical confinement [10, 27]. For example, Kang et al. tested four different crosslinkers (i.e., tetra(allyloxy)-1,4-benzoquinone (TABQ), 2-allyloxy-naphthoquinone (ANQ), 1,4-bis(allyloxy)-anthraquinone (BAAQ), and triallyloxy-triazine (TATA), as shown in Fig. 8.6a)-derived sulfur-containing polymer cathodes in Li-S batteries [28]. Among these materials, sulfur-TABQ copolymer (poly(S-TABQ), as shown in Fig. 8.6b) retrieved the best electrochemical performances, since it could provide strong polar interactions with polysulfides by the abundant heteroatoms in the molecule structure. As a result, poly(S-TABQ) yielded a high capacity of $\approx 1300 \text{ mAh g}^{-1}$ at 0.1 C, and this capacity kept stable during 100 cycles (Fig. 8.6c), which is much better than sulfur-TATA copolymer (poly(S-TATA)) and elemental sulfur. Oschmann et al. used *o*-dichlorobenzene (OCB) as the crosslinker and synthesized a thiophene-based structured sulfur-containing polymer for Li-S batteries (Fig. 8.6d) [29]. The unique structure of the as-synthesized sulfur-poly(3-hexylthiophene-2,5-diyl) (S-P3HT) copolymer provided strong chemical confinement to sulfur species via the polythiophene segment, and effectively lowered the electrical resistance of cathode. By applying such copolymer together with elemental sulfur as cathode materials, the as-developed Li-S battery delivered lower overpotential (determined from the potential difference between charging and discharging) and higher specific capacity compared to elemental sulfur cathode and simply mixing sulfur and P3HT as cathode (Fig. 8.6e).

Since carbon-carbon triple bonds can provide more reactive sites for polymerization with sulfur segments than carbon-carbon double bonds, some literatures used alkyne-based monomers as the crosslinkers to realize a high sulfur content in polymers [30]. Sun et al. synthesized a sulfur-containing polymer derived from sulfur and 1,3-diethynylbenzene (DEB), which possessed a cage-like semi-interpenetrating network (semi-IPN) structure (Fig. 8.7a) [31]. With 20 wt% DEB as crosslinker, the copolymer yielded a sulfur content of 75.7 wt%. Such material exhibited a good electrochemical activity, and it can be further improved by adding carbon black during the polymerization process (Fig. 8.7b). Dirlam et al. reported a sulfur copolymer derived from 1,4-diphenylbutadiyne (DiPhDY) [32]. Interestingly, the copolymerization of sulfur and DiPhDY induced the formation of a thiophene-based structure, as indicated in Fig. 8.7c. Such copolymer could be synthesized with a high sulfur

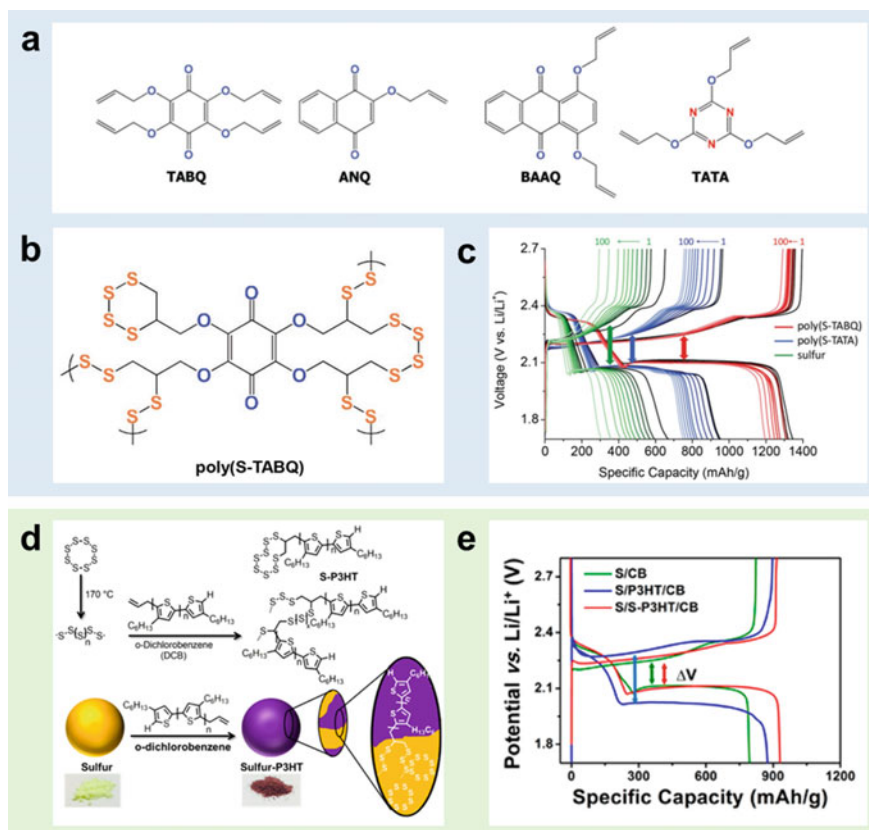


Fig. 8.6 **a** Molecular formula of TABQ, ANQ, BAAQ, and TATA. **b** Proposed molecular formula of poly(S-TABQ). **c** Charge–discharge profiles of poly(S-TABQ), poly(S-TATA), and elemental sulfur in different cycles at 0.1 C. Reprinted with permission from Ref. [28]. Copyright 2018 Wiley-VCH. **d** Synthesis procedure of S-P3HT. **e** Charge–discharge profiles of Li–S batteries with different cathode materials. Reprinted with permission from Ref. [29]. Copyright 2015 American Chemical Society

content of 90 wt%, and meanwhile provide good electrochemical performance as shown in Fig. 8.7d.

Applying natural materials as the crosslinkers for sulfur-containing polymers can further improve the environmental friendliness and cost effectiveness of Li–S batteries. Wu et al. reported a sulfur-limonene copolymer as the cathode material for Li–S batteries (Fig. 8.8a) [33]. Limonene can be easily obtained from orange and lemon peels, and has the advantages of abundant reserves, low price, environmentally friendliness and large-scale preparation. The covalent bonds formed between sulfur segments and D-limonene molecules effectively limited the dissolution and shuttle effects of Li polysulfides, and thus such copolymer exhibited favorable electrochemical performances while coupling with carbon black or carbon

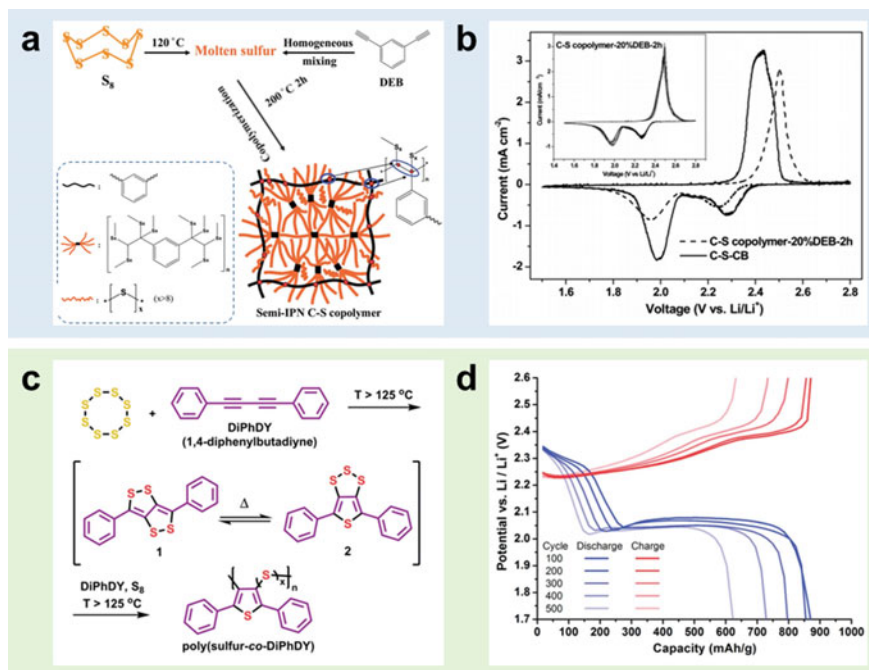


Fig. 8.7 **a** Synthesis process of S-DEB copolymer. **b** Cyclic voltammetry (CV) curves of S-DEB copolymer cathode and C-S-CB cathode (C-S-CB refers to the S-DEB copolymer with carbon black added during synthesis). Reprinted with permission from Ref. [31]. Copyright 2014 Royal Society of Chemistry. **c** Synthesis process of S-DiPhDY copolymer. **d** Charge-discharge curves of S-DiPhDY copolymer at different cycles at 0.2 C. Reprinted with permission from Ref. [32]. Copyright 2015 Royal Society of Chemistry

sphere, as shown in Fig. 8.8b. The proposed reaction mechanism for sulfur-limonene copolymer is shown in Fig. 8.8c. During the initial discharge, the polysulfide bridge bonds in copolymer transformed into $-\text{SLi}$ bonds and dispersed Li_2S nanoparticles. In the following cycles, these dispersed Li_2S nanoparticles were reversibly converted into S_8 , which also explained that the electrochemical reaction process of sulfur-limonene copolymer was similar to elemental sulfur. Moreover, commercial vegetable oils (including linseed oil, sunflower oil, olive oil) were reported to copolymerize with elemental sulfur to develop polymer cathodes for Li-S batteries (Fig. 8.8d) [34]. With a sulfur content of 70 wt%, this highly environmental-friendly material (linseed oil-sulfur copolymer) achieved a capacity of $\approx 450 \text{ mAh g}^{-1}$ after 100 cycles (Fig. 8.8e).

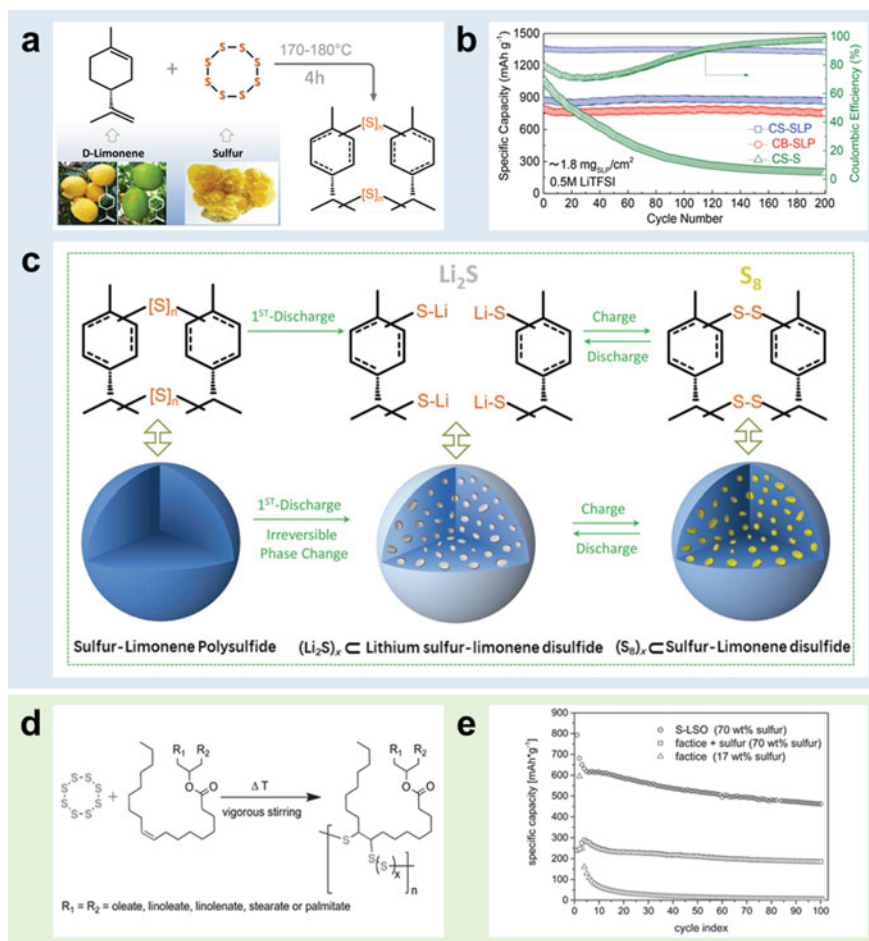


Fig. 8.8 **a** Synthesis route of sulfur-limonene copolymer. **b** Cycling performances of Li-S batteries with different cathode materials. SLP refers to sulfur-limonene polymer, CS refers to carbon sphere, CB refers to carbon black, and S refers to elemental sulfur. **c** Proposed reaction mechanism of sulfur-limonene copolymer during charge and discharge. Reprinted with permission from Ref. [33]. Copyright 2018 Wiley-VCH. **d** Synthesis procedure of sulfur-containing polymers derived from vegetable oils and elemental sulfur. **e** Cycling performance of Li-S batteries using different cathode materials. LSO refers to linseed oil. Reprinted with permission from Ref. [34]. Copyright 2017 Wiley-VCH

8.3.1.2 Thiol-Derived Polymers

Thiol-based molecule is another widely used monomer for copolymerizing sulfur-containing polymers. Since the connection between sulfur atom and hydrogen atom in thiol groups (-SH) is weak, thiol-derived sulfur-containing polymers are readily to be synthesized with a three-dimensional (3D) porous nanostructure [19]. Kim

et al. reported a trithiocyanuric acid (TTCA)-derived polymer cathode material for Li-S batteries [12]. The material preparation process was shown in Fig. 8.9a. Briefly, TTCA porous template was first synthesized by crystallization and heat treatment, then elemental sulfur was melt-infiltrated in the TTCA template and ring-opening polymerized on the thiol surface. Different solvents used for TTCA crystallization resulted in different crystal morphology. Dimethyl formamide (DMF)/water co-solvent led to TTCA rectangular tubes (noted as TTCA-I), while acetone induced TTCA splice plates (noted as TTCA-II). The strong chemical binding between TTCA segment and sulfur species and the 3D interconnected nanostructure of such copolymer could effectively limit the shuttle effect and enable the

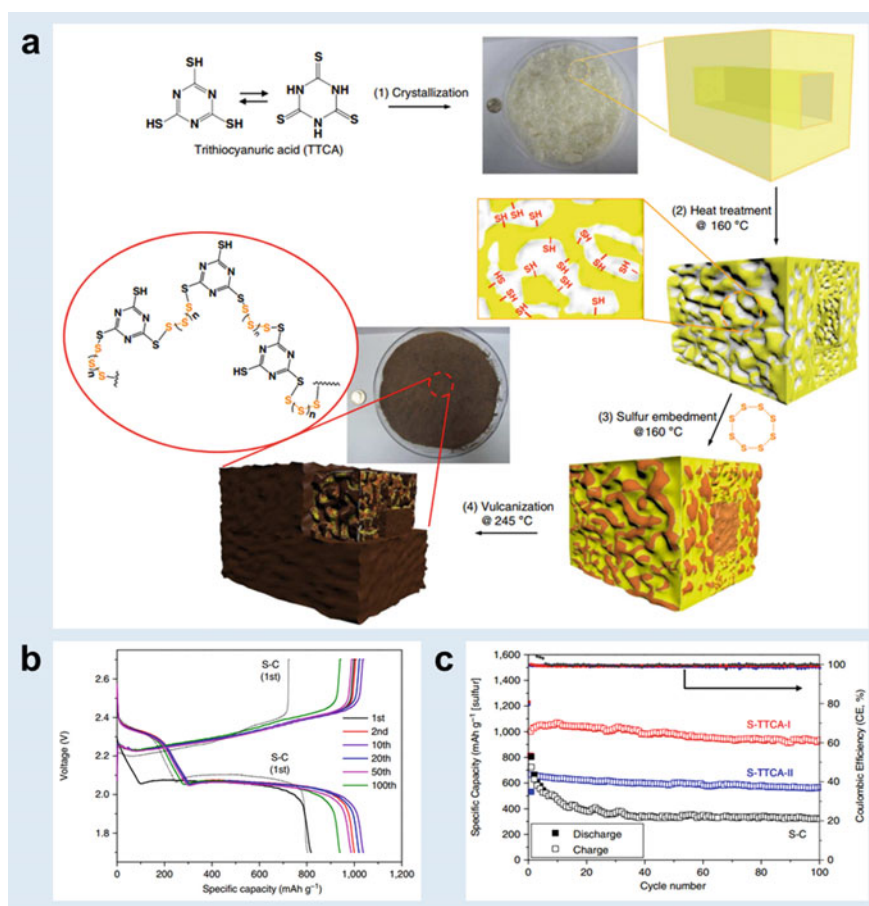


Fig. 8.9 a Schematic illustration of the preparation of sulfur-TTCA copolymer. b Charge-discharge profiles of S-TTCA-I cathodes versus sulfur-carbon cathodes at 0.2 C. c Cycling performances of Li-S batteries with different cathode materials at 0.2 C. Reprinted with permission from Ref. [12]. Copyright 2016 Nature Publishing Group

Li-S battery to deliver a decent electrochemical performance (Fig. 8.9b, c), which yielded a stable capacity of $\approx 1000 \text{ mAh g}^{-1}$ in 100 cycles (based on the mass of sulfur). Je et al. reported a sulfur-embedded polybenzoxazine (S-BOP) which was derived from hexahydro-1,3,5-triphenyl-1,3,5-triazine (TPTA), 4,4-dihydroxydiphenylsulfide (DHPDS) and elemental sulfur (Fig. 8.10d) [35]. The discharge

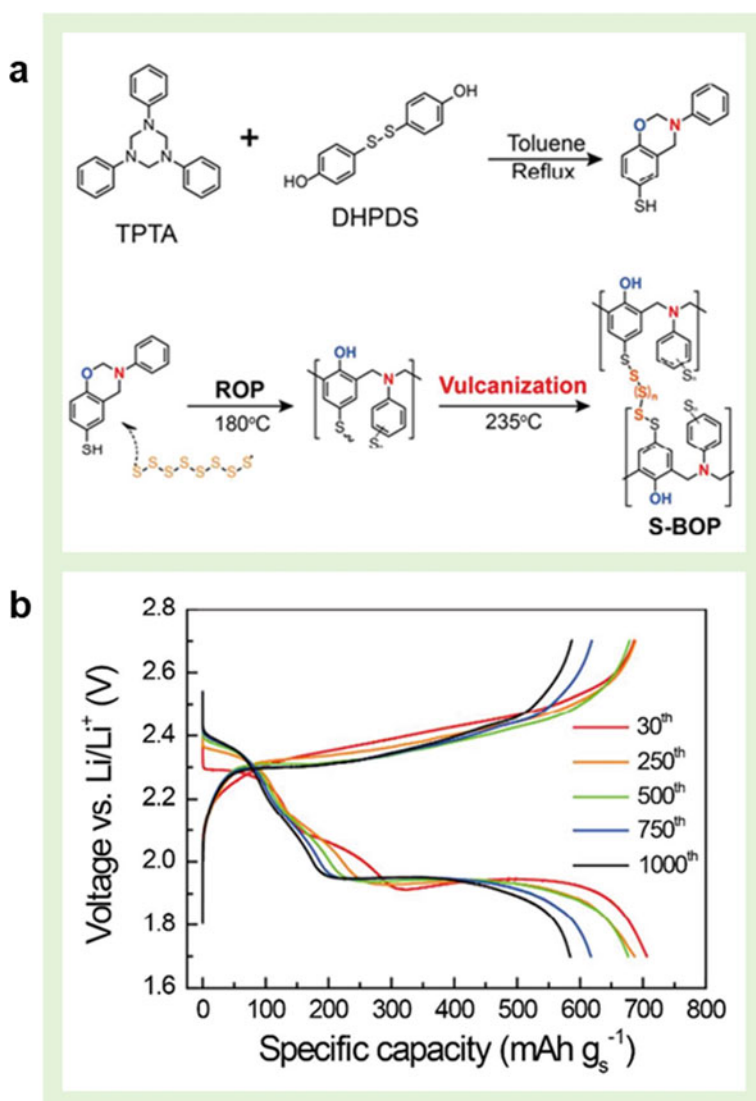


Fig. 8.10 **a** Synthesis scheme of S-BOP. ROP refers to ring-opening polymerization. **b** Charge-discharge curves of S-BOP at a current density of 720 mA g⁻¹. Reprinted with permission from Ref. [35]. Copyright 2016 American Chemical Society

curves of S-BOP exhibited two distinct plateaus, indicating its similar electrochemical behaviors with elemental sulfur (Fig. 8.10e). With a sulfur content of ≈ 72 wt%, S-BOP obtained a stable capacity of ≈ 600 mAh g^{-1} (based on the mass of sulfur) after 1000 cycles.

8.3.1.3 Covalent Triazine Framework-Based Polymers

Covalent triazine framework (CTF) is a type of microporous polymer that possess narrow distributed pore size, high specific surface area (up to 3000 m^2 g^{-1}), and moderate conductivity [36]. The unique property of CTFs enabled them to be widely used in a variety of applications, ranging from gas adsorptions to catalysis [37]. When applying elemental sulfur as mediator in the polymerization process of CTF, the as-developed sulfur-CTF copolymer can achieve a high sulfur content and can be directly used as the cathode active materials for Li-S batteries. For now, a series of monomers (e.g., 1,4-dicyanobenzene [37], perfluorinated aromatic nitrile [38], 2,2'-((perfluoro-1,4-phenylene) bis(methanyl-ylidene)) dimalononitrile [39]) have been used to copolymerize with sulfur to synthesize sulfur-CTF copolymer. Talapaneni et al. first reported the application of sulfur-containing CTFs as cathode material in Li-S batteries (Fig. 8.11a) [37]. The S-CTF copolymer (S-CTF-1) was synthesized via a sulfur-mediated trimerization of 1,4-dicyanobenzene. Such copolymer not only provided strong chemical binding and large void space for sulfur, but also enabled regular sulfur distribution and good electronic/ionic conductivity. As a result, the sulfur-containing CTF with a sulfur content of 62 wt% delivered distinct discharge platforms similar to sulfur (Fig. 8.11b), and yielded a stable capacity of ≈ 500 mAh g^{-1} (based on the mass of S-CTF-1) during 50 cycles (Fig. 8.11c). Applying electron-withdrawing groups (e.g., fluorine) to functionalize aromatic molecules can enhance their electron deficiency and thus facilitate of nucleophilic addition reactions of sulfur chains on them, which can greatly increase the sulfur content of the sulfur-CTF copolymer [40]. Regarding this strategy, Je et al. reported perfluorinated aryl cyanide as the monomer for the synthesis of sulfur-containing CTFs [40]. As shown in Fig. 8.11d, since the fluorine-substituted sites provided provides a large number of active sites for addition reaction of sulfur species (S_NAr), the as-synthesized S-CTF copolymer retrieved a high sulfur content of 86 wt%. Such copolymer yielded a capacity of ≈ 500 mAh g^{-1} (based on the mass of sulfur) after 300 cycles at 1 A g^{-1} , and this good cycling stability could be indicated by the highly reversible signals of C-C, C-S, and Li_2S in S 2p X-ray photoelectron spectroscopy (XPS) spectra (Fig. 8.11e).

Beyond the above-mentioned three molecular structures, various conventional-redox-chemistry-based sulfur-containing polymers can also be obtained via addition (e.g., on thiocarbonyl [41]), substitution (e.g., on halogen bonds [42]) or coupling [43] of sulfur chains. These polymers can also combine sulfur chains in the polymer backbone via covalent bonds to chemically limit the shuttle effect of Li polysulfides, and thus enable enhanced electrochemical performances of Li-S batteries.

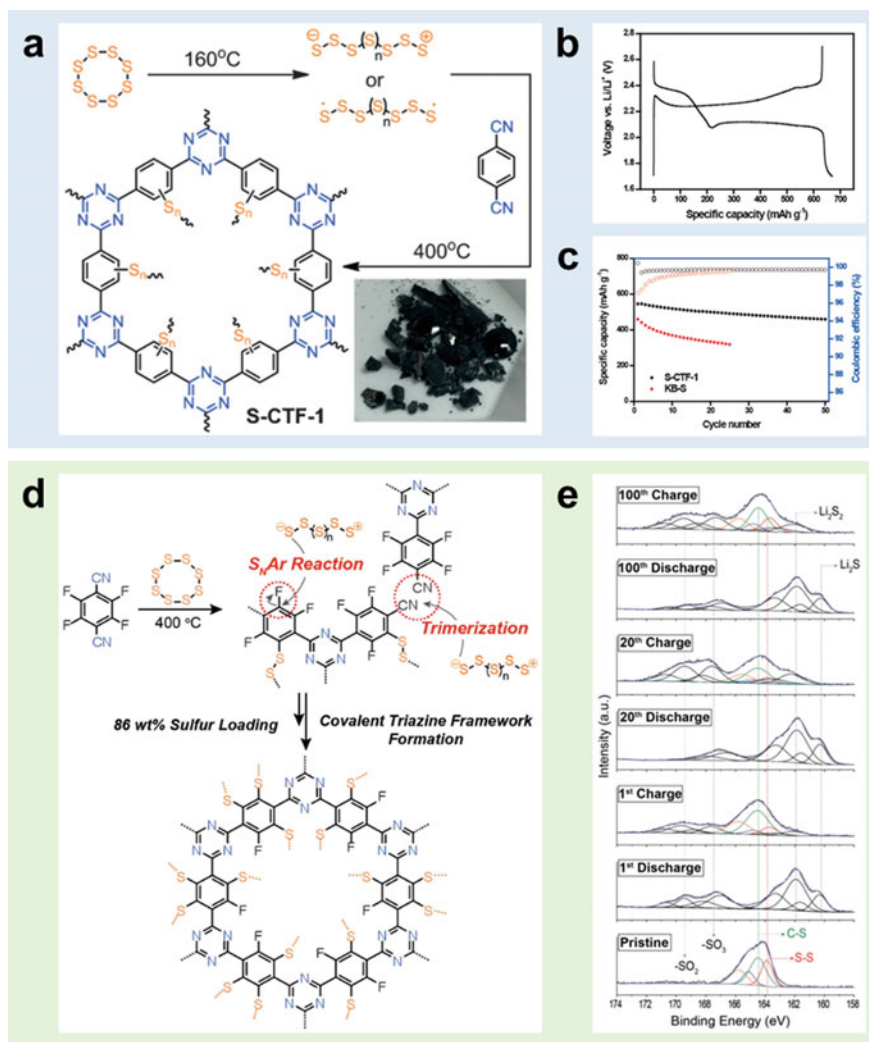


Fig. 8.11 **a** Synthesis scheme of S-CTF-1. The inset in the lower right corner is the photo of as-synthesized S-CTF-1. **b** Typical charge–discharge curves of S-CTF-1 at 0.05 C. **c** Cycling performances of S-CTF-1 and KB-S (namely Ketjen Black and elemental sulfur with a weight ratio of ≈ 1 : 1). Reprinted with permission from Ref. [37]. Copyright 2016 Wiley-VCH. **d** Synthesis scheme of sulfur-CTF copolymer from elemental sulfur and perfluorinated aryl cyanides. **e** Ex-situ S 2p XPS spectra of the sulfur-CTF copolymer at different charge–discharge state. Reprinted with permission from Ref. [40]. Copyright 2017 Wiley-VCH

8.3.2 Sulfur-Containing Polymers with Solid-Phase Conversion

In terms of sulfur-containing polymers with solid-phase conversion, the sulfur molecular chains in the polymer backbone contain fewer sulfur atoms (usually ≤ 4), and the electrochemical behaviors are very different from elemental sulfur. For example, for solid-phase-conversion polymers, there is only one slope instead of two obvious plateaus in the discharge curve, and the battery operation do not involve the generation of high-order polysulfides [19]. Due to this characteristic, solid-phase-conversion sulfur-containing polymers can achieve excellent cycling stability. However, the short sulfur molecular chains also lead to a relatively low sulfur content. Therefore, increasing the sulfur content as high as possible is an essential pursuit for the research on the solid-phase-conversion sulfur-containing polymers.

8.3.2.1 Sulfurized Polyacrylonitrile

Sulfurized polyacrylonitrile (SPAN) is a very important cathode material for Li-S batteries. SPAN is also named as pyrolyzed polyacrylonitrile-sulfur (pPAN-S) or S@pPAN [44]. Since it was first reported by Wang et al. in 2002 [45], the application of SPAN in Li-S batteries has attracted intensive research interests in recent two decades. SPAN has a variety of advantages, including inhibited shuttle effect, tiny self-discharge, and good compatibility with carbonate electrolytes, which make SPAN a highly stable cathode material for Li-S batteries and even other alkali-metal sulfur batteries (e.g., sodium-sulfur batteries [46], and potassium-sulfur batteries [10]). The basic synthesis process of SPAN is shown in Fig. 8.12a [47]. Typically, at a reaction temperature of ≈ 300 °C, the high polar nitrile groups in polyacrylonitrile (PAN) molecule cyclize into a heterocyclic compound, and meanwhile this heterocyclic compound is dehydrogenated by molten sulfur. After this reaction, SPAN molecule with sulfur chains existing as bridge bonds covalently bonded to carbon atoms is obtained. As shown in the ^{13}C solid-state NMR spectra of SPAN and PAN (Fig. 8.12b), only two different ^{13}C locations were detected in PAN, while three different ^{13}C locations were detected in SPAN due to the existence of C – S bond [14]. For now, there are two possible structures for SPAN, as shown in Fig. 8.12c. The sulfur chains in structure I exist as intermolecular bridge bonds, while the sulfur chains in the structure II exist as intramolecular bridge bonds. Wang et al. proposed that structure I is the active units in SPAN based on their solid-state NMR experimental data and the density functional theory (DFT) calculation [14]. Based on these, they speculated that the S–S bonds in SPAN broke to irreversibly convert into thiyl radicals to form a highly stable conjugative structure during the first discharge, and Li could be reversibly stored at the negative locations of these thiyl radicals and nitrogen atoms via ion-coordination bonds (Fig. 8.12d) [14].

Compared to conventional sulfur@carbon cathode which suffered from limited electronic conductivity and severe polysulfide dissolution (Fig. 8.13a), SPAN cathode

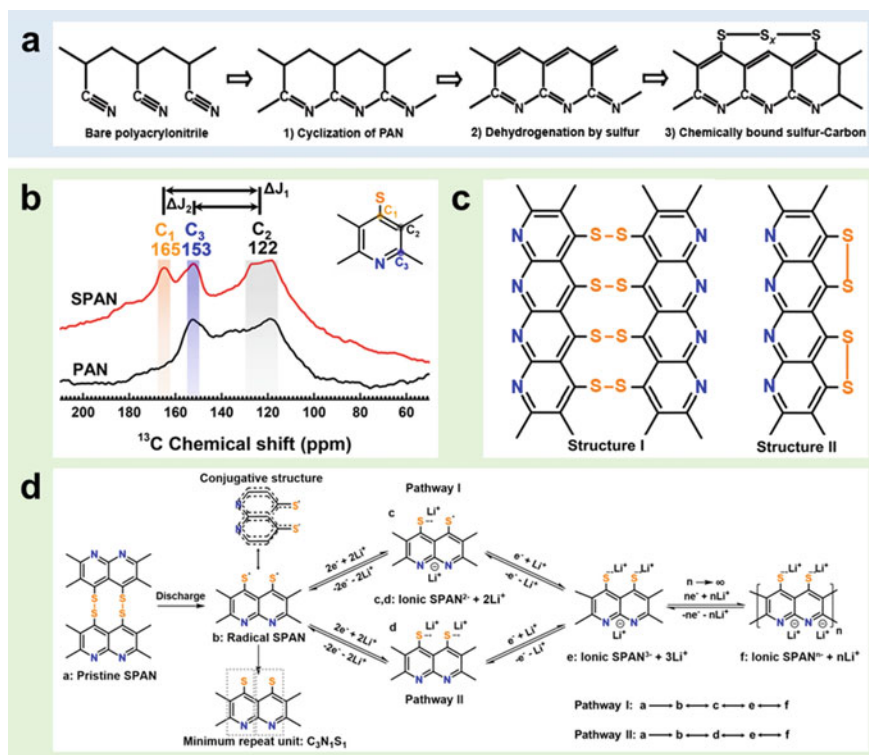


Fig. 8.12 **a** Proposed structural evolution of SPAN during synthesis process. Reprinted with permission from Ref. [47]. Copyright 2013 American Chemical Society. **b** Experimental ^{13}C CP/MAS solid-state NMR spectra of SPAN and PAN. The inset in the upper right corner indicates the corresponding different ^{13}C locations in every unit of the SPAN molecular structure. **c** Proposed two possible molecular structure of SPAN. **d** Proposed working mechanism of SPAN as Li-S battery cathode materials. Reprinted with permission from Ref. [14]. Copyright 2018 American Chemical Society

not only possesses a conductive polymer matrix that can ensure good electronic conductivity and avoid the aggregation of sulfur species, but also can react with carbonate solvents to generate a CEI layer which can prevent sulfur species from dissolution (Fig. 8.13b) [48]. Thus, most research on applying SPAN as Li-S battery cathode material was conducted in carbonate-based electrolytes due to the high stability [49–51]. In contrast, conventional Li-S batteries utilizing elemental sulfur as cathode material would suffer from a rapid capacity fading in carbonate electrolytes, mainly due to the substitution reaction or nucleophilic addition can readily occur between nucleophilic sulfide anions and carbonate solvents [52]. Xu et al. reported various carbonate-based electrolytes for SPAN||Li metal batteries [53]. Compared to conventional carbonate electrolytes (LiPF_6 in EC-DMC) that had low compatibility with Li metal anode and delivered obvious capacity decay during 400 cycles,

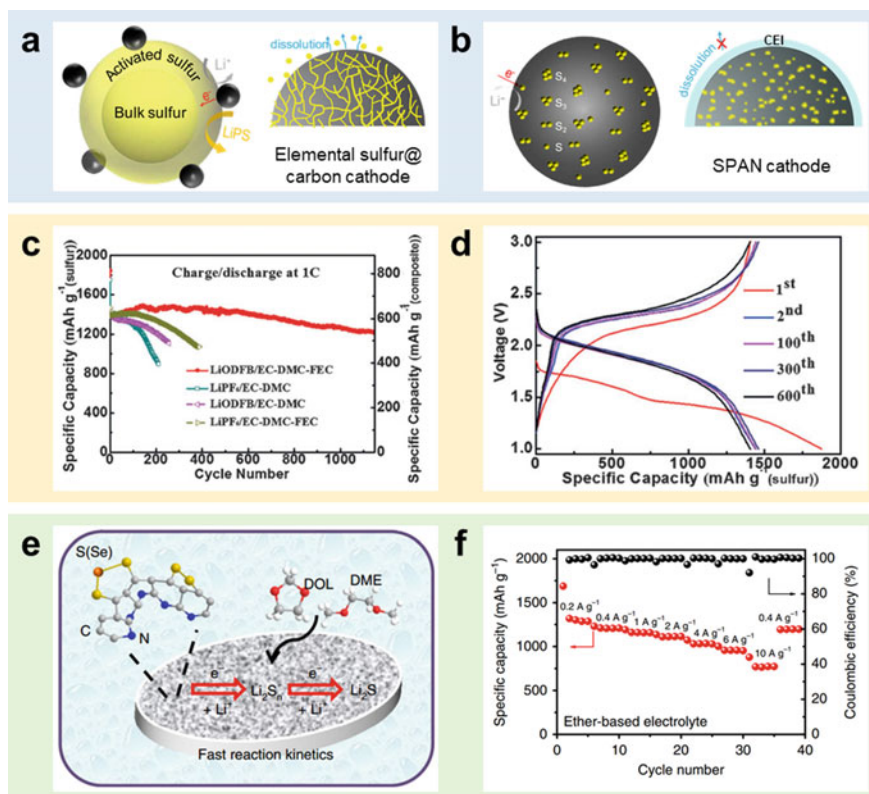


Fig. 8.13 **a** and **b** Schematic illustration indicating the reaction mechanisms of elemental sulfur@carbon cathode (**a**) and SPAN cathode (**b**). Reprinted with permission from Ref. [48]. Copyright 2020 Wiley-VCH. **c** Cycling performances of Li-S batteries using SPAN cathodes in various carbonate-based electrolytes and **d** the corresponding charge-discharge curves of that in Li-ODFB/EC-DMC-FEC electrolyte. Reprinted with permission from Ref. [53]. Copyright 2016 Wiley-VCH. **e** Schematic showing the fast reaction kinetics of Se-doped SPAN cathode in DOL-DME electrolyte. **f** Rate performances of such cathode in 1 M LiTFSI in DME and DOL (1: 1 by volume) with 2 wt% LiNO₃ electrolyte. Reprinted with permission from Ref. [54]. Copyright 2019 Nature Publishing Group

1 M lithium oxalyl difluoroborate (LiODFB) in EC-dimethyl carbonate (DMC)-fluoroethylene carbonate (FEC) (4.5: 4.5: 1 by volume) electrolyte exhibited good compatibility with Li metal anode and yielded a stable specific capacity of ≈ 1400 mAh g⁻¹ (based on the mass of sulfur) during 600 cycles at 1 C (Fig. 8.13c, d). Generally, SPAN suffers from rapid capacity decay in ether-based electrolytes, since the solution of low-order polyfulfides (Li₂S_n ($n \leq 4$)) in ethers still exists and can lead to subsequent shuttle effect [54]. Recent reports showed that SPAN could also retrieve a stable cycling performance by boosting the redox reaction kinetics [54] or accelerating the charge transfer [39]. Chen et al. reported a selenium (Se)-doped SPAN as cathode materials for Li-S batteries with both carbonate-based electrolytes

and ether-based electrolytes [54]. Since the Se doping greatly improved the reaction kinetics of SPAN, the Li polysulfide dissolution was effectively limited in ether-based electrolytes (Fig. 8.13e). As a result, with a typical ether-based electrolyte (1 M LiTFSI in DME and DOL (1: 1 by volume) with 2 wt% LiNO₃ addition), the Li–S battery using such cathode delivered stable electrochemical performance and even delivered a capacity of ≈ 750 mAh g⁻¹ (Based on the mass of sulfur and selenium) at 10 A g⁻¹ (Fig. 8.13f).

8.3.2.2 Others

In addition to SPAN, there are a variety of solid-phase-conversion sulfur-containing polymers being reported as Li–S battery cathodes. By adjusting the ratio of elemental sulfur during synthesis, the atom number of sulfur chains in the sulfur-containing polymer can be well controlled. Fewer atoms in the copolymer sulfur chains involve fewer discharge intermediates, and render simpler electrochemical reactions, which can further suppress the shuttle effect and facilitate the reaction mechanism study [19]. Preefer et al. reported a crosslinked disulfide active material for Li–S battery cathodes [15]. This material contained sulfur and carbon atoms in a ratio of 1: 1, and was expected to host six Li ions per C₆S₆ monomer unit (Fig. 8.14a). The Raman spectrum in discharge state showed the significant suppression of S–S bond signal together with the rise of Li–S bond signal, indicating the electrochemical reactions of the disulfide bonds in the polymer network (Fig. 8.14b). This unique molecular structure inhibited the formation of polysulfide intermediates and could deliver a stable capacity of ≈ 150 mAh g⁻¹ during 200 cycles. Later on, Gomez et al. synthesized poly(anthraquinonyl sulfide) (PAQS)-based polymers with different sulfur chain lengths, and investigated its influence on the electrochemical behaviors of Li–S batteries [18]. As shown in Fig. 8.14c, the PAQS-based polymer with one sulfur atom in sulfur chain undergone very different Li storage mechanism and delivered obvious different electrochemical behaviors compared to that with nine-atom sulfur chain. Fewer atoms in a PAQS-based polymer sulfur chain would inevitably reduce the sulfur content and specific capacity of Li–S batteries, but the cycle stability of the battery could be significantly improved due to avoided dissolution of Li polysulfides. Hence, it is important to regulate the number of atoms in the polymer sulfur chain for a balance between stable cycling performance and high specific capacity.

8.4 Optimization Strategies for Li–S Batteries Using Sulfur-Containing Polymer Cathode Materials

Confining sulfur to the polymer backbone via covalent bonds can greatly limit the dissolution and shuttle of sulfur species. However, these sulfur-containing polymer cathodes might still suffer from problems such as limited electronic conductivity

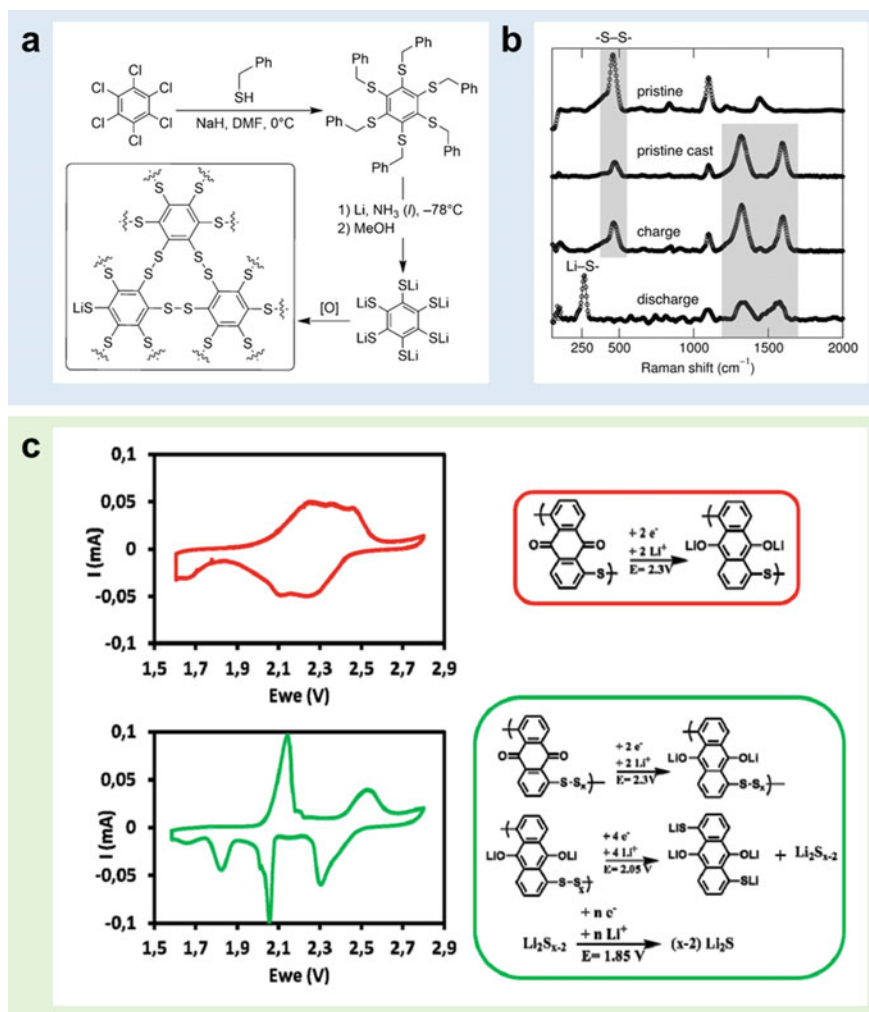


Fig. 8.14 **a** Synthesis route of the crosslinked disulfide active material. **b** Raman spectra of such materials in different state: pristine powders, casted pristine electrodes, charged state, and discharged state. Reprinted with permission from Ref. [15]. Copyright 2017 Wiley-VCH. **c** CV curves and corresponding reaction mechanisms of PAQS-based polymer with one-sulfur-atom chain (upper panel) and nine-sulfur-atom chain (lower panel). Reprinted with permission from Ref. [18]. Copyright 2018 American Chemical Society

or sluggish reaction kinetics. Moreover, when assembling full batteries, Li metal anodes, as commonly used anodes, face additional problems such as dendrite formation, which severely deteriorates the electrochemical performances of the Li-S full batteries. Regarding these issues, a series of strategies can be adopted to improve the electrochemical performances of Li-S batteries using sulfur-containing polymer

cathodes. In this section, these strategies are detailedly discussed by the following three categories, including adding conductive additives, introducing reaction accelerators, and applying quasi-solid-state or solid-state electrolytes.

8.4.1 Adding Conductive Additives

8.4.1.1 Compositing with Carbonaceous Materials

Applying carbonaceous materials to improve the electrochemical performances of sulfur-containing polymers is a widely used strategy. Carbonaceous materials can not only improve conductivity of polymer cathode, but also accommodate the volume change of the polymer cathode during battery operation and provide additional physical confinement to limit shuttle effect [55]. A general strategy to introduce carbonaceous materials is applying them as substrates for the copolymerization process of sulfur-containing polymers. These carbon materials reported to be used as copolymerization substrates include porous carbon [56], carbon nanotubes (CNTs) [57, 58], and graphene oxide (GO) [59]. Ding et al. reported a two-step synthesized porous carbon–sulfur-containing polymer composite for Li–S batteries [60]. They used a conventional melt-infusion method to load elemental sulfur in commercial conductive carbon black, then added DIB to copolymerize with the embedded elemental sulfur (Fig. 8.15a). The porous carbon framework provided good electronic transfer to sulfur species and physical confinement that could further mitigate the shuttle effect of polysulfides, and meanwhile the polymer backbone limited the aggregation of insoluble Li_2S species so that their irreversible deposition could be effectively limited. As a result, such composite material delivered favorable specific capacities of $\approx 1100 \text{ mAh g}^{-1}$ at 0.2 C and $\approx 700 \text{ mAh g}^{-1}$ at 5 C (based on the mass of sulfur, Fig. 8.15b). It is also feasible to load monomers on the carbonaceous materials first, and then to introduce sulfur to complete the copolymerization process [56]. Regarding this strategy, Yin et al. synthesized a SPAN/graphene nanosheet (GNS) composite cathode for Li–S batteries (Fig. 8.15c) [44]. The as-synthesized SPAN nanoparticles were anchored on the GNS surface with diameters less than 100 nm. The GNS in the composite materials could act as a nanosized current collector and enhance the electrochemical performances of the battery. When the content of GNS in the composite was $\approx 4 \text{ wt\%}$, such composite material yielded a capacity of $\approx 1200 \text{ mAh g}^{-1}$ after 50 cycles at 0.1 C (Fig. 8.15d). Furthermore, Chang et al. applied a chemical grafting method to synthesize covalently-grafted polysulfur-graphene sheet nanocomposites (polySGNs) for Li–S battery cathode materials [61]. The reduced GO (rGO) they used for copolymerization was functionalized with vinyl groups, which could ensure the good dispersibility of rGO nanosheets in the as-synthesized composite material (Fig. 8.15e). The rGO nanosheets formed large-sized covalently bonded Li polysulfide-graphene sheet composites. Such composites would not shuttle through the separator due to the size effect, and could deposit onto the separator at cathode side to form a conductive coating layer. Consequently, Li–S batteries using

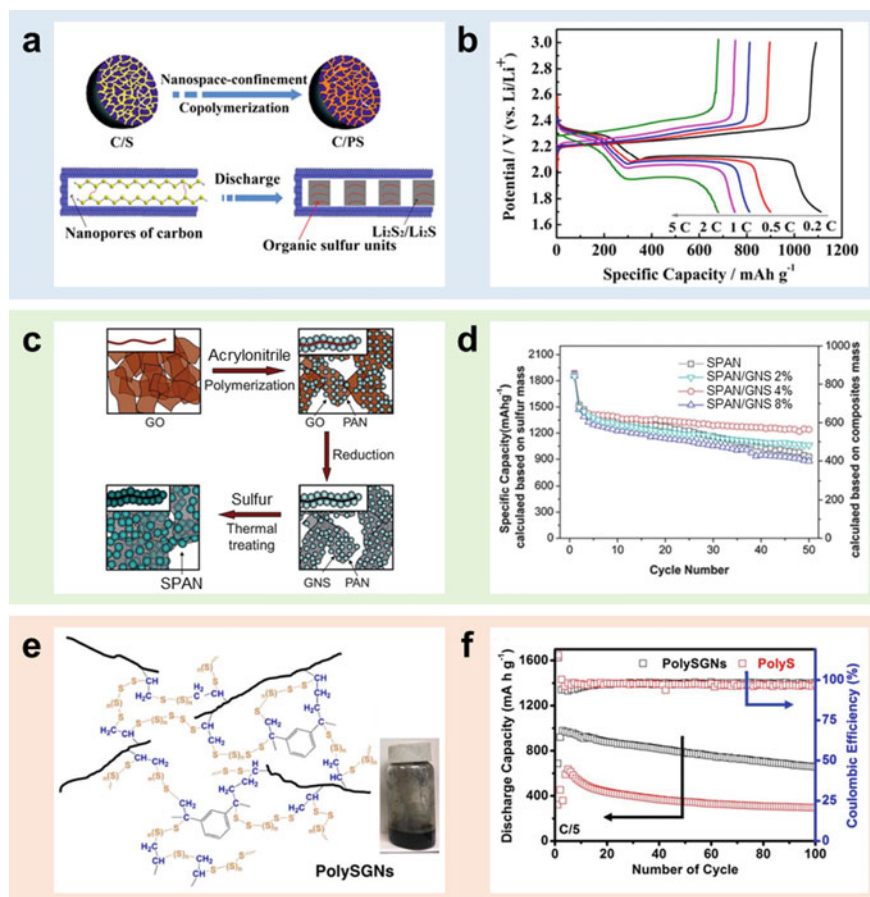


Fig. 8.15 **a** Schematic illustrations of synthesis process of porous carbon–sulfur-containing polymer composite and their discharge process in Li–S batteries. C/S refers to carbon/sulfur composite, and C/PS refers to carbon/polymeric sulfur composite. **b** Charge–discharge profiles of such composite materials in Li–S batteries at different current densities. Reprinted with permission from Ref. [60]. Copyright 2015 American Chemical Society. **c** Synthesis route of SPAN/GNS composites. Reprinted with permission from Ref. [44]. Copyright 2012 Royal Society of Chemistry. **d** Cycling performances of SPAN/GNS composites with different mass ratio of GNS. Reprinted with permission from Ref. [44]. Copyright 2012 Royal Society of Chemistry. **e** Proposed molecular structure and photo of PolySGNs. The bold black lines refer to rGO nanosheets. **f** Cycling performances of Li–S batteries with different cathode materials. PolyS refers to sulfur-DIB copolymer. Reprinted with permission from Ref. [61]. Copyright 2018 American Chemical Society

such composite cathode materials delivered a capacity of $\approx 650 \text{ mAh g}^{-1}$ (based on the mass of sulfur) after 100 cycles at 0.2 C with a sulfur loading of 3.7 mg cm^{-2} , much better than the Li–S batteries using sulfur-DIB copolymer cathodes (Fig. 8.15f).

Furthermore, Hu et al. reported CNT-encapsulated sulfur-containing polymers for Li–S batteries. As shown in Fig. 8.16a, the CNTs were synthesized via a chemical

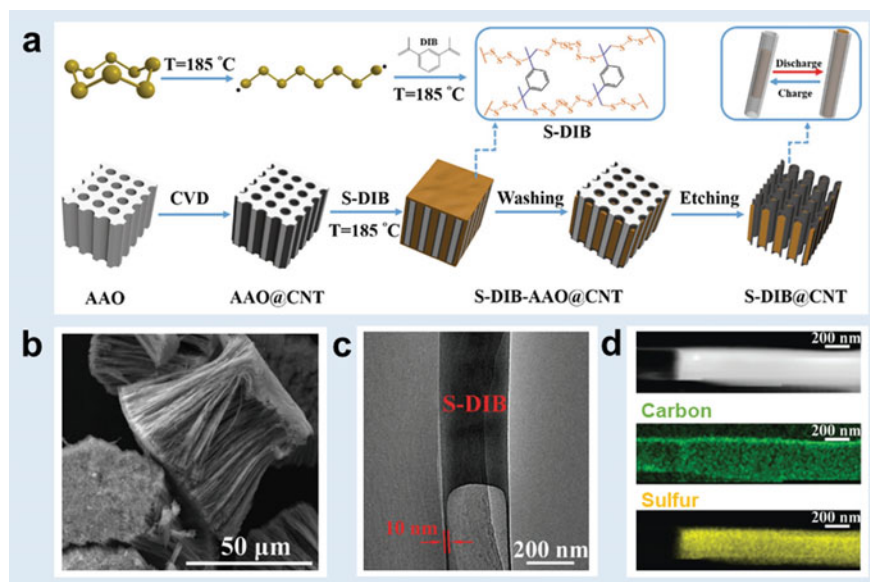


Fig. 8.16 **a** Schematic illustration of the preparation process of S-DIB@CNT cathode materials. **b** Scanning electron microscope (SEM), **c** transmission electron microscope (TEM), and **d** element mapping images of such material. Reprinted with permission from Ref. [58]. Copyright 2017 Wiley-VCH

vapor deposition (CVD) method on an anodic aluminum oxide template (AAO), and then S-DIB copolymer was thermally infiltrated into CNTs. Such composite materials possessed unique structure where sulfur copolymers were filled inside CNTs (Fig. 8.16b–d). The CNT shell provided efficient electron transfer pathway and well accommodated the volume expansion of sulfur species during discharging. As a result, the as-developed Li–S batteries obtained a high capacity of $\approx 880 \text{ mA h g}^{-1}$ (based on the mass of sulfur) after 100 cycles at 1 C. In addition, sulfur-containing polymers can be prepared into a freestanding electrode with the introduction of CNTs or graphene, which can avoid the application of binders and thus increase energy density of Li–S batteries [39, 62]. Shen et al. prepared inks composed of GO, sulfur, and DIB, and applied a 3D printing technique to convert the inks into freestanding electrodes (Fig. 8.17) [62]. Such electrode delivered good structural integrity, and yielded an initial capacity of $\approx 800 \text{ mA h g}^{-1}$ at 50 mA g^{-1} .

8.4.1.2 Grafting Conductive Polymers

Grafting conductive polymers on sulfur-containing polymers is another way to improve the conductivity of polymer cathodes. Conductive polymers are polymers with highly π -conjugated polymeric chains. These conductive polymers include polyacetylene, polyaniline, polypyrrole, polythiophene, poly(phenylenevinylene).

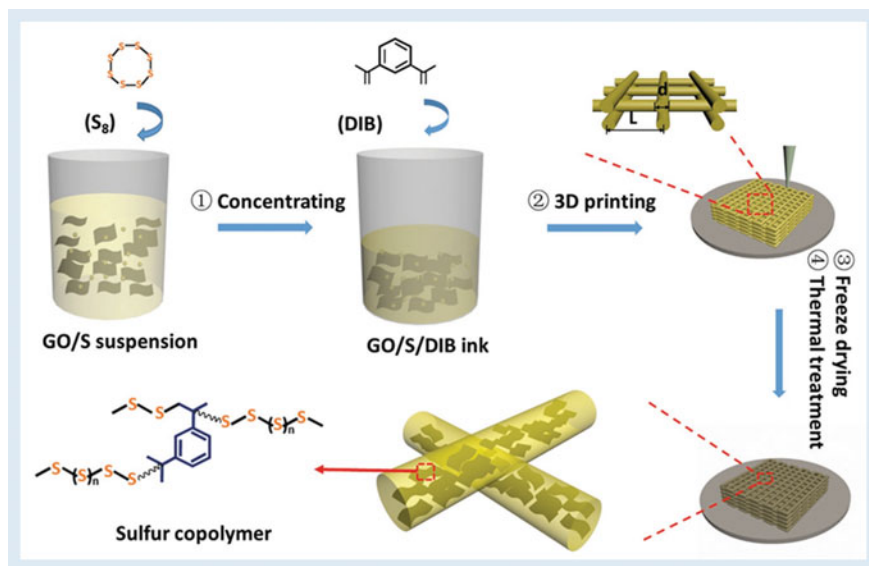


Fig. 8.17 Schematic illustration of a 3D-printing-achieved freestanding sulfur-containing polymer cathode. Reprinted with permission from Ref. [62]. Copyright 2017 Wiley-VCH

Their electronic conductivities at neutral state are very low (generally $<10^{-5}$ S cm^{-1}), but can be greatly improved to a value as high as 10^4 S cm^{-1} via doping [63]. Grafting these highly conductive polymers with sulfur-containing polymers can facilitate the transfer of electrons to the sulfur chains, and thus improve the Li-S battery performance. Kim reported a well-designed polymer structure, one-dimensional charged polypyrrole-incorporated sulfur-mediated CTF (cPpy-S-CTF, Fig. 8.18a), for Li-S battery cathodes [16]. The one-dimensional charged polypyrrole chains embedded in the two-dimensional sulfur-CTF copolymer improved the ionic and electronic conductivity, and thus the reaction kinetics and the rate capability of the sulfur-containing polymer cathodes were effectively enhanced (Fig. 8.18b).

8.4.2 Introducing Reaction Accelerators

8.4.2.1 Doping with Heteroatoms

In addition to improving electronic conductivity, enhancing reaction kinetics is also an important strategy to boost the electrochemical performances of sulfur-containing polymer cathodes. Applying heteroatoms to dope sulfur molecular chains in the polymer molecular structure can effectively achieve this goal [64]. Heteroatom doping in the sulfur chains can facilitate the formation of low-order Li polysulfides, since the heteroatom-sulfur bond can cleave during battery discharge [65]. In

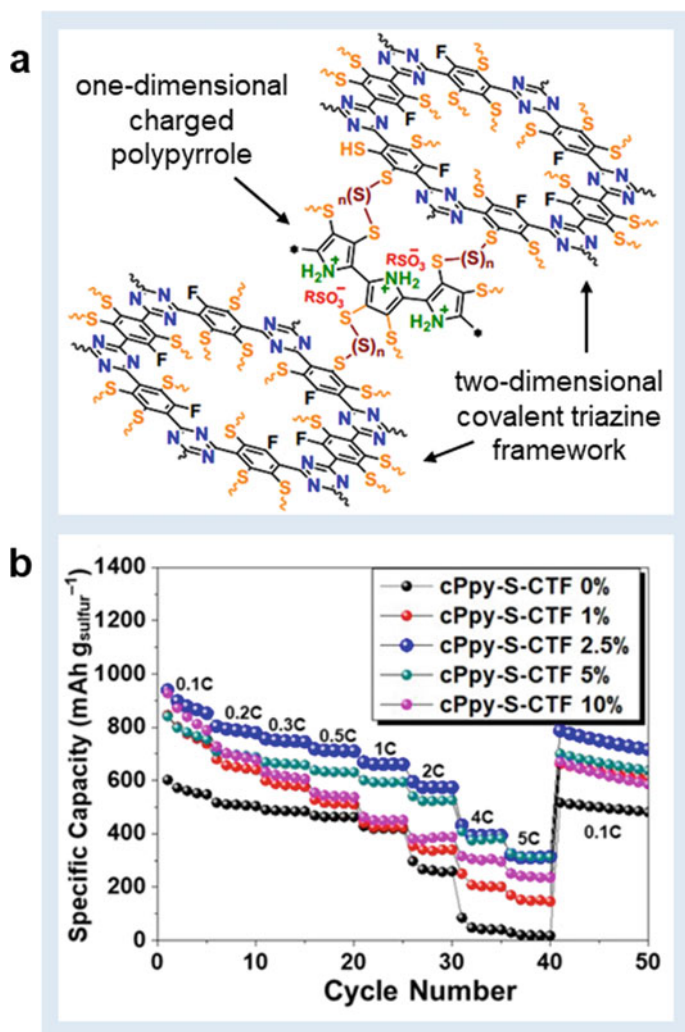


Fig. 8.18 **a** Proposed molecular structure of cPpy-S-CTF. **b** Rate performance of cPpy-S-CTF with different weight ratio of cPpy. Reprinted with permission from Ref. [16]. Copyright 2020 American Chemical Society

addition, the doping of heteroatoms (e.g., Se [54], tellurium (Te) [66]) can provide an improved electronic conductivity and a faster Li ion diffusion in the sulfur-containing polymer. For example, Dong et al. synthesized Se sulfides via co-heating elemental sulfur and SeS_2 , and used them to copolymerize with DIB to obtain S- SeS_2 -DIB copolymer (Fig. 8.19a) [17]. Solid-state NMR and XPS tests were used to prove the introduction of Se elements in the polymer molecular structure. The as-developed copolymers were melt-infused in porous carbon for battery testing. With 10 wt%

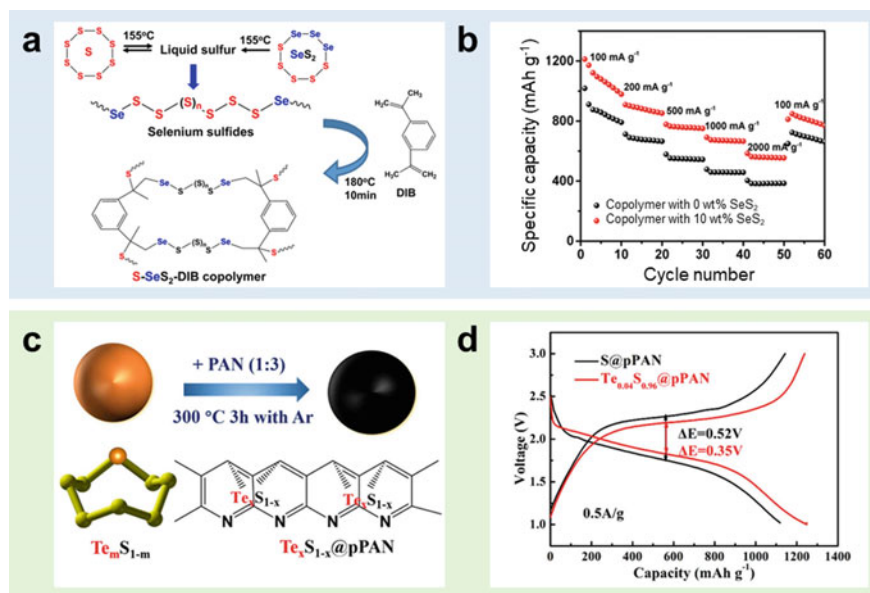


Fig. 8.19 **a** Synthesis route of S-SeS₂-DIB copolymer. **b** Rate performances of Li-S battery cathodes using such copolymer with different content of SeS₂. Reprinted with permission from Ref. [17]. Copyright 2018 American Chemical Society. **c** Synthesis process and proposed molecular structure of Te-doped SPAN. **d** Typical charge-discharge curves of Li-S batteries with different cathodes at 0.5 A g⁻¹. Reprinted with permission from Ref. [66]. Copyright 2019 Elsevier

SeS₂ addition in the copolymer synthesis, Li-S batteries delivered greatly improved rate performances (Fig. 8.19b). Similarly, Li et al. substituted Te-doped sulfur for elemental sulfur in SPAN synthesis, and obtained Te-doped SPAN (Te_xS_{1-x}@pPAN, Fig. 8.19c) [66]. Electrochemical tests and theoretical calculation indicated that the doping of Te elements reduced Li ion diffusion barrier and promoted charge transfer during battery operation. As shown in Fig. 8.19d, with a Te_{0.04}S_{0.96}@pPAN cathode, the overpotential was effectively reduced from 0.52 to 0.35 V, indicating that Te-doping facilitated the reaction kinetics and reduced the reaction overpotential in Li-S batteries.

8.4.2.2 Introducing Electrocatalysts

Introducing electrocatalysts (materials with high electrocatalytic activity) at cathode can also effectively improve the reaction kinetics of sulfur-containing polymer cathodes. This strategy has been widely applied in the research on conventional elemental-sulfur-based Li-S batteries, and a variety of materials (e.g., transition metal single atoms [67], transition metal sulfides [68]) were reported to possess high electrocatalytic activity to accelerate the conversion reaction between elemental sulfur and

Li_2S . In this regard, Liu et al. synthesized a NiS_2 -modified SPAN cathode via adding NiCO_3 in the SPAN preparation process [4]. NiS_2 not only provided strong affinity toward sulfur species, but also reduced the impedance of polymer cathode. Due to the accelerated conversion reactions of sulfur species, the as-prepared Li-S batteries using such composite cathode achieve an improved capacity of $\approx 1180 \text{ mAh g}^{-1}$ (base on the mass of sulfur) at 2 A .

8.4.3 Applying Quasi-solid-State or Solid-State Electrolytes

8.4.3.1 Applying Quasi-solid-State Electrolytes

Gel polymer electrolytes in quasi-solid state generally are composed of polymers as scaffolds and liquid electrolytes as plasticizers. The application of gel polymer electrolytes can provide much better contact at electrolyte-electrode interface than solid-state electrolytes, and meanwhile it can avoid the leakage risks of liquid electrolytes [5]. When gel polymer electrolytes are applied in Li-S batteries, they can prevent the dissolution of Li polysulfides and mechanically limit the Li metal dendrite growth. Liu et al. reported a Li-S battery based on a SPAN cathode, a Li metal anode and a polyvinylidene fluoride (PVDF)-polymethyl methacrylate (PMMA)-based gel polymer electrolyte [69]. Compared to conventional liquid electrolytes, the gel polymer electrolytes could block the diffusion of Li polysulfides and construct a stable solid electrolyte interphase (SEI) on Li metal anode (Fig. 8.20a). Considering practical application of Li-S batteries might involve heat generation which could trigger aggravated severe polysulfide dissolution and severe safety hazards, the cycling performances of Li-S batteries were investigated under $60 \text{ }^\circ\text{C}$ (Fig. 8.20b). The SPAN-based Li-S batteries with a conventional liquid electrolyte (1 M LiPF_6 in EC: DMC (1: 1 by volume)) suffered from rapid capacity decay within 40 cycles, while the batteries using gel polymer electrolyte delivered greatly improved cycling stability with a capacity of $>300 \text{ mAh g}^{-1}$ (based on the mass of SPAN) during 100 cycles.

8.4.3.2 Applying Solid-State Electrolytes

Solid-state electrolytes could not only avoid polysulfides dissolution and limit Li dendrite growth, but also provide Li-S batteries with unparalleled safety since their application could eliminate the safety risks of conventional liquid electrolytes (e.g., liquid leakage, flammability) [70, 71]. Solid-state electrolytes used in couple with sulfur-containing cathodes include three types: solid polymer electrolytes (e.g., poly(ethylene oxide) (PEO)-based electrolytes), solid inorganic electrolytes (e.g., sulfide-based electrolytes [72]), and solid composite electrolytes [73]. Gracia et al. reported an all-solid-state Li-S battery based on sulfur-divinylbenzene (DVB) copolymer cathode, Li metal anode, and LiTFSI-PEO solid-state electrolyte [74].

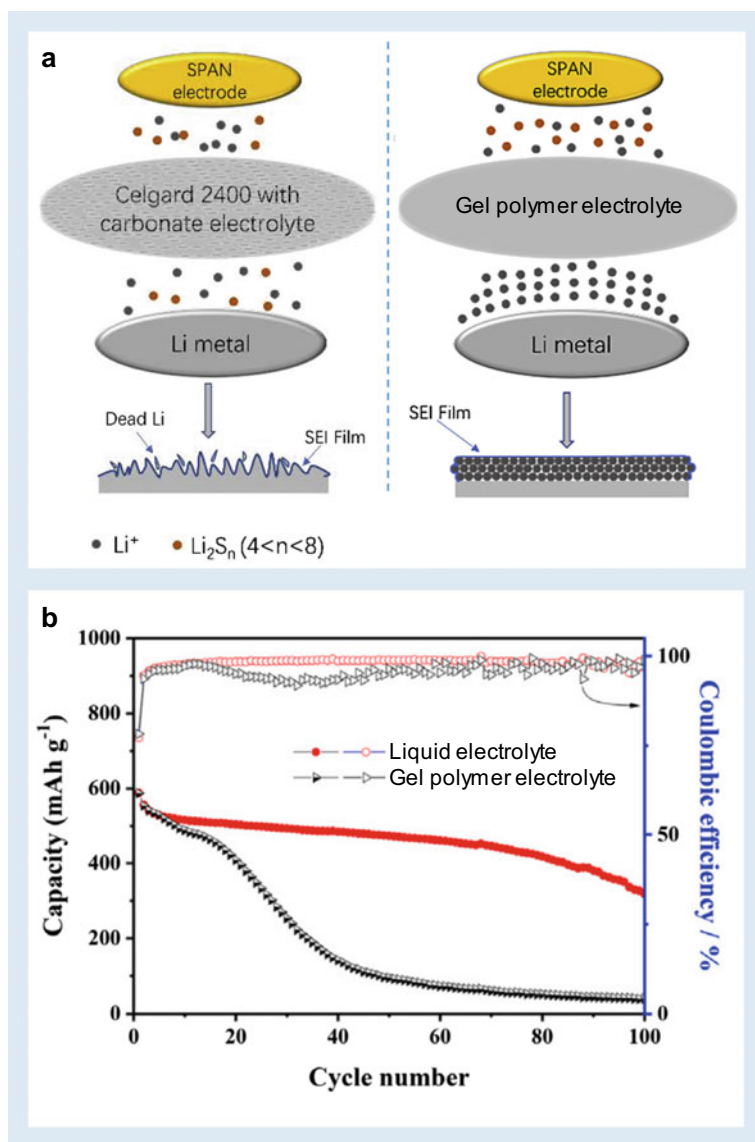


Fig. 8.20 **a** Schematic illustration of SPAN-based Li-S batteries using different electrolytes: liquid electrolytes (left column) and gel polymer electrolytes (right column). **b** Cycling performances of SPAN-based Li-S batteries using different electrolytes at 250 mA g^{-1} under 60°C . Reprinted with permission from Ref. [69]. Copyright 2019 Elsevier

Since the application of PEO-based solid-state electrolyte and polymeric sulfur cathode both had strong effects on suppressing polysulfide shuttling, the as-developed Li-S battery delivered a decent capacity of $\approx 700 \text{ mAh g}^{-1}$ after 50 cycles at 0.1 C under 70 °C. Wang et al. reported a surface modified $\text{Li}_{1.3}\text{Al}_{0.3}\text{Ti}_{1.7}(\text{PO}_4)_3$ (LATP, a lithium super ionic conductor (LISICON)-type solid-state electrolyte) solid-state electrolyte for SPAN-based Li-S batteries (Fig. 8.21a) [75]. The surface modifica-

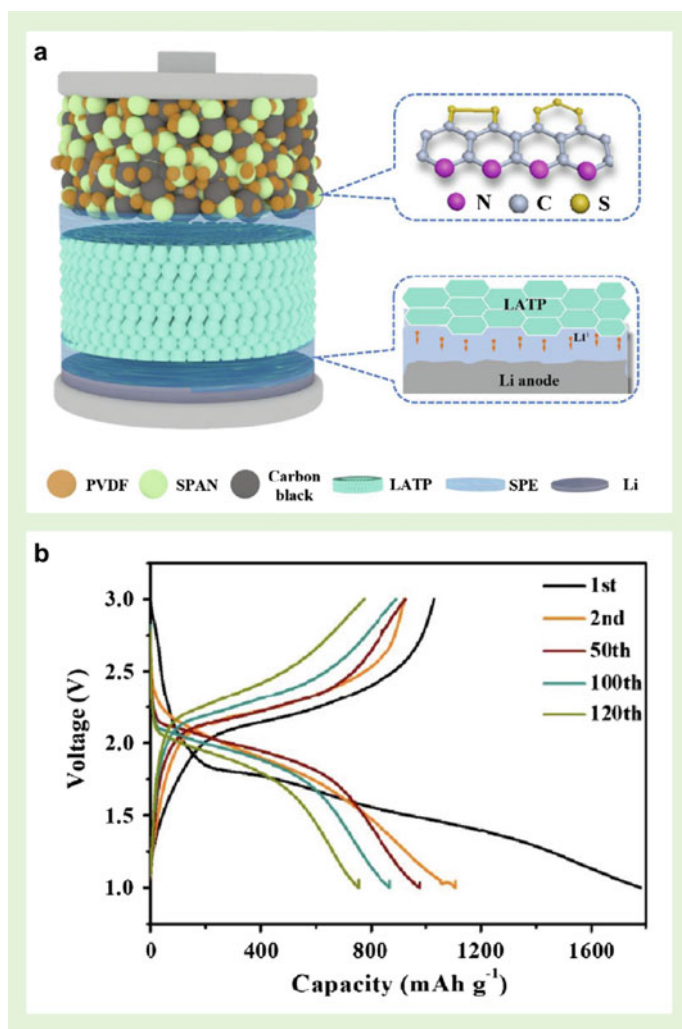


Fig. 8.21 **a** Schematic illustration of a Li-S battery using SPAN cathode and SPE-LATP-SPE sandwiched solid-state electrolyte. SPE refers to the surface solid polymer electrolyte coating layer. **b** Charge-discharge profiles of such battery in different cycles at 0.1 C under 75 °C. Reprinted with permission from Ref. [75]. Copyright 2020 Elsevier

tion was realized via a solid polymer electrolyte layer with compositions of PEO and LiTFSI (molar ratio of ethylene oxide: Li = 8: 1), which provided improved interfacial contact and avoid the side reaction between Li metal and LATP. Such batteries delivered good electrochemical performances at a relatively high temperature. In cycling tests under 75 °C, the as-developed batteries delivered a capacity of 784 mAh g⁻¹ (based on the mass of sulfur) after 120 cycles at 0.1 C (Fig. 8.21b).

8.5 Summary and Outlook

Low-cost and environmentally benign Li–S batteries are regarded as promising candidates for future high energy-density energy storage systems. Sulfur-containing polymers have attracted intensive attention in Li–S battery cathode research, since they can effectively alleviate the notorious shuttle effect and thus significantly increase the lifespan of Li–S batteries. In this chapter, we provide a systematical summarization in sulfur-containing polymer cathodes and their different electrochemical behaviors (i.e., conventional redox chemistry and solid-phase conversion) in Li–S batteries. Furthermore, we detailed the improving strategies for sulfur-containing polymer cathodes in Li–S batteries, including adding conductive additives (e.g., carbonaceous materials, conductive polymers), introducing reaction accelerators (e.g., heteroatoms, electrocatalysts), and applying quasi-solid-state or solid-state electrolytes. For now, although the research on sulfur-containing polymers greatly promoted the development of Li–S batteries, some problems such as limited mechanism understanding and insufficient practical application tests still exist and urgently need to be solved. Therefore, future research on sulfur-containing polymer cathodes in Li–S batteries should be concentrated in the following directions:

- (1) More in-depth research needs to be conducted to further investigate the working mechanisms of sulfur-containing polymer with different morphology, heteroatoms, functional groups, etc. Sulfur-containing polymers with precisely designed molecular structure and better electrochemical performance should be developed during this process. Multiple advanced testing equipment can be used to facilitate the research, e.g., in-situ solid-state NMR, in-situ XPS, in-situ Raman spectra.
- (2) Generally, the addition of polymer molecular structure can improve the cycle stability of Li–S battery cathodes, but meanwhile it could reduce the energy density and/or increase the polarization of the batteries. Therefore, optimized polymer structures coupled with few-amount addition of conductive additives or electrocatalyst needs to be further developed to effectively balance the cycle stability and energy density of Li–S batteries.
- (3) While applying the sulfur-containing polymers at cathode, attentions should be paid to the anode performances, since Li metal anodes as the frequently used anodes face many problems that result in fast battery capacity decay as well. If necessary, 3D current collectors or artificial protecting layers should be

- employed at Li metal anode to better evaluate the electrochemical performances of sulfur-containing polymer cathodes. In addition, beyond-Li metal anodes, e.g., lithiated graphite or silicon, can be studied more in couple with sulfur-containing polymer cathodes in Li–S batteries to achieve higher safety.
- (4) When evaluating electrochemical performances of sulfur-containing polymer cathodes, specific conditions including high sulfur mass loading and lean electrolyte dosage need be considered to better meet the practical application requirements. In addition, soft-packaged battery configuration needs to be adopted in testing of Li–S batteries using sulfur-containing polymer cathodes.
 - (5) Considering future practical applications, battery safety is a critical issue for Li–S batteries. Thus, developing electrolytes with higher safety is very important. This can be realized by inflammable liquid organic solvents, flame-retardant additives, and highly concentrated electrolytes. Furthermore, quasi-solid-state and solid-state electrolytes with non-leakage property and much higher safety need to be applied more in research on sulfur-containing polymer cathode-based Li–S batteries.

Although the research on sulfur-containing polymer cathode is still in its infancy and many problems need to be solved, the much-improved electrochemical performances of sulfur-containing polymer cathodes (compared to elemental sulfur) endow them to be promising cathode materials for Li–S batteries. Considering the rapid development of sulfur-containing polymer cathodes in recent years, sulfur-containing polymer cathodes can play an important role in next-generation Li–S batteries and other sulfur-based batteries.

Acknowledgements Prof. G. Wang would like to acknowledge the support by the Australian Research Council (ARC) Discovery Projects (DP200101249 and DP210101389).

References

1. Chung SH, Chang CH, Manthiram A (2018) Progress on the critical parameters for lithium-sulfur batteries to be practically viable. *Adv Funct Mater* 28:1801188
2. Fang R, Zhao S, Sun Z, Wang DW, Cheng HM, Li F (2017) More reliable lithium-sulfur batteries: status, Solutions and Prospects. *Adv Mater* 29:1606823
3. Zhao M, Li BQ, Peng HJ, Yuan H, Wei JY, Huang JQ (2020) Lithium-sulfur batteries under lean electrolyte conditions: challenges and opportunities. *Angew Chem-Int Edit* 59:12636–12652
4. Liu Y, Wang W, Wang A, Jin Z, Zhao H, Yang Y (2017) A polysulfide reduction accelerator-NiS₂-modified sulfurized polyacrylonitrile as a high performance cathode material for lithium-sulfur batteries. *J Mater Chem A* 5:22120–22124
5. Zhou D, Shanmukaraj D, Tkacheva A, Armand M, Wang G (2019) Polymer electrolytes for lithium-based batteries: advances and prospects. *Chem* 5:2326–2352
6. Su D, Zhou D, Wang C, Wang G (2018) Toward high performance lithium-sulfur batteries based on Li₂S cathodes and beyond: status, challenges, and perspectives. *Adv Funct Mater* 28:1800154
7. Zhu J, Zhu P, Yan C, Dong X, Zhang X (2019) Recent progress in polymer materials for advanced lithium-sulfur batteries. *Prog Polym Sci* 90:118–163

8. Simmonds AG, Griebel JJ, Park J, Kim KR, Chung WJ, Oleshko VP, Kim J, Kim ET, Glass RS, Soles CL, Sung Y-E, Char K, Pyun J (2014) Inverse vulcanization of elemental sulfur to prepare polymeric electrode materials for Li-S batteries. *ACS Macro Lett* 3:229–232
9. Zhou D, Chen Y, Li B, Fan H, Cheng F, Shanmukaraj D, Rojo T, Armand M, Wang G (2018) A stable quasi-solid-state sodium-sulfur battery. *Angew Chem-Int Edit* 57:10168–10172
10. Tang X, Zhou D, Li P, Guo X, Sun B, Liu H, Yan K, Gogotsi Y, Wang G (2020) MXene-based dendrite-free potassium metal batteries. *Adv Mater* 32:1906739
11. Chung WJ, Griebel JJ, Kim ET, Yoon H, Simmonds AG, Ji HJ, Dirlam PT, Glass RS, Wie JJ, Nguyen NA, Guralnick BW, Park J, Somogyi A, Theato P, Mackay ME, Sung Y-E, Char K, Pyun J (2013) The use of elemental sulfur as an alternative feedstock for polymeric materials. *Nat Chem* 5:518–524
12. Kim H, Lee J, Ahn H, Kim O, Park MJ (2016) Synthesis of three-dimensionally interconnected sulfur-rich polymers for cathode materials of high-rate lithium-sulfur batteries. *Nat Commun* 6:7278
13. Shin H, Kim D, Kim HJ, Kim J, Char K, Yavuz CT, Choi JW (2019) Fluorinated covalent organic polymers for high performance sulfur cathodes in lithium–sulfur batteries. *Chem Mater* 31:7910–7921
14. Wang W, Cao Z, Elia GA, Wu Y, Wahyudi W, Abou-Hamad E, Emwas A-H, Cavallo L, Li L-J, Ming J (2018) Recognizing the mechanism of sulfurized polyacrylonitrile cathode materials for Li-S batteries and beyond in Al-S batteries. *ACS Energy Lett* 3:2899–2907
15. Preefer MB, Oschmann B, Hawker CJ, Seshadri R, Wudl F (2017) High sulfur content material with stable cycling in lithium-sulfur batteries. *Angew Chem-Int Edit* 56:15118–15122
16. Kim J, Elabd A, Chung S-Y, Coskun A, Choi JW (2020) Covalent triazine frameworks incorporating charged polypyrrole channels for high performance lithium-sulfur batteries. *Chem Mater* 32(10):4185–4193
17. Dong P, Han KS, Lee J-I, Zhang X, Cha Y, Song M-K (2018) Controlled synthesis of sulfur-rich polymeric selenium sulfides as promising electrode materials for long-life, high-rate lithium metal batteries. *ACS Appl Mater Interfaces* 10:29565–29573
18. Gomez I, Leonet O, Blazquez JA, Grande H-J, Mecerreyes D (2018) Poly(anthraquinonyl sulfides): high capacity redox polymers for energy storage. *ACS Macro Lett* 7:419–424
19. Zhang X, Chen K, Sun Z, Hu G, Xiao R, Cheng H-M, Li F (2020) Structure-related electrochemical performance of organosulfur compounds for lithium-sulfur batteries. *Energy Environ Sci* 13:1076–1095
20. Wei S, Ma L, Hendrickson KE, Tu Z, Archer LA (2015) Metal-sulfur battery cathodes based on PAN-sulfur composites. *J Am Chem Soc* 137(37):12143–12152
21. Zhang Y, Griebel JJ, Dirlam PT, Nguyen NA, Glass RS, Mackay ME, Char K, Pyun J (2017) Inverse vulcanization of elemental sulfur and styrene for polymeric cathodes in Li-S batteries. *J Polym Sci Pol Chem* 55:107–116
22. Chen Z, Droste J, Zhai G, Zhu J, Yang J, Hansen MR, Zhuang X (2019) Sulfur-anchored azulene as a cathode material for Li-S batteries. *Chem Commun* 55:9047–9050
23. Zhao F, Li Y, Feng W (2018) Recent advances in applying vulcanization/inverse vulcanization methods to achieve high-performance sulfur containing polymer cathode materials for Li-S batteries. *Small Methods* 2:1800156
24. Nguyen DT, Hoefling A, Yee M, Nguyen GTH, Theato P, Lee YJ, Song S-W (2019) Enabling high-rate and safe lithium ion-sulfur batteries by effective combination of sulfur-copolymer cathode and hard-carbon anode. *Chemsuschem* 12:480–486
25. Hoefling A, Nguyen DT, Partovi-Azar P, Sebastiani D, Theato P, Song S-W, Lee YJ (2018) Mechanism for the stable performance of sulfur-copolymer cathode in lithium-sulfur battery studied by solid-state NMR spectroscopy. *Chem Mater* 30:2915–2923
26. Zeng S, Li L, Zhao D, Liu J, Niu W, Wang N, Chen S (2017) Polymer-capped sulfur copolymers as lithium-sulfur battery cathode: enhanced performance by combined contributions of physical and chemical confinements. *J Phys Chem C* 121:2495–2503
27. Liu X, Wang S, Wang A, Chen J, Wang Z, Zeng Q, Liu W, Li Z, Zhang L (2019) A new conjugated porous polymer with covalently linked polysulfide as cathode material for high-rate

- capacity and high coulombic efficiency lithium-sulfur batteries. *J Phys Chem C* 123:21327–21335
28. Kang H, Kim H, Park MJ (2018) Sulfur-rich polymers with functional linkers for high capacity and fast-charging lithium-sulfur batteries. *Adv Energy Mater* 1802423
 29. Oschmann B, Park J, Kim C, Char K, Sung Y-E, Zentel R (2015) Copolymerization of polythiophene and sulfur to improve the electrochemical performance in lithium-sulfur batteries. *Chem Mater* 27(20):7011–7017
 30. Tiwari VK, Song H, Oh Y, Jeong Y (2020) Synthesis of sulfur-co-polymer/porous long carbon nanotubes composite cathode by chemical and physical binding for high performance lithium-sulfur batteries. *Energy* 195:117034
 31. Sun Z, Xiao M, Wang S, Han D, Song S, Chen G, Meng Y (2014) Sulfur-rich polymeric materials with semiinterpenetrating network structure as a novel lithium-sulfur cathode. *J Mater Chem A* 2:9280–9286
 32. Dirlam PT, Simmonds AG, Kleine TS, Nguyen NA, Anderson LE, Klever AO, Florian A, Costanzo PJ, Theato P, Mackay ME, Glass RS, Charf K, Pyun J (2015) Inverse vulcanization of elemental sulfur with 1,4-diphenylbutadiyne for cathode materials in Li-S batteries. *RSC Adv* 5:24718–24722
 33. Wu F, Chen S, Srot V, Huang Y, Sinha SK, Aken PA, Maier J, Yu Y (2018) A sulfur-limonene-based electrode for lithium-sulfur batteries: high-performance by self-protection. *Adv Mater* 1706643
 34. Hoefling A, Lee YJ, Theato P (2017) Sulfur-based polymer composites from vegetable oils and elemental sulfur: a sustainable active material for Li-S batteries. *Macromol Chem Phys* 218(1):1600303
 35. Je SH, Hwang TH, Talapaneni SN, Buyukcakir O, Kim HJ, Yu J-S, Woo S-G, Jang MC, Son BK, Coskun A, Choi JW (2016) Rational sulfur cathode design for lithium-sulfur batteries: sulfur-embedded benzoxazine polymers. *ACS Energy Lett* 1(3):566–572
 36. Krishnaraj C, Jena HS, Leus K, Voort PVD (2020) Covalent triazine frameworks—a sustainable perspective. *Green Chem* 22:1038–1071
 37. Talapaneni SN, Hwang TH, Je SH, Buyukcakir O, Choi JW, Coskun A (2016) Elemental-sulfur-mediated facile synthesis of a covalent triazine framework for high-performance lithium-sulfur batteries. *Angew Chem-Int Ed* 55(9):3106–3111
 38. Xu F, Yang S, Jiang G, Ye Q, Wei B, Wang H (2017) Fluorinated, sulfur-rich, covalent triazine frameworks for enhanced confinement of polysulfides in lithium-sulfur batteries. *ACS Appl Mater Interfaces* 9:37731–37738
 39. Wang X, Qian Y, Wang L, Yang H, Li H, Zhao Y, Liu T (2019) Sulfurized polyacrylonitrile cathodes with high compatibility in both ether and carbonate electrolytes for ultrastable lithium-sulfur batteries. *Adv Funct Mater* 1902929
 40. Je SH, Kim HJ, Kim J, Choi JW, Coskun A (2017) Perfluoroaryl-elemental sulfur SNAr chemistry in covalent triazine frameworks with high sulfur contents for lithium-sulfur batteries. *Adv Funct Mater* 27:1703947
 41. Zeng S, Li L, Yu J, Wang N, Chen S (2018) Highly crosslinked organosulfur copolymer nanosheets with abundant mesopores as cathode materials for efficient lithium-sulfur batteries. *Electrochim Acta* 263:53–59
 42. Zhou H, Yu F, Wei M, Su Y, Ma Y, Wang D, Shen Q (2019) Substituting copolymeric poly(alkylenetetrasulfide) for elemental sulfur to diminish the shuttling effect of modified intermediate polysulfides for high-performance lithium-sulfur batteries. *Chem Commun* 55:3729–3732
 43. Hua H, Zhao B, Cheng H, Dai S, Kane N, Yu Y, Liu M (2019) A robust 2D organic polysulfane nanosheet with grafted polycyclic sulfur for highly reversible and durable lithium-organosulfur batteries. *Nano Energy* 57:635–643
 44. Yin L, Wang J, Lin F, Yang J, Nuli Y (2012) Polyacrylonitrile/graphene composite as a precursor to a sulfur-based cathode material for high-rate rechargeable Li-S batteries. *Energy Environ Sci* 5:6966

45. Wang J, Yang J, Xie J, Xu N (2002) A novel conductive polymer-sulfur composite cathode material for rechargeable lithium batteries. *Adv Mater* 14:963–965
46. Wang J, Yang J, Nuli Y, Holze R (2007) Room temperature Na/S batteries with sulfur composite cathode materials. *Electrochem Commun* 9:31–34
47. Hwang TH, Jung DS, Kim J-S, Kim BG, Choi JW (2013) One-dimensional carbon–sulfur composite fibers for Na-S rechargeable batteries operating at room temperature. *Nano Lett* 13:4532–4538
48. Yang H, Chen J, Yang J, Wang J (2020) Prospect of sulfurized pyrolyzed poly(acrylonitrile) (S@pPAN) cathode materials for rechargeable lithium batteries. *Angew Chem-Int Ed* 59(19):7306–7318
49. Weret MA, Kuo C-FJ, Zeleke TS, Beyene TT, Tsai M-C, Huang C-J, Berhe GB, Su W-N, Hwang B-J (2020) Mechanistic understanding of the sulfurized-poly(acrylonitrile) cathode for lithium-sulfur batteries. *Energy Storage Mater* 26:483–493
50. Fanous J, Wegner M, Grimminger J, Andresen A, Buchmeiser MR (2011) Structure-related electrochemistry of sulfur-poly(acrylonitrile) composite cathode materials for rechargeable lithium batteries. *Chem Mater* 23:5024–5028
51. Warneke S, Hintennach A, Buchmeiser MR (2018) Communication—influence of carbonate-based electrolyte composition on cell performance of SPAN-based lithium-sulfur-batteries. *J Electrochem Soc* 165:A2093–A2095
52. Gao J, Lowe MA, Kiya Y, Abruña HD (2011) Effects of liquid electrolytes on the charge-discharge performance of rechargeable lithium/sulfur batteries: electrochemical and in-situ X-ray absorption spectroscopic studies. *J Phys Chem C* 115:25132–25137
53. Xu Z, Wang J, Yang J, Miao X, Chen R, Qian J, Miao R (2016) Enhanced performance of a lithium-sulfur battery using a carbonate-based electrolyte. *Angew Chem-Int Ed* 55:10372–10375
54. Chen X, Peng L, Wang L, Yang J, Hao Z, Xiang J, Yuan K, Huang Y, Shan B, Yuan L, Xie J (2019) Ether-compatible sulfurized polyacrylonitrile cathode with excellent performance enabled by fast kinetics via selenium doping. *Nat Commun* 10:1021
55. Wang J, Yin L, Jia H, Yu H, He Y, Yang J, Monroe CW (2014) Hierarchical sulfur-based cathode materials with long cycle life for rechargeable lithium batteries. *ChemSuschem* 7:563–569
56. Zeng S-Z, Zeng X, Tu W, Huang H, Yu L, Yao Y, Jin N, Zhang Q, Zou J (2018) A universal strategy to prepare sulfur-containing polymer composites with desired morphologies for lithium-sulfur batteries. *ACS Appl Mater Interfaces* 10:22002–22012
57. Yin L, Wang J, Yang J, Nuli Y (2011) A novel pyrolyzed polyacrylonitrile-sulfur@MWCNT composite cathode material for high-rate rechargeable lithium/sulfur batteries. *J Mater Chem* 21:6807–6810
58. Hu G, Sun Z, Shi C, Fang R, Chen J, Hou P, Liu C, Cheng H-M, Li F (2017) A sulfur-rich copolymer@CNT hybrid cathode with dual-confinement of polysulfides for high-performance lithium-sulfur batteries. *Adv Mater* 1603835
59. Zeng S, Li L, Xie L, Zhao D, Zhou N, Wang N, Chen S (2017) Graphene-supported highly crosslinked organosulfur nanoparticles as cathode materials for high-rate, Long-Life Lithium-Sulfur Battery. *Carbon* 122:106–113
60. Ding B, Chang Z, Xu G, Nie P, Wang J, Pan J, Dou H, Zhang X (2015) Nanospace-confinement copolymerization strategy for encapsulating polymeric sulfur into porous carbon for lithium-sulfur batteries. *ACS Appl Mater Interfaces* 7(21):11165–11171
61. Chang C-H, Manthiram A (2018) Covalently grafted polysulfur-graphene nanocomposites for ultrahigh sulfur-loading lithium-polysulfur batteries. *ACS Energy Lett* 3(1):72–77
62. Shen K, Mei H, Li B, Ding J, Yang S (2017) 3D printing sulfur copolymer-graphene architectures for Li-S batteries. *Adv Energy Mater* 1701527
63. Shi Y, Peng L, Ding Y, Zhao Y, Yu G (2015) Nanostructured conductive polymers for advanced energy storage. *Chem Soc Rev* 44:6684–6696
64. Gomez I, Mantione D, Leonet O, Blazquez JA, Mecerreyes D (2018) Hybrid sulfur-selenium co-polymers as cathodic materials for lithium batteries. *ChemElectroChem* 5:260–265

65. Park S, Kim S-J, Sung Y-E, Char K, Son JG (2019) Short-chain polyselenosulfide copolymers as cathode materials for lithium-sulfur batteries. *ACS Appl Mater Interfaces* 11:45785–45795
66. Li S, Han Z, Hu W, Peng L, Yang J, Wang L, Zhang Y, Shan B, Xie J (2019) Manipulating kinetics of sulfurized polyacrylonitrile with tellurium as eutectic accelerator to prevent polysulfide dissolution in lithium-sulfur battery under dissolution-deposition mechanism. *Nano Energy* 60:153–161. <https://doi.org/10.1016/j.nanoen.2019.03.023>
67. Du Z, Chen X, Hu W, Chuang C, Xie S, Hu A, Yan W, Kong X, Wu X, Ji H, Wan L-J (2019) Cobalt in nitrogen-doped graphene as single-atom catalyst for high-sulfur content lithium-sulfur batteries. *J Am Chem Soc* 141:3977–3985
68. Kim SJ, Kim K, Park J, Sung YE (2019) Role and potential of metal sulfide catalysts in lithium-sulfur battery applications. *ChemCatChem* 11:2373–2387
69. Liu Y, Yang D, Yan W, Huang Q, Zhu Y, Fu L, Wu Y (2019) Synergy of sulfur/polyacrylonitrile composite and gel polymer electrolyte promises heat-resistant lithium-sulfur batteries. *iScience* 19:316–325
70. Sun C, Liu J, Gong Y, Wilkinson DP, Zhang J (2017) Recent advances in all-solid-state rechargeable lithium batteries. *Nano Energy* 33:363–386
71. Wang Y, Zhou D, Palomares V, Shanmukaraj D, Sun B, Tang X, Wang C, Armand M, Rojo T, Wang G (2020) Revitalising sodium-sulfur batteries for non-high-temperature operation: a crucial review. *Energy Environ Sci* 13:3848–3879
72. Zhang Y, Sun Y, Peng L, Yang J, Jia H, Zhang Z, Shan B, Xie J (2019) Se as eutectic accelerator in sulfurized polyacrylonitrile for high performance all-solid-state lithium-sulfur battery. *Energy Storage Mater* 21:287–296
73. Li M, Frerichs JE, Kolek M, Sun W, Zhou D, Huang CJ, Hwang BJ, Hansen MR, Winter M, Bieker P (2020) Solid-state lithium-sulfur battery enabled by thio-LiSICON/polymer composite electrolyte and sulfurized polyacrylonitrile cathode. *Adv Funct Mater* 30:1910123
74. Gracia I, Benyoucef H, Judez X, Oteo U, Zhang H, Li C, Rodriguez-Martinez LM, Armand M (2018) S-containing copolymer as cathode material in poly(ethylene oxide)-based all-solid-state Li-S batteries. *J Power Sources* 390:148–152
75. Wang Y, Wang G, He P, Hu J, Jiang J, Fan L-Z (2020) Sandwich structured NASICON-type electrolyte matched with sulfurized polyacrylonitrile cathode for high performance solid-state lithium-sulfur batteries. *Chem Eng J* 393:124705

Chapter 9

Advanced Characterization Techniques and Mechanistic Understanding



Cheng Zhou, Binbin Shuai, Xu Xu, and Liqiang Mai

Abstract With the in-depth research and rapid development of lithium sulfur (Li–S) batteries, great breakthroughs have been made in electrochemical performance, especially in cycle life and energy density. Behind a lot of success is inseparable from the support of advanced characterization technologies, which provide important structural and chemical properties analysis. In this chapter, we will focus on the special contributions brought by the various in situ/operando characterization techniques in the history of the development of Li–S batteries. And finally, we look forward to the fact that even though the commercialization of Li–S batteries is still limited by a sort of factors, we believe that in situ/operando characterization techniques will keep playing an irreplaceable role towards this ultimate purpose.

Keywords In situ/operando characterization · Polysulfide conversion · Electrochemical mechanism

9.1 Introduction

It is well known that running lithium sulfur (Li–S) batteries work in enclosed environments, which are considered black boxes, and researchers need to take apart the battery and check the electrode status during charge or discharge. However, the lithium metal anode used and the polysulfides produced in Li–S battery are very unstable in air, which makes the ex situ characterization very difficult, and the characterization results are not very consistent with the actual situation.

In 2017, Mai et al. delivered an important comment, calling for the use of advanced in situ characterization techniques for real-time monitoring of battery capacity degradation and reaction process [1]. In recent years, a large number

C. Zhou · B. Shuai · X. Xu (✉) · L. Mai (✉)
State Key Laboratory of Advanced Technology for Materials Synthesis and Processing, Wuhan University of Technology, Wuhan 430070, China
e-mail: xuxu@whut.edu.cn

L. Mai
e-mail: mlq518@whut.edu.cn



Fig. 9.1 Different in situ characterization techniques for understanding the reactions in Li-S battery

of in situ/operando characterization techniques have also been used to reveal the structural and chemical composition changes of Li-S batteries during cycling. Different from ex situ characterizations, which requires the battery to be disassembled after being charged or discharged to a specific voltage for characterization, “in situ” means to monitor the battery in real time during the battery cycle without affecting the normal cycle of the battery [2]. Based on the information reflected by different in situ characterization techniques, these characterization methods can be divided into three categories (Fig. 9.1): (1) Test phase transformation, including X-ray diffraction (XRD), (2) Observe morphology evolution, including transmission electron microscopy (TEM), atomic force microscopy (AFM), transmission X-ray microscopy (TXM), X-ray tomography (XRT), (3) Detect polysulfide intermediate phases, including Raman spectroscopy, ultraviolet visible (UV-Vis) absorption spectroscopy, X-ray absorption near-edge structure (XANES), nuclear magnetic resonance (NMR), high-performance liquid chromatography (HPLC), X-ray photoelectron spectroscopy (XPS), X-ray radiography (XRR), electron paramagnetic resonance (EPR), and Fourier transform infrared (FTIR). These in situ characterization techniques reveal the composition changes of electrode materials, electrolyte and interface during the charge/discharge process, which deepen our understanding of the reaction mechanisms of Li-S battery [3]. As shown in Table 9.1, different characterization techniques have one or more unique functions, which can’t be replaced by other characterization techniques. Based on this principle, this chapter summarizes the foundation works and the recent advances of different in situ characterization techniques in Li-S battery, including the application of in situ techniques and the development of novel in situ devices. The testing mechanisms of different in situ/operando characterization techniques and the existing problems are also summarized. Finally, possible solutions and other characterization methods are proposed. This chapter will provide a deep understanding of the application of in situ/operando characterization techniques in Li-S battery, and provide a certain reference for the development of high-performance Li-S battery.

Table 9.1 In situ/operando parameters for Li–S battery research

Technology	Unique applications
XRD	Phase change between crystal sulfur and lithium sulfide during charge and discharge
TEM	High-resolution morphological evolution of solid-phase sulfur and Li ₂ S
AFM	The formation of SEI
TXM	Distribution of sulfur
SEM	Changes in morphology during the charge and discharge cycle
XRT	Three-dimensional distribution of sulfur
XANES	Detection of amorphous solid phase and lithium polysulfide
Raman	Qualitative detection of long-chain polysulfide secondary anions
UV–Vis	The difference between long-chain and short-chain polysulfide
NMR	Detection of polysulfide species and monitoring of lithium microstructures
HPLC	Quantitative analysis of dissolved polysulfide and sulfur
FTIR	Characterizing the surface species including fragmented molecules, functional groups, and radicals of the electrodes
XRR	Macro-structure evolution
EPR/ESR	Detection of free-based species, especially free-based S ₃ ⁻
XPS	The chemical properties of interfaces have evolved

9.2 In Situ/Operando XRD

As we know, XRD is one of the earliest and most widely used techniques for in situ characterization of the phase transformation in electrode materials for Li-ion battery, as well as for Li–S batteries. The earliest application of in situ XRD in Li–S battery can be traced back to 2012 [4]. Cui et al. found that the crystalline Li₂S is not detected by in situ methods (Fig. 9.2a–e). The authors also proved that the preparation method of cathode will greatly affect the recrystallization process of sulfur. In particular, Cañas et al. reported that in the lower discharge plateau at 1.8 V, a crystalline Li₂S was formed in the discharge state (60%). In the subsequent charging reaction, Li₂S fully reacts and sulfur recrystallizes [5]. Similarly, Demir-Cakan et al. [6] and Walus et al. [7] have also reported Li₂S crystallization on the cathode in the lower discharge platform. The inconsistent results may be caused by different in situ devices and composite cathodes. As we know, it is difficult to detect Li₂S₂ ions in conventional ether-based electrolyte. In 2016, the crystalline Li₂S₂ ions were firstly detected by Paoletta et al. with a high concentration electrolyte [8]. In addition, Alloin et al. found that the α-S₈ coexisted with β-S₈ during charging. They also considered that most of the discharge products are Li₂S or Li₂S₂ [9]. The phase transformation of S₈ with different crystal structure was also confirmed by other works by in situ XRD [10].

For a long time, it was difficult to directly observe the polysulfides produced during cycling with in situ XRD characterization. Many studies have made great efforts to monitor the appearance of polysulfides directly by in situ XRD. The typical work for

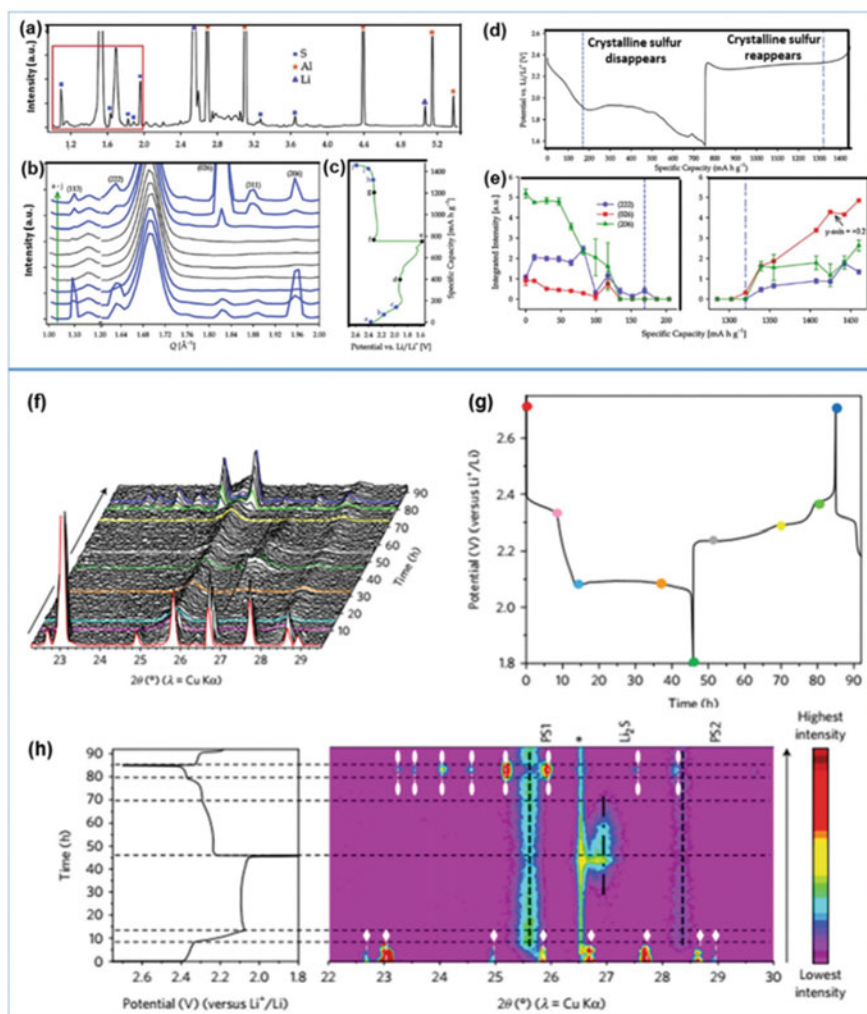


Fig. 9.2 Schematic and examples of in operando XRD measurements of Li–S batteries. **a–e** The battery was cycled with a sulfur/Super P composite electrode material at C/8. **a** XRD pattern at the start of the discharge process. **b** XRD patterns for the region of Q–space marked by the red box in **(a)**. **c** The corresponding voltage profile. **d** Integrated diffraction–peak intensities of elemental sulfur, and the corresponding voltage profile. **f–h** The battery was investigated by using fumed SiO₂ as an electrolyte additive to exploit its adsorption of polysulfides during the first cycle of the Li–S battery at a C/50 rate. **f** Waterfall representation of the XRD patterns. **g** The corresponding discharge/charge curve. **h** XRD contour plot of the data shown in **(f)**, with the same discharge/charge curve as shown in **(g)** (**a–e** Adapted with permission from Ref. [4], Copyright (2012) American Chemical Society, **f–h** Reprinted with permission from Ref. [11], Copyright (2017) Macmillan Publishers Ltd.)

directly observing polysulfides was reported by Vिलлевилле et al. By adding fumed SiO_2 into the electrolyte, the intermediate polysulfides can be attached to the surface of glass fiber, and the corresponding relationship between the formation of different polysulfides and voltage can be directly observed by in situ XRD (Fig. 9.2f–h) [11]. Using this approach, the polysulfides became visible under X-rays. On the other hand, the fumed SiO_2 can be served as an electrolyte additive, which enable efficient adsorption of soluble polysulfides [12], which will greatly promote the development of in situ XRD in the mechanism research of Li–S battery.

9.3 In Situ/Operando Morphological Characteristic Techniques

The form of electrode material is the key factor to optimize the performance of Li–S battery. So far, many model batteries were used for in situ/operation technologies, and they are assembled by working electrode and electrolyte in advanced equipment to study the interface reaction process. Because the electrochemical reaction can be better observed in the nanoscale, the electron microscope plays a decisive role in monitoring the morphological changes of the electrode microstructure, including TEM, AFM, SEM, TXM, XRT, and so on.

9.3.1 TEM

In situ TEM technology can obtain the real-time information of electrode in the process of electrochemical reaction at high spatial resolution, mainly observing the evolution of microstructure. In situ TEM has been applied in the study of Li–S battery to observe the transformation of solid sulfur and Li_2S [13]. For example, due to the good flexibility and strong van der Waals force between layers of two-dimensional materials, Tang et al. studied the detailed discharge/charging process of sulfur particles captured by MoS_2 sheet using in situ TEM [14], in which the setup of in situ TEM is similar to that reported previously (Fig. 9.3a). During discharging and charging, the morphological changes of the MoS_2 -encapsulated sulfur ball are highly reversible, as shown in Fig. 9.3b. At the same time, they found that the active sulfur particles can be hermetically confined within this two-dimensional material. In 2016, Kim et al. reported their dynamic study on the lithification of sulfur particles in carbon nanotubes [15]. Through their in situ TEM study, the authors proved that sulfur could be directly converted to Li_2S (Fig. 9.3c), without the formation of intermediate products, such as lithium polysulfide with high solubility. Their research is of great significance to solve the key problems of Li–S battery. Subsequently, Xu et al. also found that the porous carbon nanofiber/sulfur composite cathode material had a phenomenon of volume expansion at high rate of charge and discharge (Fig. 9.3d),

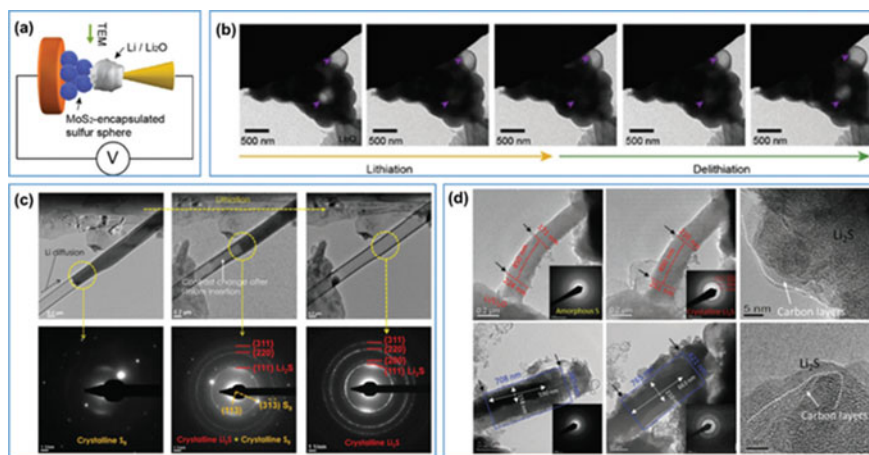


Fig. 9.3 **a** Schematic of the in situ TEM experiment setup with MoS₂-encapsulated hollow sulfur spheres. **b** Selected real-time images of the electrode material evolution during the typical lithiation–delithiation process of MoS₂-encapsulated hollow sulfur spheres to demonstrate the high reversibility. **c** In situ TEM images adopted with S confined in a carbon nanotube during lithiation reaction and their corresponding EDP patterns. **d** Collected in situ TEM images and corresponding SAED patterns with PCNF/A550/S, where the letters a, d present the initial state, letters b, e present full lithiation, letters c, f present high resolution TEM images of lithiated PCNF/A550/S (c) PCNF/A750/S (f) (**a, b** Reproduced with permission from Ref. [14], Copyright (2017) American Chemical Society. **c** Reproduced with permission from Ref. [15], Copyright (2015) Wiley-VCH. **d** Reproduced with permission from Ref. [13], Copyright (2017) Wiley-VCH.)

which provided a new understanding of the relationship between charge/discharge rate and volume expansion [13].

Due to the instability of sulfur in the vacuum environment of traditional electron microscope, especially the open-hole structure of in situ TEM, sulfur sublimates and redeposits in the vacuum environment. Therefore, it is inaccurate to characterize the sulfur distribution at the nanometer level in Li–S battery by traditional electron microscope [16]. In order to solve this problem, cryo TEM can accurately characterize the multi-scale sulfur cathode because it can inhibit the sublimation of sulfur [17].

9.3.2 AFM

In situ TEM technology mainly aimed to the direct observation of sulfur speciation evolution, while in situ AFM can be easily incorporated into the environmental conditions that simulate nanoscale cellular environment, and can be used to observe the evolution of surface morphology. In addition, in situ AFM can offer a way to detect SEI layers during battery cycles [18]. In 2016, Wan et al. used in situ AFM technology to detect nucleation, growth, and dissolution of polysulfides. The re-deposition process of the insoluble Li₂S happens on the interface between cathode

and electrolyte (Fig. 9.4) [19]. In addition, the authors combine X-ray photoelectronic energy spectrum (XPS) and Raman spectra, to supply an in-depth study of the structural–reactive dependence and performance attenuation mechanisms of Li–S batteries. Their conclusions provide visualization of interface structures and meaningful guidance on better electrode designed for Li–S batteries.

In 2019, Kiran et al. [20] reported the using of the atomic force microscope scanning electrochemical microscopy technology, which can observe the redox reaction at the interface of Li–S battery in real time with nanometer resolution. Because Li_2S particles will form conductive region and insulating region in the oxidation process, it can be directly distinguished by in situ electrochemistry and AC phase pattern. During the charging process of Li–S battery, the conductive part dissolves and the insulating part (Li_2S) reacts with the intermediate product. The main reason for capacity degradation is that the active polysulfides change into insulating products at high oxidation potential and accumulate in the cycle process, which leads to the decrease in utilization rate of active materials. By using this technique, the change of tip current was found in the particle region of $\text{Li}_2\text{S}/\text{Li}_2\text{S}_2$, and the AC contrast pattern of this region was further analyzed. The results show that the distribution of $\text{Li}_2\text{S}/\text{Li}_2\text{S}_2$ is not uniform (Fig. 9.5).

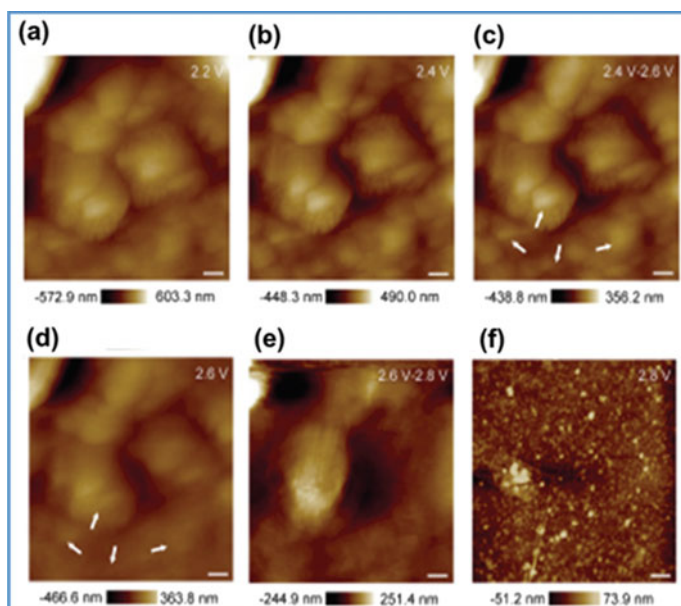


Fig. 9.4 a–f In situ AFM surface topography images at different potentials (Adapted with permission from Ref. [19], Copyright (2016) Wiley-VCH.)

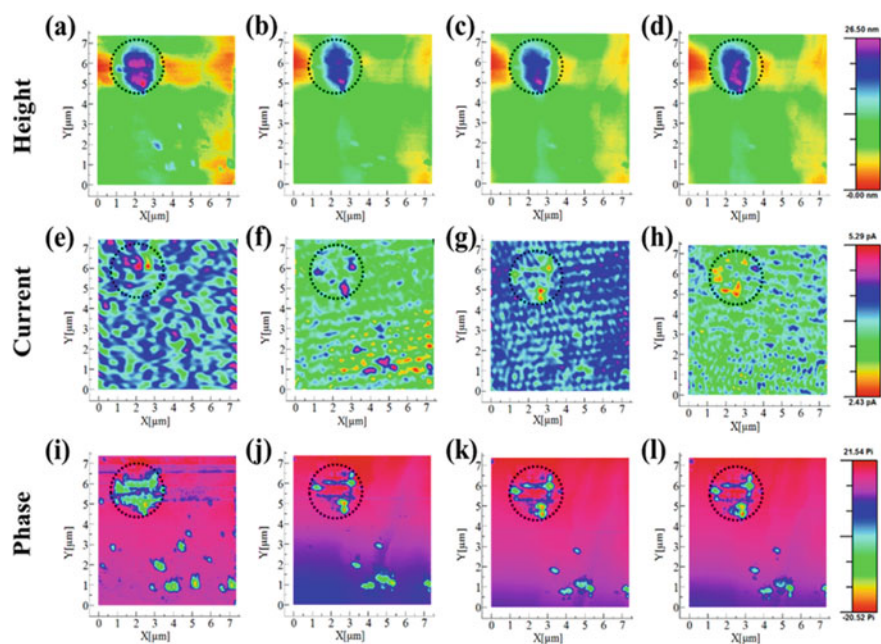


Fig. 9.5 AFM-SECM imaging of $\text{Li}_2\text{S}/\text{Li}_2\text{S}_2$ on carbon surface during oxidation: simultaneous height (first row), current (second row), and phase shift (third row) mapping of $\text{Li}_2\text{S}/\text{Li}_2\text{S}_2$ surface. First column images (a, e, i) correspond to $\text{Li}_2\text{S}/\text{Li}_2\text{S}_2$ [galvanostatically deposited] on glassy carbon before oxidation; second, third, and fourth column images correspond to the Li_2S oxidation at different substrate potentials of 2.5 (b, f, j), 2.6 (c, g, k), and 2.7 V (d, h, l) versus Li/Li respectively; $E_{\text{tip}} = 2.6$ V. Reproduced with permission from Ref. [20], Copyright (2019) American Chemical Society

9.3.3 TXM

The transmission X-ray microscope (TXM) is a non-destructive three-dimensional images approach. Because X-ray can penetrate almost all samples, the sample that can be imaged by TXM is thicker than that of TEM, while overcoming the limitations of high spatial resolution of in situ TEM in a small field of view. The application in energy devices can provide high-resolution X-ray images of electrode during battery cycle without damaging the active materials, and can reflect some additional information [21]. The in situ TXM was firstly established by Cui et al. in 2012 to track the dissolution and curing of composite sulfur cathodes during constant current (CC) charge–discharge cycle, where sample splints show the in operando of TXM for Fig. 9.6a. Surprisingly, by analyzing the dimensional changes of individual sulfur particles in the cycling battery by TXM, the authors found that the change in the size of the sulfur particles was very small, which was very different from the expected dissolution of lithium polysulfide substances [4]. As shown in Fig. 9.6c, under various potentials during the discharge process, where the letters a–i correspond to the marked

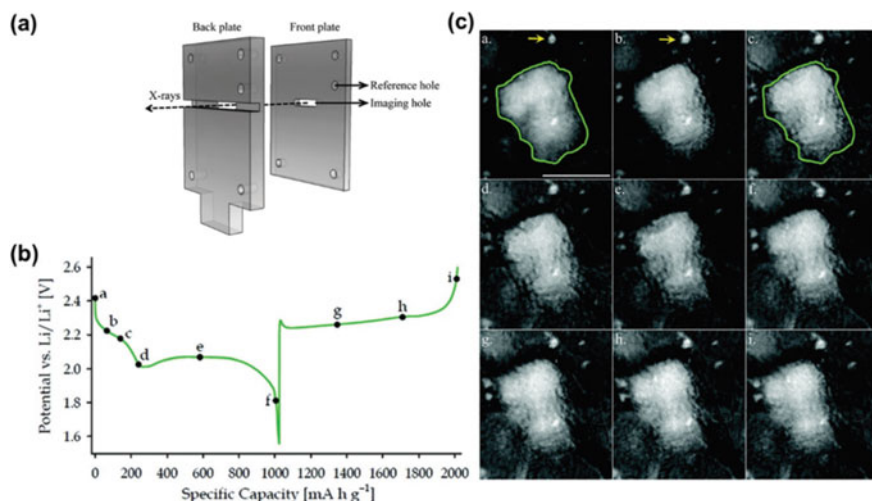


Fig. 9.6 **a** Sample holder plates of in operando TXM. **b** Discharge and charge process voltage profiles versus specific capacity of a Li-S battery cycled at C/8, where the letters a-i correspond to the capacities at different voltages. **c** In operando TXM images of a sulfur composite particle during electrochemical cycling, where the letters correspond to the points labeled a-i in (b) (Adapted with permission from Ref. [4], Copyright (2012) American Chemical Society.)

points in Fig. 9.6b, respectively. In addition, in 2014, based on operating TXM [22], Lin et al. detected that active sulfur particles exhibit complex dimensional variations in cycling batteries. The authors observed that the dissolution and re-deposition of polysulfides caused the intense contraction and expansion of sulfur particles, respectively. In addition, they suggested that the dissolution rate of polysulfides depends on the chemical metering of lithium, and the re-deposition of polysulfide is limited by the nucleation. They also reported a widespread accumulation of lithium polysulfide, resulting in significant changes in the size of active sulfur particles and poor cycle stability.

9.3.4 XRR

X-ray reflectometry (XRR) is an analytical method to determine the thickness, density, and roughness of the material by means of total reflection at or below the critical angle when X-rays are irradiated on the plane of the material at a grazing angle. The X-rays reflected at different interfaces interfere with each other and lead to the oscillation pattern, so that the longitudinal and transverse characteristics of the multilayers can be determined. A multi-dimensional device that combines electrochemical impedance spectrum (EIS), CC charging-discharging, and X-ray chemistry was proposed by Risse et al. to study Li-S batteries (Fig. 9.7a) [23]. On the basis of

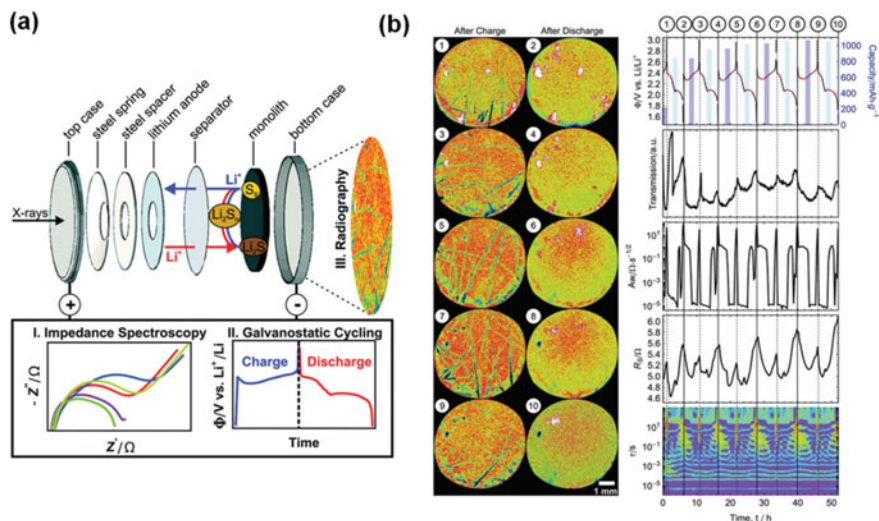


Fig. 9.7 **a** Schematic setup of the operando battery combining operando X-ray radiography with electrochemical impedance spectroscopy and galvanostatic charge/discharge cycling. **b** A multi-dimensional operando analysis of the first five cycles at $C/10$. The numbers in the voltage–time curve with the respective electrochemical capacities (blue bars), overall transmittance, Warburg coefficient, solution resistance and the distribution of relaxation times, corresponding to the radiography images points labeled 1–10 on the left (Reproduced with permission from Ref. [23], Copyright (2016) Royal Society of Chemistry.)

this device, the authors obtained ray photographic images and voltage–time curves, as well as their respective electrochemical capacities (blue bars), total transmission rates, Warburg coefficients, solution resistance and relaxation time distribution (Fig. 9.7b). The whole study clearly demonstrates the multi-dimensional power of the operations study of the Li–S battery system. Yang et al. [24] also reported their findings by applying operational measurements through a similar approach developed by Risse et al.

9.3.5 XRT

X-ray topography (XRT) mainly provides information about the spatial distribution of defects in crystals, and is very sensitive to the stress field which was caused by defects. Yermukhambetova et al. characterized the morphology of active sulfur particles by multi-scale 3D in situ tomography and the microstructure changes of active sulfur particles during battery cycle [25]. They believed that XRT can be used as an effective characterization technique for designing and optimizing cathode materials for Li–S batteries. In 2018, the morphology and crystal structure evolution of sulfur particles during cycle were observed by Yu et al., which combined in

operando XRD and XRM along with XRT [26]. The dissolution and reforming of active sulfur particle clusters can be obviously observed during the battery cycle. At the same time, they also proved that current density and temperature play an essential role in the size of sulfur clusters and Li_2S particles for the first time. This work also expands the new ideas for the development of Li–S batteries.

9.3.6 Other Morphological Characteristic Techniques

In situ/operando SEM can real-time reflect the morphological changes of the electrode materials in the battery during the charge–discharge cycle, in order to further understand the priority sites of the electrode reaction. Marceau et al. understood the degradation mechanism of polysulfides in Li–S batteries by means of in situ SEM and operating UV–Vis characterization [27]. Zhang et al. and Cui et al. have discovered a new type of highly nitrated graphene/ Li_2S active material as cathode for Li–S batteries, which can remain highly stable for thousands of cycles. Using the designed in situ SEM device, the authors observed that active Li_2S particles on graphene became smaller during charging process of the cathode material, which is mainly due to the dissolution of polysulfides. In addition, they found that the design of electrode and charging protocols could provide promising solutions for the practical application of high–energy density Li–S batteries [28].

Neutron diffraction (ND) [29] is the scattering of atomic-scale neutrons in the internal structure of materials, which is a supplement to XRD technology. Neutrons are scattered by the nucleus, so ND can provide better contrast for light atoms than X-ray, which is scattering through the electron densities outside the nucleus. Neutron reflectometer (NR) is a kind of equipment suitable for neutron scattering. At the critical angle below the total internal reflection, NR regards the scattering length density as a mapping function of the depth of neutron penetration into the material. NR can be used to observe and monitor the growth of thin-film. For example, NR is used to monitor the formation and volume changes of the SEI layer during the charge–discharge cycle of the batteries. In addition, because of the higher penetration depth of neutrons in the solid states, both electrochemical and ND measurements can be performed directly on cells to obtain information about electrode active materials. Therefore, in situ ND provides a new way to solve the long-standing technical problems in Li–S batteries.

The measurement of in situ mechanical properties is also used in the sulfur cathodes of Li–S batteries. Zhang et al. [30] linked it to the structural evolution by measuring the stress evolution on the sulfur cathode of the cell during the cycle. They found that significant stress occurred during the nucleation and growth of solid Li–S phases transition, including the irreversible stress caused by the structural rearrangement of the battery during the first cycle. However, the battery shows highly reversible elastic properties in the subsequent charge–discharge cycles. This shows great potential of long cycle in practical applications.

9.4 In Situ/Operando Detection and Tracking of Soluble Polysulfides

In the cycle of Li–S batteries, sulfur participates in the reaction and reacts with lithium, which will generate various polysulfides. In these reaction products, except the sulfur, Li_2S and Li_2S_2 , other polysulfides will dissolve in the ether-based electrolyte. Because the reactions in Li–S batteries are complex, it is extremely important to explore all the chemical reaction routes. Therefore, it is important to understand the particular chemical changes of different long-chain polysulfides and reaction between polysulfides and electrodes. The dissolution of polysulfides will reduce the content of active materials, and ultimately lead to a decrease in the electrochemical performance of the Li–S battery. At the same time, the dissolution of polysulfides will help the reduction process of sulfur [31]. Therefore, it is very important to have a deep understanding of the nature of lithium polysulfide and its dissolution mechanism in ether-based electrolytes. In this part, some in situ/operando detection methods that could specifically detect polysulfides are introduced, mainly involving XAS, UV–Vis, Raman, NMR, HPLC, and ART FTIR.

9.4.1 XAS

XAS measures the X-ray absorption coefficient of a material using X-ray photon energy as a variable to reveal information about specific elements in Li–S battery, and has no hardness requirements for whether the sample is a crystal. Because of the strong X-ray penetrating ability, the overlap of the absorption regions of various target atoms in the spectrum is not high, and it has a wide range of applications in various fields. The tested samples can be powder, liquid, and gaseous samples. This technique can help people better understand the real-time information about some elements in the battery, and to determine electrode material elements or chemical composition changes during the charge and discharge [32]. The XAS spectrum consists of the front edge, XANES, and extended X-ray absorption fine structure (EXAFS). XANES is commonly used to study the composition of various substances in Li–S batteries, and EXAFS provides local structural information. Gorlin et al. designed a special XANES setup, which placed the X-ray wicket on the side of the battery (Fig. 9.8a, b) to ensure that chemistry information between cathode and partition can be detected fully [32]. In order to accurately monitor S or lithium polysulfides, Nazar et al. prepared and calibrated the reference standards of S_8 , S_6^{2-} , S_4^{2-} , S_3^{2-} , and S^{2-} (Fig. 9.8c), and XANES results revealed the mechanism of sulfur oxidation. In addition, a three-platform reduction reaction can be observed when operating XANES compared to batteries using conventional ether-based electrolytes (Fig. 9.8d). And the concentration measured by XANES proved the appearance of S_3^{2-} in the DMA (Fig. 9.8d, e) and cracking of the S_6^{2-} [33]. In the XANES analysis (Fig. 9.8e) [34], there is a typical pre-peak that demonstrates the presence of free-based anions (S_3^{2-})

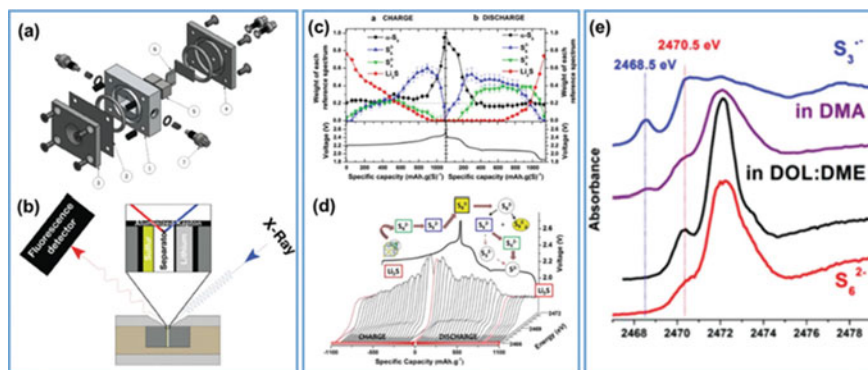


Fig. 9.8 In situ XANES tests of Li-S batteries. **a** Schematic of the spectra–electrochemical in operando battery, corresponding to its individual components. **b** schematic of the in operando XANES setup that allows detection of X-ray fluorescence from all layers in the cell. **c** A linear combination analysis of sulfur K-edge XANES based on charge/discharge cycling, four compounds (α -S₈, S₆²⁻, S₄²⁻, and Li₂S) were utilized as reference materials. **d** In situ XANES during the electrochemical cycle and the proposed reaction mechanism for Li-S cells. **e** Experimental in operando XANES around 340 mA h g⁻¹ collected during discharge in Li-S batteries using DMA or DOL: DME electrolytes compared, with S₃²⁻ and S₆²⁻ as reference materials (**a**, **b** Reproduced with permission from Ref. [32], Copyright (2015) Manchester Nh: Electrical Society; **c**, **d** reprinted with permission from Ref. [33], Copyright (2013) American Chemical Society; **e** reproduced with permission from Ref. [34], Copyright (2015) Wiley-VCH.)

in Li-S batteries. In the absorption spectrum of a variety of polysulfides, only two types of polysulfides ions are used to quantify the batteries. In operational XANES research, a great deal of effort should be invested in developing and calibrating a comprehensive absorption spectrum, which is significant for further research.

9.4.2 Raman

In the detection method of Li-S battery, Raman can qualitatively or quantitatively detect lithium polysulfides in electrolyte, which is an important reference for analyzing chemical reactions in batteries. Usually, the characteristic peaks of polysulfides and free base anions are below 550 cm⁻¹ [35]. The basic frequency of S₈ is near 219 and 474 cm⁻¹ [36]. Raman can also detect high-priced polysulfides. The characteristic peaks of free-based anions are approximately 525–535 cm⁻¹ [30]. An operational Raman device (Fig. 9.9a) was designed by Hannauer et al. to monitor the evolution of various possible polysulfide.

As shown in Fig. 9.9b, the Raman spectrum obtained from the first cycle of the positive carbon/sulfur composite cathode is demonstrated [37]. Dong et al. developed the cathode materials of Li-S battery based on Lewis. Combined with Raman spectroscopy and density functional theory (DFT), they understood the complex

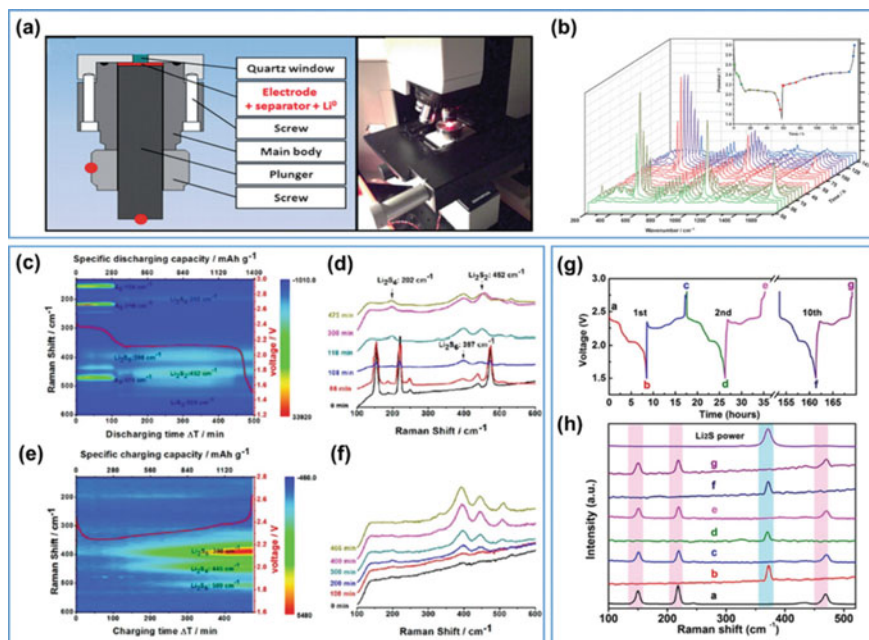


Fig. 9.9 In situ Raman measurements of a Li-S battery. **a** Schematic of the in situ Raman experiment set-up of positive carbon-sulfur (C/S) composite electrodes. **b** real-time Raman spectra, corresponding to the Li-S battery electrochemical response at C/60 during the first discharging-charging cycle. **c-f** The battery was cycled with N-doping super P carbon/sulfur. **c** and **e** In situ Raman spectra obtained during discharge and charge reactions, respectively. **d** and **f** The obtained in situ Raman spectra, corresponding to (c) and (e). **g, h** The battery was cycled with the positive electrode of nanosulfur particles on Ni foam at C/10. **g** The discharge and charge processes; **h** collected in situ Raman spectra from the points labeled a-g in (g) of a Li₂S powder (**a, b** Reproduced with permission from Ref. [37], Copyright (2015) Wiley-VCH. **c-f** reproduced with permission from Ref. [30], copyright (2015) American Chemical Society. **g, h** reproduced with permission from Ref. [35], Copyright (2015) American Chemical Society.)

chemical properties of Li-S batteries. Li₂S₈ is not detected in the redox reaction of the charge and discharge cycle of Li-S batteries, and the polysulfides completely change to Li₂S₆ and stop the reaction as shown in Fig. 9.9c-f [30]. Chen et al. also shed light on the sulfur redox of Li-S batteries with S nanodots electrical deposition in nickel foam as composite cathode. By using the in situ Raman spectrum, several charging/discharging cycles (Fig. 9.9 g, h) show a reversible reaction between S and Li₂S [35]. Hagen et al. [38] investigated the formation of lithium polysulfide in Li-S battery system (4.6 mg cm⁻² sulfur loading) with an electrolyte (0.7 m LiTFSI in 2:1 DME: DIOX) via in situ Raman. By cross-checking reference Raman peaks from the literature and DFT calculations, in situ Raman measurements prove that various lithium polysulfide phases are dependent on the state of charging. It is of interest that they could not detect three major peaks of S₈ in all the CNT-S electrodes but still claimed that S₈ occurred.

9.4.3 UV-Vis

Unlike Raman spectroscopy that uses scattered light, UV-Vis spectra are formed by the different absorption degrees of substances to ultraviolet and visible light, and it has powerful analytical capabilities for solution-based electrochemical reactions. Usually, S_8 or element S shows a feature absorption peak at 270–280 nm [39]. Between 350 and 500 nm, the free-based S_3^- has a relatively strong absorption of 620 nm [40]. For the purpose of obtaining in operando UV-Vis absorption spectral information from Li-S batteries, Dominko et al. designed the reflection configuration for the first time [41]. Qualitative and quantitative analyses are achieved by dividing the spectral solution of chemically synthesized lithium polysulfides. After that, Marceau et al. further used SEM and UV-Vis to detect and identify the formation of sulfur species [27]. Therefore, it is of great help to a deeper understanding of Li-S batteries. Their findings suggest that the discharging and charging processes are not completely reversible and are carried out in different ways. In 2017, Yan et al. assembled a battery with a special sealed glass window (Fig. 9.10b) and used reflection mode (Fig. 9.10a) to detect lithium polysulfides in electrolytes during the discharging/charging cycle [40]. The author dissolved the stoichiometric ratio of lithium sulfide and sulfur in 1 M bis(trifluoromethanesulfonyl)imide (LiTFSI) lithium electrolyte with 1,3-dioxolane (DOL) and 1,2-dimethyl Oxethane (DME)

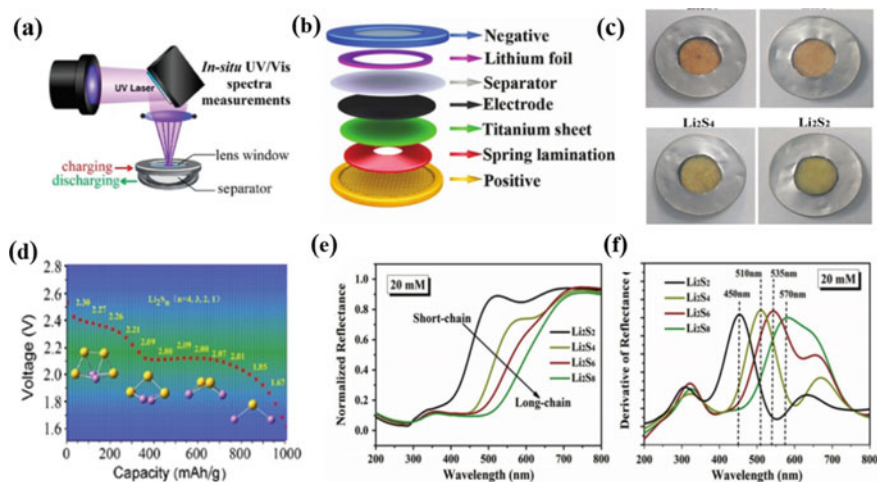


Fig. 9.10 a–f In operando UV-Vis spectra detected during the first discharge of a Li-S battery **a** the battery unit with a sealed glass window for in operando UV-Vis setup. **b** The cell configuration with a sealed glass window for in situ experiment **c** photographs of four different dissolved polysulfides (Li_2S_8 , Li_2S_6 , Li_2S_4 , Li_2S_2) **d** the collected discharge voltages were used for the in situ UV-Vis mode. **e–f** The “standards” of reflectance and the corresponding first-order derivative curves of different polysulfides (Li_2S_2 , Li_2S_4 , Li_2S_6 , and Li_2S_8) at the concentration of 20×10^{-3} m, respectively ((a), (d) Adapted with permission from Ref. [40], (b, c) (e, f) Adapted with permission from Ref. [42], Copyright (2017) American Chemical Society.)

(1:1 v/v) to make standard samples. Long-chain and short-chain polysulfide standard sample (Fig. 9.10c) made a clear distinction in color. They found that the UV–Vis spectrum corresponding to long-chain polysulfides is in the long-wave region. Combined with the research of Yan et al., it is worth noting that the selected discharge voltage will be applied to the customized battery during the in situ UV–Vis measurement, (Fig. 9.10c) and that in UV–Vis spectral analysis, the absorption wavelength of the measurement reflectivity is used as a function of the battery state. Focusing on the position of the first derivative of the ultraviolet–visible spectrum (Fig. 9.10d, e), it can be concluded that the main positions of long-chain polysulfide Li_2S_8 and Li_2S_6 are 570 nm and 535 nm, respectively. As the battery is discharged, medium-chain polysulfide Li_2S_4 is derived at 510 nm, while the short Chain polysulfides Li_2S_2 are mainly located at 450 nm locations. The difference is that Lu et al. revealed the solvent–dependent Li–S redox pathway in the operating UV spectra. It should be noted that the redox reaction of sulfur is significantly different between two different solvents [42]. These studies can provide valuable insights into the basic research of lithium battery applications. Similarly, Yan et al. recently reported a new strategy that Graft heme molecules to three functionalized carbon nanotube systems (CNT s-COOH, CNT s-OH, and CNT s-NH₂) to synthesize new biomimetic molecular catalysts. Using in situ UV technology, they found that this structure helps the catalysis and conversion of polysulfides. Although the advancement of in situ UV–visible spectroscopy technology has helped researchers better understand the mechanism of Li–S batteries, there is still a need to standardize the absorption peaks so that more accurate data can be collected to guide researchers in their research.

9.4.4 NMR

NMR is a branch of spectroscopy. NMR is used to analyze objects by absorbing a certain frequency of radiofrequency radiation through resonance. It has a wide range of applications and can be applied to semi-solid and micro samples in addition to conventional solid and liquid materials. ^7Li NMR is used to detect ^7Li signal (spin = 3/2, 92.5% abundance), mainly due to its high sensitivity to ^7Li nuclei, the ^7Li signal can be captured faster than the discharge–charge cycle on a timescale. In the research of Li–S batteries, in situ and ex situ ^7Li NMR is widely used for the detection of polysulfides [43]. The most significant advantage of in situ NMR is that it can dynamically observe the growth and exfoliation of lithium on the microscopic scale. Liu et al. assembled a special indoor cylindrical micro-battery (Fig. 9.11a) that can use in situ NMR spectroscopy to record the phase evolution of a lithium metal anode entangled with parasitic reactions (Fig. 9.11b, c) [44]. Seshadri et al. used in situ NMR to directly observe the soluble polysulfides that cause the capacity decline of Li–S batteries during battery discharge, (Fig. 9.11a, e) and also confirmed that Li_2S was formed at the beginning of the first discharge platform [45]. Hereafter, in 2017, Wang et al. reported a comprehensive method for quantitatively detecting changes in all polysulfide species produced during the cycling of Li–S batteries, which also

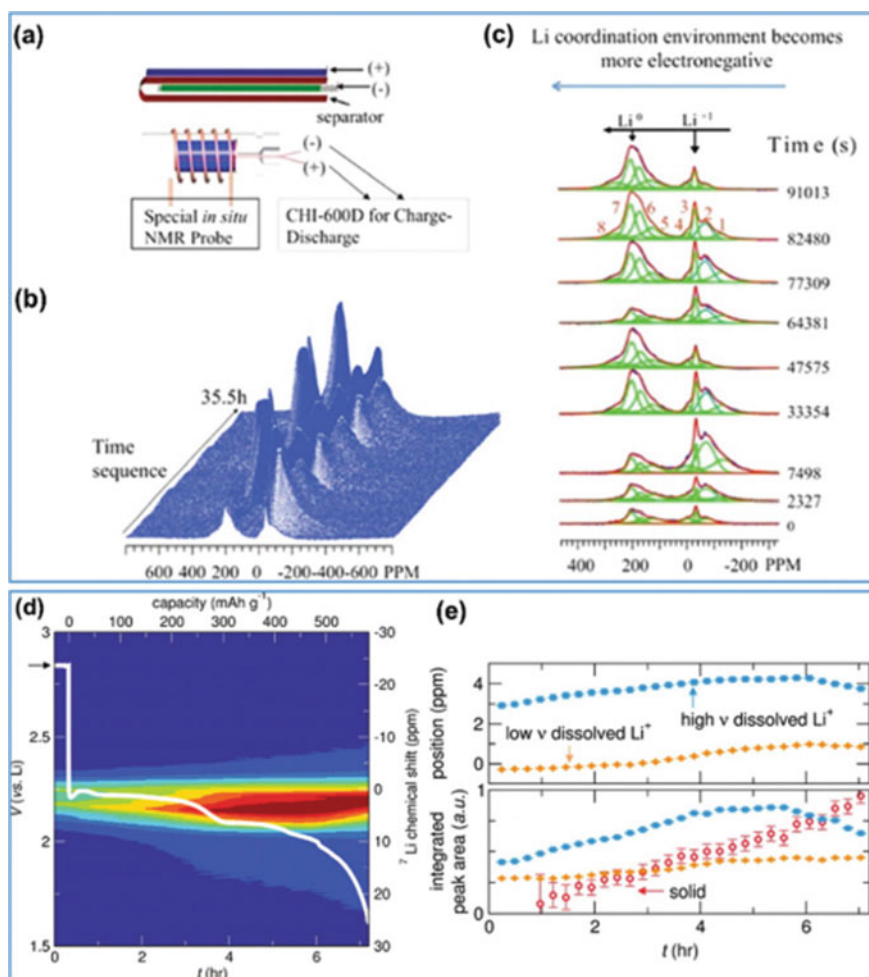


Fig. 9.11 **a** Schematic of in situ NMR experiments setup with an inhouse cylindrical micro-battery. **b** Obtained time sequence ${}^7\text{Li}$ NMR spectra in an operating Li-S micro-battery during discharge/charge. **c** Main peaks were extracted at different times by fitting the spectra. **d**, **e** A Li-S battery was cycled at $C/20$. **d** In situ ${}^7\text{Li}$ NMR signal overlaid on the electrochemical discharge curve. **e** The changes in chemical shift and integrated intensities as a function of discharge (**a**–**c** Reprinted with permission from Ref. [44], Copyright (2015) American Chemical Society; **d**–**f** reprinted with permission from Ref. [45], Copyright (2014) American Chemical Society.)

used in situ NMR spectroscopy [46]. They observed the precipitation of lithium metal during battery charge and discharge cycles, and the mossy lithium produced over time. These tests have provided more ideas for the development of electrolytes, sulfur cathode research, and lithium metal protection strategies in the development of Li-S batteries.

9.4.5 HPLC

HPLC is a useful separation technology that has been widely applied to identification and quantification. Recently, using this technique, researchers were able to identify dissolved polysulfides ions in the electrolytes of Li–S batteries [47]. A scientific study on lithium polysulfides intermediates and S₈ molecule were reported by Zheng et al. in real-time quantitative measurement with HPLC technology during discharge and charge [48]. Changes from elemental sulfur to intermediates lithium polysulfide species to insoluble Li₂S can be distinctly defined as discharge reactions (Fig. 9.12a–c). During the charging process (Fig. 9.12d–f), it is significant to conclude that Li₂S was straight oxidized to Li₂S_n and oxidized to S later. Significantly, their research provides valuable additions to guidance on other techniques and further helps people understand the redox kinetic process of Li–S batteries in a comprehensive and promising way.

9.4.6 FT-IR

Porter et al. and Kalra et al. provided innovative electrochemical devices to make the in situ infrared analysis of Li–S batteries (Fig. 9.13a, top panel) [49]. As Fig. 9.13a shows, a commercial ATR FT-IR instrument is put in the bottom part of the cell. In order to clearly observe the transformation of the polysulfides by porous nature of the cathode layer, the in-situ Li-S battery was assembled by the argon-filled atmosphere. A stainless steel plate and Cu foil disc with a 2 mm hole cut in the center was placed on top of a convex diamond crystal. The Cu foil disc here was rolled as the current collector. Then assembled the cathode, pure lithium foil anode and Celgard separator layer by layer into the CR2032 type cell. The electrolyte volume, cathode, sulfur loading is the major parts of a traditional Li–S battery, and the in situ Li–S battery assembly is almost consistent with these key components. When the infrared beam undergoes complete internal reflection in the diamond crystal, the evanescent wave penetrates the medium outside the crystal. The penetration depth of the wave is affected by some factors, such as the wavelength and the incident angle of the IR beam, the refractive indexes of the crystal and the medium used (Fig. 9.13b, bottom panel) [50]. The effective penetration depth of the evanescent wave into the working electrode is B20 mm, which can ensure detect the polysulfides in a Li–S coin cell. The quantitatively measure polysulfides as a function of in operando FTIR spectra. Therefore, it is necessary that effective measures should be taken to detect polysulfides in the coin cell by using ATR FT-IR spectroscopy. The holed structure of cathode need to be provided and sealed with the diamond crystal, the electrode design also accommodates anode layer with the in operando FTIR spectroscopy.

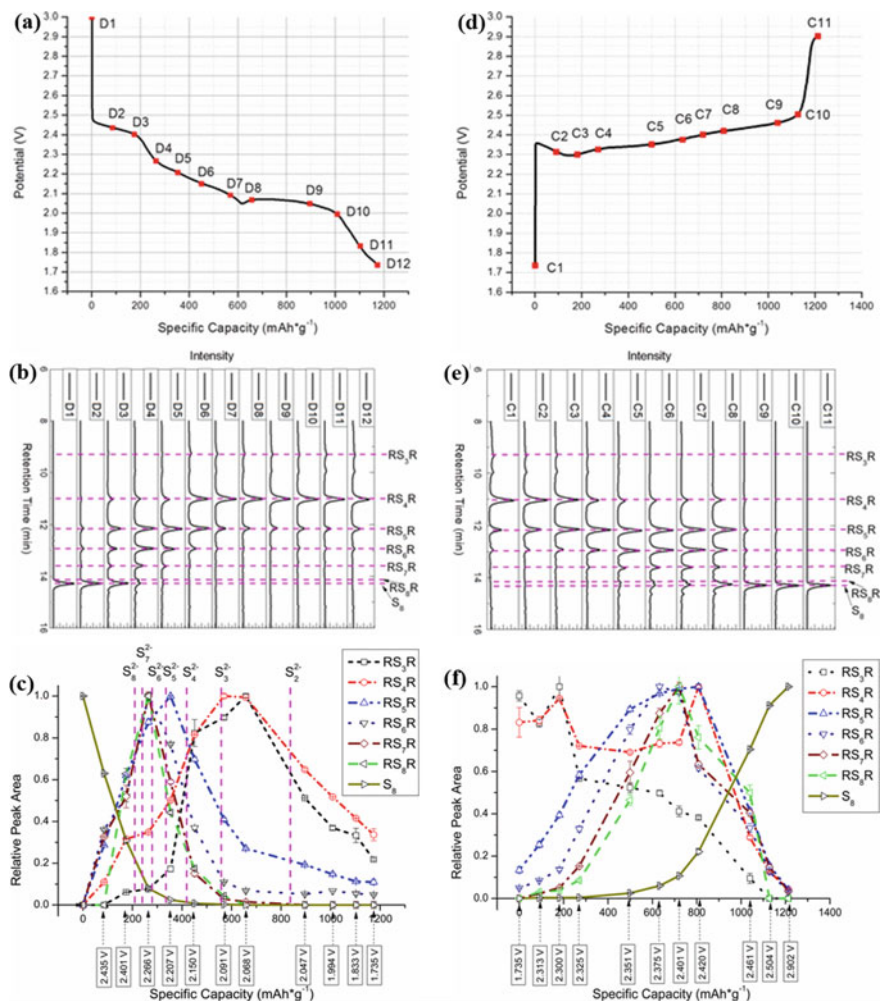
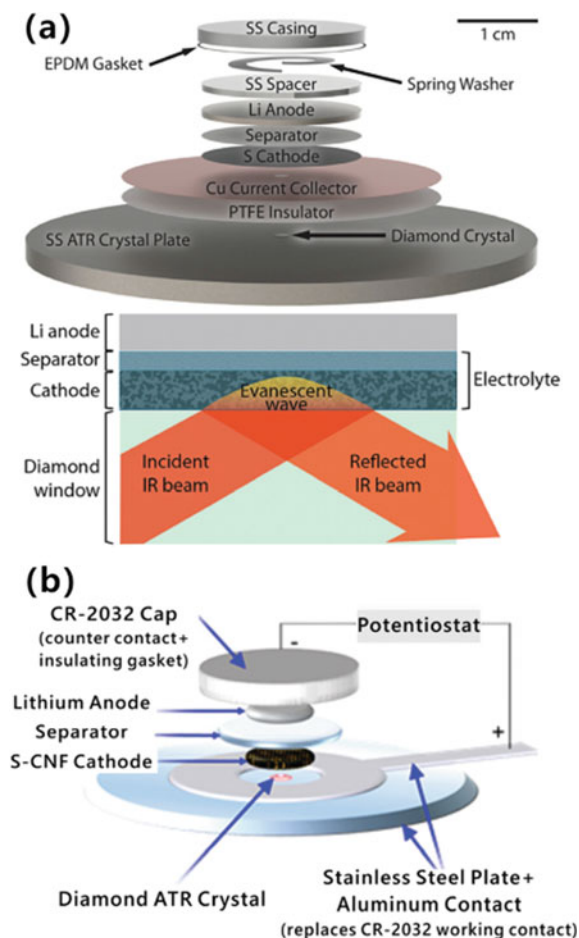


Fig. 9.12 The battery was cycled at C/70. **a** Discharge profile of the Li-S battery with sampling points (red squares from D1 to D12) during operation. **b** The corresponding HPLC chromatograms with (a). **c** Standard chromatographic peak for each parasitic polysulfide species (R = CH₃) from real-time HPLC results during discharging. **d** Charge profile of the Li-S battery with sampling points (red squares from C1 to C11) during operation. **e** The corresponding HPLC chromatograms with (d) and **f** standard chromatographic peak for each parasitic polysulfide species (R = CH₃) from real-time HPLC results during charging (Adapted with permission from Ref. [48], Copyright (2016) American Chemical Society.)

Fig. 9.13 Development of the in situ FT-IR electrochemical cell for Li-S battery investigation. **a** Top panel: schematic representation of the in situ ATR FT-IR spectro-electrochemical cell. Bottom panel: Illustration of the battery's configuration and the diamond window, the IR beam input and that reflected through the ATR crystal, absorbed by the electrolyte in a porous cathode. Reproduced with permission from Ref. [49]. Copyright 2017, Elsevier Ltd. **b** Schematic of the in situ infrared spectro-electrochemical experiment with a Li-S cell on the ATR crystal of the FT-IR spectrometer. Reproduced with permission from Ref. [50]. Copyright 2018, American Chemical Society. Tutorial Review Chem Soc Rev Pub



9.4.7 EPR

EPR technology can probe and stable the reaction intermediates with unpaired electrons by using the spin traps. Among the Li-S battery, it is reported that the application of in situ EPR technology can directly observe the transformation process of S_3^- free fundamentals in the Li-S batteries. Typically, Wang et al. [51] designed an in situ EPR device setup to directly observe the transformation of sulfur radicals during charge/discharge process. It is found that the concentration of S_3^- radicals is changing regularly with the potential fluctuation, providing significant evidences on sulfur radicals that participate in the various inner reactions in Li-S batteries, resulting in two totally different reaction paths during electrochemical process (Fig. 9.14). The unique radical mechanism may offer some diverse views to understand the generation transformation among sulfur radicals and the electrolyte, stimulating more innovative designs to explore Li-S system.

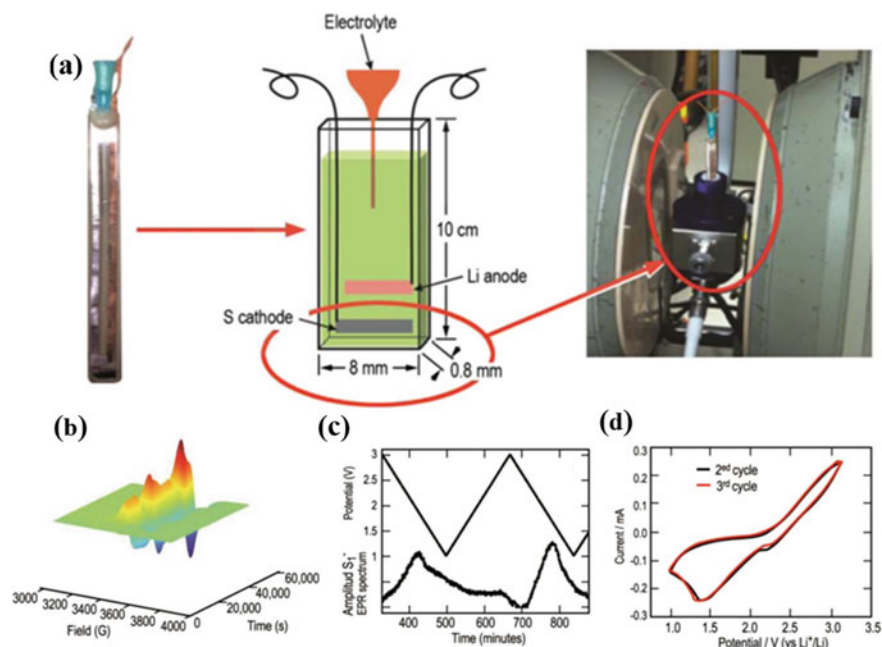


Fig. 9.14 **a** EPR cell design for in situ testing and capturing of radical resonance signals generated throughout the operation of Li–S batteries. **b** 3D plot of in situ S_3^- EPR spectra in a functioning Li–S EPR cell versus time during CV scan. **c** The concentration evolution of S_3^- radicals at different time (potentials). **d** Corresponding CV curves collected concurrently from Li–S EPR cell. Both **(c)** and **(d)** start from the second cycle with the first cycle information in supplementary information (Reproduced with permission from Ref. [51], Copyright (2015) Electrochemical Soc Inc.)

9.5 Summary and Outlook

At present, the study on the exploring of electrochemical pathways and their interactions between components in Li–S batteries stays at a relatively mature stage. Various techniques may guide the further research of next generation Li–S systems, realizing more energy storage and long cycle life to practical application. Due to ease of accessibility and low-loss, ex situ technology is mainly used. However, existing the essential post-processing and time delays, the results may not be accurate enough. In recent years, many effective measures were taken to in-depth exploring of the reaction mechanism by the in situ/operando technology. In situ/operando numbering techniques always need expensive instruments and complicated experimental devices, which can be unacceptably costly and inconvenient for researchers, so their widespread use remains limited. Despite the challenges remained, we are optimistic that Li–S batteries will be in-depth understanding of the theory and realized the practical application as soon as possible. We are confident that in situ/operando signation technology will continue to act as the key factor on achieving this goal. In the future, the

design and construction of micro/nanodevices to in situ that characterize the properties and structural changes of electrode materials is a very worthwhile exploration and development direction.

Acknowledgements This work was supported by the National Natural Science Foundation of China (51702247), the National Key Research and Development Program of China (2020YFA0715000, 2016YFA0202603), the Natural Science Foundation of Hubei Province (2019CFA001).

References

1. Mai L, Yan M, Zhao Y (2017) Track batteries degrading in real time. *Nature* 546:469–470
2. Gurlo A, Riedel R (2007) In situ and operando spectroscopy for assessing mechanisms of gas sensing. *Angew Chem Int Ed Engl* 46:3826–3848
3. Hu A et al (2020) Optimizing redox reactions in aprotic lithium–sulfur batteries. *Adv Energy Mater*
4. Nelson J et al (2012) In operando X-ray diffraction and transmission X-ray microscopy of lithium sulfur batteries. *J Am Chem Soc* 134:6337–6343
5. Cañas NA, Wolf S, Wagner N, Friedrich KA (2013) In-situ X-ray diffraction studies of lithium–sulfur batteries. *J Power Sources* 226:313–319
6. Demir-Cakan R et al (2013) Li–S batteries: simple approaches for superior performance. *Energy Environ Sci* 6
7. Walus S et al (2013) New insight into the working mechanism of lithium-sulfur batteries: in situ and operando X-ray diffraction characterization. *Chem Commun (Camb)* 49:7899–7901
8. Paoletta A et al (2016) Transient existence of crystalline lithium disulfide Li₂S₂ in a lithium-sulfur battery. *J Power Sources* 325:641–645
9. Walus S et al (2015) Lithium/sulfur batteries upon cycling: structural modifications and species quantification by in situ and operando X-ray diffraction spectroscopy. *Adv Energy Mater* 5
10. Ma L, Hendrickson KE, Wei S, Archer LA (2015) Nanomaterials: science and applications in the lithium–sulfur battery. *Nano Today* 10:315–338
11. Conder J et al (2017) Direct observation of lithium polysulfides in lithium–sulfur batteries using operando X-ray diffraction. *Nat Energy* 2
12. Ji X, Evers S, Black R, Nazar LF (2011) Stabilizing lithium-sulphur cathodes using polysulphide reservoirs. *Nat Commun* 2:325
13. Xu Z-L et al (2017) In situ TEM study of volume expansion in porous carbon nanofiber/sulfur cathodes with exceptional high-rate performance. *Adv Energy Mater* 7
14. Tang W et al (2017) In situ observation and electrochemical study of encapsulated sulfur nanoparticles by MoS₂ flakes. *J Am Chem Soc* 139:10133–10141
15. Kim H et al (2015) In situ TEM observation of electrochemical lithiation of sulfur confined within inner cylindrical pores of carbon nanotubes. *Adv Energy Mater* 5
16. Levin BD et al (2017) Characterization of sulfur and nanostructured sulfur battery cathodes in electron microscopy without sublimation artifacts. *Microsc Microanal* 23:155–162
17. Wang C-M, Liao H-G, Ross FM (2015) Observation of materials processes in liquids by electron microscopy. *MRS Bull* 40:46–52
18. Nelson Weker J, Toney MF (2015) Emerging in situ and operando nanoscale X-ray imaging techniques for energy storage materials. *Adv Funct Mater* 25:1622–1637
19. Lang SY et al (2016) Insight into the interfacial process and mechanism in lithium-sulfur batteries: an in situ AFM study. *Angew Chem Int Ed Engl* 55:15835–15839
20. Mahankali K, Thangavel NK, Reddy Arava LM (2019) In situ electrochemical mapping of lithium-sulfur battery interfaces using AFM-SECM. *Nano Lett* 19:5229–5236

21. Zhao J, Cano M, Giner-Casares JJ, Luque R, Xu G (2020) Electroanalytical methods and their hyphenated techniques for novel ion battery anode research. *Energy Environ Sci* 13:2618–2656
22. Lin C-N et al (2014) Understanding dynamics of polysulfide dissolution and re-deposition in working lithium–sulfur battery by in-operando transmission X-ray microscopy. *J Power Sources* 263:98–103
23. Risse S et al (2016) Multidimensional operando analysis of macroscopic structure evolution in lithium sulfur cells by X-ray radiography. *Phys Chem Chem Phys* 18:10630–10636
24. Yang Y et al (2017) Binder-free carbon monolith cathode material for operando investigation of high performance lithium–sulfur batteries with X-ray radiography. *Energy Storage Mater* 9:96–104
25. Yermukhambetova A et al (2016) Exploring 3D microstructural evolution in Li–Sulfur battery electrodes using in-situ X-ray tomography. *Sci Rep* 6:35291
26. Yu S-H et al (2018) Direct visualization of sulfur cathodes: new insights into Li–S batteries via operando X-ray based methods. *Energy Environ Sci* 11:202–210
27. Marceau H et al (2016) In operando scanning electron microscopy and ultraviolet–visible spectroscopy studies of lithium/sulfur cells using all solid-state polymer electrolyte. *J Power Sources* 319:247–254
28. Qiu Y et al (2015) Highly nitridated graphene–Li₂S cathodes with stable modulated cycles. *Adv Energy Mater* 5
29. Yang Y et al (2017) In situ electrochemistry of rechargeable battery materials: status report and perspectives. *Adv Mater* 29
30. Chen J-J et al (2015) Conductive Lewis base matrix to recover the missing link of Li₂S₈ during the sulfur redox cycle in Li–S battery. *Chem Mater* 27:2048–2055
31. Zhao M et al (2020) Lithium–sulfur batteries under lean electrolyte conditions: challenges and opportunities. *Angew Chem Int Ed Engl* 59:12636–12652
32. Gorlin Y et al (2015) Operando characterization of intermediates produced in a lithium–sulfur battery. *J Electrochem Soc* 162:A1146–A1155
33. Cuisinier M et al (2013) Sulfur speciation in Li–S batteries determined by operando X-ray absorption spectroscopy. *J Phys Chem Lett* 4:3227–3232
34. Cuisinier M, Hart C, Balasubramanian M, Garsuch A, Nazar LF (2015) Radical or not radical: revisiting lithium–sulfur electrochemistry in nonaqueous electrolytes. *Adv Energy Mater* 5
35. Zhao Q et al (2015) Sulfur nanodots electrodeposited on ni foam as high-performance cathode for Li–S batteries. *Nano Lett* 15:721–726
36. Yeon J-T et al (2012) Raman spectroscopic and X-ray diffraction studies of sulfur composite electrodes during discharge and charge. *J Electrochem Soc* 159:A1308–A1314
37. Hannauer J et al (2015) The quest for polysulfides in lithium–sulfur battery electrolytes: an operando confocal Raman spectroscopy study. *ChemPhysChem* 16:2709–2709
38. Hagen M et al (2013) In-situ Raman investigation of polysulfide formation in Li–S cells. *J Electrochem Soc* 160:A1205–A1214
39. Cañas NA, Fronczek DN, Wagner N, Latz A, Friedrich KA (2014) Experimental and theoretical analysis of products and reaction intermediates of lithium–sulfur batteries. *J Phys Chem C* 118:12106–12114
40. Xu N et al (2017) Greatly suppressed shuttle effect for improved lithium sulfur battery performance through short chain intermediates. *Nano Lett* 17:538–543
41. Patel MU, Dominko R (2014) Application of in operando UV/Vis spectroscopy in lithium–sulfur batteries. *Chemoschem* 7:2167–2175
42. Chen W et al (2017) A new type of multifunctional polar binder: toward practical application of high energy lithium sulfur batteries. *Adv Mater* 29
43. Huff LA, Rapp JL, Baughman JA, Rinaldi PL, Gewirth AA (2015) Identification of lithium–sulfur battery discharge products through ⁶Li and ³³S solid-state MAS and ⁷Li solution NMR spectroscopy. *Surf Sci* 631:295–300
44. Xiao J et al (2015) Following the transient reactions in lithium–sulfur batteries using an in situ nuclear magnetic resonance technique. *Nano Lett* 15:3309–3316

45. See KA et al (2014) Ab initio structure search and in situ ^7Li NMR studies of discharge products in the Li-S battery system. *J Am Chem Soc* 136:16368–16377
46. Wang H et al (2017) In situ NMR observation of the temporal speciation of lithium sulfur batteries during electrochemical cycling. *J Phys Chem C* 121:6011–6017
47. Zheng D et al (2015) Quantitative and qualitative determination of polysulfide species in the electrolyte of a lithium-sulfur battery using HPLC ESI/MS with one-step derivatization. *Adv Energy Mater* 5
48. Zheng D et al (2017) Investigation of the Li-S battery mechanism by real-time monitoring of the changes of sulfur and polysulfide species during the discharge and charge. *ACS Appl Mater Interfaces* 9:4326–4332
49. Saqib N, Ohlhausen GM, Porter JM (2017) In operando infrared spectroscopy of lithium polysulfides using a novel spectro-electrochemical cell. *J Power Sources* 364:266–271
50. Dillard C, Singh A, Kalra V (2018) Polysulfide speciation and electrolyte interactions in lithium-sulfur batteries with in situ infrared spectroelectrochemistry. *J Phys Chem C* 122:18195–18203
51. Wang Q et al (2015) Direct observation of sulfur radicals as reaction media in lithium sulfur batteries. *J Electrochem Soc* 162:A474–A478

Chapter 10

Computation and Simulation



Ying Ma

Abstract Lithium–sulfur (Li–S) batteries offer an exceptionally high energy density and have been the subject of intensive research and development efforts. Although significant progresses have been made, a few critical challenges must be addressed to achieve the full potential of Li–S batteries. Computer simulations have played an ever-increasing role in revealing the atomistic origins of these challenges, and new materials are being developed through combined experimental and computational efforts. This chapter introduces the basic principles of various computational techniques, focusing on atomistic simulations. The capabilities of computer simulations are demonstrated at three different levels ranging from simple structural optimization to the more advanced computational materials screening and selection. Emerging areas of research in Li–S research and the role of computer simulations are briefly introduced.

Keywords Lithium–sulfur batteries · Computer simulation · Multiscale modeling · Computational materials screening

10.1 Introduction

Lithium-ion batteries (LIBs) have revolutionized our society. Devices that are powered by LIBs become part of our daily lives [1, 2]. In fact, a Nobel prize for their development has long been anticipated, and the 2019 award of the Nobel Prize in Chemistry to John Goodenough, Stanley Whittingham, and Akira Yoshino attests firmly the great benefit to humankind empowered by LIBs. Unfortunately, even the most advanced LIB systems today have their limitations, the greatest one being their limited energy density (currently around 210 Wh kg^{-1} ; 650 Wh l^{-1}). A ten-fold increase in energy density is needed to match that of gasoline [3], which is unlikely due to structural limitations of currently used electrode materials. New battery chemistry has to be explored.

Y. Ma (✉)

Department of Materials Science and Biomedical Engineering, University of Wisconsin-Eau Claire, Eau Claire, USA
e-mail: yingma@uwec.edu

Sulfur (S), one of the most abundant elements on earth, offers a theoretical capacity of 1672 mAh/g, the highest among all known solid cathode materials [4]. The theoretical gravimetric energy density of lithium–sulfur (Li–S) systems is around ~2,600 Wh/kg with an open-circuit voltage of around 2 V. Not surprisingly, S has been the subject of extensive research efforts [5–15]. Interestingly, even though the concept of elementary S as a cathode material was originated [16] before the introduction of the first intercalation cathode for LIBs [17], research and development on S have largely stopped due to a number of intrinsic issues of S. The breakthrough came in 2009 when Nazar and coworkers developed highly ordered, nanostructured, mesoporous carbon (C) to encapsulate S [18]. Their success rejuvenated research efforts in S, which is apparent from the 4277 citations (from Google Scholar) received by their original paper so far. A recent literature survey indicated that out of all published papers on Li–S systems from 1960 to 2020, 96% appeared after the 2009 paper [19].

The excitement on S is understandable, given its exceptionally high energy density. However, the hope for commercialized Li–S batteries remained slim [20]. Only recently, Oxis Energy, a UK-based startup company, has developed Li–S pouch cells with a maximal density of 400 Wh/kg, while aiming at a 500 Wh/kg system by the end of 2020 (<https://www.oxisenergy.com>). These energy densities, although encouraging and impressive, fall far short of the theoretical one.

The difficulty with the Li–S system roots in the unique electrochemical properties of S. Fundamental principles and challenges of Li–S batteries, together with various experimental techniques to alleviate these challenges, have been discussed in previous chapters. This chapter will focus on the computational aspect of Li–S research. Various computational techniques will be introduced, along with examples that showcase both the advantages and limitations of a computational approach.

10.2 The Gibbs Free Energy and Cell Potential

Detailed electrochemical principles of the Li–S system have been discussed in Chap. 1. Here, we will review briefly important concepts relevant to computer simulations. Overall, the electrochemical reaction of S with Li can be written as



Under working conditions of normal battery operations, Li, S, and Li_2S crystallize in body-centered cubic (BCC), orthorhombic, and face-centered cubic (FCC) structures, respectively. The forward reaction is accompanied by a decrease in the Gibbs free energy, which is the maximum amount of non-expansion work that can be extracted. In the case of batteries, the reduction in the Gibbs free energy is converted to electrical work, and the open-circuit voltage, V_{OC} , is given by the Nernst equation, as follows:

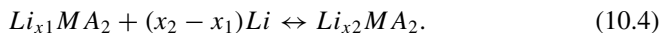
$$V_{OC} = -\frac{\Delta G_r}{nF}, \quad (10.2)$$

where ΔG_r is the change in the Gibbs free energy for the forward reaction in (10.1), F is the Faraday constant, and n is the number of charges transferred. Equivalently, V_{OC} can also be expressed as the difference in the chemical potential of Li between the cathode and the anode:

$$V_{OC} = -\frac{\mu_{Li}^C - \mu_{Li}^0}{F}, \quad (10.3)$$

where μ_{Li}^C is the Li chemical potential in the cathode, and μ_{Li}^0 is the chemical potential of Li in the anode (the Li metal). In practice, the change in the internal energy, ΔE_r , is often calculated instead because the contributions from the PV and the entropy terms are negligible [21]. Computational methods to evaluate directly entropy and Gibbs free energy change at finite temperatures also exist for more accurate calculations [22, 23].

Equations (10.2) and (10.3) form the basis for theoretical calculation of cell voltage for solid-state cathode materials including layer structured intercalation compounds [24–26] where lithium ions (Li^+) are inserted or extracted and the host structure remains stable. For example, consider the reaction given in Eq. (10.4) where an intercalation compound charges and discharges stably in between Li composition x_1 and x_2 ($x_2 > x_1$):

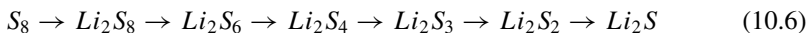


The Gibbs free energy change is given by

$$\Delta G_r = G_{Li_{x_2}MA_2} - G_{Li_{x_1}MA_2} - (x_2 - x_1)G_{Li}. \quad (10.5)$$

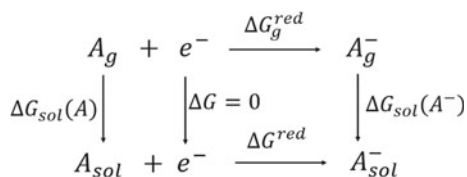
If the structures at the two intercalation limits are known, Eqs. (10.5) and (10.2) can be applied to evaluate the average redox potential between the two limits x_1 and x_2 .

The redox reaction in S, however, is not confined to the solid state, and S is not an intercalation material. In fact, crystalline S is composed of octa-atomic ring molecules, which break up and react with Li^+ , forming various intermediate species that dissolve in the electrolyte. Overall, the reaction sequence is given by



Note that the above sequence should not be understood as the actual redox sequence in S. Rather, it reflects the overall stoichiometry as S is reduced. Some of the intermediates are dissolvable in electrolyte, leading to the notorious polysulfide shuttle. A large portion of research efforts in Li–S systems has been devoted to alleviating the shuttle effect and the associated challenges.

Fig. 10.1 The thermodynamic cycle to calculate absolute free energy of reduction



Given the fact that polysulfides exist in the molecular form, the applicability of Eqs. (10.2) and (10.3) is questionable. The reference to S as the “cathode” material is not that meaningful because crystalline S is the initial reactant only. The formation of various intermediate species that often form a liquid mixture with the electrolyte necessitates a different approach to calculate the reaction voltage. Assume that a reaction intermediate A is formed and subsequently reduced through the following reaction:



Note that subscript “sol” indicates that the species is dissolved in the electrolyte solution. Equation (10.7) is the half-cell reaction at the cathode. The Gibbs free energy change associated with this equation is defined as the absolute free energy of reduction, ΔG^{red} , which can be determined through the thermodynamic cycle shown in Fig. 10.1.

The gas-phase reduction free energy, ΔG_g^{red} , is the electron affinity of species A (in the gas phase), corrected by finite-temperature (normally 298 K) contribution to the free energy. $\Delta G_{sol}(A)$ and $\Delta G_{sol}(A^-)$ are the solvation free energies of the neutral and reduced A. Since electrons are always defined to be a gas-phase species, their free energy contribution cancels out [27]. Thus, the absolute free energy of reduction is given by

$$\Delta G^{red} = \Delta G_g^{red} + \Delta G_{sol}(A^-) - \Delta G_{sol}(A). \quad (10.8)$$

Using the normal hydrogen electrode (NHE) as the anode, which has a reduction potential of 4.28 V [28], the overall cell potential, which is the difference between the reduction potential at the cathode and the anode, can be calculated by

$$V_{OC} = -\frac{\Delta G^{red}}{F} - 4.28. \quad (10.9)$$

If Li/Li⁺ redox couple is used as the reference electrode, whose reduction potential is 3.04 V lower than NHE, the cell potential is then

$$V_{OC} = -\frac{\Delta G^{red}}{F} - 1.24. \quad (10.10)$$

Equations (10.9) and (10.10) are widely used in calculating the cell potentials of various molecular species [29, 30], although different constants may appear if different reference electrodes are used.

It is noted that Li–S systems are much broader than using S as the cathode and Li as the anode. For example, the final reduced product, Li_2S , can also be used as the starting cathode materials. Except for an initial activation barrier, the electrochemical behaviors of Li_2S are similar to those observed in S in subsequent cycles [31]. A quasi-solid-state reaction has been proposed for smaller S molecules confined in a microporous carbon matrix [32]. Alumina–sulfur (Al–S) battery has also been studied, and the redox behaviors are observed to be similar to that of the Li–S system [33]. Regardless of the various forms used for S-based cathode materials, as well as other choices for the anode, the underlying electrochemical principle is the same. The challenges facing these systems are also similar: a fundamental understanding of the formation, dissolution, diffusion, and mitigation of polysulfide species remains the key aspect of S chemistry. The rest of this chapter will be devoted to a discussion of different computational techniques and their importance in revealing fundamental insights that are not always accessible by experiments.

10.3 Computational Methods: Principles and Limitations

10.3.1 Introduction and Definitions

The growth of computer simulation is intervened with the development of computational hardware and software. Today, the most powerful supercomputers can perform $\sim 10^{17}$ operations per second, and the first exaflop ($\sim 10^{18}$ operations per second) system is expected to be deployed in 2021. At the same time, computer modeling of materials has grown from earlier simulations of hard-sphere models to sophisticated electronic structure calculations. In fact, computational materials simulations are one of the top applications running on high-performance computing clusters around the world.

The advantages of a computational approach to materials research are obvious. For one thing, computational research is highly cost-effective, and for another, conditions that are inaccessible to experiments, for example, extremely high pressure, are simply adjustable parameters in a computer simulation. Most notably, the predictive power of computational modeling, i.e., predicting the structure and properties of a material before experimental discovery, has enabled a new paradigm in materials research, as exemplified by the Materials Genome Initiative (MGI) that calls for the integration of computational and experimental materials research toward expedited materials discovery.

Although the computational materials scoreboard keeps growing, designing new materials entirely on a computer is only theoretically possible, at least in the foreseeable future. For Li–S systems, computationally designed electrodes, interlayers, or

electrolyte additives that lead to an industrially applicable high energy density and long cycle life Li–S battery have yet to be seen. The limited success, although partially due to the extremely complicated redox behaviors of S, is rooted in the intrinsic limitations of various computational techniques. The purpose of this section is to present the basic principles of different techniques and discuss their respective limitations. It is hoped that the readers will be able to choose appropriate techniques for their own problems and interpret the results judiciously.

To avoid any unnecessary confusions, we will start by defining a few different structures, including the following.

Electronic structure: the distribution of electrons, or the electronic wave functions, and the corresponding energies. They are the eigenfunctions and eigenvalues of the electronic Hamiltonian eigenvalue equation (see Sect. 10.3.2). Instead of wave functions, some methods report the electronic density, which is simply the modulus square of the electronic wave function. For crystalline solids, the electronic structure is often represented by a plot of the energy band structure. Electronic structures are directly responsible for various physical and chemical properties of materials including bonding, optical excitation, and magnetic responses.

Atomistic structure: the chemical composition, arrangement, and movement of atoms in a system. If the system of study is a molecule, it is equivalent to the molecular structure; if the system is a crystal, it is equivalent to the crystalline structure. It can also be used to refer to the atomic arrangement along a surface, interface, grain boundaries, and defects. Some computational methods provide details regarding both the electronic and the atomistic structures, while other methods concern only the atomistic structures. In computational materials, atomistic structure (or sometimes atomic structure) does not concern the internal structure of atoms.

Microstructure: structures that can be revealed by an optical microscope, including the arrangement of different phases, grains, or pores. No details regarding atomistic or electronic structure are available in a microstructure analysis.

These structures are different from the macroscopic structure of a battery, which, in a simplified representation, includes the cathode and the anode immersed in the electrolyte. However, as we will see, it is these structures that dictate the overall performance of the battery. To obtain a fundamental understanding of their impacts on battery performance is a profound scientific challenge that can only be achieved through a coherent effort involving experiments, theories, and computer simulations.

10.3.2 *Ab Initio Computer Simulation Methods*

“Ab initio” means “from the beginning”, and an ab initio, or first principles, calculation indicates that it is based on the most fundamental principles and no adjustable parameters are used. When dealing with materials, which are a collection of electrons and nuclei, the governing principle is quantum mechanics. Thus, we will start from the many-body Schrödinger equation [34], given as follows:

$$i\hbar \frac{\partial \Psi(r, R, t)}{\partial t} = \hat{H} \Psi(r, R, t) \quad (10.11)$$

where \hat{H} is the Hamiltonian operator, \hbar is the reduced Planck's constant, and $\Psi(r, R)$ is the wave function, which is a function of electronic coordinates r and nuclear coordinates R . Solutions to Eq. (10.11) could give the time evolution of the wave function and thus the macroscopic properties of the system. In many cases, \hat{H} does not depend on time explicitly, and Eq. (10.11) reduces to the time-independent Schrödinger equation:

$$\hat{H} \Psi(r, R) = E \Psi(r, R). \quad (10.12)$$

Unfortunately, neither Eq. (10.11) nor (10.12) is solvable except for a limited number of simple systems and various approximations must be applied. Even after approximations, analytical solutions are not possible, and we have no choice but to find numerical ones. For this reason, modern computers are of enormous value and computer simulations are becoming increasingly important.

The first step is often to separate the nuclear and electronic motion, which is known as the Born–Oppenheimer approximation,

$$\Psi(r, R) = \chi(R)\phi(r, R), \quad (10.13)$$

where $\chi(R)$ and $\phi(r, R)$ are nuclear and electronic wave function, respectively. In the spirit of the Born–Oppenheimer approximation, the electronic wave functions are solved by treating nuclear coordinates constant. Equation (10.12) transforms into the eigenvalue equation of the electronic Hamiltonian, $H_e(r, R)$:

$$H_e(r, R)\phi(r, R) = E(R)\phi(r, R). \quad (10.14)$$

Equation (10.14), under the present form, is still not solvable. Developing accurate and efficient algorithms to solve Eq. (10.14) is at the core of computational chemistry and solid-state physics; each developed its own flavor of method. In computational chemistry, the behavior of atoms and molecules is of interest, and the concept of the linear combination of atomic orbitals (LCAO) is intuitive and powerful. Not surprisingly, the efforts in computational chemistry have been focused on determining the best wave function of the system starting from atomic wave functions. In the Hartree–Fock (HF) theory, which is widely used in computational chemistry, the many-electron wave function is approximated by the so-called Slater determinant orbitals that are formed by one-electron orbitals. Application of the variational principle leads to the well-known Hartree–Fock equation which must be solved in a self-consistent manner starting from an initial guess of the one-electron wave functions [35, 36]. A basis set, which is a set of functions, e.g., Gaussian-type and Slater-type, is used to represent the one-electron wave functions. In general, the use of a larger basis set brings more flexibility to represent different features of the “true” wave functions, which leads to an increase in the accuracy of the calculation as well

as the associated computational cost. The accuracy of the HF theory is limited to the use of an infinite basis set, known as the HF limit. However, even if an infinite basis set is used, the HF limit is not the true ground state energy of the system because electron correlation is neglected, and the difference is known as the “correlation energy” [37]. Neglecting the correlation energy is acceptable for processes where molecular bonding remains stable because the correlation energies are expected to cancel out systematically. If bond breaking and formation are involved, for example, in electrochemical conversion of S, neglecting the correlation energy can be detrimental and one needs to resort to “post” HF methods including Møller–Plesset perturbation methods in the second (MP2), third (MP3), and fourth (MP4) order, the configuration interaction (CI) method, and the quantum chemistry composite methods such as the Gaussian- n theory (G2, G3, and G4) and the complete basis set (CBS) method [38].

In solid-state physics or theoretical condensed matter physics, the systems of interest are solids. Given the inherent translation symmetry of crystalline solids and the resulting Bloch’s theorem [36, 39], the choice of using plane waves to construct crystal wave functions is a natural one (non-crystalline solids are studied with a larger supercell with periodic boundary conditions). The advent of the density function theory (DFT) [40, 41] shifted the focus further away from the wave functions to electron density, which is far more manageable. Following a similar variational process, one arrives at the Kohn–Sham equation [36], which includes explicitly the exchange and correlation effects through the so-called exchange–correlation functional, V_{xc} . This is a major advantage over the HF method, although the exact form of V_{xc} is unknown. Widely used approximations of V_{xc} include the local density approximation (LDA) [42] and the generalized gradient approximation (GGA) [43]. For more accurate calculations, various corrections are available depending on the nature of the system studied. For example, the DFT + U (LDA + U or GGA + U) method may be needed for strongly correlated systems [44, 45], and non-local correlation functionals that describe dispersion interactions are needed if the van der Waals interactions are important [46]. In this sense, DFT methods are not entirely “ab initio”, because empirical parameters do appear in some of the popular functionals. Such a distinction is not a critical one, nonetheless, the use of “ab initio” has been habitually avoided for DFT calculations.

In DFT calculations, there is no clear route to improve the accuracy, because it requires an extensive effort to refit the exchange–correlation functional. In contrast, one can always try to improve an HF calculation by resorting to, for example, a larger basis set. Once a suitable exchange–correlation functional is chosen, the Kohn–Sham equation can be solved using a similar approach as that in the case of the HF equation. Starting from an initial wave function (and thus electron density) constructed from a plane wave basis set, the energy of the system is minimized iteratively until a preset convergence criterion is satisfied. The use of a plane wave basis set is mostly out of convenience, and other types of basis sets can also be used as long as Bloch’s theorem is satisfied [47, 48].

As pointed out earlier, electron exchange and correlation are included in a DFT calculation through the exchange–correlation functionals. As a result, the DFT method enjoys a reasonably good accuracy at a lower computational cost as compared

to the HF method and is now the leading method for electronic structure calculations. It should be noted that both Hartree–Fock and DFT are ground-state methods, which is evident because both are derived following a variational procedure. For the study of electrochemical storage, excited states are involved and one may need to resort to, for example, post-HF methods and time-dependent DFT (TD-DFT) method.

Up to now, we have focused on solving Eq. (10.14) for a fixed nuclear coordinate. The process can be repeated for different values of R , leading to an effective potential, $E(R)$, on which nuclei can move (note a term stemming from nuclei–nuclei interactions should be added). The effective potential, known as the Born–Oppenheimer or adiabatic potential energy surface (PES), can be plugged into the nuclear eigenvalue equation, thus fully solving Eq. (10.12) (within the Born–Oppenheimer approximation). In many applications, quantum effects in nuclear dynamics can be neglected [49] and the dynamics of the nuclei is given by the classical Newton’s second law of motion:

$$M\ddot{R} = -\frac{\partial E(R)}{\partial R}. \quad (10.15)$$

Energies appearing in Eq. (10.15) are the effective potential obtained by solving Eq. (10.14), and the negative gradient of the energy is simply the force acting on the nuclei, which can be calculated following the Hellmann–Feynman theorem [50]. Such a quantum mechanical treatment of electrons and a classical description of nuclear dynamics enables the study of various chemical processes at finite temperatures. This group of methods is known as *ab initio* molecular dynamics (AIMD) simulations [51, 52], and two distinct flavors of implementation exist [53, 54]. It is also worthwhile to point out that the Hellmann–Feynman force can be used to find the equilibrium geometry of materials using minimization algorithms that relax the structure to the energy minimum, or zero force.

10.3.3 From “*Ab Initio*” to *Empirical Force Fields*

The computational cost of AIMD simulations remains high because Eq. (10.14) must be solved “on the fly”, which has limited its use to systems of relatively small size (<~1000 atoms). If the potential energy surface, or $E(R)$, can be determined beforehand for a wide range of nuclear configurations, then solving Eq. (10.14) is no longer needed and the computational cost will be greatly reduced, which is the basic principle of the classical molecular dynamics (MD) simulations [55]. In practice, the potential energy surface is described by an empirical force field, which is a set of functions describing pairwise, sometimes enhanced by three-body and four-body corrections, interactions between atoms. A number of parameters appear in the force field, which can be determined empirically by fitting calculated properties to experimental data. First principles interatomic potentials are also becoming popular, where the force field is fitted against potential energies or forces from electronic structure

calculations of a few different nuclear configurations. It is not possible to include all different experimental data, or all possible nuclear configurations, in the fitting of the force field. As a result, classical MD simulations are subjected to limited transferability. Before performing a classical MD simulation, the validity of the force field must be verified. Nonetheless, MD simulations enjoy the greatly reduced computational cost and have been widely used to study problems in chemistry, biochemistry, and materials science.

For the study of electrochemical systems, the ability to describe bond breaking and formation, as well as the associated changes in valence states of ions, is essential, which is beyond the scope of traditional classical MD simulations. Charge transfer potentials, or reactive force fields, including the charge-optimized many-body (COMB) potentials [56], the reactive force field (ReaxFF) [57], and the dynamically adaptive force field approach [58], are developed for this purpose, although parameterization of these potentials is challenging. The atomic charges in these potentials are generally determined based on the electronegativity equalization principle [59, 60], which requires multiple iterations for each ionic configuration, leading to a significant increase in the computational cost compared to traditional, fixed-charge MD simulations.

10.3.4 Different Scales in Computer Simulations

Computational techniques discussed so far (Sects. 10.3.2–10.3.3) are, in general, referred to as atomistic simulation techniques because these methods deal with electronic and/or atomistic structures directly. In other words, such computational studies often trace the properties of materials to their electronic and/or atomic origins. If electronic structure calculations are involved, the typical simulation time and system size are around the order of 10^{-12} s and 10^2 atoms, respectively. These measures increase to 10^{-9} s and 10^5 atoms for classical MD simulations. The growing power of supercomputers has enabled MD simulations of billions of atoms [61, 62], as well as simulations at the microsecond scale [63, 64].

The time and length scales accessible by atomistic simulations, given the computational resources available today, are still far away from macroscopic reality. Indeed, based on their typical system sizes, most atomistic simulations study problems at atomic or nanoscopic scales. Various methods are developed to further increase the time and length scales. For example, in the coarse-grained method, a group of atoms is represented by a “pseudo-atom” to reduce the degree of freedom of the problem [65]. In phase field modeling, the focus becomes the microstructure evolution of the material [66], instead of electronic or atomistic structures. This group of computational techniques is known as mesoscale methods. Note that microstructure has been conventionally used in materials science and engineering, which is a subject at the mesoscale in computer simulations.

For many engineering applications, a knowledge of the electronic, atomistic, or microstructures is not relevant. As such, these structural features are approximated

by a continuous medium. A system is composed of multiple media with different properties, and their temporal and spatial evolutions are governed by a few constitutive equations that are often in the form of partial differential equations. These equations are then solved numerically using, for example, finite element or finite difference methods. These continuum-level methods expand the scope of computer simulations to the macroscopic scale, the scale at which important battery performances, for example, rate capability, cycle stabilities, and internal resistance, can be evaluated. In the extreme case where a fast response is needed, for example, in a real-time battery management system, further simplifications are made and mathematical or equivalent circuit models are used [67]. Even though electronic and atomistic structures do not appear in macroscopic simulations, the importance of such fine structures is embedded in the physical properties of the medium, for example, density, porosity, energetics, electronic and ionic conductivity, and diffusivity of different species, which can be determined either experimentally or computationally. Sometimes, such data are not readily available and are often obtained by fitting to experimental data, which limits the applicability of macroscopic models.

As can be seen from the above discussion, the gradual increase in the time and length scales leads to the gradual loss of structural information. Ideally, a performance issue of a material system can be traced back to the properties of its component, which can be further traced back to the electronic or atomistic structure of the component, thus establishing the structure–property–performance relation. If such a relation exists, one can then design, compute, and predict the macroscopic performance of a material system entirely based on its chemical composition. However, such a “Materials by design” approach is still a “dream” of materials research and will remain so in the foreseeable future. On the one hand, we simply don’t have the computational resources to perform an electronic or atomistic calculation on a macroscopic scale; on the other hand, the direct link between some of the important engineering parameters, for example, corrosion resistance, viscosity, hardness, cycle stability (in the case of batteries), among others, and the electronic and atomistic structures has yet to be established.

Although an all-embracing computational method is at present not available, the so-called multiscale modeling approach has become popular [68]. In a multiscale model, material properties on a larger scale can be built upon information from a finer scale. For example, data obtained from atomistic simulation, including the Gibbs free energies of bulk phases and interfacial energies, are fed to a phase field model, enabling a first principles phase field method [69]. Other modes of operation also exist, all involving data exchange at different scales. The workflows of various multiscale models, as well as those of the stand-alone models, are demonstrated in Fig. 10.2. At present, bridging the gap between computational methods at different scales remains one of the foremost challenges in computational materials science.

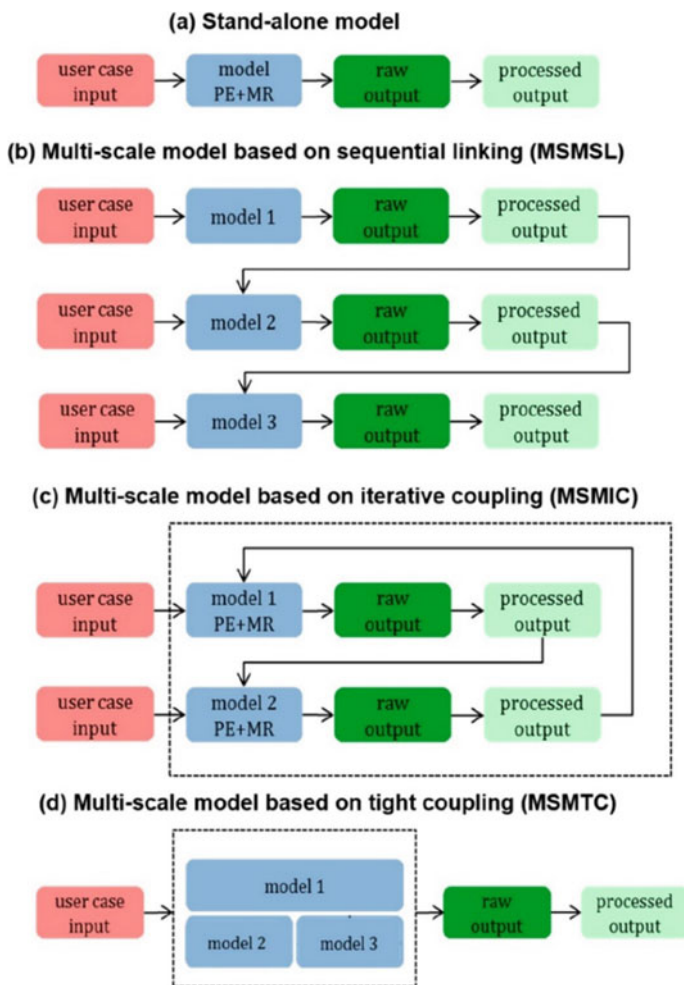


Fig. 10.2 Workflows of **a** stand-alone models, **b** multiscale models based on sequential linking (MSMSL), **c** multiscale models based on iterative coupling (MSMIC), and **d** multiscale models based on tight coupling (MSMTC). “PE” refers to “physical equation” (mathematical equation based on a fundamental physics theory which defines the relations between physics quantities of an entity) and “MR” to material relation (materials specific equation providing a value for a parameter in the physics equation). Reproduced from Ref. [68]. Copyright 2019 American Chemical Society

10.3.5 Choose an Appropriate Simulation Method

We have outlined a collection of computational tools at different time and length scales. Choosing the best tool requires an understanding of both the calculation to be performed and the tool itself. The available computational resource is an important consideration as well. Furthermore, non-“ab initio” methods are often restricted

by the available input data. For example, performing a classical MD simulation is meaningless if the force field is not available or verified; the microstructural evolution predicted from a phase field modeling could be erroneous if the interfacial and bulk-free energies are wrong. Sometimes, assumptions that are specific to the system studied are introduced, and these models must be cautiously verified before applying to a different system. In general, *ab initio* methods, either wave function-based or DFT-based, are preferred if an atomistic understanding is desired. On the other hand, if the overall device performance is needed, macroscopic methods are preferred. In the case of Li–S systems, the lack of a fundamental understanding of various molecular species that appear during charge and discharge remains the most critical issue. Thus, our computational efforts should emphasize atomistic simulations that help to improve our fundamental understandings of the S chemistry.

10.4 Computational Studies of Sulfur-Based Battery Systems

The increasing popularity of computer simulations is evident in virtually all branches of materials research. More and more experimental studies include some forms of computational work, ranging from simple structural characterization to complex computational prediction. Not surprisingly, such a trend is also observed in the study of Li–S and related systems. Most computational studies in Li–S systems are at the microscale revealing electronic or atomistic structure; mesoscale and macroscale modelings are relatively scattered. Arguably, it is due to the unique S chemistry involving the formation, dissolution, and diffusion, which necessitates a microscopic understanding of these elementary processes.

In this section, we will demonstrate how various computational methods can be used to study S-based battery systems, with an emphasis on the microscopic mechanisms of the electrochemical conversion of S. Based on the role of the computations, we will break our discussions into three categories, structures and energetics, mechanistic studies, and predictive studies. Such distinctions are made only for the purpose of illustrating the different levels of sophistication of computational studies. In fact, studies from different categories are often interdependent: mechanistic studies are based on a knowledge of the structural and energetic characteristics of the system, while computational predictions require an understanding of the underlying mechanisms.

10.4.1 Structures and Energetics

Almost all computational materials studies start from determining the molecular or crystalline structures, as well as their energies, of the systems of interest, although

pure structural and energetic calculations are rare. Computationally, if a reasonable initial structure is known, then structural optimization is relatively straightforward. Efficient algorithms exist to find the equilibrium structure, which is defined as the structure corresponding to the global minimum on the PES. In practice, experimental data, if available, are often used as the initial structure for computational structural relaxation. Structural optimization without any prior knowledge can be challenging, although it is, at least in principle, possible to predict crystal structures at any given thermodynamic conditions entirely based on the composition of the material [70]. Atomistic computational techniques, including ab initio methods and classical force field methods, are the natural choice for structural optimization. However, the resulting structure depends sensitively on the quality of the interatomic potentials if a force field method is used. As a result, ab initio methods are often preferred, especially for accurate structural determination.

10.4.1.1 Crystalline Materials

If the electrochemical reaction of S follows that given in Eq. (10.1), then there are three crystalline solids, and their structures are all well-known. Elemental S crystallizes in an orthorhombic structure composed of cyclo-octasulfur (S_8) rings, known as α -S, at room temperature. Both Li and Li_2S are cubic. Table 10.1 lists the structural parameters determined from DFT calculations, together with the experimental data. Note that because van der Waals interactions are expected to be important between S_8 rings, the DFT calculations were performed using a van der Waals density functional [71]. The accuracy (error <1%) is noteworthy. Note that the accuracy of the results depends on the exchange–correlation functionals used, and in general, an error of <3% is expected for DFT structural optimizations.

The bulk modulus can be conveniently obtained by performing structural relaxations at a few different volumes. The obtained energy–volume relation is then fitted to an equation of state and the bulk modulus is given by

$$B = V \frac{\partial^2 E}{\partial V^2}. \quad (10.16)$$

Table 10.1 Structural parameters and bulk modulus of α -S, Li, and Li_2S from DFT calculations. Experimental data are given in parentheses

	Space group	Lattice parameters (Å)			Bulk modulus (GPa)
		<i>a</i>	<i>b</i>	<i>c</i>	
α -S	<i>Fddd</i>	10.38 (10.46 [72])	12.80 (12.86 [72])	24.52 (24.48 [72])	10.8 (14.5 [73])
Li	<i>Im$\bar{3}m$</i>	3.45 (3.48 [74])	–	–	13.7 (12.9 [75])
Li_2S	<i>Fm$\bar{3}m$</i>	5.71 (5.69 [76])	–	–	40.8 (45.7 [77])

The calculated bulk moduli are also listed in Table 10.1. Note that the error is much larger than that of the lattice parameters. In fact, the error in bulk moduli from DFT calculation can be as high as 30%, although it is not an essential parameter for battery performance.

The equilibrium energy is the total energy of the system at the equilibrium structure. Such energies from DFT calculations are the internal energy of the system at zero temperature and zero pressure. Contributions from the PV term and the entropy term at finite temperatures are often negligible. Thus, the change of the Gibbs free energy for reaction (10.1) can be approximated and the open-circuit voltage is calculated to be 2.2 V. This is in the correct range of the observed voltage, although the experimental voltage profile is far from a single plateau at 2.2 V, indicating a much more complex reaction than what is given by Eq. (10.1). Computationally, the reaction voltage can also be calculated at a finite temperature. For example, vibrational contributions to the enthalpy and entropy can be calculated within the harmonic approximation [77], where the vibrational frequencies are obtained by calculating the phonon spectrum [78]. The calculated entropy contribution to the cell potential is less than 0.05 V [77], which is, indeed, negligible.

Other crystalline phases have also been reported in Li–S batteries. At ambient conditions, β -S, which is monoclinic, exists at temperatures above 95 °C, although recent experiments suggested the formation of β -S at room temperature during cycling of carbon fiber–S composites [79]. Li_2S_2 is another interesting crystalline phase, which is believed to be a reaction intermediate and is not thermodynamically stable [77]. Consequently, no experimental structural information is available. As has been pointed out earlier, it is possible to determine the crystal structure entirely based on the composition. Indeed, an evolutionary algorithm [80] was used and the seven most promising structures were predicted, as shown in Fig. 10.3 [81]. The two lowest structures are very close in energy with a reaction voltage of around 2.1 V versus Li/Li^+ , which matches the lower voltage plateau observed in Li–S systems. Subsequently, the transient existence of Li_2S_2 was observed, and the experimental X-ray diffraction pattern (XRD) matches well with that from calculated pattern using the minimal energy structure [82], as given in Fig. 10.4. The fitted lattice parameters were also in close agreement with those from computational prediction. An error of less than 3% was reported, which is within the accuracy of the DFT method.

As long as the reaction participants remain in the crystalline states, the approach described here can be applied to determine their structures and the corresponding reaction voltage. However, some of the S-based systems have a liquid cathode, for example, in the case of a Na–S battery [83], and one may need to calculate the molecular structures of various species involved in the reaction. Furthermore, amorphous materials have been used as the cathode [84]. The reaction product, Li_2S , is often found to exist in an amorphous form as well, which is evident from the missing peaks on its XRD pattern [85]. DFT calculations on such systems are more challenging due to increased system sizes.

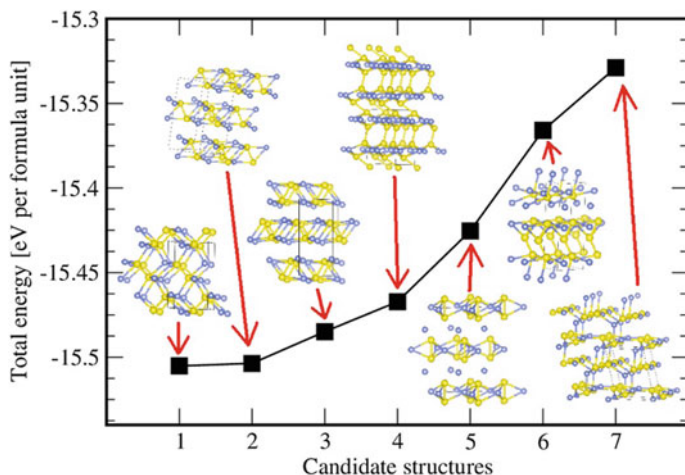
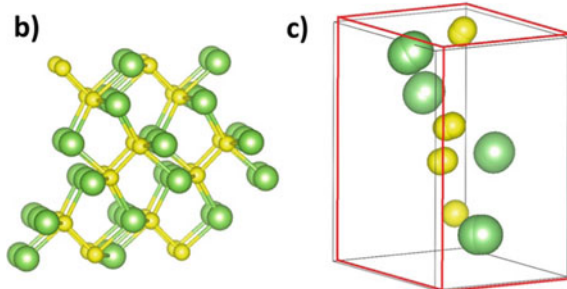
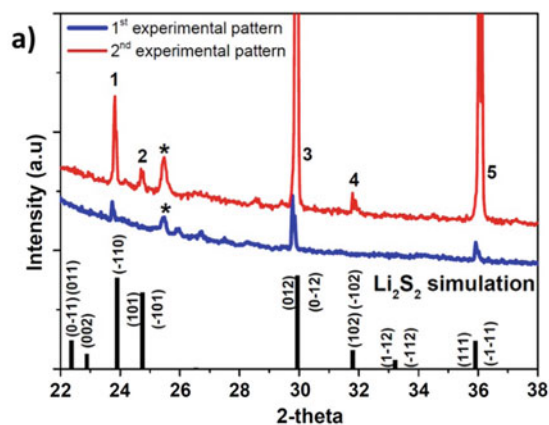


Fig. 10.3 The total energies of the seven most promising Li_2S_2 structures. Yellow and blue circles represent S and Li atoms, respectively. Reprinted with permission from Ref. [81]. Copyright 2014 Elsevier

Fig. 10.4 a Comparison between the simulated (black lines) and the observed XRD patterns (blue and red); **b** Li_2S_2 crystal structure (sulfur in yellow and lithium in green); **c** schematic diagram showing the lattice parameter differences in fitted (thin black frame) and calculated (red frame) data. Reprinted with permission from Ref. [82]. Copyright 2016 Elsevier



10.4.1.2 Molecular Species

Except for the end members of the reaction, almost all the reaction intermediates, for example, those given in Eq. (10.6), are not in the crystalline state. The α -S itself is a molecular solid composed of S_8 , and the reduction of S comes down to the reduction of S_8 . The electrochemical behavior of S is expected to be dominated by the structure, orientation, and bonding of S_8 rings and various molecular intermediate species. The appropriate tool to study such molecular behaviors are ab initio methods including wave function-based and density-based methods. AIMD and classical MD simulations are also important in the study of structural evolutions of molecular species, although the applicability of classical MD simulations is limited by available interatomic potentials.

Like polymorphism in crystals, isomerism is a similar concept that refers to structural variations in molecules. The first task in a computational study of molecular species is often to find the minimal energy isomer. Ab initio calculations have found that the crown-shaped structure with D_{4d} symmetry is the global energy minimal of S_8 , although a few other structures are close in energy [86]. Upon lithiation, the S_8 rings are expected to open and bond with incoming Li^+ , forming various lithium polysulfides Li_2S_n ($1 \leq n \leq 8$). The overall reaction sequence is given by Eq. (10.6), and the equilibrium geometry predicted from a high-level quantum chemical calculation is given in Fig. 10.5 [87]. For $2 \leq n \leq 8$, the minimal energy structure is found to be cyclic.

One important factor to consider in determining the equilibrium molecular structures is the effect of the electrolyte. Various molecular species appearing in a liquid electrolyte interact with lithium polysulfides, which may result in a change in the equilibrium geometry as compared to that in the gas phase. There are two different models in addressing the so-called solvation effect. In the explicit models, the solvent molecules are included in the calculation explicitly, whereas in the implicit models, the solvent is modeled by a continuous medium with empirically determined dielectric properties. The use of an explicit model is obviously limited by the computational cost associated with the increased system size, while the application of an implicit model needs to be carefully verified because of the empirical parameters involved. It is interesting to note that the equilibrium geometries given in Fig. 10.5 are obtained for the gas-phase molecules (single molecules in vacuum) without considering the solvation effects. Similar results have been reported using an implicit solvation model [88], while an explicit model predicts a linear geometry for Li_2S_6 and Li_2S_8 [89]. Such a discrepancy suggests the intricacy of the computational study of molecular species in solvents. Continued efforts are clearly required.

The importance of the solvation effect is also manifested in the calculation of the redox potential. Equation (10.10) is often used to calculate the redox potential for molecular species, however, the calculation of the redox Gibbs free energy involves the calculation of solvation free energies of both neutral and charged species (Fig. 10.1), which depends sensitively on the solvation model used. It is normal to have a mean unsigned error of around 0.2 V for the calculated reduction or oxidation potentials, and in some instances errors of >0.5 V were observed [90], which makes

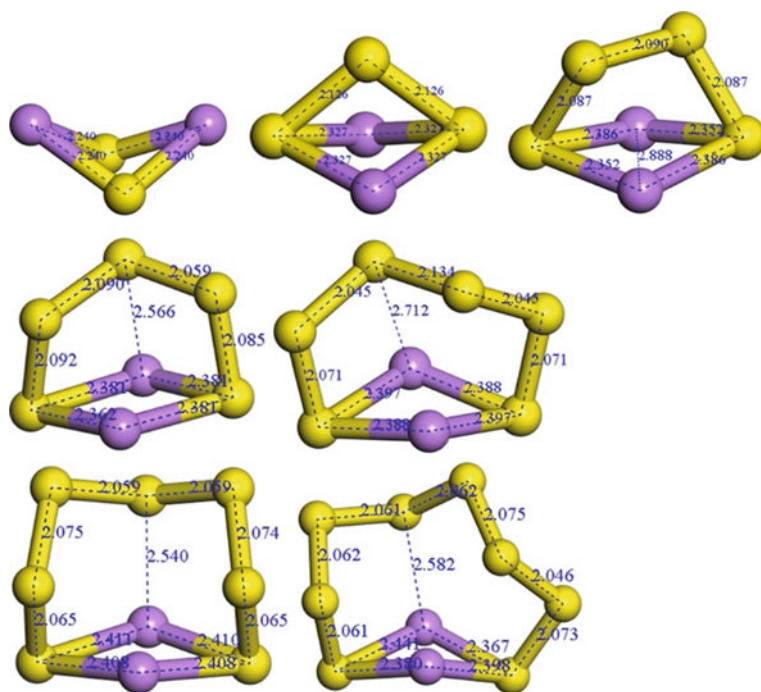


Fig. 10.5 Optimized geometries, structural parameters of Li_2S_n ($2 \leq n \leq 8$) clusters. Purple and yellow balls denote lithium and sulfur atoms, respectively. Reprinted with permission from Ref. [87]. Copyright 2019 American Chemical Society

direct comparison with experimental measurement infeasible. It is also important to note that contribution from the entropy term is not always negligible in molecular species, although computational methods are available to evaluate entropy and thus the Gibbs free energy of a given thermodynamic process [22, 23]. Nonetheless, a comparison of the reduction potentials of different species can provide useful insight regarding the reaction sequence, assuming that there is a systematic cancellation of the errors. In fact, carefully performed computations often predict reduction potentials that are within the range of observed cell voltage [29, 88].

The structural evolution of various molecules in the electrolyte solution is also of interest, which could provide important insight into the S redox chemistry. Ab initio molecular dynamics simulations showed that the energy and S–S bond length fluctuate with an energy span of 0.5 eV, as shown in Fig. 10.6 [29], which may lead to the fragmentation of the eight-member ring. However, energy calculations suggested that the S_8 rings are quite stable, and the fragmentation free energies range from 0.87 to 2.56 eV [29]. On the other hand, S_4 is the least stable that promises high electrochemical reactivity. AIMD simulations have also been performed to study the structural evolution of Li_2S_6 and Li_2S_8 , where the electrolyte molecules were included explicitly in the first solvation shell, and a polarized continuum model was

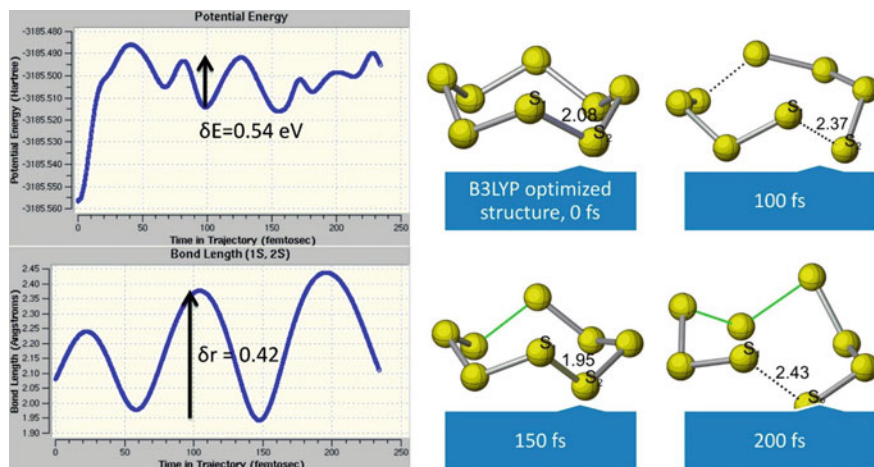


Fig. 10.6 Left: energy and S–S bond length extracted from ab initio molecular dynamics trajectories. Right: minimal energy structure as the initial structure (0 fs) and snapshots at 100, 150, and 200 fs. Reprinted with permission from Ref. [29]. Copyright 2014 American Chemical Society

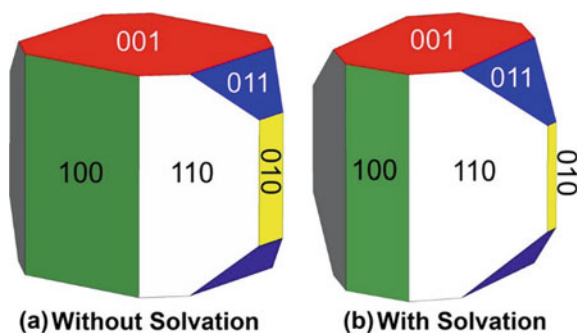
used to represent the rest of the liquid electrolyte [91]. Strong interactions between lithium and oxygen atoms in the electrolyte molecules are observed, which suggests that a stronger interaction between lithium and the cathode material is needed to achieve efficient trapping of lithium polysulfides.

Recently, organosulfides have attracted wide attention to be used as a possible cathode material, and the reduction of organosulfides shares many common characteristics with that of S [92–95]. A detailed discussion of organosulfides can be found in Chap. 7. These molecules are mixed with the electrolyte solution, forming a catholyte. Solvation models discussed above can be applied similarly to study the structures of organosulfides and predict their reduction potentials. Alternatively, the LUMO levels of different organosulfide molecules can be calculated (under the same theory level) to estimate the reaction voltage because the LUMO levels correlate approximately with the reduction potential [96–98], although such an estimation is only qualitative and deviations have been reported [99].

10.4.1.3 Surface and Interface

In computational studies of crystalline solids, the periodic boundary condition is often applied, which implies an infinite solid with no terminations. In reality, a crystalline solid terminates at various surfaces determined by the surface energies. Furthermore, an electrochemical reaction must initiate from the surface of the material. In the case of S, the initial lithiation leads to the reduction of S_8 rings that are close to the surface. It is thus important to understand the surface properties of S. Computationally, surface energies are often subject to a convergence problem, which can be alleviated by

Fig. 10.7 Equilibrium shape of α -S. **a** Neglecting the solvation effect; **b** including the solvation effect. Reprinted with permission from Ref. [77]. Copyright 2015 American Chemical Society

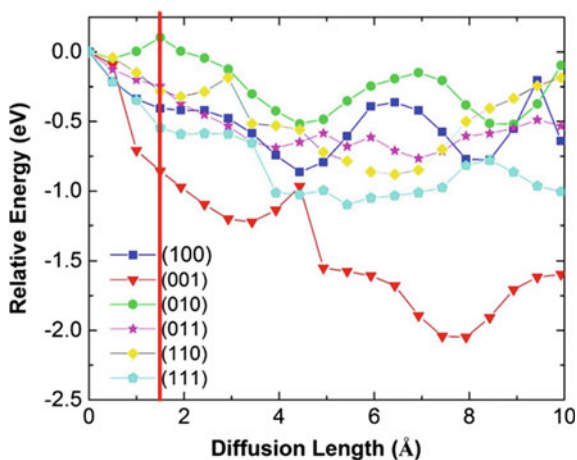


constructing two-dimensional surface slabs with varying thickness [100]. Note that surface energies are also impacted by the solvation effects. Once the surface energies are known, the Wulff construction can be used to determine the equilibrium shape of the crystal that participates in the reaction. Figure 10.7 compares the equilibrium shape of α -S with and without the solvation effects [77]. In both cases, the (110) facet has the largest fraction of the total surface area, although contributions from (100) and (001) are also obvious. Overall, the effect of solvation appears to be minor in terms of the equilibrium shape of S. In the case of Li_2S , the energy of (111) surface is significantly smaller, which leads to an equilibrium shape dominated by the (111) surfaces [77].

Different surface orientations lead to different lithium diffusivity into the surface, which is evident from the calculated surface diffusion barriers. Note that in intercalation compound, lithium diffusivity in the bulk of the cathode material is a critical parameter that determines the rate capability of the cathode. In the case of S, the bulk diffusivity is less relevant because S, as a conversion compound, does not maintain the structural integrity, and the focus has been shifted to the diffusion of various polysulfide and lithium polysulfide species, which will be discussed in Sect. 10.4.2.1. However, the surface diffusion barrier is of importance because it provides insights on the initiation of the electrochemical conversion in S. Figure 10.8 depicts the energy variation of a Li^+ into various S surfaces, indicating the existence of a driving force during lithiation, although the magnitude of this driving force depends on the surface orientation.

From Fig. 10.8, it is clear that the (001) surface, which is one of the main orientations appearing in an S particle, enjoys a larger driving force than other surface orientations. Given the existence of this driving force, Li^+ ions are expected to diffuse into a few angstroms into the surface. It is then of interest to understand how the surface structure responds to incoming Li^+ , which has been studied by AIMD simulations [101], and the structural evolution at different stages of lithiation is given in Fig. 10.9. Dimethoxyethane (DME) molecules were included in the simulation to provide a more realistic physical picture of the process. Several notable features are observed. Firstly, lithiation leads to the ring opening of S_8 molecules, which is

Fig. 10.8 Energy variation of a Li^+ along a diffusion path into S with different surface orientations. A driving force is observed for Li^+ insertion (lithiation). Red line gives the location of the surface. A few angstroms into the surface, the interfacial barrier transitions into the regular, bulk barrier



expected, although the molecules formed as a result of lithiation are far more complicated than those described by Eq. (10.6). Secondly, S_8 molecules in the second layer are almost intact, indicating a layer-by-layer conversion process. Thirdly, dissolution of polysulfides into the electrolyte is obvious, especially at the later stage of the reaction. It is again expected, and such an AIMD simulation provides an atomistic resolution of the elementary processes that determines the overall S chemistry.

Because electrolyte was included in the above simulation, it is, although rather simplified, an interfacial system. Experimentally, various forms of C are used to form the S–C composite cathode, which provides the necessary electronic conductivity to overcome the insulating nature of S. Consequently, various C–S interfaces form inside the cathode. Because C does not participate in electrochemical conversion directly, it is often neglected in computer simulations. However, the C hosts are often doped with, for example, oxygen (O), nitrogen (N), or decorating inorganic nanomaterials, to provide chemisorption of polysulfide species, which is, again, an interfacial phenomenon [102–104]. Neglecting such a contribution certainly misses out on important physics. In fact, the concept of “interfaces” in Li–S systems is exceedingly broad, and interfaces form between various components, including, but not limited to, the active material (S), the C host (including various dopants) [102], coating materials [105], interlayers [106], catalytic substrates [107], and the electrolytes (liquid or solid) [108]. These interfaces are often designed to control the electrochemical reaction in S. Regardless of the interfacial structures or materials involved, there are at least three common design principles. First, the interface must be able to bind various polysulfide species to minimize the shuttle effect and loss of active materials. Second, it should allow for fast lithium diffusion for uniform reaction. Finally, it should have sufficiently high electrical conductivity for fast reaction kinetics. Figure 10.10 depicts an example three-phase interface formed between the C matrix, a catalytic center, and the electrolyte. The role of the catalytic centers is also shown. Such interfacial systems are beyond the accessible length scales of

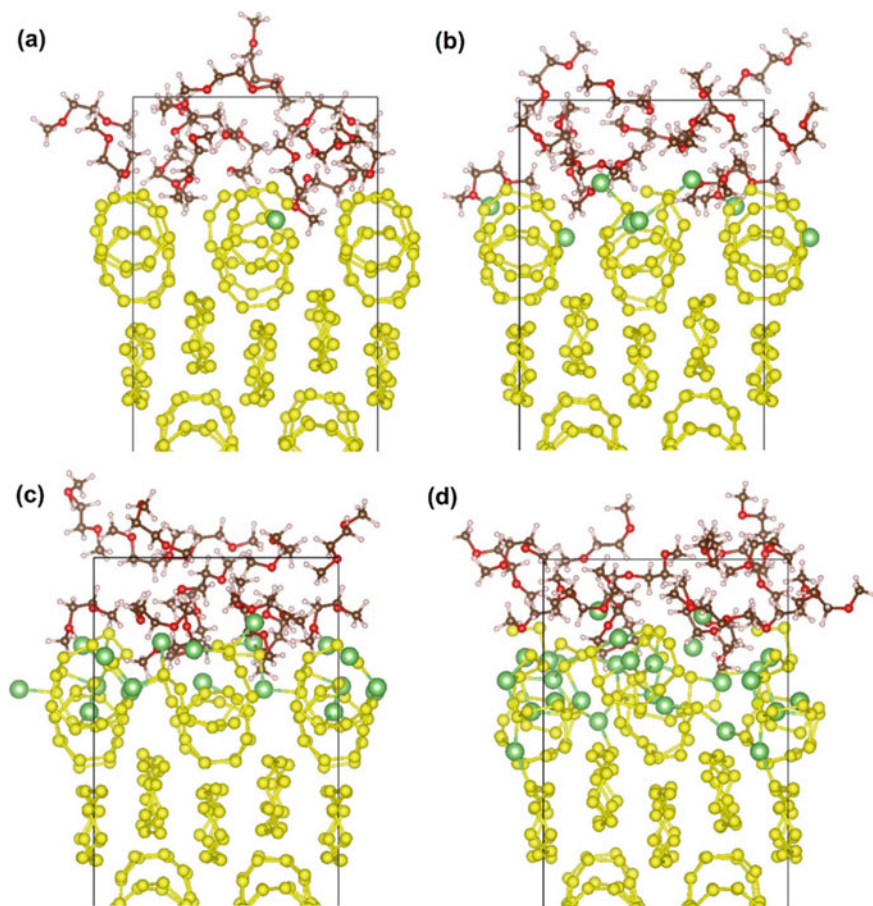


Fig. 10.9 Representative atomistic structure of the S8 (001)/electrolyte interface during different stages of the reaction. Reprinted with permission from Ref. [101]. Copyright 2018 American Chemical Society

ab initio methods at present. Atomistic simulations based on empirical force fields are the appropriate tool, although high quality interatomic potentials required to describe a large number of chemical species that may appear at these interfaces are not always available. Nevertheless, valuable insights can be obtained by calculating, for example, binding energies with polysulfides and lithium diffusion barriers without modeling the entire interfacial structure, which will be discussed in more detail in Sect. 10.4.3.

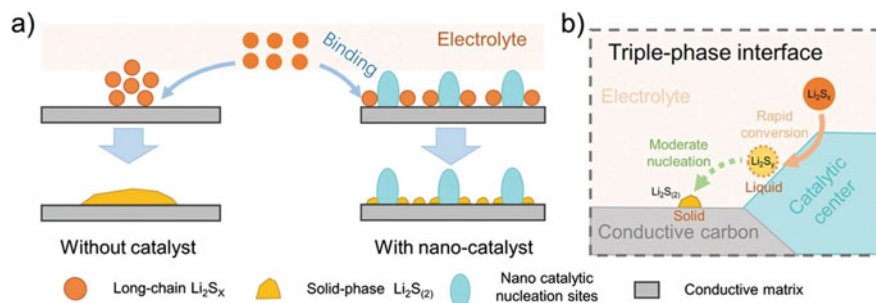


Fig. 10.10 **a** Schematic illustration of the controllable Li_2S nucleation and uniform growth on a collaborative triple-phase interface with strong adsorption, high electrical conductivity, high reactivity, and uniform distributed nucleation sites, and **b** the mechanism of lithium polysulfide redox reaction and Li_2S nucleation. Reprinted with permission from Ref. [104] Copyright 2019, Wiley-VCH

10.4.2 Mechanistic Studies

In Sect. 10.4.1, we briefly discussed how computer simulations can be used to obtain an atomistic understanding of the structural properties relevant to Li–S systems. Here, we will shift our emphasis to mechanistic studies. As we have pointed out earlier, there is no clear distinction between a structural and a mechanistic study; structures and energetics are themselves important information to achieve a mechanistic understanding of the S chemistry.

10.4.2.1 Polysulfide Dissolution, Transport, and Clustering

Alleviating polysulfide shuttle is at the heart of a successful Li–S battery. A great number of studies have been devoted to an understanding of the physical and chemical phenomena associated with polysulfides, and new techniques have been developed to control the growth and diffusion of polysulfides, leading to an improved cycling performance of the Li–S battery. Computationally, one can calculate the Gibbs free energy of dissolution. Figure 10.11 plots the Gibbs free energy of dissolution of lithium polysulfide species (dianion and radical) in dimethylformamide (DMF) and diethylene glycol dimethyl ether (Diglyme); both are frequently used in Li–S batteries. In the case of DMF, only Li_2S_2 (dianion) and Li_2S (radical) show positive free energy of dissolution, which is consistent with our knowledge that Li_2S_2 is insoluble while longer lithium polysulfides are soluble. The enthalpy of dissolution is always negative, which is expected due to the strong interactions between lithium and polar solvent molecules. For longer polysulfide species, the entropy contribution is also negative, but smaller in magnitude than enthalpy, resulting in a negative free energy of dissolution. In the case of diglyme, however, the entropy contributions are comparable to that of the enthalpy. As a result, the free energies of dissolution for

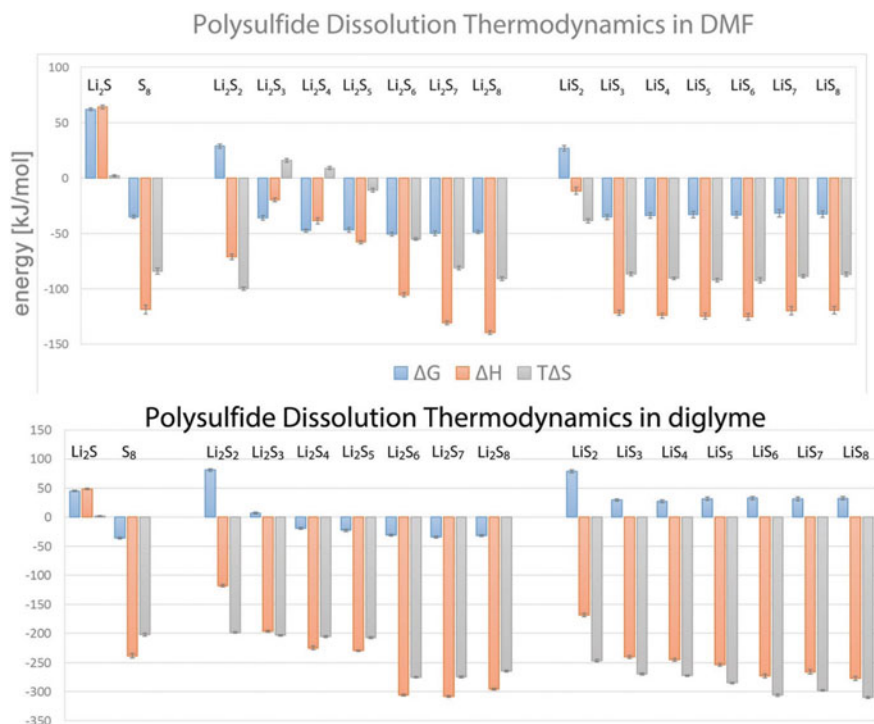


Fig. 10.11 Thermodynamics of dissolution of various lithium polysulfides in (top) DMF and (bottom) diglyme. Adapted from Ref. [110] by permission of the PCCP Owner Societies

dianions decrease in magnitude, and become positive for radical species, indicating the possibility to prevent polysulfide dissolution by using appropriate solvents. Such a study is interesting, although is rather simplified. The electrolyte solution is often a mixture of multiple solvents and salts, which should be properly accounted for to obtain accurate free energies of dissolution.

The dissolution of polysulfides is a rather complicated process, which may involve multiple intermediate species, both charged and neutral, as suggested by AIMD simulations [101]. Disproportionation of polysulfides or side reactions are also possible, resulting in complex chemical equilibria involving the co-existence of many species that might evolve during charge and discharge [109]. The best strategy to tackle this challenge is by combining experimental and computational efforts. If there are some characteristic properties of a molecule that can be experimentally measured and computationally predicted, then a match between experimental and computational data provides direct evidence of the existence of this molecule. Caution should be taken, however, when there is a mismatch, which can be a result of many factors including the difference in the experimental and computational setups.

There are a number of characteristic properties that can be probed both experimentally and computationally, including vibrational frequencies, electronic excitations, magnetic resonance (nuclear or electron spin), etc. A detailed discussion of various experimental techniques and their applications in Li–S research can be found elsewhere [111]. Because all these properties are a result of the electronic and atomistic structures, *ab initio* methods are the appropriate techniques, although classical force field methods with high-quality interatomic potentials can also generate reliable vibrational spectra. For example, vibrational frequencies have been assigned to a compendium of species through a combined DFT calculation and *in situ* Raman spectroscopic study, which provides a useful reference to interpret experimental data [112]. As another example, by comparing experimental and calculated ^6Li and ^{17}O chemical shifts in nuclear magnetic resonance (NMR) measurements, it is concluded that the dissolution of Li_2S_n was triggered by lithium exchange between solvent molecules and Li_2S_n [89]. This provides a dynamic view of the microscopic process of dissolution that is absent in energetic calculations discussed above.

If the dissolution is inevitable due to, for example, the use of a particular electrolyte solution, it is then important to understand the diffusion of polysulfide species in the electrolyte solution and its impact on the electrochemical performance. Computationally, diffusivities of various species in a solution can be calculated from the mean square displacements obtained from either *ab initio* or classical MD simulations, although the results may suffer from statistical errors if the system size is too small or the simulation time is not sufficiently long [113]. Figure 10.12 compares the calculated self-diffusion coefficients from MD simulations to those measured using pulse field gradient nuclear magnetic resonance [114, 115], and the agreement is quite impressive. If performed carefully, different studies seem to arrive at similar conclusions [89, 114, 115], even though different computational techniques were used. It is observed that the diffusion coefficients of Li^+ and polysulfide anions decrease with the addition of salt and increased polysulfide chain length. Lower order polysulfides tend to cluster, which could slow down the reaction kinetics. The addition of salts can effectively inhibit clustering, but at the same time also lead to a notable increase in the viscosity of the electrolyte solution.

Overall, both experimental and computational evidence suggests the critical role of subtle interaction among Li^+ , polysulfide anions, solvents, and salts in determining the dissolution, transport, and clustering of polysulfides, although our current understanding is far from complete. Experimentally, *in situ* experimental techniques are preferred to reproduce the working environment in a Li–S cell, although an *in situ* measurement is not always possible and may require a complicated setup [111]. Computationally, approximations, for example, various solution models, must be made due to the complex chemical and physical processes involved, and these approximations must be carefully evaluated and may lead to the omission of important insights. At present, a fundamental understanding of the dissolution, transport, and clustering of polysulfides, as well as their impacts on the electrochemical performance of Li–S batteries, has yet to be further developed.

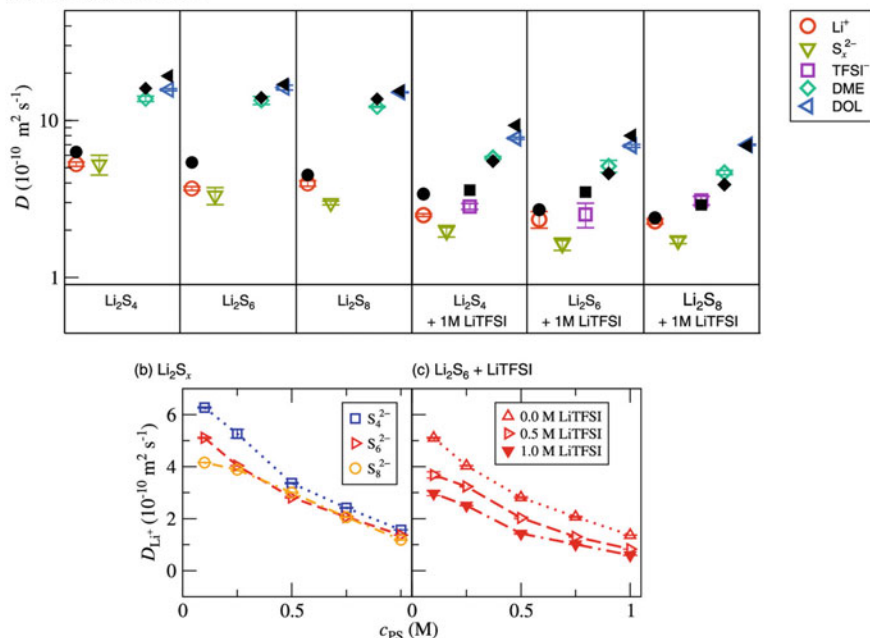
(a) 0.25M Li_2S_x in DME:DOL

Fig. 10.12 **a** Long-time self-diffusion coefficients D of all species in 0.25 M of the polysulfide as obtained from MD simulations (empty symbols) and pulse field gradient nuclear magnetic resonance measurements [114] (black filled symbols). **b** Diffusion coefficients of Li^+ in different polysulfide solutions as a function of polysulfide concentration from MD simulations. **c** Diffusion coefficients of Li^+ as a function of Li_2S_6 concentration in the presence of different amounts of lithium bistriflimide (LiTFSI) from MD simulations. Reprinted with permission from Ref. [115]. Copyright 2019 American Chemical Society

10.4.2.2 Reaction Sequences

Starting from S_8 , lithiation leads to the gradual reduction of S and formation of various lithium polysulfides. If liquid electrolyte is used, higher order lithium polysulfides (Li_2S_8 and Li_2S_6) are expected to dissolve into the solution, and continued reduction takes place in the liquid phase that requires charge transfer at the electrolyte/cathode interface. As discussed in Sect. 10.4.2.1, the liquid state reaction is complicated by subtle interactions among many species presenting in the liquid. Besides the reduction reaction, other types of reactions, for example, the fragmentation reactions of S and association/dissociation of and lithium polysulfides, are also possible. Computationally, it is possible to calculate the reduction potentials for all possible species and compare those with experimental data. However, the calculated reduction potentials are subject to intrinsic errors associated with various computational models, and it is also possible that different species give reduction potentials that are similar within computational uncertainty and thus cannot be resolved. For example, a high-level quantum chemical study predicted reduction potentials of Li_2S_8 and Li_2S_7 that differ

by merely 0.05 V, while the reduction potentials of Li_2S_6 and Li_2S_5 are numerically the same [29]. A similar problem also exists in experimental studies: signals from various characterization techniques often overlap and cannot be assigned [111].

Given these difficulties, an unambiguous identification of the reaction sequence, that is, the formation of various polysulfide species and the associated structural change, during charge and discharge, is not currently available. Nonetheless, the following sequence is generally accepted and ascribed to the characteristic two-plateau voltage profile during discharge. The higher plateau is related to S_8 reduction to long-chain polysulfides, the lower plateau is dominated by the reduction to Li_2S_2 and Li_2S , and the slope region in between is associated with the formation of S_4^{2-} . The charging process starts with extracting lithium from Li_2S with an initial voltage barrier and S_8 forms at the end of charging. The path traveled during charging is not simply the reverse of that during discharging, and the recrystallized S differs from the starting material in both amount and structure [111].

If the reaction is confined inside the cathode, i.e., there is minimal or no polysulfide dissolution, then a distinct quasi-solid-state reaction is observed, which has been attributed to smaller S molecules [32] or the formation of a solid electrolyte interphase [116]. Such a system can be studied by classical MD simulations with a reactive force field. Application of the ReaxFF approach [57], which is among the most popular reactive MD methods, has revealed some interesting atomistic features [117, 118]. The voltage profile generated from reactive MD simulations agrees with the general trend observed experimentally [117], suggesting the applicability of such an atomistic simulation approach. The calculated volume expansion due to lithium insertion also agrees well with experiments [117]. Notably, through structural (ring and fragment) analysis, a broad distribution of sulfur molecules (S_n), lithium sulfide (Li_xS), and lithium polysulfide (Li_xS_y , $y > 1$) was observed for Li_2S and Li_2S_8 nanoparticles [118]. This is significant, as it suggests that the Li–S speciation is similarly complicated even without liquid electrolyte, and the local atomic structure, due to the formation of various species, can be equally challenging to characterize experimentally.

10.4.3 Predictive Studies

The ability to predict new physical or chemical processes that have not been experimentally observed or are not experimentally accessible is the key advantage of computational studies. This section will showcase such an ability in the study of Li–S systems. Many predictive studies are also mechanistic in nature because appropriate predictions can only be made after obtaining a mechanistic understanding. Experimental verifications, although not always possible, are desired.

10.4.3.1 Polysulfide Trapping

The polysulfide dissolution, as we have discussed earlier, is really a result of the strong molecular interaction between polysulfides and the solvents. Various methods to trap lithium polysulfides, including physisorption (absorption by dispersion interaction, e.g., van der Waals bond), chemisorption (absorption by covalent/ionic bonding, e.g., lithium bond [119]), and physical confinement (e.g., physical barriers and interlayers), have been proposed [120–122], and atomistic simulations are a natural choice to study polysulfide trapping because binding energies can be readily calculated. Not surprisingly, DFT calculations suggested a rather small interaction between graphene, which is a popular material to construct the C–S cathode composite, and lithium polysulfides [123]. Consequently, third-party agents, such as functional groups and metal oxides, are added to the composite cathode to provide a stronger anchoring effect. DFT calculations predicted that the binding strength can be increased via two independent mechanisms, i.e., the Coulombic interaction between Li^+ and lone-pair electrons and hydrogen bonding, while the former dominates [124]. In principle, it is possible to calculate the binding energies of all possible third-party agents with lithium polysulfide, and an attempt was made to systematically quantify the anchoring strength of different substrates [125]. The stabilizing potential, ΔP_{S-A} , which describes the competition between adsorption of Li_2S_8 onto the substrates and its solvation into the electrolyte, was introduced. Figure 10.13 plots the optimized adsorption structure and the corresponding stabilizing potential, and the negative values in the case of poly(vinylpyrrolidone) (PVP) and phosphorylated chitosan (PCS) indicate the strong anchoring effects that can be used for effective trapping of lithium polysulfides [125], which has yet to be experimentally verified.

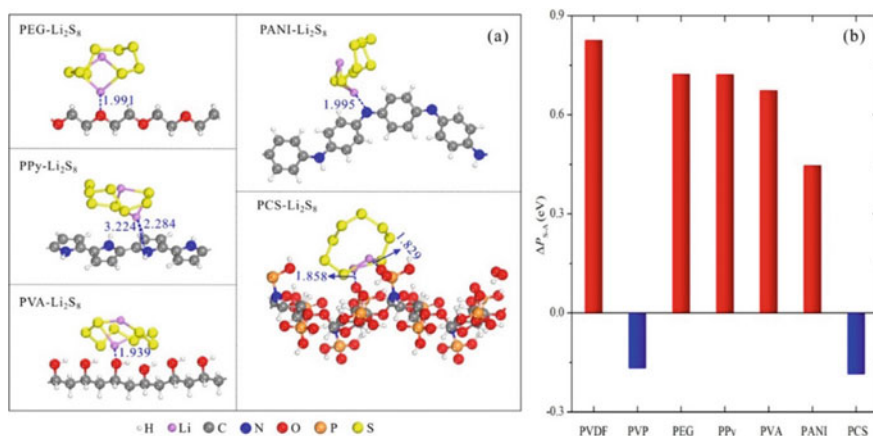


Fig. 10.13 **a** Optimized adsorption structure of Li_2S_8 on different substrates. **b** The calculated stabilizing potential. Reprinted with permission from Ref. [125]. Copyright 2017 American Chemical Society

Calculated binding energies, in many instances, corroborate well with experimental findings. For example, DFT calculations suggest that nitrogen-doped carbon nanotubes (CNT) have binding energies with Li_2S and Li_2S_4 that are 0.1–0.4 eV stronger than pristine CNTs [102]. Experimentally, N-doped CNTs show higher capacity, better reversibility, and increased stability due to the stronger affinity that reduces the loss of active material [102]. When Li_2S is charged back, an initial potential barrier is often observed due to the insulating nature of Li_2S . This potential barrier increases from 3.41 V to 3.53 V if SnS_2 is used as a substrate, and decreases to 3.47, 3.25, 3.01, 2.91, and 2.88 V for Ni_3S_2 , FeS, CoS_2 , VS_2 , and TiS_2 , respectively [107]. Since the decomposition of Li_2S involves breaking the Li–S bond, the energy required for such a process on different substrates can be calculated by DFT calculation, and the decomposition barriers are 1.03, 0.63, 0.56, 0.31, and 0.30 eV for Ni_3S_2 , FeS, CoS_2 , VS_2 , and TiS_2 , respectively [107], which correlates well with the measured charge potential. The only exception is SnS_2 , which has a small decomposition barrier of 0.32 eV and a high charge potential of 3.53 V. Because the charge process also involves electron transport, the insulating nature of SnS_2 could be the main reason for the high charge potential. In terms of the ability to anchor polysulfides, the binding strengths between Li_2S_6 and Ni_3S_2 , SnS_2 , FeS, CoS_2 , VS_2 , and TiS_2 have been calculated to be 0.72, 0.80, 0.87, 1.01, 1.04, and 1.02 eV, respectively [107]. The stronger polysulfides affinity, smaller decomposition barrier, and metallic conductivity, all of which can be determined computationally, render higher capacity, lower overpotential, and better cycling stability for VS_2 -, TiS_2 -, and CoS_2 -based cathodes compared to pure C and S cathodes [107]. The correlation between computational data and experimental battery performance is encouraging. Notably, these metal sulfides serve multiple roles including polysulfide trapping and catalytic oxidation of Li_2S . In fact, electrocatalysis has been considered as an effective approach to promote the redox conversion of polysulfides and inhibit their shuttle [19, 104].

Computational screening of materials has become an important tool in materials selection and design. In computational screening, materials with different structures are constructed and their properties calculated, based on which predictive conclusions can be drawn to inform materials selection. It is equivalent to many trial-and-error experiments, although performed computationally through either sequential or parallel calculations. In the case of polysulfide trapping, a computational screening can be used to generate a database of binding energies of various polysulfide species to different C hosts. Insights and/or trends from this collection of calculations can be further used to propose new candidate materials for additional screening. In such an attempt, a systematical DFT calculation of various heteroatom-doped nanocarbon materials was performed. While it was observed that N and O outperform other dopants, a few rules for strong anchoring effects are proposed, including the presence of a lone pair of electrons in the doping atom, a higher electronegativity of the doping atom than that of C, etc. [120]. Such mechanistic conclusions enable a predictive selection of other dopants, which will be subject to further computational screening and experimental verification.

10.4.3.2 Cathode Geometry

The S cathode is a composite material including both S and C in various forms, and the latter is required to provide necessary electronic conductivity. The interactions between C and polysulfides are mostly through van der Waals bonding, which is not strong enough for polysulfide trapping. A tremendous number of studies have been devoted to the development of new strategies for polysulfide trapping. Among these efforts, introducing metal sulfide substrate or functional groups within the C host, as those discussed above, involves modification of the cathode geometry. Similarly, metal oxides, metal nitrides, metal carbides, metal phosphides, as well as ternary and quaternary composites, have been proposed and tested [126, 127]. Here, we will discuss a slightly different approach to encapsulate S. Instead of focusing on the chemical interaction between the host and the polysulfide, the electrochemical properties of S can also be controlled by altering the size and shape of the host material, which provides a physical confinement of S and polysulfide species. As a simple example, the pore sizes in porous C can be altered, and micropores have been shown to confine S and inhibit dissolution of polysulfides, enabling a quasi-solid-state reaction [32]. In practice, both methods are often combined to achieve maximal performance. From a computational perspective, however, studying different sizes and shapes of the host material is more challenging as compared to a calculation of the binding energies. It is because that the geometry of the host, as well as S, must be properly included in the calculation, which leads to a significant increase in the system size for atomistic simulations. Reactive MD simulations are arguably best suited to study such systems. For example, the ReaxFF approach has been applied to study the electrochemical reaction of S confined in small graphene sheets [128]. The formation of smaller S molecules as a result of S confinement has been observed. As evident from Fig. 10.14a, the number of eight-member S rings (S_8) decreases

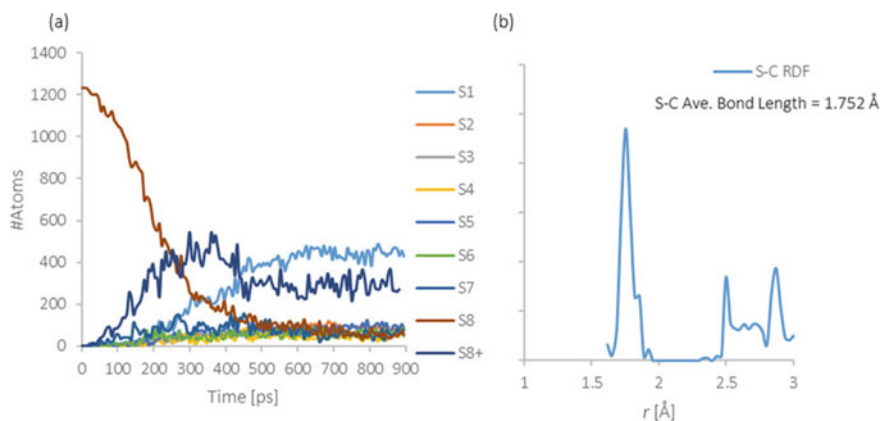


Fig. 10.14 **a** Sulfur chain distribution during the ReaxFF simulation. **b** Partial radial distribution function for sulfur and carbon at the end of isothermal stabilization. Reprinted with permission from Ref. [128]. Copyright 2018 Wiley

drastically in the first few hundred of picoseconds of the simulation, and many isolated S atoms (S_1) are observed. The pair distribution function analysis shows that S atoms are bonded to C in the graphene sheet with a bond length of around 1.75 Å, as shown in Fig. 10.14b. Such structural characteristics of confined S lead to a less pronounced volume expansion during lithiation and a different discharge voltage profile, agreeing qualitatively with earlier experimental studies. A systematic computational study of different sizes and shapes of the C host is highly desired, which could provide important insights on the design of cathode geometry.

10.4.3.3 Selection of the Electrolyte

When choosing an appropriate electrolyte solution, there are a few important considerations as well. Carbonate-based electrolytes, which are popular in Li-ion batteries, find limited usage in Li-S systems due to their detrimental reactivity with polysulfides. In other words, the electrolyte solution should have good chemical stability in the presence of other molecular species. Because batteries are charged and discharged, electrochemical stability at the operating voltage is also an important consideration, which is usually referred to as electrochemical windows. In general, solvents with a high oxidation potential and a low reduction potential give a larger electrochemical window and are preferred. A reasonably good solubility is required as well because salts are often added to improve the overall performance. Computationally, some of these properties can be calculated with relative ease, for example, the redox potentials. Other properties may be more involved, and a variety of different factors need to be considered. For example, determination of stability requires an understanding of the chemical environments, which may change during charge and discharge. A multi-step, successive screening can be used to narrow down the candidate pool, and only a small portion would need the more focused study after the screening. Figure 10.15 illustrates the general screening strategy of down-selecting a pool of candidates based on successive property evaluations [30].

In Li-S systems, we have seen that the molecular interactions between the electrolyte and various polysulfide species drive the dissolution process. Just as we can screen different doping materials for polysulfide trapping, we can also screen electrolyte molecules with minimal polysulfide interactions, which increases the number of successive steps required for the down-selection shown in Fig. 10.15. A few other properties, although important, have been left out in this kind of computational screen. Examples are ionic diffusivity and viscosity of the solution, which are much more demanding computationally. That said, the ability of computational screening in reducing the search space and predicting the most promising candidates is invaluable.

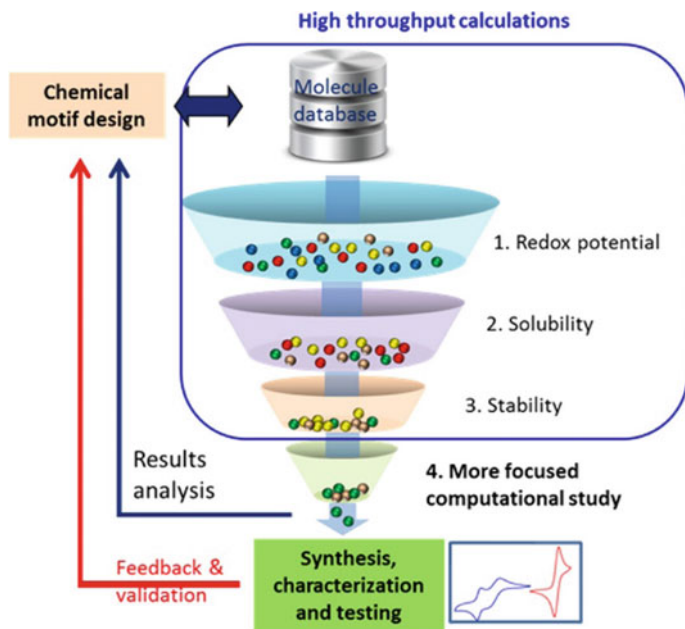


Fig. 10.15 Schematic of down-selection of candidate molecules for electrical energy storage applications based on high-throughput computations using quantum chemical calculations of specific properties. Selected molecules based on screening can be subjected to further focused computational studies and proposed for synthesis and testing. Reprinted with permission from Ref. [30]. Copyright 2015 American Chemical Society

10.5 Summary and Outlook

Computer simulations have become an increasingly important tool in materials research. A carefully performed computer simulation can provide valuable insights at a resolution that is not always accessible by experiments. Recent efforts, such as the Materials Genome Initiatives and the Integrated Computational Materials Engineering, reflect the wide recognition of the power of computer simulations in transforming materials research. The traditional trial-and-error experiments are being replaced by, at least partially, materials selection through computational screening.

In terms of Li-S research, computer simulations play an even more critical role due to the unique challenges facing Li-S batteries. The formation of various intermediate molecular species complicates the reaction pattern, requiring an understanding of the electrochemical processes at the molecular level. Atomistic simulation techniques provide the necessary resolution to address these challenges. The success and versatility of atomistic simulations have been demonstrated in determining structures and energetics of various species that appear in the reaction, providing mechanistic understandings of the microscopic processes during the electrochemical conversion of S, and predicting new materials and strategies to improve the electrochemical performance of S.

The combined experimental and computational efforts have enabled exciting progresses in Li–S batteries, and their commercial applications have become a reality. However, to achieve the full potential of Li–S chemistry, further research and development are needed. Computer simulations will continue to be an integral part of such efforts. In particular, a few emerging areas of research have gained momentum recently, which could benefit greatly from a computational perspective. These areas include the following:

- The use of organosulfides as cathode materials. Organosulfides are S containing organic molecules that have shown promising electrochemical properties [129, 130]. In general, these molecules have a much shorter S chain than S₈, thus avoiding the various problems associated with long-chain polysulfides. The electrochemical properties can be fine-tuned by using different functional groups. Computer simulations have already been used to reveal the reaction sequences and determine the redox potentials [92–94, 99, 131, 132], however, a systematic computer screening of various molecules to identify the most promising candidates for further experimental verification is highly desired.
- The design of “all-in-one” cathodes. We have discussed various ideas to promote a stable electrochemical reaction in S including physisorption and chemisorption of polysulfides, electrocatalysis, and size and shape of the cathode. These ideas can be integrated to design an “all-in-one” cathode [19]. Such a task brings new challenges to a computational screening because multiple properties need to be calculated and the system size is also increased.
- All-solid-state Li–S batteries. The use of solid electrolyte to construct all-solid-state batteries has become a subject of intensive scientific interest, especially for LIBs based on intercalation cathode materials due to safety and stability considerations [133]. It is also appealing in Li–S systems because the dissolution of polysulfides and the resulting shuttle effect can be effectively prohibited [134]. Similar to the computational screening of molecular species for liquid electrolyte, materials for solid-state electrolyte can be subject to computational screenings to expedite the materials discovery. However, many solid electrolyte materials are not crystalline. In fact, polymers, composites and gels have all been proposed, which inevitably leads to a significant increase in the computational cost. Critical properties related to solid-state electrolyte, such as ionic conductivity and interface impedance, are also difficult to assess computationally.

It is worthwhile to note that research in all these areas involves large sets of computational data, such as crystal and molecular structures, surface energies, interface energies, binding energies, reduction and oxidation potentials, lithium diffusion barriers, and ionic diffusivities. Ideally, these computational data should corroborate with experimentally derived structural, physical, chemical, and electrochemical characteristics. A coordinated, international effort to construct a comprehensive, robust, and open database that contains both computational and experimental data could provide a crucial boost to Li–S research. For example, the development of highly accurate and predictive machine learning algorithms to identify new materials and structures for Li–S batteries, which relies on robust training data sets, could benefit

greatly from such a database. Unfortunately, at least in the field of Li–S research, the creation of this database is long overdue and hindered by many non-scientific, and sometimes political, barriers. Consequently, repeated, and even erroneous, data are often reported, which is of no practical value.

Finally, we wish to point out that practical aspects are being emphasized when evaluating materials for Li–S batteries. In other words, any new materials proposed for Li–S batteries should be evaluated using industrial standards relevant to commercial implementation. The following five critical metrics are proposed: S loading $>5 \text{ mg cm}^{-2}$, C content $<5\%$, electrolyte-to-sulfur ratio $<5 \text{ } \mu\text{L mg}^{-1}$, electrolyte-to-capacity ratio $<5 \text{ } \mu\text{L (mAh)}^{-1}$, and negative-to-positive capacity ratio <5 in pouch-type cells. Note that these metrics represent the minimal requirements if Li–S batteries were to be competitive against LIBs that dominate the commercial market today. Unfortunately, a realistic study involving these parameters is beyond the capability of present atomistic simulation techniques and is best addressed by macroscopic methods. In this regard, a multiscale modeling approach that provides a coherent description from atomistic to macroscopic scale is highly desired. At present, a true “Materials by Design” for Li–S batteries, where computational materials design is driven by industrial applications and the materials as designed meet required performance targets, remains elusive and can only be achieved by a collaborative, international effort involving industry, academia, and governments.

Acknowledgements The author would like to thank the support from the Department of Materials Science and Biomedical Engineering, University of Wisconsin-Eau Claire. Computational resource is provided by the Blugold Center for High-Performance Computing at the University of Wisconsin-Eau Claire and the Center for High Throughput Computing at the University of Wisconsin-Madison.

References

1. Yoshio M, Brodd RJ, Kozawa A (2009) *Lithium-ion batteries: science and technologies*. Springer, New York
2. Manthiram A (2020) A reflection on lithium-ion battery cathode chemistry. *Nat Commun* 11(1):1550. <https://doi.org/10.1038/s41467-020-15355-0>
3. Tarascon J-M (2010) Key challenges in future Li-battery research. *Philos Trans R Soc A: Math Phys Eng Sci* 368(1923):3227–3241. <https://doi.org/10.1098/rsta.2010.0112>
4. Ji XL, Nazar LF (2010) Advances in Li-S batteries. *J Mater Chem* 20(44):9821–9826. <https://doi.org/10.1039/b925751a>
5. Manthiram A, Fu YZ, Su YS (2013) Challenges and prospects of lithium-sulfur batteries. *Acc Chem Res* 46(5):1125–1134. <https://doi.org/10.1021/ar300179v>
6. Su YS, Fu YZ, Cochell T, Manthiram A (2013) A strategic approach to recharging lithium-sulphur batteries for long cycle life. *Nat Commun* 4:2985. ARTN 2985 <https://doi.org/10.1038/ncomms3985>
7. Dong QF, Wang C, Zheng MS (2011) Research progress and prospects of lithium sulfur batteries. *Prog Chem* 23(2–3):533–539
8. Yin YX, Xin S, Guo YG, Wan LJ (2013) Lithium-sulfur batteries: electrochemistry, materials, and prospects. *Angew Chem Int Ed* 52(50):13186–13200. <https://doi.org/10.1002/anie.201304762>

9. Akridge JR, Mikhaylik YV, White N (2004) Li/S fundamental chemistry and application to high-performance rechargeable batteries. *Solid State Ionics* 175(1–4):243–245. <https://doi.org/10.1016/j.ssi.2004.07.070>
10. Manthiram A, Fu YZ, Chung SH, Zu CX, Su YS (2014) Rechargeable lithium-sulfur batteries. *Chem Rev* 114(23):11751–11787. <https://doi.org/10.1021/cr500062v>
11. Urbonaitė S, Poux T, Novak P (2015) Progress towards commercially viable Li-S battery cells. *Adv Energy Mater* 5(16):1500118. ARTN 1500118 <https://doi.org/10.1002/aenm.201500118>
12. Kolosnitsyn VS, Karaseva EV (2008) Lithium-sulfur batteries: problems and solutions. *Russ J Electrochem* 44(5):506–509. <https://doi.org/10.1134/S1023193508050029>
13. Hagen M, Hanselmann D, Ahlbrecht K, Maca R, Gerber D, Tubke J (2015) Lithium-sulfur cells: the gap between the state-of-the-art and the requirements for high energy battery cells. *Adv Energy Mater* 5(16):1401986. ARTN 1401986 <https://doi.org/10.1002/aenm.201401986>
14. Lv DP, Zheng JM, Li QY, Xie X, Ferrara S, Nie ZM, Mehdi LB, Browning ND, Zhang JG, Graff GL, Liu J, Xiao J (2015) High energy density lithium-sulfur batteries: challenges of thick sulfur cathodes. *Adv Energy Mater* 5(16):1402290. ARTN 1402290 <https://doi.org/10.1002/aenm.201402290>
15. Yang Y, Zheng GY, Cui Y (2013) Nanostructured sulfur cathodes. *Chem Soc Rev* 42(7):3018–3032. <https://doi.org/10.1039/c2cs35256g>
16. Herbert D, Ulam J (1962) Electric dry cells and storage batteries, U.S. Patent 3043896
17. Whittingham MS (1976) Electrical energy-storage and intercalation chemistry. *Science* 192(4244):1126–1127. <https://doi.org/10.1126/science.192.4244.1126>
18. Ji XL, Lee KT, Nazar LF (2009) A highly ordered nanostructured carbon-sulphur cathode for lithium-sulphur batteries. *Nat Mater* 8(6):500–506. <https://doi.org/10.1038/Nmat2460>
19. Liu T, Hu H, Ding X, Yuan H, Jin C, Nai J, Liu Y, Wang Y, Wan Y, Tao X (2020) 12 years roadmap of the sulfur cathode for lithium sulfur batteries (2009–2020). *Energy Storage Mater* 30:346–366. <https://doi.org/10.1016/j.ensm.2020.05.023>
20. Zhu K, Wang C, Chi Z, Ke F, Yang Y, Wang A, Wang W, Miao L (2019) How far away are lithium-sulfur batteries from commercialization? *Front Energy Res* 7(123). <https://doi.org/10.3389/fenrg.2019.00123>
21. Ma Y (2018) Computer simulation of cathode materials for lithium ion and lithium batteries: a review. *Energy Environ Mater* 1(3):148–173. <https://doi.org/10.1002/eem2.12017>
22. Lin S-T, Maiti PK, Goddard WA (2010) Two-phase thermodynamic model for efficient and accurate absolute entropy of water from molecular dynamics simulations. *J Phys Chem B* 114(24):8191–8198. <https://doi.org/10.1021/jp103120q>
23. Frenkel D, Smit B (2001) *Understanding molecular simulation: from algorithms to applications*, vol 1. Elsevier
24. Ceder G, Aydinol MK, Kohan AF (1997) Application of first-principles calculations to the design of rechargeable Li-batteries. *Comput Mater Sci* 8(1–2):161–169. [https://doi.org/10.1016/S0927-0256\(97\)00029-3](https://doi.org/10.1016/S0927-0256(97)00029-3)
25. Aydinol MK, Kohan AF, Ceder G, Cho K, Joannopoulos J (1997) Ab initio study of lithium intercalation in metal oxides and metal dichalcogenides. *Phys Rev B* 56(3):1354–1365
26. Gao J, Shi S-Q, Li H (2016) Brief overview of electrochemical potential in lithium ion batteries. *Chin Phys B* 25(1):018210. <https://doi.org/10.1088/1674-1056/25/1/018210>
27. Winget P, Cramer CJ, Truhlar DG (2004) Computation of equilibrium oxidation and reduction potentials for reversible and dissociative electron-transfer reactions in solution. *Theor Chem Acc* 112(4):217–227. <https://doi.org/10.1007/s00214-004-0577-0>
28. Phillips KL, Sandler SI, Chiu PC (2011) A method to calculate the one-electron reduction potentials for nitroaromatic compounds based on gas-phase quantum mechanics. *J Comput Chem* 32(2):226–239. <https://doi.org/10.1002/jcc.21608>
29. Assary RS, Curtiss LA, Moore JS (2014) Toward a molecular understanding of energetics in Li-S batteries using nonaqueous electrolytes: a high-level quantum chemical study. *J Phys Chem C* 118(22):11545–11558

30. Cheng L, Assary RS, Qu X, Jain A, Ong SP, Rajput NN, Persson K, Curtiss LA (2015) Accelerating electrolyte discovery for energy storage with high-throughput screening. *J Phys Chem Lett* 6(2):283–291. <https://doi.org/10.1021/jz502319n>
31. Yang Y, Zheng G, Misra S, Nelson J, Toney MF, Cui Y (2012) High-capacity micrometer-sized Li₂S particles as cathode materials for advanced rechargeable lithium-ion batteries. *J Am Chem Soc* 134(37):15387–15394. <https://doi.org/10.1021/ja3052206>
32. Xin S, Gu L, Zhao NH, Yin YX, Zhou LJ, Guo YG, Wan LJ (2012) Smaller sulfur molecules promise better lithium-sulfur batteries. *J Am Chem Soc* 134(45):18510–18513. <https://doi.org/10.1021/ja308170k>
33. Bhauriyal P, Das S, Pathak B (2020) Theoretical insights into the charge and discharge processes in aluminum-sulfur batteries. *J Phys Chem C* 124(21):11317–11324. <https://doi.org/10.1021/acs.jpcc.0c01358>
34. Shankar R (1994) Principles of quantum mechanics, 2nd edn. Plenum Press, New York
35. Cramer CJ (2002) Essentials of computational chemistry: theories and models. Wiley, West Sussex, England
36. Grosso G, Parravicini GP (2000) Solid state physics. Academic Press, New York
37. Löwdin P-O (1955) Quantum theory of many-particle systems. III. Extension of the Hartree-Fock scheme to include degenerate systems and correlation effects. *Phys Rev* 97(6):1509–1520. <https://doi.org/10.1103/PhysRev.97.1509>
38. Bartlett RJ, Stanton JF (2007) Applications of Post-Hartree-Fock methods: a tutorial. In: Lipkowitz KB, Boyd DB (eds) Reviews in computational chemistry. VCH, New York. <https://doi.org/10.1002/9780470125823.ch2>
39. Ashcroft NW, Mermin ND (1976) Solid state physics. Thomson Learning
40. Hohenberg P, Kohn W (1964) Inhomogeneous electron gas. *Phys Rev* 136(3B):B864–B871. <https://doi.org/10.1103/PhysRev.136.B864>
41. Kohn W, Sham LJ (1965) Self-consistent equations including exchange and correlation effects. *Phys Rev* 140(4A):A1133–A1138. <https://doi.org/10.1103/PhysRev.140.A1133>
42. Ziegler T (1991) Approximate density functional theory as a practical tool in molecular energetics and dynamics. *Chem Rev* 91(5):651–667
43. Perdew JP, Chevary JA, Vosko SH, Jackson KA, Pederson MR, Singh DJ, Fiolhais C (1992) Atoms, molecules, solids, and surfaces: applications of the generalized gradient approximation for exchange and correlation. *Phys Rev B* 46(11):6671
44. Vladimir IA, Aryasetiawan F, Lichtenstein AI (1997) First-principles calculations of the electronic structure and spectra of strongly correlated systems: the LDA + U method. *J Phys: Condens Matter* 9(4):767
45. Loschen C, Carrasco J, Neyman KM, Illas F (2007) First-principles LDA+U and GGA+U study of cerium oxides: dependence on the effective U parameter. *Phys Rev B* 75(3):035115. <https://doi.org/10.1103/PhysRevB.75.035115>
46. Kristian B, Valentino RC, Kyuho L, Elsebeth S, Thonhauser T, Per H, Bengt IL (2015) van der Waals forces in density functional theory: a review of the vdW-DF method. *Rep Prog Phys* 78(6):066501
47. Ching W-Y, Rulis P (2012) Electronic structure methods for complex materials: the orthogonalized linear combination of atomic orbitals. Oxford University Press
48. Soler JM, Artacho E, Gale JD, García A, Junquera J, Ordejón P, Sánchez-Portal D (2002) The SIESTA method for ab initio order-N materials simulation. *J Phys: Condens Matter* 14(11):2745–2779. <https://doi.org/10.1088/0953-8984/14/11/302>
49. Markland TE, Ceriotti M (2018) Nuclear quantum effects enter the mainstream. *Nat Rev Chem* 2(3):0109. <https://doi.org/10.1038/s41570-017-0109>
50. Feynman RP (1939) Forces in molecules. *Phys Rev* 56(4):340–343. <https://doi.org/10.1103/PhysRev.56.340>
51. Kühne TD (2014) Second generation Car-Parrinello molecular dynamics. *WIREs Comput Mol Sci* 4(4):391–406. <https://doi.org/10.1002/wcms.1176>
52. Iftimie R, Minary P, Tuckerman ME (2005) Ab initio molecular dynamics: Concepts, recent developments, and future trends. *Proc Natl Acad Sci USA* 102(19):6654–6659. <https://doi.org/10.1073/pnas.0500193102>

53. Car R, Parrinello M (1985) Unified approach for molecular dynamics and density-functional theory. *Phys Rev Lett* 55(22):2471–2474. <https://doi.org/10.1103/PhysRevLett.55.2471>
54. Kresse G, Hafner J (1993) Ab initio molecular dynamics for liquid metals. *Phys Rev B* 47(1):558–561. <https://doi.org/10.1103/PhysRevB.47.558>
55. Rapaport DC (2004) *The art of molecular dynamics simulation*, 2nd edn. Cambridge University Press, Cambridge
56. Phillpot SR, Antony AC, Shi L, Fullarton ML, Liang T, Sinnott SB, Zhang Y, Biner SB (2018) Charge optimized many body (COMB) potentials for simulation of nuclear fuel and clad. *Comput Mater Sci* 148:231–241. <https://doi.org/10.1016/j.commatsci.2018.02.041>
57. Senftle TP, Hong S, Islam MM, Kylasa SB, Zheng Y, Shin YK, Junkermeier C, Engel-Herbert R, Janik MJ, Aktulga HM, Verstraelen T, Grama A, van Duin ACT (2016) The ReaxFF reactive force-field: development, applications and future directions. *NPJ Comput Mater* 2:15011. <https://doi.org/10.1038/npjcompumats.2015.11>
58. Ma Y, Garofalini SH (2012) Atomistic insights into the conversion reaction in iron fluoride: a dynamically adaptive force field approach. *J Am Chem Soc* 134(19):8205–8211
59. Mortier WJ, Vangenechten K, Gasteiger J (1985) Electronegativity equalization—application and parametrization. *J Am Chem Soc* 107(4):829–835. <https://doi.org/10.1021/ja00290a017>
60. Rappe AK, Goddard WA (1991) Charge equilibration for molecular-dynamics simulations. *J Phys Chem* 95(8):3358–3363. <https://doi.org/10.1021/j100161a070>
61. Shibuta Y, Sakane S, Miyoshi E, Okita S, Takaki T, Ohno M (2017) Heterogeneity in homogeneous nucleation from billion-atom molecular dynamics simulation of solidification of pure metal. *Nat Commun* 8(1):10. <https://doi.org/10.1038/s41467-017-00017-5>
62. Jung J, Nishima W, Daniels M, Bascom G, Kobayashi C, Adedoyin A, Wall M, Lappala A, Phillips D, Fischer W, Tung C-S, Schlick T, Sugita Y, Sanbonmats KY (2019) Scaling molecular dynamics beyond 100,000 processor cores for large-scale biophysical simulations. *J Comput Chem* 40(21):1919–1930. <https://doi.org/10.1002/jcc.25840>
63. Lindert S, Kekenus-Huskey Peter M, McCammon JA (2012) Long-timescale molecular dynamics simulations elucidate the dynamics and kinetics of exposure of the hydrophobic patch in troponin C. *Biophys J* 103(8):1784–1789. <https://doi.org/10.1016/j.bpj.2012.08.058>
64. Klepeis J, Lindorff-Larsen K, Dror R, Shaw D (2009) Long-timescale molecular dynamics simulations of protein structure and function. *Curr Opin Struct Biol* 19:120–127. <https://doi.org/10.1016/j.sbi.2009.03.004>
65. Kmiecik S, Gront D, Kolinski M, Wieteska L, Dawid AE, Kolinski A (2016) Coarse-grained protein models and their applications. *Chem Rev* 116(14):7898–7936. <https://doi.org/10.1021/acs.chemrev.6b00163>
66. Chen LQ (2007) 3—Phase-field modelling of material microstructure. In: Guo ZX (ed) *Multi-scale materials modelling*. Woodhead Publishing, pp 62–83. <https://doi.org/10.1533/9781845693374.62>
67. Fotouhi A, Auger DJ, Propp K, Longo S, Wild M (2016) A review on electric vehicle battery modelling: from lithium-ion toward lithium-sulphur. *Renew Sustain Energy Rev* 56:1008–1021. <https://doi.org/10.1016/j.rser.2015.12.009>
68. Franco AA, Rucci A, Brandell D, Frayret C, Gaberscek M, Jankowski P, Johansson P (2019) Boosting rechargeable batteries R&D by multiscale modeling: myth or reality? *Chem Rev* 119(7):4569–4627. <https://doi.org/10.1021/acs.chemrev.8b00239>
69. Bhattacharyya S, Sahara R, Ohno K (2019) A first-principles phase field method for quantitatively predicting multi-composition phase separation without thermodynamic empirical parameter. *Nat Commun* 10(1):3451. <https://doi.org/10.1038/s41467-019-11248-z>
70. Glass CW, Oganov AR, Hansen N (2006) USPEX—evolutionary crystal structure prediction. *Comput Phys Commun* 175(11):713–720. <https://doi.org/10.1016/j.cpc.2006.07.020>
71. Klimeš J, Bowler DR, Michaelides A (2009) Chemical accuracy for the van der Waals density functional. *J Phys: Condens Matter* 22(2):022201. <https://doi.org/10.1088/0953-8984/22/2/022201>
72. Rettig SJ, Trotter J (1987) Refinement of the structure of orthorhombic sulfur, [alpha]-S8. *Acta Crystallogr C* 43(12):2260–2262. <https://doi.org/10.1107/S0108270187088152>

73. Luo H, Ruoff AL (1993) X-ray-diffraction study of sulfur to 32 GPa: amorphization at 25 GPa. *Phys Rev B* 48(1):569–572. <https://doi.org/10.1103/PhysRevB.48.569>
74. Berliner R, Fajen O, Smith HG, Hitterman RL (1989) Neutron powder-diffraction studies of lithium, sodium, and potassium metal. *Phys Rev B* 40(18):12086–12097. <https://doi.org/10.1103/PhysRevB.40.12086>
75. Slotwinski T, Trivisonno J (1969) Temperature dependence of the elastic constants of single crystal lithium. *J Phys Chem Solids* 30(5):1276–1278. [https://doi.org/10.1016/0022-3697\(69\)90386-2](https://doi.org/10.1016/0022-3697(69)90386-2)
76. Buehrer W, Altorfer F, Mesot J, Bill H, Carron P, Smith HG (1991) Lattice dynamics and the diffuse phase transition of lithium sulphide investigated by coherent neutron scattering. *J Phys: Condens Matter* 3(9):1055–1064. <https://doi.org/10.1088/0953-8984/3/9/002>
77. Park H, Koh HS, Siegel DJ (2015) First-principles study of redox end members in lithium-sulfur batteries. *J Phys Chem C* 119(9):4675–4683. <https://doi.org/10.1021/jp513023v>
78. Wei S, Chou MY (1992) Ab initio calculation of force constants and full phonon dispersions. *Phys Rev Lett* 69(19):2799–2802. <https://doi.org/10.1103/PhysRevLett.69.2799>
79. Villevieille C, Novák P (2013) A metastable β -sulfur phase stabilized at room temperature during cycling of high efficiency carbon fibre–sulfur composites for Li–S batteries. *J Mater Chem A* 1(42):13089–13092. <https://doi.org/10.1039/C3TA13072J>
80. Oganov AR, Glass CW (2006) Crystal structure prediction using ab initio evolutionary techniques: principles and applications. *J Chem Phys* 124(24):244704. <https://doi.org/10.1063/1.2210932>
81. Feng Z, Kim C, Vijh A, Armand M, Bevan KH, Zaghbi K (2014) Unravelling the role of Li_2S_2 in lithium–sulfur batteries: a first principles study of its energetic and electronic properties. *J Power Sources* 272:518–521. <https://doi.org/10.1016/j.jpowsour.2014.07.078>
82. Paoletta A, Zhu W, Marceau H, Kim C-s, Feng Z, Liu D, Gagnon C, Trottier J, Abdelbast G, Hovington P, Vijh A, Demopoulos GP, Armand M, Zaghbi K (2016) Transient existence of crystalline lithium disulfide Li_2S_2 in a lithium-sulfur battery. *J Power Sources* 325:641–645. <https://doi.org/10.1016/j.jpowsour.2016.06.086>
83. Lu X, Kirby BW, Xu W, Li G, Kim JY, Lemmon JP, Sprenkle VL, Yang Z (2013) Advanced intermediate-temperature Na–S battery. *Energy Environ Sci* 6(1):299–306
84. Liu Y, Cui C, Liu Y, Liu W, Wei J (2020) Application of MoS_2 in the cathode of lithium sulfur batteries. *RSC Adv* 10(13):7384–7395. <https://doi.org/10.1039/C9RA09769D>
85. Noh H, Song J, Park J-K, Kim H-T (2015) A new insight on capacity fading of lithium–sulfur batteries: the effect of Li_2S phase structure. *J Power Sources* 293:329–335. <https://doi.org/10.1016/j.jpowsour.2015.05.072>
86. Wong MW, Steudel Y, Steudel R (2002) Novel species for the sulfur zoo: isomers of S_8 . *Chem Phys Lett* 364(3):387–392. [https://doi.org/10.1016/S0009-2614\(02\)01342-8](https://doi.org/10.1016/S0009-2614(02)01342-8)
87. He Q, Liao X, Xia L, Li Z, Wang H, Zhao Y, Truhlar DG (2019) Accurate binding energies for lithium polysulfides and assessment of density functionals for lithium-sulfur battery research. *J Phys Chem C* 123(34):20737–20747. <https://doi.org/10.1021/acs.jpcc.9b05235>
88. Wang L, Zhang T, Yang S, Cheng F, Liang J, Chen J (2013) A quantum-chemical study on the discharge reaction mechanism of lithium-sulfur batteries. *J Energy Chem* 22(1):72–77. [https://doi.org/10.1016/S2095-4956\(13\)60009-1](https://doi.org/10.1016/S2095-4956(13)60009-1)
89. Vijayakumar M, Govind N, Walter E, Burton SD, Shukla A, Devaraj A, Xiao J, Liu J, Wang CM, Karim A, Thevuthasan S (2014) Molecular structure and stability of dissolved lithium polysulfide species. *Phys Chem Chem Phys* 16(22):10923–10932. <https://doi.org/10.1039/c4cp00889h>
90. Guerard JJ, Arey JS (2013) Critical evaluation of implicit solvent models for predicting aqueous oxidation potentials of neutral organic compounds. *J Chem Theory Comput* 9(11):5046–5058. <https://doi.org/10.1021/ct4004433>
91. Kamphaus EP, Balbuena PB (2017) First-principles investigation of lithium polysulfide structure and behavior in solution. *J Phys Chem C* 121(39):21105–21117. <https://doi.org/10.1021/acs.jpcc.7b04822>

92. Wu M, Cui Y, Bhargava A, Losovyj Y, Siegel A, Agarwal M, Ma Y, Fu Y (2016) Organotrисульфид: a high capacity cathode material for rechargeable lithium batteries. *Angew Chem Int Ed* 55(34):10027–10031. <https://doi.org/10.1002/anie.201603897>
93. Bhargava A, Ma Y, Shashikala K, Cui Y, Losovyj Y, Fu Y (2017) The unique chemistry of thiuram polysulfides enables energy dense lithium batteries. *J Mater Chem A* 5(47):25005–25013. <https://doi.org/10.1039/C7TA07460C>
94. Cui Y, Ackerson JD, Ma Y, Bhargava A, Karty JA, Guo W, Zhu L, Fu Y (2018) Phenyl selenosulfides as cathode materials for rechargeable lithium batteries. *Adv Funct Mater* 28(31):1801791. <https://doi.org/10.1002/adfm.201801791>
95. Guo W, Fu Y (2018) A perspective on energy densities of rechargeable Li-S batteries and alternative sulfur-based cathode materials. *Energy Environ Mater* 1(1):20–27. <https://doi.org/10.1002/eem2.12003>
96. Liang Y, Zhang P, Yang S, Tao Z, Chen J (2013) Fused heteroaromatic organic compounds for high-power electrodes of rechargeable lithium batteries. *Adv Energy Mater* 3(5):600–605. <https://doi.org/10.1002/aenm.201200947>
97. Liang Y, Zhang P, Chen J (2013) Function-oriented design of conjugated carbonyl compound electrodes for high energy lithium batteries. *Chem Sci* 4(3):1330–1337. <https://doi.org/10.1039/C3SC22093A>
98. Park M, Shin D-S, Ryu J, Choi M, Park N, Hong SY, Cho J (2015) Organic-catholyte-containing flexible rechargeable lithium batteries. *Adv Mater* 27(35):5141–5146. <https://doi.org/10.1002/adma.201502329>
99. Guo W, Bhargava A, Ackerson JD, Cui Y, Ma Y, Fu Y (2018) Mixture is better: enhanced electrochemical performance of phenyl selenosulfide in rechargeable lithium batteries. *Chem Commun* 54(64):8873–8876. <https://doi.org/10.1039/C8CC04076A>
100. Boettger JC (1994) Nonconvergence of surface energies obtained from thin-film calculations. *Phys Rev B* 49(23):16798–16800. <https://doi.org/10.1103/PhysRevB.49.16798>
101. Arneson C, Wawrzyniakowski ZD, Postlewaite JT, Ma Y (2018) Lithiation and delithiation processes in lithium-sulfur batteries from ab initio molecular dynamics simulations. *J Phys Chem C* 122(16):8769–8779. <https://doi.org/10.1021/acs.jpcc.8b00478>
102. Peng HJ, Hou TZ, Zhang Q, Huang JQ, Cheng XB, Guo MQ, Yuan Z, He LY, Wei F (2014) Strongly coupled interfaces between a heterogeneous carbon host and a sulfur-containing guest for highly stable lithium-sulfur batteries: mechanistic insight into capacity degradation. *Adv Mater Interfaces* 1(7):1400227. ARTN 1400227 <https://doi.org/10.1002/admi.201400227>
103. Peng H-J, Zhang Z-W, Huang J-Q, Zhang G, Xie J, Xu W-T, Shi J-L, Chen X, Cheng X-B, Zhang Q (2016) A cooperative interface for highly efficient lithium-sulfur batteries. *Adv Mater* 28(43):9551–9558. <https://doi.org/10.1002/adma.201603401>
104. Yuan H, Peng H-J, Huang J-Q, Zhang Q (2019) Sulfur redox reactions at working interfaces in lithium-sulfur batteries: a perspective. *Adv Mater Interfaces* 6(4):1802046. <https://doi.org/10.1002/admi.201802046>
105. Li X, Sun X (2018) Interface design and development of coating materials in lithium-sulfur batteries. *Adv Funct Mater* 28(30):1801323. <https://doi.org/10.1002/adfm.201801323>
106. Qian J, Wang F, Li Y, Wang S, Zhao Y, Li W, Xing Y, Deng L, Sun Q, Li L, Wu F, Chen R (2020) Electrocatalytic interlayer with fast lithium-polysulfides diffusion for lithium-sulfur batteries to enhance electrochemical kinetics under lean electrolyte conditions. *Adv Funct Mater* 30(27):2000742. <https://doi.org/10.1002/adfm.202000742>
107. Zhou G, Tian H, Jin Y, Tao X, Liu B, Zhang R, Seh ZW, Zhuo D, Liu Y, Sun J, Zhao J, Zu C, Wu DS, Zhang Q, Cui Y (2017) Catalytic oxidation of Li₂S on the surface of metal sulfides for Li–S batteries. *Proc Natl Acad Sci* 114(5):840–845. <https://doi.org/10.1073/pnas.1615837114>
108. Yu X, Manthiram A (2017) Electrode-electrolyte interfaces in lithium-sulfur batteries with liquid or inorganic solid electrolytes. *Acc Chem Res* 50(11):2653–2660. <https://doi.org/10.1021/acs.accounts.7b00460>

109. Chen X, Hou T, Persson KA, Zhang Q (2019) Combining theory and experiment in lithium–sulfur batteries: current progress and future perspectives. *Mater Today* 22:142–158. <https://doi.org/10.1016/j.mattod.2018.04.007>
110. Pascal TA, Wujcik KH, Wang DR, Balsara NP, Prendergast D (2017) Thermodynamic origins of the solvent-dependent stability of lithium polysulfides from first principles. *Phys Chem Chem Phys* 19(2):1441–1448. <https://doi.org/10.1039/C6CP06889H>
111. Zhang G, Zhang Z-W, Peng H-J, Huang J-Q, Zhang Q (2017) A toolbox for lithium-sulfur battery research: methods and protocols. *Small Methods* 1(7):1700134. <https://doi.org/10.1002/smt.201700134>
112. Hagen M, Schiffels P, Hammer M, Dörfler S, Tübke J, Hoffmann MJ, Althues H, Kaskel S (2013) In-situ Raman investigation of polysulfide formation in Li-S cells. *J Electrochem Soc* 160(8):A1205–A1214. <https://doi.org/10.1149/2.045308jes>
113. He X, Zhu Y, Epstein A, Mo Y (2018) Statistical variances of diffusional properties from ab initio molecular dynamics simulations. *NPJ Comput Mater* 4(1):18. <https://doi.org/10.1038/s41524-018-0074-y>
114. Rajput NN, Murugesan V, Shin Y, Han KS, Lau KC, Chen J, Liu J, Curtiss LA, Mueller KT, Persson KA (2017) Elucidating the solvation structure and dynamics of lithium polysulfides resulting from competitive salt and solvent interactions. *Chem Mater* 29(8):3375–3379. <https://doi.org/10.1021/acs.chemmater.7b00068>
115. Park C, Ronneburg A, Risse S, Ballauff M, Kanduč M, Dzubielia J (2019) Structural and transport properties of li/s battery electrolytes: role of the polysulfide species. *J Phys Chem C* 123(16):10167–10177. <https://doi.org/10.1021/acs.jpcc.8b10175>
116. Markevich E, Salitra G, Rosenman A, Talyosef Y, Chesneau F, Aurbach D (2015) The effect of a solid electrolyte interphase on the mechanism of operation of lithium–sulfur batteries. *J Mater Chem A* 3(39):19873–19883. <https://doi.org/10.1039/C5TA04613K>
117. Islam MM, Ostadhossain A, Borodin O, Yeates AT, Tipton WW, Hennig RG, Kumar N, van Duin ACT (2015) ReaxFF molecular dynamics simulations on lithiated sulfur cathode materials. *Phys Chem Chem Phys* 17(5):3383–3393. <https://doi.org/10.1039/C4CP04532G>
118. Li Y, Romero NA, Lau KC (2018) Structure-property of lithium-sulfur nanoparticles via molecular dynamics simulation. *ACS Appl Mater Interfaces* 10(43):37575–37585. <https://doi.org/10.1021/acsami.8b09128>
119. Hou TZ, Xu WT, Chen X, Peng HJ, Huang JQ, Zhang Q (2017) Lithium bond chemistry in lithium-sulfur batteries. *Angew Chem Int Ed* 56(28):8178–8182. <https://doi.org/10.1002/anie.201704324>
120. Hou T-Z, Chen X, Peng H-J, Huang J-Q, Li B-Q, Zhang Q, Li B (2016) Design principles for heteroatom-doped nanocarbon to achieve strong anchoring of polysulfides for lithium-sulfur batteries. *Small* 12(24):3283–3291. <https://doi.org/10.1002/sml.201600809>
121. Liao K, Mao P, Li N, Han M, Yi J, He P, Sun Y, Zhou H (2016) Stabilization of polysulfides via lithium bonds for Li–S batteries. *J Mater Chem A* 4(15):5406–5409. <https://doi.org/10.1039/C6TA00054A>
122. Park K, Cho JH, Jang J-H, Yu B-C, De La Hoz AT, Miller KM, Ellison CJ, Goodenough JB (2015) Trapping lithium polysulfides of a Li–S battery by forming lithium bonds in a polymer matrix. *Energy Environ Sci* 8(8):2389–2395. <https://doi.org/10.1039/C5EE01809A>
123. Jand SP, Chen Y, Kaghadzchi P (2016) Comparative theoretical study of adsorption of lithium polysulfides (Li₂S_x) on pristine and defective graphene. *J Power Sources* 308:166–171. <https://doi.org/10.1016/j.jpowsour.2016.01.062>
124. Ji Z, Han B, Li Q, Zhou C, Gao Q, Xia K, Wu J (2015) Anchoring lithium polysulfides via affinitive interactions: electrostatic attraction, hydrogen bonding, or in parallel? *J Phys Chem C* 119(35):20495–20502. <https://doi.org/10.1021/acs.jpcc.5b06373>
125. Zhou C, Ji Z, Han B, Li Q, Gao Q, Xia K, Wu J (2017) Computational criteria for evaluating polysulfide cohesion, solvation, and stabilization: approach for screening effective anchoring substrates. *J Phys Chem C* 121(1):308–314. <https://doi.org/10.1021/acs.jpcc.6b09577>
126. Li F, Liu Q, Hu J, Feng Y, He P, Ma J (2019) Recent advances in cathode materials for rechargeable lithium–sulfur batteries. *Nanoscale* 11(33):15418–15439. <https://doi.org/10.1039/C9NR04415A>

127. Dong C, Gao W, Jin B, Jiang Q (2018) Advances in cathode materials for high-performance lithium-sulfur batteries. *iScience* 6:151–198. <https://doi.org/10.1016/j.isci.2018.07.021>
128. Perez Beltran S, Balbuena PB (2018) Formation of multilayer graphene domains with strong sulfur-carbon interaction and enhanced sulfur reduction zones for lithium-sulfur battery cathodes. *Chemosuschem* 11(12):1970–1980. <https://doi.org/10.1002/cssc.201702446>
129. Wang D-Y, Guo W, Fu Y (2019) Organosulfides: an emerging class of cathode materials for rechargeable lithium batteries. *Acc Chem Res* 52(8):2290–2300. <https://doi.org/10.1021/acs.accounts.9b00231>
130. Bhargav A, Manthiram A (2020) Xanthogen polysulfides as a new class of electrode material for rechargeable batteries. *Adv Energy Mater* n/a (n/a):2001658. <https://doi.org/10.1002/aenm.202001658>
131. Wu M, Bhargav A, Cui Y, Siegel A, Agarwal M, Ma Y, Fu Y (2016) Highly reversible diphenyl trisulfide catholyte for rechargeable lithium batteries. *ACS Energy Lett* 1(6):1221–1226. <https://doi.org/10.1021/acseenergylett.6b00533>
132. Guo W, Wawrzyniakowski ZD, Cerda MM, Bhargav A, Pluth MD, Ma Y, Fu Y (2017) Bis(aryl) tetrasulfides as cathode materials for rechargeable lithium batteries. *Chem Eur J* 23(67):16941–16947. <https://doi.org/10.1002/chem.201703895>
133. Ding Z, Li J, Li J, An C (2020) Review—interfaces: key issue to be solved for all solid-state lithium battery technologies. *J Electrochem Soc* 167(7):070541. <https://doi.org/10.1149/1945-7111/ab7f84>
134. Wang H, Cao X, Liu W, Sun X (2019) Research progress of the solid state lithium-sulfur batteries. *Front Energy Res* 7(112). <https://doi.org/10.3389/fenrg.2019.00112>

Index

A

- Activation, 33, 43, 52, 53, 83, 85–89,
91–93, 101, 102, 168, 173, 174, 179,
185, 190, 191, 197, 201, 204–206,
299, 359
- Additives, 12, 26, 41, 45, 46, 55, 87, 93, 99,
101, 116, 122, 123, 142, 145–147,
155, 166, 227, 228, 232, 235–238,
241, 242, 275, 291, 296, 316, 325,
326, 334, 335, 360
- Adsorption, 22, 26, 27, 29, 32–36, 42, 44,
45, 55, 60, 62, 64, 66, 68, 71, 89, 92,
101, 111, 114, 117, 118, 121, 124,
126, 127, 130, 131, 134, 135, 139,
147, 148, 150, 151, 155, 157, 166,
172, 173, 177, 178, 181, 182, 184,
195, 197, 199, 202, 206, 209, 211,
213, 253, 255, 309, 334, 335, 377,
382
- Anode, 1, 2, 7, 8, 10, 11, 13, 22, 83, 84, 87,
93–102, 111, 113, 115, 126, 147,
156, 158, 159, 166–170, 172, 189,
202, 225–233, 235–242, 288, 296,
312, 313, 315, 322, 325, 326, 331,
346, 348, 357–360
- Application, 1–3, 19, 20, 26, 72, 83–85, 89,
111, 120, 151, 159, 167, 173, 201,
202, 211, 225–227, 229, 239, 242,
256, 269, 291, 295, 309, 311, 318,
322, 324–326, 332, 333, 338, 341,
342, 346, 350, 351, 359, 361, 363,
364, 371, 379, 381, 386–388

C

- Capacity, 1–3, 6, 8–10, 12, 13, 19–22, 27,
28, 30–37, 41, 43–45, 47, 48, 50–55,
57, 58, 60–70, 84, 87–90, 92–102,
111, 113, 114, 118, 121, 123, 124,
126, 128, 131, 141, 146, 153, 154,
156, 159, 167–172, 174–184, 192,
206, 209, 225, 227, 228, 231, 239,
242, 247, 248, 250–253, 255, 256,
258, 261, 263, 264, 266, 269–277,
279–282, 284–290, 295, 296, 300,
303, 305, 308, 309, 312–314,
316–318, 322, 324, 325, 331, 337,
339, 340, 346, 356, 383, 388
- Carbon materials, 19–24, 26, 31, 33, 36, 37,
55, 56, 61, 64, 67, 70–72, 111, 119,
126, 127, 132, 134, 135, 152, 155,
159, 174, 184, 316
- Carbon nanotubes, 20, 24, 25, 45–47, 53,
70, 119, 123, 134, 153, 156, 170,
207, 210, 248, 253, 255, 291, 316,
335, 336, 346, 383
- Catalytic, 91, 126, 145, 155, 165, 166,
173–175, 177, 179–185, 190,
195–197, 201, 202, 204, 210–214,
253, 287, 288, 375, 383
- Cathode, 1–11, 13, 19–22, 25–41, 43–48,
50–72, 83–85, 87–102, 111–113,
115–117, 119–128, 133, 134,
136–138, 141, 143–159, 166–173,
177–190, 198, 203, 205, 206, 212,
213, 225–229, 231, 241, 242, 247,
248, 250, 252, 253, 255–260,
262–265, 270, 275, 279–282,
284–287, 289, 290, 293, 295–307,
309, 311–314, 316–319, 321, 322,

- 324–326, 333, 335, 336, 338,
340–344, 347, 348, 350, 356–360,
369, 373–375, 380–385, 387
- Challenges, 1, 2, 4, 5, 7, 8, 13, 84, 85, 94,
111, 170, 171, 184, 206, 225–230,
239, 241, 242, 351, 355–357, 359,
360, 365, 378, 386, 387
- Characterization, 87, 90, 95, 102, 111, 115,
118, 124, 135, 165, 166, 169, 182,
201, 202, 204, 206, 208–211, 213,
214, 242, 248, 260, 266, 291,
331–333, 340, 341, 367, 381
- Composite, 9, 19, 20, 22–70, 72, 84, 89,
119–125, 134–137, 140–142, 147,
151–154, 170, 171, 177, 181, 183,
184, 186–188, 205–209, 226, 229,
237, 238, 255, 259, 261, 262, 279,
282, 287, 289, 316–318, 322,
333–335, 338, 339, 343, 344, 362,
369, 375, 382, 384, 387
- Computation, 102, 367, 372, 386
- Conductive, 3, 5, 9, 10, 22, 23, 25, 26, 31,
41, 44–47, 49–51, 53–55, 57–59, 66,
68–71, 87, 90, 122, 123, 125, 134,
141, 142, 144–146, 150, 151, 155,
156, 170, 176, 187, 198, 200, 240,
291, 296, 298, 312, 316, 318, 319,
325, 337
- Confinement, 22, 47, 52, 111, 119, 125,
126, 134, 170, 208, 213, 303, 316,
382, 384
- Conversion, 1, 3–5, 19–21, 44, 66, 70, 71,
91, 93, 95, 102, 113, 117, 126, 155,
165, 168, 173–185, 187–190,
192–194, 197–199, 202, 204–207,
211–213, 225–227, 229–231, 235,
242, 250, 251, 253, 283, 288, 290,
296–299, 311, 314, 321, 322, 325,
346, 362, 367, 374, 375, 383, 386
- Covalent, 248, 274, 289, 295–297, 300,
304, 309, 314, 382
- Current density, 27, 30, 31, 35–38, 43, 44,
47, 50–52, 124, 128, 133, 154, 156,
171, 176, 178, 186–189, 192, 204,
228, 232, 235, 286, 288, 292, 308,
317, 341
- Cyclic organosulfides, 247, 248, 264, 266
- 230–232, 235–237, 316, 318, 336,
339, 344
- Doping, 59, 61, 64, 66, 71, 90, 101, 127,
128, 131–135, 171, 178, 179, 195,
276, 287, 290, 314, 319–321, 344,
383, 385
- E**
- Electrocatalysts, 87, 91, 101, 102, 180, 185,
188–190, 193, 194, 196, 198, 199,
204, 296, 321, 325
- Electrolyte, 1–4, 6–13, 21, 25–30, 32–36,
44, 51, 52, 55, 59, 63, 64, 84–87,
93–102, 111, 113, 114, 116–118,
120, 124, 125, 128, 136, 140–142,
146, 147, 151, 159, 166–170,
173–175, 180, 186, 192, 198–200,
204, 208, 210, 212, 213, 225–237,
239–242, 247, 248, 250, 253–257,
266, 271–273, 279, 281, 282, 287,
288, 291, 296, 299, 311–314, 316,
322–326, 332–335, 337, 342–345,
347, 348, 350, 357, 358, 360,
371–373, 375, 376, 378–382, 385,
387, 388
- Energy, 1–3, 5, 7, 9–11, 13, 14, 21, 26, 29,
44, 53, 55, 58, 60, 62, 70, 72, 84, 85,
90, 91, 94, 100–102, 111, 119, 126,
127, 130, 131, 133, 137–139,
141–145, 149–151, 154, 155, 157,
165–168, 170, 173, 174, 177, 178,
180, 181, 184, 185, 190, 191,
193–195, 197–199, 201, 204–206,
208, 212, 213, 225–227, 231, 239,
241, 242, 248, 250–252, 256, 258,
260, 261, 264, 271, 275, 276, 291,
295, 300, 318, 325, 331, 337, 338,
341, 342, 351, 355–358, 360, 362,
363, 365, 367–378, 382–384, 386,
387
- F**
- Formation, 5, 7, 10, 28, 29, 39, 40, 71, 85,
86, 90, 94, 95, 99, 115, 134, 148,
153, 168, 173, 175, 182, 194, 210,
228–230, 233, 235, 236, 239, 241,
247, 255, 259, 263, 264, 266, 270,
273, 277, 280–282, 284, 287, 298,
303, 314, 315, 319, 333, 335, 341,
344, 345, 358, 359, 362, 364, 367,
369, 380, 381, 384, 386

Framework, 5, 8–13, 50, 51, 66, 70, 134, 151, 153, 157, 170, 172, 184, 195, 248, 259, 287, 297, 300, 309, 316

Full cell, 94–96, 98–102

H

Host, 2, 9, 10, 25, 26, 36, 38, 44, 51, 59, 61, 68, 117, 126, 128, 148–150, 154, 159, 170, 182–186, 195, 196, 198, 203, 207, 208, 211, 212, 229, 314, 357, 375, 383–385

Hybrid, 7, 20, 64–67, 70, 71, 115, 118, 134, 135, 211, 237, 238, 279, 280, 284, 285

I

In situ, 86, 114, 115, 117, 122, 141, 144, 157–159, 177, 179, 182, 211, 212, 235, 236, 242, 282, 283, 331–333, 335–338, 340–348, 350–352

Interlayer, 101, 111, 156–159, 166, 171, 172, 177, 180, 181, 203, 359, 375, 382

L

Li₂S, 5, 9, 21, 22, 26, 28, 83–102, 112–115, 118, 119, 124, 131, 137–142, 144, 145, 148, 149, 165, 166, 168–170, 173–181, 183, 184, 188, 189, 192–195, 198–200, 203, 205, 210, 213, 226, 229, 231, 232, 235, 236, 248, 250, 255, 263, 264, 266, 270, 277, 280, 281, 289, 296, 298, 299, 303, 305, 309, 316, 322, 333, 335–338, 341–344, 346, 348, 356, 359, 368, 369, 377, 381, 383

Li-metal anode, 8, 10, 13, 326

Linear organosulfides, 247, 248, 271

LiPS, 116, 169–171, 176, 181, 203, 211, 227, 229–232, 235–237, 239–242

Li-S battery, 1–4, 6–14, 20, 21, 26, 29, 44, 55, 64, 70, 72, 101, 111–114, 123, 124, 146, 156, 157, 159, 165–175, 177, 179–182, 184–186, 189, 190, 194–203, 208, 210, 211, 213, 214, 247, 291, 295–301, 303–309, 311–319, 321–326, 331–333, 335–337, 339–344, 346–348, 350, 355, 356, 360, 369, 377, 379, 386–388

Lithium-ion batteries, 1–3, 295, 355

M

Mediators, 86, 87, 92, 93, 101, 117, 155, 192, 198–200, 226, 253, 309

Metal sulfides, 91, 126, 149, 150, 157, 174, 177, 182–184, 213, 383, 384

O

Optimization, 22, 71, 72, 159, 211, 229, 232, 235, 295, 298, 314, 355, 368

Organosulfide, 247–251, 255, 259, 264, 268, 270, 271, 275–277, 279, 281, 284, 290, 291, 293, 373, 387

Outlook, 101, 111, 159, 225, 227, 241, 290, 325, 351, 386

P

Perspective, 13, 27, 28, 55, 72, 83, 124, 151, 159, 165, 166, 201, 213, 242, 247, 296, 384, 387

Polymer, 56–59, 98, 100, 123–125, 134–142, 144, 145, 155, 170, 171, 184, 247, 248, 259–261, 263, 284–289, 291, 296–300, 303, 305–307, 309, 311, 312, 314–316, 318–320, 322–325, 387

Polysulfides, 1, 5–13, 20, 22, 25–36, 38–45, 47, 49–52, 54–64, 66, 68, 70, 71, 84–87, 89–93, 95, 98–102, 111, 113–120, 122–128, 131, 134, 135, 137–144, 146–157, 159, 165–172, 174–185, 187, 189, 198, 204–206, 209–213, 225, 226, 229–231, 239, 241, 247, 248, 252, 253, 255, 259, 261, 263, 264, 269, 271, 273, 284, 286–290, 295, 296, 298, 300, 303–305, 309, 311, 314, 316, 319, 322, 324, 331–339, 341–346, 348, 349, 357–359, 371, 373–385, 387

Porous, 9, 20, 22, 23, 25, 26, 32–39, 43, 44, 50–54, 56, 58, 61, 66, 68–70, 85, 119, 120, 122–124, 126, 128, 134, 150, 151, 155, 156, 170, 176, 180, 184, 187, 193, 207, 211, 237, 259, 263, 306, 307, 316, 317, 320, 335, 350, 384

R

Redox, 2, 5, 6, 19–22, 26, 29, 30, 33, 34, 41, 44, 47, 49, 51, 53, 62–64, 71, 87, 92, 93, 111, 126, 133, 153, 155, 157,

- 159, 165, 166, 168, 170, 171,
173–178, 180–187, 189–191,
197–200, 202–204, 211, 214, 226,
247, 248, 250, 253–255, 266,
268–270, 273, 277–285, 288, 290,
291, 296–300, 309, 313, 325, 337,
344, 346, 348, 357–360, 371, 372,
377, 383, 385, 387
- S**
- Se, 93, 247, 275–277, 279–290, 313, 314,
320
- Separator, 3, 7, 9, 101, 116, 117, 156–158,
169, 171, 172, 176–178, 180–183,
204, 228, 232, 316, 348
- Simulation, 90, 92, 93, 137, 180, 271, 273,
355, 356, 359–361, 363–367, 371,
372, 374–382, 384–388
- Small molecules, 275
- Solid–electrolyte interphase (SEI), 7, 8, 10,
95, 99, 186, 226–233, 235–242, 322,
333, 336, 341
- Structures, 2, 7, 20–22, 25–27, 29, 30, 32,
33, 35, 36, 38, 40, 41, 43–45, 47–56,
60–62, 64, 66–72, 85–87, 90, 93,
101, 102, 118, 119, 123, 124, 126,
128, 130, 131, 134, 136, 141–145,
147, 149–152, 154, 155, 170–172,
177, 179, 180, 184, 206–209, 211,
213, 227, 228, 230–233, 239, 241,
242, 248, 250, 255, 257, 258,
264–266, 269, 271–273, 277,
279–281, 284, 289, 290, 295, 300,
303, 309, 311, 312, 314, 317–321,
325, 332, 333, 336, 337, 340–342,
346, 348, 356, 357, 359, 360,
363–365, 367–371, 373–377, 379,
381–383, 386, 387
- Sulfur-carbon, 9, 19, 20, 22–25, 28, 31, 33,
45, 51–53, 58–61, 64, 67, 70, 72,
121, 170, 307
- Sulfur-containing polymer, 295–300, 303,
304, 306, 309, 311, 314–321, 325,
326
- Sulfurized polyacrylonitrile (SPAN), 287,
289, 299, 311–314, 316, 317,
321–324, 372
- T**
- Techniques, 86, 87, 111, 114, 116, 117,
124, 165, 166, 169, 182, 201, 202,
205, 206, 208, 210, 211, 213, 214,
248, 252, 255, 260, 266, 291, 318,
331–333, 335, 337, 340–342, 348,
351, 355, 356, 359, 360, 364, 368,
377, 379, 381, 386, 388
- U**
- Unsaturated, 180, 198, 284, 297, 300